UNIVERSITÀ
DEGLI STUDI
DI BRESCIA

DOTTORATO DI RICERCA IN
INGEGNERIA MECCANICA E INDUSTRIALE

ICAR/08 Scienza delle Costruzioni

CICLO
XXXIII

THE RESPONSE OF ENDOTHELIAL CELLS TO ANGIOGENIC STIMULI: EXPERIMENTS, MODELING, AND SIMULATIONS

DOTTORANDO:
MATTIA SERPELLONI

RELATORI:
Prof. ALBERTO SALVADORI
Prof.ssa STEFANIA MITOLA

COORDINATORE DEL DOTTORATO:
Prof.ssa LAURA ELEONORA DEPERO

Indice

Sommario

La seguente tesi è il completamento di un percorso di dottorato ambientato nel campo della meccanobiologia. Tale ambito di ricerca necessita competenze che sono fortemente interdisciplinari che attraversano ambiti specifici della biologia, della chimica, della fisica e dell'ingegneria. Pertanto, una fruttuosa collaborazione tra due gruppi di ricerca appartenenti all'Università degli Studi di Brescia e guidati dai Professori Alberto Salvadori (Dipartimento di Ingegneria Meccanica e Industriale - DIMI) e Stefania Mitola (Dipartimento di Medicina Molecolare e Traslazionale - DMMT) si è dimostrata essenziale nell'affrontare un tema così profondamente intersettoriale.

L'obiettivo del presente manoscritto è generare modelli matematici capaci di interpretare e predire le osservazioni sperimentali costruite in modelli biologici che sono finalizzati allo studio dell'angiogenesi (a livello cellulare), ovvero la crescita di nuovi vasi sanguigni da quelli già esistenti. Tale fenomeno, che può essere fisiologico e/o patologico, viene innescato dall'interazione chimica tra specifici fattori di crescita (ligandi) e distinte proteine transmembranali (recettori) presenti sulla membrana cellulare delle cellule endoteliali (CE) ricoprenti la parete interna dei vasi sanguigni. In particolare, sono state affrontate le dinamiche di due recettori: VEGFR-2 e intregrina. Il primo è il principale regolatore dell'innesco dello stimolo angiogenico all'interno di una CE; questo stimolo, che porta alla proliferazione e alla migrazione delle CE, viene attivato dall'interazione chimica di VEGFR2 con ligandi canonici come VEGF-A o non canonici come gremlin. Il secondo recettore, è rappresentato dalla molecola primaria d'adesione nelle CE; esso sostiene lo scambio di impulsi meccanici con l'ambiente extracellulare attraverso l'interazione con molecole presenti nella matrice extracellulare (MEC) come la fibronectina o il fibrinogeno.

Pertanto, è stato costruito un modello biologico con l'intento di comprendere come VEGFR2 e integrina vengano reclutati e ricollocati sulla membrana cellulare di una CE da parte dei corrispettivi ligandi. Di conseguenza, diversi esperimenti in-vitro sono stati effettuati su una singola CE adagiata su un substrato rigido arricchito con ligandi immobilizzati. Infatti, nonostante le conoscenze biologiche riguardo questi recettori siano ampie, lo studio della loro ricollocazione è ancora carente. Nel caso in esame, è possibile osservare come la dinamica recettoriale sia fortemente influenzata dall'interazione chimica recettore-ligando, dalla motilità delle proteine transmembranali e dalla meccanica cellulare. Nello specifico, i dati mostrano come il primo contatto cellula-substrato porti ad una immediata formazione di complessi che successivamente aumentano grazie all'incremento della superficie di contatto tra membrana cellulare e substrato in seguito al fenomeno dell'accasciamento della CE sul substrato stesso e alla diffusione dei recettori. Tale fenomeno permane e domina la parte terminale dell'esperimento durante la quale la geometria della cellula è sostanzialmente invariata.

Nel corso del corrente manoscritto sono stati proposti due modelli multifisici paradigmatici costruiti sulla base di due formulazioni termodinamicamente coerenti. Le equazioni che governano questi modelli risultano da uno studio complesso delle leggi fisiche che guidano la realtà sperimentale. Tali formulazioni sono state adattate agli esperimenti sopra menzionati al fine di descrivere la diffusione di recettori liberi sulla membrana cellulare durante il progressivo accasciamento meccanico di una CE, includendo la loro capacità di interagire chimicamente con ligandi immobili ricoprenti il substrato a contatto con la cellula stessa. Tali modelli hanno la capacità di descrivere l'esaurimento dei recettori liberi sulla membrana cellulare a favore della generazione di complessi che inducono una cascata di segnali intracellulari volti ad innescare lo stimolo angiogenico. Nello specifico, nel primo modello, grazie ad un'ipotesi semplificativa della dinamica di contatto tra cellula e substrato chiamata *meccanica surrogata*, si è codificato il processo chemo-diffusivo delle proteine transmembranali su una geometria cellulare assunta come sferica e rigida. Il secondo modello invece, considera la deformabiltà meccanica della cellula in grandi deformazioni e il processo di formazione di protrusioni cellulari (lamellopodi) sostenuto dall'evoluzione del reticolo di actina all'interno del citoplasma di una CE.
Infine, le equazioni governanti entrambe le formulazioni sono determinate nella loro forma forte ed in seguito rimodellate nella corrispondente forma debole al fine di essere discretizzate numericamente ed implementate nel software deal.ii (https://www.dealii.org/), ovvero una libreria C++ e open source che supporta la creazione di codici ad elementi finiti e di calcolo ad alte prestazioni.

Un'analisi approfondita del concetto di equilibrio termodinamico è preliminare alla costruzione di qualsiasi modello fisico, a maggior ragione per descrivere stati di non equilibrio termodinamico. Tali argomentazioni sono affrontate nella parte finale della tesi dove è riassunto il lavoro svolto durante l' esperienza all'estero, dell'autore della tesi, presso il Dipartimento di Ingegneria dell'Università di Cambridge sotto la supervisione del Professor Vikram Deshpande. Durante tale periodo, finanziato dalla *Fondazione Guido Berlucchi* attraverso la borsa di studio denominata *Young Researchers Mobility Programme*, l'argomento di studio è stato codificare termodinamicamente, attraverso un modello di meccanica statistica, il concetto di equilibrio omeostatico e le contestuali fluttuazioni esibite dalle cellule.

Chapter 1

Introduction

Mechanobiology is an emerging subject of the science of living matter[1] that focuses on the study of biological responses by cells to mechanical stimuli [2]. Particularly, it arises from the awareness that mechanical signals play a fundamental role in several biological processes, revealing an interconnected and complex reality. Investigations in such an intersectoral scenario require interdisciplinary skills, including physics, engineering, and biology, which must be merged with accuracy and competence. Multidisciplinarity assumes a profound understanding of the methodologies that the individual disciplines have built during the centuries. Therefore, without any desire to be exhaustive in the solution of the topic, I will provide a brief introduction and some food for thought on the main difficulties that arise in mechanobiology, including a description of the topics that will be addressed in the current thesis.

1.1 Mechanobiological insight

Intuitively and instinctively, it is spontaneous to associate the majority of biological phenomena with biochemical processes that regulate the evolution and state of living organisms. However,

[1] Preliminary and fundamental to address this topic is to understand the main differences between animate and inanimate matter. Taking cues from [1] (pages 2-4) it is possible to provide four characteristics of living beings able to distinguish them from non-living organisms:

- a specifically defined complexity: living matters have a recursive complexity specific for each species living on Earth. Such a characteristic implicitly states that a huge amount of information has to be transferred from generation to generation. Today we know that such information is strictly correlated with the DNA;
- the ability for growth and regeneration: living beings have the ability to grow and heal their own injuries. These processes are a prelude to sophisticated chemical processes that transform inanimate matter and energy, taken from the outside world, into organic matter. All this occurs in standard conditions: room temperature, atmospheric pressure, pH close to neutrality, and an almost total absence of electrical charges. This is the reason for the existence of the catalyst enzymes that, in a very specific way, accelerate chemical reactions that would otherwise take times incompatible with life;
- the capacity to reproduce: every living being arises from others, which transfer at the new generation their genetic information;
- adaptation to the environment: random mutations of the genetic patrimony of a given species, can prove to be favorable or unfavorable to survival in an environment that can also change over time. This process triggers the natural selection mechanism which is the basis of Darwin's theory of evolution.

there are cases in which a strong mechanical sensitivity of the human body is revealed (as for fractures to bones and trauma to tissue or surgical repairs or tympanic membrane) [3] (pages 4-8).

Arguably, it's less intuitive grasping that in many cases during a biological process, at the cellular level, the same systems change and actively respond to changes in mechanical forces. In mechanobiology, a substantial and fundamental distinction must be made between biological systems that have mechanical functions (e.g. tympanic membrane, skeletal system, etc.) and biological systems that actively respond to mechanical stimuli at the cellular level [3] (pages 4-8). Fig. 1.1 shows the process of intravasation[2] of a cancer cell in a blood vessel (early stages of metastasis of cancer).

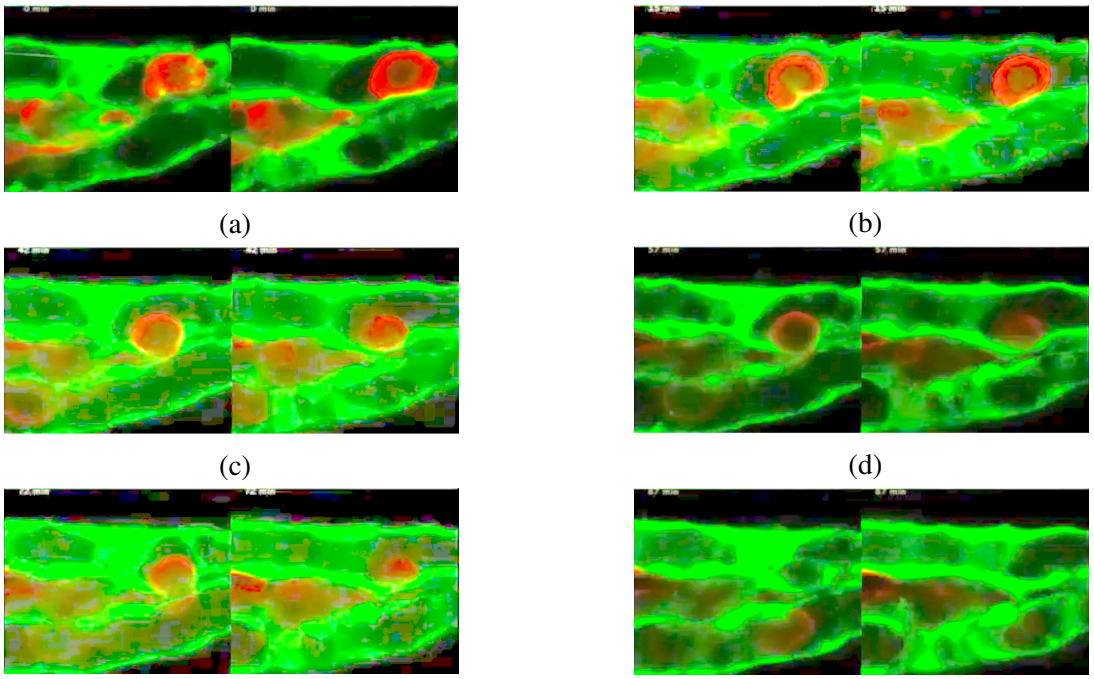

(a) (b) (c) (d) (e) (f)

Figure 1.1: A sequence of frames taken from a time-lapse video (adapted from *https://youtu.be/6URUH4y8dbE*) of a tumor cell (red) within a zebrafish blood vessel (green). Here we can observe how the cancer cell is able to adhere and then penetrated to a vessel wall.

[2]characteristic phenomenon of the phases of metastasis of a tumor, corresponds to the invasion of a blood (or lymphatic) vessel by tumor cells.

It strikes how the process of metastasization of a cancer cell is characterized by a high number of mechanical phenomena: cancer cell large deformations, cell-blood vessel contact dynamic (adhesion, migration, and intravasation), fluid-structure interactions (blood fluid, which is notoriously a non-Newtonian fluid), etc. These, which are extremely complex mechanical problems individually, are characteristic of many other physiological and/or pathological biological processes.
All the cells that make up the human body are sensitive to mechanical stimuli and actively organize themselves to bear them. Hence, from this assumption, it is possible to come to the conclusion that there is no aspect of life that is not directly or indirectly influenced by the mechanics. Even the cardinal phenomena of the reproduction of a virus within the human body, that nowadays determine many aspects of our life, are characterized by a sequence of mechanical events. To reproduce, a virus must transfer a cargo of genetic material into the host cells and it does by means of two mechanisms (membrane fusion and endocytosis) of which one of these is certainly mechanically mediated (endocytosis) [3].

1.2 Thermodynamics: a meta-discipline

In accordance with what has been said so far, we recognize in thermodynamics all the characteristics necessary to provide a pervasive scientific background and the ability to link several fields of physics and engineering. Such a perspective is not innovative rather it is shared by many influential scientists in the last few decades.

Einstein, the father of relativity theory, was also a grandmaster of thermodynamics, and in one of his famous citations, he stated that: *“A law is more impressive the greater the simplicity of its premises, the more different are the kinds of things it relates, and the more extended its range of applicability. Thermodynamics is the only physical theory of universal content, which I am convinced, that within the framework of applicability of its basic concepts will never be overthrown.”*.

Probably, Einstein’s devotion for thermodynamics is correlated to the following very interesting perspective provide by Bejan in his work [4]: *"...the object of thermodynamics is “any system” (with any imaginable boundary, any interactions, and any constitution)..."*.

Referring to a continuum thermodynamics framework (a topic that plays a pivotal role in the current work), we mentioned two definitions that highlight the role of thermodynamics in this field. The former is provided by the authors of the book [5] (see the Preface):*"...Together, continuum mechanics and thermodynamics form the fundamental theory lying at the heart of many disciplines in sciences and engineering..."*. The second one is always given by the book [5] (page 129) but actually inherited from Callen’s book [6], state that: "*Thermodynamics is the study of the restrictions on the possible properties of matter that follow from the symmetry properties of the fundamental laws of physics*".

Hence, we will approach mechanobiology by means of consistent thermodynamic frames that provide the theoretical backdrop at every mathematical model presented in this thesis. Such modelings are the simplified representation of a complex and interconnected reality; sometimes different formulations arise from the attempt to describe the same phenomenologies but from alternative viewpoints, depending on the purpose and the aspect of reality that we are interested in under-

standing, describing, predicting.

Think of the angiogenesis system, which is a branched structure incredibly challenging to describe (see Fig. 1.2).
Such topics are a great example of how nature could be intricated and knotty. According to some interesting works by Bejan (constructal law[3]), these structures are created and evolved in order to optimize flows (or from another point of view, they could be driven by the tendency to increase the production of entropy - Steepest Entropy Ascent [8]). However there is no blood vessel equal to the other, and again we have an enormous internal complexity.

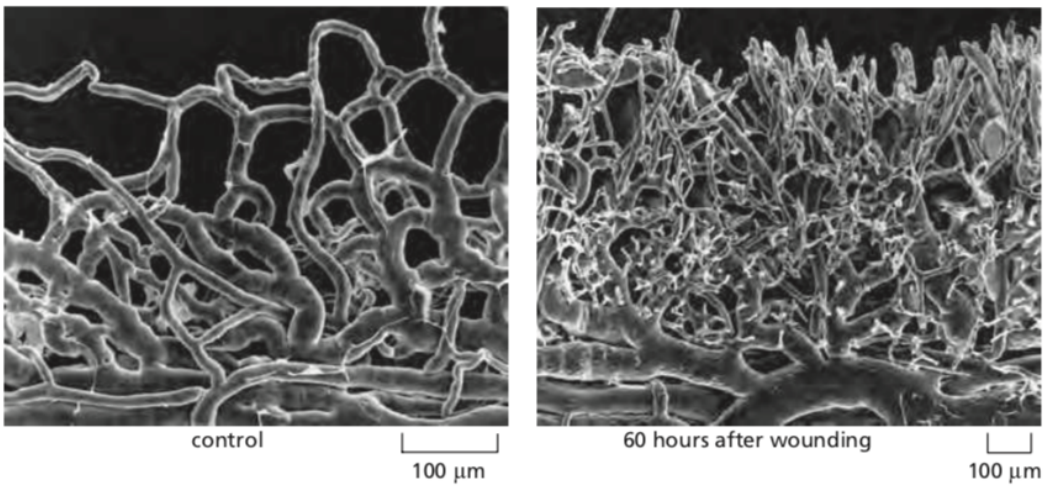

Figure 1.2: New capillary formation in response to wounding. The intricate new blood vessel formation is depicted. New capillaries generation could be triggered to favor wound healing. Adapted from [9].

It would therefore seem impossible that models for such different aspects of reality could have commonalities. Richard Feynman calls them in one of his famous lectures [10] "*The Great Conservation Principles*". The generality of these principles, which are closely related to the subjects of thermodynamics, is further proof of the pervasiveness of this discipline. Hopefully, thermodynamics would be the discipline acting as a lock pick and provide the mathematical tools to conform to the vision of living matter given by Paul A. Weiss in his 1960 lecture: "*lest our necessary and highly successful preoccupation with cell fragments and fractions obscure the fact that the cell is not just an inert playground for a few almighty masterminding molecules, but is a system, a hierarchically ordered system, of mutually interdependent species of molecules, molecular groupings, and supramolecular entities; and that life, through cell life, depends on the order of their interactions*" [11].

[3]For a finite-size flow system to persist in time (to live) it must evolve such that it provides greater and greater access to the currents that flow through it [7]

1.2.1 Statistical mechanics and continuum thermodynamics

Two complementary approaches will be adopted during the thesis, namely the continuum thermodynamics theory (Part II and III) and the statistical mechanics scheme (Part IV and conclusions 10).

Continuum thermodynamics is a theoretical framework able to draws conclusions from fundamental principles based on experience and so deduced from phenomenologies at the macro-scale (also called phenomenological approach), i.e. with no information with regard to the microscopic aspects of the matter.

The aim of statistical mechanics is to bridge the microscopical description of the matter and the macroscopical one (everyday life scale) [12]. Such a goal is perfectly embodied by the Boltzmann formula $S(E,V,N) = \kappa_B \ln \Omega(E,V,N)$, which connect the entropy (S, i.e. a macroscopic state variable) with the possible number of the microstates associated to a given one macro [12].

It is evident how the two above mentioned theories seems antithetic; nevertheless, together, they provide a very powerful tool for the interpretation and prediction of biological experimental results.
Typically, continuum thermodynamics allows doing precise calculations involving a few state variables[4]. Statistical mechanics, instead, provides details on how the physics of the micro-constituents rule the macroscopic observables, and so how matter microscopically works (attribute that a coarse-grained procedure does not permit) [13] (pages 3-4). Therefore, the matching of these two schemes could provide massive improvements of the current knowledge on the physical laws ruling living systems.

The capability of by statistical mechanics to connect macroscopical quantities and the motion of the micro-components of a system, is, inside mechanobiology, employed to elucidate the crucial physical mechanisms of the cytoskeletal activity.
Hence, by relying on the description of cytoskeletal polymers interaction by statistically-based theory it is possible to match and enrich the phenomenological description of the mechanical behavior of a cell. Consistently, cell constituents (e.g. cytoskeletal networks rather than cellular organelles), are unavoidably affected by thermal fluctuations, due to their sizes are close to the thermodynamic limit.

Actually, throughout this thesis, specifically in the Part IV, we will provide a further method to exploit the statistical mechanics architecture, which will be a real paradigmatic change in the study of cellular activities.

In order to satisfy either the several observations that attest to cells fluctuating response during in-vitro experiments and in order to bypass the uncertainty and ignorance on the determination of all intracellular processes that happen in every biological phenomenon (lack of information), it has been introduced in the paper [14], a statistical mechanics framework for living cells. Such a theory

[4]Following the book [5] (page 133), it is possible to found the following definition of state variable: "*The macroscopic observables that are well defined and single-valued when the system is in a state of thermodynamic equilibrium are called state variables. Those state variables which are related to the kinematics of the system (volume, strain, etc.) are called kinematic state variables.*"

allow the accounting of a very relevant concept, cellular homeostasis.

Intriguingly, in the end, aided by these considerations, we can infer how the study of cell mechanical behavior can really (and radically) change some paradigms of mechanics, that from decades have persisted, up to affirm that "the cell is an applied mechanics grand challenge" [3] (pages 8-9).

1.3 Motivations and research objectives of the current work

The current work, aims at building multi-physical models able to describe, interpret, and predict the key mechanisms that rule the angiogenic stimulus inside endothelial cells. Such an aim is reached by means of a multidisciplinary sodality between the group of biologists headed by Professor Stefania Mitola (Department of Molecular and Translational Medicine of the University of Brescia) and the group of engineers led by Professor Alberto Salvadori (Department of Mechanical and Industrial Engineering of the University of Brescia). The former group focuses on the experimental models' formulation, whereas the latter, manages the mathematical models' elaboration. The present work has to be included in a broader framework; indeed, this project is the first step of a long term-plan, concerning several multiphysics models able to describe the main phases of the metastasis of cancer (briefly summarized in Fig. 1.3). We have identified tumor angiogenesis[5] as the first phase of our goal. The reason is that it plays a pivotal role at the very early stage of metastasis of cancer.

[5]Tumor angiogenesis is a pathological condition presented in many cancer diseases that reassume the phenomena of the new blood vessel formation from preexisting one, connected with the cancer growth, proliferation, and metastasis.

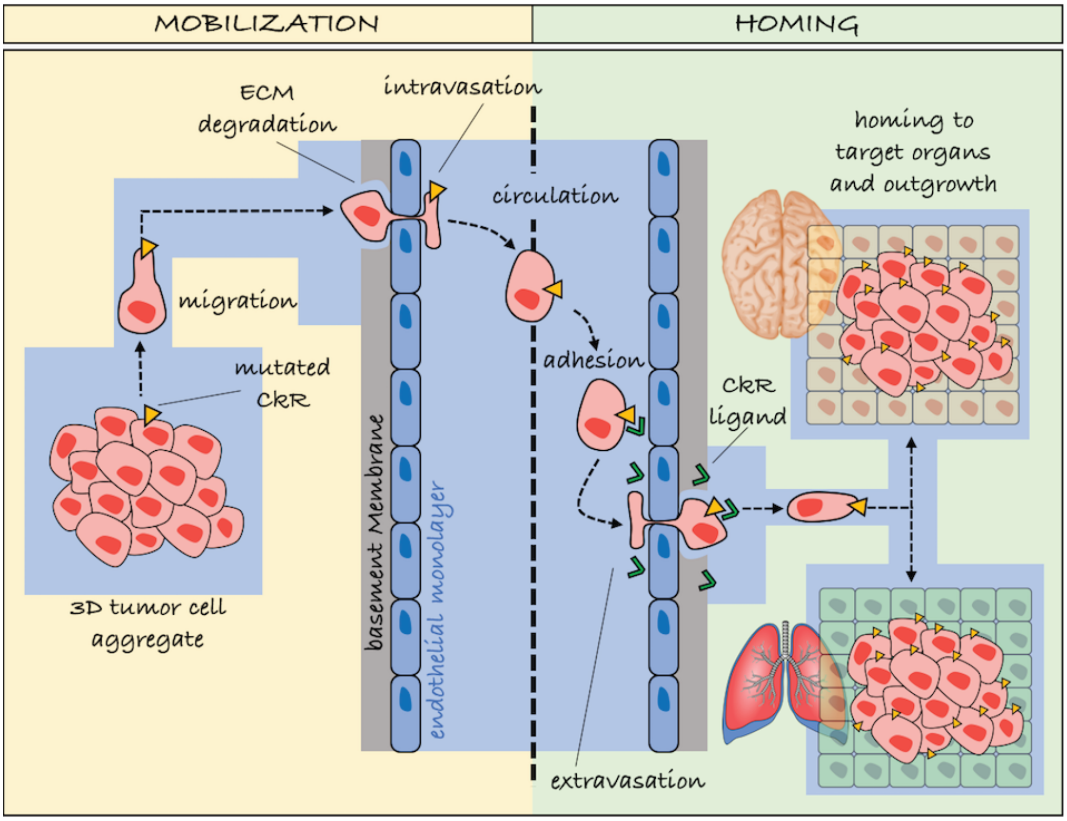

Figure 1.3: The drawing depicts some of the main events characterizing the process of metastasis of a cancer. Importantly, tumor angiogenesis plays a relevant role at the early stage of metastasis of cancer. Courtesy of Dr. Elisabetta Grillo

In fact, a solid tumor (see cancer cell aggregate in Fig. 1.3), to grow and survive, needs to exchange nutrients and waste with the surrounding environment. Such a process owing to the growth of new blood vessels from preexisting ones (angiogenesis) that sprinkle the tumor mass allowing it to survive. This phenomenon is triggered by the release of specific growth factors (also called ligands) by the tumor cells, which stimulate endothelial cells (the cells that cover the inner wall of blood vessels Figs. 1.4) to initiate the process of angiogenesis. The new blood vessels that envelop the tumor mass can favor its survival but also support the migration of the cancer cells, initiating the process called metastasis.

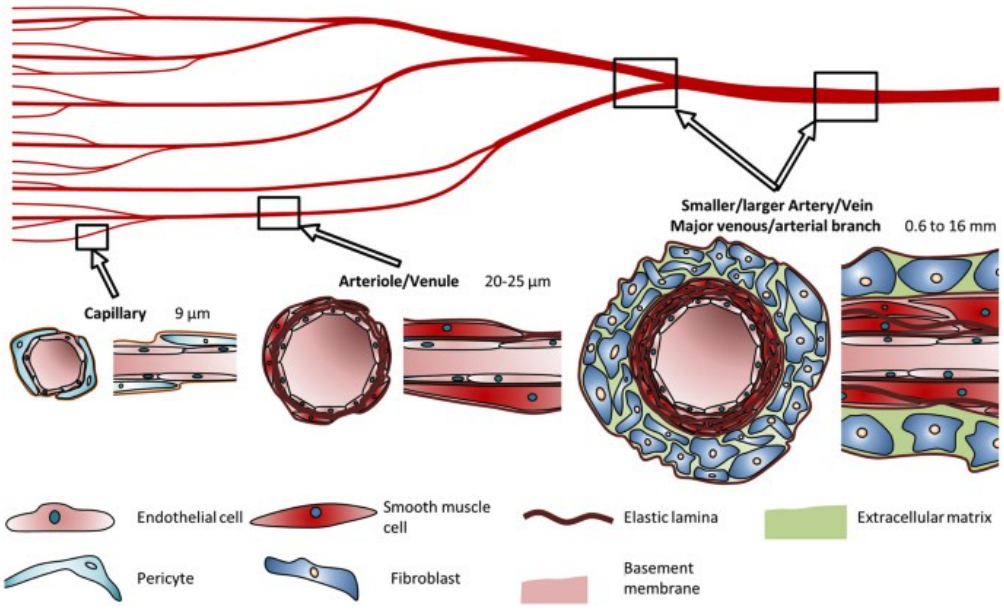

Figure 1.4: The diameters of vascular channels are here depicted as well as the corresponding composition and cell typology. The role and placement of endothelial cells in each of these structures (arteries - veins, arterioles - venules, and capillaries) are relevant for the current thesis. Adapted from [15]

1.3.1 Research objectives

The main aim of the current research is to build mathematical models able to describe, predict, and interpret the phenomenology that characterizes the triggering of the angiogenic stimulus at the cellular level, specifying the role of the mechanical behavior of ECs in these processes. According to this, we analyze angiogenesis from the perspective of a single endothelial cell (EC) setting in-vitro experiment, where we can observe and study the relocation and recruitment of VEGFR-2, and other receptors like integrin, during the mechanical spreading of this EC on a ligands-coated substrate. We are aware that enhancing the knowledge about the dynamics of VEGFR-2 and integrins can lead to major improvements of the pro- and anti-angiogenic therapies.
In fact, despite these models represent a very early step of a series of patterns characterizing the phenomenon of tumor metastasis, they can be adapted to all those processes, pathological or physiological, in which angiogenesis plays a major role, either pro- or anti-angiogenic strategy. Angiogenesis, at the molecular level, is ruled mainly by the VEGFR2 activation and polarization; hence, studying the interaction of this receptor with co-receptors and corresponding ligands, could be used to find a way to switch-off or switch-on the angiogenic stimulus as needed. Indeed, the identification of the laws that regulate VEGFR2 and integrin polarization could, ultimately, open new perspectives toward developing innovative anti- or pro-angiogenic strategies.

The thesis has been divided into four distinct yet connected Parts.

In Part I, we offer a description of the basic notions of biology necessary and functional to under-

stand the experimental phenomenologies that will be defined and then modeled in the subsequent parts. Specifically, this segment of the thesis will contain, in addition to the biological background (chapter 2), a section (2.5) describing the state of the art (to the best of our knowledge) corresponding to the cell mechanical patterns existents in literature. This is the prelude to the introduction to the further Parts, wherein it will be developed and deeply described our way to undertake and study cell mechanics, particularly, when it is coupled with the chemo-diffusive activities of proteins on the cell membrane of ECs.

In the successive two Parts of the thesis, II and III, we will deal with the construction of multiphysics models embedded in the field of continuum thermodynamics. Specifically, in the former one part, we build a chemo-transport thermodynamically consistent model, in which the mechanical behavior of an EC is appropriately codified, in our formulation, by the aid of the *Surrogated mechanics hypothesis* (cell membrane rigid and spheric). This means describing the complex mechanism of contact dynamics between the cell membrane and its microenvironment through the introduction of a fictitious source term in the mass balance equations of chemical species (see chapter 3). In the third part instead, we set a thermodynamically motivated chemo-transport-mechanical formulation, hence a model that mathematically accounts for the real mechanical behavior of EC. In detail, we provide a description of the mechanical passive and active (involving actin polymerization) behavior of this kind of cell, and so a one-way coupled framework describing membrane dynamics (see chapter 6).

Consequently, we will write the corresponding weak formulation of governing equations, with the related numerical discretization (implemented in deal.ii framework[6] - https://www.dealii.org/ -) for the surrogated mechanics formulation as well as for a large deformation framework (proposed in Part III). Finally, through the co-design between in-vitro (show and motivated in chapter 4) and in-silico experiments, we are capable to provide insight on the relocation and recruitment of VEGF (with or without genetic mutations) and integrin receptor on a cell membrane that remains rigid and spheric (see chapter 5) or that advects (see chapters 7 and 8). Furthermore, having a model in which mechanical behaviors are described, it will be possible to quantify the forces that regulate the adhesion and the mechanical spreading of an EC.

In the end, through the Part IV, we provide a paradigmatic change in the cell mechanical description of living cells, able to account for their tendency to reach the so-called (dynamic) homeostatic equilibrium and based on the formulation inherited by the work [14]. Effectively, this part of the thesis arises from a collaboration with Professor Vikram Deshpande of the Department of Engineering of the University of Cambridge and financed by a scholarship provided by Guido Berlucchi Foundation (Young Researchers Mobility Programme)[7], of whom the author of the thesis is grateful.
Specifically, in [14] it is assumed that cells are entropic and so that they manifest fluctuations in order to support the homeostasis; such an attitude is here modeled accounting for a specific internal constraint during entropy maximisation procedure for the definition of homeostatic equilibrium. In this part of the thesis, we offer an exhaustive introduction on the innovative formulation here

[6] deal.ii is an open-source C + + software library that supports the creation of high performance computing finite element codes.

[7] Experience abroad, which was prematurely interrupted after 2 months on the six planned, due to coronavirus pandemic.

described (see sections 1.2.1 and 9.1), aimed at understanding the section (9.2) where the corresponding numerical results on the behavior of the cell, constrained to maintain an elliptic shape, are shown.

Part I

Biological background

Chapter 2

Biological background

The study and understanding of the process that leads to the triggering of the angiogenic stimulus can be the starting point for improving all anti- and pro-angiogenic therapies. In order to do that, we have focused on the behavior of a single Endothelial Cell (EC) and on its interaction with the surrounding microenvironment (different according to the experimental condition - in vivo or in-vitro-).

Therefore, the aim of the current chapter is to provide a background of biological notions, suitable summarized, in order to understand the biological goal of the thesis. We start with the introduction of the general morphology of a eukaryotic cell (section 2.1), pointing out the description of the components that are relevant for our scopes (cell membrane (section 2.1.1), cytoskeleton (section 2.1.2), and some of their molecules). Subsequently, the growth factors and the extracellular matrix (ECM) are introduced and defined (sections 2.2.1 and 2.2.2 respectively). Finally, a suitable designation of transmembrane proteins is provided in section 2.3, in order to be able to include a final and exhaustive description of the tissue vascularization machinery (section 2.4). Indeed, we must bear in mind that we are interested in angiogenesis at the molecular level that actually is not an event confined inside an EC rather involves multiple interconnections among several kinds of cells and ECM as well.

2.1 Morphology of a eukaryotic cell

A botanist, Mathias Schleiden, in 1830 was the first scientist that gave the exact designation of an eukaryotic cell [1]. He noted, inside the vegetal tissues, the correct characteristic arrangement of this type of cell having identified both cytoplasm and nucleus [1]. Actually, this recognition was corroborated by the presence of the cellulose wall that well delineates the boundaries of these kinds of cells, differently by the animal ones, that for this reason, they took a long time more to be certified and observed [1]. About this, was Theodor Schwann, a zoologist, to observe an animal eukaryotic cell, for the first time, from cartilage tissue. Such an event was favored by a high presence of extracellular matrix material that facilitated a well define contours of the cells into this biological substance [1]. Together, Schleiden and Schwann proposed the cellular theory, which is grounded on three postulates:

- cells constitute every living organism on the planet Earth [1];

- the primary unit of such organisms are cells [1];
- the division of pre-existing cells generate new cells (actually, this statement was proposed by Rudolf Virchow later) [1].

The degree of complexity of a cell is very high and although some mechanisms are now known to the scientific community, there are just as many that are unknown or unclear.

The endothelial cell is a eukaryotic cell (see Fig. 2.1) and as such, it is made of two main portions: the cytoplasm and the nucleus. The first is enclosed inside the cell membrane and it is made by several compartments call cytoplasmatic organelles, which are the following: rough and smooth endoplasmic reticulum (RER and SER respectively), the Golgi apparatus, the mitochondria, the lysosomes, and the peroxisomes. Beyond the organelles, there is a further compartment inside the cytoplasm, i.e. a fluid matrix called cytosol that represents about half of the volume of a cell and 50 % of the mass of the cytoplasm, where several cell processes actually happen [1]. In early observations, it was thought that the cytosol was simply a colloid, devoid of any structure, in which cell organelles fluctuate [1]. Nowadays, it has been understood that this cellular compartment, is actually structured and stabilized by a tridimensional proteins matrix called the cytoskeleton [1]. These proteins are arranged as filaments and fibers able to organize themself in a matrix in order to confer mechanical stability to the whole cell. Intriguingly, the cytoskeletal matrix connects the nucleus with the cell membrane, up to connecting such a structural matrix with the extracellular microenvironment [1].
Finally, the second portion composing the cell, i.e. the nucleus, is the place where the majority of the genetic heritage is located inside the cell. Such a compartment is split by a double membrane by the cytoplasm and its presence makes it possible to discriminate eukaryotic cells from prokaryotic cells [1] (page 6 and chapter 3).

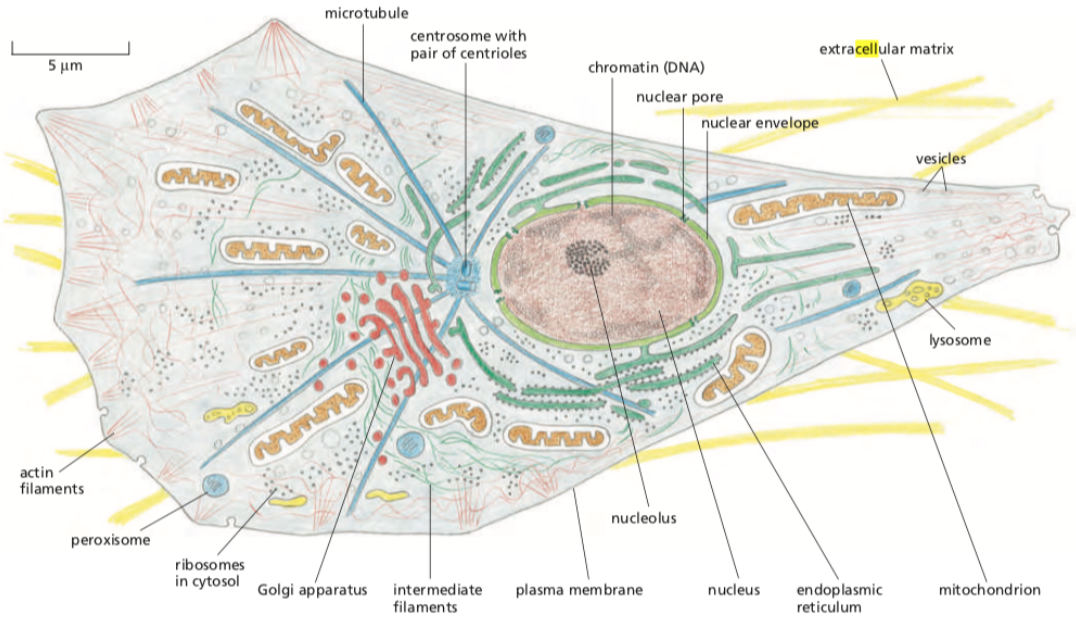

Figure 2.1: A characteristic animal cell is shown in this drawing. Adapted from [9]

2.1.1 The cellular membrane and its domains

Now we want to focus on a further organelle [1], [9] (page 88 and page 649, respectively), that is also the main regulator for every interaction between the cell and the extracellular environment, namely the cell membrane (thickness about 5 *nm* [9] (page 566). Interestingly, cell membrane presides over the homeostasis [1] (page 90) and works also as an insulator with shiftable resistance able to rule an electric signal by means of the flux in/out of specific ions [16].

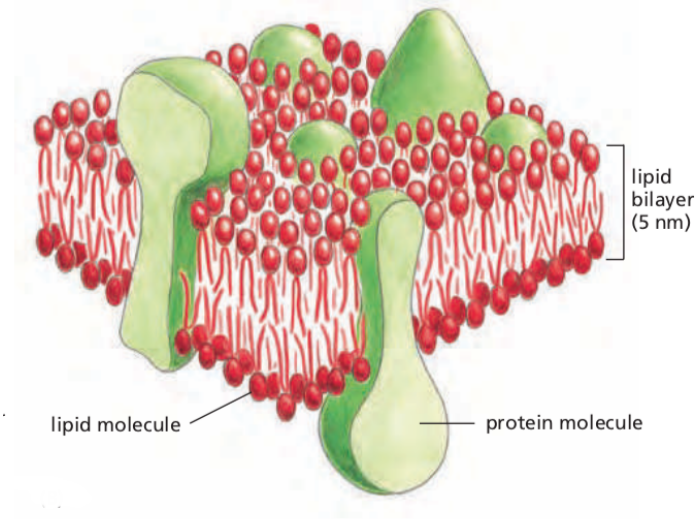

Figure 2.2: Cell membrane architecture through proteins and lipids representations is depicted by means of this three-dimensional drawing. Adapted from [9]

Lipids such as cholesterol and phospholipids are the main constituents of the cellular membrane jointly with sugar and proteins, and all together can generate glycolipid and/or glycoprotein complexes. In particular, phosphoric acid and two fatty acids united to glycerol give rise to phospholipids (amphipathic molecules). Interestingly, these are usually enriched by choline or serine (electrically charged molecule), which generate the hydrophilic group polar, differently by the apolar one denoted by the two fatty acids [17]. Consequently, owing to the diverse polarities present in the phospholipids, borns the so-called lipid bilayer, with hydrophilic heads oriented towards the cytoplasm and the ECM (internal and external sides of the cell respectively) and hydrophobic tails paired on the inside of the membrane.
A profound asymmetry of the lipid bilayer determines several important qualities of the cell membrane. Indeed, the differences in charge, fluidity, or phase transition are guaranteed by an asymmetrical arrangement of these phospholipids in the membrane. Also, this implicitly leads to an asymmetry in the orientation of the membrane proteins themself [18].

Cholesterol, a further pivotal constituent of the plasma membrane, has the role, inside the membrane, to regulate its physical properties. In fact, it has an apolar tail with a rigid polar head with rings. A reduction of protein and lipid motility, as well as membrane permeability and molecular surface, can be a consequence of cellular membrane cholesterol integration, orthogonally inserted into the membrane [18].

Concerning proteins, they can be classified considering the way in which they bind the membrane, specifically it is possible to distinguish integral, peripherals, and superficial proteins. The first ones are characterized by the fact they cross one or more times the lipid bilayer and the only way to separate them from the membrane is to dissolve it. Frequently a α-helix structure or sometimes a folded β-sheets are the hydrophobic domains that traverse the membrane. The second ones instead are interconnected with the membrane by means of weak interactions and they are partially immersed in the membrane itself. Such proteins can be dissociated from the lipid bilayer with the aid of polar substances. Finally, the last typology sees proteins that are associated with the membrane by means of bonds with glycolipids or lipids.
Moreover, membrane proteins can also work as channel proteins allowing some kinds of molecules to cross the membrane itself [19]. Carbohydrates are the last constituent of the membrane and they exist as chemical groups affiliated to glycoproteins and glycolipids. Finally, we can state that: ion exchange, cell-ECM interaction, and cell-cell interplay, as well as the molecules uptake and signaling transduction, are among the major functions performed by proteins and glycoproteins [16].

The non-homogeneous distribution exhibit by the cellular membrane, either in time and space, revealed by the lipids and protein distributions, appear highly dynamic. Such dynamism is characteristic at multiple spatial scales and is necessary in order to organize an opportune cellular response to different biochemical and mechanical inputs.

2.1.1.1 Lipid rafts and caveolae

Proteins and lipids thicken in peculiar areas of the membrane called membrane domains. The discovery of the dynamical nature of these components and their non-homogeneity has been imposed an overcoming of the model of the plasmatic membrane as a "fluid mosaic" proposed by Singer and Nicholson in the 1972 [20]. Such domains have a specific biological task and so far, their theoretical prediction is not been possible. Hereto, only two kinds of domains have been observed, i.e. short-range structures at protein or lipid base [21, 22, 23]. Usually, intracellular proteins are relevant components of those domains delineate by protein scaffolds and play an important role in the confinement and internalization of transmembrane proteins [24]. Lipid rafts are a clear instance of lipid-based ordered structures. These are made up of cholesterol, sphingolipids, and numerous proteins, that can be integral or alternatively anchored by glycolipids [23] (doi: 10.1038/42408).

Lipid rafts are planar structures, whose size varies dynamically between tens and hundreds of nanometers, are anchored to about 35% of the proteins present on the cell membrane. Not only that, about one-third of this 35% are transmembrane proteins [25], which are stabilized by structures such as lipid rafts possessing a greater density and thickness than the surrounding membrane [26]. Such a characteristic of the lipid rafts favors the chemical interaction between a transmembrane protein with co-receptors or second intracellular messengers. This happens inasmuch as the interplay with lipid rafts slow-down the diffusivity of these transmembrane proteins until they are immobilized.
Particular types of lipid rafts are identified in caveolae, whose non-planar (flask) structure gives the cell membrane the ability to lengthen, when required, acting as a real "reserve" of the membrane itself [27, 28]. This structure has a size that is around 50-100 nanometers [29] and is due to the presence of caveolins 1,2,3 and cavine. The former deform the oligomers interacting with lipid rafts resulting in bending of the cell membrane (transduction of a mechanical signal); the second stabilize this peculiar structure. Could exist a correlation between caveolae and endocytosis although it is not necessary [30]. In conformity with well-defined conditions, caveolae can support the internalization of the membrane proteins and fill a fundamental role in the mechanical characterization of the cell membrane. Nevertheless, nowadays the general agreement is that they are primarily stable membrane domains [29].

2.1.2 The cytoskeleton

Generally, a eukaryotic cell, and therefore also an EC, during its movement is able to stand-up to deformation and shape chancing thanks to the cytoskeleton [11]. This is a complex network of filaments and tubules that dynamically evolve, provide at the cell the mechanical properties necessary for carrying out of the biological processes interest, and confer to the cell the spatial organization conforms at the extracellular state. The cytoskeleton is prevalently made up of three kinds of networks: actin filaments, microtubules, and intermediate filaments [9] (chapter 16). These three architectures are distinguishable owing to different functions, polarity, mechanical stiffness, assembly-dynamics, and finally molecular motors with which they are connected.

Actin filaments are strictly correlated with the shape management of the cell surface with decisive effects on the locomotion of the whole-cell. The microtubules, instead, play a pivotal role in

the intracellular transport and cell division (mitotic spindle) as well as fixing membrane-enclosed organelles. Finally, the intermediate filaments have the utility of reinforcing the cytoskeletal structure confers mechanical strength [9] (chapter 16), [31] (chapter 1).
All these are interconnected to each other and are capable of support and generate physical forces affecting local mechanical features and whole cellular attitude. Moreover, intriguingly, fate, shape, and functions of a cell, could be arranged by long-lived cytoskeletal structure acting as an epigenetic determinant [11].

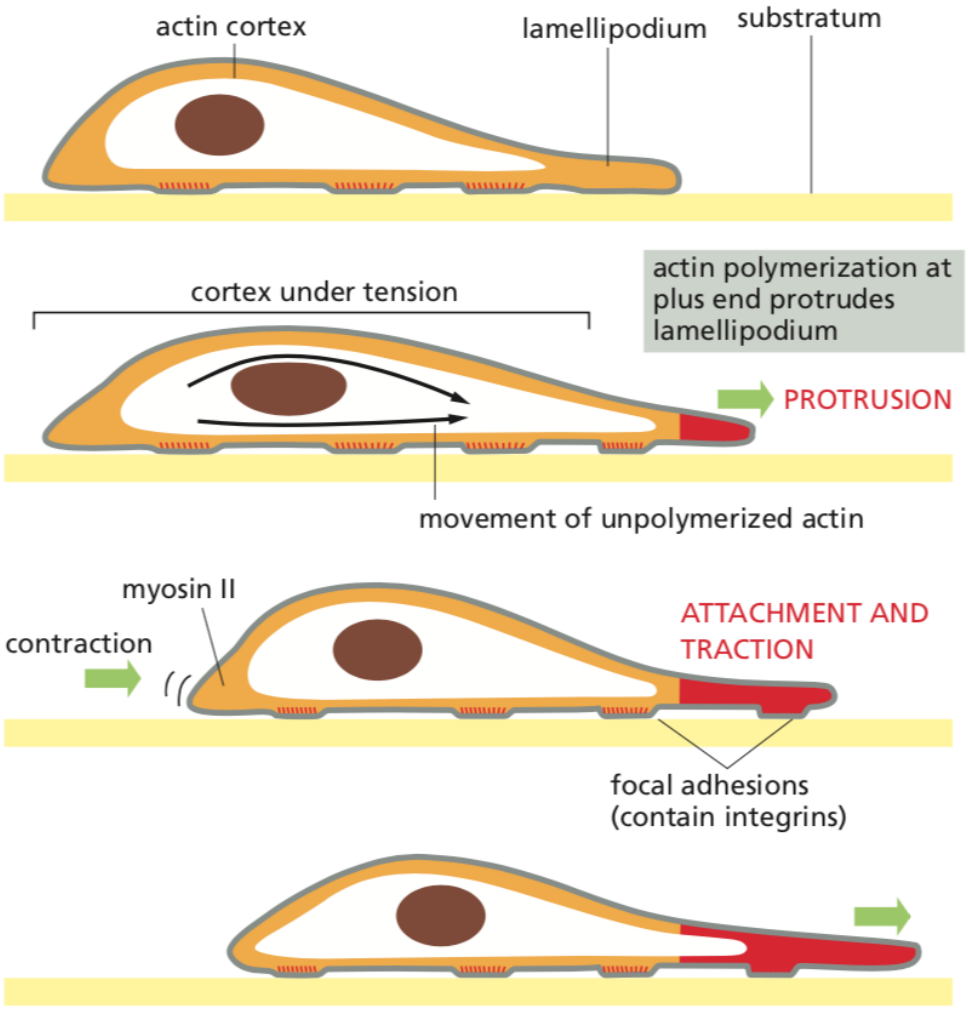

Figure 2.3: This drawing shows how the actin-rich cortex promotes cell-motion inside protrudes lamellipodia. Importantly, if the actin polymerization in the actin cortex allowing the push-forward of the cell, in the rear of the cell, contraction happens (correlated with myosin activity). Moreover, a pivotal role is played by focal adhesions which anchor the cell to the substrate, granting their forces exchange, required to cell for motion. Adapted from [9]

It is possible to catch three main functions provided by the cytoskeleton [11]:

- biochemically and physically connector of the cell with the surrounding environment;

- spatial organizer of what is present inside the cell;
- force generator able to move the cell and make it change shape.

These tasks are absolved with the help of several organelles and a plethora of cytoplasmic proteins. Although the cytoskeleton is frequently labeled as the "skeleton" of the cell this should not lead to thinking that it is a static structure. On the contrary, is a really dynamic arrangement able to adapt to the environmental characteristics, ruled by a continuous flux of each regulatory protein [11].

Importantly, we know that many pivotal building blocks of the cytoskeletal network have been discovered and characterized in-vitro experiments. Nowadays, by means of advanced light microscopy, scientists are determining the evolution in space and time of these proteins during specific biological processes (e.g cell motility and cell division) [11]. Specifically, actin is one of the fundamental proteins that form the cytoskeleton, being its polymerizes the main way for generating filaments inside the cells. Remarkably, have been found a huge number of molecules (a number larger than 150 proteins) that embeds actin-binding domains. For instance, the WAVE complex is a macromolecular aggregate constituted by a series of actin controllers supporting at the edge of moving cells the assembly of actin filament network [11].

In the remainder of the section, we will list the major constituents of the cytoskeleton and we connecting them to their task inside the cytoskeletal network. According to [11] we need to stress three notions on the subjects:

- spatial signals and physical limitations rule self-assembly of matrix constituents giving rise the long-range order;
- physical features of the cell are driven by the arrangement of the cytoskeleton;
- cellular behavior either at short- that long-timescale could be affected by the matrix-bound to the surrounding microenvironment

2.1.2.1 The microtubules

Among the above-mentioned matrix, the microtubule one is surely the stiffest and it certainly has the most complicated dynamics of assembly and disassembly [11]. The microtubule's persistence length, a mechanical feature identifying the flexibility of a filament (proportional with its stiffness), is very large compared to its true length (~ 5 mm [11]), which entails that microtubules can assume an almost linear trajectory that crosses the whole-cell [11]. This is true despite this kind of structures are known to be sensitive, and so buckling, to the compressive cargo [11]. Microtubule's rigidity is a property that can corroborate many biological functions. For instance, in the course of the interphase, namely that period of the cellular cycle antecedent to the cellular division, microtubules have a radial arrangement; in this way, thay can work as the main road and fulcrum for intracellular traffic [11]. Not only that, throughout the cellular chromosomes separating cycle (mitosis), the microtubule matrix organizes itself in order to form the mitotic spindle, namely a real machine capable of tracking down and line up chromosomes [11]. Interestingly, the ability of the mitotic spindle to do this is correlated to the dynamics of the assembly of each microtubule. Importantly, a microtubule is undergone dynamic instability, i.e. it may switch between the rapidly

shrinking states to the stably growing and vice-versa [11]. Unstableness allows quick rearrangement of the microtubule matrix, leading to a massive improvement in cellular space exploration of these molecules [11]. Consequently, this instability induces an impressive sensitiveness enhancement that could be 1000-fold rapid than can exhibit a classical biopolymer [11]. In fact, a polymer is usually responsive to the activity of regulatory proteins, the variation of cellular, as well as its subassembly components concentration [11].

2.1.2.2 The role of actin monomer and the actin filaments network

Actin has a preeminent role in the cytoskeleton activity. It is one of its prevalent components and its filaments are placed mainly in the cortex (actin cortex, located under the plasma membrane) [31] (chapter 1). Monomeric globular subunits (G-actin) are generated and placed inside the cytoplasm. Here, their polymerization engenders actin filaments (F-actin) which actively participate in cell motility. Such filaments generating the forces necessary for the locomotions by means of two paradigmatic mechanisms: polymerization and the actin-myosin contraction [31] (chapter 1).
The first one provides the force against the cell membrane able to produce cell protrusion throughout cell migration. The second one confers at the cell, by the aid of myosin II, the contractile features required during motility. Myosin II is a motor protein that converts the energy of ATP hydrolysis into mechanical work [31] (chapter 1). In fact, similarly to microtubules and differently to intermediate filaments, actin filaments are polarized polymers. This means that either microtubule that actin filaments have, at the molecular level, an asymmetrical arrangement, resulting in proper trails for molecular motors [11]. Specifically, if for the actin filaments we have denoted the myosin proteins as molecular motors, for what concern the microtubules these turn out to be the members of dynein or kinesin families [11]. Moreover, these motors can also act as transporters through the microtubules-rails among different intracellular compartments [11]. For instance, the microtubule-associated motors play a pivotal role in their array arrangements, either during the interphase that throughout the mitotic spindle [11]. Instead, from the actin-myosin interaction arise the bundles of contractile filaments called stress fibers (SFs), able to make several kinds of cells contract in many biological processes. SFs generation is strictly connected to either the Rho-A signaling and the force exerted by the SFs itself as well [31] (chapter 1).
Intriguingly, there are further peculiar differences between the actin filaments network and the microtubules ones [11]. Firstly, actin filaments do not shift between polymerization and depolymerization discrete states as we happen for microtubules. Secondly, microtubules have an arrangement that sets organize around one or two focal points, whereas actin filaments net is always in dynamic evolution, it assembles and disassembles, as a consequence of the signaling activeness scheme [11].

The actin filaments are polymers certainly fewer stiff than microtubules [11]. In a completely counterintuitive way, such a feature does not affect the ability of actin filaments to assemble themself in a well structured and stiff arrangement that, mainly happens, thanks to the existence of many crosslinkers (such as α-Actinin [32]). Polymeric structures base on actin filaments can be given rise, among the other, isotropic or branched rather than the above mentioned bundled networks (see SFs) [11].
Particularly, in order to assist the development of filopodial protrusions, usually during chemotaxis and cell-cell communication, a network of bundles of aligned filaments arise. Differently, into the frontier of a motile cell, a generation of a net of branched filaments, result to be necessary in order to produce either the force able to modify the cell shape and to prop the front line itself [11]. Such a

mechanism of support is made possible by the ability of actin filaments to elongate by means of the adding of the nucleotide-bound monomers [11]. These, continuing to join at the actin filaments, allow them steady extensions.
For instance, as an answer to the signaling downstream induce by chemotaxis, guided by the cell-surface receptors, we observe in the frontier of crawling leukocytes, a formation of branched actin filament networks [11]. Consistently, in fibroblast, integrin-ligand interaction guide the arrangement of SFs [11]. Focal adhesions (FAs see section 2.1.2.2.1) are usually located at the ends of SFs and such adhesion sites arise for unloading the contractile forces exerts by these bundles filaments, on the ECM, or vice-versa.

Furthermore, other complex interactions involving actin filaments happen when these interplay with members of the cofilin family (disassembly factors) or the formin family (polymerases) [11]. In the end, among the many biological processes supported by the actin cytoskeletal filaments, there is a recognizable mechanobiology interest phenomenon call endocytosis, namely a mechanism that allows the cells to embed extracellular molecules. In order to efficacy conclude this process, the portion of membrane involve in this phenomenon, release a signal able to induce the local actin filaments assembly. In this way, the network can support that portion of the membrane ready to become an endocytic vesicle and so internalize it [11]. Interestingly, endocytosis is one of the mechanisms that can sustain the viral replication cycle. In fact, viruses are not cells and so they can not exploit the cellular division machinery to reproduce themself. Therefore, for the purpose of surviving and replicate, viruses need to make use of the metabolism of cells that host them. In fact, with the aim to inoculated and then replay their genome, some viruses have firstly to attach to the cell membrane (receptors-mediated process) and then enter inside the cell. Depending on the kind of virus, exist different way in which this can happen, one of these is just about guided by endocytosis.

The filaments of actin that cover the inner side of the cell membrane have several functions in cell activity. In fact, besides it confers to the cell the suitable shape adapting to the morphology evolution of the cell itself, the cell cortex plays a key role in vehicular transmembrane proteins inside a specific domain (such as Ras proteins [33]). Here, transmembrane proteins can improve their interaction with other proteins [34, 35, 36, 37]. Such statements are sustained by experimental evidence that should show how the protein complex formation induces the lipid engagement and later the rafts formation [38, 39, 40, 41, 42]. In fact, is possible to induce instability and precariousness of the cluster proteins through deprivation of cholesterol or/and by hindering the remodeling of cortical actin [43]. It is conceivable that small lipids rafts (tens of nanometers) arise from the clustering of proteins and lipids, which subsequently at activator stimuli develop until the generation of mature lipid rafts with the aim to become macromolecular signaler (e.g. cell-cell adhesion complexes, immunological synapses, and structures driving the migrating cells) [43].

2.1.2.2.1 Focal adhesions and stress fibers Focal adhesions (FAs) are complex clusters of protein whose (dynamic) structure evolves in response to the chemo-mechanical interactions between components of the ECM (e.g. fibrinogen and fibronectin) and actin bundles of the cytoskeleton (see subsection 2.1.2.2). Such an interplay is mediated by means of the transmembrane protein called integrin confers at FAs the ability to be actual adhesion sites transducing either mechanical

that chemical cues. It has to be clear that integrins are linked to the actin bundles of the cytoskeleton by means of a plaque of multi-proteins, located in the area adjacent to the inner side of the cell membrane, that actively belongs to the cluster macromolecular domain of the FAs; these could be talin, kindlin, vinculin, paxillin, focal adhesion kinase (FaK), numerous others [9] (pages 863-867 and 952-956 and 1079-1081), [31] (chapter 1).

The size, position of FAs are determined by the organization of the cytoskeletal machinery, the signaling properties, as well as the responsiveness of cells at the substrate characteristics. Hence, the mechanical features of the ECM/substrate are strictly correlated with the dynamic of the generation of FAs and SFs as well, pointing out again, that the conduct of a cell is not limited to its own singular attitude, rather to active interaction with the rest of the extracellular microenvironment, in order to maintain the homeostatic state. Intriguingly, altogether these mechanisms affect, either in-vivo that in-vitro, the cell differentiation, and proliferation.
Ventral (the most common) and dorsal FAs arise at the end of SFs which are the main structure able to provide intracellular contractility at the cells.
Evidently, mechanical forces experienced by cells within tissues can dramatically modulate cell signaling and behavior. Consequently, interaction involving FAs can lead to several biological responses like cytoskeletal reorganization, cell motility cell death or growth, and gene expression (communication with the cell nucleus). During cell migration, FAs arise to contain the cell membrane contraction and favors the formation of protrusion at the front of the cell. Cell adhesion as well is promoted by FAs which allows suitable stability for the cell shape. Focal adhesions guide the cytoskeletal reorganization during ECs motility, and consequently are pivotal for the cellular morphology regulation [44].

2.1.2.3 The intermediate filaments

Among all the three cytoskeletal matrix constituents, intermediate filaments are surely the less stiff. Consistent with this, they work largely better to tensile load than the compressive one [11]. Intermediate filament arrangements can take advantage of by microtubules or actin filaments interplay [11]. In fact, crosslinks among intermediate filaments rather than the other networks forming the cytoskeleton are frequently, and specifically, plectins are the proteins devoted to this reticulation. Intriguingly, mechanical stress induces intermediate filament formations. In fact, it is possible to observe how the generation of keratin intermediate filaments, allow the epithelial cells of the respiratory tract to support shear stress [11]. Importantly, different from microtubules and actin filaments, intermediate filaments can not prop the molecular motors directed motion inasmuch unpolarized polymers. Finally, we mention the class of intermediate filaments called polymerized nuclear lamins [11]. These support the eukaryotic nucleus mechanical integrity and equivalently important, at the origin of mitosis, their phosphorylation due to cyclin-dependent kinases provides the stimuli that lead to the nuclear-envelop collapse [11].

2.2 The cellular microenvironment

2.2.1 The growth factors

Growth factors are signaling molecules able to diffuse in the intracellular space and ECM. These can trigger and support many biological processes for many kinds of cells (including ECs). Usually, these molecules are secreted by nearby cells, as well as glands and tissues rather than tumor cells. Importantly, whoever it is the organic entity that secretes and releases them into the surrounding environment, it does in order to draw some specific biological advantage. For instance, we can think of the growth factors released by cancer cells in response to a state of hypoxia of a solid tumor. These trigger a subsequent generation of blood vessels that will allow the tumor itself to continue to grow and develop. Anyhow, all the angiogenesis-dependent diseases are characterized by the uncontrolled release of angiogenic growth factors, leading to EC activation.

Growth factors, by binding their cognate cell surface receptors during angiogenesis, are responsible for the activation of signaling pathways that sustain cell survival, proliferation, and migration [45]. Practically, ECM can govern cell behavior managing cytokines and growth factors (e.g. vascular endothelial growth factor (VEGF), platelet-derived growth factor (PDGF), fibroblast growth factor-2 (FGF2), insulin-like growth factor receptor-1 (IGF1R), and transforming-growth factor-β1 (TGFβ11) [46]), among which there are those necessary for physiological and pathological angiogenesis. Moreover, although growth factors are considered soluble molecules, many of them bind extracellular matrix components leading to the formation of immobilized ECM-bound complexes. Hence, immobilized (within ECM network) growth factors, maintain long-term stimulation of target cells (growth factors that work like chemoattractants and mitogens [46]), mostly if they achieve high local concentration, and so, preserving the ability to recruit their specific signaling receptors (e.g. TKR and integrins) [31] (chapter 1).

Effectively, TKR-integrins cross-talk (exhaustively explained in section 2.3.2) affects cellular responses, through a fine adjustment. Moreover, cell migration, which usually is correlated to cellular contractility, leads to an incremental strengthening of the ECM and the tissue in general. Therefore, cellular contractility favors the generation of actin bundles which, through integrins, discharge traction forces on the ECM; as a consequence, ECM reacts by becoming more rigid, inducing an increment in the traction forces, supporting the growth and therefore the survival of the cells [31] (chapter 1).

2.2.1.1 The cystine-knot proteins family (CK)

In the current work, we will focus on two main groups of growth factors: the Dan and VEGF family, both belonging to the cystine-knot proteins family. Particularly, it has been a priority for us to study the member of the VEGF family VEGF-A, and the component of the group of the BMP (bone morphogenetic protein) antagonists called gremlin-1 [47, 48].

VEGF-A form part of the VEGFs family that is composed of another four members (VEGF-B, VEGF-C, VEGF-D, and VEGF-E). We have concentrated on VEGF-A inasmuch as is the most important specific mitogen for the ECs inside the blood vessels. Such a ligand has several isoforms correlative to the number of amino acids exhibits; VEGF-A_{165} is the most prevalent in the

human body. It, once generated, pervades the tissues and goes to settle adjacent to the ECs stimulating them to migrate (chemotaxis). VEGF-A is accumulated in the extracellular matrix, inducing the recruitment of VEGFR-2 at the basal portion of the basal membrane, receptor dimerization, and the activation of intracellular signaling through a series of phosphorylations.
Moreover, this ligand is overexposed in several kinds of tumor, and its interaction with ECs induce a succession of phenomena that lead to angiogenesis facilitating the vascular permeability [31] (chapter 1).
Interestingly, the EC response to this ligand differs upon its physical state. Upon VEGF stimulation, the phosphorylation grade of VEGFR-2 is slighter in confluent cells compared to that observed in sparse cells [49].

Gremlin-1, instead, is a non-canonical ligand for VEGFR2 [50]. Also, it is a member of C-terminal cystine-knot proteins (CTCK) and an antagonist of the BMP, which is, instead, part of the group of the growth factor cystine-knots proteins called TGF-β.
Recently it has been proved that gremlin-1 induce angiogenesis either in-vivo that in-vitro [51, 52, 53]. This is a new role for this protein that so far was known as a controller of bone formation during human growth. Hence, gremlin-1 becomes an agonist for VEGFR2 and it could play a fundamental role in tumor angiogenesis, being, in addition, a protein generated by tumor endothelium [31] (chapter 1).

2.2.2 ECM and its components

All the cells have a continuous talk with the microenvironment circling them; they dynamically evolve together with the surroundings through the exchange of cues (e.g. biochemical and biomechanical) aiming to absolve specific biological processes and compliance with the homeostasis of the cells, tissues, and hence body. Several biological behaviors are connected with the micromechanical signals among ECM and cells, among these, we have the invasion, neoplastic evolution, and metastases [54]. The sensitivity of the target cells to these factors is modulated by the microenvironment. Hence, ECM plays multiple roles on cells and particularly on ECs that are stably adhere to it; in fact, as well as establishing mechanical support, it can influence their mobility, shape, polarity, and even differentiation [31] (chapter 1). The cellular response to ECM biophysical stimuli, including the mechanical ones [3], depends on the hierarchy of the mechano-chemical systems which provide adhesion receptors (such as integrins), intracellular focal adhesions, cytoskeletal networks, and molecular motors. Integrin (properly explained in the section 2.3.2), namely a large family of transmembrane heterodimeric receptors, allows cells the possibility to dialogue, interoperate, and perceive the ECM [31] (chapter 1). Integrins play a relevant role in many cellular phenomena; in fact, besides aiding the mechanical support of ECs, their engagement leads to an intracellular signaling cascade that is the kick-off of several biological processes.

Following, a description of the main components of ECM together with a suitable characterization of the transmembrane protein called integrin are therefore provided below with the aim to render clear the adhesion mechanism ruling the cells.

The extracellular matrix, composed of the substance developed by eukaryotes cells inside the human body, is an elaborate network of macromolecules that plays different roles at the service of the tissues (supports to the skeleton, dermis, tendons, etc.) and cells (actively participation at cellular

adhesion, motility, and migration) that constitute it [1] (page 120).
Collagens with elastins, laminins, fibronectin, growth factors, and matrix metalloproteases (MMPs) are among the principal constituents of the ECM. Moreover, ECM is made by a hydrated compound gel of glycosaminoglycans (GAGs) and proteoglycans (among others HSPGs), whose interlinking protein fibers are embeds in the matrix network [46, 31] (chapter 1). Other non-fibrous glycoproteins (thrombospondins) are contained in ECM with members of the hemostatic system (von Willebrand factor (vWF), fibrinogen, and vitronectin), as well as specific growth factor associated proteins (insulin-like growth factor binding proteins) [31, 55, 56].

ECM is not a static entity; in fact, it undergoes continuous remodeling, with the breakdown that constantly happens by proteases (particularly metalloproteases) [57]. Importantly, every molecule constituent of the ECM has specific skills that determine its structural, chemical, and mechanical characteristics relevant to the blood vessel function and vascular activity [46].

Actually, ECM is prevalently defined by a collagen scaffold, with variability on the type of this protein (different families); the remanent molecules are anchored to the scaffold itself and they are able to interact with the cells embedded or neighbor to the ECM [57].
Inside the vascular wall, it has been found 13 collagen family members, on 28 that has been discovered so far inside the matrix. ECs, vascular smooth muscle cells (VSMCs), and fibroblast produce and interact with this matrix protein, which is the most copious among those exhibit by the ECM [46]. For instance, VSMCs migration and growth is induced by the interplay with collagen 1. Not only that, this interaction stimulates the generation of matrix-degrading enzymes, MMP2 as well [46].
Collagen mechanical (tensile) strength is granted by fibrils, i.e. the way in which the triple-stranded helical structure of collagen itself is organized [46]. Particularly, collagen can bind to other proteins (e.g. fibronectin), with the aim to maintain ECM. Such interactions allow either the stabilization of fibronectin itself when a mechanical load is present that the government of the assembly of collagen [46].

However, ECM is predominantly made by GAGs (e.g. hyaluronan and heparan sulfate), namely a set of elements of disaccharides that repeat themself like unramified chains. Arising from the covalent link of GAG chains with a protein core are the proteoglycans (e.g. syndecan, versican, and aggrecan) [46], that result to be pivotal in preserving tissue hydration. The reason for that is correlated to the fact that proteoglycans can assume large dimensions and so move a high amount of volume of water [46]. Moreover, they have the peculiarity to interplay with other ECM proteins among which integrins, growth factors, cytokines, and chemokines [46]. Such interactions can corroborate to modulate several cellular processes and govern the signal transduction as well as the in/out of molecules from the ECM itself [46].

A further molecules embedded inside the ECM is the elastin, i.e. a pivotal protein for the preservation of the structure and the elasticity of the vessel walls. This protein is first synthesized as a monomer (greatly soluble) call tropoelastin (precursor of elastin) and then reticulate into insoluble elastin fibers after post-translational modification [46]. Tropoelastin can induce, in ECs, the production of endothelial nitric oxide synthase (eNOS). Such phenomena can trigger the consequent liberation of nitric oxide (NO), a relevant molecule in the vascular system inasmuch able to provide protective functions at the blood vessel [46].

Inside the matrix are also present proteases (i.e. MMPs) produced by ECs, VSMCs, and fibroblasts. These are enzymes able to deteriorate the ECM proteins and therefore capable of liberating the so-called growth factors and cytokines. Such a process leads to the bioactive shard formations adapted to provide the blood vessel reshape [46]. Contextual with MMPs (MMP1, 2, and 9 are the most frequent types in the vessel walls) there are the tissue inhibitors of metalloproteinases (TIMPs). The latter is necessary to counterbalance the MMPs generated through the ECM-cell interplays, highlighting a biological mechanism that allows sustaining homeostasis [46].

A further ECM relevant molecule is fibronectin (dimer), namely, a large glycoprotein (with numerous isoforms) and part of the constituent fibers of the matrix itself [46]. On the ECM it is present as fibronectin fibrils, they produced on the cell surface by means of an integrin-mediated process, proving that these two proteins, jointly with other molecules, generate a pivotal network for the signaling during vessel formation [46]. It has been proved that the inhibition of fibronectin synthesization leads to a diminution of the generation of ECM by VSMC, cellular proliferation, vascular remodeling, as well as the correct regulation of the collagen I formation [46].
Moreover, fibronectin is also identify as a specific ligand of integrins possessing the $\alpha_5 - \beta_1$ subunits [9] (pages 1066-1068 and 1076-1077).

Another important molecule is fibrinogen, i.e. a member of the hemostatic system that is usually located inside the ECM. This protein interacts with the β_3 and $\alpha_{||b} - \beta_3$ integrins that are present on platelets and so fundamental in blood coagulation [9] (pages 1076-1077). Also, a careful analysis of the value of fibrinogen present in the blood lumen could be revealed severe infections in the patience.
The use and purpose that fibronectin and fibrinogen will have within future experimental and numerical models will be clarified in the next chapters.

2.3 Transmembrane proteins

2.3.1 Receptors Tyrosine Kinase

A very important class of transmembrane proteins is represented by the Receptors Tyrosine Kinase (RTK). These have an N-terminal extracellular domain that favors interaction with growth factors (but also with cytokines and hormones) and a C-terminal intracellular domain important to the intracellular activities of the receptors [58]. RTK/extracellular microenvironment interaction rules and induces several intracellular signaling such as migration, growth, differentiation, and cellular metabolism [59]. RTK are monomers that, thanks to the chemical interplay with ligands, dimerize reaching self-phosphorylation [60], [61], [62]. Actually, experimental pieces of evidence show that dimerization can happen without ligands as well, inside of micro and macro membrane-domains, but with lower probability [63]. RTK distribution and signaling are governed by membrane dynamics. Ligand/RTK interaction induces receptors redistribution on the cell membrane, leading to the relocation and the modulation of receptor activities in blood vessels during angiogenic events. Accordingly, it has been suggested that aberrant spatial regulation of RTKs may play a role in cancer progression. In this context, the cortical cytoskeleton, the actin filaments, and other cy-

toskeletal components closely apposed to the plasma membrane, surely play a role not only in cell adhesion and motility, growth, endocytosis, exocytosis, signal transduction but also in driving receptor motion on the membrane, internalization, and receptor recycling (lateral adjustment of the RTK). These membrane-associated components are parts of dynamic structures involved in stabilizing membrane (and thus of the cell homeostasis).
Interestingly, exist just about 20 subfamilies of receptors with tyrosine kinase activity [64]. Among all these families exist the VEGFR one, to which it belongs VEGFR2, an integral membrane protein that we will deal with extensively in the course of the thesis and in the next sections.

2.3.1.1 VEGFR-2 and its spatial regulation

VEGFR2 ($210 - 230\ KDa$) is a protein usually expressed in several kinds of cells, such as ECs and some kinds of cancer cells. VEGFR2 is the main pro-angiogenic receptor expressed by these cells, playing a pivotal role in neovessel formation. In fact, VEGFR2-ligands interplay allows a conformational change of the kinase domain of the receptor, revealing the sites where ATP can bind [65, 66, 67, 68]. Subsequently, we will see how the ligands VEGF-A [69] and gremlin [51] can induce the polarization of VEGFR-2. Specifically, these interactions include a homodimerization or heterodimerization of the transmembrane protein and consequently lead to phosphorylation and an intracellular signaling cascade that rules the triggering of the above mentioned angiogenic stimulus and so the prelude of cellular proliferation and migration. For instance, during tumor angiogenesis VEGFR2 is overexposed either from endothelial cells, that form the nearby blood vessels at the tumoral mass, that from the cancer cells themself that are able to multiply in consequence of VEGFR2 activation. We can conclude that VEGF/VEGFR2 system may play a dual role during tumor progression, by modulating both stromal and parenchymal tumor compartments.

Cytoskeleton activities are also correlated with the pursuits of VEGFR2 which act on improving the permeability of the vascular plexus favoring intracellular pores generation (phenomenology that could be related to caveolae activities) and the transient opening of paracellular junctions [70, 71]. Moreover, caveolae could favor the internalization of VEGFR2. During this phenomenon, VEGFR2 can manifest its activation releasing its intracellular signaling from the endosome compartment favoring some second messengers activation like Akt, and, in the end, it can be degraded or recycled on the membrane [72, 73, 74, 75, 76].

It is hence evident how the VEGFR2 spatial regulation is pivotal to manage the magnitude of extracellular stimuli for all that cells able to overexpose it. Inside lipids rafts, VEGFR2 can be stabilized and could chemically interplay with co-receptors such as integrin.

2.3.1.2 Co-receptors for VEGFR2

It is known how the adhesion to different ECM can modulate the VEGFR-2 response [52, 69]. Such distinctive features may be attributed to the VEGFR-2 association with different transmembrane proteins, which form distinct multi-molecular complexes that interact with cytosolic transducers. Effectively, VEGFR-2 forms a complex with Ve-Cadherin and β-catenin into cell-cell contacts [77], with the vascular endothelial-phosphotyrosine phosphatase (VE-PTP) into cell-cell junctions [78], with neuropilin 1 [79] and $\alpha_v\beta_3$ in lipid raft domains [52]. As we will see in the section 2.3.2 $\alpha_v\beta_3$, integrin mediates cell-matrix interactions, and, similarly to VEGFR-2, transmits "outside-in"

cues to the cell, which triggers a large array of intracellular signaling events. Interestingly, It has been also proved that integrin participates in VEGFR-2 full activation, sparking the propagation of intracellular signaling cascades that affect the cell mechanical response. This correlation shows to be particularly efficient in prolonging and strengthening the intracellular signal released by the VEGFR-2-Ligand complex [52, 80, 51].

However, $\alpha_v\beta_3$ integrin is one of the most important survival systems for nascent vessels and participates in the full activation of VEGFR-2 triggered by VEGF-A or gremlin, which are important angiogenic inducers in the tumor, inflammation, and tissue regeneration. Although the role of productive crosstalk between VEGFR-2 and $\alpha_v\beta_3$ in the angiogenic response is well characterized in terms of intracellular signaling, ECs migration, and proliferation, the effects of complex formation on the membrane dynamic of both receptors is still missing.

2.3.1.3 Somatic mutations of VEGFR2

In recent years, the expression of VEGFR2 on tumor cells, including lung cancer, neuroendocrine neoplasm, and melanoma has been reported, thus suggesting a direct role of the VEGF/VEGFR2 system in tumor biology. VEGFR2 is expressed by $78-89\%$ of tumor cells in advanced-stage melanomas [81], which show increased adhesiveness to the vascular wall, invasivity of the ECM, and even ability to shape functional channels similar to vascular vessels (vasculogenic mimicry).

Genetic mutations play a fundamental role in the study of tumors. In fact, somatic mutations have a key role to discriminate cancer cells from the "healthy" cells surrounding the tumor. Such mutations act on the DNA altering it; in a sense, we can state that cancer is a genetic disease [9] (chapter 20). Concerning VEGFR2 correlations with cancer evolutions, we push forward our studies on several human cancer, accounting for some possible mutations in the kinase domain of this RTK receptor.

VEGFR2 mutations correlated to cancers are identified by means of Next-generation sequencing analysis [82, 83, 84]. Such mutations, that including the substitutions D717V, G800D/R, L840F, G843D, S925F, R1022Q, L1049W, S1100F, and R1032Q (the most recurrent one), could be associated with an altered response to targeted drugs and/or to cancer growth. Among these just mentioned there are those that can support, in a xenograft model of colon cancer, tumor growth, such as D717V, G800D/R, G843D, S925F, R1022Q, R1032Q, and S1100F [82, 83, 84]. Whereas L840F mutation can promote, in colon cancer patients, therapy refractoriness [82, 85]. Interestingly, it has been shown that treatment with pazopanib stimulates a good metabolic response in a patient with metastatic basal cell carcinoma expressing the mutation of VEGFR2, specifically substitution R1032Q (where 1032 indicates the position of the mutation in the kinase domain of VEGFR2) of [84]. Significantly, low levels of phospho-KDR and phospho-MAPK make-believe to a considerably decrease receptor (exhibiting R1032Q substitution) functioning. Nevertheless, when they are exposed to VEGF, VEGFR2-R1032Q expressed in cancer cells, trigger cancer growth.

2.3.2 Integrin, an adhesion molecule

Integrin is a further transmembrane protein that plays a key role in many physiological and pathological manifestations, including angiogenesis; indeed, its spatial distribution on the cell surface can have massive consequences on the mechanical evolution of the EC [31] (chapter 1).

Integrin is a dimer made by $\beta-$ and $\alpha-$ chain genes. Different combinations of the 8 different $\beta-$ with the 18 $\alpha-$ give rise to the 24 kinds of integrins present in the human body [9] (chapter 19). Its own flexible structure allows it to be an adhesive dynamic machine playing a pivotal role in chemo-mechanical transduction signaling. $\alpha_v\beta_3$ integrin mediates cell-matrix interactions, and, similarly to VEGFR-2, transmits "outside-in" signals to the cell, which triggers a large array of intracellular signaling events. Effectively, the tension discharged by the SFs through the FAs, and therefore on the integrins, give rise to a mechanical signal that strengthens the protein cluster itself and therefore at the signal as well emanating from it.
Integrins intervene in the correct activation of cytokine. Particularly, for triggering the pathway Erk1/Erk2 MAP kinase that mainly ruling the ECs proliferation [86]. Moreover, adhesion induces a further important channel of signaling activation, namely the Erk1/Erk2 MAP kinase pathway that supports ECs survival in favor of apoptosis [86]. It can therefore be observed that without the contribution of adherence to the ECM the ECs undergo apoptosis [86].

$\alpha_v\beta_3$ exists in an inactive form with a bent-clasped conformation (low-affinity integrin), in an activable form with an unbent-clasped conformation or in an active form with an unbent and unclasped conformation (high-affinity configuration) [87, 88, 89]. The conformation and the affinity of $\alpha_v\beta_3$ for its ligands fibrin(ogen), fibronectin, thrombospondin, von Willebrand factor, and vitronectin are subjected to short-term modulation by phorbol esters, Mn2+, ADP, vascular endothelial growth factor, basic fibroblast growth factor, and elevations in intracellular cyclic AMP (cAMP) [90]. It is crucial to understand, for the aim of the current thesis, that integrin that chemically interplays with ECM ligands are found in the active state, whereas we infer in a low conformation during the interaction, like co-receptor, with the VEGFR2 inside the lipid rafts.

Integrin involvement can activate several signaling pathways inside the cell, among the others the most note are: Src, focal adhesion kinase (FAK), MAPKs, Rho-GTPase, phosphoinositide-3-kinase (PI3K) [31]. Moreover, integrins expression, together with ECM arrangement, have the ability to regulate the responsiveness, in the course of angiogenesis, of EC to growth factors [31]. In fact, it is common in biology to assist at the phenomenon called crosstalk, namely that phenomenon wherein one or more members involved in a specific signal transduction path can be implicated in another distinct pathway. Consistently with our aims, a clear example of crosstalk is provided by tyrosine kinase receptor (TKR) and integrins [31]. Specifically, integrin and VEGFR2, which follow two different paths of signaling transduction, interact, and relate to each other in order to optimize their own behavior increasing the regulation of cellular riposte. Interestingly, VEGF, and FGF ligands, which usually guide angiogenesis, are also regulated and sustains by $\alpha_v\beta_3-$integrin [31].

2.4 Tissue Vascularization

Every cell in the human body has to be stocked with oxygen and nutrients and at the same time free oneself from the waste substances like carbon dioxin. The apparatus that performs this task is the cardio-circulatory system through a closed system of blood vessels (arteries, arterioles, capillaries, venules, and veins [46]). Usually, the majority of blood vessels are formed by three distinct layers: tunica intima, tunica media, and tunica adventitia. The first one is a real primary defense barrier against the spill of blood lumen and itis composed of a monolayer of ECs that is backed, in the sub-endothelial-space, by connective tissue [46]. The second one, split by the first by means of the internal elastic lamina, is composed principally of VSMCs and a circular manner arrangement of elastic and connective tissues. Such a layer can be of massive importance in blood pressure control, thanks to the constrict and dilate activities of VSMCs [46]. Fibroblast and connective tissue fibers make up the tunica adventitia, which is externally bounded by the external elastic lamina [46]. Despite these structures are easily found to surround many types of blood vessels, it is possible to observe existing cases wherein such an articulate architecture is not present. In fact, the capillaries, namely the smallest ones among the blood vessels, are made by mural cells known as pericytes that encircle by a thin tube of ECs [46].

The blood vessels resulting to be a prerequisite for the normal development of tissue and arise through two processes: vasculogenesis and angiogenesis (also named neovascularization). Vasculogenesis occurs in the embryo, where new vessels form de novo via the assembly of endothelial cells (ECs) precursors (angioblasts) [91], giving rise to a primitive vascular plexus. Subsequently, to generate a mature vasculature, vessels originate from the primary plexus by either intussusceptive or sprouting angiogenesis. These are phenomena correlated to the growth and branching of vessels resulting from the stimulation of the ECs that covers the inner wall of the already existing blood vessels [9] (chapter 22). Explicitly, partition and growth of blood vessels in-situ are what characterizes intussusceptive angiogenesis. In contrast, sprouting angiogenesis involves mechanisms that require the development of a blood vessel branch guided by a tip cell (see 2.4) that is stimulated by specific signaling proteins (also called growth factors or ligands) [31] (chapter 1).

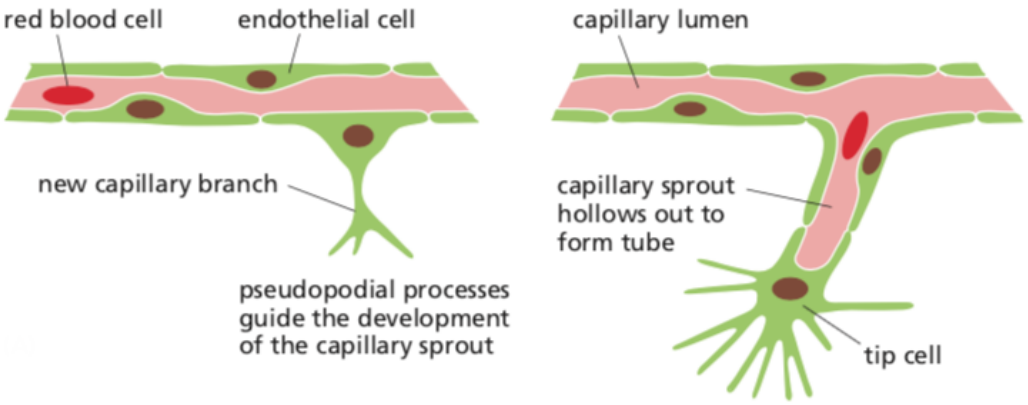

Figure 2.4: A new blood vessel (capillary) arises owing to the phenomenon called sprouting angiogenesis. This process is guided by an endothelial tip cell that promotes the advancement of the capillary sprout. Adapted from [9]

It is therefore clear how the birth of new blood vessels can play a pivotal role in many byological processes of the human body, both physiological and pathological. Effectively, angiogenesis plays a major role in tissues' growth, scarring of wounds, and repairing processes connected with the menstrual cycle (physiological phenomena), as at the same time in numerous diseases such as ischemia (e.g. acute limb ischemia, coronary artery ischemia, cardiac ischemia, and cerebral ischemia), cancer (both solid[1] and hematological tumors), and chronic inflammation like rheumatoid arthritis, Crohn's disease, and diabetic retinopathy [31] (chapter 1). Moreover, such phenomena are corroborated by the fact that, in a vertebrate, it is possible to observe that the majority of cells in most tissues are close to a blood capillary (approximately 50–100 μm) [9] (chapter 22).

A first potential classification of angiogenic phenomena arises from the experimental remark of the previous biological processes (particularly the pathological ones); in fact, it is possible to observe that some of these diseases are connected with a reduction of vascular perfusion (e.g. ischemia), others with an excess of revascularization (e.g. tumor angiogenesis[2]). Therefore, in the former case, the triggering of the angiogenetic implantation is desirable inasmuch phenomenon necessary for the reconstitution of the health of a tissue, in the second case has to be defused. Such a characterization is ineludible and crucial at the same time, such that plays a relevant role in the choice of medical strategy to fight the above-mentioned diseases. Two juxtaposed medical strategies arose after these considerations, i.e. the so-called pro- and anti-angiogenic therapies, which intervene in the balancing among the pro- and anti-angiogenic signals. It is therefore understood how governing the angiogenic system can bring considerable advantages both in the case in which it is desired to be triggered and in the case in which it is desired to disable it [31] (chapter 1).

2.4.1 Therapeutic Angiogenesis and Vasculogenesis

Pro-angiogenic strategies are therapies that have the aim to improve or recover, the vascular network in response to reduced vascular perfusion that leads to a state of hypoxia that causes the degeneration of tissue. Just think of tissue engineering, wherein, at the early stages of tissue implantation, if it is not well perfused (and therefore oxygenated), it can rapidly degenerate to death. A further example concerns wound healing in diabetic conditions or even tissues that due to ischemias are subjected to a decrease of vascular perfusion [31] (chapter 1).

Anti-angiogenic strategies have the opposite aim of the previous ones, i.e. to drastically reduce the onset of the angiogenic stimuli. Such a goal is common to every therapeutic strategy that has to defeat diseases that benefit from the uncontrolled growth of blood vessels. As already mentioned, in many cases, cancer is sustained by the growth of new vessels that favors their survival, development, and diffusion (metastatic cancer) inside the human body [31] (chapter 1).

[1] The observation by Tannock [92] that the vasculature is in rapid proliferation within the tumor was followed a few years later by the work of Folkman who postulated that the growth of new blood vessels is an essential requirement for tumors to grow beyond a certain size.

[2] It has to be clear that hypoxia generally induces angiogenesis. Therefore, in all cells in which hypoxia occurs, the production of vascular endothelial growth factor (VEGF) is stimulated; this acts on endothelial cells inducing proliferation and new revascularization of the hypoxic tissue [9] (chapter 22)

2.4.2 The angiogenic stimulus at the molecular level

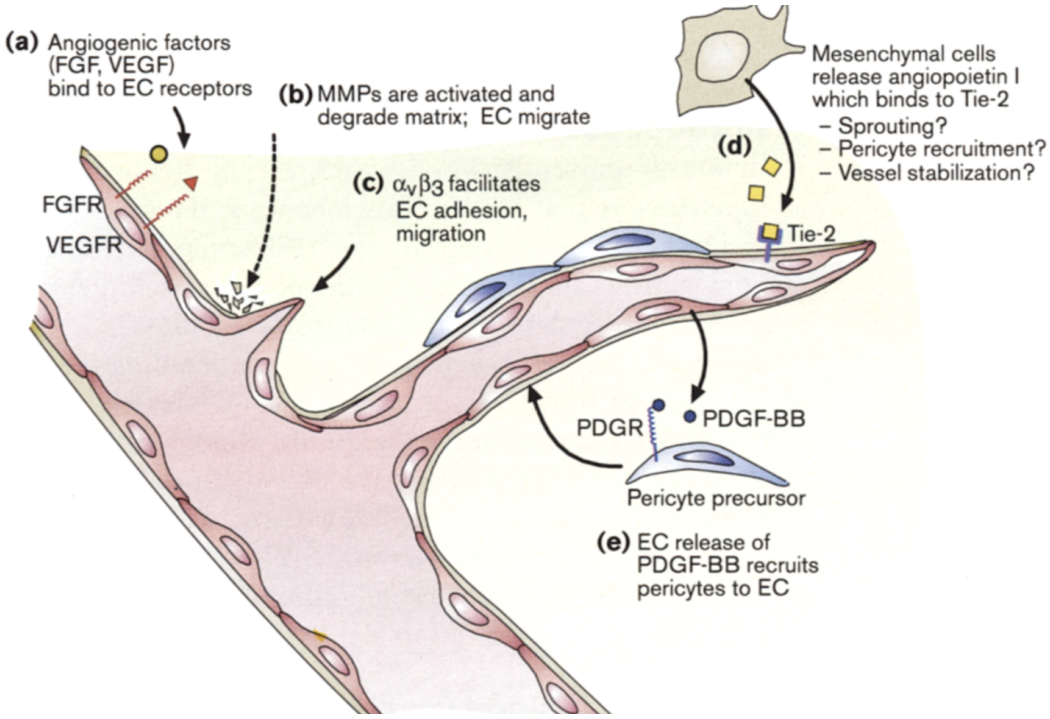

Figure 2.5: In this drawing, the multistep processes connected to blood vessel formation is depicted. Adapted from [91]

A monolayer of quiescent ECs covers the inner surface of blood vessels and their tight connection is guaranteed by means of the so-called tight cell adhesion junctions. The endothelium is surrounded by an extracellular matrix (ECM), namely the vascular basement membrane, constituted mainly by proteins and proteoglycans (among the others: collagen type IV, lamins, perlecan, and heparan sulfate proteoglycan [86]), that confers shape and stability to the blood vessel. In the basement of the membrane are incorporated accessory cells, among others there are smooth muscle cells and pericytes (also known as mural cells); this kind of cells monitoring the development and the maturation, and at the same time providing stability, at the ECs. Hence, several kinds of cells and proteins (soluble factors, ECM components, and surface receptors) are involved (see Fig 2.5) in sprouting angiogenesis but mainly ECs have a pivotal role. [31] (chapter 1).

From here on we focus on how the sprouting angiogenesis process can alter the state of undisturbed blood vessels, highlighting how this complex multistep phenomenon producing an impressive change in vessel morphology.

During hypoxia, inflammation, or tumor growth, the release of angiogenic signals (including the Vascular Endothelial Growth Factor (VEGF) and fibroblast growth factor (FGF)) causes the detachment of pericytes from the vessel wall, the loosening of inter-endothelial cell contacts, and the increase of vascular permeability [93]. The lack of oxygen inside a tissue effectively leads to the augmentation, basically inside any kind of cell, of a specific transcription factor, i.e. the so-called

hypoxia-inducible factor 1α (HIF1α). HIF1α induces gene transcription of specific genes necessary in a shortage of oxygen state (e.g. Vegf and other genes) that practically cause the secretion of angiogenic inducers like VEGF [9] (chapter 22) (see 2.6).

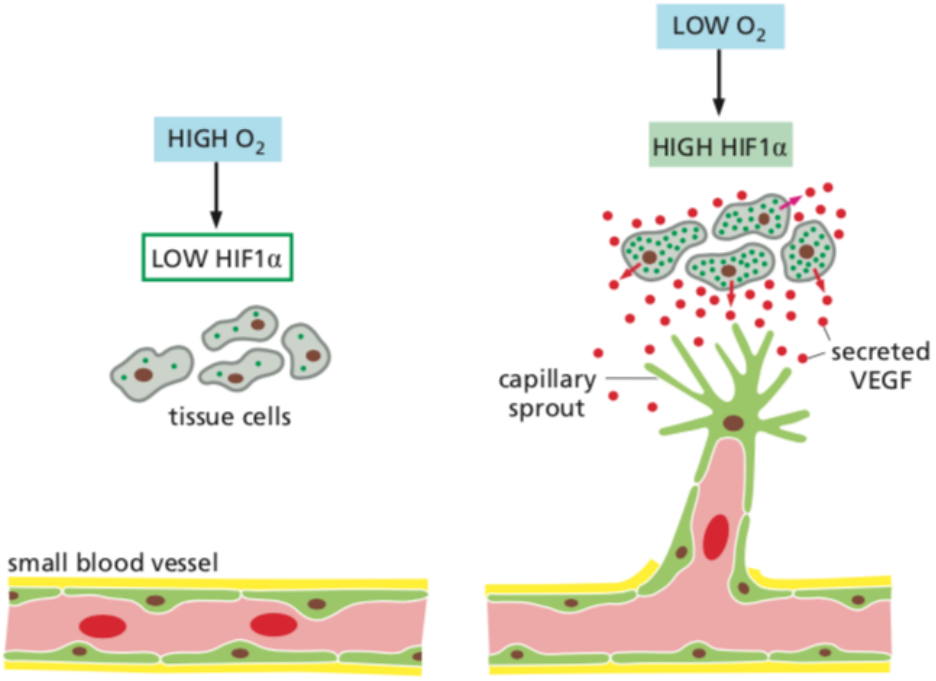

Figure 2.6: This drawing depicts how the VEGF secretion is favor by a state of hypoxia. Adapted from [9].

These early events allow the extravasation of serum proteins such as urokinase plasminogen activator (uPA) and matrix metalloproteases (MMPs) from the vascular lumen, concurring to the disruption of the endothelial basement membrane. This first stage of angiogenesis, wherein we attested degradation of the vascular basement membrane and activation of quiescent ECs [86], opens the doors to the second stage, i.e. the migration and proliferation of ECs within provisional ECM [86]. In fact, MMPs can degrade collagen and other constituents of the extracellular matrix and so break up the basement membrane barrier, providing the necessary space for ECs to migrate [91].

Next, upon stimulation with angiogenic factors, quiescent ECs acquire a characteristic "angiogenic phenotype". Activated ECs modify their morphology, proliferate, and migrate into the stroma following the concentration of the angiogenic stimuli (chemotactic migration). During this process, $\alpha_v\beta_3$-integrin tailored expressed on the surface of ECs play a key role, by providing them with the ability to adhere to the ECM, by interacting with proteases, and modulating the activity of angiogenic factors. $\alpha_v\beta_3$-integrins are receptors susceptible to Arg-Gly-Asp (RGD), i.e. a peptide motive present in many matrix components (among others fibrinogen and fibronectin), that favor the cell adhesion on the ECM and so play a pivotal role in cell migration. Although integrin activity is usually correlated to the mechanical interaction between EC and ECM, the inhibition on

the newly formed blood vessel birth played by its antagonist proves that these adhesion molecules are significant for the good success of the sprouting angiogenesis itself [91].
After migration and proliferation, ECs have to assemble and forming new nascent tubes (third stage). Assemble is roled by endothelial cell-cell contacts (favor, for example, by the transmembrane glycoprotein E-selectin). Finally, progressive remodeling of the nascent EC tubes and the recruitment of mural cells provide stability and regulate perfusion. In fact, ECs nascent tubes are not stable and recruitment of mesenchymal cells (which can differentiate in pericytes) is necessary in order to consolidate them. Precisely, recruitment is triggered by specif growth factors (e.g. Platelet-derived growth factor PDGF, particularly the PDGF-BB isoform), that are also released by ECs [94] in their microenvironment. Therefore, the ECs tubes uncovered by pericytes are dismantled whereas those covered are progressive stabilized [91].

2.4.3 Endothelial cells interactions during angiogenesis

All the cells have a continuous talk with the microenvironment circling them. Usually, an EC located in the inner wall of blood vessels actively interacts with different biological entities: other cells (e.g. other ECs, Vascular Smooth Muscle Cells), the ECM, and the blood flow and everything that is carried by it. These ways to interface with the environment, which imply different ways of the single EC to interplay with the surrounding microenvironment (cell-cell interactions, cell-matrix interaction, fluid-structure interactions), involve a huge degree of chemical and physical interactions engaged during the angiogenic process.

It has to be clear that frequently, in biology, the shape of a biological entity is intertwined with its function. In such a framework ECs are no exception. In fact, ECs that cover the inner side of blood vessels, are in closed contact with the flowing lumen, which, therefore, can exchange mechanical cues with these kinds of cells [32]. Precisely, ECs present an elongated form inside the blood vessels, namely aligned with the blood flux direction. Instead, they often assume a cuboidal shape, near branches, and bifurcations manifesting none preferential proclivity [44].
Normally, ECs can undergo high-shear laminar flow in straight sections of the arterial organization, as well as low-shear disturbed flow upon the arterial branches [32]. The latter because of the existence of secondary vortices flows could be also the causes of atherosclerosis and endothelial dysfunction [32].

Concerning in-vitro experiments studying SFs inside human aortic endothelial cells (HAECs), it is possible to reproduce the above mentioned in-vivo conditions (disturbed flow, and laminar flow), by means of a microfluidic system, as well as the static condition on Petri dishes [32]. Interestingly, SF inside HAECs subjected to laminar flow are directed as the flux itself (orientation angles among 0–30°) [32]. Vice-versa, with disturbed flow conditions, SF are orthogonally oriented with respect to the flow (orientation angles among 60–90°) [32]. Finally, according to statical condition, it is possible to ascertain that SF are randomly oriented [11, 32] Moreover, a slow return at the random expression of SF is expected when an interruption of the mechanical stimulus (shear load) is applied [11].

Membrane tension susceptibility of the ECs and muscle cells are insignificant either at the stretching that at osmotic swelling [29]. Therefore, applying a load on the plasma membrane an instanta-

neous membrane tension buffering happens. This is due to the ATP and the flattening of caveolae (actin-independent). Interestingly, flattening is joined with a quick dismantling of the caveolar architecture [29]. This is corroborated by free diffusion of caveolins, in less a 30 s, in the cell membrane [29]. Eliminating the load on the lipid bilayer, we can see a regained of the initial concentration of caveolae, letting us imagine a reversible behavior [29]. Nonetheless, if disassembly is guided only from the mechanical state of the membrane, reassembly is actin- and ATP-dependent [29]. Importantly, caveolar flattening is actin cytoskeleton independent only in the first few minutes of the mechanical stress. Yet, it has been shown that SF as well can control trafficking and caveolae flattening [29]. Finally, it is possible to assist after a long time of observation, to a rearrangement of the cytoskeleton, behavior that surrogate caveolae clearing why not all caveolae are solicited at the beginning of the load history [29].

Interestingly, it is has been observed in bovine aortic ECs that, in an integrin-kinase-dependent and src kinase-dependent way, Cav1 is engaged and phosphorylated with integrin complexes [29]. Not only that, Cav1 and caveolae are also pivotal in murine intact blood vessels where they support either the long-term mechano-transduction that the rapid one [29]. Moreover, the persistent effect of the blood shear flux is the cause of an increment of the density of caveolae on the ECs surface. This phenomenon is connected with the triggering of MAPK and endothelial nitric oxide synthase (eNOS) [29]. Caveolae are generally prominently present in many kinds of cells subjected to mechanical constraints/loads and, among these, there are surely the ECs that cover the inner wall of the in-vivo blood vessels, which are undergone shear stress owing to blood flux [29].

Most notably, it has been observed [95] how, during the adhesion of non-embedded bovine aortic ECs on Formvar-coated gold grids, a restructuring of the cytoplasmic system happen [95]. Particularly, it has been denoted four successive phases. During the first one cell membrane spread and of the unstructured cytoplasmic matrix occurs [95]. Nextly, propagation of microfilament bundles, microtubules happens, namely the diffusion of the cytoplasmic fiber system (second phase) [95]. After that, we witness the alinement of microfilament bundles contextually with the microtubules arrangement as radial tracts (third stage) [95]. Finally, following these stellate tracts, a centripetal shift of the organelles has been observed (last stage) [95].
Anyhow, among all the ways that ECs can communicate with the environment, we are interested in that mediated by the receptor-ligand chemical interaction, particularly VEGFR2-VEGF-A/gremlin and integrin-fibronectin/fibrinogen.
We have already mentioned how ligands play a pivotal role in the mechanism of chemotaxis, haptotaxis, and mechanotaxis; namely, those mechanisms that rule the directional migration of ECs during angiogenesis following a gradient of soluble chemoattractants, immobilized ligands, and mechanical forces, respectively [31] (chapter 1), [96].

According to this, in the current thesis, we will prioritize the EC-ECM interaction (and at its experimental modeling) stressing how the molecular interactions between transmembrane proteins on the cell membrane of an EC and the molecules embedded in the ECM are the basis of the processes of formation of new blood vessels. In fact, ECM plays a pivotal role in every phase of angiogenesis provide structural supports to ECs, conferring molecular signaling necessary to guides the new blood vessel formation, and offering itself as an immobilizing scaffold for cytokines [86].

2.4.3.1 The role of ECM during angiogenesis

It has been proved that more than half of the mass of the blood vessels wall is made by ECM [46]. Particularly, ECM is placed within the space among the tunica layers and cells and, it is generated (or better synthesized) by ECs VSMCs and fibroblasts. Interestingly, in a capillaries structure, the basement membrane (i.e. a narrow stratum of ECM) is positioned among ECs and pericytes [46]. Accordingly, ECs can be subjected to various types of stimulations that require the mediation of integrins (e.g. integrin-collagen I interactions role the new formations of capillaries [46]); for this reason, different integrins, corresponding to diverse physio/pathological conditions, can provide the required flexibility to organize the cellular response.

During in-vitro experiments (despite the absence of in-vivo validations) it is possible to attest the ability of concentration gradients of constituent elements of the ECM (haptotaxis) to induce cell motility of ECs independently by angiogenic cytokines [86]. In the end, it is possible to state that migration of ECs during sprouting angiogenic mechanism, is connected to a reaction to either a gradient of angiogenic cytokine (chemotaxis) that a gradient of ECM constituents (haptotaxis) [86].

ECM does not play only the role of structural supports for the cellular components but also is crucial in the initializing of several stimuli (e.g. biochemical and biomechanical) that are pivotal for many biological processes both physiological that pathological [31] (page 8). In fact, ECM plays the role of a storage reservoir of growth factors for vasculature cells [46]. Such behavior happens by means of sequestering, binding, and finally accumulating available signaling molecules by ECM, that according to this kind of attitude, acts just as a "reservoir".

Although the pivotal role cover by ECM during ECs proliferation, migration, and survival has been demonstrated, there is little clarity in the identification of the single contributes of ECM members. Nevertheless, experimental evidence shows how multiple ECM constituents can cooperate in order to improve the promotion of ECs survival [86].

As is evident, angiogenesis follows a well-documented, in the current scientific literature, trigger mechanism. Nevertheless, although the importance of the role of VEGFR2 in the management of the angiogenic stimulus is widely recognized, the understanding and identification of the laws that govern its dynamic behavior on the cell membrane, during the activation phase of ECs, are still poorly understood.

2.5 Mathematical models on the cellular mechanics

Receptor-mediated interplay with the ECM, drive cell migration, spreading, and adhesion in the course of processes such as wound healing as well as tissue regeneration. Cell shape, motility, growth, and proliferation, evolve, hence, by means of the mutual interactions among ECM, growth factors, and cytokines. Also, cell morphology is dictated by tractions exerted by cellular receptors on the ECM, highlighting the important role of cell-substrate interactions in cell activities [97].
Mechanical aspects of cell deformation have been treated more extensively by many authors. The mechanical response of the cell during its spreading has been attributed merely to the lipid mem-

brane (by means of the underlying cortical actin network) in several contributions. In the so-called *active gel theory* [98, 99, 100, 101], the lipid membranes are regarded as two-dimensional liquid crystals whose structure is conferred by the oriented lipid molecules, through an approach apparently originated in [102]. General cell-substrate contact conditions have been developed for lipid membranes interacting with curved substrates along their edges in [103], through a variational energy principle. The same authors extended these ideas to the electromechanics of lipid bilayers in [104], accounting for flexo-electricity so to include deformations in the presence of applied electric fields, as well as to include the effects of a continuous distribution of transmembrane proteins [105].

Cell adhesion is one of the most common and widely studied biological processes wherein receptor dynamics cover a significant role. Both cell-cell and cell-substrate adhesion can be likewise analyzed, insofar a fixed surface can be viewed as either a tissue substrate or as the symmetry plane between two identical cells with compatible binders [106]. To the best of our knowledge, among the first works on cell adhesion, the pioneering studies of Bell [107] and co-workers [108] have paved the way to study and develop models devoted to describe such biological process. Here, the variation in receptors density was accounted in a thermodynamic framework for cell-cell adhesion mediated by receptor-ligand binding, and the competition between attractive receptor-ligand interactions and repulsive electrostatic interaction was investigated in the adhesion process. During those same years, Goldstein, Wofsy, and Bell [109] studied the interaction of low-density lipoprotein (LDL) receptors with coated pits and compared the presented theoretical study with experiments. They evaluated both the 2-D diffusion limits for the forward rate constant for the binding of an LDL receptor to a coated pit on a human fibroblast and the meantime an LDL receptor spends on the cell surface before being captured by a coated pit. It is worth noting that, few months later the first work proposed by Bell [107], Dembo and Goldstein presented a theoretical study of equilibrium binding of symmetric bivalent haptens to cell surface antibody wherein 2-D antibody molecules diffuse in the plane of cell surface not intersecting to each other [110].

Lee et al. [111] studied the balance between electromigration and mutual diffusion of cell surface receptors, by means of an application of a sinusoidal electric field. A finite-difference mathematical model was proposed for describing charged receptor transport in the plane of the plasma membrane. Boulbitch et al. [112] accounted for receptor dynamics in the study of a giant vesicle membrane adhesion on a substrate. The displacement of the front of the tight adhesion region was analyzed showing a time dependence on ligands concentration. Freund and Lin [106] analyzed the process of transient growth of an adhesion zone due to receptors dynamic, starting from an initially curved elastic plate, by adopting the constitutive assumption that receptors diffuse at a speed proportional to the local gradient in chemical potential. Such a model was also adopted for investigating the expansion of a circular adhesion zone by accounting for insufficient receptors density to overcome the repulsive barrier which provides resistance to cell adhesion [113]. Based on this framework, the adhesive receptor-ligand interactions were taken into account by proposing the adhesion-traction separation model, which provides an additional contribution to the flux of receptors otherwise merely governed by Fickian diffusion. Indeed, the role of non-specific force was here accounted for considering a driving force for the recruitment of receptors towards the adhesion front. It was therefore presumed that the diffusion flux as a consequence of the attractive traction exerted by the ligands on the substrate is proportional to the traction tangential to

the membrane surface [114]. Such model, developed for studying vesicles adhesion, was further enriched [115] for performing computer simulations of attachment-detachment of a red blood cell to a substrate, and a novel chemical reaction equation was proposed for specific receptor-ligand interactions. A similar assumption concerning a flux of receptors driven by a force was adopted by Golestaneh and Nadler [116] for studying adhesion and deformation of small biological cells. Here, receptor diffusion due to receptor-receptor interactions was assumed to be driven by Fick's Law, whereas a nonlinear binding force, based on charge-induced dipole interaction, was assumed to model the flux generated by receptor-ligand interactions. Additionally, the effect of the presence of receptors on the deformation and adhesion of the cell membrane was accounted for through the introduction of spontaneous area dilation.

Mechano-sensitive cellular contractility models that account for the stress fibers (SFs) reorganization in the bulk of the cell have also been proposed in a number of phenomenological models (to cite a few see the large repertoire of Deshpande and co-workers [117, 118, 119, 120, 121, 122, 123], as well as [124, 125]).
In 2008 Deshpande and co-workers proposed a biomechanical model for coupling cell contractility with the generation of focal adhesion (FA) [118], which was then widely used, and broadened, in later years. Here, the diffusion of low-affinity integrins along the cell membrane was accounted for in a three-fold FA model wherein low and high-affinity integrins are in thermodynamic equilibrium, low-affinity integrins diffuse on the cell membrane and the contractile forces generated by the stress fibers (SFs) are in mechanical equilibrium and change the free energies of the integrins. The mobility of low-affinity integrins was likewise taken into account in devising a signaling model, based on the generation of IP_3 molecules during focal adhesion growth, for coupling stress fiber contractility and mechano-sensitive focal adhesion models [126]. The same framework was used by Ronan et al. [122, 123] for investigating and simulating the role of the actin cytoskeleton in compression resistance of cells and cell adhesion.
Vigliotti et al. [127] investigated the response of osteoblasts on grooved substrates by means of a model that accounts for the cooperative feedback between intracellular signaling, FA development, and SF contractility. This last one thermodynamically based SF model [127] was adapted by McEvoy et al. [128] for implementing a non-local finite element setting, also accounting for global conservation cytoskeletal proteins within the cell, global conservation of binding integrins on the cell membrane, and adhesion limiting ligand density on the substrate surface. With the aim to summarize the model proposed in Deshpande et al. [119, 129], and to show some results obtained with it, McMeeking and Deshpande [121] presented a user element bio-chemo-mechanical model installed in a finite element code for simulating cell behavior in vitro. Such model targets contractility, adhesion, signaling, and cytoskeleton formation and, focused on actomyosin SFs, remodeling. It has been used to describe some experiments either of inspiration for the development of their models or that have been successfully simulated.

Receptors dynamic along cell membrane is also involved in other biological phenomena, e.g. in endocytosis and exocytosis, a crucial process of entering and leaving of viruses and bioparticles in animal cells. In this regard, based on the mathematical framework developed in [106, 113], Gao, Shi and Freund [130], presented a receptor-mediated endocytosis study for analyzing how a cell membrane with diffusive mobile receptors wraps around a cylindrical or spherical particle coated with compatible ligands. A similar study was performed by Decuzzi and Ferrari [131] for accounting for the endocytosis of non-spherical particles, considering elliptical cylindrical ones, in

a continuum energetic approach. The same model proposed in [130] was re-presented by Gao in an overview aimed to develop a systematic, multiscale theoretical framework for modeling uptake and release of nanoparticles in human and animal cells [132]. To the best of our knowledge, the latest work concerning receptor driven endocytosis regards a numerical simulation of the influence of the binder mobility in the viral entry driven by receptor diffusion, described by a diffusion differential equation with two boundary conditions, *i.e.* the former for the flux balance and the latter for energy balance at the adhesion front [133].

Of the most recent papers wherein receptor dynamics along the cell membrane was accounted, the hypothesis that cell surface-associated caveolae may participate in mechanotransduction was investigated by Shin et al. [134]. Exploiting, at low Reynolds numbers, the equation of motion for the flow of plasma and presuming no slip-condition on the membrane, they examined the fluid flow in and around caveolae. Liberman et al. [135] elucidated the interactions between single cells by means of the use of an agent-based model. They implemented a realistic cell-cell interaction model based on biophysical principles, validated the model against the results of a mean-field model of Notch receptors and ligands in two neighboring cells, and tested the effect of filopodial geometry on Notch signaling. Carotenuto et al. [136], in order to investigate how ligand-receptor interactions along with the cell membrane trigger raft formation, developed a multiphysics approach that relied on the interaction among energetics, multiscale geometrical changes, and mass balance of active G-protein-coupled receptors (GPCRs), and Multidrug Resistance Proteins (MRPs). Based on the fact that lipid rafts often serve as an entry port for viruses, such a model may help in better understanding membrane-mediated phenomena such as the novel debated COVID-19 virus-cell interaction. Bubba et al. [137] proposed a discrete model of chemotaxis that takes into account possible alterations in cellular motility. Here, the coupling between a discrete-time biased random walk on a regular lattice and a discrete balance equation for the concentration of chemoattractant governs cell movement.

Two recent publications [138, 139] have been devoted to the modeling and simulation of VEGF receptors recruitment in angiogenesis, adopting strong simplifying assumptions on the mechanics of the lipid membrane. Specifically, it was taken as rigid, surrogating the effects of the change in geometry through a suitable fictitious source term of the ligand within the chemo-diffusive equations. Such model has been recently broadened in [140] wherein the concurrent membrane dynamics of both VEGFR-2 and integrins was accounted in order to identify how ligands stimulation induces the polarization of receptors in cell protrusions and in the basal aspect of endothelial cells plated on a ligand-enriched extracellular matrix.

The present thesis deals with the motion of the same receptors on a cell membrane, accounting for different physics (chemical affinity, mechanical deformations, transport on the membrane, long and short-range electronic interactions), and for the mechanical deformation in the bulk of the cell. Whereas all processes that take place on the membrane are influenced by the bulk deformation, two-ways coupling may not occur, i.e. the mechanical deformation of the nucleus and of the cytosol may not be significantly influenced by receptors recruitment on the membrane.

Part II

Model formulation with a "surrogated" mechanical description

Recent technological advances made available a large number of experimental data in biology. On one hand, this is a motivation for great excitement. On the other, it pushes interpretative abilities to the limit. For this sake, the ability of multi-physics models to predict the time-space evolution of complex processes and to unravel their intimate nature is more and more becoming of pivotal importance in science[3].

In the present part of the thesis, we provide a contribution in understanding how VEGFR-2 and integrins regulate tumor angiogenesis, by means of a chemo-transport-mechanical model, set in the thermodynamics of continua, that actually is an extension of our earliest formulations ([140]) shown in the works [138], [139].

This model couples three chemical reactions (see 3.1.1) to continuity equations for mass (see 3.1.2), energy, and entropy (see 3.2.1 and 3.2.2, respectively). Thermodynamic restrictions (Clausius-Duhem inequality) set limits for the Helmholtz free-energy (see 3.2.3), and ultimately, on constitutive relations (see 3.2.4).
Two simplifying assumptions are taken in this large section of the thesis and will be removed in the next: *surrogated mechanics* (see 3.1.3) and *infinitely fast kinetics* (see 3.3). By the first one, the cell-substrate contact dynamics is surrogated by means of a fictitious term in the mass balance equations of the ligands. The second makes chemical reactions always at equilibrium; such a scenario stems from experimental evidence, which shows that the time required to reach the chemical equilibrium is orders of magnitude lower than the timescale of all other physical processes.

The formal derivation of the governing equations has been achieved both in strong and weak forms (see 3.4.1, 5.1, and 5.2). Such a weak form naturally leads to a semi-discrete problem, by approximating the space-time unknown scalar concentration fields into suitable finite-dimensional spaces, thus rephrasing the weak form into a system of ordinary differential equations, whose solution is an approximation of the exact solution for each instant. A Backward Euler scheme for the finite element approximation of the chemo-transport model has been implemented. To avoid poor computational accuracy, numerical simulations require a very small time discretization step, thus leading to a very high computational cost in properly capturing the spreading process. The time-dependent partial differential equations have been therefore rephrased in order to apply higher-order time integration schemes. The non-linear discretized equations have been implemented in the deal.ii framework (https://www.dealii.org/), an open-source $\mathsf{C}++$ software library that supports the creation of high performance computing finite element codes. The different time scales that characterize the chemical, mechanical and diffusive phenomena lead to a clear identification of three predominant phases of the trapping of free receptors by the corresponding ligands. The time-space evolution of the receptor dynamics has been discussed at large in the simulation chapters (3.4 and 5).

Specifically, in the first chapter of this part of the thesis (chapter 3), we present the upgrade of the multiphysics model at the case wherein manifold chemical reactions are involved among the proteins belonging to the lipid bilayer and those in the extracellular matrix. In the second one

[3]What is said here is closely connected what Professor Gretar Tryggvason (Department Head Mechanical Engineering and Charles A. Miller Jr. Distinguished Professor at Johns Hopkins University) has declared in his famous citation: "*Simple, single-physics problems, have already been solved by our generation*".

(chapter 3.4), instead, we test the numerical capacity of this model, studying the in-silico results without any comparison with experimental outcomes. Over the course of the third chapter (chapter 4), instead, we will introduce some experimental results such as the time-lapse microscopy analysis adhesion assays rather than FRAP analysis, in order to identify what are the numerical values of the material parameters and data that we want to reply by means of in-silico analysis. Finally, in the last chapter (chapter 5), through a co-design among numerical and experimental resultants, we are able to provide further insight into identifications on the laws that rule the receptor-dynamics of VEGFR2 and integrin during angiogenesis.
Intriguingly, equations that govern the problem of the relocation of VEGFR-2 and integrin motion on the membrane, driven by their specific ligands, will ultimately be expressed in a strong and dimensionless formalism, in terms of four space-time unknown scalar concentration fields in the chapter 3.4, while will be rephrased in a six scalar concentration fields in the chapter 5.

Chapter 3

A model of integrin and VEGF receptors recruitment on endothelial cells

Uncontrolled release of angiogenic growth factors can lead to EC activation in angiogenesis-dependent diseases. Growth factors and extracellular matrix components chemical binding leads to the formation of immobilized ECM-bound complexes. Among these, VEGF-A [69] and gremlin [51, 138] are produced by tumor or inflammatory cells and accumulate in ECM, in order to interact with its tyrosine kinase receptor VEGFR-2 and causing its polarization. Moreover, ECM-anchored VEGF or gremlin induces the recruitment of VEGFR-2 at the basal portion of the basal membrane, receptor dimerization, and the activation of intracellular signaling through a series of phosphorylations.

Actually, VEGFR-2 response could be affected by adhesion to different kinds of ECMs [52], [69]. Such distinctive features may be attributed to the VEGFR-2 association with different transmembrane proteins, which form distinct multi-molecular complexes that interact with cytosolic transducers. Particularly, we are interested in $\alpha_v\beta_3$ integrin, which participates in the full activation of VEGFR-2 triggered by gremlin. It has been proved, in fact, that integrin participates in VEGFR-2 full activation, sparking the propagation of intracellular signaling cascades that affect the cell mechanical response. This correlation shows to be particularly efficient in prolonging and strengthening the intracellular signal released by the VEGFR-2-Ligand complex. Intriguingly, in this macromolecular complex, $\alpha_v\beta_3$ integrin is found in a low-affinity configuration. $\alpha_v\beta_3$ integrin also mediates directly cell-matrix interactions by means of specific receptor-ligand (e.g. fibrin(ogen), fibronectin) interaction, where usually it manifests a high-affinity configuration. In fact, similarly to VEGFR-2, integrin transmits "outside-in" signals to the cell, which trigger a large array of intracellular signaling events, including the organization of the mechanical response of the EC.

Although the role of productive crosstalk between VEGFR-2 and $\alpha_v\beta_3$ in the angiogenic response is well characterized in terms of intracellular signaling, ECs migration, and proliferation, the effects of complex formation on the membrane dynamic of both receptors is still missing.

Hence, starting from imaging experimental data and a rigorous thermodynamic approach [141], we modeled in recent publications [138], [139] the relocation of VEGFR-2 on ECs membrane during the angiogenic process. The developed chemo-transport-mechanics model captures the VEGFR-

2 recruitment at the basal portion of EC inside active blood vessels and highlights three different phases in receptor relocation, driven by three main regulatory factors: *extracellular ligand/receptor chemical interaction, cell mechanical deformation, and receptor diffusion*.

Particularly, In the present part of the chapter, we aim at theoretically modeling the interplay between VEGFR-2, $\alpha_v\beta_3$ in its different conformations, VEGFR-A or gremlin, and ECM components (e.g. fibronectin and fibrinogen). The receptor dynamics is combined with the cell mechanical deformation and with the chemical interactions in the framework of the thermodynamics of continua [142].

Nomenclature

Notation

Vectors $\vec{a}$ will be denoted by an over-right-arrow, second-order tensors $\boldsymbol{A}, \boldsymbol{a}$ by bold face. This notation does not apply to operators.

Operators

- the symbol $\mathrm{tr}[-]$ denotes the trace operator
- the symbol $\mathrm{div}[-]$ denotes the divergence operator in the current configuration, i.e. $\mathrm{div}\left[\vec{f}\right] = \partial f_i/\partial x_i$
- the symbol $\mathrm{div}_{\mathcal{P}}[-]$ denotes the divergence operator restricted at the surface $\mathcal{P}$ in the current configuration
- the symbol $\mathrm{Div}[-]$ denotes the referential divergence operator, i.e. $\mathrm{Div}\left[\vec{f}\right] = \partial f_i/\partial X_i$
- the symbol $\mathrm{Div}_{\mathcal{P}_R}[-]$ denotes the referential divergence operator restricted at the surface $\mathcal{P}_{\mathcal{R}}$
- the symbol $\nabla[-]$ denotes the gradient operator in the current configuration
- the symbol $\nabla_{\mathcal{P}}[-]$ denotes the gradient operator restricted at the surface $\mathcal{P}$ in the current configuration
- the symbol $\mathrm{Grad}[-]$ denotes the referential gradient operator
- the symbol $\mathrm{Grad}_{\mathcal{P}_R}[-]$ denotes the referential gradient operator restricted at the surface $\mathcal{P}_{\mathcal{R}}$
- the symbol $\mathrm{curl}[-]$ denotes the curl operator in the current configuration
- the symbol $\mathrm{Curl}[-]$ denotes the curl operator in the referential configuration
- the symbol $\Delta[-]$ denotes the Laplace operator in the current configuration
- the symbol $\Delta_{\mathcal{P}}[-]$ denotes the Laplace operator restricted at the surface $\mathcal{P}$ in the current configuration
- the symbol $\bigtriangleup[-]$ denotes the Laplace operator in the referential configuration
- the symbol $\bigtriangleup_{\mathcal{P}_{\mathcal{R}}}[-]$ denotes the Laplace operator restricted at the surface $\mathcal{P}_{\mathcal{R}}$ in the referential configuration
- the symbol $\cdot$ denotes the single contraction of two vectors
- the symbol : denotes the double contraction of two tensors
- the symbol $\otimes$ denotes the tensor product between two vectors
- the symbol $\times$ denotes the vector or cross product between two vectors

- the symbols $||\vec{a}||^2$, $||\boldsymbol{A}||^2$ denote the squared norm of vector $\vec{a}$ or tensor $\boldsymbol{A}$
- the symbol ^{T} denotes transposition of a tensor
- the symbol $^{-1}$ denotes the inverse of a tensor

Variables and fields

- the symbol t denotes time
- the symbol $\Omega(t) \in \mathbb{R}^3$ denotes a volume that advects, where referential counterparts inherit the subscript $_R$
- the symbol $\partial\Omega(t)$ denotes the surface of $\Omega(t)$, where referential counterparts inherit the subscript $_R$
- the symbol $\mathcal{P}(t) \subset \partial\Omega(t)$ denotes a part of $\partial\Omega(t)$, where referential counterparts inherit the subscript $_R$
- the symbol $\partial\mathcal{P}(t)$ denotes the boundary of $\mathcal{P}(t)$, where referential counterparts inherit the subscript $_R$
- the symbol $\vec{v}_{adv}(\vec{x},t)$ denotes the velocity of advection at place $\vec{x}$ and time t
- the symbol $\vec{n}(\vec{x},t)$ denotes the outward normal at place $\vec{x}$ and time t
- the symbol $\vec{t}_{\perp}(\vec{x},t)$ denotes the normal to the curve $\partial\mathcal{P}(t)$ at a generic place $\vec{x}$ and time t
- the symbol $\vec{t}_{||}(\vec{x},t)$ denotes the vector tangent to the curve $\partial\mathcal{P}(t)$ at a generic place $\vec{x}$ and time t
- the symbol $\boldsymbol{l}(\vec{x},t)$ denotes the velocity gradient at place $\vec{x}$ and time t
- the symbol $\boldsymbol{d}(\vec{x},t)$ denotes the stretching at place $\vec{x}$ and time t
- the symbol $\boldsymbol{F}(\vec{X},t)$ denotes the deformation gradient at point $\vec{X}$ and time t
- the symbol $\boldsymbol{C}(\vec{X},t)$ denotes the right Cauchy-Green tensor at point $\vec{X}$ and time t
- the symbol $\boldsymbol{P}(\vec{X},t)$ denotes the first Piola stress tensor at point $\vec{X}$ and time t
- the symbol $J(\vec{X},t)$ denotes the determinant $\det[\boldsymbol{F}]$ at point $\vec{X}$ and time t
- the symbol $j(\vec{X},t)$ denotes the areal jacobian at point $\vec{X}$ and time t
- the symbol $\vec{n}_R(\vec{X},t)$ denotes the outward normal at point $\vec{X}$ and time t
- the symbol $\mathbb{1}$ denotes the identity matrix

- the symbol c_e denotes the molarity of a generic species e
- the symbol ς_E denotes the the rate in number of molecules per unit area per unit time at which species e is generated by sources.
- the symbol s_e denotes the rate of generation/depletion of molecules e per unit volume per unit of time, non-correlated with the chemical reaction
- the symbol $\vec{h}_e$ denotes the molar flux of a generic species e
- the symbol μ_e^u denotes the change in specific energy provided by a unit supply of moles of a generic species e
- the symbol μ_e^η denotes the change in specific entropy provided by a unit supply of moles of a generic species e
- the symbol μ_e denotes the chemical potential of a generic species e
- the symbol $c_e^{\max}$ denotes the saturation limit of a generic species e
- the symbol ϑ_e denotes the non-dimensional ratio between the concentration of a generic species e and $c_e^{\max}$
- the symbol P_e^e denotes the Peclet number of a generic species e
- the symbol w denotes the reaction rate of a reaction

- the symbol A denotes the affinity of a reaction
- the symbols k_f and k_b denote the kinetic constants of the forward and backward reaction
- the symbols $\Delta G^0(T)$ denotes the standard Gibbs free-energy of formation
- the symbols K_{eq} denotes the equilibrium constant

Constants and parameters

- the symbol κ_B denotes the Boltzmann constant
- the symbol $\mathcal{N}_A$ denotes the Avogadro's number
- the symbol R denotes the universal gas constant
- the symbol $\mathbb{\mu}$ denotes the receptor mobility
- the symbol $\mathbb{D}$ denotes the receptor diffusivity
- the symbol $\overline{\chi}$ denotes the exchange parameter
- the symbol α denotes the infinitely fast kinetics parameter

3.1 Modeling VEGFR-2 and Integrin motion is driven by their specific ligands

The equations that model the motion of integrins and VEGFR-2 on the lipid membrane are detailed in this section. The relocation of these proteins is assumed to take place merely along the lipid bilayer, i.e. internalization processes as well as the supply of proteins from the cytosol are neglected. Governing equations emanate from a chemo-transport-mechanical model in terms of balance equations coupled to thermodynamic restrictions. These two items will be separately dealt with in the next two subsections.

3.1.1 Chemical reactions

Proteins relocation could be guided by their corresponding ligands, i.e. *VEGF-A* or *gremlin* for VEGFR-2 and *fibronectin* or *fibrinogen* for integrins. The interactions between ligands and receptors are modeled as three chemical reactions, accompanied by the mass balance equations. They are defined on the cell membrane, which will be henceforth denoted with Ω.

The first chemical reaction

$$V + L_V \underset{k_b^1}{\overset{k_f^1}{\rightleftarrows}} C_1 \tag{3.1}$$

describes the interaction between VEGFR-2 (V) and VEGF-A or gremlin (L_V), which provides complex C_1 and induces a cascade of intracellular signals that ultimately lead to the activation of angiogenesis. Reaction (3.1) alone was studied thoroughly in the two publications [138] and [139].

The second chemical reaction

$$I + C_1 \underset{k_b^2}{\overset{k_f^2}{\rightleftarrows}} C_2 \tag{3.2}$$

depicts the interplay between the complex C_1, supplied by reaction (3.1), and the integrin receptors I. Reaction 3.2 ultimately provides another complex, denoted with C_2, which supports and allows the long-term VEGFR-2 phosphorylation.

The last chemical reaction that this thesis concerns with, i.e.

$$I + L_I \underset{k_b^3}{\overset{k_f^3}{\rightleftarrows}} \underbrace{I_h L_I}_{C_3} \tag{3.3}$$

accounts for the interaction between the diffusing, not engaged integrin receptors (I) with fibronectin (or fibrinogen) (L_I), which leads to the formation of complex C_3. The subscript h emphasizes that integrin molecules bound to fibronectin (or fibrinogen) within the complex C_3 are in a high-affinity state, i.e. they are transmembrane proteins that manifest modest relocation propensity on the lipid bilayer. Reaction (3.3) induces a cascade of intracellular signals, which lead to the formation of macromolecular clusters (so-called focal adhesions) through which mechanical forces and regulatory signals are transmitted between the ECM and ECs.

3.1.2 Mass balance equations

In order to include the rate of reactions (3.1) - (3.3), depicted in section 3.1.1, into appropriate mass balance equations, the three chemical reactions will be here stated in the following abstract form

$$a\mathrm{A} + b\mathrm{B} \underset{k_b}{\overset{k_f}{\rightleftarrows}} c\mathrm{C}\,, \tag{3.4}$$

where A represents a protein that is free to move on the cell membrane (e.g. receptors or transmembrane proteins), B an immobilized molecule (ligands or fixed complexes), while C is the correspondent product. Parameters a, b, and c are the specific stoichiometric coefficients. Eq. (3.4) pinpoints that the trapping mechanism presented in [141] is triggered by means of the chemical affinity between a molecule free to diffuse on the cell membrane, later trapped due to chemically binds, by a further molecule that here has mobility equal to zero.

The mass balance equation for the generic species $E = A, B, C$ is defined as follows

$$\frac{\mathrm{d}}{\mathrm{d}t}\int_{\mathcal{P}(t)} c_E(\vec{x},t)\,\mathrm{d}A = -\oint_{\partial\mathcal{P}(t)} \vec{h}_E \cdot \vec{t}_\perp\,\mathrm{d}l + \int_{\mathcal{P}(t)} \varsigma_E(\vec{x},t)\,\mathrm{d}A\,, \tag{3.5}$$

on a subpart $\mathcal{P}(t)$ of the membrane, as shown in Fig. 3.1. In eq. (3.5), vector $\vec{t}_\perp$ is normal to the curve $\partial\mathcal{P}(t)$ at a generic point $\vec{x}$ on the cell membrane. As shown in Fig. 3.1, the so-called (mobile) trihedron of Frenet is completed by the vectors $\vec{n}$ and $\vec{t}_{||}$, i.e. the cell membrane unit normal and the vector tangent to the curve $\partial\mathcal{P}(t)$, respectively. Furthermore:

- c_E is the molarity of species E (i.e. the number of molecules per unit area);
- $\vec{h}_E$ is the mass flux in terms of molecules, i.e. the number of molecules of species E measured per unit length per unit time, and is a tangent vector field on the membrane;
- ς_E is the rate in number of molecules per unit area per unit time at which species E is generated by sources.

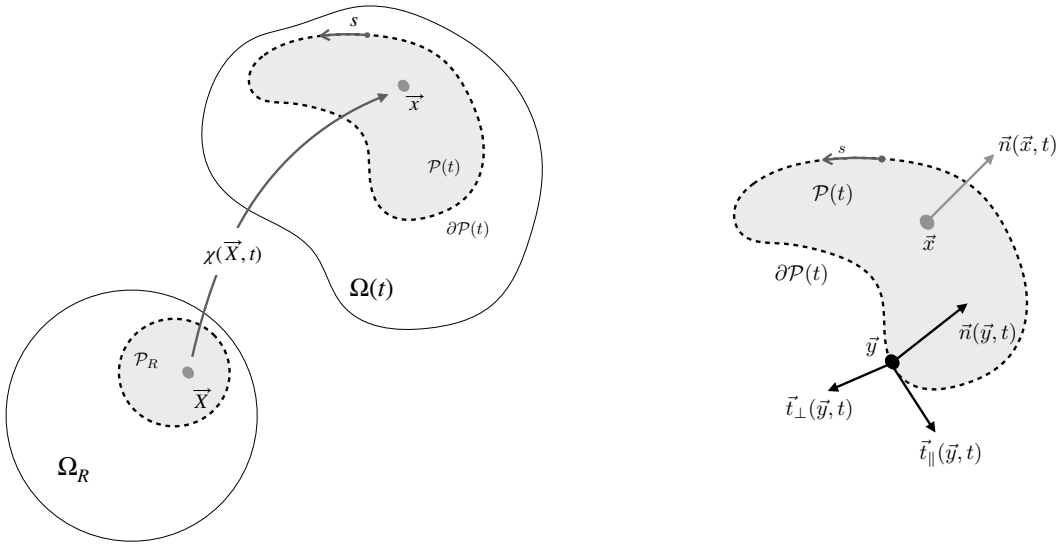

(a) (b)

Figure 3.1: Notation. (a) The reference body Ω_R and the deformed body $\Omega(t)$. Note that $\vec{x} \in \mathcal{P}(t)$ implies $\vec{X} \in \mathcal{P}_R$. (b) Frenet frame at point $\vec{y} \in \partial\mathcal{P}(t)$ and the normal vector $\vec{n}$ at point $\vec{x} \in \mathcal{P}(t)$.

Exploiting Stokes' theorem, the line integral in equation (3.5) can be written as

$$\oint_{\partial\mathcal{P}} \vec{h}_E \cdot \vec{t}_\perp \, \mathrm{d}l = \oint_{\partial\mathcal{P}} \vec{h}_E \cdot (\vec{t}_{||} \times \vec{n}) \, \mathrm{d}l = \oint_{\partial\mathcal{P}} (\vec{n} \times \vec{h}_E) \cdot \vec{t}_{||} \, \mathrm{d}l = \oint_{\partial\mathcal{P}} (\vec{n} \times \vec{h}_E) \cdot \vec{\mathrm{d}l} = \int_{\mathcal{P}} \mathrm{curl} \left[\vec{n} \times \vec{h}_E \right] \cdot \vec{n} \, \mathrm{d}A \, .$$

By denoting (see Appendix D - section D.1.1 -) as usual with

$$\mathrm{div}_{\mathcal{P}} \left[\vec{h}_E \right] = \mathrm{curl} \left[\vec{n} \times \vec{h}_E \right] \cdot \vec{n} \, ,$$

the mass balance equation can be finally recast in the form

$$\frac{\mathrm{d}}{\mathrm{d}t} \int_{\mathcal{P}(t)} c_E(\vec{x},t) \, \mathrm{d}A + \int_{\mathcal{P}(t)} \mathrm{div}_{\mathcal{P}} \left[\vec{h}_E \right] \mathrm{d}A = \int_{\mathcal{P}(t)} \varsigma_E(\vec{x},t) \, \mathrm{d}A \, . \tag{3.6}$$

It is straightforward to show that Reynold's theorem on $\mathcal{P}(t)$ (see next part for an exhaustive description of the subject, section 6.2.1) reads as follows:

$$\frac{\mathrm{d}}{\mathrm{d}t} \int_{\mathcal{P}(t)} c_E \, \mathrm{d}A = \int_{\mathcal{P}(t)} \frac{\mathrm{d}\, c_E}{\mathrm{d}t} + c_E \, \mathrm{div}_{\mathcal{P}} \left[\vec{v}_{adv}(\vec{x},t) \right] \mathrm{d}A \, , \tag{3.7}$$

where $\vec{v}_{adv}(\vec{x},t)$ is the velocity of advection at point $\vec{x}$ and time t. Replacing eq. (3.7) into eq. (3.6) leads to localize the mass balance equation (3.5) for species E at point $\vec{x}$ and time t in the form

$$\frac{\mathrm{d}\, c_E}{\mathrm{d}\, t} + c_E \ \mathrm{div}_{\mathcal{P}}\left[\vec{v}_{adv}(\vec{x},t)\right] + \mathrm{div}_{\mathcal{P}}\left[\vec{h}_E\right] = \varsigma_E(\vec{x},t) \ , \tag{3.8}$$

which can be pulled back to a reference configuration using standard arguments of continuum mechanics [142] as follows

$$\frac{\partial c_{E_R}}{\partial t} + \mathrm{Div}_{\mathcal{P}}\left[\vec{h}_{E_R}\right] = \varsigma_{E_R}(\vec{X},t) \ , \tag{3.9}$$

where the subscript $_R$ denotes quantities in the reference configuration.
Separating in the contribution $\varsigma_{E_R}(\vec{X},t)$ the source term given by the chemical reaction (3.4), from other possible physical phenomena, we derive:

$$\frac{\partial c_{E_R}}{\partial t} + \mathrm{Div}_{\mathcal{P}}\left[\vec{h}_{E_R}\right] = s_{E_R}\left(\vec{X},t\right) - e\ w_R^{(3.4)}\left(\vec{X},t\right) \ , \tag{3.10}$$

where:

- $w_R^{(3.4)}$ is the reaction rate of the reaction (3.4);
- s_{E_R} represents a rate of generation/depletion of molecules E per unit volume per unit of time, non-correlated with the chemical reaction (3.4).

Parameters $e = a,\ b,\ -c$ represent the stoichiometric coefficients that account for the positive sign for reactants and negative for the product (see [143]).

In this part of the thesis, however, we will follow a different path of reasoning, borrowed from [138] and [139].

3.1.3 Surrogated mechanics

Describing the evolution of the geometry of the cell membrane is a complex task, a result of intricate biological phenomena that couple purely membrane events with others arising in the bulk of the cell. From a mechanical point of view, this corresponds to consider two limit behaviors, namely, consider either the cell membranes like the surface of a deformable body or a stand-alone structure with shell behavior (see 2.5).

In the first case, we are implicitly assuming that the cell membrane evolution is the mere result of deformation that arises from the bulk of the cell. Usually, these deformations are the result of the interaction between an active and passive behavior of the activity of the cell. The first one is the result of the cytoskeleton machinery (e.g. stress fibers activity). The second one is due to the mechanical properties of the individual components of the cell which passively respond to external loads as in usual, non-active, materials.

In the second case, it is implicitly meant that the cell membrane has specific mechanical properties, usually conferred by the so-called cell cortex, i.e. a protein net in support of the cell membrane

itself.

However, the cell is living matter, its composition and its attitudes adapt according to the state of the surrounding environment which, in turn, is modified by the behavior of the cell itself, in a continuous dance that aims at the dynamic equilibrium called homeostasis. Hence, the problem is not to establish which of the two models is the most correct, rather the most suitable to describe the behavior of the type of cell of interest, accounting of the specificity of the biological process to be described. For the current part and for the rest of the thesis, we believe that the first case, which considers the cell membrane as the surface of a deforming body, the most suitable.

The geometrical evolution of the cell during its spreading on the substrate is matched with the relocation of receptors along the lipid membrane. Mathematically, the coupling occurs through the velocity of advection in eq. (3.8) and through the mass supply $\varsigma_{E_R}(\vec{X},t)$ in eq. (3.9). Specifically, the latter accounts for the spreading by setting the amount of the cell geometry that, being in contact with the substrate, interacts with ligands, ensuring that the chemical reaction (3.4) takes place.

Notwithstanding, in this part, we adopt a paradigmatic simplification in the study of the mechanical behavior of an EC. Accordingly, we decided to introduce the hypothesis of surrogate mechanics, already assumed in the works [138, 139] and [140]. Such assumption will be removed in Part III. Surrogate mechanics means that the evolution of the cell-substrate contact dynamic is codified by means of a calibrated source of ligands inserted in the mass balance equations. In such a view, the geometrical evolution of the cell membrane will be neglected and the cell maintains the shape of a rigid sphere for the duration of the analysis. Henceforth, following the standard imposed by the surrogated mechanics hypothesis,, the subscript $_R$ will be neglected, inasmuch, under this assumption, there is no difference between imposing the mass balance equation in the current or in the reference configuration ($\vec{x} \equiv \vec{X}$).

Therefore, a priori given supplies of ligands L_V and L_I (see the reactions (3.1) - (3.3)), calibrated from experimental investigations of the mechanics of cell spreading, implicitly considers the membrane-substrate contact dynamics. We chose this form[1]

$$s_{L_V}(x,t) = \frac{\overline{c_{L_V}}}{\bar{t}}\mathcal{H}\left[t-\frac{x}{v}\right]\mathcal{H}\left[\bar{t}-t+\frac{x}{v}\right], \tag{3.11a}$$

$$s_{L_I}(x,t) = \frac{\overline{c_{L_I}}}{\bar{t}}\mathcal{H}\left[t-\frac{x}{v}\right]\mathcal{H}\left[\bar{t}-t+\frac{x}{v}\right], \tag{3.11b}$$

where:

- $\overline{c_{L_V}}$ and $\overline{c_{L_I}}$ are the concentrations of substrate immobilized ligands;
- $\mathcal{H}[-]$ is the Heaviside step function;
- t_f is the time experimentally required to a complete mechanical deformation;

[1]Following this path of reasoning, the identification of a reference configuration is unnecessary. Therefore, the suffix $_R$ will be removed from now on. The notation $\mathrm{div}_{\mathcal{P}}[\,]$ is equivalent to $\mathrm{Div}_{\mathcal{P}}[\,]$.

- $v = \dfrac{\pi r}{2t_f}$ is the velocity of the mechanical deformation (assumed constant up to t_f);
- r is the cell radius;
- $\bar{t} \ll t_f$ is a parameter that identifies a finite time required for chemical binding;
- x is the curvilinear abscissa on the meridian plane of the sphere;

By this approach, the relocation of receptors can be solved without numerical simulations of the real spreading process. Whereby questionable quantitative response is expected, the physics of the relocation of receptors is captured with fidelity.
Application of the surrogated mechanics approach to equations (3.4) and (3.10) finally leads to the following set of paradigmatic mass balance equations

$$\frac{\partial c_A}{\partial t} + \mathrm{div}_{\mathcal{P}}\left[\vec{h}_A\right] + a\, w^{((3.4))} = s_A\,, \tag{3.12a}$$
$$\frac{\partial c_B}{\partial t} + \mathrm{div}_{\mathcal{P}}\left[\vec{h}_B\right] + b\, w^{((3.4))} = s_B\,, \tag{3.12b}$$
$$\frac{\partial c_C}{\partial t} + \mathrm{div}_{\mathcal{P}}\left[\vec{h}_C\right] - c\, w^{((3.4))} = s_C\,. \tag{3.12c}$$

Clearly, in the set of equations (3.12), the source s_B (ligand) is strictly correlated with the cell-substrate contact dynamic, but what about s_A and s_C? s_A and s_C could be linked to other biological phenomena. For instance, correct calibration of these components could describe the up or down-regulation of proteins on the cell membrane, i.e., the decrease or increase of the amount of protein on the cell membrane owing to internalization of the invaginations present on the lipid bilayer or the exposure of vesicles present in the cytosol. Nevertheless, it has to be clear that in the current thesis, the terms s_A and s_C are always set equal to zero.

Hence, thanks to assumptions that the ligands on the substrate are not free to move (mass fluxes equal to zero), and neither are the complex molecules after activation, it follows that equations (3.12) particularize to the integrin - VEGFR reactions (3.1) - (3.3) in the following form:

$$\frac{\partial c_V}{\partial t} + \mathrm{div}_{\mathcal{P}}\left[\vec{h}_V\right] + w^{((3.1))} = 0\,, \tag{3.13a}$$
$$\frac{\partial c_{L_V}}{\partial t} + w^{((3.1))} = s_{L_V}\,, \tag{3.13b}$$
$$\frac{\partial c_{C_1}}{\partial t} - w^{((3.1))} + w^{((3.2))} = 0\,, \tag{3.13c}$$
$$\frac{\partial c_{C_2}}{\partial t} - w^{((3.2))} = 0\,, \tag{3.13d}$$
$$\frac{\partial c_I}{\partial t} + \mathrm{div}_{\mathcal{P}}\left[\vec{h}_I\right] + w^{((3.3))} + w^{((3.2))} = 0\,, \tag{3.13e}$$
$$\frac{\partial c_{L_I}}{\partial t} + w^{((3.3))} = s_{L_I}\,, \tag{3.13f}$$
$$\frac{\partial c_{C_3}}{\partial t} - w^{((3.3))} = 0\,, \tag{3.13g}$$

(3.13h)

where, henceforth, for reasons of brevity, the reaction rates will be renamed as follow:

$$w^{((3.1))} = w^{(1)}\,, \quad w^{((3.2))} = w^{(2)}\,, \quad w^{((3.3))} = w^{(3)}\,. \tag{3.14}$$

3.2 Construction of a thermodynamically consistent model

Due to the hypothesis of surrogated mechanics, similarly to the hypothesis of small displacements, the reference and current configurations will be completely superimposable. From this consideration, it follows that specific properties could be defined both for a unit of mass and unit of surface, without appreciable differences.

3.2.1 Energy Balance

As discussed in [141], the energy balance reads:

$$\frac{dU(\mathcal{P})}{dt} = \mathcal{W}_u(\mathcal{P}) + \mathcal{Q}_u(\mathcal{P}) + \mathcal{T}_u(\mathcal{P})\,, \tag{3.15}$$

where:

- $\mathcal{P} \subset \Omega$ is an arbitrary sub-region inside Ω,
- U denotes the net internal energy associated to $\mathcal{P}$, defined as follows:

$$U(\mathcal{P}) = \int_{\mathcal{P}} u\, dA\,; \tag{3.16}$$

- $\mathcal{W}_u$ is the power that arises from the mechanical interaction, here equal to zero because of surrogated mechanics hypothesis;
- $\mathcal{Q}_u$ is the power due to heat interaction:

$$\mathcal{Q}_u = \int_{\mathcal{P}} b_q dA - \int_{\partial\mathcal{P}} \vec{q}\cdot\vec{n} dl\,, \tag{3.17}$$

  where b_q is the heat supply by external agents and $\vec{q}$ is the heat flux vector;

- $\mathcal{T}_u$ is the power associated with the mass transfer interaction:

$$\mathcal{T}_u = \int_{\mathcal{P}} \mu^u_{L_I} s_{L_I} dA + \int_{\mathcal{P}} \mu^u_{L_V} s_{L_V} dA - \int_{\partial\mathcal{P}} \left(\mu^u_I \vec{h}_I\right)\cdot\vec{n} dl - \int_{\partial\mathcal{P}} \left(\mu^u_V \vec{h}_V\right)\cdot\vec{n} dl\,, \tag{3.18}$$

  in which μ^u_δ denotes the change in specific energy provided by a unit supply of moles of species $\delta = I, V$.

A standard application of the surface divergence theorem (see Appendix D - section D.1.1 -) leads to the following:

$$\mathcal{Q}_u = \int_{\mathcal{P}} b_q dA - \int_{\mathcal{P}} div_{\mathcal{P}}\left[\vec{q}\right] dA \,, \tag{3.19a}$$

$$\mathcal{T}_u = \int_{\mathcal{P}} \mu^u_{L_I} s_{L_I} dA + \int_{\mathcal{P}} \mu^u_{L_V} s_{L_V} dA - \int_{\mathcal{P}} div_{\mathcal{P}}\left[\mu^u_I \vec{h}_I\right] dA - \int_{\mathcal{P}} div_{\mathcal{P}}\left[\mu^u_V \vec{h}_V\right] dA \,. \tag{3.19b}$$

By doing so, the first law of thermodynamics assumes the expression:

$$\begin{aligned} \int_{\mathcal{P}} \frac{du}{dt}\, dA = \int_{\mathcal{P}} b_q dA - \int_{\mathcal{P}} div_{\mathcal{P}}\left[\vec{q}\right] dA + \\ + \int_{\mathcal{P}} \mu^u_{L_I} s_{L_I} dA + \int_{\mathcal{P}} \mu^u_{L_V} s_{L_V} dA - \int_{\mathcal{P}} div_{\mathcal{P}}\left[\mu^u_I \vec{h}_I\right] dA - \int_{\mathcal{P}} div_{\mathcal{P}}\left[\mu^u_V \vec{h}_V\right] dA \,. \end{aligned} \tag{3.20}$$

Finally, the local form of the first principle is here deduced considering that $\mathcal{P}$ is an arbitrary sub-region inside Ω, therefore:

$$\frac{du}{dt} = b_q - div_{\mathcal{P}}\left[\vec{q}\right] + \mu^u_{L_I} s_{L_I} + \mu^u_{L_V} s_{L_V} - div_{\mathcal{P}}\left[\mu^u_I \vec{h}_I\right] - div_{\mathcal{P}}\left[\mu^u_V \vec{h}_V\right] \,. \tag{3.21}$$

3.2.2 Entropy balance equations

A suitable interpretation of the second law of thermodynamics is here presented by showing the interplay among the internal production of entropy with the contribution arising from the heat and mass interaction as follows:

$$\frac{dS(\mathcal{P})}{dt} = \mathcal{Q}_\eta(\mathcal{P}) + \mathcal{T}_\eta(\mathcal{P}) + \frac{dS_{irr}(\mathcal{P})}{dt} \,. \tag{3.22}$$

Where:

- S expresses the net internal entropy of $\mathcal{P}$,
- $\mathcal{Q}_\eta$ denotes the entropy per unit time due to heat interaction:

$$\mathcal{Q}_\eta = \int_{\mathcal{P}} \frac{b_q}{T} dA - \int_{\partial\mathcal{P}} \frac{\vec{q}}{T} \cdot \vec{n} dl \,, \tag{3.23}$$

  in which T is the temperature;

- $\mathcal{T}_\eta$ is the entropy per unit time due to mass interaction:

$$\mathcal{T}_\eta = \int_{\mathcal{P}} \mu^\eta_{L_I} s_{L_I} dA + \int_{\mathcal{P}} \mu^\eta_{L_V} s_{L_V} dA - \int_{\partial\mathcal{P}} \left(\mu^\eta_I \vec{h}_I\right) \cdot \vec{n} dl - \int_{\partial\mathcal{P}} \left(\mu^\eta_V \vec{h}_V\right) \cdot \vec{n} dl \,, \tag{3.24}$$

  wherein the scalar μ^η_δ denotes the change in specific entropy provided by a unit supply of moles of species $\delta = I, V$;

- S_{irr} is the entropy produced inside $\mathcal{P}$ and owing to the second law of thermodynamics states that: $\dfrac{dS_{irr}}{dt} \geq 0$.

Standard application of the divergence theorem set on a the sub-surface $\mathcal{P}$, leads to:

$$\int_{\mathcal{P}} \left\{ \frac{ds}{dt} - \frac{b_q}{T} + div_{\mathcal{P}} \left[\frac{\vec{q}}{T} \right] - \mu_{L_I}^{\eta} s_{L_I} - \mu_{L_V}^{\eta} s_{L_V} + div_{\mathcal{P}} \left[\mu_I^{\eta} \vec{h}_I \right] + div_{\mathcal{P}} \left[\mu_V^{\eta} \vec{h}_V \right] \right\} dA \geq 0 \,. \tag{3.25}$$

In the local form:

$$\frac{ds}{dt} - \frac{b_q}{T} + div_{\mathcal{P}} \left[\frac{\vec{q}}{T} \right] - \mu_{L_I}^{\eta} s_{L_I} - \mu_{L_V}^{\eta} s_{L_V} + div_{\mathcal{P}} \left[\mu_I^{\eta} \vec{h}_I \right] + div_{\mathcal{P}} \left[\mu_V^{\eta} \vec{h}_V \right] \geq 0 \,. \tag{3.26}$$

Multiplying by T and after simple algebra on the $div_{\mathcal{P}} \left[\dfrac{\vec{q}}{T} \right]$, we obtain:

$$\begin{aligned} T\frac{ds}{dt} - b_q + div_{\mathcal{P}} \left[\vec{q} \right] - \frac{1}{T} \vec{q} \cdot \nabla_{\mathcal{P}} \left[T \right] + \\ -T\mu_{L_I}^{\eta} s_{L_I} - T\mu_{L_V}^{\eta} s_{L_V} + T div_{\mathcal{P}} \left[\mu_I^{\eta} \vec{h}_I \right] + T div_{\mathcal{P}} \left[\mu_V^{\eta} \vec{h}_V \right] \geq 0 \,. \end{aligned} \tag{3.27}$$

Hence, comparing (3.27) with (3.21) through the terms $b_q + div_{\mathcal{P}} \left[\vec{q} \right]$, we attain:

$$\begin{aligned} T\frac{ds}{dt} - \frac{du}{dt} + s_{L_I} \underbrace{\left(\mu_{L_I}^{u} - T\mu_{L_I}^{\eta} \right)}_{\mu_{L_I}} + s_{L_V} \underbrace{\left(\mu_{L_V}^{u} - T\mu_{L_V}^{\eta} \right)}_{\mu_{L_V}} + \\ - \left\{ \nabla_{\mathcal{P}} \left[\mu_I^{u} - T\mu_I^{\eta} \right] \cdot \vec{h}_I + \underbrace{\left(\mu_I^{u} - T\mu_I^{\eta} \right)}_{\mu_I} div_{\mathcal{P}} \left[\vec{h}_I \right] \right\} \\ - \left\{ \nabla_{\mathcal{P}} \left[\mu_V^{u} - T\mu_V^{\eta} \right] \cdot \vec{h}_V + \underbrace{\left(\mu_V^{u} - T\mu_V^{\eta} \right)}_{\mu_V} div_{\mathcal{P}} \left[\vec{h}_V \right] \right\} \\ - \frac{1}{T} \underbrace{\left\{ \vec{q} + T\mu_I^{\eta} \vec{h}_I + T\mu_V^{\eta} \vec{h}_V \right\}}_{\underline{\vec{q}}} \cdot \nabla_{\mathcal{P}} \left[T \right] \geq 0 \,, \end{aligned} \tag{3.28}$$

and:

$$\begin{aligned} T\frac{ds}{dt} - \frac{du}{dt} + s_{L_I} \left(\mu_{L_I} \right) + s_{L_V} \left(\mu_{L_V} \right) - \frac{1}{T} \underline{\vec{q}} \cdot \nabla_{\mathcal{P}} \left[T \right] + \\ - \left\{ \nabla_{\mathcal{P}} \left[\mu_I \right] \cdot \vec{h}_I + \left(\mu_I \right) div_{\mathcal{P}} \left[\vec{h}_I \right] \right\} + \\ - \left\{ \nabla_{\mathcal{P}} \left[\mu_V \right] \cdot \vec{h}_V + \left(\mu_V \right) div_{\mathcal{P}} \left[\vec{h}_V \right] \right\} \geq 0 \,. \end{aligned} \tag{3.29}$$

We can reformulated equation (3.29) as follows:

$$\begin{aligned} T\frac{ds}{dt} - \frac{du}{dt} - \nabla_{\mathcal{P}}[\mu_I]\cdot\vec{h}_I - \nabla_{\mathcal{P}}[\mu_V]\cdot\vec{h}_V - \frac{1}{T}\underline{\vec{q}}\cdot\nabla_{\mathcal{P}}[T] + \\ +\mu_{L_I}\left\{\frac{\partial c_{L_I}}{\partial t} + w^{(3)}\right\} + \mu_{L_V}\left\{\frac{\partial c_{L_V}}{\partial t} + w^{(1)}\right\} + \\ +\mu_I\left\{\frac{\partial c_I}{\partial t} + w^{(3)} + w^{(2)}\right\} + \mu_V\left\{\frac{\partial c_V}{\partial t} + w^{(1)}\right\} + \\ +\mu_{C_1}\left\{\frac{\partial c_{C_1}}{\partial t} - w^{(1)} + w^{(2)}\right\} + \mu_{C_2}\left\{\frac{\partial c_{C_2}}{\partial t} - w^{(2)}\right\} + \\ +\mu_{C_3}\left\{\frac{\partial c_{C_3}}{\partial t} - w^{(3)}\right\} \geq 0\,, \end{aligned} \tag{3.30}$$

$$\begin{aligned} A_1 &= -\mu_V - \mu_{L_V} + \mu_{C_1}\,, \\ A_2 &= -\mu_I - \mu_{C_1} + \mu_{C_2}\,, \\ A_3 &= -\mu_I - \mu_{L_I} + \mu_{C_3}\,, \end{aligned} \tag{3.31}$$

the entropy imbalance finally result:

$$\begin{aligned} T\frac{ds}{dt} - \frac{du}{dt} - \nabla_{\mathcal{P}}[\mu_I]\cdot\vec{h}_I - \nabla_{\mathcal{P}}[\mu_V]\cdot\vec{h}_V - \frac{1}{T}\underline{\vec{q}}\cdot\nabla_{\mathcal{P}}[T] + \mu_\gamma\frac{\partial c_\gamma}{\partial t} + \\ -w^{(1)}A_1 - w^{(2)}A_2 - w^{(3)}A_3 \geq 0\,, \\ \text{where } \gamma = L_I,\, L_V,\, I,\, V,\, C_1,\, C_2,\, C_3\,. \end{aligned} \tag{3.32}$$

3.2.3 Thermodynamic restrictions

In a continuum field description and under the hypothesis of surrogated mechanics, we can state that the Helmholtz free-energy density (ψ) has the following features:

$$\begin{aligned} \psi = \psi(T, c_\gamma) \;&\longrightarrow\; \frac{d\psi}{dt} = \frac{\partial\psi}{\partial T}\frac{\partial T}{\partial t} + \frac{\partial\psi}{\partial c_\gamma}\frac{\partial c_\gamma}{\partial t} \\ \psi = u - Ts \;&\longrightarrow\; \frac{d\psi}{dt} = \frac{du}{dt} - \frac{dT}{dt}s - \frac{ds}{dt}T \end{aligned} \tag{3.33}$$

$$T\frac{ds}{dt} - \frac{du}{dt} = -\frac{\partial T}{\partial t}s - \frac{\partial\psi}{\partial T}\frac{\partial T}{\partial t} - \frac{\partial\psi}{\partial c_\gamma}\frac{\partial c_\gamma}{\partial t} = -(\frac{\partial\psi}{\partial T} + s)\frac{\partial T}{\partial t} - \frac{\partial\psi}{\partial c_\gamma}\frac{\partial c_\gamma}{\partial t} \tag{3.34}$$

Identifying the quantities $T\frac{ds}{dt} - \frac{du}{dt}$, either in the expression (3.32) that in (3.34), we can couple them and deduce the so-called Clausius-Duhem inequality:

$$\begin{aligned} (\mu_\gamma - \frac{\partial\psi}{\partial c_\gamma})\frac{\partial c_\gamma}{\partial t} - (\frac{\partial\psi}{\partial T} + s)\frac{\partial T}{\partial t} - \nabla_{\mathcal{P}}[\mu_I]\cdot\vec{h}_I + \\ -\nabla_{\mathcal{P}}[\mu_V]\cdot\vec{h}_V - \frac{1}{T}\underline{\vec{q}}\cdot\nabla_{\mathcal{P}}[T] - w^{(1)}A_1 - w^{(2)}A_2 - w^{(3)}A_3 \geq 0\,. \end{aligned} \tag{3.35}$$

The time derivative of T and c_γ appears linearly in the (3.35); consequently, this inequality must hold for any value of $\dfrac{\partial T}{\partial t}$ and $\dfrac{\partial c_\gamma}{\partial t}$. Consequently:

$$\mu_\gamma = \frac{\partial \psi}{\partial c_\gamma}\,, \quad s = -\frac{\partial \psi}{\partial T}\,. \tag{3.36}$$

As a result, μ_γ acquires the meaning of chemical potential and hence A_1, A_2, A_3 of the affinity of the reactions (3.1),(3.2), and (3.3) respectively. Finally, the Clausius-Duhem inequality (3.35) became:

$$\begin{gathered} \underbrace{-\nabla_{\mathcal{P}}\left[\mu_I\right]\cdot\vec{h}_I - \nabla_{\mathcal{P}}\left[\mu_V\right]\cdot\vec{h}_V +}_{\text{diffusive}} \\ \underbrace{-\frac{1}{T}\underline{\vec{q}}\cdot\nabla_{\mathcal{P}}\left[T\right]}_{\text{thermal}}\ \underbrace{-w^{(1)}A_1 - w^{(2)}A_2 - w^{(3)}A_3}_{\text{chemical}} \geq 0\,. \end{gathered} \tag{3.37}$$

i.e. the so-called Clausius-Plank inequality. Because the thermodynamic forces of different tensorial order do not couple (Curie symmetry principle [144] (pages 33-34)), the (3.35) can be written separately as:

$$\begin{aligned} &-\nabla_{\mathcal{P}}\left[\mu_I\right]\cdot\vec{h}_I - \nabla_{\mathcal{P}}\left[\mu_V\right]\cdot\vec{h}_V - \frac{1}{T}\underline{\vec{q}}\cdot\nabla_{\mathcal{P}}\left[T\right] \geq 0\,, \\ &-w^{(1)}A_1 - w^{(2)}A_2 - w^{(3)}A_3 \geq 0\,. \end{aligned} \tag{3.38}$$

3.2.3.1 Expression of μ^u and μ^η as a function of Helmholtz free energy

In this section, we want to establish the expressions of μ^u and μ^η as a function of the Helmholtz free-energy density ψ. It is known from the previous section that entropy is a function of c_γ and T (see relations (3.36)) and so, also the internal energy density (usually in the form $u = u(s, c_\gamma)$), becomes a function of the same state variable. Hence:

$$\begin{gathered} u = u(s(T, c_\gamma), c_\gamma) \text{ and } \psi = u - Ts \\ \Longrightarrow \\ \psi(c_\gamma, T) = u(s(T, c_\gamma), c_\gamma) - Ts(c_\gamma, T) \end{gathered} \tag{3.39}$$

Owing to the definition of the Helmholtz free-energy density, we deduce:

$$\begin{aligned} d\psi &= \frac{\partial u}{\partial s}\frac{\partial s}{\partial c_\gamma}dc_\gamma + \frac{\partial u}{\partial s}\frac{\partial s}{\partial T}dT + \frac{\partial u}{\partial c_\gamma}dc_\gamma - dTs - T\frac{\partial s}{\partial c_\gamma}dc_\gamma - T\frac{\partial s}{\partial T}dT\,, \\ \left.\frac{\partial \psi}{\partial c_\gamma}\right|_T &= \left.\frac{\partial u}{\partial s}\frac{\partial s}{\partial c_\gamma}\right|_T + \left.\frac{\partial u}{\partial c_\gamma}\right|_T - T\left.\frac{\partial s}{\partial c_\gamma}\right|_T\,. \end{aligned} \tag{3.40}$$

Similarly, for the internal energy, it is found that

$$\begin{aligned} du(s(c_\gamma, T), c_\gamma) &= \frac{\partial u}{\partial s}\left(\frac{\partial s}{\partial c_\gamma}dc_\gamma + \frac{\partial s}{\partial T}dT\right) + \frac{\partial u}{\partial c_\gamma}dc_\gamma\,, \\ \frac{du}{dc_\gamma} &= \frac{\partial u}{\partial s}\frac{\partial s}{\partial c_\gamma} + \frac{\partial u}{\partial c_\gamma}\,. \end{aligned} \tag{3.41}$$

Therefore, taking advantage of the expression $\left.\frac{\partial u}{\partial s}\frac{\partial s}{\partial c_\gamma}\right|_T + \left.\frac{\partial u}{\partial c_\gamma}\right|_T$, embedded into expressions (3.40) and (3.41), it is trivial to see that:

$$\left.\frac{\partial \psi}{\partial c_\gamma}\right|_T = \frac{du}{dc_\gamma} - T\left.\frac{\partial s}{\partial c_\gamma}\right|_T . \tag{3.42}$$

Knowing the Eqs. (3.36) and the relations $\mu_\gamma = \mu_\gamma^u - T\mu_\gamma^\eta$, it is easy to deduce:

$$\left.\frac{\partial \psi}{\partial c_\gamma}\right|_T = \frac{du}{dc_\gamma} - T\frac{\partial}{\partial c_\gamma}\left(-\left.\frac{\partial \psi(T,c_\gamma)}{\partial T}\right|_{c_\gamma}\right), \tag{3.43}$$

$$\frac{\partial \psi}{\partial c_\gamma} = \frac{du}{dc_\gamma} + T\frac{\partial}{\partial c_\gamma}\left(\frac{\partial \psi(T,c_\gamma)}{\partial T}\right), \tag{3.44}$$

and, consequently, the following expressions:

$$\mu_\gamma^\eta = \left.\frac{\partial s(T,c_\gamma)}{\partial c_\gamma}\right|_T = -\frac{\partial}{\partial c_\gamma}\frac{\partial \psi(T,c_\gamma)}{\partial T} = -\frac{\partial}{\partial T}\frac{\partial \psi(T,c_\gamma)}{\partial c_\gamma} = -\frac{\partial}{\partial T}\mu_\gamma(T,c_\gamma), \tag{3.45}$$

$$\mu_\gamma^u = \mu_\gamma + T\mu_\gamma^\eta = \left.\frac{\partial \psi(c_\gamma,T)}{\partial c_\gamma}\right|_T - T\frac{\partial}{\partial T}\mu_\gamma(c_\gamma,T) = \frac{du}{dc_\gamma}, \tag{3.46}$$

that are consistent with the local form of the first principle and the Gibbs relation[2]. In fact, it holds:

$$\frac{\partial \psi}{\partial c_\gamma} = \frac{du}{dc_\gamma} + T\frac{\partial}{\partial c_\gamma}\frac{\partial \psi}{\partial T} = \frac{\partial u}{\partial c_\gamma} + \underbrace{\frac{\partial u}{\partial s}\frac{\partial s}{\partial c_\gamma}}_{T\frac{\partial s}{\partial c_\gamma}} + \underbrace{T\frac{\partial}{\partial c_\gamma}\frac{\partial \psi}{\partial T}}_{-\frac{\partial s}{\partial c_\gamma}} = \frac{\partial u}{\partial c_\gamma} = \mu_\gamma . \tag{3.47}$$

According to the expression $\psi_\gamma = \mu_\gamma = \mu_\gamma^u - T\mu_\gamma^\eta$, it is worth:

$$\mu_\gamma^\eta = -\frac{\partial^2 \psi}{\partial c_\gamma \partial T} \quad \text{and} \quad \mu_\gamma^u = \frac{\partial \psi}{\partial c_\gamma} - T\frac{\partial^2 \psi}{\partial c_\gamma \partial T} . \tag{3.48}$$

A further way to prove that μ_γ^u and μ_γ^η are not partial properties is given in the Appendix C (see section C.2.1).

3.2.3.2 Dependence on the temperature gradient

In view of the expression $\vec{\underline{q}} = \vec{q} + T\mu_I^\eta \vec{h}_I + T\mu_V^\eta \vec{h}_V$, the following identity:

$$\begin{aligned} &-\vec{h}_I \cdot \nabla_{\mathcal{P}}[\mu_I] - \vec{h}_V \cdot \nabla_{\mathcal{P}}[\mu_V] - \frac{1}{T}\vec{\underline{q}} \cdot \nabla_{\mathcal{P}}[T] = \\ &= -\vec{h}_I(\nabla_{\mathcal{P}}[\mu_I] + \mu_I^\eta \nabla_{\mathcal{P}}[T]) - \vec{h}_V(\nabla_{\mathcal{P}}[\mu_V] + \mu_V^\eta \nabla_{\mathcal{P}}[T]) - \frac{1}{T}\vec{q} \cdot \nabla_{\mathcal{P}}[T] \end{aligned} \tag{3.49}$$

[2]Gibbs relations under the hypothesis of surrogate mechanics: $u = u(s, c_i)$ and so $du = Tds + \mu_i dc_i$.

holds.
Combining the expression (3.49) with the properties of the $\nabla_{\mathcal{P}}$ operator[3], the subsequent relations arise:

$$\begin{aligned}
&\nabla_{\mathcal{P}}[\mu_\delta] = \nabla_{\mathcal{P}}\left[\frac{\partial \psi(T,c_\gamma)}{\partial c_\delta}\right] = \frac{\partial}{\partial c_\delta}\left[\nabla_{\mathcal{P}}\psi(T,c_\gamma)\right] = \frac{\partial}{\partial c_\delta}\left[\frac{\partial \psi}{\partial T}\nabla_{\mathcal{P}}[T] + \frac{\partial \psi}{\partial c_\gamma}\nabla_{\mathcal{P}}[c_\gamma]\right] , \\
&\nabla_{\mathcal{P}}[\mu_\delta] + \mu_\delta^\eta \nabla_{\mathcal{P}}[T] = \frac{\partial^2 \psi}{\partial c_\delta \partial T}\nabla_{\mathcal{P}}[T] + \frac{\partial^2 \psi}{\partial c_\delta \partial c_\gamma}\nabla_{\mathcal{P}}[c_\gamma] - T\frac{\partial^2 \psi}{\partial c_\delta \partial T} = \frac{\partial^2 \psi}{\partial c_\delta \partial c_\gamma}\nabla_{\mathcal{P}}[c_\gamma] , \\
&\text{where } \delta = I, V, \text{ and } \gamma = I, L_I, V, L_V, C_1, C_2, C_3.
\end{aligned} \tag{3.52}$$

Finally, by means of the relations (3.48) and (3.49), we can show that the expressions $\nabla_{\mathcal{P}}[\mu_I] + \mu_I^\eta \nabla_{\mathcal{P}}[T]$ and $\nabla_{\mathcal{P}}[\mu_V] + \mu_V^\eta \nabla_{\mathcal{P}}[T]$ are independent upon the gradient of temperature.

$$\begin{aligned}
&\nabla_{\mathcal{P}}[\mu_I] + \mu_I^\eta \nabla_{\mathcal{P}}[T] = \frac{\partial^2 \psi}{\partial c_I^2}\nabla_{\mathcal{P}}[c_I] + \frac{\partial^2 \psi}{\partial c_I \partial c_\iota}\nabla_{\mathcal{P}}[c_\iota] , \\
&\text{where } \iota = L_I,\ L_V,\ V,\ C_1,\ C_2,\ C_3 ,
\end{aligned} \tag{3.53}$$

$$\begin{aligned}
&\nabla_{\mathcal{P}}[\mu_V] + \mu_V^\eta \nabla_{\mathcal{P}}[T] = \frac{\partial^2 \psi}{\partial c_V^2}\nabla_{\mathcal{P}}[c_V] + \frac{\partial^2 \psi}{\partial c_V \partial c_\kappa}\nabla_{\mathcal{P}}[c_\kappa] , \\
&\text{where } \kappa = L_I,\ L_V,\ I,\ C_1,\ C_2,\ C_3 .
\end{aligned} \tag{3.54}$$

3.2.4 Constitutive theory

We can deduce the structure of the constitutive relations of the problem at hand starting from the Clausius-Duhem inequality (3.35). We rewrote the (3.37) as follows:

$$\begin{cases}
-\dfrac{1}{T}\vec{\underline{q}} \cdot \nabla_{\mathcal{P}}[T] - \nabla_{\mathcal{P}}[\mu_I] \cdot \vec{h}_I - \nabla_{\mathcal{P}}[\mu_V] \cdot \vec{h}_V \geq 0 , \\
-w^{(1)}A_1 - w^{(2)}A_2 - w^{(3)}A_3 \geq 0 .
\end{cases} \tag{3.55}$$

Considering that $\nabla_{\mathcal{P}}[\mu_I] + \mu_I^\eta \nabla_{\mathcal{P}}[T]$ does not depend on the temperature gradient, we deduce from the (3.55) that

$$-\frac{1}{T}\vec{q} \cdot \nabla_{\mathcal{P}}[T] - \vec{h}_I \cdot \left(\nabla_{\mathcal{P}}[\mu_I] + \mu_I^\eta \nabla_{\mathcal{P}}[T]\right) - \vec{h}_V \cdot \left(\nabla_{\mathcal{P}}[\mu_V] + \mu_V^\eta \nabla_{\mathcal{P}}[T]\right) \geq 0 , \tag{3.56a}$$

$$-w^{(1)}A_1 - w^{(2)}A_2 - w^{(3)}A_3 \geq 0 . \tag{3.56b}$$

[3]Properties of the operator $\nabla_{\mathcal{P}}$ for the following generic functions $f(y,z)$ and $g(\vec{u},\vec{v})$:

$$\nabla_{\mathcal{P}} f(y,z) = \frac{\partial f}{\partial y}\nabla_{\mathcal{P}}[y] + \frac{\partial f}{\partial z}\nabla_{\mathcal{P}}[z] , \tag{3.50}$$

$$\nabla_{\mathcal{P}}[g(\vec{u},\vec{v})] = \frac{\partial g}{\partial \vec{u}}\nabla_{\mathcal{P}}[\vec{u}] + \frac{\partial g}{\partial \vec{v}}\nabla_{\mathcal{P}}[\vec{v}] , \tag{3.51}$$

see also the Appendix D (see section D.2.5).

3.2.4.1 Flows and generalized forces

Equilibrium systems played a relevant role throughout the history of thermodynamic; nevertheless, assisted only by the equilibrium framework, we could describe very few phenomena observed in nature. However, the whole theoretical structure that supports equilibrium thermodynamics extends to non-equilibrium states that remain locally close to equilibrium. This is the so-called local-equilibrium hypothesis, wherein the intensive variable is now a function of the position [145]. A state variable can be defined as a function of the position if its fluctuations are small compared to the value of the variable itself [145] (page 217). In a thermodynamic of continua framework[4], at each continuum particle[5] [5] (page 71), the intensive variables such as, for instance, strain, stresses, temperature, pressure, concentrations, etc., have to be homogeneous inside the infinitesimal volume defined at the neighborhood of the particles.

Describing processes outside the field of thermodynamic equilibrium implies an explicit expression of the term which represents the production of entropy [146].

$$\frac{dS_{irr}}{dt} = \sigma = \sum_i J_i \Gamma_i \geq 0 \text{ with } i \text{ an irreversible process .} \tag{3.57}$$

Where:

- σ is the local production of entropy [145] (page 224);
- J_i are the rates of variation of the processes involved, i.e. flows (heat flow, chemical reactions, diffusion, ...);
- Γ_i are generalized forces (temperature gradient, affinities, gradients of chemical potentials, ...);
- $J_i = 0$ and $\Gamma_i = 0$ at thermodynamic equilibrium.

Actually, Eq. (3.57) is not an explicit expression of the entropy production; further assumptions are necessary to reach this aim.
For instance, close to equilibrium, it seems entirely legitimate to assume linear and homogeneous correlations between flows and forces (theory called "linear thermodynamics of irreversible process" [146]):

$$J_i = L_{ij} \Gamma_j \, . \tag{3.58}$$

The assumptions are based on awareness arisen from experimental evidence that led to the notorious empirical laws of Fourier, Ohm, and Fick [145] (page 227), [146]. The linear thermodynamics of irreversible process[6] is a theory characterized by the so-called Onsager reciprocity relation ($L_{ij} = L_{ji}$ - wherein, phenomenological coefficients are evaluated at equilibrium - [145]

[4] Citing by [5] (page 169): *By accepting the "continuum assumptions" and the existence of state variable fields, we are in fact accepting the postulate of local thermodynamic equilibrium. This postulate states that the local and instantaneous relations between thermodynamic quantities in a system out of equilibrium are the same as for a uniform system in equilibrium.*

[5] We are implicitly accepting the continuity hypothesis

[6] Another interesting result belonging to this theory is the theorem of the minimum entropy produced (it applies to stationary states close to equilibrium that need much more restrictive assumptions than the Onsager relations) [145].

(page 230)) [145] (pages 228-230). Such relations are due to Onsager in his milestone work [147] on the "*principle of microscopic reversibility*" (see the book [145] - pages 205-211 and 228-230 -). Further discussions on the topic, embedded in the field of the thermodynamics of continuum, are provided by [5] - pages 190-191 - and [144] (chapter 4, 6, 9). In the Steepest Entropy Ascent Principle[7] [8], [148], the Onsager principle, becomes a particular case.
In addition to the symmetry condition $L_{ij} = L_{ji}$, it is possible to infer, thanks to Curie's Principle (see [144] (page 5 and chapter 6)), that not all couplings between flows and forces are likely [145] (page 230); this is due to spatial symmetries of the material system that impose that the thermodynamic force of different tensorial order can not couple (see [144] (page 5 and chapter 6)).

Back to the Eq. (3.56a) and assuming that all phenomena can be described through linear relationships between flows and generalized forces (Onsager's relations), we come to write:

$$\begin{cases} \vec{h}_\delta = -\boldsymbol{M}_\delta \left(\nabla_{\mathcal{P}}[\mu_\delta] + \mu_\delta^\eta \nabla_{\mathcal{P}}[T] \right) \quad \text{where } \delta = I, V. \\ \vec{q} = -\boldsymbol{K} \nabla_{\mathcal{P}}[T] \, . \end{cases} \tag{3.59}$$

where $\boldsymbol{M}_\delta$ and $\boldsymbol{K}$ are respectively the positive defined mobility and heat conductivity tensor. The two reciprocal phenomena *Dufur* and *Soret effects*, describing mutual action of the gradient of chemical species concentration on temperature and the gradient temperature on concentrations (thermophoresis), are not accounted for in this thesis, owing to the hypothesis of isothermal processes that here we embrace. Hence, placing $\nabla_{\mathcal{P}}[T] = \vec{0}$, we focus on the mobility tensor, which is definite as:

$$\boldsymbol{M}_\delta = \mathfrak{u}_\delta c_\delta^{\max} \vartheta_\delta \left(1 - \vartheta_\delta\right) \mathbb{1} \quad [149] \, , \tag{3.60}$$

where the saturation limit of receptors is taken into account by means of $\vartheta_\delta = \dfrac{c_\delta}{c_\delta^{\max}}$. Trough the definition (3.60), we satisfy the request that the two different phases, that is $c_\delta = 0$ and $c_\delta = c_\delta^{\max}$ (saturation) have vanishing mobilities.
$\mathfrak{u}_\delta$ is the so-called receptor mobility, namely the average velocity when applying a force of $1\, N/mol$, regardless of the origin of the force. Also, we assume that $\mathfrak{u}_\delta$ and ϑ_δ don't change throughout the time.

3.2.4.2 The expression of the Helmholtz free energy density

We assume that the ECs in our in-vitro experiments are undergoing isothermal processes exclusively, and in the next section, we will add a further hypothesis concerning the chemical equilibrium of the species involved in this model. Under the hypothesis of isothermal processes

$$\psi(c_\gamma) = \psi_0 + \psi_{\text{diff}}(c_\gamma) \, . \tag{3.61}$$

In the current thermodynamics framework, we observe a total set-up made by an EC (closed system) in thermal equilibrium with a thermal bath ("reservoir"). As usual in continuum thermody-

[7] This principle together with Zigler's maximum entropy production principle, and the principle of entropy production invariance under time reversal, provide methods to how deduced Onsager relations without ergodic hypothesis [148]

namics, for this kind of problem (T, *suitable kinematics state variables*[8], $\mathbf{c}$) is the more appropriate thermodynamics variables capable to describe the evolution of the system (EC), which reach the thermodynamic equilibrium in correspondence of the minimum values assumed by the Helmholtz free-energy $\psi = \psi(T,\ \text{suitable kinematics state variables},\ \mathbf{c})$ [12]. Under the surrogated mechanics assumption and assuming isothermal processes, the number of the thermodynamics variables are reduced to the only chemical species concentrations $\psi = \psi(\mathbf{c})$ (see expression (3.61)). The correlation between the entropy function of an isolated system and the function density of microstates (Ω), is very well known in a statistical mechanics scheme. Furthermore, when a two-state system, as in the case of the trapping model used here and well definite in the paper [141], Ω corresponds to the number of molecular configurations [141, 150]. Similarly to what has been deduced for the number of interstitial species atoms in an ideal crystalline lattice [141], via Stirling's approximation, we offer the following expression for the combination formula for the potential conformations of proteins concentrations on a cell membrane:

$$\Omega_\gamma = \left[\vartheta_\gamma^{\vartheta_\gamma}\left(1-\vartheta_\gamma\right)^{\left(1-\vartheta_\gamma\right)}\right]^{-\mathcal{N}_A c_\gamma^{\max}}\ , \tag{3.62}$$

where $\mathcal{N}_A$ is the Avogadro's number and $\gamma = I, V, L_V, L_I, C_1, C_2, C_3$. By means the Boltzmann's equation we obtain:

$$\begin{aligned}\eta_\gamma^{\text{diff}} &= \kappa_B \ln\left[\Omega_\gamma\right] \\ &= \kappa_B \ln\left[\vartheta_\gamma^{\vartheta_\gamma}\left(1-\vartheta_\gamma\right)^{\left(1-\vartheta_\gamma\right)}\right]^{-\mathcal{N}_A c_\gamma^{\max}} \\ &= -\underbrace{\kappa_B \mathcal{N}_A}_{R} c_\gamma^{\max}\left(\vartheta_\gamma \ln\left[\vartheta_\gamma\right] + \left(1-\vartheta_\gamma\right)\ln\left[1-\vartheta_\gamma\right]\right)\ .\end{aligned} \tag{3.63}$$

Again, similarly to what has been done for mobile guest atoms interplaying with a host medium [141], [149], [151], we introduce ψ_{diff} for the continuum approximation of mixing for the current problem:

$$\psi_{\text{diff}}(c_\gamma) = \mu_\gamma^0 - T\eta_\gamma^{\text{diff}} + RT c_\gamma^{\max}\vartheta_\gamma\left(1-\vartheta_\gamma\right)\overline{\chi}\ , \tag{3.64}$$

where μ_β^0 corresponds to the reference values of each chemical potentials and $\overline{\chi}$ is a real constant, that specifies the energy of interaction among mobile species (receptors) and the fixed ones (ligands or complexes) [141]. Specifically, the reference chemical potentials are correlated with the trap binding-energy (ΔE^T [141]) and the equilibrium constant via:

$$\begin{aligned}\Delta E^T_{(3.1)} &= \mu_V + \mu_{L_V} - \mu_{C_1} = \kappa_B T \ln\left[K_{eq}^{(3.1)}\right]\ , \\ \Delta E^T_{(3.2)} &= \mu_I + \mu_{C_1} - \mu_{C_2} = \kappa_B T \ln\left[K_{eq}^{(3.2)}\right]\ , \\ \Delta E^T_{(3.3)} &= \mu_I + \mu_{L_I} - \mu_{C_3} = \kappa_B T \ln\left[K_{eq}^{(3.3)}\right]\ ,\end{aligned} \tag{3.65}$$

where the trap binding-energy is the negative of ΔG^0, namely the so-called Gibbs free-energy change [141]. The (3.64) takes into account both the energetic interaction that the entropy of mixing, which contributes is equal to zero if the *exchange parameter* ($\overline{\chi} = 0$) [141, 150] is equal

[8]The *kinematic state variables* are those state variables connected with the position and shape of the system (i.e. its motion). Usually, in continuum thermodynamics, these could be the Volume or the elements of the Lagrangian strain tensor [5]

to zero. This happens when all the chemical interplay among ligands and receptors are equivalent [141].

Now, we limit our study at the constituents $\delta = I, V$ assuming the parameter $\overline{\chi} = 0$:

$$\begin{aligned} \psi_\delta(c_\delta) &= \mu_\delta^0 c_\delta + RT c_\delta^{\max} \left[\vartheta_\delta \ln(\vartheta_\delta) + (1-\vartheta_\delta)\ln(1-\vartheta_\delta)\right] , \\ \mu_\delta &= \frac{\partial \psi_\delta(c_\delta)}{\partial c_\delta} = \mu_\delta^0 + RT\left[\ln(\vartheta_\delta) - \ln(1-\vartheta_\delta)\right] . \end{aligned} \tag{3.66}$$

Since $\vec{h}_\delta$ is related to the gradient of the chemical potentials (see 3.59 considering that $\nabla_{\mathcal{P}}[T] = \vec{0}$), one writes:

$$\begin{aligned} \nabla_{\mathcal{P}}[\mu_\delta] &= RT\frac{1}{\vartheta_\delta}\nabla_{\mathcal{P}}[\vartheta_\delta] + RT\frac{1}{(1-\vartheta_\delta)}\nabla_{\mathcal{P}}[\vartheta_\delta] = RT\frac{1}{c_\delta^{\max}}\frac{1}{\vartheta_\delta(1-\vartheta_\delta)}\nabla_{\mathcal{P}}[c_\delta] , \\ \vec{h}_\delta &= -\mathbb{u}_\delta c_\delta^{\max}\vartheta_\delta(1-\vartheta_\delta)\mathbf{I}\nabla_{\mathcal{P}}[\mu_\delta] = -\mathbb{u}_\delta RT\nabla_{\mathcal{P}}[c_\delta] = -\underbrace{\mathbb{D}_\delta}_{\text{diffusivity}}\nabla_{\mathcal{P}}[c_\delta] , \end{aligned} \tag{3.67}$$

which are the well known Fick's constitutive equations, that in extenso can be written as

$$\vec{h}_I = -\mathbb{D}_I\nabla_{\mathcal{P}}[c_I] \tag{3.68a}$$

$$\vec{h}_V = -\mathbb{D}_V\nabla_{\mathcal{P}}[c_V] . \tag{3.68b}$$

Fick's constitutive relations satisfy thermodynamic restrictions as long as diffusivities are positive definite, as well known (see an extended motivation in [142] (pages 382-383)). Note, though, that in the current formulation the gradient operator in equations (3.68) is defined on the surface, i.e.

$$\nabla_{\mathcal{P}}[c] = \nabla[c] - (\vec{n}\cdot\nabla[c])\vec{n} . \tag{3.69}$$

$\nabla_{\mathcal{P}}[c]$ is, hence, the projected gradient operator of a scalar field c, pointing out how, in the current formulation, the mobile proteins are constrained to remain on the spherical surface $\mathcal{P}$.

3.3 Chemical kinetics

The chemical kinetics of the paradigmatic reaction (3.4), after the surrogated mechanics hypothesis, is modeled as for ideal systems via the law of mass action [144] (pages 204-206):

$$w^{(3.4)} = k_f\left[\frac{\vartheta_B}{(1-\vartheta_B)}\right]^b\left[\frac{\vartheta_A}{(1-\vartheta_A)}\right]^a - k_b\left[\frac{\vartheta_C}{(1-\vartheta_C)}\right]^c . \tag{3.70}$$

In eq. (3.70), ϑ_A denotes the non-dimensional ratio between the concentration of species A and its amount $c_A^{\max}$ at saturation,

$$\vartheta_A = c_A/c_A^{\max} ,$$

similarly ϑ_B and ϑ_C for species B and C.

The expression (3.70) could be upgraded accounting for the hypothesis of a dilute solution, which is here supported by experimental evidence that shows how species concentration remains far from saturation limit in their own binding sites.
Therefore, under this specific condition, $(1-\vartheta_A) \sim 1$ (the same for species B and C) and the mass action law (3.70) simplifies as

$$w^{(3.4)} = \tilde{k}_f \, [c_B]^b \, [c_A]^a - \tilde{k}_b \, [c_C]^c \ , \tag{3.71}$$

having denoted with

$$\tilde{k}_f = \frac{k_f}{\left[c_B^{\max}\right]^b \left[c_A^{\max}\right]^a} \ , \qquad \tilde{k}_b = \frac{k_b}{\left[c_C^{\max}\right]^c} \ .$$

3.3.1 Infinitely fast kinetics

We observe that the interaction kinetics of these proteins is orders of magnitude faster than the mechanical spreading of the cell and the diffusion of the free molecules on the cell membrane. This makes us infer that the concentrations of the species $[A]$, $[B]$, and $[C]$ can be assumed at chemical equilibrium at all times, i.e. $w^{(3.4)} = 0$, namely leads us to formulate the *infinitely fast kinetic hypothesis*.

3.3.1.1 The necessary conditions for chemical equilibrium

The necessary conditions for chemical equilibrium are well expressed in [143] by:

$$\sum_i \nu_i^j \mu_i(T, c_\gamma^\circ) = 0 \, , \tag{3.72}$$

where ν_i^j is the stoichiometric coefficient of the generic i-th constituent in the chemical reaction j-th, T is temperature and c_γ° the concentrations of constituents at the equilibrium state. Finally, $\mu_i = \mu_{ii} + RT\ln(a_i)$, represents the chemical potential of a non-ideal solution with μ_{ii} the chemical potential for the corresponding pure substance and a_i the activity of the generic species i [143].
At the chemical equilibrium, chemical kinetics for a non-ideal solution is ruled by:

$$\begin{aligned} \sum_i \nu_i^j \left[\mu_{ii} + RT\ln(a_i)\right] &= 0 \, , \\ -\frac{1}{RT}\sum_i \nu_i^j \mu_{ii} = \sum_i \nu_i^j \ln(a_i) &= \sum_i \ln(a_i)^{\nu_i^j} \ , \\ \exp\left[-\frac{\Delta\left(G^0(T)\right)_j}{RT}\right] &= \prod_i (a_i)^{\nu_i^j} \ . \end{aligned} \tag{3.73}$$

Afterward, assuming that a_i depend only on ϑ_i in the following way $a_i = \dfrac{\vartheta_i}{1-\vartheta_i}$,

$$K_{eq}^j = \exp\left[-\frac{\Delta\left(G^0(T)\right)_j}{RT}\right] = \prod_i \left(\frac{\vartheta_i}{1-\vartheta_i}\right)^{\nu_i^j} \ , \tag{3.74}$$

where $\Delta\left(G^0(T)\right)_j$ and K_{eq}^j are the standard Gibbs free-energy of formation and the constant of equilibrium of the $j-th$ chemical reaction, respectively [143].

3.3.1.2 A new governing equation

Hence, at chemical equilibrium, as $w^{(3.4)}=0$, the concentrations in eq. (3.70) obey the relation

$$\frac{k_f}{k_b}=\left[\frac{\vartheta_C^{\mathrm{eq}}}{1-\vartheta_C^{\mathrm{eq}}}\right]^c\left[\frac{1-\vartheta_A^{\mathrm{eq}}}{\vartheta_A^{\mathrm{eq}}}\right]^a\left[\frac{1-\vartheta_B^{\mathrm{eq}}}{\vartheta_B^{\mathrm{eq}}}\right]^b=K_{\mathrm{eq}}^{(3.4)}\,, \tag{3.75}$$

which defines the constant of equilibrium $K_{\mathrm{eq}}^{(3.4)}$ of reaction (3.4).

Making reference again to the paradigmatic equation (3.71), the concentration of complex c_C is linked to the others in the case of *infinitely fast kinetics*.
Far from saturation, equating the reaction rate to zero, i.e. $w^{(3.4)}=0$, implies

$$[c_{C_R}]^c=\frac{[c_A]^a\,[c_B]^b}{\alpha^{(3.4)}}\,, \tag{3.76}$$

$$\alpha^{(3.4)}=\frac{\tilde{k}_b}{\tilde{k}_f}=\frac{\left[c_{C_A}^{\max}\right]^a\left[c_B^{\max}\right]^b}{\left[c_C^{\max}\right]^c}\frac{1}{K_{eq}^{(3.4)}}\,. \tag{3.77}$$

Consequently, the infinitely fast kinetics hypothesis, Eq. (3.76), acquires the dignity of a governing equation like Eq. (3.10).

3.4 Governing equations and their numerical discretization

3.4.1 Governing equations

The paradigmatic problem (3.12) in the surrogated mechanics approach can be written in terms of concentrations after imposing that species B and C are immobile, that the Fick law (3.68a) relates the mass flux $\vec{h}_A$ to the concentration c_A, and either imposing the mass action law in the form (3.70) ((3.71) when far from saturation) or assuming infinitely fast kinetics in the form (3.76). In this last case, the two concentrations c_A and c_B describe the problem, as follows:

$$\frac{\partial c_A}{\partial t}\left(1+\frac{c_B}{\alpha}\right)+\frac{c_A}{\alpha}\frac{\partial c_B}{\partial t}+\mathrm{div}_{\mathcal{P}}\left[-\mathbb{D}_A\nabla_{\mathcal{P}}\left[c_A\right]\right]=0\,, \tag{3.78a}$$

$$\frac{\partial c_B}{\partial t}\left(1+\frac{c_A}{\alpha}\right)+\frac{c_B}{\alpha}\frac{\partial c_A}{\partial t}=s_B\,. \tag{3.78b}$$

Parameter α depicts the influence of chemistry at infinitely fast kinetics. $\mathbb{D}_A$ is the parameter associated with the diffusion process of the species A on the surface. s_B, instead, is a function that accounts for mechanics, in a surrogated way. All these multi-physics processes impact the discretization parameters for the numerical simulation.

Equations (3.78) can be properly rephrased to model to the integrin - VEGFR reactions (3.1)-(3.3). Four unknown fields, $c_I(\vec{x},t)$, $c_{L_I}(\vec{x},t)$, $c_V(\vec{x},t)$, $c_{L_V}(\vec{x},t)$ describe the evolution of the system through the following non-linear partial differential equations:

$$\frac{\partial c_{L_V}}{\partial t}\left(1+\frac{c_V}{\alpha_1}+\frac{c_V}{\alpha_1}\frac{c_I}{\alpha_2}\right)+\frac{c_V c_{L_V}}{\alpha_1\alpha_2}\frac{\partial c_I}{\partial t}+\frac{\partial c_V}{\partial t}\left(\frac{c_{L_V}}{\alpha_1}+\frac{c_{L_V}}{\alpha_1}\frac{c_I}{\alpha_2}\right)-s_{L_V}=0\,, \tag{3.79a}$$

$$\frac{\partial c_V}{\partial t}+\mathrm{div}_{\mathcal{P}}\left[-\mathbb{D}_V\nabla_{\mathcal{P}}[c_V]\right]-\frac{\partial c_{L_V}}{\partial t}+s_{L_V}=0\,, \tag{3.79b}$$

$$\frac{\partial c_I}{\partial t}\left(1+\frac{c_V c_{L_V}}{\alpha_1\alpha_2}\right)+\mathrm{div}_{\mathcal{P}}\left[-\mathbb{D}_I\nabla_{\mathcal{P}}[c_I]\right]-\frac{\partial c_{L_I}}{\partial t}+\frac{c_I}{\alpha_2}\frac{c_{L_V}}{\alpha_1}\frac{\partial c_V}{\partial t}+\frac{c_I}{\alpha_2}\frac{c_V}{\alpha_1}\frac{\partial c_{L_V}}{\partial t}+s_{L_I}=0\,, \tag{3.79c}$$

$$\frac{\partial c_{L_I}}{\partial t}\left(1+\frac{c_I}{\alpha_3}\right)+\frac{c_{L_I}}{\alpha_3}\frac{\partial c_I}{\partial t}-s_{L_I}=0\,. \tag{3.79d}$$

Initial conditions are dictated by experimental evidences and model assumptions and hold:

$$\begin{aligned} &c_I(\vec{x},0)=?\ molecules/\mu m^2, \quad c_{L_I}(\vec{x},0)=0\ molecules/\mu m^2,\\ &c_V(\vec{x},0)=?\ molecules/\mu m^2, \quad c_{L_V}(\vec{x},0)=0\ molecules/\mu m^2\,, \end{aligned} \tag{3.80}$$

where the numerical values of the initial concentrations of VEGFR2 and integrin, at this point of the thesis, are still unknowns (for this reason denoted with "?" in eq. 3.80) but will be appropriately deduced in chapter 4.

3.4.1.1 Dimensionless Equations

The interplay among the multi-physics processes in the governing equations (3.79) can be captured in a dimensionless formulation. To this aim, denote with L_d a reference length, with t_d a problem timescale, with c_{bulk} a reference concentration, and finally, define the dimensionless (starred) amounts

$$\vec{x}=L_d\vec{x}^{\star}\,,\ t=t_d t^{\star}\,,\ c_A=c_{bulk}c_A^{\star}\,,\ \alpha_i=c_{bulk}\alpha_i^{\star}\,.$$

with $i=1,2,3$. Exploiting the simple identities

$$\frac{\partial c_A}{\partial t}=\frac{c_{bulk}}{t_d}\frac{\partial c_A^{\star}}{\partial t^{\star}}\,,\qquad s_A=\frac{c_{bulk}}{t_d}s_A^{\star}\,, \tag{3.81a}$$

$$\nabla_{\mathcal{P}}[c_a]=\frac{c_{bulk}}{L_d}\nabla_{\mathcal{P}}^{\star}[c_A^{\star}]\,,\qquad \mathrm{div}_{\mathcal{P}}[f]=\frac{1}{L_d}\mathrm{div}_{\mathcal{P}}^{\star}[f]\,. \tag{3.81b}$$

and defining the Peclet number [152] for a generic species A as

$$\mathrm{P}_e^A=\frac{L_d^2}{\mathbb{D}_A t_d}\,,$$

the following dimensionless governing equations of the problem come out:

$$\frac{\partial c_{L_V}^{\star}}{\partial t^{\star}}\left(1+\frac{c_V^{\star}}{\alpha_1^{\star}}+\frac{c_V^{\star}}{\alpha_1^{\star}}\frac{c_{I^{\star}}}{\alpha_2^{\star}}\right)+\frac{c_V^{\star}c_{L_V}^{\star}}{\alpha_1^{\star}\alpha_2^{\star}}\frac{\partial c_I^{\star}}{\partial t^{\star}}+\frac{\partial c_V^{\star}}{\partial t^{\star}}\left(\frac{c_{L_V}^{\star}}{\alpha_1^{\star}}+\frac{c_{L_V}^{\star}}{\alpha_1^{\star}}\frac{c_I^{\star}}{\alpha_2^{\star}}\right)-s_{L_V}^{\star}=0\,, \tag{3.82a}$$

$$\frac{\partial c_V^{\star}}{\partial t^{\star}}-\mathrm{div}_{\mathcal{P}}^{\star}\left[\frac{1}{\mathrm{P}_e^V}\nabla_{\mathcal{P}}^{\star}[c_V^{\star}]\right]-\frac{\partial c_{L_V}^{\star}}{\partial t^{\star}}+s_{L_V}^{\star}=0\,, \tag{3.82b}$$

$$\frac{\partial c_I^\star}{\partial t^\star}\left(1+\frac{c_V^\star c_{L_V}^\star}{\alpha_1^\star\alpha_2^\star}\right)-\mathrm{div}_{\mathcal{P}}^\star\left[\frac{1}{\mathrm{P}_e^I}\,\nabla_{\mathcal{P}}^\star[c_I^\star]\right]-\frac{\partial c_{L_I}^\star}{\partial t^\star}+\frac{c_I^\star}{\alpha_2^\star}\frac{c_{L_V}^\star}{\alpha_1^\star}\frac{\partial c_V^\star}{\partial t^\star}+\frac{c_I^\star}{\alpha_2^\star}\frac{c_V^\star}{\alpha_1^\star}\frac{\partial c_{L_V}^\star}{\partial t^\star}+s_{L_I}^\star=0\,, \quad (3.82c)$$

$$\frac{\partial c_{L_I}^\star}{\partial t^\star}\left(1+\frac{c_I^\star}{\alpha_3^\star}\right)+\frac{c_{L_I}^\star}{\alpha_3^\star}\frac{\partial c_I^\star}{\partial t^\star}-s_{L_I}^\star=0\,. \quad (3.82d)$$

These initial values PDEs will be solved for the unknown fields $c_{L_V}^\star$, $c_V^\star$, $c_I^\star$, and $c_{L_I}^\star$ once initial and boundary conditions will be given. Whereby the transport process is ruled by the Peclet numbers P_e^V and P_e^I, other dimensionless amounts control chemistry (the three parameters $\alpha_i^\star$) and spreading ($s_{L_V}^\star$ and $s_{L_I}^\star$). The ratios between those numbers define the limiting factors during the evolution in time of the whole system. It will be clarified in discussing the numerical approximation of problem (3.82), that stems from its weak form.

3.4.1.2 Weak formulation and finite elements discretization

Formally speaking, the weak formulation is obtained after the multiplication of the strong form of the governing equations by a suitable set of time-independent test functions (expressed here with a superposed caret), and performing an integration upon the domain, exploiting Green's formula with the aim of reducing the order of differentiation. Such a weak form, in terms of the unknown fields $c_{L_V}^\star$, $c_V^\star$, $c_I^\star$, and $c_{L_I}^\star$, reads as follows:

$$\begin{aligned}
&\int_{\mathcal{P}^\star}\hat{c}_{L_V}^\star\left[\frac{\partial c_{L_V}^\star}{\partial t^\star}\left(1+\frac{c_V^\star}{\alpha_1^\star}+\frac{c_V^\star}{\alpha_1^\star}\frac{c_I^\star}{\alpha_2^\star}\right)+\frac{c_V^\star c_{L_V}^\star}{\alpha_1^\star\alpha_3^\star}\frac{\partial c_I^\star}{\partial t^\star}+\frac{\partial c_V^\star}{\partial t^\star}\left(\frac{c_{L_V}^\star}{\alpha_1^\star}+\frac{c_{L_V}^\star}{\alpha_1^\star}\frac{c_I^\star}{\alpha_2^\star}\right)\right]+\\
&\hat{c}_V^\star\left[\frac{\partial c_V^\star}{\partial t^\star}-\frac{\partial c_{L_V}^\star}{\partial t^\star}\right]+\frac{1}{\mathrm{P}_e^V}\nabla_{\mathcal{P}}^\star[c_V^\star]\cdot\nabla_{\mathcal{P}}^\star[\hat{c}_V^\star]+\frac{1}{\mathrm{P}_e^I}\nabla_{\mathcal{P}}^\star[c_I^\star]\cdot\nabla_{\mathcal{P}}^\star[\hat{c}_I^\star]+\\
&\hat{c}_I^\star\left[\frac{\partial c_I^\star}{\partial t^\star}\left(1+\frac{c_V^\star c_{L_V}^\star}{\alpha_1^\star\alpha_2^\star}\right)-\frac{\partial c_{L_I}^\star}{\partial t^\star}+\frac{c_I^\star}{\alpha_2^\star}\frac{c_{L_V}^\star}{\alpha_1^\star}\frac{\partial c_V^\star}{\partial t^\star}+\frac{c_I^\star}{\alpha_2^\star}\frac{c_V^\star}{\alpha_1^\star}\frac{\partial c_{L_V}^\star}{\partial t^\star}\right]+\\
&\hat{c}_{L_I}^\star\left[\frac{\partial c_{L_I}^\star}{\partial t^\star}\left(1+\frac{c_I^\star}{\alpha_3^\star}\right)+\frac{c_{L_I}^\star}{\alpha_3^\star}\frac{\partial c_I^\star}{\partial t^\star}\right]\,\mathrm{d}\mathcal{P}^\star=\int_{\mathcal{P}^\star}\hat{c}_{L_V}^\star\,s_{L_V}^\star-\hat{c}_V^\star\,s_{L_V}^\star-\hat{c}_I^\star\,s_{L_I}^\star+\hat{c}_{L_I}^\star\,s_{L_I}^\star\,\mathrm{d}\mathcal{P}^\star\,. \quad (3.83)
\end{aligned}$$

Note that there is no contribution defined on the boundary because the cell membrane Ω is a closed surface. The problem to be solved can be written in a more abstract setting: we seek for unknown fields $c_G^\star(\vec{x}^\star,t^\star)$ - with G denoting L_V, V, I, or L_I - in the functional space $\mathcal{V}^{[0,t_f^\star]}$ that satisfy initial conditions $c_G^\star(\vec{x}^\star,0)=c_{0G}^\star(\vec{x}^\star)$ such that

$$a\left(\left\{\frac{\partial}{\partial t^\star}c_G^\star(\vec{x}^\star,t^\star),c_G^\star(\vec{x}^\star,t^\star)\right\},\hat{c}_G^\star(\vec{x}^\star)\right)=(f_G(\vec{x}^\star,t^\star),\hat{c}_G^\star(\vec{x}^\star))\,, \quad (3.84)$$

for all $\hat{c}_G^\star(\vec{x}^\star)$ that belong to a suitable functional space $\mathcal{V}$. In the abstract form (3.84), $a(\cdot,\cdot)$ is non-linear functional (3.83) and (f,c) denotes the standard scalar product between f and c. The identification of the functional spaces $\mathcal{V}^{[0,t_f^\star]},\mathcal{V}$ falls beyond the scope of the thesis.

The weak form (3.84) naturally leads to a semi-discrete problem, by approximating the space $\mathcal{V}$ by a finite dimensional space $\mathcal{V}_h$. To this aim, unknown fields $c_G^\star(\vec{x}^\star,t^\star)$ - with G denoting L_V, V, I, or L_I - will be approximated as a product of separated variables, by means of a basis $\{\varphi_i^G(\vec{x}^\star)\}$ of spatial shape functions and nodal unknowns that depend solely on time

$$c_{hG}^\star(\vec{x}^\star,t^\star)=\varphi_i^G(\vec{x}^\star)\,c_i^{\star G}(t^\star)\,. \quad (3.85)$$

The Einstein summation convention is taken for repeated indexes. The semi-discrete approximate problem reads as follows: given $c_{0h_G^\star}^\star(\vec{x}^\star)$ a suitable approximation of the initial datum $c_{0_G^\star}^\star(\vec{x}^\star)$, for each $t^\star \in [0, t_f^\star]$ find $c_{h_G^\star}^\star$ such that

$$a\left(\varphi_j^G(\vec{x}^\star)\ \left\{\frac{\partial}{\partial t^\star}c_j^{\star G}(t^\star), c_j^{\star G}(t^\star)\right\}, \varphi_i^G(\vec{x}^\star)\right) = \left(f_G(\vec{x}^\star, t^\star), \varphi_i^G(\vec{x}^\star)\right). \tag{3.86}$$

The weak form (3.83) is thus rephrased into the system of ordinary differential equations (3.86), whose solution is an approximation of the exact solution for each $t^\star$.

In order to obtain a full discretization of the weak form (3.83), we consider a uniform mesh for the time variable $t^\star$ and define $t_n^\star = n\Delta t^\star$ with $n = 0, 1, ...$, and $\Delta t^\star > 0$ being the time step. The time derivative will be replaced by suitable difference quotients

$$\frac{\partial c_i^{\star G}}{\partial t^\star} \simeq \frac{c_i^{\star G}(t_n^\star + \Delta t^\star) - c_i^{\star G}(t_n^\star)}{\Delta t^\star}, \tag{3.87}$$

thus constructing a sequence $c_{h_A}^{n\star}(\vec{x}^\star)$ that approximates the exact solution $c_G^\star(\vec{x}^\star, t_n^\star)$ [152]. Making recourse to the Backward Euler method leads to the non-linear problem depicted in Appendix A.

The Backward Euler scheme for the finite element approximation of the chemo-transport model was implemented exploiting the high-performance computing open-source library deal.ii (https://www.dealii.org/).
Numerical simulations have shown that it is mandatory to use a very small time discretization step $\Delta t^\star$ when a first-order accuracy numerical integration scheme is used. The limiting time scale is imposed by the mechanical deformation of the cell (identified within the equations by the terms of fictitious sources $s_{L_V}^\star$ and $s_{L_I}^\star$). Therefore, properly capturing the spreading process leads to a very high computational cost.

The time-dependent partial differential equations (3.82) can be conveniently rephrased in order to apply higher order time integration schemes. A variable change will be adopted, namely

$$c_A^\star = c_{L_V}^\star + c_{C_1}^\star + c_{C_2}^\star, \quad c_B^\star = c_V^\star - c_{L_V}^\star, \quad c_D^\star = c_I^\star + c_{C_2}^\star - c_{L_I}^\star, \tag{3.88}$$

having denoted with

$$c_{C_1}^\star = \frac{c_V^\star c_{L_V}^\star}{\alpha_1^\star}, \quad c_{C_2}^\star = \frac{c_I^\star c_V^\star c_{L_V}^\star}{\alpha_1^\star \alpha_2^\star}, \quad c_{C_3}^\star = \frac{c_I^\star c_{L_I}^\star}{\alpha_3^\star}. \tag{3.89}$$

Simple algebra leads to the following set of time-dependent PDEs,

$$\frac{\partial c_A^\star}{\partial t^\star} - s_{L_V}^\star = 0, \tag{3.90a}$$

$$\frac{\partial c_B^\star}{\partial t^\star} - \frac{1}{\mathrm{P}_e^V}\mathrm{div}_{\mathcal{P}}^\star\left[\nabla_{\mathcal{P}}^\star\left[c_V^\star\right]\right] + s_{L_V}^\star = 0, \tag{3.90b}$$

$$\frac{\partial c_D^\star}{\partial t^\star} - \frac{1}{\mathrm{P}_e^I}\mathrm{div}_{\mathcal{P}}^\star\left[\nabla_{\mathcal{P}}^\star\left[c_I^\star\right]\right] + s_{L_I}^\star = 0, \tag{3.90c}$$

$$\frac{\partial c_E^\star}{\partial t^\star} - s_{L_I}^\star = 0\,. \tag{3.90d}$$

subject to the constraints

$$c_V^\star c_V^\star\,(\alpha_2^\star + c_I^\star) + c_V^\star\,(\alpha_1^\star\alpha_2^\star - \alpha_2^\star c_B^\star - c_I^\star c_B^\star) - \alpha_1^\star\alpha_2^\star\,(c_B^\star + c_A^\star) = 0 \tag{3.91a}$$

$$\begin{aligned} &c_I^\star c_I^\star\,(\alpha_1^\star\alpha_2^\star + c_V^\star c_V^\star - c_V^\star c_B^\star) + c_I^\star\,(-\alpha_1^\star\alpha_2^\star c_D^\star + \alpha_1^\star\alpha_2^\star\alpha_3^\star + \alpha_3^\star c_V^\star c_V^\star - \alpha_3^\star c_V^\star c_B^\star) + \\ &\quad - \alpha_1^\star\alpha_2^\star\alpha_3^\star\,(c_E^\star + c_D^\star) = 0\,, \end{aligned} \tag{3.91b}$$

and initial conditions

$$c_A^\star(0) = 0\,, \qquad c_B^\star(0) = \frac{?}{c_{bulk}}\,, \qquad c_D^\star(0) = \frac{?}{c_{bulk}}\,, \qquad c_E^\star(0) = 0\,, \tag{3.92}$$

where the symbol "?" means that the numerical value of the concentrations c_B and c_D are not known yet. In fact, such values will be defined once the initial concentrations of VEGFR2 and integrin will be suitably introduced in chapter 4, further considering that $c_{L_V}^\star(0) = c_{L_V}^\star(0) = c_{L_I}^\star(0) = c_{C_1}^\star(0) = c_{C_2}^\star(0) = c_{C_3}^\star(0) = 0$ inasmuch, at instant $t = 0$ s, there is no contact between the cell membrane and the ligands coated substrate. Analytical integration of (3.90a) and (3.90d) together with relevant initial conditions (3.92) leads to:

$$c_A^\star(\vec{x}^\star, t^\star) = S_{L_V}^\star(\vec{x}^\star, t^\star)\,, \qquad c_E^\star(\vec{x}^\star, t^\star) = S_{L_I}^\star(\vec{x}^\star, t^\star)\,,$$

where $S_{L_V}^\star$ and $S_{L_I}^\star$ are the integral over time of the source terms. They correspond to the value of ligands that at every instant $t^\star$ are in contact with the cell membrane at point $\vec{x}^\star$ due to the (surrogated) mechanics of spreading and are also available for the reaction with relevant counterparts. As such, they shall be assumed as experimental data, whereby the source terms $s_{L_V}^\star$ and $s_{L_I}^\star$ are much harder to identify.

Since $c_A^\star$ and $c_E^\star$ have been analytically solved, the weak form of problem (3.90) can be recast in a standard [152] abstract setting: we seek for unknown fields $c_Z^\star(\vec{x}^\star, t^\star)$ - with Z denoting B or D - in the functional space $\mathcal{V}^{[0,t_f^\star]}$ that satisfy initial conditions (3.92) and subject to the constraints (3.91) such that

$$\frac{\partial}{\partial t^\star} b\,(c_Z^\star(\vec{x}^\star, t^\star), \hat{c}_Z^\star(\vec{x}^\star)) + a\,(c_Z^\star(\vec{x}^\star, t^\star), \hat{c}_Z^\star(\vec{x}^\star)) = (f_Z(\vec{x}^\star, t^\star), \hat{c}_Z^\star(\vec{x}^\star))\,, \tag{3.93}$$

for all $\hat{c}_Z^\star(\vec{x}^\star)$ that belong to a suitable functional space $\mathcal{V}$. In the abstract form (3.93), $a(\cdot,\cdot)$ and $b(\cdot,\cdot)$ are the usual bilinear forms of the Laplace operator written on a non-Riemann manifold $\mathcal{P}^\star$. The weak form (3.93) can be conveniently integrated in time, providing the following approximation scheme

$$\begin{aligned} &b\,(c_Z^\star(\vec{x}^\star, t_n^\star), \hat{c}_Z^\star(\vec{x}^\star)) - b\left(c_Z^\star(\vec{x}^\star, t_{n-1}^\star), \hat{c}_Z^\star(\vec{x}^\star)\right) \\ &\quad + \int_{t_{n-1}^\star}^{t_n^\star} a\,(c_Z^\star(\vec{x}^\star, \tau^\star), \hat{c}_Z^\star(\vec{x}^\star))\,\mathrm{d}\tau^\star = (\int_{t_{n-1}^\star}^{t_n^\star} f_Z(\vec{x}^\star, \tau^\star)\mathrm{d}\tau^\star, \hat{c}_Z^\star(\vec{x}^\star))\,, \end{aligned} \tag{3.94}$$

for all $\hat{c}_Z^\star(\vec{x}^\star)$, whereby $c_Z^\star(\vec{x}^\star, \tau^\star)$ must satisfy initial conditions (3.92) and is subject to the constraints (3.91). Note that the integral

$$\int_{t_{n-1}^\star}^{t_n^\star} f_Z(\vec{x}^\star, \tau^\star)\mathrm{d}\tau^\star$$

is given in closed form and involves the functions $S^{\star}_{L_V}(\vec{x}^{\star},t^{\star})$ and $S^{\star}_{L_I}(\vec{x}^{\star},t^{\star})$ evaluated in $t^{\star}_{n-1}$ and $t^{\star}_{n}$. In view of this feature, the contribution of cell spreading in terms of surrogated mechanics is captured with high accuracy, whereas the accuracy in the approximation of the transport term

$$\int_{t^{\star}_{n-1}}^{t^{\star}_{n}} a\left(c^{\star}_{Z}(\vec{x}^{\star},\tau^{\star}),\hat{c}^{\star}_{Z}(\vec{x}^{\star})\right)\mathrm{d}\tau^{\star}$$

appears not to require too small time steps in view of the longer timescale of the diffusivity compared to the other two physics involved (see also the similar conclusions reached in [138]). The extended version of the weak form (3.94) is following depicted. Specifically, the (3.90a) and (3.90d) are firstly analytically integrated in time (with $\int_0^t s_{L_V}(\vec{x},\tau)d\tau = S_{L_V}(\vec{x},t)$ and $\int_0^t s_{L_I}(\vec{x},\tau)d\tau = S_{L_I}(\vec{x},t)$ see section B.1.1) and then they have been write in a weak form and discretized through the (3.85). For what concerns the weak formulations corresponding to (3.90b), and (3.90c), instead, has been done either a spatial and temporal discretization. The first one by means of the (3.85), i.e. approximating the unknown concentrations fields through the product of the separated variables: spatial shape functions, and nodal unknowns that depend solely on time. The second one, subdividing the time span interval $[0,t]$ into n steps, it has been possible to deduce the expressions (3.96) and (3.97) integrating between the steps $[t_{n-1},t_n]$, where a Newton-Cotes quadrature formula has applied (see (3.101) and (3.102)) to the diffusive terms. Finally, the corresponding weak formulation of the constraints (3.91a), and (3.91b), have been discretized by the finite element method giving expressions (3.99) and (3.100).

First Equation (3.90a)

$$\begin{gathered}\int_{\mathcal{P}^{\star}} \varphi^{\star A}_{i}(\vec{x}^{\star})\varphi^{\star A}_{j}(\vec{x}^{\star})c^{\star A}_{j}(t^{\star})d\mathcal{P}^{\star} - \int_{\mathcal{P}^{\star}} \varphi^{\star A}_{i}(\vec{x}^{\star})S^{\star}_{L_V}(\vec{x}^{\star},t^{\star})d\mathcal{P}^{\star} = 0\,,\\ c^{\star}_{A}(\vec{x}^{\star},0) = 0\,.\end{gathered} \tag{3.95}$$

Second Equation (3.90b)

$$\begin{gathered}\int_{\mathcal{P}^{\star}} \varphi^{\star B}_{i}(\vec{x}^{\star})\varphi^{\star B}_{l}(\vec{x}^{\star})c^{\star B}_{l}(t^{\star}_{n})d\mathcal{P}^{\star} - \int_{\mathcal{P}^{\star}} \varphi^{\star B}_{i}(\vec{x}^{\star})\varphi^{\star B}_{l}(\vec{x}^{\star})c^{\star B}_{l}(t^{\star}_{n-1})d\mathcal{P}^{\star} +\\ \frac{1}{\mathrm{P}^{V}_{e}}\int_{\mathcal{P}^{\star}} \nabla^{\star}_{\mathcal{P}}\left[\,\varphi^{\star B}_{i}(\vec{x}^{\star})\,\right]\cdot\nabla^{\star}_{\mathcal{P}}\left[\,\varphi^{\star V}_{k}(\vec{x}^{\star})\,\right]d\mathcal{P}^{\star}\int_{t^{\star}_{n-1}}^{t^{\star}_{n}} c^{\star V}_{k}(\tau^{\star})d\tau^{\star} +\\ \int_{\mathcal{P}^{\star}} \varphi^{\star B}_{i}(\vec{x}^{\star})S^{\star}_{L_V}(\vec{x}^{\star},t^{\star}_{n})d\mathcal{P}^{\star} - \int_{\mathcal{P}^{\star}} \varphi^{\star B}_{i}S^{\star}_{L_V}(\vec{x}^{\star},t^{\star}_{n-1})d\mathcal{P}^{\star} = 0\,,\\ c^{\star}_{B}(\vec{x}^{\star},0) = \frac{?}{c_{bulk}}\,.\end{gathered} \tag{3.96}$$

Third Equation (3.90c)

$$
\begin{aligned}
&\int_{\mathcal{P}^\star} \varphi_i^{\star D}(\vec{x}^\star)\varphi_m^{\star D}(\vec{x}^\star)c_m^{\star D}(t_n^\star)d\mathcal{P}^\star - \int_{\mathcal{P}^\star} \varphi_i^{\star D}(\vec{x}^\star)\varphi_m^{\star D}(\vec{x}^\star)c_m^{\star D}(t_{n-1}^\star)d\mathcal{P}^\star + \\
&\frac{1}{\mathrm{P}_e^I}\int_{\mathcal{P}^\star} \nabla_{\mathcal{P}}^\star\left[\,\varphi_i^{\star D}(\vec{x}^\star)\,\right]\cdot\nabla_{\mathcal{P}}^\star\left[\,\varphi_p^{\star I}(\vec{x}^\star)\,\right]d\mathcal{P}^\star \int_{t_{n-1}^\star}^{t_n^\star} c_p^{\star I}(\tau^\star)d\tau^\star + \\
&\int_{\mathcal{P}^\star} \varphi_i^{\star D}(\vec{x}^\star)S_{L_I}^\star(\vec{x}^\star,t_n^\star)d\mathcal{P}^\star - \int_{\mathcal{P}^\star} \varphi_i^d S_{L_I}^\star(\vec{x}^\star,t_{n-1}^\star)d\mathcal{P}^\star = 0\,, \\
&c_D^\star(\vec{x}^\star,0) = \frac{?}{c_{bulk}}\,.
\end{aligned}
\tag{3.97}
$$

Fourth Equation (3.90d)

$$
\begin{aligned}
&\int_{\mathcal{P}^\star} \varphi_i^{\star E}(\vec{x}^\star)\varphi_s^{\star E}(\vec{x}^\star)c_s^{\star E}(t^\star)d\mathcal{P}^\star - \int_{\mathcal{P}^\star} \varphi_i^{\star E}(\vec{x}^\star)S_{L_I}^\star(\vec{x}^\star,t^\star)d\mathcal{P}^\star = 0\,, \\
&c_E^\star(\vec{x}^\star,0) = 0\,.
\end{aligned}
\tag{3.98}
$$

Fifth Equation (3.91a)

$$
\begin{gathered}
\alpha_2^\star \int_{\mathcal{P}^\star} \varphi_i^{\star V}(\vec{x}^\star)\varphi_k^{\star V}(\vec{x}^\star)\varphi_k^{\star V}(\vec{x}^\star)c_k^{\star V}(t^\star)c_k^{\star V}(t^\star)d\mathcal{P}^\star + \\
\int_{\mathcal{P}^\star} \varphi_i^{\star V}(\vec{x}^\star)\varphi_k^{\star V}(\vec{x}^\star)\varphi_k^{\star V}(\vec{x}^\star)\varphi_p^{\star I}(\vec{x}^\star)c_k^{\star V}(t^\star)c_k^{\star V}(t^\star)c_p^{\star I}(t^\star)d\mathcal{P}^\star + \\
\alpha_1^\star\alpha_2^\star \int_{\mathcal{P}^\star} \varphi_i^{\star V}(\vec{x}^\star)\varphi_k^{\star V}(\vec{x}^\star)c_k^{\star V}(t^\star)d\mathcal{P}^\star - \\
\alpha_2^\star \int_{\mathcal{P}^\star} \varphi_i^{\star V}(\vec{x}^\star)\varphi_k^{\star V}(\vec{x}^\star)\varphi_l^{\star B}(\vec{x}^\star)c_k^{\star V}(t^\star)c_l^{\star B}(t^\star)d\mathcal{P}^\star - \\
\int_{\mathcal{P}^\star} \varphi_i^{\star V}(\vec{x}^\star)\varphi_k^{\star V}(\vec{x}^\star)\varphi_p^{\star I}(\vec{x}^\star)\varphi_l^{\star B}(\vec{x}^\star)c_k^{\star V}(t^\star)c_p^{\star I}(t^\star)c_l^{\star B}(t^\star)d\mathcal{P}^\star - \\
\alpha_1^\star\alpha_2^\star \int_{\mathcal{P}^\star} \varphi_i^{\star V}(\vec{x}^\star)\varphi_l^{\star B}(\vec{x}^\star)c_l^{\star B}(t^\star)d\mathcal{P}^\star - \\
\alpha_1^\star\alpha_2^\star \int_{\mathcal{P}^\star} \varphi_i^{\star V}(\vec{x}^\star)\varphi_j^{\star A}(\vec{x}^\star)c_j^{\star A}(t^\star)d\mathcal{P}^\star = 0\,, \\
c_V^\star(\vec{x}^\star,0) = \frac{?}{c_{bulk}}\,.
\end{gathered}
\tag{3.99}
$$

Sixth Equation (3.91b)

$$
\begin{gathered}
\alpha_1^\star\alpha_2^\star \int_{\mathcal{P}^\star} \varphi_i^{\star I}(\vec{x}^\star)\varphi_p^{\star I}(\vec{x}^\star)\varphi_p^{\star I}(\vec{x}^\star)c_p^{\star I}(t^\star)c_p^{\star I}(t^\star)d\mathcal{P}^\star + \\
\int_{\mathcal{P}^\star} \varphi_i^{\star I}(\vec{x}^\star)\varphi_p^{\star I}(\vec{x}^\star)\varphi_p^{\star I}(\vec{x}^\star)\varphi_k^{\star V}(\vec{x}^\star)\varphi_k^{\star V}(\vec{x}^\star)c_p^{\star I}(t^\star)c_p^{\star I}(t^\star)c_k^{\star V}(t^\star)c_k^{\star V}(t^\star)d\mathcal{P}^\star - \\
\int_{\mathcal{P}^\star} \varphi_i^{\star I}(\vec{x}^\star)\varphi_p^{\star I}(\vec{x}^\star)\varphi_p^{\star I}(\vec{x}^\star)\varphi_k^{\star V}(\vec{x}^\star)\varphi_l^{\star B}(\vec{x}^\star)c_p^{\star I}(t^\star)c_p^{\star I}(t^\star)c_k^{\star V}(t^\star)c_l^{\star B}(t^\star)d\mathcal{P}^\star - \\
\alpha_1^\star\alpha_2^\star \int_{\mathcal{P}^\star} \varphi_i^{\star I}(\vec{x}^\star)\varphi_p^{\star I}(\vec{x}^\star)\varphi_m^{\star D}(\vec{x}^\star)c_p^{\star I}(t^\star)c_m^{\star D}(t^\star)d\mathcal{P}^\star + \\
\alpha_1^\star\alpha_2^\star\alpha_3^\star \int_{\mathcal{P}^\star} \varphi_i^{\star I}(\vec{x}^\star)\varphi_p^{\star I}(\vec{x}^\star)c_p^{\star I}(t^\star)d\mathcal{P}^\star + \\
\alpha_3^\star \int_{\mathcal{P}^\star} \varphi_i^{\star I}(\vec{x}^\star)\varphi_p^{\star I}(\vec{x}^\star)\varphi_k^{\star V}(\vec{x}^\star)\varphi_k^{\star V}(\vec{x}^\star)c_p^{\star I}(t^\star)c_k^{\star V}(t^\star)c_k^{\star V}(t^\star)d\mathcal{P}^\star - \\
\alpha_3^\star \int_{\mathcal{P}^\star} \varphi_i^{\star I}(\vec{x}^\star)\varphi_p^{\star I}(\vec{x}^\star)\varphi_k^{\star V}(\vec{x}^\star)\varphi_l^{\star B}(\vec{x}^\star)c_p^{\star I}(t^\star)c_k^{\star V}(t^\star)c_l^{\star B}(t^\star)d\mathcal{P}^\star - \\
\alpha_1^\star\alpha_2^\star\alpha_3^\star \int_{\mathcal{P}^\star} \varphi_i^{\star I}(\vec{x}^\star)\varphi_s^{\star E}(\vec{x}^\star)c_s^{\star E}(t^\star)d\mathcal{P}^\star - \\
\alpha_1^\star\alpha_2^\star\alpha_3^\star \int_{\mathcal{P}^\star} \varphi_i^{\star I}(\vec{x}^\star)\varphi_m^{\star D}(\vec{x}^\star)c_m^{\star D}(t^\star)d\mathcal{P}^\star = 0\,, \\
c_I^\star(\vec{x}^\star,0) = \frac{?}{c_{bulk}}\,.
\end{gathered}
\tag{3.100}
$$

In which the following Newton-Cotes quadrature formula will be given:

$$\begin{gathered}\int\limits_{\mathcal{P}^\star}\frac{1}{\mathrm{P}_e^V}\nabla_{\mathcal{P}}^\star\left[\,\varphi_i^{\star B}(\vec{x}^\star)\,\right]\cdot\nabla_{\mathcal{P}}^\star\left[\,\varphi_k^{\star V}(\vec{x}^\star)\,\right]d\mathcal{P}^\star\int\limits_{t_{n-1}^\star}^{t_n^\star}c_k^{\star V}(\tau^\star)d\tau^\star\\ \simeq\\ \int\limits_{\mathcal{P}^\star}\frac{1}{\mathrm{P}_e^V}\nabla_{\mathcal{P}}^\star\left[\,\varphi_i^{\star B}(\vec{x}^\star)\,\right]\cdot\nabla_{\mathcal{P}}^\star\left[\,\varphi_k^{\star V}(\vec{x}^\star)\,\right]d\mathcal{P}^\star\frac{\Delta t^\star}{2}\left(c_k^{\star V}(t_n^\star)+c_k^{\star V}(t_{n-1}^\star)\right)\,,\end{gathered}\tag{3.101}$$

$$\begin{gathered}\int\limits_{\mathcal{P}^\star}\frac{1}{\mathrm{P}_e^I}\nabla_{\mathcal{P}}^\star\left[\,\varphi_i^{\star D}(\vec{x}^\star)\,\right]\cdot\nabla_{\mathcal{P}}^\star\left[\,\varphi_p^{\star I}(\vec{x}^\star)\,\right]d\mathcal{P}^\star\int\limits_{t_{n-1}^\star}^{t_n^\star}c_p^{\star I}(\tau^\star)d\tau^\star\\ \simeq\\ \int\limits_{\mathcal{P}^\star}\frac{1}{\mathrm{P}_e^I}\nabla_{\mathcal{P}}^\star\left[\,\varphi_i^{\star D}(\vec{x}^\star)\,\right]\cdot\nabla_{\mathcal{P}}^\star\left[\,\varphi_p^{\star I}(\vec{x}^\star)\,\right]d\mathcal{P}^\star\frac{\Delta t^\star}{2}\left(c_p^{\star I}(t_n^\star)+c_p^{\star I}(t_{n-1}^\star)\right)\,.\end{gathered}\tag{3.102}$$

Finally, it is possible deduce the follow six equations:

First equation (3.90a)

$$\begin{gathered}\int_{\mathcal{P}^\star}\varphi_i^{\star A}(\vec{x}^\star)\varphi_j^{\star A}(\vec{x}^\star)d\mathcal{P}^\star\left[c_j^{\star A}(t^\star)\right]-\int_{\mathcal{P}^\star}\varphi_i^{\star A}(\vec{x}^\star)S_{L_V}^\star(\vec{x}^\star,t^\star)d\mathcal{P}^\star=0\,,\\ c_A^\star(\vec{x}^\star,0)=0\,.\end{gathered}\tag{3.103}$$

Second equation (3.90b)

$$\begin{gathered}\int_{\mathcal{P}^\star}\varphi_i^{\star B}(\vec{x}^\star)\varphi_l^{\star B}(\vec{x}^\star)d\mathcal{P}^\star\left[c_l^{\star B}(t_n^\star)\right]-\int_{\mathcal{P}^\star}\varphi_i^{\star B}(\vec{x}^\star)\varphi_l^{\star B}(\vec{x}^\star)d\mathcal{P}^\star\left[c_l^{\star B}(t_{n-1}^\star)\right]+\\ \frac{1}{\mathrm{P}_e^V}\int\limits_{\mathcal{P}^\star}\nabla_{\mathcal{P}}^\star\left[\,\varphi_i^{\star B}(\vec{x}^\star)\,\right]\cdot\nabla_{\mathcal{P}}^\star\left[\,\varphi_k^{\star V}(\vec{x}^\star)\,\right]d\mathcal{P}^\star\left[\frac{\Delta t^\star}{2}\left(c_k^{\star V}(t_n^\star)+c_k^{\star V}(t_{n-1}^\star)\right)\right]+\\ \int_{\mathcal{P}^\star}\varphi_i^{\star B}(\vec{x}^\star)S_{L_V}^\star(\vec{x}^\star,t_n^\star)d\mathcal{P}^\star-\int_{\mathcal{P}^\star}\varphi_i^{\star B}S_{L_V}^\star(\vec{x}^\star,t_{n-1}^\star)d\mathcal{P}^\star=0\,,\\ c_B^\star(\vec{x}^\star,0)=\frac{?}{c_{bulk}}\,.\end{gathered}\tag{3.104}$$

Third equation (3.90c)

$$\begin{gathered}\int_{\mathcal{P}^\star}\varphi_i^{\star D}(\vec{x}^\star)\varphi_m^{\star D}(\vec{x}^\star)d\mathcal{P}^\star\left[c_m^{\star D}(t_n^\star)\right]-\int_{\mathcal{P}^\star}\varphi_i^{\star D}(\vec{x}^\star)\varphi_m^{\star D}(\vec{x}^\star)d\mathcal{P}^\star\left[c_m^{\star D}(t_{n-1}^\star)\right]+\\ \frac{1}{\mathrm{P}_e^I}\int\limits_{\mathcal{P}^\star}\nabla_{\mathcal{P}}^\star\left[\,\varphi_i^{\star D}\,\right]\cdot\nabla_{\mathcal{P}}^\star\left[\,\varphi_p^{\star I}(\vec{x}^\star)\,\right]d\mathcal{P}^\star\left[\frac{\Delta t^\star}{2}\left(c_p^{\star I}(t_n^\star)+c_p^{\star I}(t_{n-1}^\star)\right)\right]+\\ +\int_{\mathcal{P}^\star}\varphi_i^{\star D}(\vec{x}^\star)S_{L_I}^\star(\vec{x}^\star,t_n^\star)d\mathcal{P}^\star-\int_{\mathcal{P}^\star}\varphi_i^{d}(\vec{x}^\star)S_{L_I}^\star(\vec{x}^\star,t_{n-1}^\star)d\mathcal{P}^\star=0\,,\\ c_D^\star(\vec{x}^\star,0)=\frac{?}{c_{bulk}}\,.\end{gathered}\tag{3.105}$$

Fourth equation (3.90d)

$$\begin{gathered}\int_{\mathcal{P}^\star} \varphi_i^{\star E}(\vec{x}^\star)\varphi_s^{\star E}(\vec{x}^\star)d\mathcal{P}^\star\left[c_s^{\star E}(t^\star)\right] - \int_{\mathcal{P}^\star} \varphi_i^{\star E}(\vec{x}^\star)S_{L_I}^\star(\vec{x}^\star,t^\star)d\mathcal{P}^\star = 0\,,\\ c_E^\star(\vec{x}^\star,0) = 0\,.\end{gathered} \tag{3.106}$$

Fifth equation (3.91a)

$$\begin{gathered}\alpha_2^\star \int_{\mathcal{P}^\star} \varphi_i^{\star V}(\vec{x}^\star)\varphi_k^{\star V}(\vec{x}^\star)\varphi_k^{\star V}(\vec{x}^\star)d\mathcal{P}^\star\left[c_k^{\star V}(t^\star)c_k^{\star V}(t^\star)\right] +\\ \int_{\mathcal{P}^\star} \varphi_i^{\star V}(\vec{x}^\star)\varphi_k^{\star V}(\vec{x}^\star)\varphi_k^{\star V}(\vec{x}^\star)\varphi_p^{\star I}(\vec{x}^\star)d\mathcal{P}^\star\left[c_k^{\star V}(t^\star)c_k^{\star V}(t^\star)c_p^{\star I}(t^\star)\right] +\\ \alpha_1^\star\alpha_2^\star \int_{\mathcal{P}^\star} \varphi_i^{\star V}(\vec{x}^\star)\varphi_k^{\star V}(\vec{x}^\star)d\mathcal{P}^\star\left[c_k^{\star V}(t^\star)\right] -\\ \alpha_2^\star \int_{\mathcal{P}^\star} \varphi_i^{\star V}(\vec{x}^\star)\varphi_k^{\star V}(\vec{x}^\star)\varphi_l^{\star B}(\vec{x}^\star)d\mathcal{P}^\star\left[c_k^{\star V}(t^\star)c_l^{\star B}(t^\star)\right] -\\ \int_{\mathcal{P}^\star} \varphi_i^{\star V}\varphi_k^{\star V}(\vec{x}^\star)\varphi_p^{\star I}(\vec{x}^\star)\varphi_l^{\star B}(\vec{x}^\star)d\mathcal{P}^\star\left[c_k^{\star V}(t^\star)c_p^{\star I}(t^\star)c_l^{\star B}(t^\star)\right] -\\ \alpha_1^\star\alpha_2^\star \int_{\mathcal{P}^\star} \varphi_i^{\star V}(\vec{x}^\star)\varphi_l^{\star B}(\vec{x}^\star)d\mathcal{P}^\star\left[c_l^{\star B}(t^\star)\right] -\\ \alpha_1^\star\alpha_2^\star \int_{\mathcal{P}^\star} \varphi_i^{\star V}(\vec{x}^\star)\varphi_j^{\star A}(\vec{x}^\star)d\mathcal{P}^\star\left[c_j^{\star A}(t^\star)\right] = 0\,,\\ c_V^\star(\vec{x}^\star,0) = \frac{?}{c_{bulk}}\,.\end{gathered} \tag{3.107}$$

Sixth equation (3.91b)

$$\begin{gathered}\alpha_1^\star\alpha_2^\star \int_{\mathcal{P}^\star} \varphi_i^{\star I}(\vec{x}^\star)\varphi_p^{\star I}(\vec{x}^\star)\varphi_p^{\star I}(\vec{x}^\star)d\mathcal{P}^\star\left[c_p^{\star I}(t^\star)c_p^{\star I}(t^\star)\right] +\\ \int_{\mathcal{P}^\star} \varphi_i^{\star I}(\vec{x}^\star)\varphi_p^{\star I}(\vec{x}^\star)\varphi_p^{\star I}(\vec{x}^\star)\varphi_k^{\star V}(\vec{x}^\star)\varphi_k^{\star V}(\vec{x}^\star)d\mathcal{P}^\star\left[c_p^{\star I}(t^\star)c_p^{\star I}(t^\star)c_k^{\star V}(t^\star)c_k^{\star V}(t^\star)\right] -\\ \int_{\mathcal{P}^\star} \varphi_i^{\star I}(\vec{x}^\star)\varphi_p^{\star I}(\vec{x}^\star)\varphi_p^{\star I}(\vec{x}^\star)\varphi_k^{\star V}(\vec{x}^\star)\varphi_l^{\star B}(\vec{x}^\star)d\mathcal{P}^\star\left[c_p^{\star I}(t^\star)c_p^{\star I}(t^\star)c_k^{\star V}(t^\star)c_l^{\star B}(t^\star)\right] -\\ \alpha_1^\star\alpha_2^\star \int_{\mathcal{P}^\star} \varphi_i^{\star I}(\vec{x}^\star)\varphi_p^{\star I}(\vec{x}^\star)\varphi_m^{\star D}(\vec{x}^\star)d\mathcal{P}^\star\left[c_p^{\star I}(t^\star)c_m^{\star D}(t^\star)\right] +\\ \alpha_1^\star\alpha_2^\star\alpha_3^\star \int_{\mathcal{P}^\star} \varphi_i^{\star I}(\vec{x}^\star)\varphi_p^{\star I}(\vec{x}^\star)d\mathcal{P}^\star\left[c_p^{\star I}(t^\star)\right] +\\ \alpha_3^\star \int_{\mathcal{P}^\star} \varphi_i^{\star I}(\vec{x}^\star)\varphi_p^{\star I}(\vec{x}^\star)\varphi_k^{\star V}(\vec{x}^\star)\varphi_k^{\star V}(\vec{x}^\star)d\mathcal{P}^\star\left[c_p^{\star I}(t^\star)c_k^{\star V}(t^\star)c_k^{\star V}(t^\star)\right] -\\ \alpha_3^\star \int_{\mathcal{P}^\star} \varphi_i^{\star I}(\vec{x}^\star)\varphi_p^{\star I}(\vec{x}^\star)\varphi_k^{\star V}(\vec{x}^\star)\varphi_l^{\star B}(\vec{x}^\star)d\mathcal{P}^\star\left[c_p^{\star I}(t^\star)c_k^{\star V}(t^\star)c_l^{\star B}(t^\star)\right] -\\ \alpha_1^\star\alpha_2^\star\alpha_3^\star \int_{\mathcal{P}^\star} \varphi_i^{\star I}(\vec{x}^\star)\varphi_s^{\star E}(\vec{x}^\star)d\mathcal{P}^\star\left[c_s^{\star E}(t^\star)\right] -\\ \alpha_1^\star\alpha_2^\star\alpha_3^\star \int_{\mathcal{P}^\star} \varphi_i^{\star I}(\vec{x}^\star)\varphi_m^{\star D}(\vec{x}^\star)d\mathcal{P}^\star\left[c_m^{\star D}(t^\star)\right] = 0\,,\\ c_I^\star(\vec{x}^\star,0) = \frac{?}{c_{bulk}}\,.\end{gathered} \tag{3.108}$$

The discretized weak formulations here presented led to the results presented in Appendix B; here, exploiting the high-performance computing library deal.ii (see https://www.dealii.org), has been implemented a fully coupled Newton-Raphson solver for the solution of this set of approximated expressions. These numerical outcomes are appropriately based on experimental parameters, although they are slightly different from those that we will deduce in the next chapter 4. These preliminary results (those of Appendix B) stem from our first approach of a multiple chemical reactions problem (see [140]), and they have provided a qualitative conclusion on how VEGFR2 and integrin can evolve in time when both are recruited in the basal side of an EC spread on a substrate enriched of ligands. Nonetheless, the non-linearities introduced by the change of variables (3.88), specifically owing to the expressions (3.91a) and (3.91b), give rise to several computational problems that have been overtaken by the formulations presented in chapter 5. Here, a further way to implement the balance equations (3.13) has been performed.

Chapter 4

Experimental data and constitutive parameters

In the current chapter, we present a scenario of the experimental results that we want to replay by means of in-silico simulation, and contextually, the value of the constitutive parameters that the multi-fields model needs. Specifically, some of these have been deduced by the group of biologists guided by Professor Stefania Mitola, and others inferred from literature. Importantly, Professor Stefania Mitola and Dr. Cosetta Ravelli realized, in the newborn "Imaging core facility" of the Preventive and Personalized Medicine Laboratory of the University of Brescia, imaging experiments. Moreover, those variables that we will be not able to quantify experimentally will be the specific subject of calibration, in chapter 5, throughout the co-designing of experimental and numerical simulations.

Single-molecule (SM) imaging, as well as bulk (or ensemble) fluorescence imaging, are two combinable experimental approaches, through which it is possible to examine the receptor dynamics on the cell membrane.

FRAP (see Appendix E.1), namely Fluorescence recovery after photobleaching is surely among the most noted ensemble techniques available to examine the receptor dynamics on the cell membrane. This methodology provides that a fluorescent protein is fused with the molecule under study, allowing to visualize its mobility on the cell membrane [9] (chapter 9). Particularly, specific regions of the cell membrane are bleached (bleached region - ROI -) by means of a laser beam, in order to achieve pieces of information through the calculation of time necessary to recover the fluorescence in the ROI itself. Specifically, the amount of *immobile* and *mobile* fraction, as well as the diffusivity of molecules of interest on the cell membrane, are guaranteed by FRAP. However, only averaged information, in time and space, on a large number of fluorescent particles, is provided by this method. Moreover, if molecules can not migrate in ROI, only through the aid of FRAP we are not able to understand the reason for this peculiar behavior [9] (chapter 10).

Qualitative and quantitatively pieces of knowledge of the trajectories and so of the evolution in time of the single-molecule position, are guaranteed by SM imaging and tracking (single-particle tracking, SPT - see Appendix E.3 -). This methodology works trailing single-molecules movement by video microscopy, by labeling it with antibodies matched with fluorescent coloring or minute gold particles [9] (chapter 10). Importantly, the particle path could actually reveal the key mecha-

nisms of molecule dynamics, including membrane lateral movements.

We can not neglect further experimental methodologies, namely the Surface Plasmon Resonance (SPR - see Appendix E.4 -), FRET analysis (see Appendix E.1), and Time-lapse imaging (see next section 4.1). The first provides key results in the affinity measurements among molecules and in the association and dissociation constant rate of specific chemical reactions. Hence, equilibrium binding and interaction kinetics analysis is possible by means of SPR. The second one allows us to study molecular structures of biological molecules, as well as protein interactions on the cell membrane. The last one allows the study of the spatial and temporal evolution of the labeled protein on the cell membrane by means of a series of photograms.

Following we provide a brief introduction to the management of the above-mentioned experimental methodologies and their results. Such a specification is deemed necessary in order to understand how practically work the experimental setting of a biological experiment with the aim to grasp how to deduce the experimental parameters characterizing our mathematical models.

4.1 Experimental data on time-lapse analysis adhesion assays

4.1.1 Experimental insight

Either spatial that temporal information is enclosed in the so-called time-lapse experiments. In fact, thanks to an incessant development over the years of the tools available to biologists (e.g electronic imaging sensor, labeling methods, and light microscopy), we dispose of sensitive time-lapse imaging of cells and single molecules [31] (chapter 2).

It is possible to resume the time-lapse imaging studies in the following four successive steps [31] (chapter 2):

- programming of the experiments and gaining of the image data;
- preprocessing of the data in order to reduce and correct both systemic and random errors;
- data analysis identifying the molecules of interest for the study;
- reconstruction of the trajectories and analysis of the experimental results in order to validate the hypotheses underlying the experimental model, refute them, or deduce new knowledge.

Time-lapse analysis adhesion assays have been setting in order to prove the recruitment of VEGFR2 by the non-canonical ligand gremlin (henceforth called the experiment "type one"). Contextually, a further experiment (henceforth called the experiment "type two"), similar to the "type one", has been set up replacing gremlin with the specific integrin ligand, fibrinogen.

It has to be clear, that for the current work of thesis, the "type one" is always the experiment that embeds and describes the aims of the biological model, namely, in this case, the prove of VEGFR2 recruitment due to the presence of gremlin on the substrate. Viceversa, the "type two", is the so so-called control experiment. Such an experiment is necessary to prove that the recruitment of

VEGFR2 happens due to gremlin and not for another biological factor. In fact, in biology, we can not practically obtain absolute deductions from a single experiment, rather we need to build a further one (experiment "type two"), which ensures that what we are seeing, is a specific phenomenon of the experiment "type one". Particularly, for the purpose of attesting to the recruiting of VEGFR2 by gremlin, a control experiment is arranged to show how VEGFR2 is not recruited when fibrinogen (a non-specific ligand for this receptor) coat the substrate.

VEGFR2 is not the only molecule labeled in these adhesion experiments. Indeed, either in the experiment "type one" that "type two", we take a view of the dynamic of a further receptor, i.e. integrin. Therefore, both VEGFR2 and integrin have been fused with suitable fluorescence molecules in order to allow the biologists to follow their movements on the cell membrane.

In the end, what we observe is that in the experiment "type one" (Fig. 4.1), gremlin recruits VEGFR2, and interestingly, also integrin is engaged by these ligands, even if this takes place only after longer times of observation. On the contrary, instead, in the experiment "type two" (Fig. 4.2), the integrin recruitment by fibrinogen happens rapidly, but no VEGFR2 engagement is detected (see [51], and [52]).

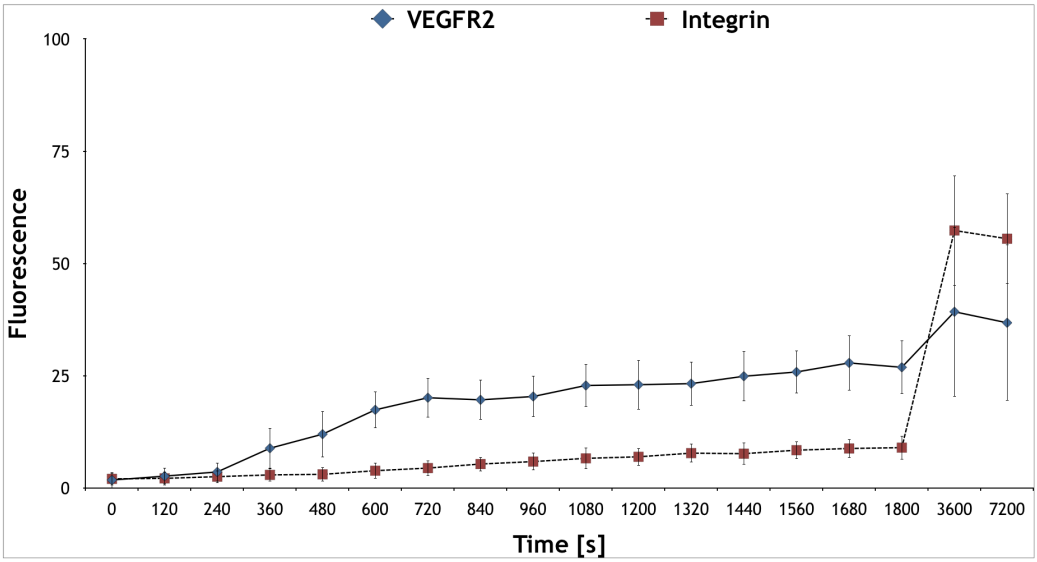

Figure 4.1: Fluorescence intensity time evolution of VEGFR2 and integrin perceived at the basal side of ECs lying on a substrate enriched of gremlin (*experiment "type one"*) [52]. Importantly, both VEGFR2 and integrin are recruited by this ligand, even if the latter only for long periods of observation [52].

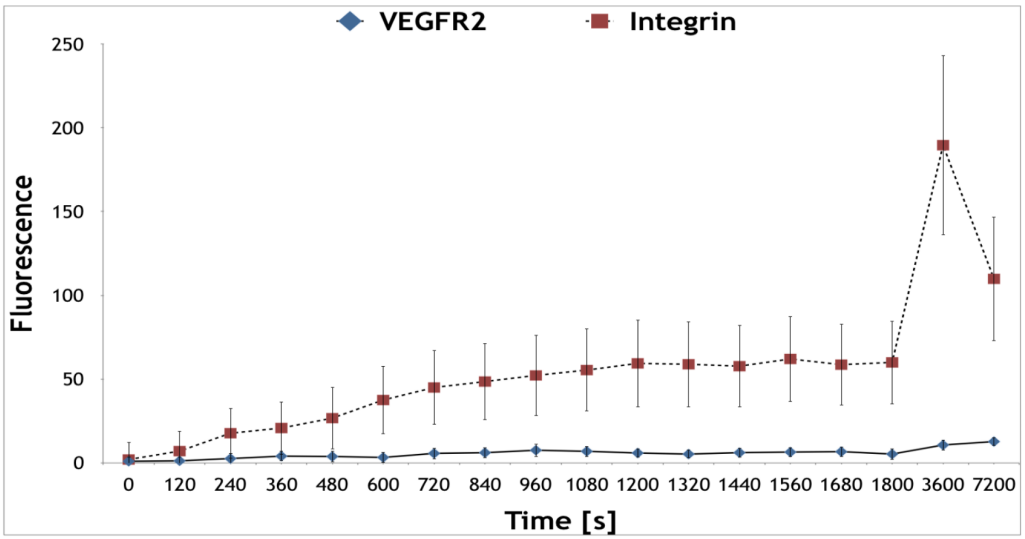

Figure 4.2: Fluorescence intensity time evolution of VEGFR2 and integrin perceived at the basal side of ECs lying on a substrate enriched of fibrinogen (*experiment "type two"*) [52]. Importantly, integrin is recruited from this ligand as opposed to VEGFR2 which shows no affinity [52].

Summing up:

- gremlin induces recruitment of both VEGFR2 and integrin (after a long time);
- fibrinogen induces only integrin relocation but not VEGFR2.

4.1.1.1 Experimental evidence of receptors colocalization

Immunofluorescence experiments [51] and [52], shown VEGFR2 and integrin interactions in subcellular structures. Hence, using three different markers, either in triple and double colocalization, it has been proved that VEGFR-2 and integrin are located inside the same membrane structures.

Such a procedure has been possible owing to the features of GM1, namely a lipid that is part of the cell membrane. Indeed, GM1 is recruited in denser structures, from the lipidic point of view, where VEGFR2 is stabilized and the intracellular signaling takes place. Hence, from these experiments in colocalization, emerges two interesting data. The first shows that 33% of VEGFR2 located on the basal side of the cell is colocalized with the integrin receptor. The second one, instead, displays how the 13% of integrin placed in the cell-substrate contact zone is touching with VEGFR2. Importantly, these percentages refer to the final arrangement of proteins on ECs during experimental trials (i.e. $t = 7200\ s$).

Actually, Immunofluorescence and colocalization experiments do not have the precision to guarantee direct observations of the physical interaction of the VEGFR2-complex and integrin. In fact, through this type of experiment, we can only estimate how much of a VEGFR2 population is recruited overall, and how much it is not. To demonstrate the direct interaction between VEGFR2 and integrin, biologists have means like FRET, a system that goes to the scale of a few angstroms.

In the end, hence, having proved by FRET the physical interaction between VEGFR-2-gramlin-complex and integrin, we can consider the estimates with immunofluorescence and colocalization, valid.

4.2 Biologically observation corroborate model parameters

Analyzing the current experimental data it will be possible to formulate preliminary hypotheses that will support the simplified drafting of constitutive relations. Such relations respect the thermodynamic constraints imposed by the inequalities (3.55).

4.2.1 Values of diffusivity for VEGFR2 and integrin

VEGFR2 and integrin are transmembrane proteins able to move laterally (lateral diffusion) on the lipid bilayer providing. Lateral diffusion is a relevant ability for these receptors in order to become the main regulators of angiogenic and mechanics intracellular signaling, respectively (see chapter 2). Therefore, the measure of such a parameter is a pivotal biological goal for the current thesis.

Receptors dynamics have suffered impressive improvement afterward the development of Green and Red Fluorescent Protein (GFP and DsRED) from jellyfish Aequorea victoria and anemone Discosoma striata respectively. These fluorescent proteins are bind to the receptors and subsequently, they re-emit light once excited with the aid of beam light. In this way, interaction, mobility, and concentrations of receptors have been observed [31] (chapter 2).

The expression (3.10) is a compact notation that could describe three multiple mass balance equations, one for each costituent involved in the reaction (3.4). It has already been said that A is a free protein able to diffuse on the cell membrane, whereas B a fixed protein linked to a substrate able to bind A and trap it. Consequently, the respective complex C is assumed not capable of diffuse on the cell membrane. In agreement with this, the flux terms correlated with B and C assume the following values: $\vec{h}_B = \vec{h}_C = \vec{0}$. Different considerations must be made for A, where its mass balance equation needs a constitutive law able to correlate the mass fluxes with the respective concentrations of species. This task is accomplished thanks to Fick's law (as well-motivated in section 3.2.4) by means of the relation (3.67) that here assume the following structure: $\vec{h}_A = -\mathbb{D}_A \mathrm{Grad}_{\mathcal{P}}[c_A]$. Where $\mathbb{D}_A$ is the so-called diffusivity, a material parameter that will be quantified through the experiments implemented by biologists (FRAP analysis), and that, in the current model, it will be assumed independent by the variables $(\vec{x},t)$. Consequently, the set of equations represented by the (3.12), it will be written like a function of only concentrations.

Concerning VEGFR2 and integrin, we observe in [138] (for VEGFR2) and we deduce from [153] (for integrin), the following values of diffusivities:

Table 4.1: Numerical values of both *free diffusivities* and *confined diffusivities* are tabulated either for VEGFR2 that integrin, respectively.

Recptor	Free diffusivity	Confined diffusivity	Units
VEGFR2	0.198	0.052	$\frac{\mu m^2}{s}$
Integrin	0.289	0.043	$\frac{\mu m^2}{s}$

Actually, concerning the adhesion molecule, the experiments in [153] involve β_3-integrin and they are done on platelets; the reason derives from the fact that in platelets there are very few types of integrins and mainly β_3, unlike the EC. However, this is not an β_3 associated with α_v, so it is not conformationally exactly what we need, but it is an approximation that we consider acceptable.

The distinction between *free diffusivity* and *confined diffusivity* derives from the behavior that the receptors assume once engaged by the immobilized ligands. Specifically, henceforth, we call *free* the diffusivity of a receptor that is interplaying with none ligand, and we call *confined* the diffusivity of a receptor that is interacting with the correspondent binder. The latter definition is corroborated by the experimental observation of the trajectory of the receptor which is, juxtaposed, limited around the ligands. Such behavior, confirmed by the numerical result show in Tab. 4.1, supports, in the first instance, the trapping behavior defined in the previous chapters.

4.3 Further experimental considerations

We need now to introduce further consideration on the chemical reactions (3.1) - (3.3), particularly on their stochiometric expression.

It is known that the activity of the VEGFR2 is connected with the angiogenic stimuli; in this section, we are interested in the VEGFR2-gremlin interaction (first chemical reaction (3.1)), where gremlin is a non-canonical ligand for VEGFR2. The reduction to a single event characterizing the processes of triggering angiogenesis makes clear the idea that VEGFR2 get a pivotal role in the management of this phenomenon, but can underestimate its complexity.

In this regard, it has been shown that further transmembrane receptors co-participate in angiogenic stimulation (see 2.3.1.2), with the aim, for example, of making it more long-lasting and stable. This is the task that has been recognized for the integrin, which, binding with the VEGFR2-gremlin-complex (second chemical reaction (3.2)), increases its intracellular signal. Also, integrin plays a fundamental role in regulating the adhesion and migration processes of ECs during angiogenesis. In this circumstance this transmembrane protein binds with specific ligands, creating protein clusters that give rise to the formation of focal adhesions. At these adhesion points, the cell and the

substrate actively exchange mechanical forces. In particular, in this part of the thesis, we focus on the integrin-fibrinogen interaction (third chemical reaction of interest (3.3)).

Below we will deepen some biological issues related to these three chemical reactions, deducing important information for the purposes of in-silico modeling.

4.3.1 VEGFR2-gremlin chemical reaction

The stoichiometry of the chemical reaction between VEGFR2 and gremlin and its main regulator mechanisms are well known. VEGFR2 is a single molecule, a monomer, which during the phenomenon of angiogenesis is overexposed on the cell membrane of an EC in order to intensify the angiogenic signal. Gremlin interacts with a VEGFR2 monomer causing a conformation change of the latter. This change allows the dimerization of the receptor and, therefore, its activation. Gremlin itself turns out to be a dimer, and this characteristic assists the dimerization process of VEGFR2. Consequently, a single complex C_1 is composed of two VEGFR2 and two gremlin monomers. However, owing to the technological tools in the experiments, it is possible to follow and trace the individual monomers of VEGFR2 on the cell membrane. This means that we have experimental data that express the diffusion and reaction of a single monomer of VEGFR2. Hence, in light of this, the following stoichiometry is assumed:

$$\underbrace{\text{VEGFR2}}_{V} + \underbrace{\text{Gremlin}}_{L_V} \underset{k_b}{\overset{k_f}{\rightleftarrows}} \text{C}_1 \ . \tag{4.1}$$

It must, therefore, be clear that the complex identified in the reaction (4.1) is only half of the real one.

The material parameters related to this chemical reaction, including those connected to the hypothesis of surrogated mechanics, have been used in in-silico experiments shown in Appendix B.1 and work [140].
Nevertheless, a further parameter has to be determined, namely the concentration of ligands effectively available to interact with the free receptors on the cell membrane. In fact, not all gremlin present on the substrate is in the ideal conditions to favor chemical interaction with VEGFR2 (e.g. favorable orientation of the molecules) and their amount needs to be calibrated through the in-silico analysis processes.

4.3.2 Integrin-fibrinogen chemical reaction

Similarly to (4.1), the chemical reaction (4.2) describes the interaction between a receptor (integrin), free to relocate itself on the cell membrane of EC, and a ligand (fibrinogen), assumed fixed on the substrate. The mechanism leading to the entrapment of VEGFR2 and integrin receptors with the corresponding ligands, gremlin, and fibrinogen, from our point of view, is totally analogous. Also, experimental evidence legitimizes us to assume a one-to-one relationship between the receptor molecules and those of the ligands, confirming the following relationship:

$$\underbrace{\text{Integrin}}_{I} + \underbrace{\text{Fibrinogen}}_{L_I} \underset{k_b}{\overset{k_f}{\rightleftarrows}} \text{C}_3 \ . \tag{4.2}$$

Moreover, from experimental observation it can be deduced that the timing of receptor-ligand bind and the mechanical spreading time, are aligned to the experiment on gremlin, therefore $\bar{t} = 1\ s$ and $t_f = 600\ s$. Consequently, also the radius $r = 20\mu m$ of the spreading EC remains unchanged from the previous case. Standard Gibbs free energy is here inherited from the work [154] and adapted by assuming the value $\Delta G_0^{(4.2)} = -44000\ \frac{J}{mol}$. The current equilibrium constant hence assumes the following expression:

$$K_{eq}^{(4.2)} = \left[-\frac{\Delta G_0^{(4.2)}}{RT} \right] = 25716896.47906 \tag{4.3}$$

where $T = 310.15\ K$ and $R = 8.314462618\ \frac{J}{K\ mol}$.
Accepting the hypothesis that the concentration of complex and receptor are equal at saturation is valid ($[c_I^{\max}] = \left[c_{C_3}^{\max}\right]$), all that remains is to deduce $\left[c_{L_I}^{\max}\right]$. Such a value is derivable from the paper [155]. In this work, soluble fibrinogen dimers for SPR experiments have been used. The molecular weight of this dimer results to be $330\ kDa$, which is equivalent to $0.000000000547990700763866\ ng$. The concentration for immobilization in SPR can be considered about $9\ \frac{ng}{mm^2}$. What we want to calculate is the number of molecules per μm^2, therefore:

$$\left[c_{L_I}^{\max}\right] = \frac{9}{5.479907 \times 10^{-10}} 10^{-6} = 16423.6364\ \frac{molecules}{\mu m^2} \tag{4.4}$$

$$\alpha^{(4.2)} = \left[c_{L_I}^{\max}\right] \frac{1}{K_{eq}^{(4.1)}} \tag{4.5}$$

Finally, we assume for integrin an initial homogeneous concentration on the surface of EC in suspension equal to $c_I^0 = 1.25\ \frac{molecules}{\mu m^2}$. This is deducible from the total value of molecules of integrin on the cell membrane of an EC, equal to 6.2×10^3 suggested by [156].
Once again, as in the case of VEGFR2 and gremlin, the only parameter that needs calibration is the actual quantity of ligands interacting with the free receptors.

4.3.2.1 Integrin-VEGFR2-Gremlin-Complex Chemical reaction

In this paragraph, we discuss the chemical reaction that describes the interaction between the VEGFR2-Gremlin complex and integrin. By its nature, such a chemical reaction makes sense if and only if, in our model, is coupled with the (4.1). The trapping mechanism, in this reaction, is triggered by the affinity between the free integrin receptor and the C_1 complex (given by the (4.1) reaction), which is anchored to the substrate through the fixed ligands. If on one hand, VEGFR2-ligands interactions have been studied extensively over the years, on the other, the chemical reaction (4.6), exhibits multiple lacks of knowledge. Stoichiometry is not a priori known, and the study of chemical kinetics reserves several complications. Not only that, deduce from experimental evidence the values of the saturation concentrations of the molecules involved in this chemical reaction is a very complicated purpose to achieve.

In first approximations, in order to deal with this chemical reaction, we assume that the stoichiometric coefficient f is equal to one, and the diffusivity, necessary to describe the free relocation of

integrin is equal to that introduced for the chemical reaction (4.2). Therefore:

$$d \underbrace{\text{integrin}}_{I} + e \, \mathrm{C}_1 \underset{k_b}{\overset{k_f}{\rightleftarrows}} f \, \mathrm{C}_2 \,, \tag{4.6}$$

$$\alpha^{(4.6)} = \frac{\left[c_I^{\max}\right]^d \left[c_{C_1}^{\max}\right]^e}{\left[c_{C_2}^{\max}\right]} \frac{1}{K_{eq}^{(4.6)}} \,, \tag{4.7}$$

where either the saturation limits and the equilibrium constant are unknown. This makes the calibration of the $\alpha^{(4.6)}$ parameter together with the stoichiometry of the reaction (4.6) the main objective for this section.

Also, it must be clear that the integrins involved in C_2 and C_3 exhibit different conformation states: i.e. bent-clasped (low-affinity state) and unbent and unclasped conformation state (high-affinity state) respectively [87], [88], [89].

4.3.3 Summary of biological objectives and parameters values

In the end, from a biological viewpoint, it was achieved a double aim: first, to prove that the VEGFR2 is recruited in the basal side of an EC that spreads on a substrate coated by gremlin. Second, the demonstrations of how integrin promotes the long-lasting activation and polarization of VEGFR2 initially triggered by gremlin. Specifically, these phenomena have been described in the following works [157], [51], [52], and also in [31], and here reexamined in section 4.1.

At the end of this chapter, we have collected almost the total amount of material parameters necessary for the purpose of the numerical simulation, and by means of the Tab. 4.2 and 4.3 we propose a suitable summarization:

Table 4.2: Model papameters

Material parameters	values	Units
$\mathbb{D}_V$	0.198	$\mu m^2/s$
$\mathbb{D}_I$	0.289	$\mu m^2/s$
$\alpha_{(4.1)}$	0.04519	$mol./\mu m^2$
$\alpha_{(4.2)}$	0.00062	$mol./\mu m^2$
$\alpha_{(4.6)}$	unknown	$mol./\mu m^2$
s_{L_V}	unknown	$mol./(s\ \mu m^2)$
s_{L_I}	unknown	$mol./(s\ \mu m^2)$

Table 4.3: Initial concentrations

Initial concentrations	values	Units
c_V^0	4.8	$mol./\mu m^2$
c_I^0	1.25	$mol./\mu m^2$
$c_{L_V}^0$	0	$mol./\mu m^2$
$c_{L_I}^0$	0	$mol./\mu m^2$
$c_{C_1}^0$	0	$mol./\mu m^2$
$c_{C_2}^0$	0	$mol./\mu m^2$
$c_{C_3}^0$	0	$mol./\mu m^2$

Chapter 5

Numerical simulations provide insights into the relocation of integrins and VEGF receptor on a lipid membrane

By co-designing experimental (base on [52] and on the whole previous chapter in general) and numerical investigation, we decipher the regulatory laws underlying the mechanisms of the VEGFR2-interaction, either with gremlin that with co-receptors like integrin. The matching of in-vitro and in-silico experiments, allow us to interpret reality and deduce those material parameters that cannot be computed by means of experimental analyses.

5.1 Governing Equations

We develop mathematical models able to describe the relocation of VEGFR2 and integrin on the cell membrane of an EC during its mechanical spreading on a substrate enriched by gremlin or/and fibrinogen, employing the thermodynamic model built-in chapter 3, namely continuum chemo-transport thermodynamically consistent model. Such a formulation led to the governing equations (3.79), which in the current chapter, will be reframed differently with respect to the precedent ones. Here, we will follow a new strategy where we will reduce the degree of non-linearity introduced by the equations 3.90 and 3.91 to the detriment of an increasing number of balance equations to discretized.
The primary goal is therefore to combine the scientific experimental methodology introduced by biologists, with mathematical modeling provided by engineers and/or physicists (see section 5.2). In this way, scientific theories addressed to the science of living matter, can be both predicting and interpreting.

According to the constitutive choices shown in the previous chapter, we can reduce the local form of governing equations (3.12) as follow:

$$\frac{\partial c_A}{\partial t}(\vec{x},t) - \mathbb{D}_A \Delta_{\mathcal{P}}[c_A(\vec{x},t)] + a\, w^{(3.4)}(\vec{x},t) = 0 \ , \tag{5.1a}$$

$$\frac{\partial c_B}{\partial t}(\vec{x},t) + b\, w^{(3.4)}(\vec{x},t) = s_B(\vec{x},t) \ , \tag{5.1b}$$

$$\frac{\partial c_C}{\partial t}(\vec{x},t) - c\, w^{(3.4)}(\vec{x},t) = 0 \ , \tag{5.1c}$$

where $\Delta_{\mathcal{P}}[\,] = \mathrm{div}_{\mathcal{P}}[\nabla_{\mathcal{P}}[\,]]$ is the Laplacian operator restricted on the surface. Therefore, supported by the infinitely fast kinetics and surrogated mechanics hypothesis, we can replace the Eq. (5.1c) in the Eq. (5.1a) and (5.1b), and reintroducing the Eq. (3.77), the Eq. (5.1) become:

$$\frac{\partial c_A}{\partial t}(\vec{x},t) - \mathbb{D}_A \Delta_{\mathcal{P}}[c_A(\vec{x},t)] + \frac{a}{c}\frac{\partial c_C}{\partial t}(\vec{x},t) = 0 \,, \tag{5.2a}$$

$$\frac{\partial c_B}{\partial t}(\vec{x},t) + \frac{b}{c}\frac{\partial c_C}{\partial t}(\vec{x},t) = s_B(\vec{x},t) \ , \tag{5.2b}$$

$$[c_C]^c = \frac{[c_A]^a [c_B]^b}{\alpha^{(3.4)}} \,. \tag{5.2c}$$

These are the rephrased (with respect to the equations (3.78)) local governing equations for a multi-physical problem describing trapping phenomena of free molecules A (on a cell membrane), by means of the fixed molecules B (attached to a substrate), during the spreading of an EC on specific ligands coated substrate.

5.2 Multi-physical models and numerical results

Four models will be built with the aim to characterize the biological mechanisms, above-describes, ruling the triggering of the angiogenic stimulus.
The firsts two models will be able to capture the evolution in time of the depletion of a receptor located on the cell membrane during the spreading of an EC on a substrate coated with a specific ligand. Hence, supported by the experimental data introduced in the papers [51], [52], we will calibrate the evolution over time of VEGFR2 when EC adheres to gremlin (experiment "type one"), and integrin when EC adheres to fibrinogen (experiment "type two"). Through these models, we will calibrate the respective concentrations of ligands actually interacting with the free membrane receptors.

The next step will see the construction of a further model that couple the chemical reaction (4.1) and (4.6). Here, the final objective will be the calibration of $\alpha^{(4.2)}$ parameter and the stoichiometric coefficients d and e which best interpolate the experimental data that express the relationship of VEGFR2 and integrin on gremlin substrate.

Finally, a model that takes into account all the chemical reactions (4.1), (4.6), and (4.2) will be set in order to predict the trend of the receptors recruitment by gremlin and fibrinogen that simultaneously and homogeneously cover the substrate on which an EC is spreading.

5.2.1 Weak formulation

In order to do that, weak formulations of the local governing equations of the type (5.2), rendered dimensionless, are implemented through the open-source finite elements library deal.ii (https://www.dealii.org/) that exploits high-performance computing technique. The weak forms

here mentioned can be deduced from (5.2) through a premultiplication of each term for corresponding test functions and subsequent integration on the spatial domain, which in the specific case, result in the rigid surface identified in Fig. 5.1. The discretization of the unknown field $c_E(\vec{x},t)$ lead to the separation of independent variables $\vec{x}$ and t through the following expression:

$$c_E(\vec{x},t) = \sum_{i=1}^{n} \varphi_i^E(\vec{x}) c_i^E(t) \,, \tag{5.3}$$

where n is the number of nodes of the tessellation, and $\varphi_i^E(\vec{x})$ are the so-called shape functions, while $c_i^E(t)$ the nodal unknowns. Doing that, the partial non-linear differential equations system became a non-linear ordinary differential equations system (ODE) in the t variable, and by means of ODE discretization methods, it will be rendered numerically implementable. Therefore, the weak formulation corresponding to the eq. (5.2) reads:

$$\begin{aligned}
&\int_{\mathcal{P}} \varphi_i^A(\vec{x})\varphi_j^A(\vec{x})dA \left[c_j^A(t_n)\right] - \int_{\mathcal{P}} \varphi_i^A(\vec{x})\varphi_j^A(\vec{x})dA \left[c_j^A(t_{n-1})\right] + \\
&+ \int_{\mathcal{P}} \nabla_{\mathcal{P}} \left[\varphi_i^A(\vec{x})\right] \cdot \nabla_{\mathcal{P}} \left[\varphi_j^A(\vec{x})\right] dA \left[\int_{t_{n-1}}^{t_n} c_j^A(\tau)d\tau\right] + \\
&\frac{a}{c}\int_{\mathcal{P}} \varphi_i^A(\vec{x})\varphi_k^C(\vec{x})dA \left[c_k^C(t_n)\right] - \frac{a}{c}\int_{\mathcal{P}} \varphi_i^A(\vec{x})\varphi_k^C(\vec{x})dA \left[c_k^C(t_{n-1})\right] = 0 \,,
\end{aligned} \tag{5.4a}$$

$$\begin{aligned}
&\int_{\mathcal{P}} \varphi_i^B(\vec{x})\varphi_p^B(\vec{x})dA \left[c_p^B(t_n)\right] - \int_{\mathcal{P}} \varphi_i^B(\vec{x})\varphi_p^B(\vec{x})dA \left[c_p^B(t_{n-1})\right] + \\
&- \int_{\mathcal{P}} \varphi_i^B(\vec{x}) \left[\int_{t_{n-1}}^{t_n} s_{L_B}(\vec{x},\tau)d\tau\right] dA + \\
&\frac{b}{c}\int_{\mathcal{P}} \varphi_i^B(\vec{x})\varphi_k^C(\vec{x})dA \left[c_k^C(t_n)\right] - \frac{b}{c}\int_{\mathcal{P}} \varphi_i^B(\vec{x})\varphi_k^C(\vec{x})dA \left[c_k^C(t_{n-1})\right] = 0 \,,
\end{aligned} \tag{5.4b}$$

$$\begin{aligned}
&\alpha^{(3.4)} \int_{\mathcal{P}} \varphi_i^C(\vec{x}) \left[\varphi_k^C(\vec{x})\right]^c dA \left[c_k^C(t_n)\right]^c + \\
&- \int_{\mathcal{P}} \varphi_i^C(\vec{x}) \left[\varphi_j^A(\vec{x})\right]^a \left[\varphi_p^B(\vec{x})\right]^b dA \left[c_k^A(t_n)\right]^a \left[c_p^B(t_n)\right]^b = 0 \,,
\end{aligned} \tag{5.4c}$$

where $\int_{t_{n-1}}^{t_n} s_{L_B}(\vec{x},\tau)d\tau$ will be solved analytically and then implemented, whereas $\int_{t_{n-1}}^{t_n} c_j^A(\tau)d\tau$ will be discretized by means Newton-Cotes quadrature formula and then implemented [140].

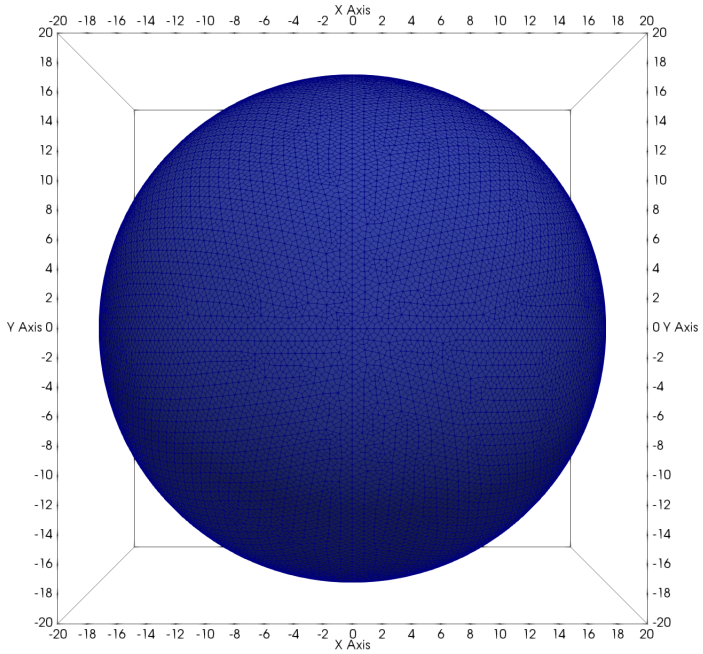

Figure 5.1: Tessellation of the cell membrane consists of 6437 quadrilaterals.

5.2.2 Approximation of eq. (3.11)

To avoid discontinuities, a "gaussian" approximation on the relationships (3.11) has been implemented:

$$s_{L_V} \simeq a \exp[-((t-b)^2)/(c^2)] \,, \tag{5.5a}$$

$$s_{L_I} \simeq d \exp[-((t-e)^2)/(f^2)] \,, \tag{5.5b}$$

in which the coefficients $a,\ b,\ c,\ d,\ e,\ f$ characterize the shape of s_{L_V} and s_{L_I}.

Time integration can be performed analytically

$$\int_0^t s_{L_V}(\vec{x},\tau)d\tau = S_{L_V}(\vec{x},t) - S_{L_V}(\vec{x},0) = \frac{1}{2}ac\sqrt{\pi}(Erf[b/c] - Erf[(b-t)/c]) \,, \tag{5.6a}$$

$$\int_0^t s_{L_I}(\vec{x},\tau)d\tau = S_{L_I}(\vec{x},t) - S_{L_I}(\vec{x},0) = \frac{1}{2}df\sqrt{\pi}(Erf[e/f] - Erf[(e-t)/f]) \,. \tag{5.6b}$$

Expressions (5.6) are consistent with the requirements $S_{L_V}(\vec{x},0) = 0$ and $S_{L_I}(\vec{x},0) = 0$.

We approximate the expression (3.11) by means of expression (5.5) that needs to be integrated over time (see (5.4b)) as shown by the (5.6). Below we can observe at fixed time $t = 300\ s$ the shape of both functions s_{L_B} (Fig. 5.2a) and S_{L_B} (Fig. 5.2b). Finally, thanks to experimental observation, we assume that at the end of the mechanical spreading (600 s [138] and [139]), only about $1/3$ of the total amount of the spread cell membrane goes in contact with the substrate (see the trend of s_B by the Fig. 5.3).

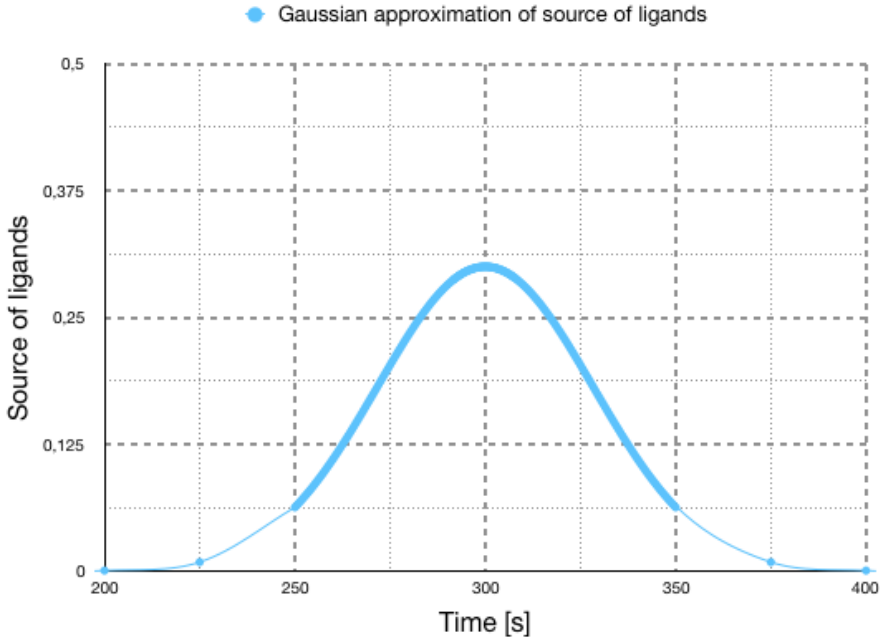

(a) t=300 s

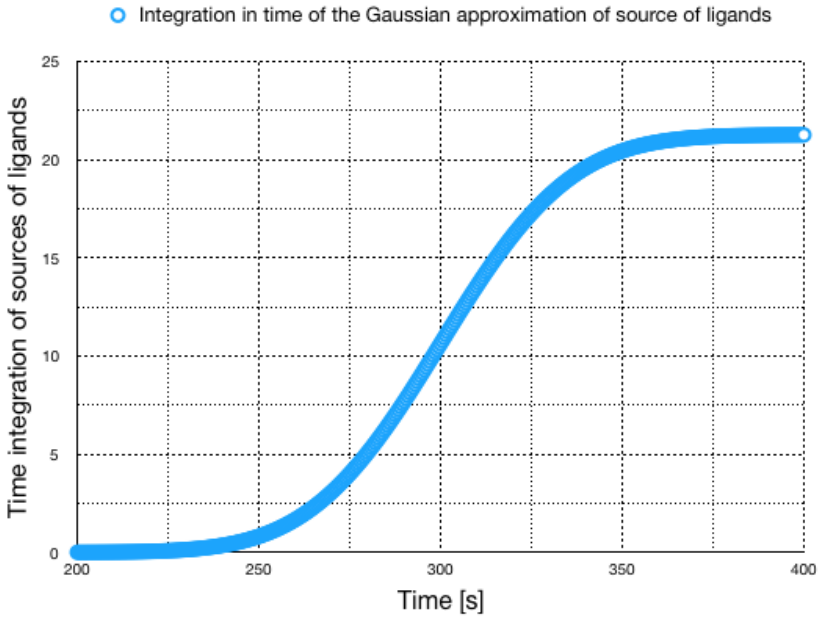

(b) t=300 s

Figure 5.2: Time evolution of the approximated expression of s_{L_B} (5.5) and its time integration S_{L_B}. Case with $a = 0.3$ $b = 300$ s and $c = 40$, is here depicted.

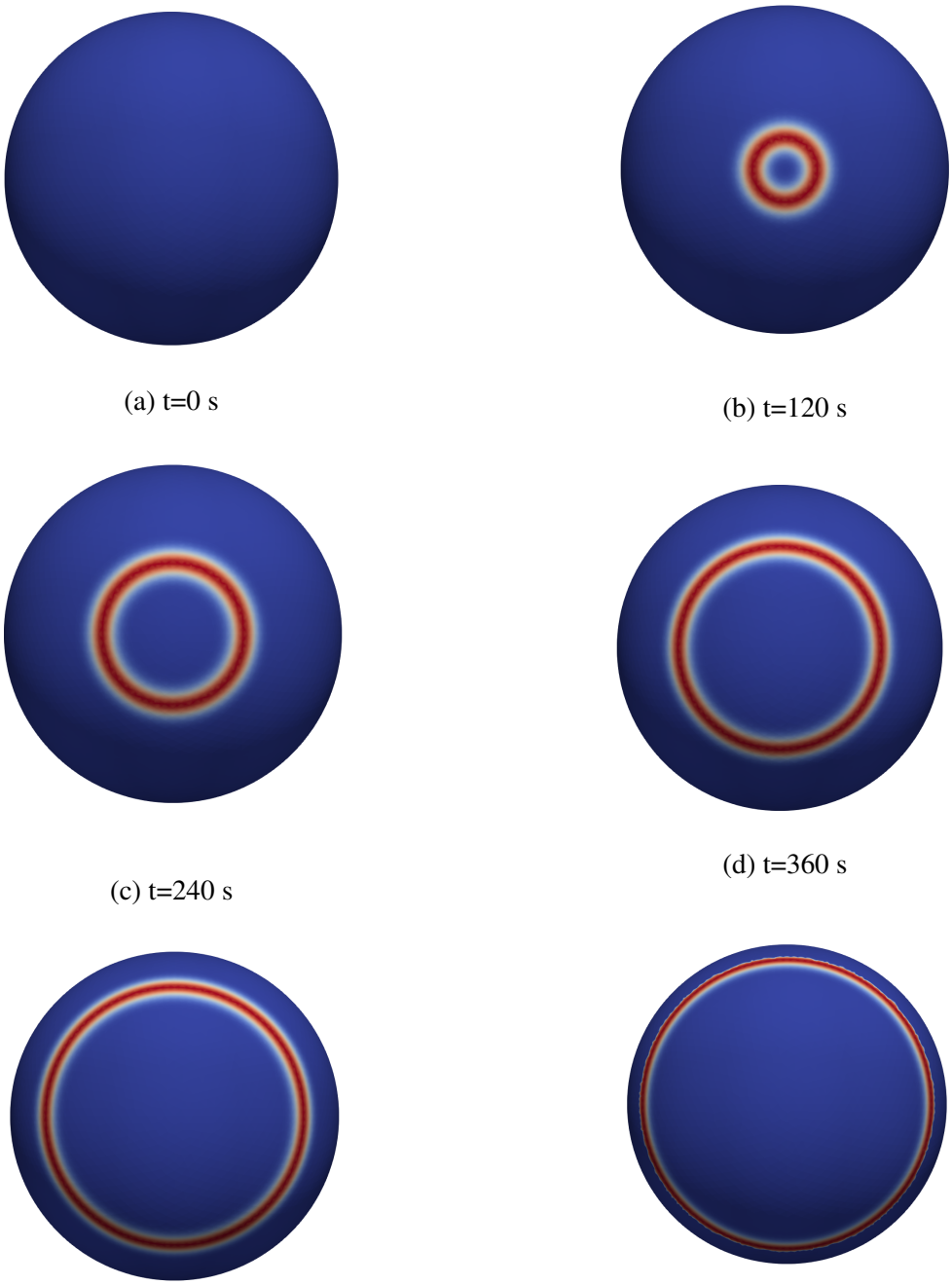

(a) t=0 s

(b) t=120 s

(c) t=240 s

(d) t=360 s

(e) t=480 s

(f) t=600 s

Figure 5.3: Time evolution of the s_B function through six pictures of the in-silico trial. Specifically at instant $t = 0,\ 120,\ 240,\ 360,\ 600\ s$.

5.2.3 Model based on one chemical reaction: VEGFR2-gremlin interaction

As a result of what has been introduced so far, we show the governing equations concerning the model for the reaction VEGFR2-gremlin:

$$\underbrace{\text{VEGFR2}}_{V} + \underbrace{\text{Gremlin}}_{L_V} \underset{k_b}{\overset{k_f}{\rightleftarrows}} \text{C}_1 \,. \tag{5.7}$$

$$\frac{\partial c_V}{\partial t} - \mathbb{D}_V \, \Delta_{\mathcal{P}} [\, c_V \,] + \frac{\partial c_{C_1}}{\partial t} \;=\; 0 \,, \tag{5.8a}$$

$$\frac{\partial c_{L_V}}{\partial t} + \frac{\partial c_{C_1}}{\partial t} = s_{L_V} \;\;, \tag{5.8b}$$

$$[c_{C_1}] = \frac{[c_V]\,[c_{L_V}]}{\alpha^{(5.7)}} \,. \tag{5.8c}$$

In the current model, we want to fit numerical data through the experimental ones, by means of the calibration of s_{L_V}. Basically, that means finding the exact combination of the values of the parameters characterizing the Eq. (5.5). In an attempt to do this, another experimental datum has been accounted for. Indeed, experimental evidence shows that EC avoids the complete depletion of free receptors on its own cell membrane, leaving about 30% of the total amount (about 24000) on the apical side. This observation is specular to that reported by the work [138] where has been highlighted that 77% of the VEGFR2 on the cell membrane is free to move on the cell membrane, while the remaining result to be anchored at the actin filaments of the cytoskeleton and so can not move. Such data are supported by FRAP analysis, which has displayed a failure recovery of fluorescence after photobleaching. Interestingly, immobilized receptors (that are not bound to any ligands) could have a very low diffusivity owing to their interaction with the cytoskeletal filaments or due to the diffusion impediments caused by other molecules on the lipid bilayer. It has to be clear, that in the current model such a kind of constraint is not embedded; rather, we need to impose it externally, playing with the ligand quantities. This kind of approximation is acceptable, if, as it actually is, through the current models, we are mostly interested in the dynamical evolution of receptors on the cell membrane rather than their interaction with the cytoskeleton and with the surrounding environment.

5.2.3.1 The gremlin calculation

Comparing numerical with experimental outcomes (see Tab. 5.1), we obtain the availability of ligands of 21.2694 $molecules/\mu m^2$.

Table 5.1: Co-designing between VEGFR2-fluorescence intensity (in-vitro experiments) and the number of complexes generating on the cell membrane (in-silico simulation) is provided. Specifically, both total and dimensionless quantities are tabulated.

Time	FRAP	Error bars	Complex	Adimensional Complex	Adimensional FRAP	Adimensional error bars
0	1.8125	1.7470	0.0000	0.0000	0.0674	0.0649
120	2.6775	1.7774	660.6680	0.0557	0.0995	0.0661
240	3.6175	2.0371	2105.2400	0.1774	0.1344	0.0757
360	8.8875	4.5427	3992.4000	0.3364	0.3303	0.1688
480	12.0225	5.1638	6069.1400	0.5113	0.4468	0.1919
600	17.4375	4.0251	7329.1500	0.6175	0.6481	0.1496
720	20.1325	4.3776	8050.8500	0.6783	0.7482	0.1627
840	19.6650	4.4217	8659.5400	0.7296	0.7308	0.1643
960	20.4075	4.5417	9192.9900	0.7745	0.7584	0.1688
1080	22.8600	4.7168	9672.0600	0.8149	0.8496	0.1753
1200	23.0375	5.5135	10108.8000	0.8517	0.8562	0.2049
1320	23.2725	4.8333	10511.0000	0.8856	0.8649	0.1796
1440	24.9150	5.5791	10884.6000	0.9171	0.9260	0.2073
1560	25.8650	4.7980	11233.5000	0.9465	0.9613	0.1783
1680	27.8800	6.0900	11560.8000	0.9740	1.0361	0.2263
1800	26.9075	5.9243	11868.9000	1.0000	1.0000	0.2202
3600	39.2718	18.8742	14967.9000	1.2611	1.4595	0.7014
7200	36.8140	17.3697	16218.7000	1.3665	1.3682	0.6455

where the numerical results correspond to the concentration of the complex generated in the basal part of the EC, while the experimental one is the evolution over time, on the basal side of the EC, of the fluorescence of VEGFR2, both normalized to the respective values at time $t = 1800\ s$. According to this data, at the end of the process (7200 s), 75% of the total amount of VEGFR2 is located in the basal side of the cell, while 67% of this total amount corresponds to C_1.
Likewise of the works [138], [139], here the shape of the experimental curve identifies three-part: a very short initial plateau, a subsequent steep branch, and, in the end, a long branch of curve characterized by a lower formation rate of complexes.
Thanks to the multi-physics model we understood that the plateau-phase is correlated with the first contact phase between membrane and substrate. Practically, the moment we lay down the cell on the substrate, all the free receptors present in that part of the cell are instantaneously trapped by gremlin. Subsequently, there is an exposure of VEGFR2 in contact with the substrate due to the mechanical spreading of the cell, which brings a new portion of the membrane in contact with the ligands. Finally, we interpret the last process as diffusive-dominant; i.e., free receptors, following Fick's Law, are recruited at the basal side of the cell where they are trapped again by gremlin.
A further relevant consideration emerges from the comparison between numerical and experimental data, namely that the assumption made of $s_V = 0$ would seem correct. In fact, observing Fig. 5.4 we can appreciate how the numerical curve always remains embedded among the error bars of the numerical one.

Actually, this can be interpreted in two different ways: either no phenomenon of internalization and new synthesis (exposure on the cell membrane) of VEGFR2 occur during the adhesion of an EC on a substrate covered with gremlin or happen but their contributions cancel each other out. We infer that the second option is the correct one, inasmuch supported by experimental observations given by biologists. The internalization of VEGFR2, as well as the synthesis of new receptors, are pivotal phenomena in the process that corroborates the angiogenic stimulus. In the current experiment, the slow synthesis process of new VEGFR2 proteins is compensated by an internalization phenomenon that starts late with respect to the relocation process of this receptor.

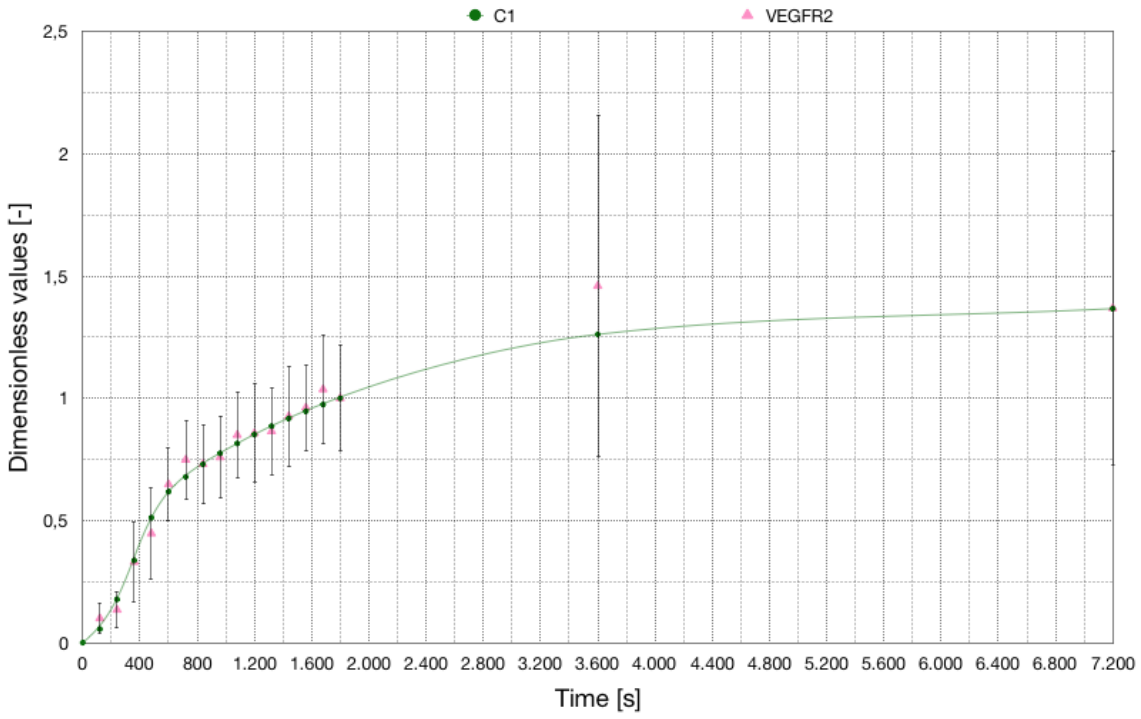

Figure 5.4: Numerical (dots with continuous line) and experimental (triangles with error bars) outcomes. Evolution in time of the normalized total amount of complexes is depicted.

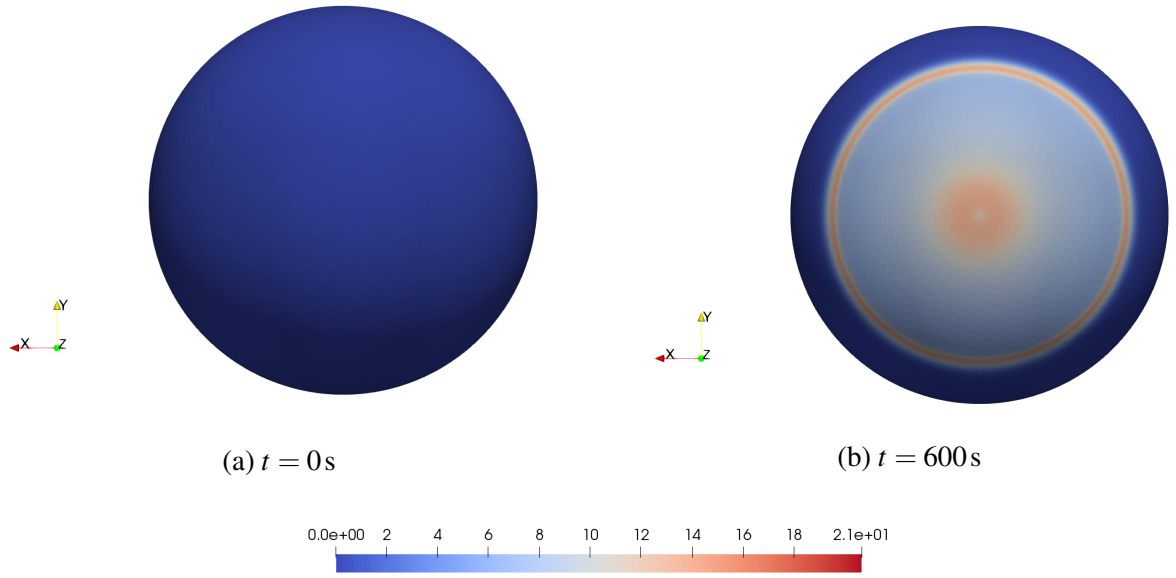

(a) $t = 0\,\mathrm{s}$

(b) $t = 600\,\mathrm{s}$

(c) Legend

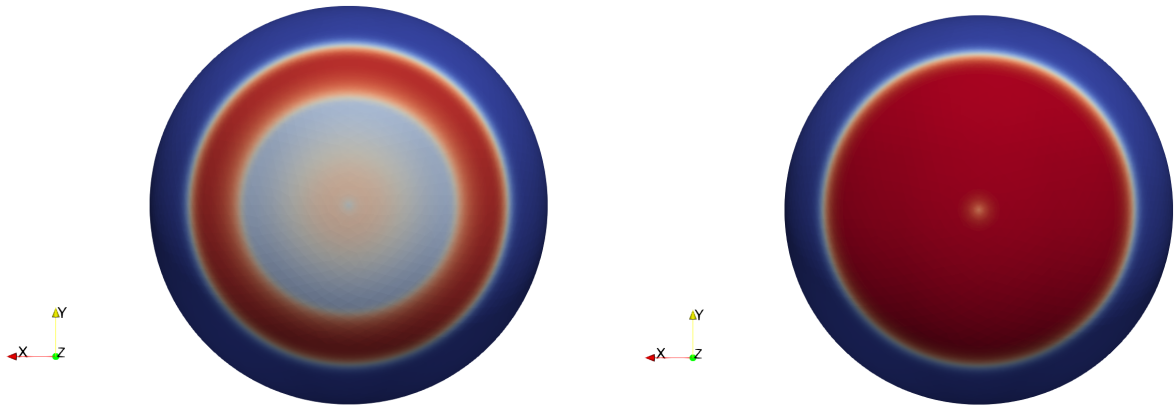

(d) $t = 1800\,\mathrm{s}$

(e) $t = 7200\,\mathrm{s}$

Figure 5.5: Basal distribution of complexes at the instant $t = 0,\ 600,\ 1800,\ 7200\,\mathrm{s}$.

Below we show two new cases corresponding to different concentrations of available gremlin.

5.2.3.2 High amount of gremlin

In the current section, we approach the case of an EC that spread on a substrate with a concentration of ligands equal to 42.5389 $molecules/\mu m^2$ (i.e. doubled with respect to the previous case). In Tab. 5.2 we compare the evolution in time of the concentration of complex C_1 with the fluorescence of molecules of VEGFR2. Referring to the total amount of receptors (bound or free) at the time $t = 7200\ s$, we see that 87.72% of these are in contact with the substrate where the 86.35% (of the total amount) result be bound. Such percentages show that less than 15% of the global amount of receptors remain on the apical side, violating the biological insights above mentioned.

Table 5.2: Co-designing between VEGFR2-fluorescence intensity (in-vitro experiments) and the number of complexes generating on the cell membrane (in-silico simulation), correspondent to a high amount of gremlin, is provided. Specifically, both the total that dimensionless quantities are tabulated.

Time	FRAP	Error bars	Complex	Adimensional Complex	Adimensional FRAP	Adimensional error bars
0	1.8125	1.7470	0.0000	0.0000	0.0674	0.0649
120	2.6775	1.7774	817.0600	0.0630	0.0995	0.0661
240	3.6175	2.0371	2301.7900	0.1774	0.1344	0.0757
360	8.8875	4.5427	4221.5300	0.3254	0.3303	0.1688
480	12.0225	5.1638	6302.9800	0.4858	0.4468	0.1919
600	17.4375	4.0251	7652.2700	0.5898	0.6481	0.1496
720	20.1325	4.3776	8457.4600	0.6519	0.7482	0.1627
840	19.6650	4.4217	9145.7200	0.7049	0.7308	0.1643
960	20.4075	4.5417	9760.7900	0.7523	0.7584	0.1688
1080	22.8600	4.7168	10320.5000	0.7955	0.8496	0.1753
1200	23.0375	5.5135	10835.7000	0.8352	0.8562	0.2049
1320	23.2725	4.8333	11315.0000	0.8721	0.8649	0.1796
1440	24.9150	5.5791	11765.9000	0.9069	0.9260	0.2073
1560	25.8650	4.7980	12190.8000	0.9396	0.9613	0.1783
1680	27.8800	6.0900	12592.5000	0.9706	1.0361	0.2263
1800	26.9075	5.9243	12974.0000	1.0000	1.0000	0.2202
3600	39.2718	18.8742	17090.1000	1.3173	1.4595	0.7014
7200	36.8140	17.3697	20825.0000	1.6051	1.3682	0.6455

What has been discussed so far, has a visual correspondence in the graphic representation in Fig. 5.6 and 5.7. Generally, we can observe how the numerical curve Fig. 5.6 fit less-well the experimental one, compared to 5.4. Such a phenomenon should be consistent with the failure to satisfy the constraint on the immobilized receptors that previously has been established through a tailored calibration of the terms s_{L_V}. Nonetheless, the C_1-curve remains always inside the error-bars and the shape of the numerical curve is similar to the experimental one. Moreover, by means the Fig. 5.7e,

we can appreciate how changed the representation of the spatial distribution at the time $t = 7200\ s$ of the concentration complex C_1 compared to Fig. 5.5e. Unlike what happens in the 5.2.3.1 section, we do not see a homogeneous distribution in contact with the substrate of the VEGFR2-gremlin complexes. On the contrary, due to the excessive availability of ligands, the free receptors that flow from the apical to the basal part of the cell are immediately trapped. The result is the formation of a high-intensity ring of C_1 concentration on the edge of the extreme contact zone between the cell membrane and substrate.

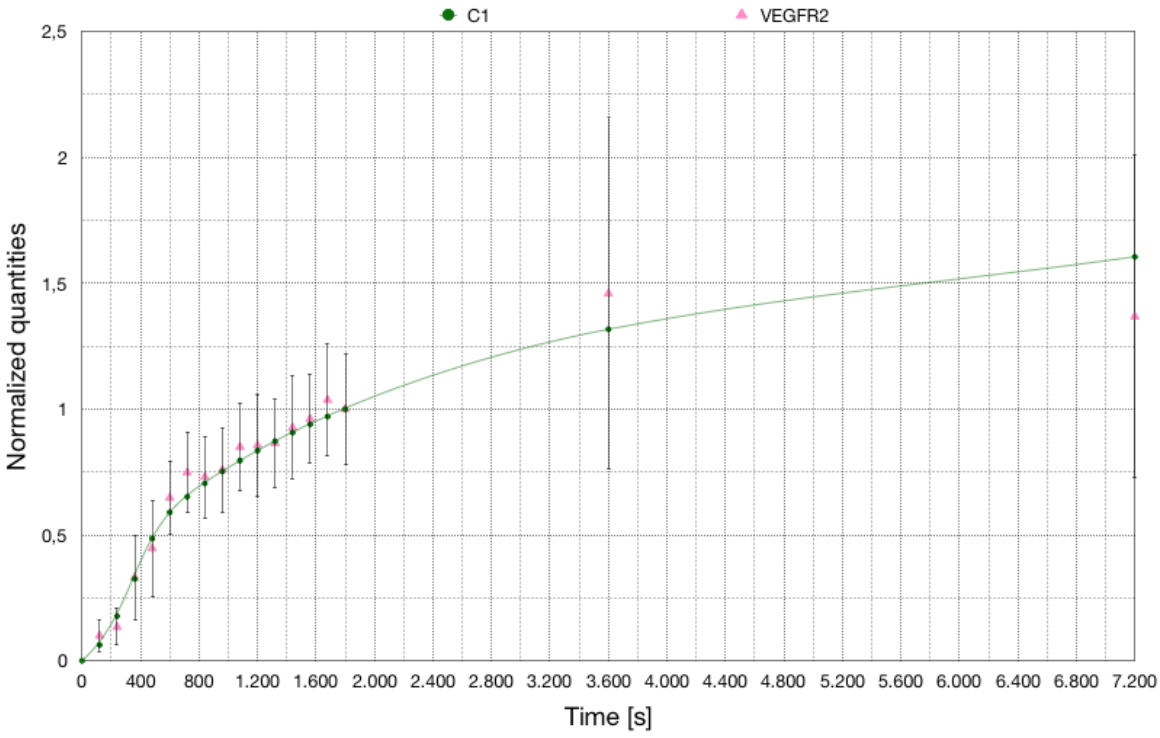

Figure 5.6: Numerical (dots with continuous line) and experimental (triangles with error bars) outcomes. Evolution in time of the normalized total amount of complexes correspondent to a high amount of gremlin is depicted.

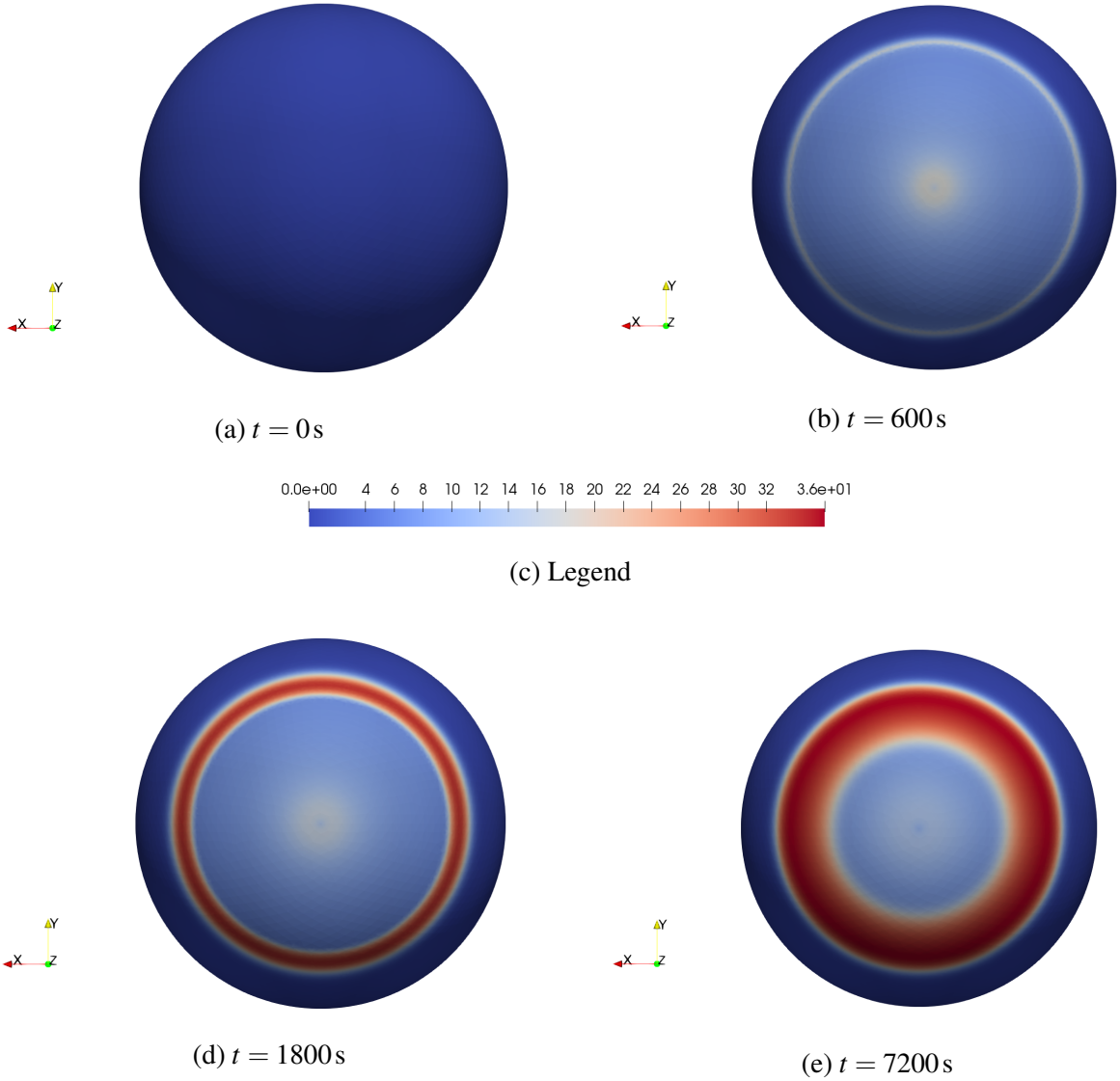

(a) $t = 0\,\mathrm{s}$

(b) $t = 600\,\mathrm{s}$

(c) Legend

(d) $t = 1800\,\mathrm{s}$

(e) $t = 7200\,\mathrm{s}$

Figure 5.7: Basal distribution of complexes (C_1) at the instant $t = 0,\ 600,\ 1800,\ 7200\,\mathrm{s}$ correspondent to a high amount of gremlin.

5.2.3.3 Low amount of gremlin

In the current section, we try to understand what happens in the case of a low-amount of ligands concentration. By analogy with the Tables 5.2 and 5.1 in the Tab. 5.3 we show the trend of the numerical and experimental outcomes when the concentration of ligands is equal to 10.6347 $molecules/\mu m^2$(i.e. the half of those shown in 5.2.3.1).

Table 5.3: Co-designing between VEGFR2-fluorescence intensity (in-vitro experiments) and the number of complexes generating on the cell membrane (in-silico simulation), correspondent to a low amount of gremlin, is provided. Specifically, both the total that dimensionless quantities are tabulated.

Time	FRAP	Error bars	Complex	Adimensional Complex	Adimensional FRAP	Adimensional error bars
0	1.8125	1.7470	0.0000	0.0000	0.0674	0.0649
120	2.6775	1.7774	395.8180	0.0484	0.0995	0.0661
240	3.6175	2.0371	1724.6600	0.2108	0.1344	0.0757
360	8.8875	4.5427	3597.2400	0.4396	0.3303	0.1688
480	12.0225	5.1638	5665.4000	0.6924	0.4468	0.1919
600	17.4375	4.0251	6713.9400	0.8205	0.6481	0.1496
720	20.1325	4.3776	7173.5700	0.8767	0.7482	0.1627
840	19.6650	4.4217	7495.2000	0.9160	0.7308	0.1643
960	20.4075	4.5417	7725.1600	0.9441	0.7584	0.1688
1080	22.8600	4.7168	7893.0100	0.9646	0.8496	0.1753
1200	23.0375	5.5135	8012.9600	0.9793	0.8562	0.2049
1320	23.2725	4.8333	8086.6300	0.9883	0.8649	0.1796
1440	24.9150	5.5791	8127.7500	0.9933	0.9260	0.2073
1560	25.8650	4.7980	8153.1200	0.9964	0.9613	0.1783
1680	27.8800	6.0900	8170.2700	0.9985	1.0361	0.2263
1800	26.9075	5.9243	8182.6100	1.0000	1.0000	0.2202
3600	39.2718	18.8742	8230.7200	1.0059	1.4595	0.7014
7200	36.8140	17.3697	8236.8700	1.0066	1.3682	0.6455

In Fig. 5.9 we can see a non-well-match between numerical and experimental data. Particularly, the numerical curve has several values out of the error-bars and its shape is different compared to the experimental curve.
Therefore, we definitely exclude the values of the concentrations of ligands that are significantly lower than 21.2694 $molecules/\mu m^2$, setting such a concentration as the lower bound for the number of ligands for the current problem.

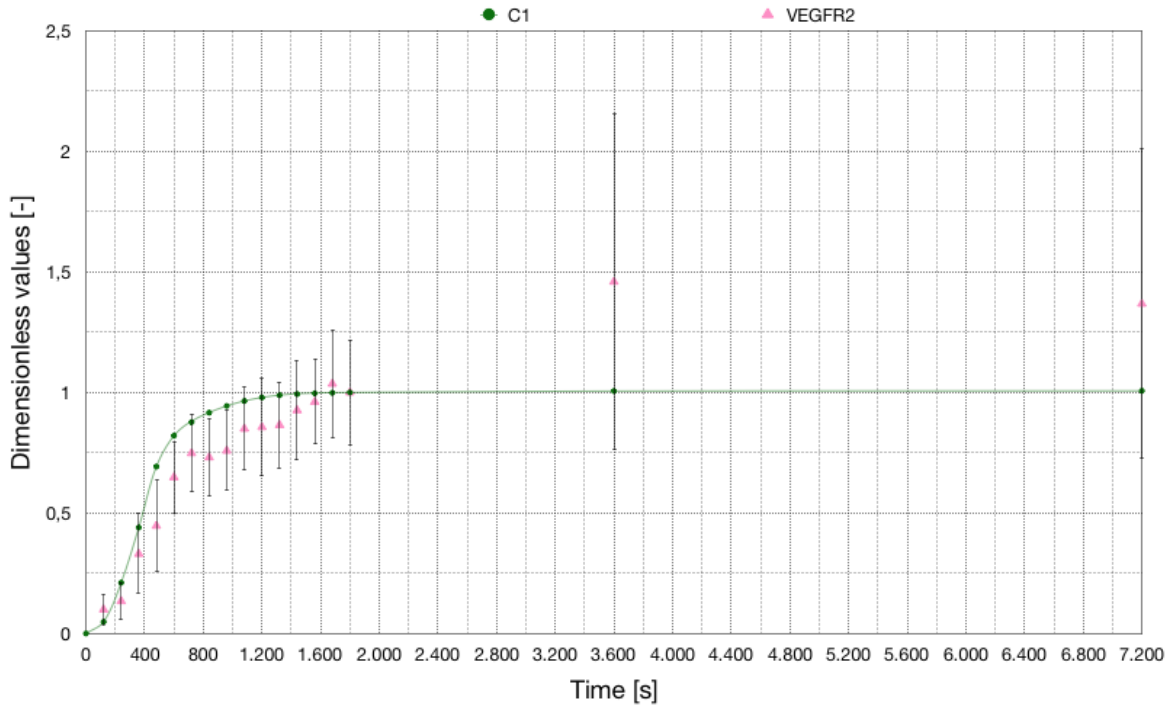

Figure 5.8: Numerical (dots with continuous line) and experimental (triangles with error bars) outcomes. Evolution in time of the normalized total amount of complexes correspondent to a low amount of gremlin is depicted.

Interestingly, different from Fig. 5.5, and 5.7, due to a low gremlin availability, in Fig. 5.9 it is possible to observe a full ligands depletion yet at the instant $t = 1800$ s.

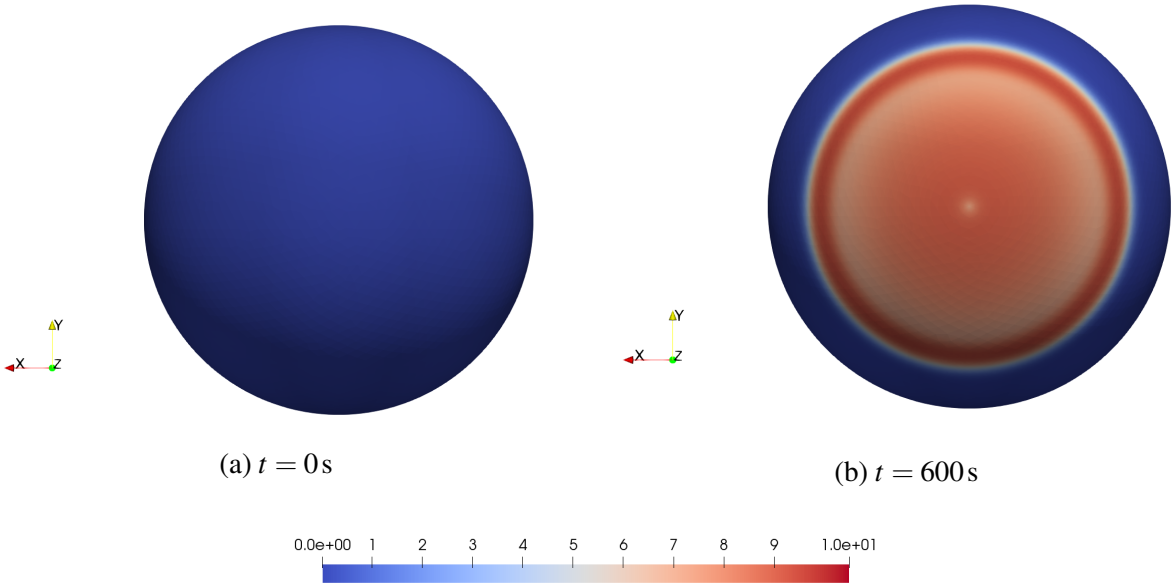

(a) $t = 0\,\mathrm{s}$

(b) $t = 600\,\mathrm{s}$

(c) Legend

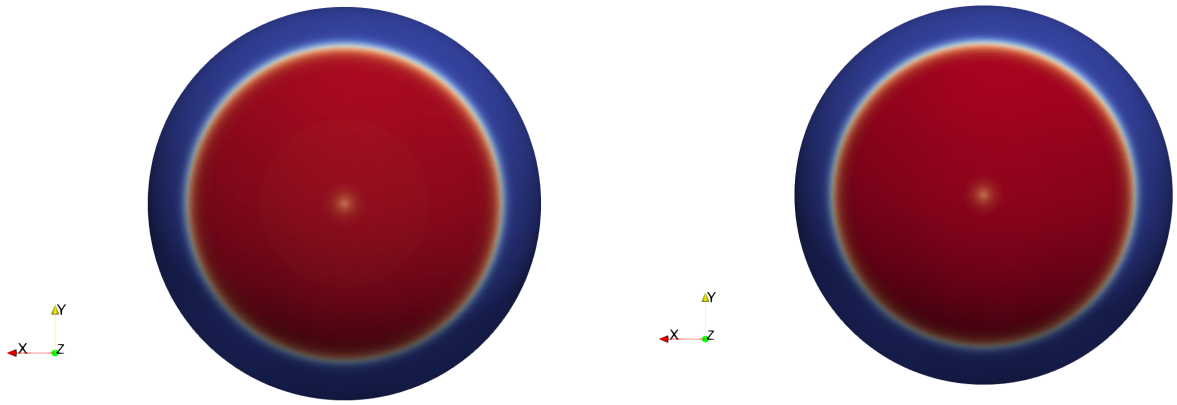

(d) $t = 1800\,\mathrm{s}$

(e) $t = 7200\,\mathrm{s}$

Figure 5.9: Basal distribution of complexes (C_1) at the instant $t = 0,\ 600,\ 1800,\ 7200\,\mathrm{s}$ correspondent to a low amount of gremlin.

5.2.4 Model based on one chemical reaction: integrin-fibrinogen interaction

In this section, we study the relocation of integrin when an EC is spreading on the fibrinogen coated substrate. The generic formulation aforementioned (eq. (5.2)) is below particularized as follows:

$$\underbrace{\text{integrin}}_{I} + \underbrace{\text{Fibrinogen}}_{L_I} \underset{k_b}{\overset{k_f}{\rightleftarrows}} \text{C}_3 \ . \tag{5.9}$$

$$\frac{\partial c_I}{\partial t} - \mathbb{D}_I \Delta_{\mathcal{P}}[c_I] + \frac{\partial c_{C_3}}{\partial t} = 0 \,, \tag{5.10a}$$

$$\frac{\partial c_{L_I}}{\partial t} + \frac{\partial c_{C_3}}{\partial t} = s_{L_I} \ , \tag{5.10b}$$

$$[c_{C_3}] = \frac{[c_I]\,[c_{L_I}]}{\alpha^{(5.9)}} \ . \tag{5.10c}$$

The mechanism underlying the chemical interaction between integrin and its specific ligand dominates the active part of the mechanical behavior of EC. Specifically, during the interaction with fibrinogen, integrin changes its own conformation from inactive (low-affinity) to active (high-affinity), trigger an internal signaling cascade that leads to the generation of adhesion sites in order to exchange mechanical stimuli between the cell and its microenvironment.

5.2.4.1 The fibrinogen calculation

Below the results of numerical analysis, where, relying on the fact that the molecules of gremlin and fibrinogen have comparable dimensions (see 4.3.2), we have decided to extend the value of the availability of ligands of gremlin to fibrinogen (21.2694 $molecules/\mu m^2$).

Table 5.4: Co-designing between integrin-fluorescence intensity (in-vitro experiments) and the number of complexes generating on the cell membrane (in-silico simulation) is provided. Specifically, both the total that dimensionless quantities are tabulated.

Time	FRAP	Error bars	Complex	Adimensional Complex	Adimensional FRAP	Adimensional error bars
0	2.0200	10.3196	0.0000	0.0000	0.0337	0.1720
120	7.0275	11.8379	292.5320	0.0715	0.1172	0.1973
240	17.7100	14.9573	757.3920	0.1851	0.2952	0.2494
360	20.8125	15.7440	1331.1500	0.3253	0.3470	0.2625
480	26.7050	18.4065	1934.3600	0.4727	0.4452	0.3069
600	37.5350	20.3823	2346.8300	0.5735	0.6257	0.3398
720	45.0000	22.2337	2619.1900	0.6400	0.7502	0.3707
840	48.5450	22.8354	2850.8800	0.6966	0.8093	0.3807
960	52.2100	24.0112	3061.3200	0.7480	0.8704	0.4003
1080	55.4000	24.6039	3243.6700	0.7926	0.9236	0.4102
1200	59.3875	26.0124	3420.8300	0.8359	0.9900	0.4336
1320	58.8700	25.5831	3592.0400	0.8777	0.9814	0.4265
1440	57.7225	24.5200	3736.9300	0.9131	0.9623	0.4088
1560	62.0475	25.5762	3859.5100	0.9431	1.0344	0.4264
1680	58.6325	24.3768	3967.2400	0.9694	0.9775	0.4064
1800	59.9850	24.7566	4092.4600	1.0000	1.0000	0.4127
3600	189.6127	53.7018	5287.6300	1.2920	3.1610	0.8953
7200	109.8590	36.9739	6054.5700	1.4794	1.8314	0.6164

Similar to what was done for VEGFR2, either numerical and experimental quantities have been normalized through their correspondent values at $t = 1800\ s$. In the following, we have fixed in a graph (Fig. 5.10) the temporal evolution of the above-normalized quantities.

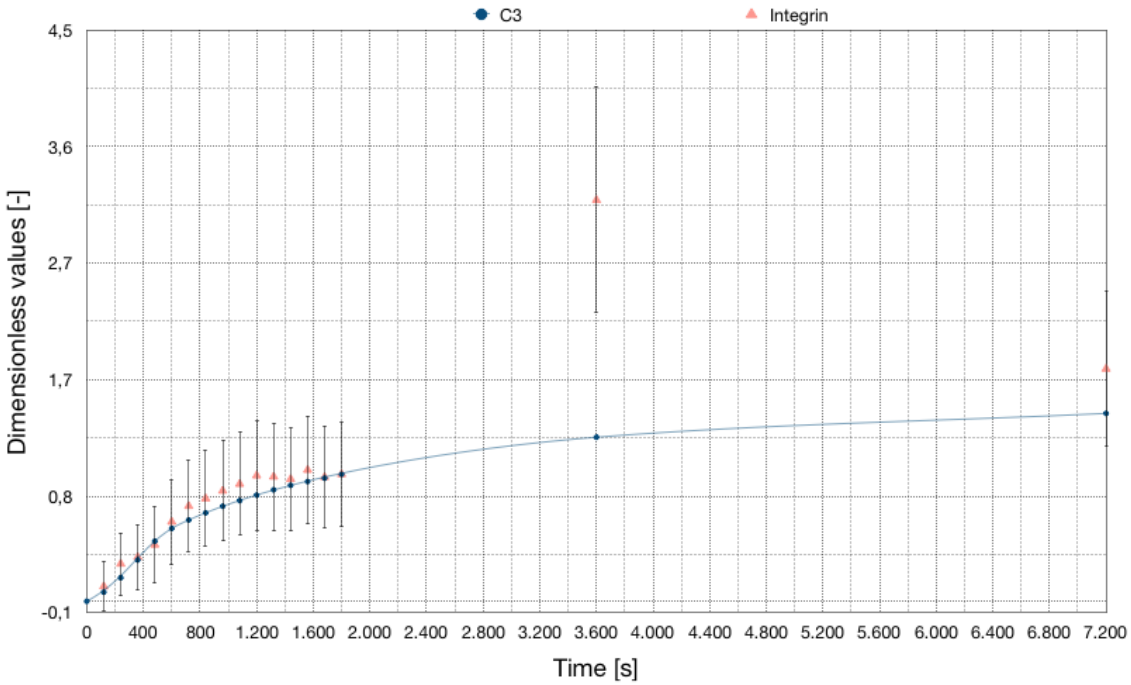

Figure 5.10: Numerical (dots with continuous line) and experimental (triangles with error bars) outcomes. Evolution in time of the normalized total amount of complexes is depicted.

From this analysis, we observe that 97% of the total amount of integrin (about 6300 molecules), of which 96% of complexes, are located in the basal side of the cell, showing a completely different result from what emerged to the VEGFR2 study. Comparing this observation with the evidence arising from Fig. 5.10 we can infer that a new physics is influencing the relocation of this receptor. It is, in fact, possible to see how the model we built intercepts the experimental curve, with well-approximation, up to $t = 1800\ s$. Differently, after this moment, the behavior of integrin is not governed, as for VEGFR2, by means of a purely diffusive phenomenon. It would seem evident that the hypothesis $s_I = 0$ is here not valid.

It is indeed known how huge quantities of integrin are exposed to the cell membrane by means of vesicles embedded in the inner part of the cell. In fact, dissimilarly from VEGFR2, integrin is already preformed in these vesicles; therefore, the cell does not need to synthesize them from scratch and so, these receptors result to be easily available for being exposed on the membrane. This phenomenon could justify the huge amount of integrin observed at the instant $t = 3600\ s$. We conclude by inferring that the high affinity between integrin and fibrinogen, together with the low availability of receptors on the cell membrane at the beginning of the analysis, leads to a quick depletion of the receptor that, in the reality, could induce a relevant exposition of s_I.

Once again it is possible to appreciate the potentiality of a mathematical model applied to biology. In fact, despite the evident inability to intercept every discrete point of the experimental curve, the current model can interpret reality discovering that further events, not taken into consideration inside the framework itself, has to happen to describe the experiment. Intriguingly, we can also predict the order of magnitude of the quantity of integrin that should be correlated with s_I. In

fact, through an easy dimensionless relationship between the experimental and numerical value at $t = 3600\ s$, we can deduce the following result: $\frac{3.1610}{1.2920} = 2.4465$. Hence, the number of integrins that actually are present on the real cell membrane at time $t = 3600\ s$ are nearly 2.5 times respect to that provided by the in-silico simulations (see Tab. 5.4).

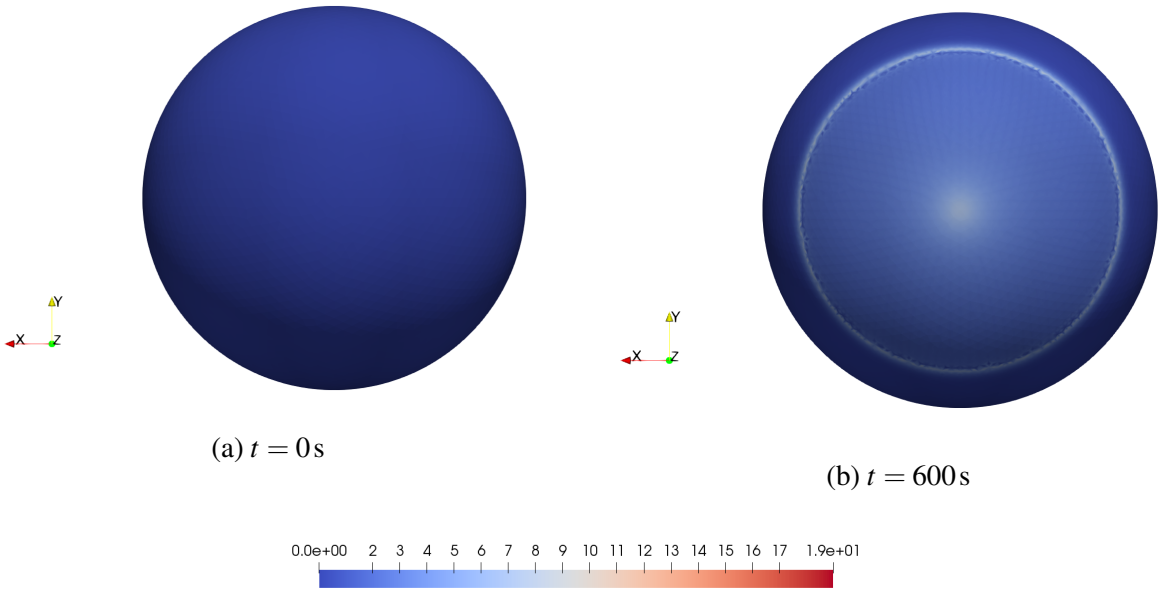

(a) $t = 0\,\mathrm{s}$

(b) $t = 600\,\mathrm{s}$

(c) Legend

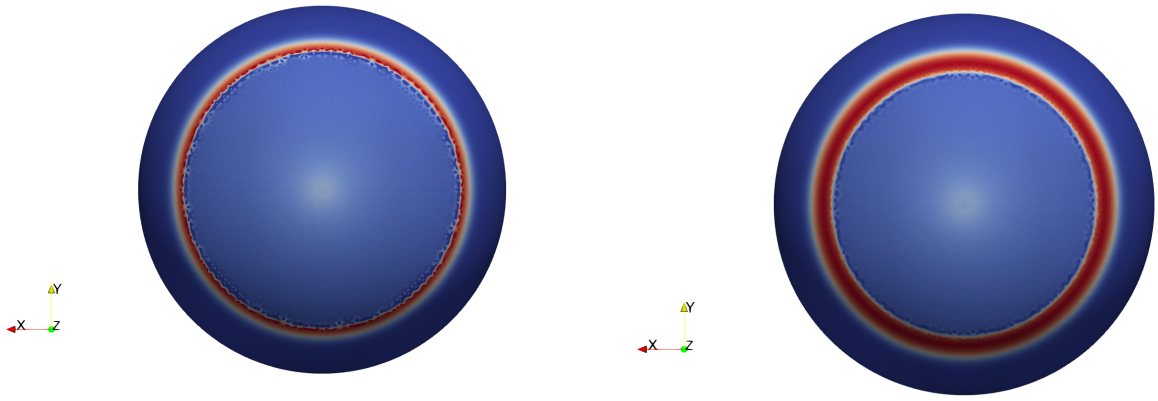

(d) $t = 1800\,\mathrm{s}$

(e) $t = 7200\,\mathrm{s}$

Figure 5.11: Basal distribution of complexes (C_3) at the instant $t = 0,\ 600,\ 1800,\ 7200\,\mathrm{s}$.

Similar to what is shown in the previous sections, we are going to study what happens at the numerical outcomes if the substrate is coated with a doubled and then halved ligand concentration (42.5389 $molecules/\mu m^2$ and 10.6347 $molecules/\mu m^2$ respectively).

5.2.4.2 High amount of fibrinogen

The low ratio between the number of receptors available on the cell membrane and the ligands on the substrate leads to considerably different results to the equivalent VEGFR2-gremlin case. In fact, Tab. 5.5 and Tab. 5.4 have no substantial differences in the numerical values.

Table 5.5: Co-designing between integrin-fluorescence intensity (in-vitro experiments) and the number of complexes generating on the cell membrane (in-silico simulation), correspondent to a high amount of fibrinogen, is provided. Specifically, both the total that dimensionless quantities are tabulated.

Time	FRAP	Error bars	Complex	Adimensional Complex	Adimensional FRAP	Adimensional error bars
0	2.0200	10.3196	0.0000	0.0000	0.0337	0.1720
120	7.0275	11.8379	323.8780	0.0766	0.1172	0.1973
240	17.7100	14.9573	797.7110	0.1886	0.2952	0.2494
360	20.8125	15.7440	1377.5000	0.3257	0.3470	0.2625
480	26.7050	18.4065	1979.2600	0.4680	0.4452	0.3069
600	37.5350	20.3823	2409.4800	0.5697	0.6257	0.3398
720	45.0000	22.2337	2687.1200	0.6353	0.7502	0.3707
840	48.5450	22.8354	2917.6400	0.6898	0.8093	0.3807
960	52.2100	24.0112	3166.3100	0.7486	0.8704	0.4003
1080	55.4000	24.6039	3341.1300	0.7900	0.9236	0.4102
1200	59.3875	26.0124	3490.0000	0.8252	0.9900	0.4336
1320	58.8700	25.5831	3636.5100	0.8598	0.9814	0.4265
1440	57.7225	24.5200	3798.2300	0.8980	0.9623	0.4088
1560	62.0475	25.5762	3961.7600	0.9367	1.0344	0.4264
1680	58.6325	24.3768	4105.3300	0.9706	0.9775	0.4064
1800	59.9850	24.7566	4229.5300	1.0000	1.0000	0.4127
3600	189.6127	53.7018	5428.1700	1.2834	3.1610	0.8953
7200	109.8590	36.9739	6095.5400	1.4412	1.8314	0.6164

Particularly, the main difference is represented in the pictures of Fig. 5.12 and Fig. 5.13e. Here, the greater amount of ligands, shown in the second figure, leads to a reduction of the width of the red ring that encircles the EC and, at the same time, an increase in the value of the concentration of C_3.

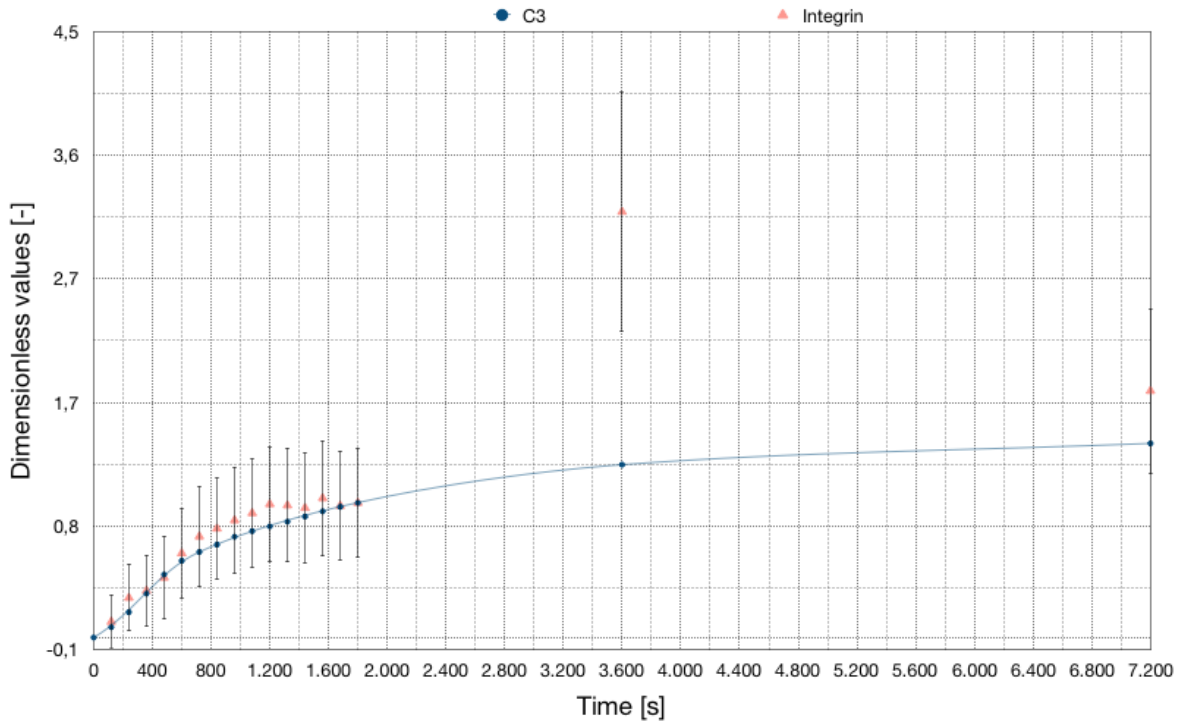

Figure 5.12: Numerical (dots with continuous line) and experimental (triangles with error bars) outcomes. Evolution in time of the normalized total amount of complexes correspondent to a high amount of fibrinogen is depicted.

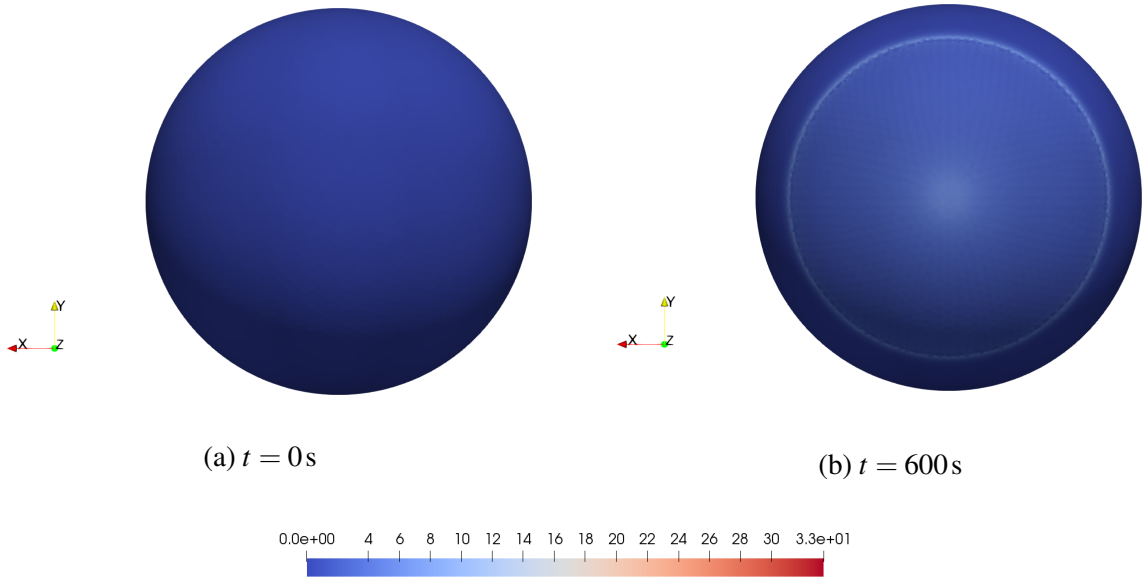

(a) $t = 0\,\mathrm{s}$

(b) $t = 600\,\mathrm{s}$

(c) Legend

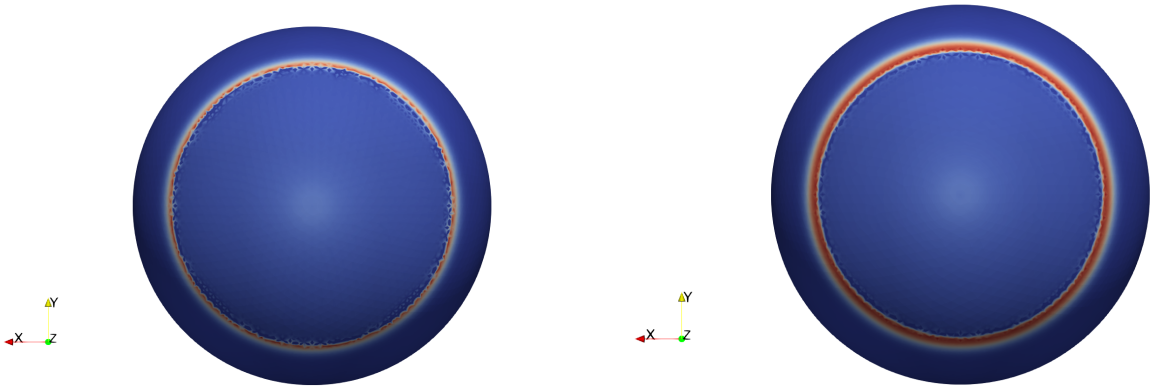

(d) $t = 1800\,\mathrm{s}$

(e) $t = 7200\,\mathrm{s}$

Figure 5.13: Basal distribution of complexes (C_3) at the instant $t = 0,\ 600,\ 1800,\ 7200\,\mathrm{s}$ correspondent to a high amount of fibrinogen.

5.2.4.3 Low amount of fibrinogen

Regarding the case with the availability of ligands equal to 10.6347 $molecules/\mu m^2$, we can observe a slight difference in the results already presented in the Tab. 5.6 compared to the 5.4.

Table 5.6: Co-designing between integrin-fluorescence intensity (in-vitro experiments) and the number of complexes generating on the cell membrane (in-silico simulation), correspondent to a low amount of fibrinogen, is provided. Specifically, both the total that dimensionless quantities are tabulated.

Time	FRAP	Error bars	Complex	Adimensional Complex	Adimensional FRAP	Adimensional error bars
0	2.0200	10.3196	0.0000	0.0000	0.0337	0.1720
120	7.0275	11.8379	253.4940	0.0642	0.1172	0.1973
240	17.7100	14.9573	709.2570	0.1795	0.2952	0.2494
360	20.8125	15.7440	1276.9600	0.3232	0.3470	0.2625
480	26.7050	18.4065	1881.2800	0.4761	0.4452	0.3069
600	37.5350	20.3823	2280.1400	0.5770	0.6257	0.3398
720	45.0000	22.2337	2539.9100	0.6428	0.7502	0.3707
840	48.5450	22.8354	2752.3900	0.6966	0.8093	0.3807
960	52.2100	24.0112	2963.5000	0.7500	0.8704	0.4003
1080	55.4000	24.6039	3124.8100	0.7908	0.9236	0.4102
1200	59.3875	26.0124	3299.3100	0.8350	0.9900	0.4336
1320	58.8700	25.5831	3428.1600	0.8676	0.9814	0.4265
1440	57.7225	24.5200	3591.3400	0.9089	0.9623	0.4088
1560	62.0475	25.5762	3714.6400	0.9401	1.0344	0.4264
1680	58.6325	24.3768	3825.0000	0.9680	0.9775	0.4064
1800	59.9850	24.7566	3951.4000	1.0000	1.0000	0.4127
3600	189.6127	53.7018	5085.3300	1.2870	3.1610	0.8953
7200	109.8590	36.9739	5905.6700	1.4946	1.8314	0.6164

Everything would hence seem to lead to the same deductions made for the case with a high concentration of fibrinogen and therefore presume the validity of the current model as well. Nevertheless, we find such an inference unreasonable. In fact, the practical equivalence of the saturation values between gremlin and fibrinogen (shown in section 4.3.2), suggest similar available concentrations either for these ligands. Moreover, such a value, for the current in-vitro experiment (see 4.1), has to be independent of the kind of cell that spread on the substrate, rather is strictly dependent on the structural characteristic of the molecule of the ligand itself. All together these considerations induce us to infer that, again, the lower-bound for the concentration of available fibrinogen is 21.2694 $molecules/\mu m^2$.

Hence, considering the results achieved so far it has been possible to assume that the concentration of S_{L_V} and S_{L_I} can not be lower than 21.2694 $molecules/\mu m^2$. Such a result will be accounted for in the next model formulations, where no numerical analysis with a concentration of available ligands lower than this, will be set.

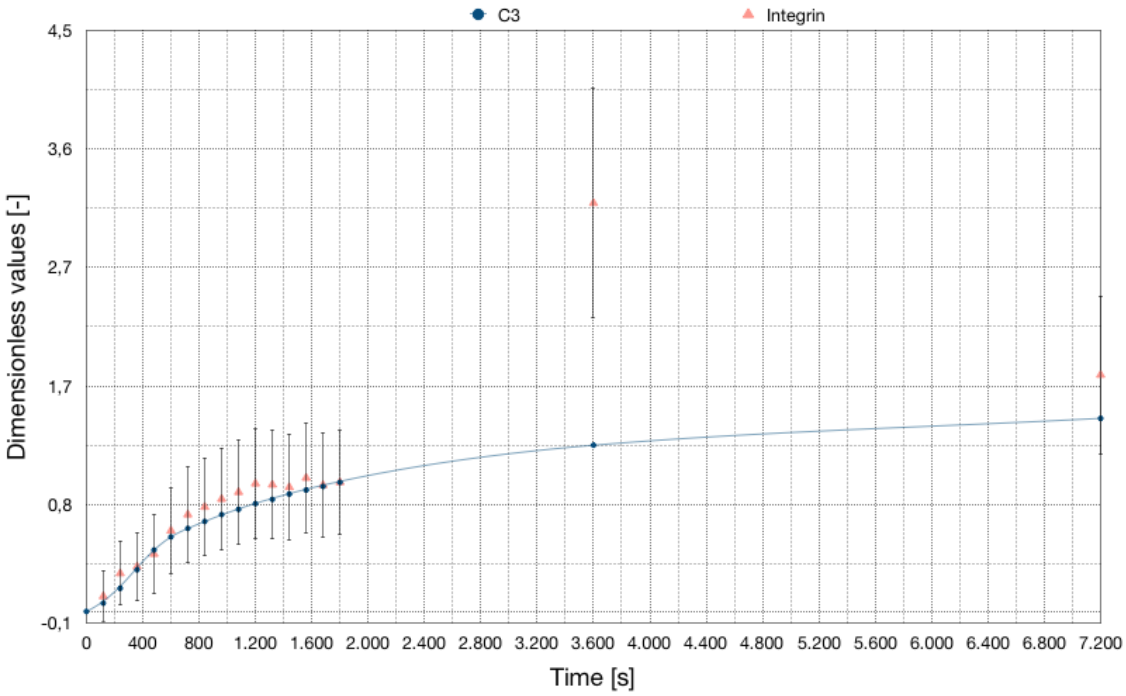

Figure 5.14: Numerical (dots with continuous line) and experimental (triangles with error bars) outcomes. Evolution in time of the normalized total amount of complexes correspondent to a low amount of fibrinogen is depicted.

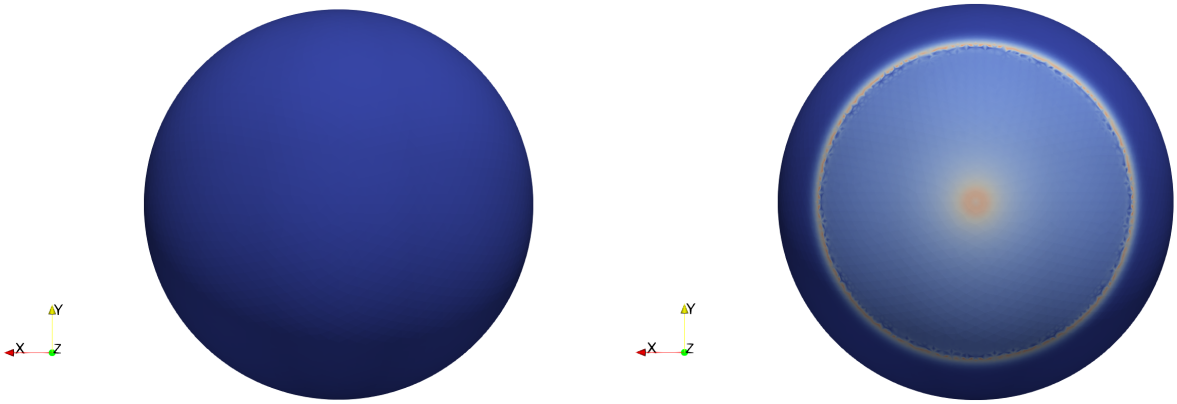

(a) $t = 0\,\mathrm{s}$

(b) $t = 600\,\mathrm{s}$

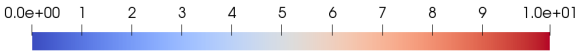

(c) Legend

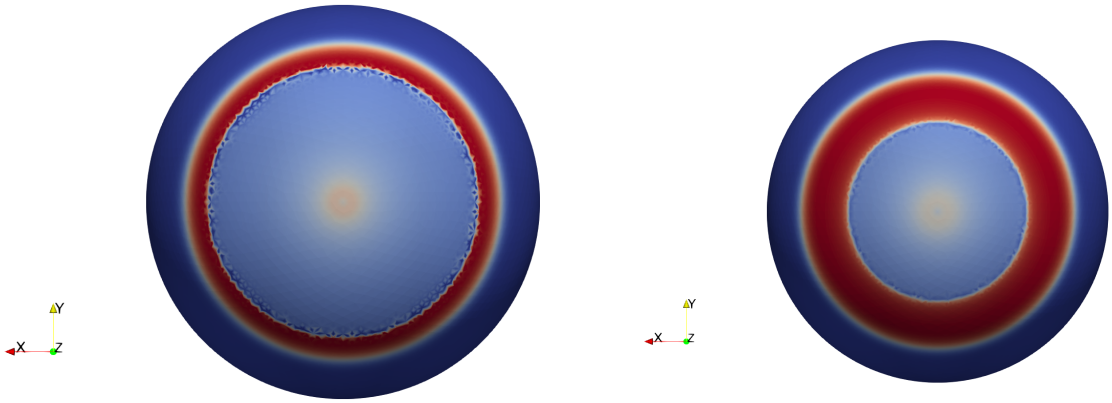

(d) $t = 1800\,\mathrm{s}$

(e) $t = 7200\,\mathrm{s}$

Figure 5.15: Basal distribution of complexes (C_3) at the instant $t = 0,\ 600,\ 1800,\ 7200\,\mathrm{s}$ correspondent to a low amount of fibrinogen.

5.2.5 Model based on two chemical reactions: integrin interacts with VEGFR2-gremlin-complex

Experimental evidence showed that integrin promotes long-lasting activation of VEGFR2 [52]. Accordingly, the following chemical reactions are embedded in the framework of our model:

$$\underbrace{\text{VEGFR2}}_{V} + \underbrace{\text{Gremlin}}_{L_V} \underset{k_b}{\overset{k_f}{\rightleftarrows}} \text{C}_1 \,, \tag{5.11a}$$

$$d\ \underbrace{\text{Integrin}}_{I} + e\ \text{C}_1 \underset{k_b}{\overset{k_f}{\rightleftarrows}} \text{C}_2 \,. \tag{5.11b}$$

The governing equations coupled to the chemical reactions 5.11a and 5.11b, reads as follows:

$$\frac{\partial c_V}{\partial t} - \mathbb{D}_V \Delta_{\mathfrak{P}}[c_V] + \frac{\partial c_{C_1}}{\partial t} + e\,\frac{\partial c_{C_2}}{\partial t} = 0\,, \tag{5.12a}$$

$$\frac{\partial c_{L_V}}{\partial t} + \frac{\partial c_{C_1}}{\partial t} + e\,\frac{\partial c_{C_2}}{\partial t} = s_{L_V}\,, \tag{5.12b}$$

$$\frac{\partial c_I}{\partial t} - \mathbb{D}_I \Delta_{\mathfrak{P}}[c_I] + d\,\frac{\partial c_{C_2}}{\partial t} = 0\,, \tag{5.12c}$$

$$[c_{C_1}] = \frac{[c_V]\,[c_{L_V}]}{\alpha^{(5.11a)}}\,, \tag{5.12d}$$

$$[c_{C_2}] = \frac{[c_I]^d\,[c_{C_1}]^e}{\alpha^{(5.11b)}}\,. \tag{5.12e}$$

The values calibrated by model 5.2.3 will be here inherited, particularly s_{L_V}.
Moreover, the calibration of the parameter $\alpha_{(5.11b)}$ goes hand in hand with that of the stoichiometric coefficients d and e. In particular, it is shown in the work [52] that, at the end of the experiment of time-lapse analysis adhesion assay ($t = 7200\ s$), nearly the 33% of VEGFR2, located in the basal side of the cell, interact with integrin, while about the 13% of integrin, in the same portion of the cell, is colocalized with VEGFR2 (see section4.1.1.1).
Concerning the stoichiometry that rules the chemical interaction between integrin-VEGFR2-gremlin-complex, we have neither any information from previous in-silico analysis nor biological pieces of information. However, in view of the percentages just discussed and of the fact that the initial number of VEGFR2 is about four times the number of integrin at the initial time, we retain lawful to infer that the coefficient d is lower, or at least equal, than e.

Finally, the strategy will be to find the most reasonable combination between the values of parameters d, e, and $\alpha_{(5.11b)}$ and to evaluate a posteriori the eventually good match between in-silico and in-vitro simulations.

The best-fitting have been obtained by the following stoichiometric coefficients:

Table 5.7: In-silico results describing colocalization of VEGFR2 and integrin at the and of the experiments. Gremlin concentration equal to 21.2694 $molecules/\mu m^2$

Stoichiometric coefficients	$\alpha_{(5.11b)}$	% of VEGFR2 colocalized with integrin	% of integrin colocalized with VEGFR2
$d = 1, e = 4$	0.00138	88.50	88.20
$d = 1, e = 2$	0.14464	62.05	98.61
$d = 1, e = 1$	0.04519	31.96	99.05

We notice a fair matching between experimental and numerical data for all three cases above-showed, but mainly for the cases with $e = 1$ and $e = 2$ (see the Fig 5.16, Fig. 5.17 and Fig. 5.18)).

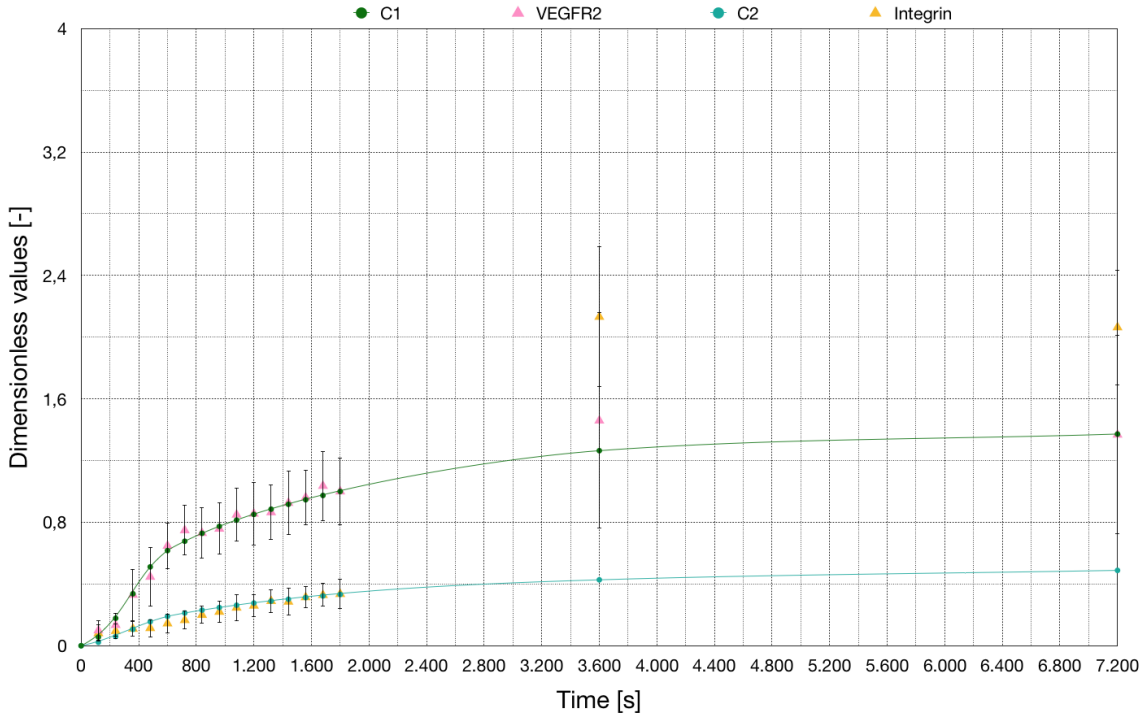

Figure 5.16: Numerical (dots with continuous line) and experimental (triangles with error bars) outcomes. Evolutions in time of the normalized total amounts of complexes are depicted for $d = e = 1$.

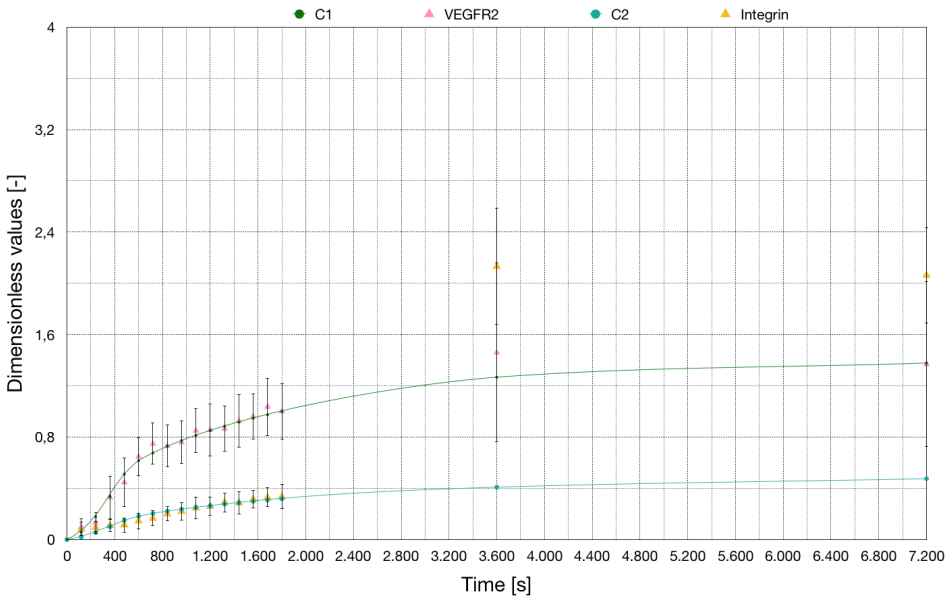

Figure 5.17: Numerical (dots with continuous line) and experimental (triangles with error bars) outcomes. Evolutions in time of the normalized total amounts of complexes are depicted for $d = 1$ and $e = 2$.

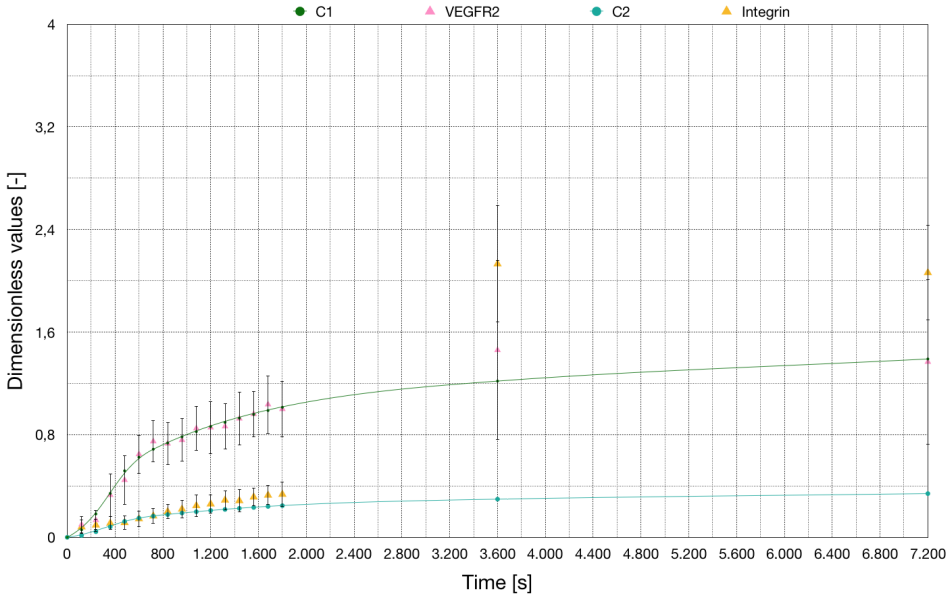

Figure 5.18: Numerical (dots with continuous line) and experimental (triangles with error bars) outcomes. Evolutions in time of the normalized total amounts of complexes are depicted for $d = 1$ and $e = 4$.

Analyzing the trend of the percentages in Tab. 5.7, we notice two things:

1. little by little e tends to one, the percentage of VEGFR2 in contact with integrin decreases, and the percentage of integrin that colocalize with VEGFR2 increases;

2. again, as in the case of integrin-fibrinogen interaction (section 5.2.4), we have a strong discrepancy between the experimental and numerical data for times $t > 1800\ s$.

Similarly to section 5.2.4, we have a strong exposure of integrin (embedded in the vesicles inside the cell), on the cell membrane: a phenomenon that we know neglected in the current framework. This implies that a comparison between the percentages of colocalization deduced from the numerical outcomes with the experimental ones is not feasible. Indeed, these values are experimentally evaluated at $t = 7200\ s$ but, we already know, for $t > 1800\ s$ exists a discrepancy between numerical and experimental data. Therefore, an attempt to compare these data would seem complete in vain.

Nevertheless, matching the results we can observe how, concerning the case with $d = 1$ and $e = 1$, the percentage of VEGFR2 colocalized with integrin corresponds to the experimental, about 33%, whereas the data describing how many integrins are interacting with VEGFR2 is completely different. These data corroborate our belief that by incrementing the amount of integrin by means of the source term s_I we may reach a complete fit with the experimental result. Hence, these pieces of information could be closely related and they make us opt for a one-to-one stoichiometry between integrin - C_1.

Following, we tabling the evolution on time of the depletion of the receptors by the aids of Tab. 8.2 and 8.3 and together the Fig. 5.16.

Table 5.8: Co-designing between VEGFR2 and integrin fluorescence intensity (in-vitro experiments) and the number of complexes generating on the cell membrane (in-silico simulation), is provided. Specifically, the total quantities are tabulated.

Time	FRAP VEGFR2	Error bars VEGFR2	FRAP integrin	Error bars integrin	C_2	C_1
0	1.8125	1.7470	2.0700	1.3727	0.0000	0.0000
120	2.6775	1.7774	2.1825	1.4993	269.3160	671.6870
240	3.6175	2.0371	2.5650	1.3584	714.1570	2125.3170
360	8.8875	4.5427	2.9550	1.4014	1269.7700	4019.9100
480	12.0225	5.1638	3.0775	1.5473	1859.5500	6101.9100
600	17.4375	4.0251	3.8900	1.7371	2271.3600	7363.4200
720	20.1325	4.3776	4.4750	1.6674	2532.8000	8087.9800
840	19.6650	4.4217	5.3775	1.5673	2756.2900	8700.9700
960	20.4075	4.5417	5.9175	1.9579	2954.8100	9238.4600
1080	22.8600	4.7168	6.6400	2.3900	3134.8800	9721.8400
1200	23.0375	5.5135	6.9850	1.9568	3300.1900	10162.4800
1320	23.2725	4.8333	7.8000	2.0404	3453.1300	10568.5800
1440	24.9150	5.5791	7.6800	2.4520	3595.4900	10945.8200
1560	25.8650	4.7980	8.4550	1.9578	3728.4700	11298.3500
1680	27.8800	6.0900	8.8375	2.0512	3853.0400	11629.1000
1800	26.9075	5.9243	9.0225	2.5968	3969.9700	11940.6800
3600	39.2718	18.8742	57.3603	12.2651	5101.3000	15094.6400
7200	36.8140	17.3697	55.5292	10.0477	5832.0000	16382.5000

Table 5.9: Co-designing between VEGFR2 and integrin fluorescence intensity (in-vitro experiments) and the number of complexes generating on the cell membrane (in-silico simulation), is provided. Specifically, the dimensionless quantities are tabulated.

Time	Adimensional C_2	Adimensional C_1	Adimensional VEGFR2	Adimensional error bars VEGFR2	Adimensional integrin	Adimensional error bars integrin
0	0.0000	0.0000	0.0674	0.0649	0.0769	0.0510
120	0.0226	0.0563	0.0995	0.0661	0.0811	0.0557
240	0.0598	0.1780	0.1344	0.0757	0.0953	0.0505
360	0.1063	0.3367	0.3303	0.1688	0.1098	0.0521
480	0.1557	0.5110	0.4468	0.1919	0.1144	0.0575
600	0.1902	0.6167	0.6481	0.1496	0.1446	0.0646
720	0.2121	0.6773	0.7482	0.1627	0.1663	0.0620
840	0.2308	0.7287	0.7308	0.1643	0.1999	0.0582
960	0.2475	0.7737	0.7584	0.1688	0.2199	0.0728
1080	0.2625	0.8142	0.8496	0.1753	0.2468	0.0888
1200	0.2764	0.8511	0.8562	0.2049	0.2596	0.0727
1320	0.2892	0.8851	0.8649	0.1796	0.2899	0.0758
1440	0.3011	0.9167	0.9260	0.2073	0.2854	0.0911
1560	0.3122	0.9462	0.9613	0.1783	0.3142	0.0728
1680	0.3227	0.9739	1.0361	0.2263	0.3284	0.0762
1800	0.3325	1.0000	1.0000	0.2202	0.3353	0.0965
3600	0.4272	1.2641	1.4595	0.7014	2.1318	0.4558
7200	0.4884	1.3720	1.3682	0.6455	2.0637	0.3734

By analogy with what we did in the section 5.2.4, we compute, by means a ratio between the experimental and numerical normalized values, how many integrins, should be provided through s_I for find a well-match between numerical and experimental results. In particular, it is trivial to compute: $\frac{2.1318}{0.4272} \sim 4.9898$ for $t = 3600\ s$ and $\frac{2.0637}{0.4884} \sim 4.2253$ for $t = 7200\ s$. We can deduce that at time $t = 3600\ s$ we should have a five-time larger amount of integrin in the basal side of the cell and about four-time at $t = 7200\ s$.

A significant discrepancy, therefore, emerges between the missing values of integrin in the case of integrins interaction with fibrinogen (about 2 times that expected by the model) and in the case of interplay with the VEGFR2-Gremlin complex (about 5 times that expected by the model). These data are very surprising, merely for the fact that the first interaction (involving high-affinity integrin) should lead to a greater demand for integrin receptors in the basal part of the cell compared to the other chemical reaction mentioned above.

Interestingly, this data can be explained, from an experimental point of view, through the so-called clustering of integrin receptors at the adhesion sites (focal adhesions). Such a phenomenon can distort the perceived fluorescence of the receptors during time-lapse analysis, misrepresenting their experimental interpretation. Consequently, we think that the fluorescence datum, shown in Fig 5.10, underestimates the real quantity of integrins overexpose by the EC, and so, we infer that the

real quantity can be at least the one calculated in the current section (about 5 times that expected by the model).

The possibility of correctly calibrating membrane externalization of integrin receptors has impressive importance in order to include in the current models a correct description of the organization of the cytoskeleton and of the adhesion sites.

Finally, regarding Fig. 5.19 and 5.20, we can observe the complementarities between the pictures Fig. 5.19e and 5.20e. In fact, the red ring formed by C_2 is superimposable with the external zone of C_1, similarly to the results in Appendix B.2.1. Such a phenomenon is supported by the diffusion of the integrin receptor from the apical to the basal side of the cell.

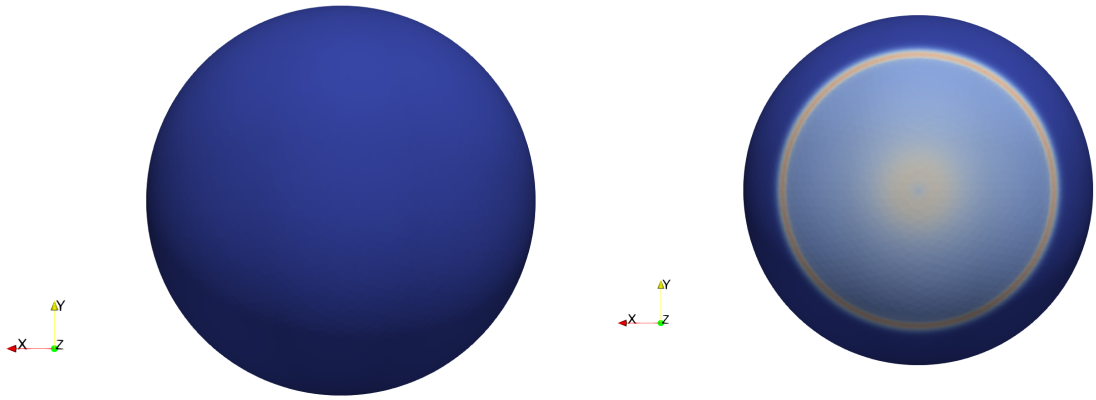

(a) $t = 0\,\mathrm{s}$

(b) $t = 600\,\mathrm{s}$

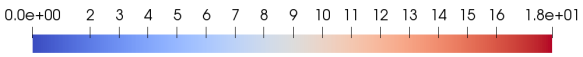

(c) Legend

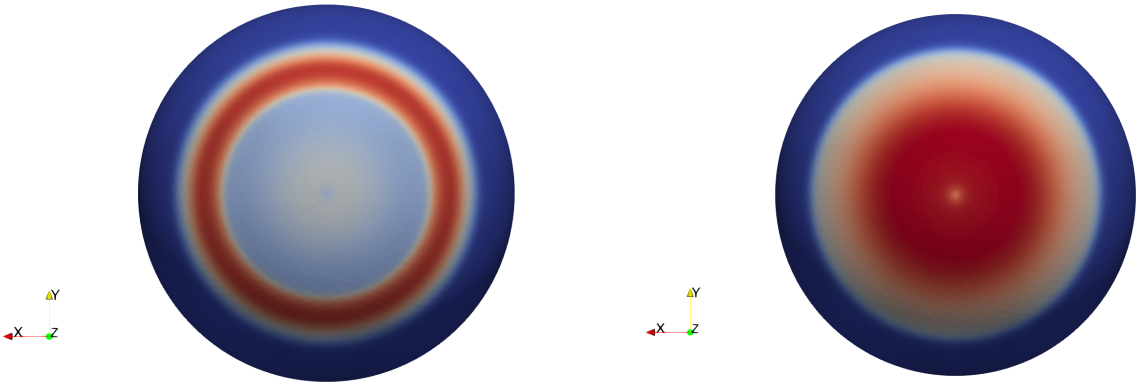

(d) $t = 1800\,\mathrm{s}$

(e) $t = 7200\,\mathrm{s}$

Figure 5.19: Basal distribution of complexes (C_1) at the instant $t = 0,\ 600,\ 1800,\ 7200\,\mathrm{s}$.

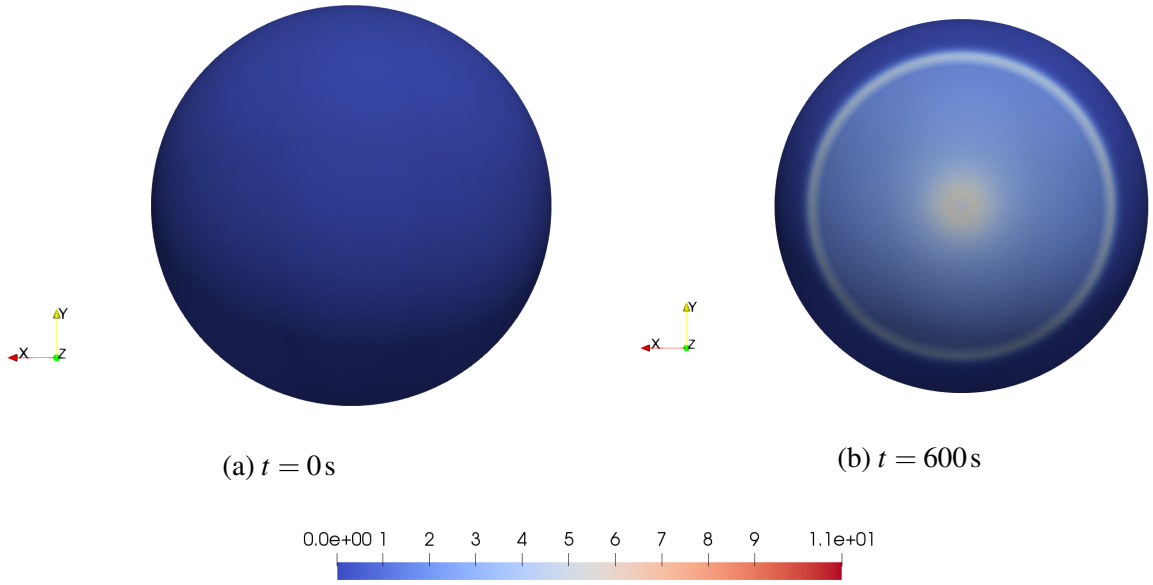

(a) $t = 0\,\mathrm{s}$ (b) $t = 600\,\mathrm{s}$

(c) Legend

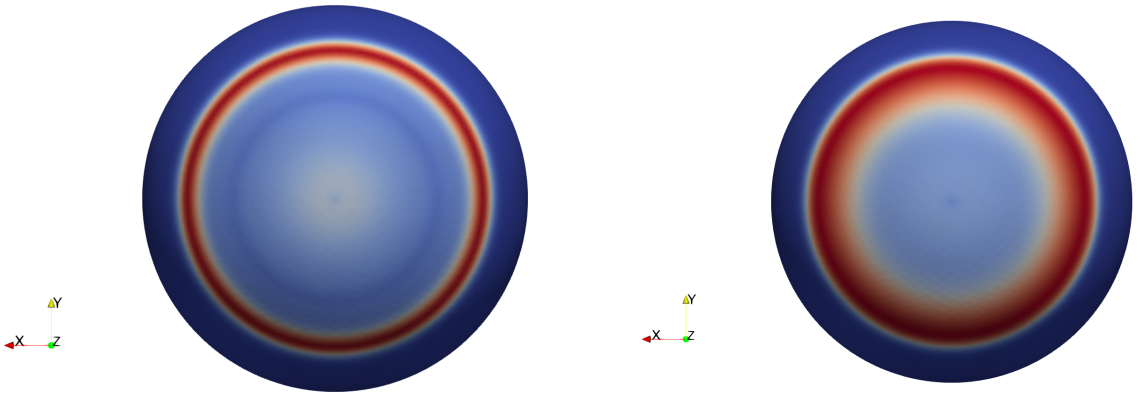

(d) $t = 1800\,\mathrm{s}$ (e) $t = 7200\,\mathrm{s}$

Figure 5.20: Basal distribution of complexes (C_2) at the instant $t = 0,\ 600,\ 1800,\ 7200\,\mathrm{s}$.

5.2.5.1 Model based on two chemical reactions with a high amount of gremlin

Similar to what has just been done in the previous section, we analyze the results drawn from a numerical model with a high concentration of ligands. Again, the numerical result that better fitting the experimental ones correspond to the following values of d, e, and $\alpha_{(5.11b)}$.

Table 5.10: In-silico results describing colocalization of VEGFR2 and integrin at the and of the experiments. Gremlin concentration equal to 42.5389 $molecules/\mu m^2$

Stoichiometric coefficients	$\alpha_{(5.11b)}$	% of VEGFR2 colocalized with integrin	% of integrin colocalized with VEGFR2
$d = 1, e = 4$	0.00138	94.33	95.65
$d = 1, e = 2$	0.14464	56.28	99.66
$d = 1, e = 1$	0.04519	27.99	99.40

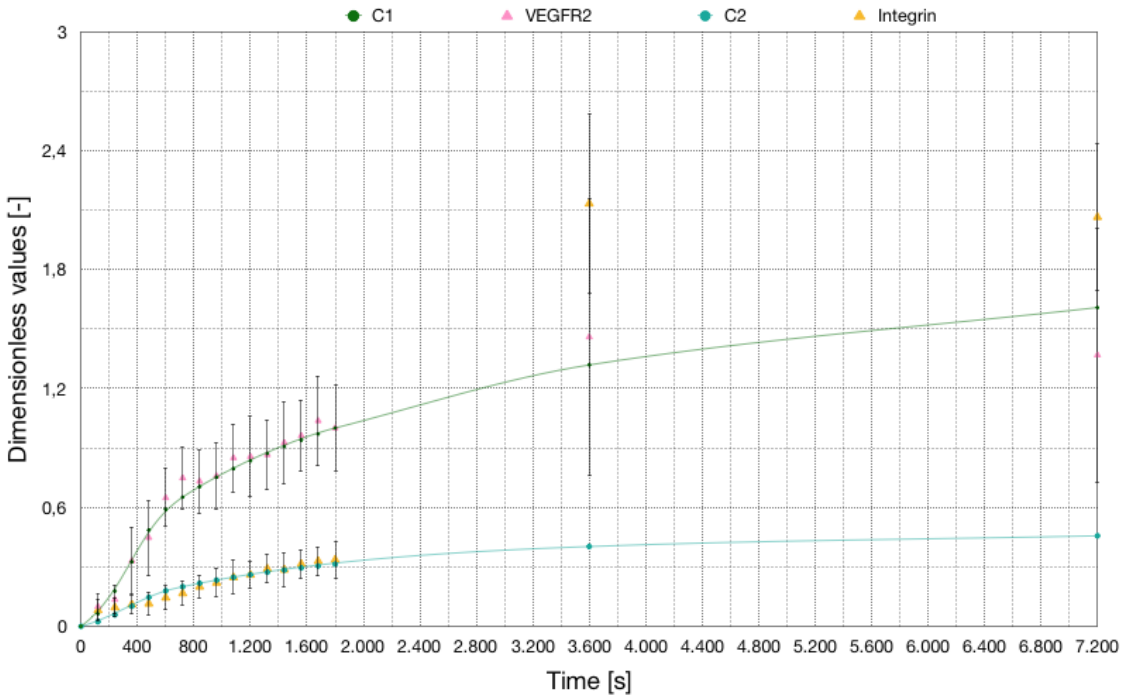

Figure 5.21: Numerical (dots with continuous line) and experimental (triangles with error bars) outcomes correspondent to a high amount of gremlin. Evolutions in time of the normalized total amounts of complexes are depicted for $d = e = 1$.

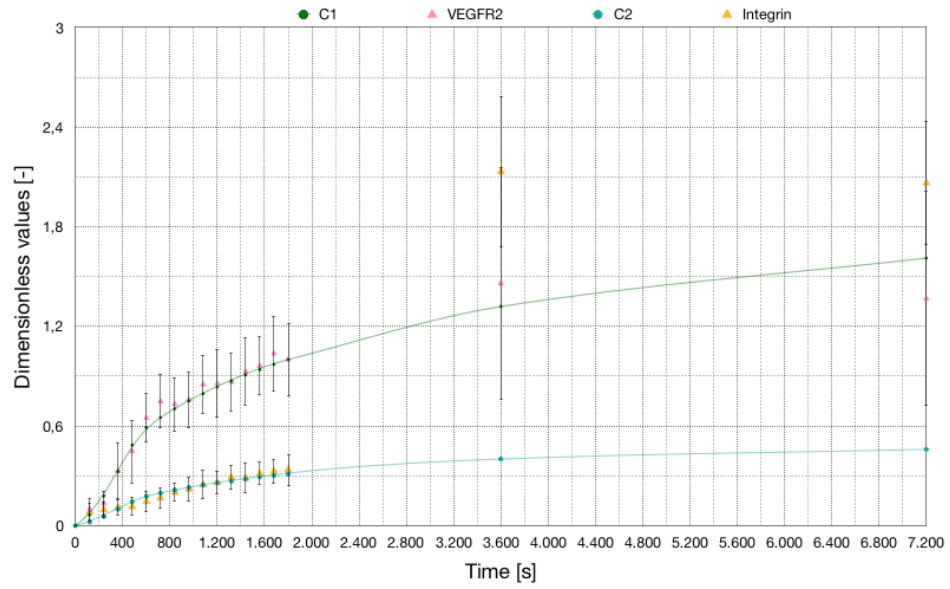

Figure 5.22: Numerical (dots with continuous line) and experimental (triangles with error bars) outcomes correspondent to a high amount of gremlin. Evolutions in time of the normalized total amounts of complexes are depicted for $d = 1$ and $e = 2$.

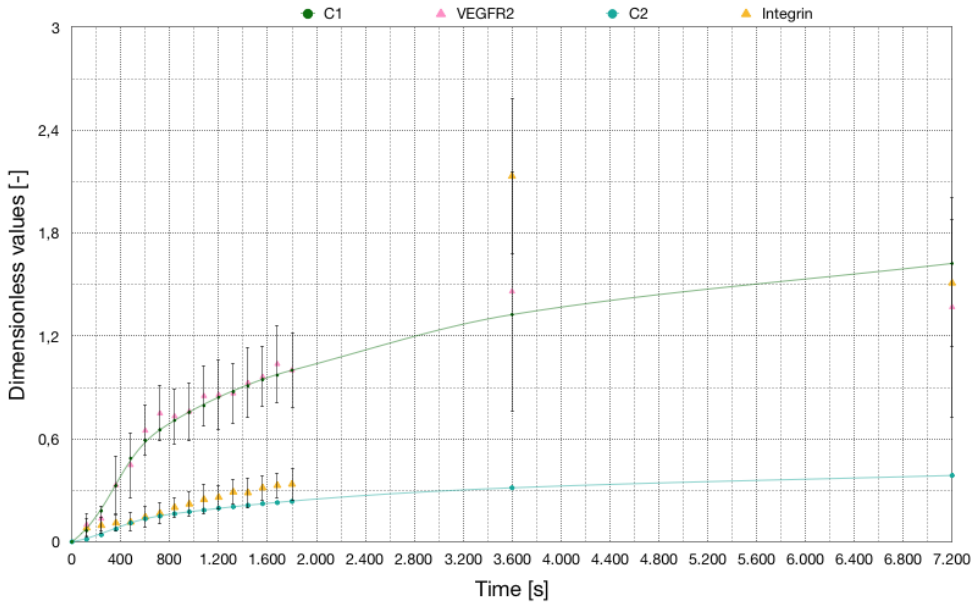

Figure 5.23: Numerical (dots with continuous line) and experimental (triangles with error bars) outcomes correspondent to a high amount of gremlin. Evolutions in time of the normalized total amounts of complexes are depicted for $d = 1$ and $e = 4$.

Through careful observation of Tab. 5.10 and Fig. 5.21, 5.22, and 5.23, we infer that a stoichiom-

etry one-to-one between d and e is the most desirable. Moreover, comparing the results embedded in Tab. 5.7 and 5.10 we can appreciate a decrease in the percentage of VEGFR2 colocalized with integrin in the basal part of the cell, from about 32% to 28%. Hence, would seem that increasing the availability of ligands in the substrate implies a reduction of the percentage of colocalization of VEGFR2. This coincides with what observed on the ratio between non-dimensional, experimental, and numerical quantities, at the temporal instants $t = 3600\ s$ $\frac{2.1318}{0.4024} \sim 5.2981$ and $t = 7200\ s$ $\frac{2.0637}{0.4564} \sim 4.5222$ (see Tab. 5.12).

Table 5.11: Co-designing between VEGFR2 and integrin fluorescence intensity (in-vitro experiments) and the number of complexes generating on the cell membrane (in-silico simulation), correspondent to a high amount of gremlin, is provided. Specifically, the total quantities are tabulated.

Time	FRAP VEGFR2	Error bars VEGFR2	FRAP integrin	Error bars integrin	C_2	C_1
0	1.8125	1.7470	2.0700	1.3727	0.0000	0.0000
120	2.6775	1.7774	2.1825	1.4993	300.7140	826.7230
240	3.6175	2.0371	2.5650	1.3584	755.0610	2318.6010
360	8.8875	4.5427	2.9550	1.4014	1317.1500	4244.0100
480	12.0225	5.1638	3.0775	1.5473	1906.3700	6328.9200
600	17.4375	4.0251	3.8900	1.7371	2331.3600	7679.3100
720	20.1325	4.3776	4.4750	1.6674	2601.5000	8485.9200
840	19.6650	4.4217	5.3775	1.5673	2831.1800	9177.9800
960	20.4075	4.5417	5.9175	1.9579	3036.2200	9794.3000
1080	22.8600	4.7168	6.6400	2.3900	3222.3400	10357.8700
1200	23.0375	5.5135	6.9850	1.9568	3393.0800	10875.8000
1320	23.2725	4.8333	7.8000	2.0404	3551.1500	11357.6800
1440	24.9150	5.5791	7.6800	2.4520	3698.4200	11810.5500
1560	25.8650	4.7980	8.4550	1.9578	3835.9700	12238.4600
1680	27.8800	6.0900	8.8375	2.0512	3964.6600	12642.7900
1800	26.9075	5.9243	9.0225	2.5968	4085.3800	13026.5300
3600	39.2718	18.8742	57.3603	12.2651	5241.3600	17171.0600
7200	36.8140	17.3697	55.5292	10.0477	5944.7200	20940.2200

Table 5.12: Co-designing between VEGFR2 and integrin fluorescence intensity (in-vitro experiments) and the number of complexes generating on the cell membrane (in-silico simulation), correspondent to a high amount of gremlin, is provided. Specifically, the dimensionless quantities are tabulated.

Time	Adimensional C_2	Adimensional C_1	Adimensional VEGFR2	Adimensional error bars VEGFR2	Adimensional integrin	Adimensional error bars integrin
0	0.0000	0.0000	0.0674	0.0649	0.0769	0.0510
120	0.0231	0.0635	0.0995	0.0661	0.0811	0.0557
240	0.0580	0.1780	0.1344	0.0757	0.0953	0.0505
360	0.1011	0.3258	0.3303	0.1688	0.1098	0.0521
480	0.1463	0.4858	0.4468	0.1919	0.1144	0.0575
600	0.1790	0.5895	0.6481	0.1496	0.1446	0.0646
720	0.1997	0.6514	0.7482	0.1627	0.1663	0.0620
840	0.2173	0.7046	0.7308	0.1643	0.1999	0.0582
960	0.2331	0.7519	0.7584	0.1688	0.2199	0.0728
1080	0.2474	0.7951	0.8496	0.1753	0.2468	0.0888
1200	0.2605	0.8349	0.8562	0.2049	0.2596	0.0727
1320	0.2726	0.8719	0.8649	0.1796	0.2899	0.0758
1440	0.2839	0.9067	0.9260	0.2073	0.2854	0.0911
1560	0.2945	0.9395	0.9613	0.1783	0.3142	0.0728
1680	0.3044	0.9705	1.0361	0.2263	0.3284	0.0762
1800	0.3136	1.0000	1.0000	0.2202	0.3353	0.0965
3600	0.4024	1.3182	1.4595	0.7014	2.1318	0.4558
7200	0.4564	1.6075	1.3682	0.6455	2.0637	0.3734

The results so far commented leave room for interpretation of the correct concentration of gremlin which must be available in the substrate, but nevertheless, they provide an estimate of the material parameters connected to the chemical reaction 5.11b. Moreover, having identified the more probably stoichiometry with the current models, it will possible to understand how the introduction of well-calibrated receptor sources, in future works, will affect the value of s_{L_V} and the other parameters.

Finally, similarly to what is seen in section 5.2.3.2, we observe an increase in the concentration of complexes with a simultaneous space reduction of the C_1 high-intensity band. Again, the reason is to be attributed to the high-availability of ligands, which trap the free receptors coming from the apical side of the cell in the external side of the cell-substrate contact zone (see Fig. 5.24 and 5.25).

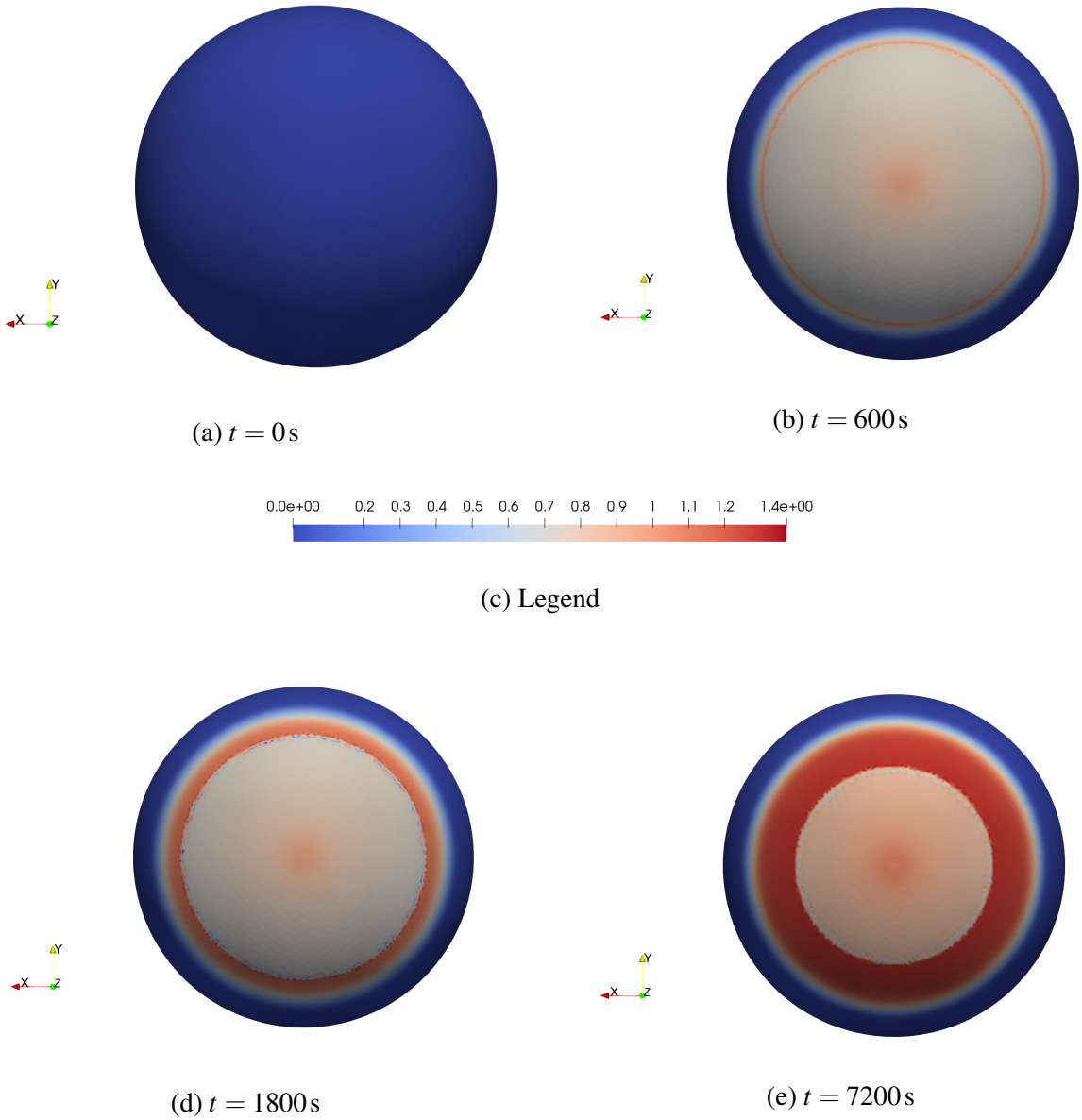

(a) $t = 0\,\mathrm{s}$

(b) $t = 600\,\mathrm{s}$

(c) Legend

(d) $t = 1800\,\mathrm{s}$

(e) $t = 7200\,\mathrm{s}$

Figure 5.24: Basal distribution of complexes (C_1) at the instant $t = 0,\ 600,\ 1800,\ 7200\,\mathrm{s}$ correspondent to a high amount of gremlin.

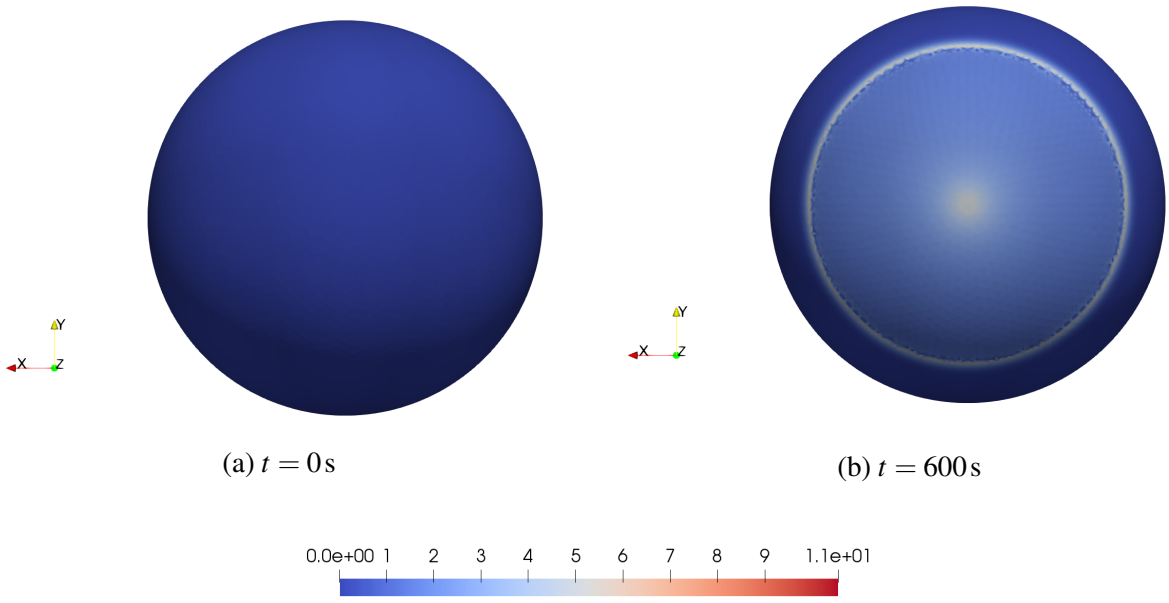

(a) $t = 0\,\mathrm{s}$

(b) $t = 600\,\mathrm{s}$

(c) Legend

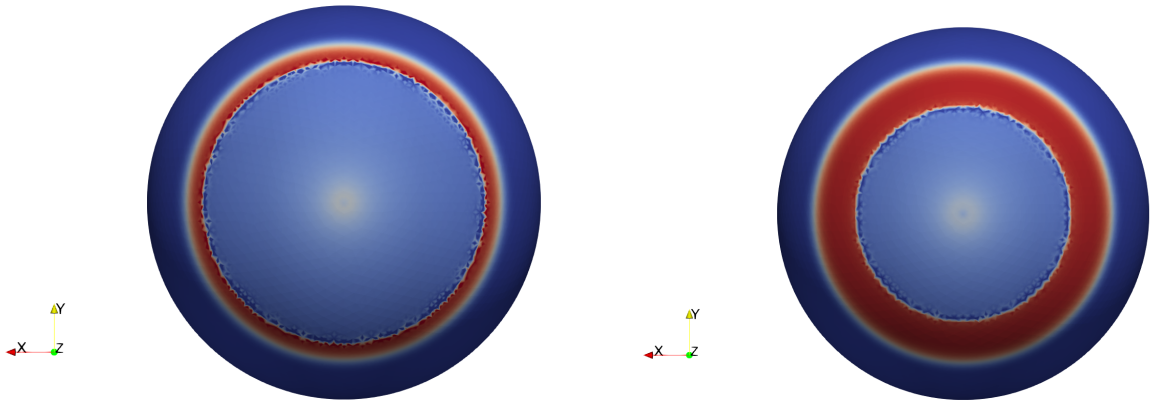

(d) $t = 1800\,\mathrm{s}$

(e) $t = 7200\,\mathrm{s}$

Figure 5.25: Basal distribution of complexes (C_2) at the instant $t = 0,\ 600,\ 1800,\ 7200\,\mathrm{s}$ correspondent to a high amount of gremlin.

5.2.6 Model based on three chemical reactions

In line with what has been done so far, we try to extend our work in order to study a fully coupled model involving all the previous chemical reactions. No parameters need to be calibrated in this formulation, inasmuch as no in-vitro experiments have been set involving all these species. Hence, the main goals of the current model are to predict the respective proportionality of concentrations of the complexes in the case of co-presence of the following chemical interactions (5.13). In order to do that, further experimental consideration is here introduced, namely that VEGFR2 and integrin can colocalize only outside the adhesion sites (Focal Adhesion).

$$V + L_V \underset{k_b}{\overset{k_f}{\rightleftarrows}} \mathrm{C}_1 \,, \qquad (5.13a)$$

$$I + \mathrm{C}_1 \underset{k_b}{\overset{k_f}{\rightleftarrows}} \mathrm{C}_2 \,, \qquad (5.13b)$$

$$I + L_I \underset{k_b}{\overset{k_f}{\rightleftarrows}} \mathrm{C}_3 \,. \qquad (5.13c)$$

$$\frac{\partial c_V}{\partial t} - \mathbb{D}_V \Delta_{\mathcal{P}}[c_V] + \frac{\partial c_{C_1}}{\partial t} + \frac{\partial c_{C_2}}{\partial t} = 0 \,, \qquad (5.14a)$$

$$\frac{\partial c_{L_V}}{\partial t} + \frac{\partial c_{C_1}}{\partial t} + \frac{\partial c_{C_2}}{\partial t} = s_{L_V} \,, \qquad (5.14b)$$

$$\frac{\partial c_I}{\partial t} - \mathbb{D}_I \Delta_{\mathcal{P}}[c_I] + \frac{\partial c_{C_2}}{\partial t} + \frac{\partial c_{C_3}}{\partial t} = 0 \,, \qquad (5.14c)$$

$$\frac{\partial c_{L_I}}{\partial t} + \frac{\partial c_{C_3}}{\partial t} = s_{L_I} \,, \qquad (5.14d)$$

$$[c_{C_1}] = \frac{[c_V]\,[c_{L_V}]}{\alpha^{(5.13a)}} \,, \qquad (5.14e)$$

$$[c_{C_2}] = \frac{[c_I]\,[c_{C_1}]}{\alpha^{(5.13b)}} \,, \qquad (5.14f)$$

$$[c_{C_3}] = \frac{[c_I]\,[c_{L_I}]}{\alpha^{(5.13c)}} \,. \qquad (5.14g)$$

Below, the outcomes are tabulated in Tab. 5.13, and then depicted in Fig. 5.26.

Table 5.13: Total and dimensionless quantities of complexes generating on the cell membrane (in-silico simulation), are tabulated.

Time	C_2	C_1	C_3	Adimensional C_2	Adimensional C_1	Adimensional C_3
0	0.0000	0.0000	0.0000	0.0000	0.0000	0.0000
120	23.9587	661.3557	288.8260	0.0020	0.0557	0.0243
240	29.2289	2106.3289	750.2990	0.0025	0.1773	0.0632
360	33.7717	3993.7917	1320.2800	0.0028	0.3362	0.1111
480	37.2486	6070.7586	1916.9600	0.0031	0.5110	0.1614
600	126.5970	7332.3770	2262.2500	0.0107	0.6172	0.1904
720	238.3150	8055.6850	2426.7800	0.0201	0.6781	0.2043
840	315.1300	8665.5700	2580.6200	0.0265	0.7294	0.2172
960	379.8290	9199.9390	2709.7600	0.0320	0.7744	0.2281
1080	434.0610	9679.8210	2859.8000	0.0365	0.8148	0.2407
1200	481.7200	10117.3400	2989.0400	0.0405	0.8516	0.2516
1320	526.4700	10520.2700	3102.7900	0.0443	0.8855	0.2612
1440	567.9750	10894.5750	3208.6300	0.0478	0.9170	0.2701
1560	604.5440	11244.0440	3311.0700	0.0509	0.9464	0.2787
1680	636.9160	11571.9160	3417.7800	0.0536	0.9740	0.2877
1800	665.6620	11880.5620	3518.8300	0.0560	1.0000	0.2962
3600	856.2090	14985.0090	4498.1200	0.0721	1.2613	0.3786
7200	701.7660	16237.9660	5361.2800	0.0591	1.3668	0.4513

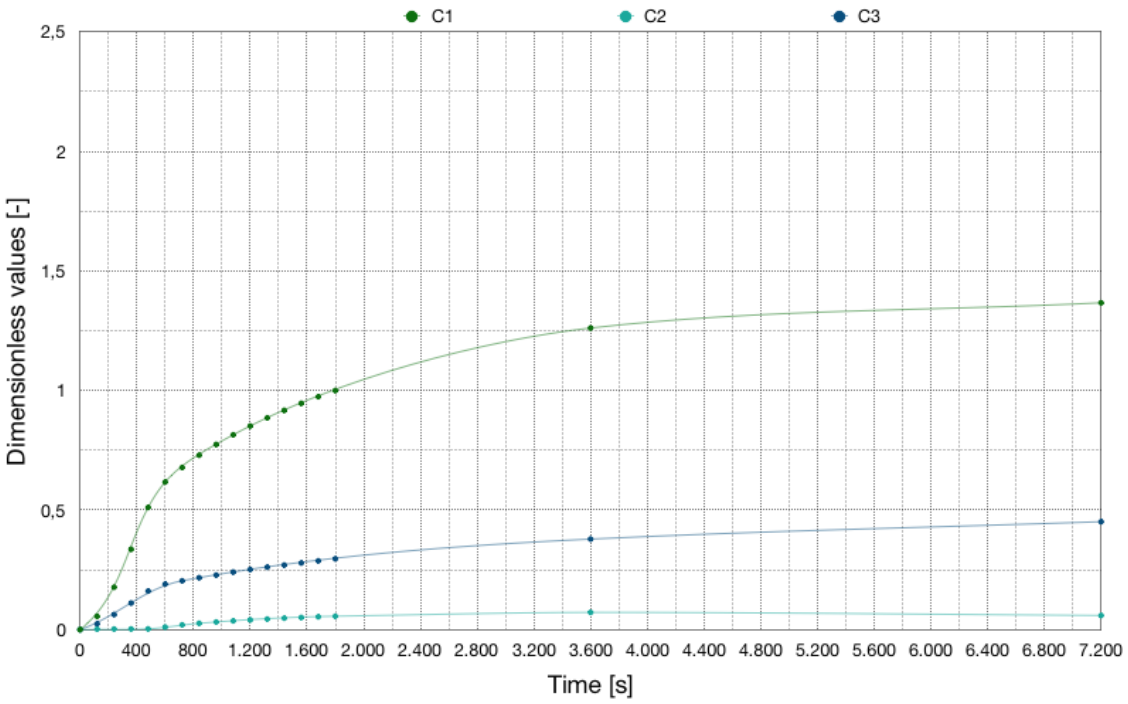

Figure 5.26: Numerical (dots with continuous line) outcomes correspondent to the evolutions in time of the normalized total amounts of complexes are depicted.

Forcedly, we will assume valid the inferences built by the previous models. The concurrent observation in the models 5.2.4 and 5.2.5, of an impressive increase of availability of integrin (after $t > 1800\ s$), leads us to assume that the same phenomenon is likely to repeat for a problem such as the one here analyzed. Therefore, every numerical comparison among the complexes values deduced for times greater than $t = 1800\ s$ will be considered meaningless.

In particular, it is interesting to observe the ratio between the normalized values of C_2 and C_3 at time $t = 1800\ s$, which turns out to be equal at $\frac{0.0560}{0.2962} \sim 0.1892$.
The outcomes would seem to confirm a predominance of the integrin-fibrinogen interaction with respect to integrin-C_1, showing a ratio among C_2/C_3 about 19%, i.e. the quantity of C_3 is five-time larger than C_2. This phenomenon is to be caused to the double-contemporary contribution of a "presumed" higher chemical affinity between integrin-fibrinogen with respect to integrin-C_1 and the larger availability of ligands L_I compared to C_1. We have to use the word "presumed" because it is very likely that the chemical affinity between integrin and its specific ligand is greater than that between integrin-C_1, but unfortunately, we can not prove it neither experimentally nor through the current model formulation in a definitive way. Indeed, despite it is possible to calibrate the parameter $\alpha_{(5.13b)}$ we may not state with certainty if $\alpha_{(5.13b)} > \alpha_{(5.13c)}$ because of the value of equilibrium constant $K_{eq}^{(5.13c)}$ or due to the value assume by ratio $\frac{c_I^{\max} c_{C_1}^{\max}}{c_{C_2}^{\max}}$. In fact, we have not elements for deducing neither the values of $c_I^{\max}$, $c_{C_1}^{\max}$, $c_{C_2}^{\max}$ nor $K_{eq}^{(5.13c)}$. Furthermore, the hypothesis of a dilute solution as well (as assume in section 3.3.1.2) could be distorting the veracity of the model response. Nevertheless, the good results obtained in section 5.2.5 make us lean towards the validity of this hypothesis.

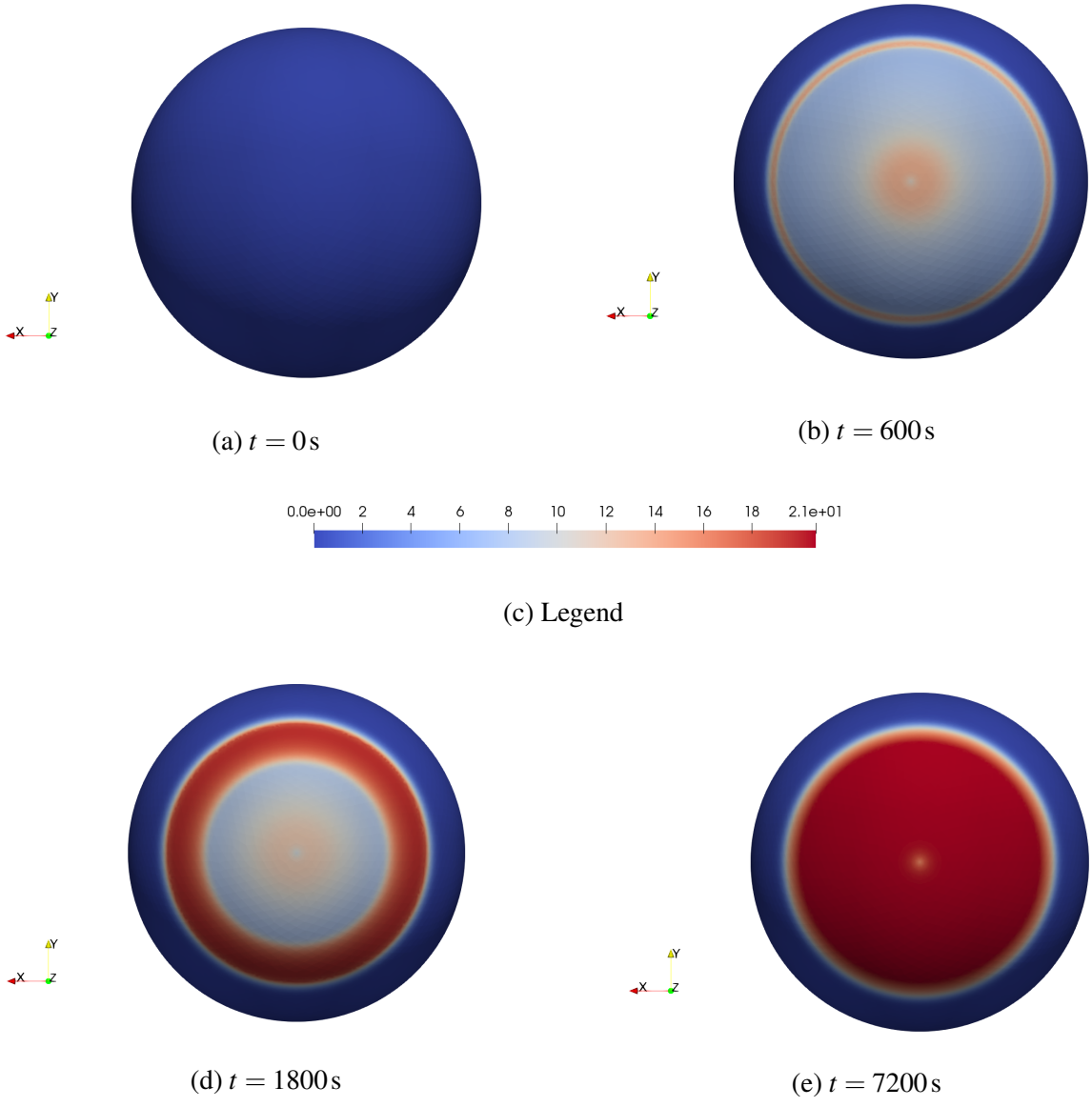

(a) $t = 0\,\mathrm{s}$

(b) $t = 600\,\mathrm{s}$

(c) Legend

(d) $t = 1800\,\mathrm{s}$

(e) $t = 7200\,\mathrm{s}$

Figure 5.27: Basal distribution of complexes (C_1) at the instant $t = 0,\ 600,\ 1800,\ 7200\,\mathrm{s}$.

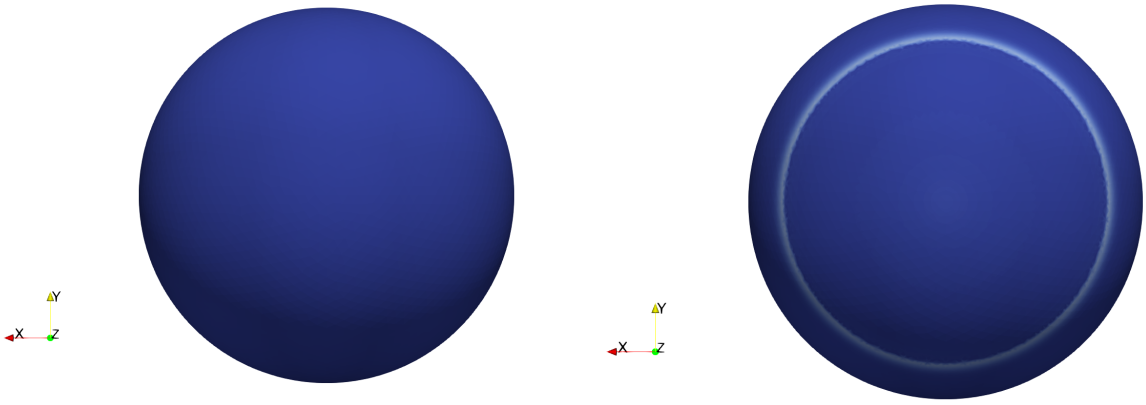

(a) $t = 0\,\mathrm{s}$ (b) $t = 600\,\mathrm{s}$

(c) Legend

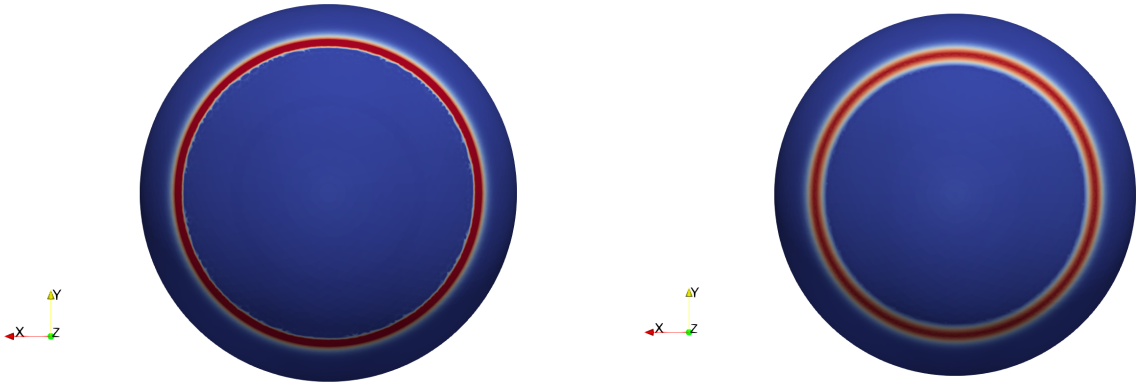

(d) $t = 1800\,\mathrm{s}$ (e) $t = 7200\,\mathrm{s}$

Figure 5.28: Basal distribution of complexes (C_2) at the instant $t = 0,\ 600,\ 1800,\ 7200\,\mathrm{s}$.

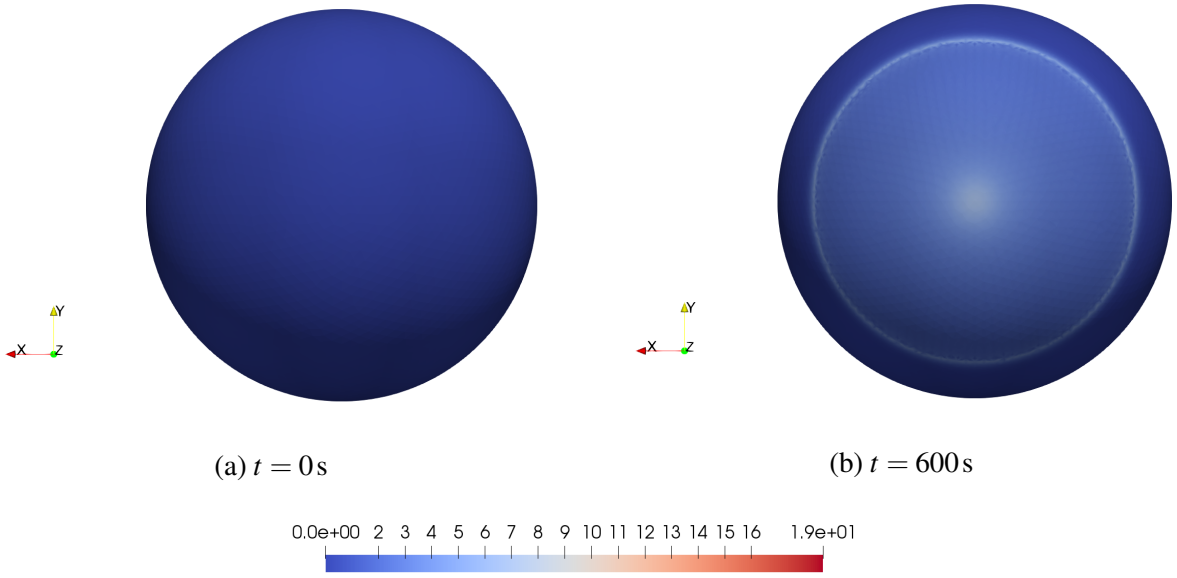

(a) $t = 0\,\mathrm{s}$

(b) $t = 600\,\mathrm{s}$

(c) Legend

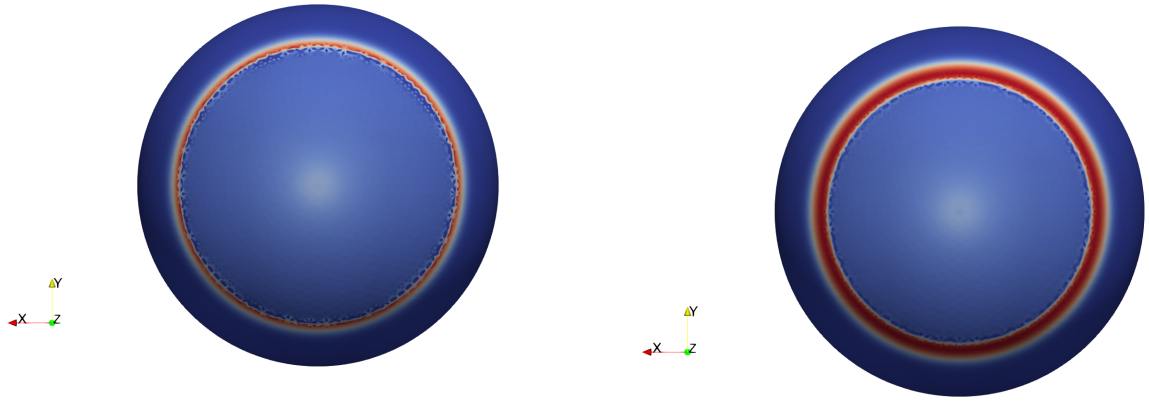

(d) $t = 1800\,\mathrm{s}$

(e) $t = 7200\,\mathrm{s}$

Figure 5.29: Basal distribution of complexes (C_3) at the instant $t = 0,\ 600,\ 1800,\ 7200\,\mathrm{s}$.

5.2.6.1 Model based on three chemical reactions with a high amount of ligands

Following, we show the relevant data associated with an availability of ligands equal to 42.5389 $molecules/\mu m$
both for gremlin and fibrinogen.

Table 5.14: Total and dimensionless quantities of complexes generating on the cell membrane (in-silico simulation), are tabulated in correspondence of high amounts of gremlin and fibrinogen.

Time	C_2	C_1	C_3	Adimensional C_2	Adimensional C_1	Adimensional C_3
0	0.0000	0.0000	0.0000	0.0000	0.0000	0.0000
120	20.1274	817.7314	319.6010	0.0016	0.0630	0.0246
240	23.6757	2302.8357	791.6680	0.0018	0.1774	0.0610
360	26.4551	4222.8351	1369.2700	0.0020	0.3253	0.1055
480	28.2369	6304.4769	1966.4900	0.0022	0.4856	0.1515
600	102.7550	7655.1350	2340.0700	0.0079	0.5896	0.1802
720	213.1870	8461.6770	2507.5600	0.0164	0.6517	0.1931
840	284.6810	9151.0510	2670.9900	0.0219	0.7048	0.2057
960	339.9840	9766.5040	2809.6900	0.0262	0.7522	0.2164
1080	389.6340	10326.9140	2983.1200	0.0300	0.7954	0.2298
1200	431.6720	10842.7720	3135.7500	0.0332	0.8351	0.2415
1320	467.3690	11322.6690	3258.4800	0.0360	0.8721	0.2510
1440	499.6840	11773.8840	3359.3800	0.0385	0.9069	0.2587
1560	529.5940	12199.3940	3454.5400	0.0408	0.9396	0.2661
1680	555.8790	12601.3790	3549.6000	0.0428	0.9706	0.2734
1800	578.4350	12983.1350	3648.6500	0.0446	1.0000	0.2810
3600	673.0810	17101.0810	4749.4400	0.0518	1.3172	0.3658
7200	461.9290	20832.9290	5632.8800	0.0356	1.6046	0.4339

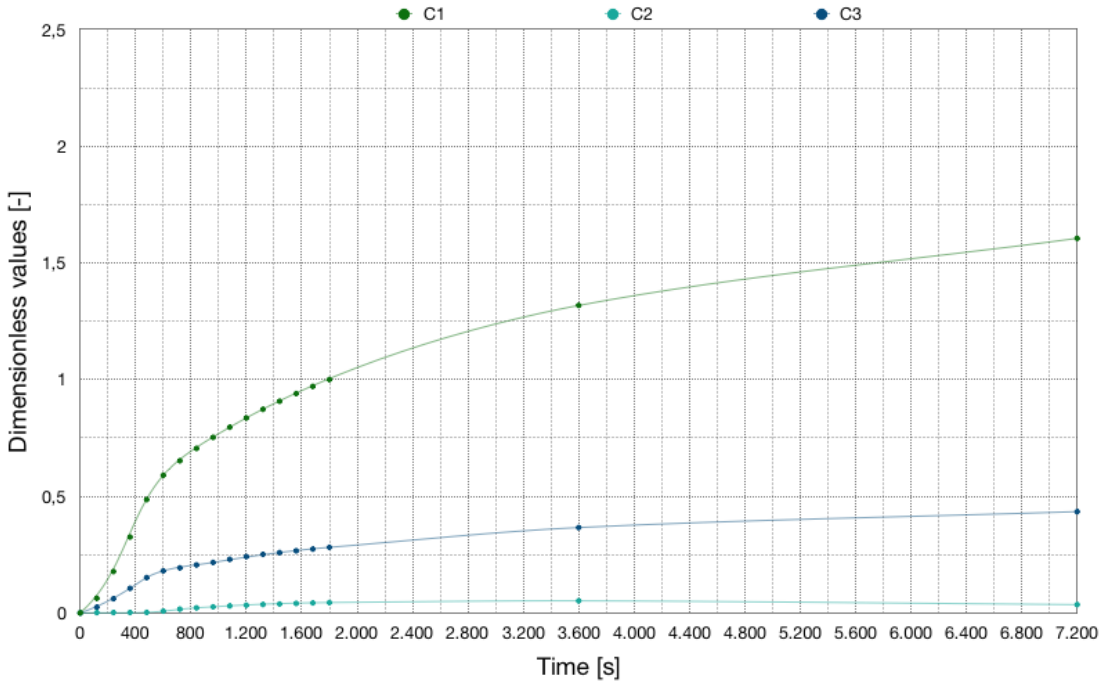

Figure 5.30: Numerical (dots with continuous line) outcomes correspondent to the evolutions in time of the normalized total amounts of complexes are depicted in correspondence of high amounts of gremlin and fibrinogen.

The trend of the curves shown in Fig. 5.30 is completely equivalent to what is seen in Fig. 5.26. However, through the numerical representation in Tab. 5.14 we can observe how it changed the ratio between the non-dimension value (at $t = 1800\ s$) assumed by C_2 and C_3, from the case with ligands concentration equal to 21.2694 $molecules/\mu m^2$ to 42.5389 $molecules/\mu m^2$: i.e., from $\frac{0.0560}{0.2962} \sim 0.1892$ to $\frac{0.0446}{0.2810} \sim 0.1585$. This result shows a tendency to decrease the concentration of integrin in the low-affinity form with respect to the high one when the concentration of ligands available is greater.

In the end, the numerical model suggests a possible extension of the experimental model that would allow deducing two biologically important pieces of information: the relationship between the concentrations of complexes concerning integrin, and once again the values of the concentrations of the aforementioned ligands.

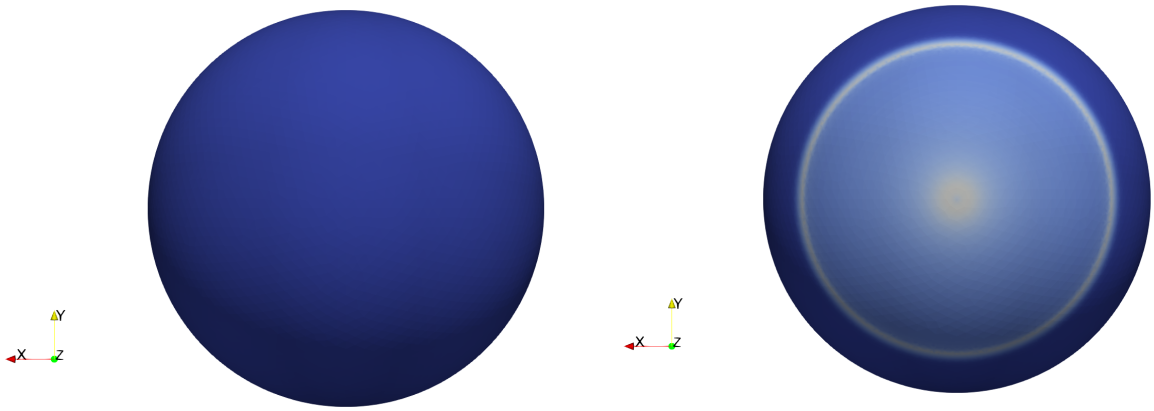

(a) $t = 0\,\mathrm{s}$

(b) $t = 600\,\mathrm{s}$

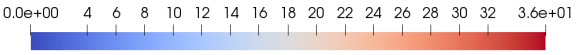

(c) Legend

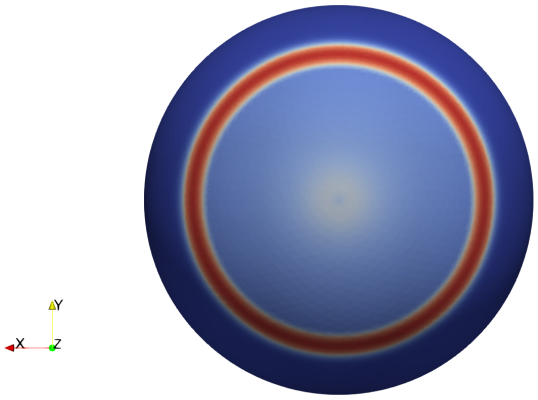

(d) $t = 1800\,\mathrm{s}$

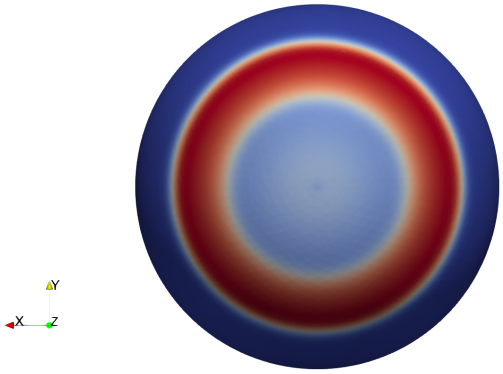

(e) $t = 7200\,\mathrm{s}$

Figure 5.31: Basal distribution of complexes (C_1) at the instant $t = 0,\ 600,\ 1800,\ 7200\,\mathrm{s}$ correspondent to a high amount of gremlin and fibrinogen.

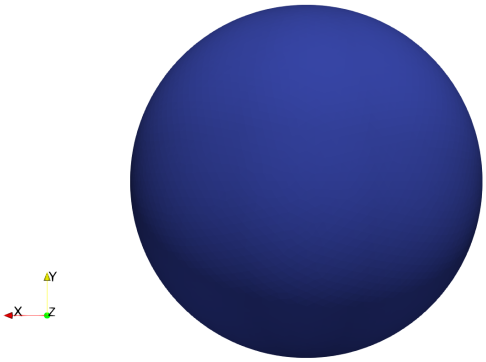

(a) $t = 0\,\mathrm{s}$

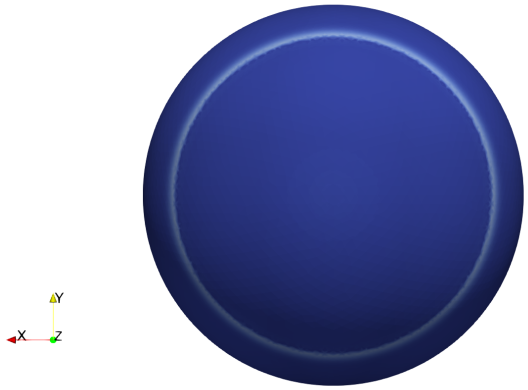

(b) $t = 600\,\mathrm{s}$

(c) Legend

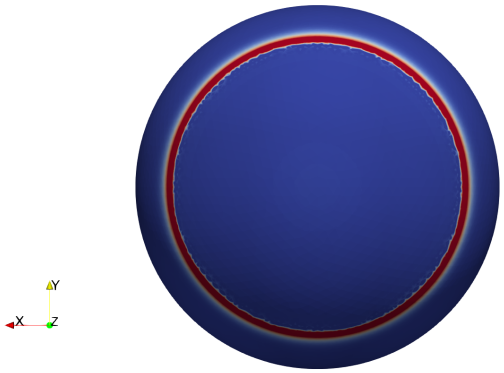

(d) $t = 1800\,\mathrm{s}$

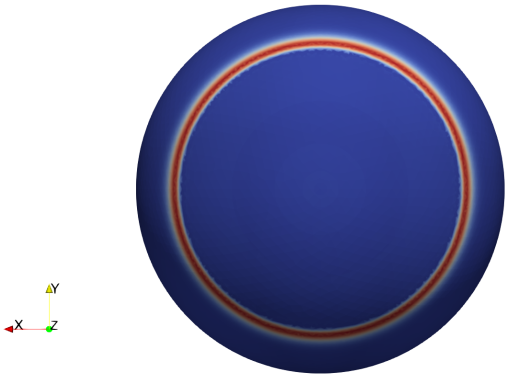

(e) $t = 7200\,\mathrm{s}$

Figure 5.32: Basal distribution of complexes (C_2) at the instant $t = 0,\ 600,\ 1800,\ 7200\,\mathrm{s}$ correspondent to a high amount of gremlin and fibrinogen.

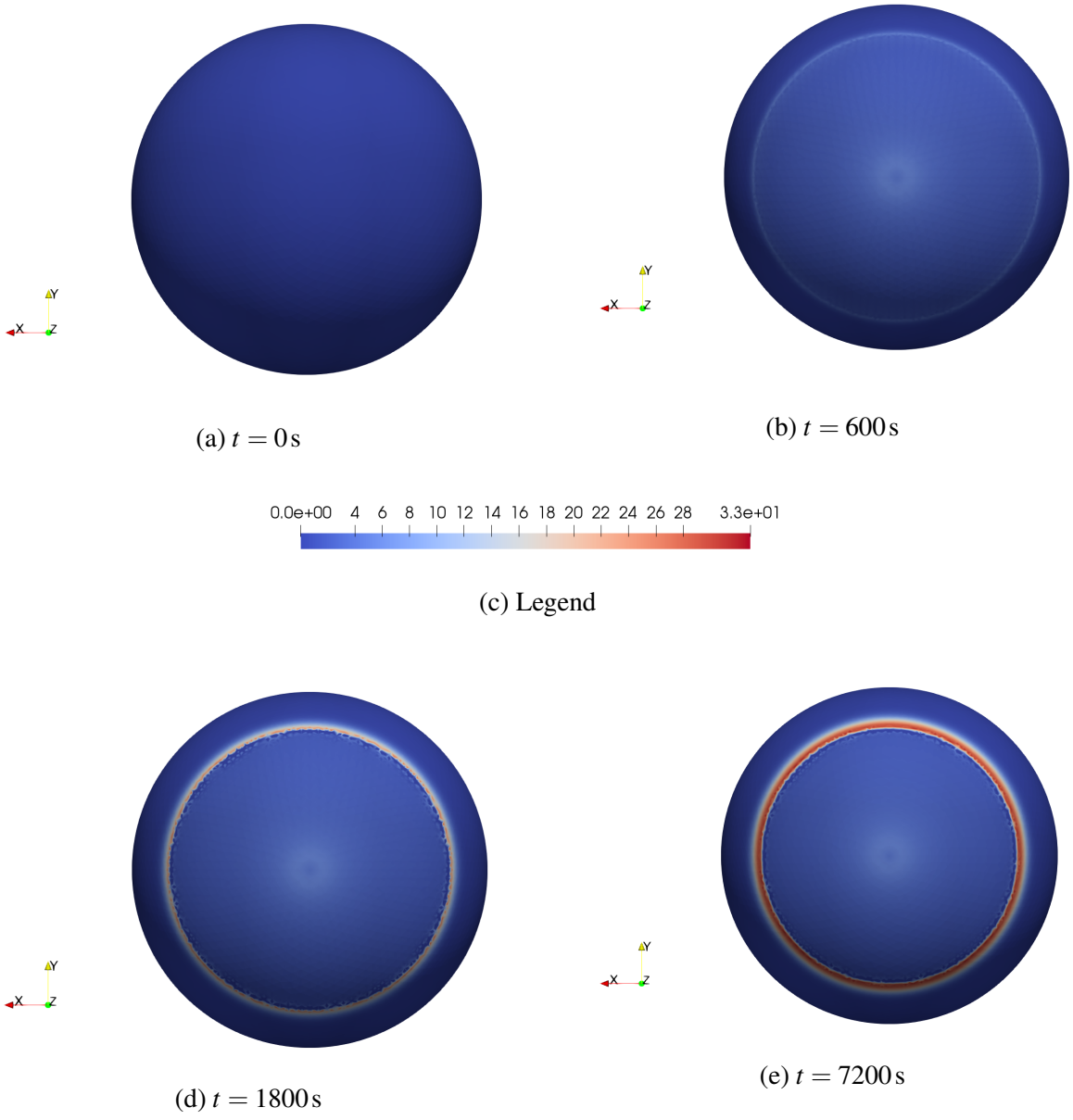

(a) $t = 0\,\mathrm{s}$ (b) $t = 600\,\mathrm{s}$

(c) Legend

(d) $t = 1800\,\mathrm{s}$ (e) $t = 7200\,\mathrm{s}$

Figure 5.33: Basal distribution of complexes (C_3) at the instant $t = 0,\ 600,\ 1800,\ 7200\,\mathrm{s}$ correspondent to a high amount of gremlin and fibrinogen.

In conclusion, it is important to note that Figures 5.11, 5.13, 5.15, 5.24, 5.25, 5.28, 5.29, 5.32, and 5.33 show slight oscillations into the back of the traveling wave. This phenomenon is correlated either to mesh effects connected to the relationship between the temporal and spatial discretization step and to the modeling non-linearities, which increases by the close connection between the governing equations induced by the coupling of the chemical reactions.

5.2.7 Conclusions

In the current work, a multidisciplinary approach among biologists and engineers was set with the aim to describe, at the molecular level, the events that arise at the early stages of angiogenesis. Concurrently to the in-vitro analyses presented in the works [51], [52], and section 4.1, we implemented in the C++ software library called deal.ii (https://www.dealii.org/ - used for solving PDEs by means of Finite Element codes -) four different patterns based on a multi-physics model thermodynamically consistent and framed in the continuum thermodynamics [138], [139] and [140] and well described in section 3.1. Here, the above-mentioned chemical reactions are described by means of the trapping model presented in [141], where the trapping mechanism is governed by the chemical reaction between proteins that are free to move on the cell membrane with molecules fixed at the substrate.
This combined work led to the quantification of numerous experimental parameters, highlighting how the availability of a mathematical model changes the way we observe reality.
A gradual approach has been here adopted in order to come to the complete calibration of the model parameters. Therefore, two models of the four above-mentioned have been set with the goal to describe a single receptor-ligand chemical reaction. In particular, these models describe the relocation of a receptor, VEGFR2, or integrin, on the cell membrane of an EC in contact with a substrate enriched with a specific ligand, respectively gremlin or fibrinogen.
A third model has been built as an extension of the VEGFR2-gremlin model; here, a further chemical reaction has been added, namely that concerning integrin and VEGFR2-gremlin-complex. Lastly, we have introduced the last model able to couple all the three chemical reactions so far have been mentioned.

5.2.7.1 Qualitative results

The evolution in time of the curve that describes the evolution of the total amount of complexes on the basal side of the EC allows distinguishing three characteristic events associated with just as many physics phenomena: pure chemical (initial contact between the cell and substrated), chemo-mechanical (until 600 s) and a final mechanism driven primarily by the diffusive properties of free molecules. All this is correlated with the hypothesis to neglect the receptors' internalization/externalization phenomena inside our model. Indeed, such a hypothesis seems like a legitim for VEGFR2-gremlin, which is ruled, in its final branch of the curve by a pure diffusive mechanism Fig. 5.5. Viceversa, for what concerns integrin-fibrinogen, we observe a discrepancy with the experimental results in the same area of the curve, either for integrin-fibrinogen interaction, that for the one integrin-VEGFR2-gremlin-Complex (Fig. 5.10 and Fig.5.16). However, thanks to the current model it is possible to approx quantify the lack of receptors in both cases, i.e. 2 times for integrin in the high-affinity state and 4-5 times for the low one, with respect to the numerical outcomes. Such a difference in the amount of integrin externalized between the model presented in section 5.2.4 and 5.2.5, which appears surprising, could be related to possible clustering phenomena of integrin at the sites of adhesion with fibrinogen, which can lead to an underestimation of the fluorescence of the receptor itself in the problem presented in section 5.2.4. This result has important consequences in the correct extension of the current model to one describing the cytoskeletal activity of an EC. Finally, matching all three chemical-reaction exclusively by means of an in-silico experiment, we can state a prediction on the trend of the curves of depletion of free receptors when two ligands coexist on the substrate. In this frame, we can predict the probable

ratio in which each complex could be found respectively to the others. Particularly, it has been observed that the quantity of complex C_3, at instant $t = 1800\ s$, is about five-time C_2.

5.2.7.2 Quantitative results

In-silico outcomes allow quantifying the numeric values of several material parameters. This result is the main reason that forces us to gradually approach the above mentioned four models, from patterns embedding a single chemical reaction to that with three. In fact, by means of the model describing only ligand-receptor chemical interaction, we have calibrated the minimum value of ligands-concentrations that effectively interact with free receptors on the cell membrane: $21.2694\ molecules/\mu m^2$ both for gremlin and fibrinogen. Having calibrated the appropriate values the concentrations of ligands available, we moved on to interpreting the results of the two chemical reaction model where it has been possible to deduce a probable stoichiometry between the molecules of integrin and VEGFR2-gremlin-Complex, that reads as follows:

$$\underbrace{\text{Integrin}}_{I} + \text{C}_1 \underset{k_b}{\overset{k_f}{\rightleftarrows}} \text{C}_2 \ . \tag{5.15}$$

The achieved comprehension, in spite of the two major simplifying assumptions taken (infinitely fast kinetics hypothesis and surrogated mechanics), encourages us to devote efforts towards more sophisticated formulations (see Part III), so as to further lessen the numerical approximations introduced herein. We will see how this improvement will enhance the predictive capabilities of the current model by, for instance, properly accounting for the mechanical deformation of the cell.

Appendix A

Backward Euler formulation

Equation (3.82b)

$$\int_{\mathcal{P}^\star} \varphi_i^{\star V}(\vec{x}^\star)\varphi_k^{\star V}(\vec{x}^\star)d\mathcal{P}^\star \left(\frac{c_k^{\star V}(t^\star+\Delta t^\star)-c_k^{\star V}(t^\star)}{\Delta t^\star}\right) -$$
$$\int_{\mathcal{P}^\star} \varphi_i^{\star V}(\vec{x}^\star)\varphi_l^{\star L_V}(\vec{x}^\star)d\mathcal{P}^\star \left(\frac{c_l^{\star L_V}(t^\star+\Delta t^\star)-c_l^{\star L_V}(t^\star)}{\Delta t^\star}\right) +$$
$$\int_{\mathcal{P}^\star} \nabla_{\mathcal{P}}^\star\left[\,\varphi_k^{\star V}(\vec{x}^\star)\,\right]\cdot\nabla_{\mathcal{P}}^\star\left[\,\varphi_i^{\star V}(\vec{x}^\star)\,\right]d\mathcal{P}^\star\frac{c_k^{\star V}(t^\star+\Delta t^\star)}{\mathrm{P}_e^V}+ \tag{A.1}$$
$$\int_{\mathcal{P}^\star} \varphi_i^{\star V}(\vec{x}^\star)\varphi_l^{\star L_V}(\vec{x}^\star)s_{L_V}^\star d\mathcal{P}^\star = 0\,,$$
$$c_V^\star(\vec{x}^\star,0)=\frac{?}{c_{bulk}}\,.$$

Equation (3.82d)

$$\int_{\mathcal{P}^\star} \varphi_i^{\star L_I}(\vec{x}^\star)\varphi_m^{\star L_I}(\vec{x}^\star)d\mathcal{P}^\star \left(\frac{c_m^{\star L_I}(t^\star+\Delta t^\star)-c_m^{\star L_I}(t^\star)}{\Delta t^\star}\right) +$$
$$\int_{\mathcal{P}^\star} \varphi_i^{\star L_I}(\vec{x}^\star)\varphi_m^{\star L_I}(\vec{x}^\star)\varphi_p^{\star I}(\vec{x}^\star)d\mathcal{P}^\star \left(\frac{c_m^{\star L_I}(t^\star+\Delta t^\star)-c_m^{\star L_I}(t^\star)}{\Delta t^\star}\right)\frac{c_p^{\star I}(t^\star+\Delta t^\star)}{\alpha_3^\star}+$$
$$\int_{\mathcal{P}^\star} \varphi_i^{\star L_I}(\vec{x}^\star)\varphi_p^{\star I}(\vec{x}^\star)\varphi_m^{\star L_I}(\vec{x}^\star)d\mathcal{P}^\star \left(\frac{c_p^{\star I}(t^\star+\Delta t^\star)-c_p^{\star I}(t^\star)}{\Delta t^\star}\right)\frac{c_m^{\star L_I}(t^\star+\Delta t^\star)}{\alpha_3^\star}- \tag{A.2}$$
$$\int_{\mathcal{P}^\star} \varphi_i^{\star L_I}(\vec{x}^\star)s_{L_I}^\star d\mathcal{P}^\star = 0\,,$$
$$c_{L_I}^\star(\vec{x}^\star,0)=0\,.$$

Equation (3.82a)

$$\int_{\mathcal{P}^\star} \varphi_i^{\star L_V}(\vec{x}^\star)\varphi_l^{\star L_V}(\vec{x}^\star)d\mathcal{P}^\star\left(\frac{c_l^{\star L_V}(t^\star+\Delta t^\star)-c_l^{\star L_V}(t^\star)}{\Delta t^\star}\right)+$$

$$\int_{\mathcal{P}^\star} \varphi_i^{\star L_V}(\vec{x}^\star)\varphi_l^{\star L_V}(\vec{x}^\star)\varphi_k^{\star V}(\vec{x}^\star)d\mathcal{P}^\star\left(\frac{c_l^{\star L_V}(t^\star+\Delta t^\star)-c_l^{\star L_V}(t^\star)}{\Delta t^\star}\right)\frac{c_k^{\star V}(t^\star+\Delta t^\star)}{\alpha_1^\star}+$$

$$\int_{\mathcal{P}^\star} \varphi_i^{\star L_V}(\vec{x}^\star)\varphi_k^{\star V}(\vec{x}^\star)\varphi_l^{\star L_V}(\vec{x}^\star)d\mathcal{P}^\star\left(\frac{c_k^{\star V}(t^\star+\Delta t^\star)-c_k^{\star V}(t^\star)}{\Delta t^\star}\right)\frac{c_l^{\star L_V}(t^\star+\Delta t^\star)}{\alpha_1^\star}+$$

$$\int_{\mathcal{P}^\star} \varphi_i^{\star L_V}(\vec{x}^\star)\varphi_l^{\star L_V}(\vec{x}^\star)\varphi_k^{\star V}(\vec{x}^\star)\varphi_p^{\star I}(\vec{x}^\star)d\mathcal{P}^\star\frac{c_l^{\star L_V}(t^\star+\Delta t^\star)}{\Delta t^\star}\frac{c_k^{\star V}(t^\star+\Delta t^\star)c_p^{\star I}(t^\star+\Delta t^\star)}{\alpha_1^\star\alpha_2^\star}-$$

$$\int_{\mathcal{P}^\star} \varphi_i^{\star L_V}(\vec{x}^\star)\varphi_l^{\star L_V}(\vec{x}^\star)\varphi_k^{\star V}(\vec{x}^\star)\varphi_p^{\star I}(\vec{x}^\star)d\mathcal{P}^\star\frac{c_l^{\star L_V}(t^\star)}{\Delta t^\star}\frac{c_k^{\star V}(t^\star+\Delta t^\star)c_p^{\star I}(t^\star+\Delta t^\star)}{\alpha_1^\star\alpha_2^\star}+$$

$$\int_{\mathcal{P}^\star} \varphi_i^{\star L_V}(\vec{x}^\star)\varphi_p^{\star I}(\vec{x}^\star)\varphi_k^{\star V}(\vec{x}^\star)\varphi_l^{\star L_V}(\vec{x}^\star)d\mathcal{P}^\star\frac{c_p^{\star I}(t^\star+\Delta t^\star)}{\Delta t^\star}\frac{c_k^{\star V}(t^\star+\Delta t^\star)c_l^{\star L_V}(t^\star+\Delta t^\star)}{\alpha_1^\star\alpha_2^\star}- \tag{A.3}$$

$$\int_{\mathcal{P}^\star} \varphi_i^{\star L_V}(\vec{x}^\star)\varphi_p^{\star I}(\vec{x}^\star)\varphi_k^{\star V}(\vec{x}^\star)\varphi_l^{\star L_V}(\vec{x}^\star)d\mathcal{P}^\star\frac{c_p^{\star I}(t^\star)}{\Delta t^\star}\frac{c_k^{\star V}(t^\star+\Delta t^\star)c_l^{\star L_V}(t^\star+\Delta t^\star)}{\alpha_1^\star\alpha_2^\star}+$$

$$\int_{\mathcal{P}^\star} \varphi_i^{\star L_V}(\vec{x}^\star)\varphi_k^{\star V}(\vec{x}^\star)\varphi_l^{\star L_V}(\vec{x}^\star)\varphi_p^{\star I}(\vec{x}^\star)d\mathcal{P}^\star\frac{c_k^{\star V}(t^\star+\Delta t^\star)}{\Delta t^\star}\frac{c_l^{\star L_V}(t^\star+\Delta t^\star)c_p^{\star I}(t^\star+\Delta t^\star)}{\alpha_1^\star\alpha_2^\star}-$$

$$\int_{\mathcal{P}^\star} \varphi_i^{\star L_V}(\vec{x}^\star)\varphi_k^{\star V}(\vec{x}^\star)\varphi_l^{\star L_V}(\vec{x}^\star)\varphi_p^{\star I}(\vec{x}^\star)d\mathcal{P}^\star\frac{c_k^{\star V}(t^\star)}{\Delta t^\star}\frac{c_l^{\star L_V}(t^\star+\Delta t^\star)c_p^{\star I}(t^\star+\Delta t^\star)}{\alpha_1^\star\alpha_2^\star}-$$

$$\int_{\mathcal{P}^\star} \varphi_i^{\star L_V}(\vec{x}^\star)s_{L_V}^\star d\mathcal{P}^\star = 0\,,$$

$$c_{L_V}^\star(\vec{x}^\star,0) = 0\,.$$

Equation (3.82c)

$$\int_{\mathcal{P}^\star} \varphi_i^{\star I}(\vec{x}^\star)\varphi_p^{\star I}(\vec{x}^\star)d\mathcal{P}^\star \left(\frac{c_p^{\star I}(t^\star+\Delta t^\star)-c_p^{\star I}(t^\star)}{\Delta t^\star}\right) -$$

$$\int_{\mathcal{P}^\star} \varphi_i^{\star I}(\vec{x}^\star)\varphi_m^{\star L_I}(\vec{x}^\star)d\mathcal{P}^\star \left(\frac{c_m^{\star L_I}(t^\star+\Delta t^\star)-c_m^{\star L_I}(t^\star)}{\Delta t^\star}\right) +$$

$$\int_{\mathcal{P}^\star} \varphi_i^{\star I}(\vec{x}^\star)\varphi_p^{\star I}(\vec{x}^\star)\varphi_k^{\star V}(\vec{x}^\star)\varphi_l^{\star L_V}(\vec{x}^\star)d\mathcal{P}^\star \frac{c_p^{\star I}(t^\star+\Delta t^\star)}{\Delta t^\star}\frac{c_k^{\star V}(t^\star+\Delta t^\star)c_l^{\star L_V}(t^\star+\Delta t^\star)}{\alpha_1^\star\alpha_2^\star} -$$

$$\int_{\mathcal{P}^\star} \varphi_i^{\star I}(\vec{x}^\star)\varphi_p^{\star I}(\vec{x}^\star)\varphi_k^{\star V}(\vec{x}^\star)\varphi_l^{\star L_V}(\vec{x}^\star)d\mathcal{P}^\star \frac{c_p^{\star I}(t^\star)}{\Delta t^\star}\frac{c_k^{\star V}(t^\star+\Delta t^\star)c_l^{\star L_V}(t^\star+\Delta t^\star)}{\alpha_1^\star\alpha_2^\star} +$$

$$\int_{\mathcal{P}^\star} \varphi_i^{\star I}(\vec{x}^\star)\varphi_k^{\star V}(\vec{x}^\star)\varphi_p^{\star I}(\vec{x}^\star)\varphi_l^{\star L_V}(\vec{x}^\star)d\mathcal{P}^\star \frac{c_k^{\star V}(t^\star+\Delta t^\star)}{\Delta t^\star}\frac{c_p^{\star I}(t^\star+\Delta t^\star)c_l^{\star L_V}(t^\star+\Delta t^\star)}{\alpha_1^\star\alpha_2^\star} -$$

$$\int_{\mathcal{P}^\star} \varphi_i^{\star I}(\vec{x}^\star)\varphi_k^{\star V}(\vec{x}^\star)\varphi_p^{\star I}(\vec{x}^\star)\varphi_l^{\star L_V}(\vec{x}^\star)d\mathcal{P}^\star \frac{c_k^{\star V}(t^\star)}{\Delta t^\star}\frac{c_p^{\star I}(t^\star+\Delta t^\star)c_l^{\star L_V}(t^\star+\Delta t^\star)}{\alpha_1^\star\alpha_2^\star} + \tag{A.4}$$

$$\int_{\mathcal{P}^\star} \varphi_i^{\star I}(\vec{x}^\star)\varphi_l^{\star L_V}(\vec{x}^\star)\varphi_p^{\star I}(\vec{x}^\star)\varphi_k^{\star V}(\vec{x}^\star)d\mathcal{P}^\star \frac{c_l^{\star L_V}(t^\star+\Delta t^\star)}{\Delta t^\star}\frac{c_p^{\star I}(t^\star+\Delta t^\star)c_k^{\star V}(t^\star+\Delta t^\star)}{\alpha_1^\star\alpha_2^\star} -$$

$$\int_{\mathcal{P}^\star} \varphi_i^{\star I}(\vec{x}^\star)\varphi_l^{\star L_V}(\vec{x}^\star)\varphi_p^{\star I}(\vec{x}^\star)\varphi_k^{\star V}(\vec{x}^\star)d\mathcal{P}^\star \frac{c_l^{\star L_V}(t^\star)}{\Delta t^\star}\frac{c_p^{\star I}(t^\star+\Delta t^\star)c_k^{\star V}(t^\star+\Delta t^\star)}{\alpha_1^\star\alpha_2^\star} +$$

$$\int_{\mathcal{P}^\star} \nabla_{\mathcal{P}}^\star\left[\varphi_p^{\star I}(\vec{x}^\star)\right]\cdot\nabla_{\mathcal{P}}^\star\left[\varphi_i^{\star I}(\vec{x}^\star)\right]d\mathcal{P}^\star \frac{c_p^{\star I}(t^\star+\Delta t^\star)}{\mathrm{P}_e^I} +$$

$$\int_{\mathcal{P}^\star} \varphi_i^{\star I}(\vec{x}^\star)\varphi_p^{\star I}(\vec{x}^\star)s_{L_I}^\star d\mathcal{P}^\star = 0\,,$$

$$c_I^\star(\vec{x}^\star,0) = \frac{?}{c_{bulk}}\,.$$

Appendix B

Simulations

The relocation of VEGFR-2 and integrin along the cell membrane of an endothelial cell during its adhesion and spreading onto a ligands-enriched substrate has been simulated implementing a fully coupled Newton-Raphson solver for the discretized weak form (3.94) exploiting the high performance computing library deal.ii (see *https://www.dealii.org*).

B.1 Parameters and data

The process was investigated over a time span of $t = 3900\ s$, an adequate extent for the deployment of the experimentally observed multi-field processes. The parameter t_f, which represents the time required for a complete adhesion, was calibrated as $t_f = 600\ s$ from experimental pieces of evidence. Since spreading has been mechanically surrogated in the present note, half of the sphere that geometrically recovers the shape of the membrane is taken as covered by ligands at time t_f. The finite time required for binding two reactants has been set to $\bar{t} = 1\ s$.

The size $l = 20\mu m$ of the radius of the cell-sphere has been deduced from an average of 50 measurements on different endothelial cells [138, 139]. Utilizing two different experimental techniques, Fluorescence Recovery After Photobleaching (FRAP) and Surface Plasmon Resonance (SPR), the diffusivity of the VEGFR-2 and the kinetic parameters of gremlin/VEGFR-2 chemical reaction have been estimated.

Hence, VEGFR2 diffusivity was estimated $\mathbb{D}_V = 0.198\ \dfrac{\mu m^2}{s}$, as in the work [138].

Through the SPR, we deduce the kinetics parameters and so the standard Gibbs free energy ($\Delta G_0^{(1)} = -32949.0\ \dfrac{J}{mol}$), that is correlated with the equilibrium constant by the following relation:

$$K_{eq}^{(1)} = \left[-\frac{\Delta G_0^{(1)}}{RT} \right] = 354058.31692\,, \tag{B.1}$$

where $T = 310.15\ K$ and $R = 8.314462618\ \dfrac{J}{K\ mol}$ are the absolute temperature and the gas constant, respectively. The value of $K_{eq}^{(1)}$ turns out to be prominent for the current work in order to

deduce the parameter $\alpha^{(1)} = \dfrac{\left[c_V^{\max}\right]\left[c_{L_V}^{\max}\right]}{\left[c_{C_1}^{\max}\right]} \dfrac{1}{K_{eq}^{(1)}}$. Finally, assuming $\left[c_V^{\max}\right] = \left[c_{C_1}^{\max}\right]$ and computing (from SPR analysis) the value of $c_{L_V}^{\max} = 16000 \, \dfrac{molecules}{\mu m^2}$ [138], we can find $\alpha^{(1)}$.

The amount of VEGFR-2 on the cell membrane per μm^2 at the beginning of the process (i.e. 24000 *molecules* [158, 48]), $c_V(\vec{x},0) = 4.8 \, \frac{molecules}{\mu m^2}$, come out dividing the number of high-affinity binding sites for cell surface area.

Consistent with in vitro observations, it has been taken $c_V^{\max} = c_{C_1}^{\max} = c_{C_2}^{\max}$ and $c_I^{\max} = c_{C_3}^{\max}$. Furthermore, the following parameters have been deduced from preliminary experimental results:

- $\mathbb{D}_I$, is the diffusivity of integrin: here assumed equal to $0.23 \, \frac{\mu m^2}{s}$;
- $K_{eq}^{(2)}$ and $K_{eq}^{(3)}$, are the equilibrium constants for the chemical reactions (3.2) and (3.3): here taken equal to $K_{eq}^{(1)}$ (assumption);
- $c_I(\vec{x},0)$, is the initial concentration of free integrin that has been taken to be equal to $8 \, \frac{molecules}{\mu m^2}$ (a value that is reasonably larger than the initial concentration of VEGFR-2 but without experimental confirmation);
- $c_{L_I}^{\max}$ and $c_I^{\max}$, are the saturation limits for the fibronectin (or fibrinogen) and integrin: here assumed equal to $c_{L_V}^{\max}$, the saturation limit for gremlin.

B.1.1 Numerical approximation of s_{L_V} and s_{L_I}.

To avoid discontinuities, a "gaussian" approximation on the relationships (3.11) has been implemented:

$$s_{L_V} \simeq a \exp[-((t-b)^2)/(c^2)] \, , \tag{B.2a}$$

$$s_{L_I} \simeq d \exp[-((t-e)^2)/(f^2)] \, , \tag{B.2b}$$

in which the coefficients a, b, c, d, e, f characterize the shape of s_{L_V} and s_{L_I}.
Time integration can be performed analytically

$$\int_0^t s_{L_V}(\vec{x},\tau) d\tau = S_{L_V}(\vec{x},t) - S_{L_V}(\vec{x},0) = \frac{1}{2} ac\sqrt{\pi}(Erf[b/c] - Erf[(b-t)/c]) \, , \tag{B.3a}$$

$$\int_0^t s_{L_I}(\vec{x},\tau) d\tau = S_{L_I}(\vec{x},t) - S_{L_I}(\vec{x},0) = \frac{1}{2} df\sqrt{\pi}(Erf[e/f] - Erf[(e-t)/f]) \, . \tag{B.3b}$$

Expressions (B.3) are consistent with the requirements $S_{L_V}(\vec{x},0) = 0$ and $S_{L_I}(\vec{x},0) = 0$.
The function (B.3) provides a supply of ligands, at the end of the cell-substrate contact dynamic process, equal to $16 \, \frac{molecules}{\mu m^2}$. Such a total density of ligands is almost as twice as compared to the initial concentration of integrins (here fixed at $8 \, \frac{molecules}{\mu m^2}$) and more than three times compared to VEGFR-2 (here fixed at $4.8 \, \frac{molecules}{\mu m^2}$).

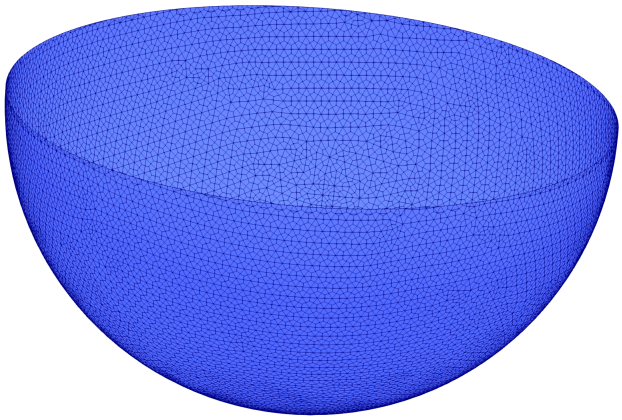

Figure B.1: Half-sphere tessellation via hexagons.

B.1.2 Discretization of geometry.

The tessellation of the cell membrane consists of 37650 quadrilaterals, uniformly distributed over the spherical surface. The discretization, depicted in Fig. B.1, remained unchanged throughout the analysis, with no re-meshing.

B.2 Outcomes

In addition to the values of $c_V^\star$ and $c_I^\star$, which are derived from the linear system solution together with $c_A^\star, c_B^\star, c_D^\star, c_E^\star$, the values of $c_{Lv}^\star$, $c_{Ll}^\star$, $c_{C_1}^\star$, $c_{C_2}^\star$, $c_{C_3}^\star$ will be evaluated and converted back into dimensional quantities, at each Gauss point, during the post-processing, by means of the identities (3.88) and (3.89).

B.2.1 Evolution in space and in time of free receptors and complexes

The evolution in space and time of free receptors and complexes is regulated by three mechanism: *chemistry* - chemical interaction among ligands-receptors (chemical reactions (3.1), (3.3)) and receptor-complex (chemical reaction (3.2)), *mechanics* - mechanical spreading of the cell that puts ligands into contact with receptors, and *diffusion* - due to the Brownian motion of unbound receptors. Chemical reaction (3.2) connects the reactions (3.1) and (3.3). Accordingly, the evolution in space and time of free receptors is connected to the history of complexes.

B.2.2 Depletion of VEGFR-2

A major depletion of free VEGFR-2 on the entire membrane is observed in numerical simulations (Fig. B.2): the concentration of free VEGFR-2 decreases from the initial amount ($4.8 \frac{molecules}{\mu m^2}$) to a value one order of magnitude smaller on the apical side (after 3900 s). Free VEGFR-2 receptors on the basal membrane are essentially absent. Concerning the chemical interactions

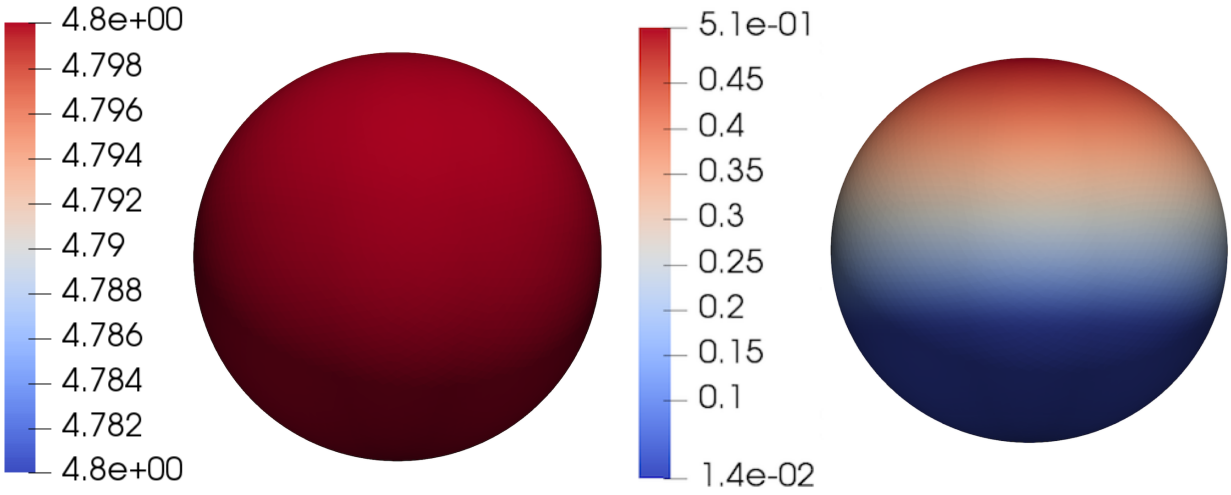

(a) t=0 s (b) t=3900 s

Figure B.2: Comparison between the concentration distribution of VEGFR2 at the initial and final time of the analyses.

involving VEGFR-2, since there is a much higher quantity of integrin and gremlin than VEGFR-2, it emerges that:

1. the equilibrium constants of the reactions (3.1) and (3.2), are extremely high (and comparable in magnitude). As such, they favor the production of complexes;
2. when a receptor c_V gets in contact with the corresponding ligand c_{L_V}, c_{C_1} is immediately generated;
3. the newly produced complex instantly interacts with the available integrin, giving c_{C_2}.

This chemical-loop concerning c_V, c_{L_V}, c_I, c_{C_1} and c_{C_2}, occurs whenever two reactants of a specific chemical reaction meet on the cell membrane.

The physics that presides the motion of the reagents changes according to the time of observation of the events. Because the time scale of the mechanics is much faster than that of diffusion, one discriminates a first *chemo-mechanically-dominated* period, which begins at the instant $t = 0\ s$ (pure chemo-dominant) and terminates at the end of the mechanical spreading of the cell ($t_f = 600\ s$). During this time, the basal part of the cell completely adheres to the substrate, and the VEGFR-2 receptors get trapped [141] by the ligands.

A second phase, *chemo-diffusive-dominated*, exists from $t = t_f$ until the end of the analysis, at $t = 3900\ s$. During this period, free receptors diffuse across the cell membrane, from the apical to the basal side of the cell. As soon as they meet ligands, they are immediately captured on the substrate.

In order to visualize the overall information mentioned above, a few frames of the evolution of VEGFR-2 over time are shown in Fig. B.3.

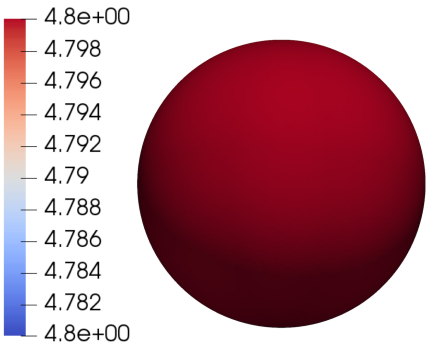

(a) t=0 s

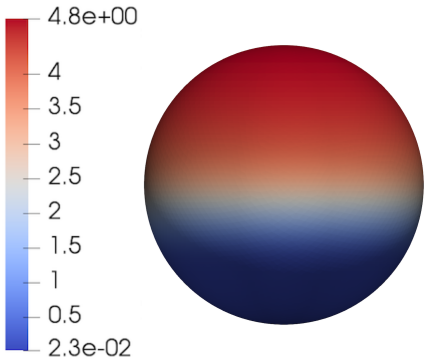

(b) t=500 s

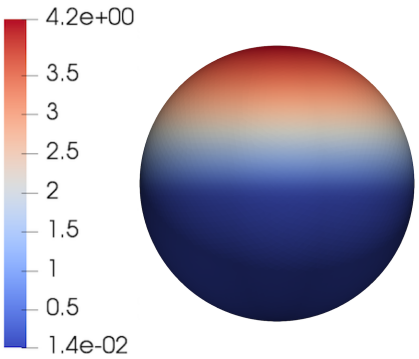

(c) t=1000 s

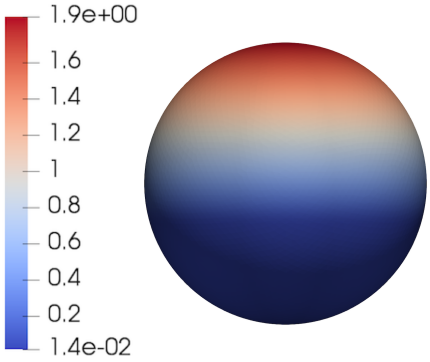

(d) t=2000 s

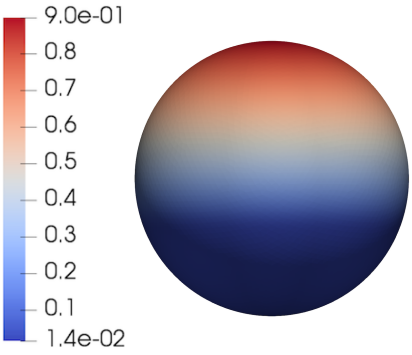

(e) t=3000 s

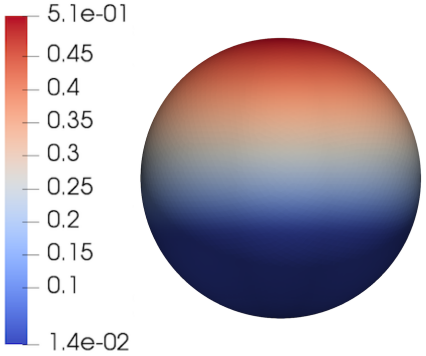

(f) t=3900 s

Figure B.3: Distribution of the concentration of the VEGFR-2 at times $t = 0, 500, 1000, 2000, 3000, 3900\ s$.

B.2.3 Evolution of C_1 and C_2.

From the frames in Fig. B.4 it is seen that two “rings" of complexes C_1 exist on the cell membrane in contact with ligands.

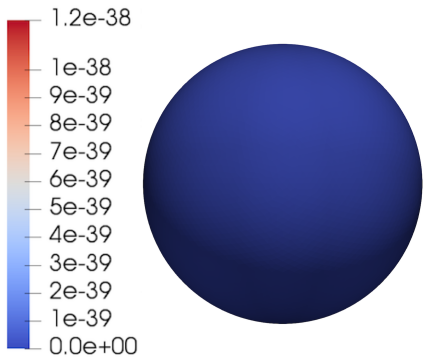

(a) t=0 s

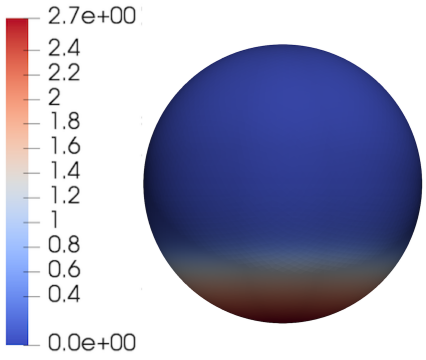

(b) t=500 s

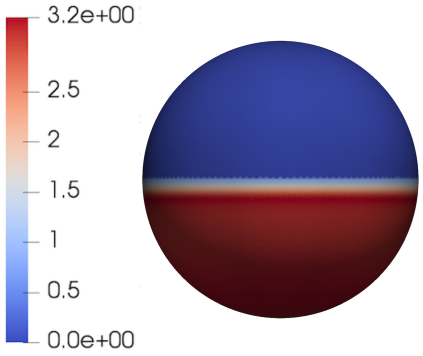

(c) t=1000 s

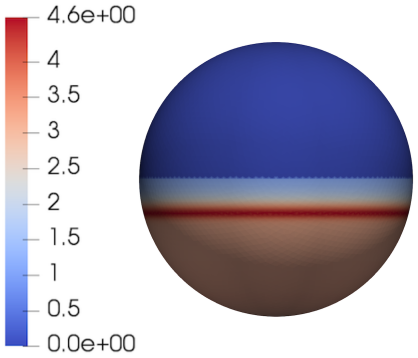

(d) t=2000 s

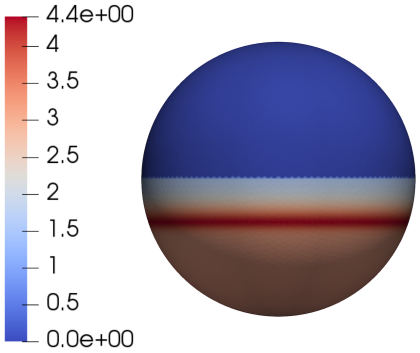

(e) t=3000 s

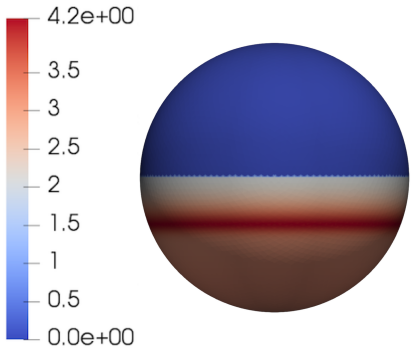

(f) t=3900 s

Figure B.4: Distribution of the concentration of the complex c_{C_1} at time $t = 0,\ 500,\ 1000,\ 2000,\ 3000,\ 3900\ s$.

Moving from the pole at the basal side of the cell towards the equatorial area of the sphere, three homogeneous bands are clearly visible. They show different intensities: medium (about 3.2 $\frac{molecules}{\mu m^2}$), high (about 4.2 $\frac{molecules}{\mu m^2}$) and low (about 2.2 $\frac{molecules}{\mu m^2}$), respectively. These different areas of complexes accumulation generate progressively. The medium zone is essentially completed at the end of the chemo-mechanical-dominated phase ($t_f = 600\ s$), whereupon the two rings grow throughout the chemo-diffusive-dominated phase.

Once again, we highlight that it is not possible to study the outcome of a single reaction, because all three are intimately linked. If one considers the distribution of the complex C_2, in Fig. B.5, an accumulation at the edge that delimitates the area of contact between cell and substrate becomes evident. It is easy to figure out that the low concentration ring for C_1 in Fig. B.4 is, at the same time, a zone for the high accumulation of complex C_2.

In fact, C_1 would accumulate at the boundary between cell and substrate. This phenomenon has been illustrated in depth in [138] and motivated by the diffusion of VEGFR-2 from the apical side toward the basal membrane coupled to the chemical reaction (3.1), which highly favors the production of C_1. As soon as the latter is formed, reaction (3.2) is triggered and it proceeds until integrin receptors are available. The latter, however, are rapidly consumed by reactions (3.2) and (3.3) and once they are fully depleted, C_1 cannot be converted to C_2 anymore and it stores itself in its own accumulation ring. Note that in view of the diffusion of VEGFR-2, the C_1 accumulation ring moves in time towards the basal pole of the cell. In conclusion, the complexes c_{C_1} and c_{C_2}, evolve driven by a large flow of receptors from the apical part of the cell towards the basal part. These free receptors, meeting the corresponding reactants in the cell-substrate contact zone, generate complexes and become trapped. In this regard, it is useful to analyze the trend of the integrin receptor and the corresponding complex c_{C_3} generated in the chemical reaction (3.3).

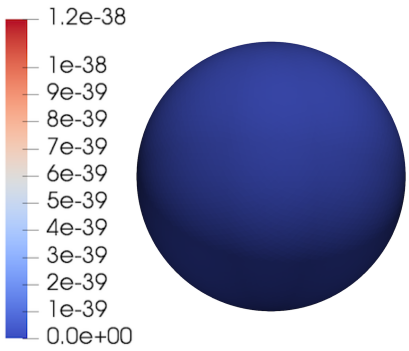

(a) t=0 s

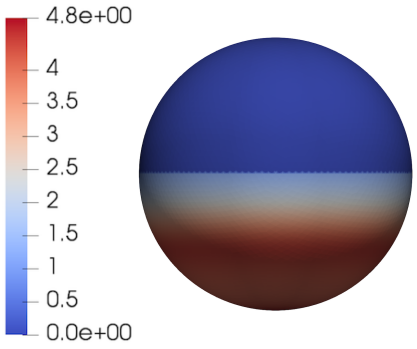

(b) t=500 s

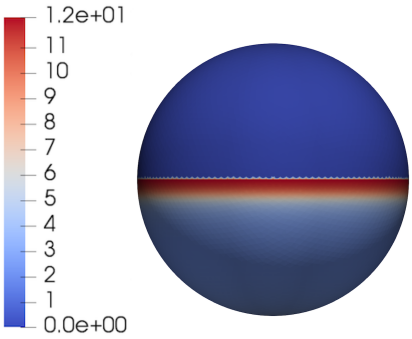

(c) t=1000 s

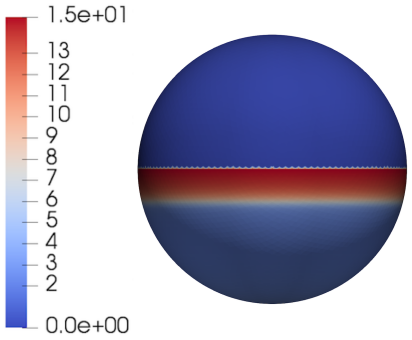

(d) t=2000 s

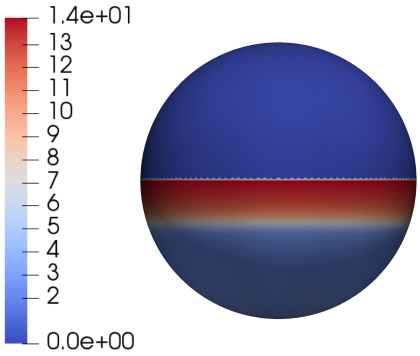

(e) t=3000 s

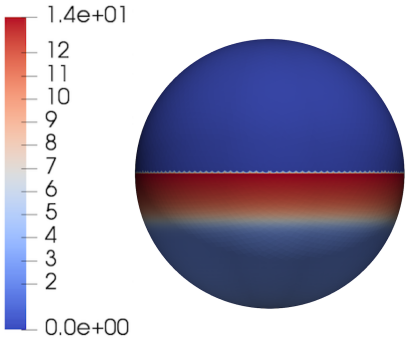

(f) t=3900 s

Figure B.5: Distribution of the concentration of the complex c_{C_2} at time $t = 0, 500, 1000, 2000, 3000, 3900\ s$.

B.2.4 Evolution of C_I.

The free integrin receptor I and VEGFR-2 undergo a similar evolution[1]. Free integrin concentration ranges from 8 $\frac{molecules}{\mu m^2}$ (value at time $t = 0$ s) to a value of the order of magnitude of $10^{-1} \div 10^{-2}$ $\frac{molecules}{\mu m^2}$ at the end of the analysis, at time $t = 3900$ s. The reasons for the global consumption of integrin, visible in Fig. B.6, are to be found in the receptors-ligands chemical interactions (3.1)-(3.3).

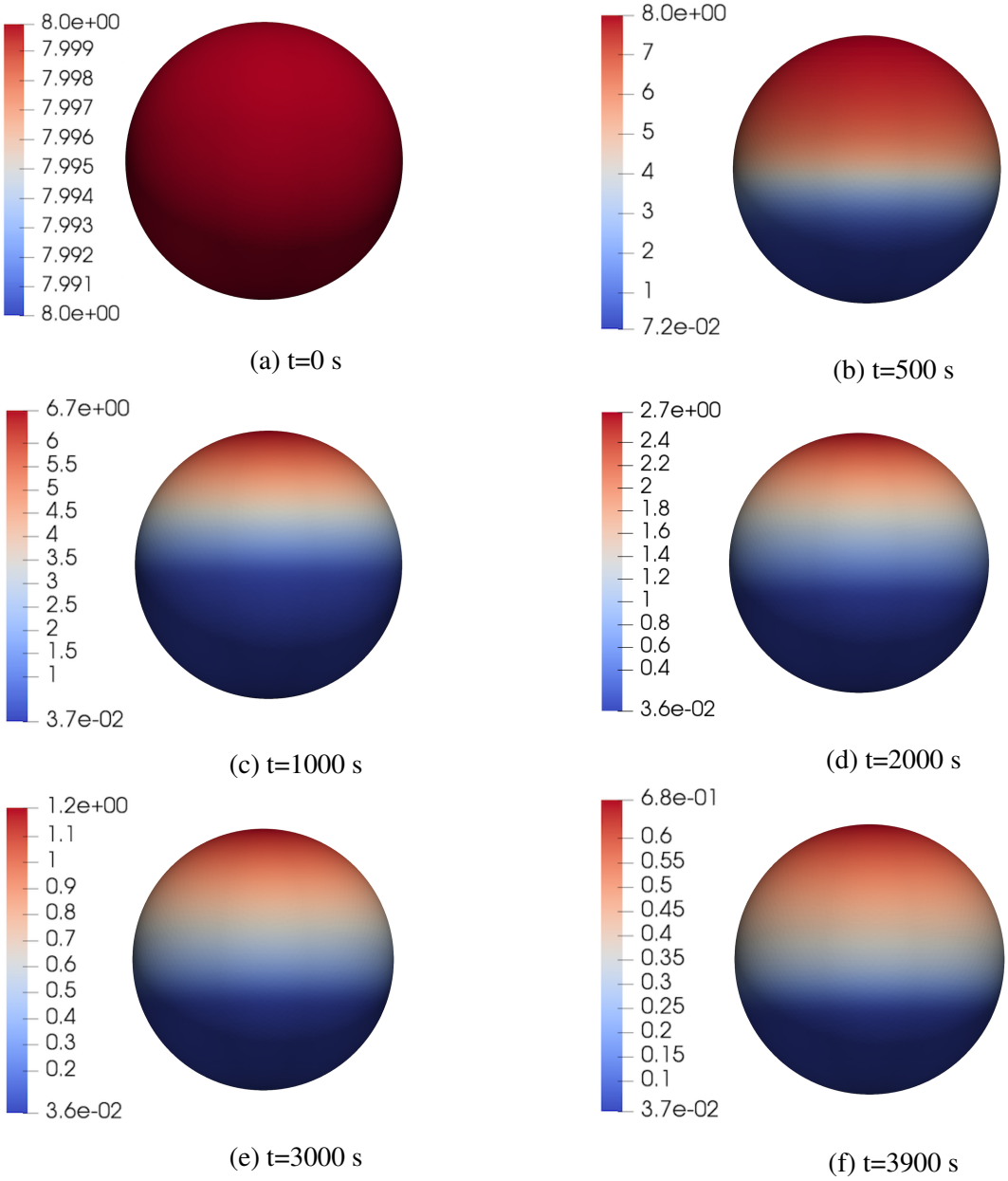

(a) t=0 s

(b) t=500 s

(c) t=1000 s

(d) t=2000 s

(e) t=3000 s

(f) t=3900 s

Figure B.6: Distribution of the concentration of integrin at time $t = 0$, 500, 1000, 2000, 3000, 3900 s.

[1]As for the VEGFR-2, a first chemo-mechanical-dominated period and a following chemo-diffusive-dominated phase holds for the integrin as well.

Figures B.5 and B.7 show an accumulation of complexes C_2 and C_3 at the edge between cell and substrate. The magnitude of the concentrations is similar because similar are the equilibrium constants of chemical reactions (3.2) and (3.3) and the saturation limits of integrins and fibronectin (or fibrinogen). Unlike the complex C_1, which shows three homogeneous areas with different magnitudes, the concentration of C_2 and C_3 locates in two (high intensity and low intensity) zones. Diffusion guides the free integrin and the VEGFR-2 from the apical part towards the basal one, leading to the accumulation of complexes in a relatively narrow zone of high availability of ligands and C_1. When free integrins cross the border that identifies the cell-substrate contact zone, they are immediately captured by L_I and C_1, which have the same affinity with I. The difference in concentrations between c_{C_3} and c_{C_2} ($c_{C_3} \simeq 14 \frac{molecules}{\mu m^2}$ is greater than $c_{C_2} \simeq 13.5 \frac{molecules}{\mu m^2}$) is due to the different physics that supply ligands and C_1. The (larger) availability of fibronectin (or fibrinogen) is provided by the chemo-mechanics, whereas the C_1 at hand is generated from 3.1 and in the high-intensity narrow zone is mostly due to the chemo-diffusive phase that causes the migration of VEGFR-2 from the apical to the basal side of the cell.

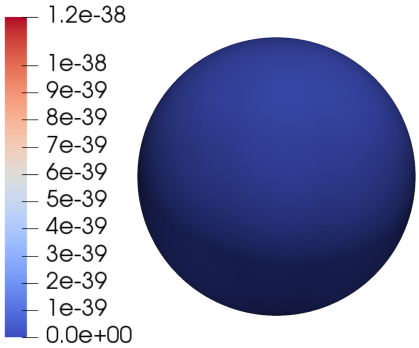

(a) t=0 s

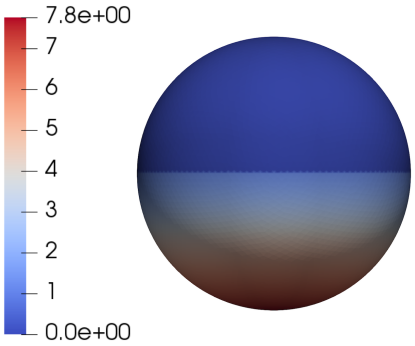

(b) t=500 s

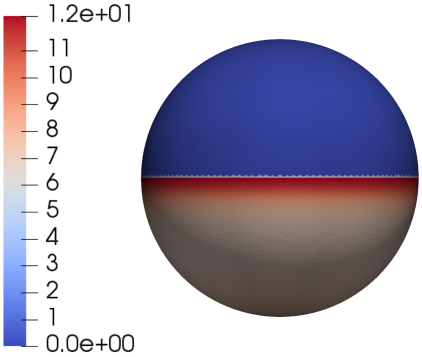

(c) t=1000 s

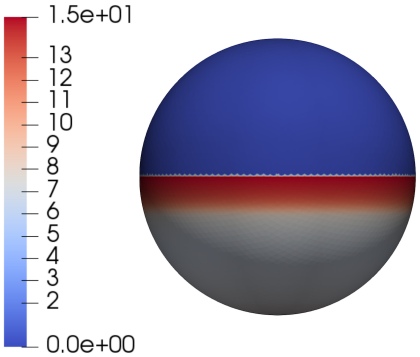

(d) t=2000 s

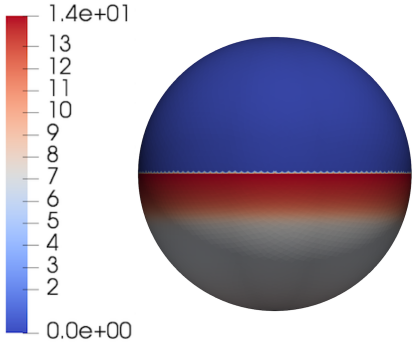

(e) t=3000 s

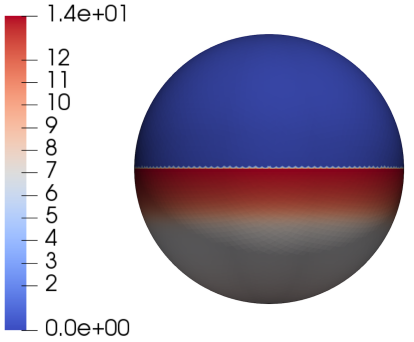

(f) t=3900 s

Figure B.7: Distribution of the concentration of the complex c_{C_3} at time $t = 0, 500, 1000, 2000, 3000, 3900\ s$.

In the low-intensity zone, c_{C_3} and c_{C_2} reach the values of about $7\frac{molecules}{\mu m^2}$ and $2.6\frac{molecules}{\mu m^2}$, respectively. The gap is due again to the larger availability of fibronectin (or fibrinogen) for the reaction (3.3) compared to the C_1 at hand for the reaction (3.2).
It should be emphasized that the flux of integrins is higher than that of VEGFR-2 because $\mathbb{D}_I$ is bigger than $\mathbb{D}_V$ and integrins are consumed concurrently by two chemical reactions. The latter justifies a large concentration gradient of I.

The main aim of this thesis is to provide insights into receptor dynamics through a co-design between in-vitro and in-silico experiments. This section has allowed testing the goodness of the multiphysical model presented in chapter 3 by means of in-silico formulations construction. Practically, we have discretized and then implemented, in a rephrased form (see 3.90 and 3.91), the set of governing equations 3.82 deduced from the thermodynamically consistent model presented in paragraph 3.2. However, no comparison has been made with the experimental results, a subject that we deal with in detail throughout chapter 5. In fact, the numerical analyzes presented in the current chapter do not correspond to any real biological experiments, although, the model parameters that have been introduced in section B.1 are realistic. Hence, satisfied with the results hereto obtained, through the next two chapters we are preparing to carry out a coordinated approach between biology and engineering, adapting the formulations constructed so far in order to describe real in-vitro experiments.

Appendix C

Partial properties and non-partial properties

In the current section, we prove, in an alternative way, that the quantities μ^u and μ^η are not partial properties.

Under the hypothesis of simple system (see [143]) and starting from the fundamental relation (see [143]), it is possible to deduce and arrange the following pivotal expressions (see [143]):

- Gibbs relation

$$dU = TdS - pdV + \mu_i dn_i \quad \text{where } i = 1, ..., r \text{ is the number of constituents;} \tag{C.1}$$

- Euler relation

$$U = TS - pV + \mu_i n_i \quad \text{where } i = 1, ..., r \text{ is the number of constituents;} \tag{C.2}$$

- Gibbs-Duhem relation

$$SdT - Vdp + n_i d\mu_i = 0 \quad \text{where } i = 1, ..., r \text{ is the number of constituents.} \tag{C.3}$$

Thanks to specific hypotheses (see [143]), it is possible to infer, that the knowledge of the single chemical potentials, written as a function of (T, p, y_i), allows calculating all the properties at the thermodynamic equilibrium state of a multi-constituent system. However, the measurements of the values of all these chemical potentials are not a small feat. Consequently, any expressions that link the properties of a system with multiple constituents with the properties of a one-constituent system are relevant in this framework, resulting in a massive simplification either on the experimental phase that in the theoretical one [143].

For such a system, it will be feasible to express every possible thermodynamic potential $Z = S,\ U,\ H, G...$[1] by means of the following specific partial derivative:

$$\begin{aligned} &Z = Z(T, p, \mathbf{n}) \longrightarrow\ z_i = \left(\frac{\partial Z}{\partial n_i}\right)_{T,p,\mathbf{n}}, \\ &\text{such that: } Z(T, p, \mathbf{n}) = \sum_i n_i z_i(T, p, \mathbf{y}), \end{aligned} \tag{C.10}$$

[1] Following, a list of some of the possible characteristic function (see [143]) is shown (in addition to the internal energy $U = U(S, V, \mathbf{n})$ and the entropy $S = S(U, V, \mathbf{n})$:

where: $y_i = \dfrac{n_i}{\sum_i n_i}$ is the mole fraction and $\mu_i(T,p,\mathbf{n}) = \mu_i(T,p,\mathbf{y})$ ([143] chapter 17) knowing that $\sum_i y_i = 1$.
Hence, z_i is the contribution per unit amount of each constituent to the corresponding extensive property of the multi-constituent "simple" system (see [143]).

C.1 T,p-partial and T,V- partial properties

Now, together with fondamental relations in energetic ($U = U(S,V,\mathbf{n})$) or entropic form ($S = S(U,V,\mathbf{n})$) we dispose of several expressions that define the chemical potential, particularly one for each characteristic function:

$$\begin{aligned}
\mu_i = \mu_i(S,V,\mathbf{n}) &= \frac{\partial U(S,V,\mathbf{n})}{\partial n_i} \\
&= \mu_i(U,V,\mathbf{n}) = \frac{\partial S(U,V,\mathbf{n})}{\partial n_i} \\
&= \mu_i(S,p,\mathbf{n}) = \frac{\partial H(S,p,\mathbf{n})}{\partial n_i} \\
&= \mu_i(T,V,\mathbf{n}) = \frac{\partial \Psi(T,V,\mathbf{n})}{\partial n_i} \\
&= \mu_i(T,p,\mathbf{n}) = \frac{\partial G(T,p,\mathbf{n})}{\partial n_i} \,.
\end{aligned} \tag{C.11}$$

Starting from $G = G(T,p,\mathbf{n})$ and its differential $dG = -SdT + Vdp + \mu \cdot d\mathbf{n}$ and using Maxwell's relations (see [143]),we can define the so-called partial properties (see [143]).

partial entropy

$$s_i = s_i(T,p,\mathbf{n}) = \frac{\partial S(T,p,\mathbf{n})}{\partial n_i} = -\frac{\partial^2 G(T,p,\mathbf{n})}{\partial T \partial n_i} = -\frac{\partial \mu_i(T,p,\mathbf{n})}{\partial T} \,, \tag{C.12}$$

- enthalpy, define as

$$H = U + pV \,. \tag{C.4}$$

Differentiating the C.4 and coupling it with the Gibbs relation we obtain:

$$dH = TdS + Vdp + \mu_i n_i, \text{ i.e. } H = H(S,p,\mathbf{n}) \,. \tag{C.5}$$

- Helmholtz free-energy, define as

$$\Psi = U - TS \,. \tag{C.6}$$

Differentiating C.6 and coupling it with Gibbs relation we obtain:

$$d\Psi = -SdT - pdV + \mu_i dn_i, \text{ i.e. } \Psi = \Psi(T,V,\mathbf{n}) \,. \tag{C.7}$$

- Gibbs free-energy, define as

$$G = U - TS + pV \,. \tag{C.8}$$

Differentiating C.8 and coupling it with Gibbs relation we obtain:

$$dG = -SdT + Vdp + \mu_i n_i, \; G = G(T,p,\mathbf{n}) \,. \tag{C.9}$$

where we used the relationship $S(T,p.\mathbf{n}) = -\left(\dfrac{\partial G(T,p.\mathbf{n})}{\partial T}\right)_{p,\mathbf{n}}$.

partial volume

$$v_i = v_i(T,p,\mathbf{n}) = \frac{\partial V(T,p,\mathbf{n})}{\partial n_i} = \frac{\partial^2 G(T,p,\mathbf{n})}{\partial p \partial n_i} = \frac{\partial \mu_i(T,p,\mathbf{n})}{\partial p}\,, \tag{C.13}$$

where we used the relationship $V(T,p.\mathbf{n}) = \left(\dfrac{\partial G(T,p.\mathbf{n})}{\partial p}\right)_{T,\mathbf{n}}$.
Employing the Gibbs relation C.1, we can further found

partial internal energy

$$\begin{aligned} u_i = u_i(T,p,\mathbf{n}) = \frac{\partial U(T,p,\mathbf{n})}{\partial n_i} = Ts_i(T,p,\mathbf{n}) - pv_i(T,p,\mathbf{n}) + \mu_i(T,p,\mathbf{n}) = \\ = -T\frac{\partial \mu_i(T,p,\mathbf{n})}{\partial T} - p\frac{\partial \mu_i(T,p,\mathbf{n})}{\partial p} + \mu_i(T,p,\mathbf{n}) = \left[\frac{\partial \frac{\mu_i}{T}}{\partial \frac{1}{T}}\right]_{p,\mathbf{n}} - p\frac{\partial \mu_i(T,p,\mathbf{n})}{\partial p}\,. \end{aligned} \tag{C.14}$$

The relation $dH = TdS + Vdp + \mathbf{n}\cdot d\mu$ leads to:

partial enthalpy

$$\begin{aligned} h_i = h_i(T,p,\mathbf{n}) = \frac{\partial H(T,p,\mathbf{n})}{\partial n_i} = \\ = Ts_i(T,p,\mathbf{n}) + \mu_i(T,p,\mathbf{n}) = -T\frac{\partial \mu_i(T,p,\mathbf{n})}{\partial T} + \mu_i(T,p,\mathbf{n}) = \left[\frac{\partial \frac{\mu_i}{T}}{\partial \frac{1}{T}}\right]_{p,\mathbf{n}}\,. \end{aligned} \tag{C.15}$$

Similarly, using the relationship $d\Psi = -SdT - pdV + \mu\cdot d\mathbf{n}$, we can also find:

partial Helmholtz free-energy

$$\begin{aligned} \psi_i = \psi_i(T,p,\mathbf{n}) = \frac{\partial \Psi(T,p,\mathbf{n})}{\partial n_i} = \\ = -pv_i(T,p,\mathbf{n}) + \mu_i(T,p,\mathbf{n}) \\ = -p\frac{\partial \mu_i(T,p,\mathbf{n})}{\partial p} + \mu_i(T,p,\mathbf{n}) = \left[\frac{\partial \frac{\mu_i}{p}}{\partial \frac{1}{p}}\right]_{T,\mathbf{n}}\,, \end{aligned} \tag{C.16}$$

and finally[2]:

$$\textbf{partial Gibbs free energy}$$
$$g_i = g_i(T,p,\mathbf{n}) = \frac{\partial G(T,p,\mathbf{n})}{\partial n_i} = \\ = \mu_i(T,p,\mathbf{n})\,. \tag{C.20}$$

For all of these, the term "partial properties" will be justified in the next paragraph.

C.1.1 Gibbs free energy and Duhem-Margules relation

Let C.21 be the differential of the expression $\mu_i(T,p,\mathbf{n})$.

$$d\mu_i = \left(\frac{\partial \mu_i}{\partial T}\right)_{p,\mathbf{n}} dT + \left(\frac{\partial \mu_i}{\partial p}\right)_{T,\mathbf{n}} dp + \sum_j \left(\frac{\partial \mu_i(T,p,\mathbf{n})}{\partial n_j}\right)_{T,p,\mathbf{n}'} dn_j \\ = \\ -s_i dT + v_i dp + \sum_j \left(\frac{\partial \mu_i(T,p,\mathbf{n})}{\partial n_j}\right)_{T,p,\mathbf{n}'} dn_j\,. \tag{C.21}$$

[2]Alternatively, we provide a further way to deduce these partial properties.
Partial energy:

$$G = U + pV - TS \Longrightarrow\ G - pV(G) + TS(G) = U(G)$$
$$u_i = u_i(T,p,\mathbf{n}) = \frac{\partial U(T,p,\mathbf{n})}{\partial n_i} = \\ = \frac{\partial G(T,p,\mathbf{n})}{\partial n_i} - p\frac{\partial V(T,p,\mathbf{n})}{\partial n_i} + T\frac{\partial S(T,p,\mathbf{n})}{\partial n_i} \\ = Ts_i(T,p,\mathbf{n}) - pv_i(T,p,\mathbf{n}) + \mu_i(T,p,\mathbf{n}) = \\ u_i(T,p,\mathbf{n}) = -T\frac{\partial \mu_i(T,p,\mathbf{n})}{\partial T} - p\frac{\partial \mu_i(T,p,\mathbf{n})}{\partial p} + \mu_i(T,p,\mathbf{n}) = \\ = \left[\frac{\partial \frac{\mu_i}{T}}{\partial \frac{1}{T}}\right]_{p,\mathbf{n}} - p\frac{\partial \mu_i(T,p,\mathbf{n})}{\partial p}\,. \tag{C.17}$$

Partial enthalpy:

$$G = U + pV - TS \Longrightarrow\ G + TS(G) = H(G)$$
$$h_i = h_i(T,p,\mathbf{n}) = \frac{\partial H(T,p,\mathbf{n})}{\partial n_i} = \frac{\partial G(T,p,\mathbf{n})}{\partial n_i} + T\frac{\partial S(T,p,\mathbf{n})}{\partial n_i} \\ = Ts_i(T,p,\mathbf{n}) + \mu_i(T,p,\mathbf{n}) \\ h_i(T,p,\mathbf{n}) = -T\frac{\partial \mu_i(T,p,\mathbf{n})}{\partial T} + \mu_i(T,p,\mathbf{n}) = \left[\frac{\partial \frac{\mu_i}{T}}{\partial \frac{1}{T}}\right]_{p,\mathbf{n}}\,. \tag{C.18}$$

Partial Helmholtz free-energy:

$$G = U + pV - TS \Longrightarrow\ G - pV(G) = \Psi(G)$$
$$\psi_i = \psi_i(T,p,\mathbf{n}) = \frac{\partial \psi(T,p,\mathbf{n})}{\partial n_i} = \frac{\partial G(T,p,\mathbf{n})}{\partial n_i} - p\frac{\partial V(T,p,\mathbf{n})}{\partial n_i} \\ = -pv_i(T,p,\mathbf{n}) + \mu_i(T,p,\mathbf{n}) \\ \psi_i(T,p,\mathbf{n}) = -p\frac{\partial \mu_i(T,p,\mathbf{n})}{\partial p} + \mu_i(T,p,\mathbf{n}) = \left[\frac{\partial \frac{\mu_i}{p}}{\partial \frac{1}{p}}\right]_{T,\mathbf{n}}\,. \tag{C.19}$$

By means of Euler relation C.2 and Gibbs-Duhem relation C.3, and with the contribution of the C.21 we can prove the term "partial properties".
Multiplying the C.21 by n_i and making explicit all the summations on the index i and j (where inside the double summation we swapped the indices), we can see that:

$$\begin{aligned} \sum_i n_i d\mu_i = -\sum_i n_i s_i dT + \sum_i n_i v_i dp + \\ + \sum_i n_i \left[\sum_j \left(\frac{\partial \mu_i(T,p,\mathbf{n})}{\partial n_j} \right)_{T,p,\mathbf{n}'} dn_j \right] . \end{aligned} \tag{C.22}$$

Also, coupling the C.3 with the C.22, it is possible to conclude:

$$\begin{aligned} dT \left(S - \sum_i n_i s_i \right) - dp \left(V - \sum_i n_i v_i \right) + \\ + \sum_i \left(\sum_j n_j \left(\frac{\partial \mu_i(T,p,\mathbf{n})}{\partial n_j} \right)_{T,p,\mathbf{n}'} \right) dn_i = 0 . \end{aligned} \tag{C.23}$$

where the terms in brackets must be identically null.

C.1.2 Alternative expression to demonstrate the term partial

Substituting the Euler relation (C.2) in Gibbs free energy definition (C.8), we get:

$$G = \sum_i n_i \mu_i . \tag{C.24}$$

Through the coupling of C.24 with C.20 is trivial deduce $G = \sum_i n_i g_i(T,p,\mathbf{n}) = \sum_i n_i \mu_i(T,p,\mathbf{n})$, whose differentiation becomes:

$$dG = \sum_i \left(dn_i \mu_i + n_i d\mu_i \right) , \tag{C.25}$$

where the expression of $d\mu_i$ has been already inferred in C.21, and so we get:

$$\begin{aligned} dG = \sum_i dn_i \mu_i + \\ + \sum_i \left[n_i \left(-s_i dT + v_i dp + \sum_j \left(\frac{\partial \mu_i(T,p,\mathbf{n})}{\partial n_j} \right)_{T,p,\mathbf{n}'} dn_j \right) \right] . \end{aligned} \tag{C.26}$$

Finally, comparing C.26 with C.9, we obtain:

$$\begin{aligned} \sum_i dn_i \mu_i + \sum_i \left[n_i \left(-s_i dT + v_i dp + \sum_j \left(\frac{\partial \mu_i(T,p,\mathbf{n})}{\partial n_j} \right)_{T,p,\mathbf{n}'} dn_j \right) \right] \\ = \\ -SdT + Vdp + \mu \cdot d\mathbf{n} \\ dT \left(S - \sum_i n_i s_i \right) - dp \left(V - \sum_i n_i v_i \right) + \\ + \sum_i \left(\sum_j n_j \left(\frac{\partial \mu_i(T,p,\mathbf{n})}{\partial n_j} \right)_{T,p,\mathbf{n}'} \right) dn_i = 0 . \end{aligned} \tag{C.27}$$

It follows that the terms in brackets must be identically null and therefore, comparing term to term:

$$\begin{gathered} S = \sum_i n_i s_i(T,p,\mathbf{n}) = -\sum_i n_i \left(\frac{\partial \mu_i}{\partial T}\right)_{p,\mathbf{n}} , \\ V = \sum_i n_i v_i(T,p,\mathbf{n}) = \sum_i n_i \left(\frac{\partial \mu_i}{\partial p}\right)_{T,\mathbf{n}} , \\ \sum_j n_j \left(\frac{\partial \mu_i(T,p,\mathbf{n})}{\partial n_j}\right)_{T,p,\mathbf{n}'} = 0 \text{ Duhem-Margules equations} , \\ \text{but also:} \\ U = \sum_i n_i u_i(T,p\mathbf{n}) , \\ \Psi = \sum_i n_i \psi_i(T,p\mathbf{n}) , \\ H = \sum_i n_i h_i(T,p\mathbf{n}) . \end{gathered} \tag{C.28}$$

Therefore, $Z = \sum_i n_i z_i(T,p,\mathbf{n})$ for $Z = S,V,U,H,\Psi,G$ and $z = s,v,u,h,\psi,g$ can be called partial properties.

C.2 Helmholtz free energy and properties T,V-"partial"

Let's try to do a similar procedure starting from $\Psi = \Psi(T,V,\mathbf{n})$ and from its differential C.7: $d\Psi = -SdT - pdV + \mu \cdot d\mathbf{n}$, where henceforth the apex "^{a}" is affixed to identify the $T-V$-"partial" properties. Knowing that:

$$\begin{gathered} S(T,V\mathbf{n}) = -\left(\frac{\partial \Psi}{\partial T}\right)_{V,\mathbf{n}} , \\ p(T,V\mathbf{n}) = -\left(\frac{\partial \Psi(T,V\mathbf{n})}{\partial V}\right)_{T,\mathbf{n}} , \\ \mu_i(T,V\mathbf{n}) = -\left(\frac{\partial \Psi(T,V\mathbf{n})}{\partial n_i}\right)_{T,V,\mathbf{n}'} , \end{gathered} \tag{C.29}$$

we can deduce the following expressions:

T-V entropy

$$\begin{gathered} s_i^a = s_i^a(T,V,\mathbf{n}) = \frac{\partial S(T,V,\mathbf{n})}{\partial n_i} = \\ = -\frac{\partial^2 \Psi(T,V,\mathbf{n})}{\partial T \partial n_i} = -\frac{\partial \mu_i(T,V,\mathbf{n})}{\partial T} \end{gathered} \tag{C.30}$$

T-V pressure

$$\begin{gathered} p_i^a = p_i^a(T,V,\mathbf{n}) = \frac{\partial p(T,V,\mathbf{n})}{\partial n_i} = \\ -\frac{\partial^2 \Psi(T,V,\mathbf{n})}{\partial V \partial n_i} = -\frac{\partial \mu_i(T,V,\mathbf{n})}{\partial V} \end{gathered} \tag{C.31}$$

Through the Gibbs relation it is possible to find:

T-V energy

$$\begin{gathered} u_i^a = u_i^a(T,V,\mathbf{n}) = \frac{\partial U(T,V,\mathbf{n})}{\partial n_i} = \\ = Ts_i^a(T,V,\mathbf{n}) + \mu_i(T,V,\mathbf{n}) = -T\frac{\partial^2 \Psi(T,V,\mathbf{n})}{\partial T \partial n_i} + \mu_i(T,V,\mathbf{n}) = \\ = -T\frac{\partial \mu_i(T,V,\mathbf{n})}{\partial T} + \mu_i(T,V,\mathbf{n}) \end{gathered} \tag{C.32}$$

and using the relation C.5 we also find:

T-V enthalpy

$$\begin{gathered} h_i^a = h_i^a(T,V,\mathbf{n}) = \frac{\partial H(T,V,\mathbf{n})}{\partial n_i} = \\ = Ts_i^a(T,V,\mathbf{n}) + Vp_i^a(T,V,\mathbf{n}) + \mu_i(T,V,\mathbf{n}) \end{gathered} \tag{C.33}$$

By analogy, exploiting the relation C.7:

T-V Helmholtz free-energy

$$\psi_i^a = \psi_i^a(T,V,\mathbf{n}) = \frac{\partial \Psi(T,V,\mathbf{n})}{\partial n_i} = \mu_i(T,V,\mathbf{n}) \tag{C.34}$$

Finally, from $dG = -SdT + Vdp + \mu \cdot d\mathbf{n}$ it is possibile deduce[3]:

T-V Gibbs free-energy

$$g_i^a = g_i^a(T,V,\mathbf{n}) = \frac{\partial G(T,V,\mathbf{n})}{\partial n_i} = V p_i^a + \mu_i(T,V,\mathbf{n}) \tag{C.38}$$

Again, similar to section C.1.1, we try to understand if the term "partial properties" is justified in such a context.
By differentiating the $\mu_i = \mu_i(T,V,\mathbf{n})$, we obtain:

$$\begin{aligned} d\mu_i &= \left(\frac{\partial \mu_i(T,V,\mathbf{n})}{\partial T}\right)_{V,\mathbf{n}} dT + \\ &+ \left(\frac{\partial \mu_i(T,V,\mathbf{n})}{\partial V}\right)_{T,\mathbf{n}} dV + \sum_j \left(\frac{\partial \mu_i(T,V,\mathbf{n})}{\partial n_j}\right)_{V,\mathbf{n}} dn_j \,, \\ d\mu_i &= -s_i^a dT - p_i^a dV + \sum_j \frac{\partial \mu_i(T,V,\mathbf{n})}{\partial n_j} dn_j \,. \end{aligned} \tag{C.39}$$

The Gibbs-Duhem relation becomes:

$$\begin{aligned} 0 &= -SdT + Vdp - \mathbf{n} \cdot d\mu \,, \\ 0 &= -[S - \sum_i n_i s_i^a]dT + [Vdp - \sum_i n_i p_i^a dV] - \sum_j [\sum_i n_i \frac{\partial \mu_i(T,V,\mathbf{n})}{\partial n_j}] dn_j \,, \end{aligned} \tag{C.40}$$

[3] Alternatively, we provide a further way to deduce these properties.
T-V energy: :

$$\begin{aligned} &\Psi = U - TS \Longrightarrow U(\Psi) = \Psi + TS(\Psi) \,, \\ u_i^a = u_i^a(T,V,\mathbf{n}) &= \frac{\partial U(T,V,\mathbf{n})}{\partial n_i} = \frac{\partial \Psi(T,V,\mathbf{n})}{\partial n_i} + T\frac{\partial S(T,V,\mathbf{n})}{\partial n_i} = \\ &= T s_i^a(T,V,\mathbf{n}) + \mu_i(T,V,\mathbf{n}) = -T\frac{\partial \mu_i(T,V,\mathbf{n})}{\partial T} + \mu_i(T,V,\mathbf{n}) \,. \end{aligned} \tag{C.35}$$

T-V enthalpy:

$$\begin{aligned} &\Psi = U - TS = H - pV - TS \Longrightarrow H(\Psi) = \Psi + TS(\Psi) + p(\Psi)V \\ &h_i^a = h_i^a(T,V,\mathbf{n}) = \frac{\partial H(T,V,\mathbf{n})}{\partial n_i} \\ &= \frac{\partial \Psi(T,V,\mathbf{n})}{\partial n_i} + T\frac{\partial S(T,V,\mathbf{n})}{\partial n_i} + V\frac{\partial p(T,V,\mathbf{n})}{\partial n_i} = \\ &= T s_i^a(T,V,\mathbf{n}) + V p_i^a(T,V,\mathbf{n}) + \mu_i(T,V,\mathbf{n}) \\ &= -T\frac{\partial \mu_i(T,V,\mathbf{n})}{\partial T} - V\frac{\partial \mu_i(T,V,\mathbf{n})}{\partial V} + \mu_i(T,V,\mathbf{n}) \,. \end{aligned} \tag{C.36}$$

T-V Gibbs free-energy:

$$\begin{aligned} &G = U - TS + pV = \Psi + pV \Longrightarrow G(\Psi) = \Psi + p(\Psi)V \\ &g_i^a = g_i^a(T,V,\mathbf{n}) = \frac{\partial G(T,V,\mathbf{n})}{\partial n_i} = \\ &= \frac{\partial \Psi(T,V,\mathbf{n})}{\partial n_i} + V\frac{\partial p(T,V,\mathbf{n})}{\partial n_i} = V p_i^a(T,V,\mathbf{n}) + \mu_i(T,V,\mathbf{n}) \\ &= -V\frac{\partial \mu_i(T,V,\mathbf{n})}{\partial V} + \mu_i(T,V,\mathbf{n}) \,. \end{aligned} \tag{C.37}$$

firstly, we need to express dp in terms of dT, dV, and dn_i, that is, we have to write the differential of the equation of state $p(T,V,\mathbf{n})$, let's write it like this:

$$dp = \alpha(T,V,\mathbf{n})dT + \beta(T,V,\mathbf{n})dV + \sum_j \gamma_j(T,V,\mathbf{n})dn_j \,, \tag{C.41}$$

therefore, the Eq. C.40 becomes:

$$\begin{aligned} 0 = &-[S - V\alpha - \sum_i n_i s_i^a]dT + [V\beta - \sum_i n_i p_i^a]dV \\ &- \sum_j [\sum_i n_i \frac{\partial \mu_i(T,V,\mathbf{n})}{\partial n_j} - V\gamma_j]dn_j \,, \end{aligned} \tag{C.42}$$

where, because the terms in square brackets must be identically null, we obtain:

$$\begin{aligned} S &= V\alpha(T,V,\mathbf{n}) + \sum_i n_i s_i^a(T,V,\mathbf{n}) \,, \\ V\beta(T,V,\mathbf{n}) &= \sum_i n_i p_i^a(T,V,\mathbf{n}) \,, \\ V\gamma_j(T,V,\mathbf{n}) &= \sum_i n_i \frac{\partial \mu_i(T,V,\mathbf{n})}{\partial n_j} \,. \end{aligned} \tag{C.43}$$

The relations C.43 are less interpretable than those expressed as a function of Gibbs free energy.

C.2.1 $\mu_i^u(T,V,n_i)$ and $\mu_i^\eta(T,V,n_i)$ in the current framework

Now, we would like to connect the current framework, with the one presented in 3.2: In order to do that, it is necessary comparing the expressions 3.48 with the C.30 and C.32.In fact, unless the terms **n** and **c** these equations are totally equivalent.

$$\begin{aligned} \mu_i^\eta(T,V,c_i) &= -\frac{\partial^2 \Psi}{\partial T \partial c_i} \,, \\ s_i^a = s_i^a(T,V,\mathbf{n}) &= \frac{\partial S(T,V,\mathbf{n})}{\partial n_i} = -\frac{\partial^2 \Psi(T,V,\mathbf{n})}{\partial T \partial n_i} \,. \end{aligned} \tag{C.44}$$

$$\begin{aligned} \mu_i^u(T,V,c_i) &= \frac{\partial \Psi}{\partial c_i} - T\frac{\partial^2 \Psi}{\partial T \partial c_i} \,, \\ u_i^a = u_i^a(T,V,\mathbf{n}) &= \frac{\partial U(T,V,\mathbf{n})}{\partial n_i} = \\ = Ts_i^a(T,V,\mathbf{n}) + \mu_i(T,V,\mathbf{n}) &= -T\frac{\partial^2 \Psi(T,V,\mathbf{n})}{\partial T \partial n_i} + \frac{\partial \Psi(T,V,\mathbf{n})}{\partial n_i} \,. \end{aligned} \tag{C.45}$$

Appendix D

Operators

In this section, we want to clarify the mathematical structure of several operators $div_{\mathcal{P}}[]$ exploited in the surrogated mechanics framework.

D.1 Calculation of the divergence and gradient operators on the surface of a sphere

D.1.1 $div_{\mathcal{P}}[\vec{h}]$

We decide to start from a generic mass balance equation, hence:

$$\int_{\mathcal{P}} \frac{\partial c}{\partial t} dS = -\int_{\partial\mathcal{P}} \Phi dl + \int_{\mathcal{P}} s dS \,, \tag{D.1}$$

where:

- $\mathcal{P}$ and $\partial\mathcal{P}$ are respective the surface immersed in a three-dimensional space and its frontier.
- c is the molarity.
- Φ is flux, identified by the scalar product $\int_{\partial\mathcal{P}} \Phi dl = \int_{\partial\mathcal{P}} \vec{h}\cdot\vec{t}_{\perp} dl$, in which:
  - $\vec{h}$ is the mass flow in terms of moles;
  - $\vec{t}_{\perp}$ is the unit vector along which the flow is projected.
- s is the rate at which species is generated by sources.

Exploiting the properties of the vector product and the mixed product, conjugated to Stokes' Theorem, we can derive:

$$\int_{\partial\mathcal{P}} \Phi dl = \int_{\partial\mathcal{P}} \vec{h}\cdot\vec{t}_{\perp} dl = \int_{\partial\mathcal{P}} \left(\vec{n}\times\vec{h}\right)\cdot\vec{t}_{\parallel} dl = \int_{\partial\mathcal{P}} \left(\vec{n}\times\vec{h}\right) d\vec{l} = \int_{\mathcal{P}} \left[\text{ rot } \left(\vec{n}\times\vec{h}\right)\right]\cdot\vec{n} dS \,, \tag{D.2}$$

wherein $\vec{n}$ is the normal unit vector to the surface $\mathcal{P}$. Following, we focus on the terms:

$$\begin{aligned} \text{rot}\ \left(\vec{n}\times\vec{h}\right) &= \nabla\times\left(\vec{n}\times\vec{h}\right) \\ \nabla\times\left(\vec{n}\times\vec{h}\right) &= \vec{n}\left(\nabla\cdot\vec{h}\right)-\vec{h}\left(\nabla\cdot\vec{n}\right)+\left(\vec{h}\cdot\nabla\right)\vec{n}-\left(\vec{n}\cdot\nabla\right)\vec{h} \end{aligned} \tag{D.3}$$

$$\int\limits_{\mathcal{P}}\left[\nabla\times\left(\vec{n}\times\vec{h}\right)\right]\cdot\vec{n}dS=\int\limits_{\mathcal{P}}\left[\vec{n}\left(\nabla\cdot\vec{h}\right)-\vec{h}\left(\nabla\cdot\vec{n}\right)+\left(\vec{h}\cdot\nabla\right)\vec{n}-\left(\vec{n}\cdot\nabla\right)\vec{h}\right]\cdot\vec{n}dS \tag{D.4}$$

But:

$$\left[\vec{h}\left(\nabla\cdot\vec{n}\right)\right]\cdot\vec{n}=\left[\left(\vec{h}\cdot\nabla\right)\vec{n}\right]\cdot\vec{n}=0 \tag{D.5}$$

indeed:

$$\begin{gathered} \left[\vec{h}\left(\nabla\cdot\vec{n}\right)\right]\cdot\vec{n}=n_{q,q}h_pn_p=\left(\vec{h}\cdot\vec{n}\right)\left(\nabla\cdot\vec{n}\right) \\ \text{this expression is equal to zero if:} \\ \left(\vec{h}\cdot\vec{n}\right)=0\ \text{ or }\ \left(\nabla\cdot\vec{n}\right)=0 \end{gathered} \tag{D.6}$$

Actually, in the current framework, the vector flow remains always orthogonal to the normal unit vector at the surface, hence: $\left(\vec{h}\cdot\vec{n}\right)=0$.
Concerning the expression $n_{p,q}h_qn_p$, instead:

$$n_{p,q}h_qn_p=\left[\left(\vec{h}\cdot\nabla\right)\vec{n}\right]\cdot\vec{n}=\left(\left[\begin{array}{ccc}\vec{h}\cdot\nabla n_1 & \vec{h}\cdot\nabla n_2 & \vec{h}\cdot\nabla n_3\end{array}\right]\right)\left[\begin{array}{c}n_1\\n_2\\n_3\end{array}\right] \tag{D.7}$$

$$\begin{aligned} &=h_1n_1\frac{\partial n_1}{\partial x_1}+h_2n_1\frac{\partial n_1}{\partial x_2}+h_3n_1\frac{\partial n_1}{\partial x_3}+ \\ &+h_1n_2\frac{\partial n_2}{\partial x_1}+h_2n_2\frac{\partial n_2}{\partial x_2}+h_3n_2\frac{\partial n_2}{\partial x_3}+h_1n_3\frac{\partial n_3}{\partial x_1}+h_2n_3\frac{\partial n_3}{\partial x_2}+h_3n_3\frac{\partial n_3}{\partial x_3}= \\ &=\frac{1}{2}h_1\frac{\partial\left(n_1n_1\right)}{\partial x_1}+\frac{1}{2}h_2\frac{\partial\left(n_1n_1\right)}{\partial x_2}+\frac{1}{2}h_3\frac{\partial\left(n_1n_1\right)}{\partial x_3}+ \\ &+\frac{1}{2}h_1\frac{\partial\left(n_2n_2\right)}{\partial x_1}+\frac{1}{2}h_2\frac{\partial\left(n_2n_2\right)}{\partial x_2}+\frac{1}{2}h_3\frac{\partial\left(n_2n_2\right)}{\partial x_3}+\frac{1}{2}h_1\frac{\partial\left(n_3n_3\right)}{\partial x_1}+\frac{1}{2}h_2\frac{\partial\left(n_3n_3\right)}{\partial x_2}+\frac{1}{2}h_3\frac{\partial\left(n_3n_3\right)}{\partial x_3}= \\ &=\frac{1}{2}h_1\frac{\partial}{\partial x_1}\left(n_1^2+n_2^2+n_3^2\right)+\frac{1}{2}h_2\frac{\partial}{\partial x_2}\left(n_1^2+n_2^2+n_3^2\right)+\frac{1}{2}h_3\frac{\partial}{\partial x_3}\left(n_1^2+n_2^2+n_3^2\right)= \\ &=\frac{1}{2}h_1\frac{\partial}{\partial x_1}\left(\|\vec{n}\|^2\right)+\frac{1}{2}h_2\frac{\partial}{\partial x_2}\left(\|\vec{n}\|^2\right)+\frac{1}{2}h_3\frac{\partial}{\partial x_3}\left(\|\vec{n}\|^2\right)=\frac{1}{2}\vec{h}\cdot\nabla\left(\|\vec{n}\|^2\right)=0\,. \end{aligned} \tag{D.8}$$

Therefore:

$$\int\limits_{\mathcal{P}}\left[\nabla\times\left(\vec{n}\times\vec{h}\right)\right]\cdot\vec{n}dS=\int\limits_{\mathcal{P}}\left[\vec{n}\left(\nabla\cdot\vec{h}\right)-\left(\vec{n}\cdot\nabla\right)\vec{h}\right]\cdot\vec{n}dS\,, \tag{D.9}$$

where $(\vec{n}\cdot\nabla)\vec{h} = \left(\nabla\vec{h}\right)\vec{n}$.

$$(\vec{n}\cdot\nabla)\vec{h} = \left(\begin{bmatrix} n_1 & n_2 & n_3 \end{bmatrix} \begin{bmatrix} \frac{\partial}{\partial x_1} \\ \frac{\partial}{\partial x_2} \\ \frac{\partial}{\partial x_3} \end{bmatrix} \right) \begin{bmatrix} h_1 \\ h_2 \\ h_3 \end{bmatrix} = \left(n_1\frac{\partial}{\partial x_1} + n_2\frac{\partial}{\partial x_2} + n_3\frac{\partial}{\partial x_3} \right) \begin{bmatrix} h_1 \\ h_2 \\ h_3 \end{bmatrix} =$$
$$= \begin{bmatrix} n_1\frac{\partial h_1}{\partial x_1} + n_2\frac{\partial h_1}{\partial x_2} + n_3\frac{\partial h_1}{\partial x_3} \\ n_1\frac{\partial h_2}{\partial x_1} + n_2\frac{\partial h_2}{\partial x_2} + n_3\frac{\partial h_2}{\partial x_3} \\ n_1\frac{\partial h_3}{\partial x_1} + n_2\frac{\partial h_3}{\partial x_2} + n_3\frac{\partial h_3}{\partial x_3} \end{bmatrix} = \begin{bmatrix} \vec{n}\cdot\nabla h_1 \\ \vec{n}\cdot\nabla h_2 \\ \vec{n}\cdot\nabla h_3 \end{bmatrix}, \tag{D.10}$$

$$\left(\nabla\vec{h}\right)\vec{n} = \left(\begin{bmatrix} \frac{\partial h_1}{\partial x_1} & \frac{\partial h_1}{\partial x_2} & \frac{\partial h_1}{\partial x_3} \\ \frac{\partial h_2}{\partial x_1} & \frac{\partial h_2}{\partial x_2} & \frac{\partial h_2}{\partial x_3} \\ \frac{\partial h_3}{\partial x_1} & \frac{\partial h_3}{\partial x_2} & \frac{\partial h_3}{\partial x_3} \end{bmatrix} \right) \begin{bmatrix} n_1 \\ n_2 \\ n_3 \end{bmatrix} = \begin{bmatrix} n_1\frac{\partial h_1}{\partial x_1} + n_2\frac{\partial h_1}{\partial x_2} + n_3\frac{\partial h_1}{\partial x_3} \\ n_1\frac{\partial h_2}{\partial x_1} + n_2\frac{\partial h_2}{\partial x_2} + n_3\frac{\partial h_2}{\partial x_3} \\ n_1\frac{\partial h_3}{\partial x_1} + n_2\frac{\partial h_3}{\partial x_2} + n_3\frac{\partial h_3}{\partial x_3} \end{bmatrix} = \begin{bmatrix} \vec{n}\cdot\nabla h_1 \\ \vec{n}\cdot\nabla h_2 \\ \vec{n}\cdot\nabla h_3 \end{bmatrix}. \tag{D.11}$$

This entails $(\vec{n}\cdot\nabla)\vec{h} = \left(\nabla\vec{h}\right)\vec{n}$, and so:

$$\int_{\mathcal{P}} \left[\nabla\times\left(\vec{n}\times\vec{h}\right)\right]\cdot\vec{n}dS = \int_{\mathcal{P}} \left\{\left(\nabla\cdot\vec{h}\right) - \left[\left(\nabla\vec{h}\right)\vec{n}\right]\cdot\vec{n}\right\}dS = \int_{\mathcal{P}} div_{\mathcal{P}}[\vec{h}]dS\,. \tag{D.12}$$

D.1.2 $div_{\mathcal{P}}[\widehat{c}\vec{h}]$

Similarly, we can write:

$$\int_{\partial\mathcal{P}} \widehat{\Phi} dl = \int_{\partial\mathcal{P}} \underbrace{\widehat{c}\vec{h}}_{\vec{g}} \cdot \vec{t}_{\perp} dl = \int_{\partial\mathcal{P}} \vec{g} \cdot \vec{t}_{\perp} dl \,,$$

where thanks to what we have seen in the previous section, we can state that: (D.13)

$$\int_{\partial\mathcal{P}} \vec{g} \cdot \vec{t}_{\perp} dl = \int_{\partial\mathcal{P}} (\vec{n} \times \vec{g}) \, d\vec{l} = \int_{\mathcal{P}} [\text{ rot } (\vec{n} \times \vec{g})] \cdot \vec{n} dS \,.$$

It is known that:

$$\nabla \times (\vec{n} \times \vec{g}) = \vec{n} (\nabla \cdot \vec{g}) - \vec{g} (\nabla \cdot \vec{n}) + (\vec{g} \cdot \nabla) \vec{n} - (\vec{n} \cdot \nabla) \vec{g} \,, \tag{D.14}$$

where:

$$\begin{gathered} \vec{n} (\nabla \cdot \vec{g}) = \vec{n} \left[\nabla \cdot \left(\widehat{c}\vec{h} \right) \right] = \vec{n} \left[(\nabla \widehat{c}) \cdot \vec{h} + \widehat{c} \left(\nabla \cdot \vec{h} \right) \right] \,, \\ (\nabla \vec{g}) \vec{n} = \left[\nabla \left(\widehat{c}\vec{h} \right) \right] \vec{n} = \left[(\nabla \widehat{c}) \otimes \vec{h} + \widehat{c} \left(\nabla \vec{h} \right) \right] \vec{n} \\ \Longrightarrow \\ \nabla \times (\vec{n} \times \vec{g}) = \vec{n} \left[(\nabla \widehat{c}) \cdot \vec{h} + \widehat{c} \left(\nabla \cdot \vec{h} \right) \right] - \left\{ \left[(\nabla \widehat{c}) \otimes \vec{h} + \widehat{c} \left(\nabla \vec{h} \right) \right] \vec{n} \right\} - \vec{g} (\nabla \cdot \vec{n}) + (\vec{g} \cdot \nabla) \vec{n} \,. \end{gathered} \tag{D.15}$$

Exploiting the conditions on the orthogonality:

$$[\vec{g} (\nabla \cdot \vec{n})] \cdot \vec{n} = [(\vec{g} \cdot \nabla) \vec{n}] \cdot \vec{n} = 0 \,, \tag{D.16}$$

we can infer that:

$$\begin{aligned} [\nabla \times (\vec{n} \times \vec{g})] \cdot \vec{n} &= \left[(\nabla \widehat{c}) \cdot \vec{h} + \widehat{c} \left(\nabla \cdot \vec{h} \right) \right] - \left\{ \left[(\nabla \widehat{c}) \otimes \vec{h} \right] \vec{n} \right\} \cdot \vec{n} - \left\{ \left[\widehat{c} \left(\nabla \vec{h} \right) \right] \vec{n} \right\} \cdot \vec{n} \\ &= \underbrace{\left\{ \widehat{c} \left(\nabla \cdot \vec{h} \right) - \left\{ \left[\widehat{c} \left(\nabla \vec{h} \right) \right] \vec{n} \right\} \cdot \vec{n} \right\}}_{\widehat{c} div_{\mathcal{P}}[\vec{h}]} + \left\{ (\nabla \widehat{c}) \cdot \vec{h} - \left\{ \left[(\nabla \widehat{c}) \otimes \vec{h} \right] \vec{n} \right\} \cdot \vec{n} \right\} \,. \end{aligned} \tag{D.17}$$

Having proved that $\left\{\left[(\nabla\widehat{c})\otimes\vec{h}\right]\vec{n}\right\}\cdot\vec{n}=\{[\vec{n}\cdot(\nabla\widehat{c})]\,\vec{n}\}\cdot\vec{h}$, we can deduce:

$$
\begin{aligned}
\left\{\left[(\nabla\widehat{c})\otimes\vec{h}\right]\vec{n}\right\}\cdot\vec{n} &= \left\{\left(\begin{bmatrix}\frac{\partial\widehat{c}}{\partial x_1}\\ \frac{\partial\widehat{c}}{\partial x_2}\\ \frac{\partial\widehat{c}}{\partial x_3}\end{bmatrix}\begin{bmatrix} h_1 & h_2 & h_3\end{bmatrix}\right)\begin{bmatrix} n_1\\ n_2\\ n_3\end{bmatrix}\right\}^T\begin{bmatrix} n_1\\ n_2\\ n_3\end{bmatrix}\\
&= \left\{\begin{pmatrix} h_1\frac{\partial\widehat{c}}{\partial x_1} & h_2\frac{\partial\widehat{c}}{\partial x_1} & h_3\frac{\partial\widehat{c}}{\partial x_1}\\ h_1\frac{\partial\widehat{c}}{\partial x_2} & h_2\frac{\partial\widehat{c}}{\partial x_2} & h_3\frac{\partial\widehat{c}}{\partial x_2}\\ h_1\frac{\partial\widehat{c}}{\partial x_3} & h_2\frac{\partial\widehat{c}}{\partial x_3} & h_3\frac{\partial\widehat{c}}{\partial x_3}\end{pmatrix}\begin{bmatrix} n_1\\ n_2\\ n_3\end{bmatrix}\right\}^T\begin{bmatrix} n_1\\ n_2\\ n_3\end{bmatrix}\\
&= \begin{bmatrix} n_1h_1\frac{\partial\widehat{c}}{\partial x_1}+n_2h_2\frac{\partial\widehat{c}}{\partial x_1}+n_3h_3\frac{\partial\widehat{c}}{\partial x_1}\\ n_1h_1\frac{\partial\widehat{c}}{\partial x_2}+n_2h_2\frac{\partial\widehat{c}}{\partial x_2}+n_3h_3\frac{\partial\widehat{c}}{\partial x_2}\\ n_1h_1\frac{\partial\widehat{c}}{\partial x_3}+n_2h_2\frac{\partial\widehat{c}}{\partial x_3}+n_3h_3\frac{\partial\widehat{c}}{\partial x_3}\end{bmatrix}^T\begin{bmatrix} n_1\\ n_2\\ n_3\end{bmatrix}\\
&= \begin{bmatrix} \underbrace{(n_1h_1+n_2h_2+n_3h_3)}_{A}\frac{\partial\widehat{c}}{\partial x_1}\\ (n_1h_1+n_2h_2+n_3h_3)\frac{\partial\widehat{c}}{\partial x_2}\\ (n_1h_1+n_2h_2+n_3h_3)\frac{\partial\widehat{c}}{\partial x_3}\end{bmatrix}^T\begin{bmatrix} n_1\\ n_2\\ n_3\end{bmatrix}\\
&= A\begin{bmatrix}\frac{\partial\widehat{c}}{\partial x_1} & \frac{\partial\widehat{c}}{\partial x_2} & \frac{\partial\widehat{c}}{\partial x_3}\end{bmatrix}\begin{bmatrix} n_1\\ n_2\\ n_3\end{bmatrix} = A\left(n_1\frac{\partial\widehat{c}}{\partial x_1}+n_2\frac{\partial\widehat{c}}{\partial x_2}+n_3\frac{\partial\widehat{c}}{\partial x_3}\right),
\end{aligned}
\tag{D.18}
$$

$$
\begin{aligned}
\{[\vec{n}\cdot(\nabla\widehat{c})]\,\vec{n}\}\cdot\vec{h} &= \left\{\left(\begin{bmatrix} n_1 & n_2 & n_3\end{bmatrix}\begin{bmatrix}\frac{\partial\widehat{c}}{\partial x_1}\\ \frac{\partial\widehat{c}}{\partial x_2}\\ \frac{\partial\widehat{c}}{\partial x_3}\end{bmatrix}\right)\begin{bmatrix} n_1\\ n_2\\ n_3\end{bmatrix}\right\}^T\begin{bmatrix} h_1\\ h_2\\ h_3\end{bmatrix} =\\
&\left\{\left(\underbrace{n_1\frac{\partial\widehat{c}}{\partial x_1}+n_2\frac{\partial\widehat{c}}{\partial x_2}+n_3\frac{\partial\widehat{c}}{\partial x_3}}_{B}\right)\begin{bmatrix} n_1\\ n_2\\ n_3\end{bmatrix}\right\}^T\begin{bmatrix} h_1\\ h_2\\ h_3\end{bmatrix} = B\begin{bmatrix} n_1 & n_2 & n_3\end{bmatrix}\begin{bmatrix} h_1\\ h_2\\ h_3\end{bmatrix}\\
&= B\left(n_1h_1+n_2h_2+n_3h_3\right),
\end{aligned}
\tag{D.19}
$$

and hence:

$$
\begin{aligned}
\left\{\left[(\nabla\widehat{c})\otimes\vec{h}\right]\vec{n}\right\}\cdot\vec{n} &= A\left(n_1\frac{\partial\widehat{c}}{\partial x_1}+n_2\frac{\partial\widehat{c}}{\partial x_2}+n_3\frac{\partial\widehat{c}}{\partial x_3}\right)\\
&= (n_1h_1+n_2h_2+n_3h_3)\left(n_1\frac{\partial\widehat{c}}{\partial x_1}+n_2\frac{\partial\widehat{c}}{\partial x_2}+n_3\frac{\partial\widehat{c}}{\partial x_3}\right)\\
&= \left(n_1\frac{\partial\widehat{c}}{\partial x_1}+n_2\frac{\partial\widehat{c}}{\partial x_2}+n_3\frac{\partial\widehat{c}}{\partial x_3}\right)(n_1h_1+n_2h_2+n_3h_3)\\
&= B\left(n_1h_1+n_2h_2+n_3h_3\right)\\
&= \{[\vec{n}\cdot(\nabla\widehat{c})]\,\vec{n}\}\cdot\vec{h}\,.
\end{aligned}
\tag{D.20}
$$

Finally:

$$\int_{\partial\mathcal{P}} \widehat{\Phi} dl = \int_{\partial\mathcal{P}} \underbrace{\widehat{c}\vec{h}}_{\vec{g}} \cdot \vec{t}_{\perp} dl = \int_{\mathcal{P}} [\nabla \times (\vec{n} \times \vec{g})] \cdot \vec{n} dS$$

$$= \int_{\mathcal{P}} \underbrace{\left\{ \widehat{c}\left(\nabla \cdot \vec{h}\right) - \left\{ \left[\widehat{c}\left(\nabla \vec{h}\right) \right] \vec{n} \right\} \cdot \vec{n} \right\}}_{\widehat{c} div_{\mathcal{P}}[\vec{h}]} dS + \int_{\mathcal{P}} \left\{ (\nabla \widehat{c}) \cdot \vec{h} - \left\{ \left[(\nabla \widehat{c}) \otimes \vec{h} \right] \vec{n} \right\} \cdot \vec{n} \right\} dS$$

$$= \int_{\mathcal{P}} \widehat{c} div_{\mathcal{P}}[\vec{h}] dS + \int_{\mathcal{P}} \underbrace{\left\{ (\nabla \widehat{c}) \cdot \vec{h} - \{ [\vec{n} \cdot (\nabla \widehat{c})] \vec{n} \} \cdot \vec{h} \right\}}_{\nabla_{\mathcal{P}}[\widehat{c}] \cdot \vec{h}} dS \tag{D.21}$$

$$= \int_{\mathcal{P}} \widehat{c} div_{\mathcal{P}}[\vec{h}] dS + \int_{\mathcal{P}} \nabla_{\mathcal{P}}[\widehat{c}] \cdot \vec{h} dS = \int_{\mathcal{P}} div_{\mathcal{P}}[\widehat{c}\vec{h}] dS \,.$$

D.1.3 $div_{\mathcal{P}}[\frac{\vec{q}}{T}]$

Similarly, we can write:

$$\int_{\partial\mathcal{P}} \widetilde{\Phi} dl = \int_{\partial\mathcal{P}} \underbrace{\frac{\vec{q}}{T}}_{\vec{p}} \cdot \vec{t}_{\perp} dl = \int_{\partial\mathcal{P}} \vec{p} \cdot \vec{t}_{\perp} dl \,,$$

where, thanks to what we have seen in the previous section, we can state that: (D.22)

$$\int_{\partial\mathcal{P}} \vec{p} \cdot \vec{t}_{\perp} dl = \int_{\partial\mathcal{P}} (\vec{n} \times \vec{p}) \, d\vec{l} = \int_{\mathcal{P}} [\text{ rot } (\vec{n} \times \vec{p})] \cdot \vec{n} dS \,,$$

It is known that:

$$\nabla \times (\vec{n} \times \vec{p}) = \vec{n} (\nabla \cdot \vec{p}) - (\nabla \vec{p}) \vec{n} + (\vec{p} \cdot \nabla) \vec{n} - \vec{p} (\nabla \cdot \vec{n}) \ . \tag{D.23}$$

where:

$$\begin{gathered} \vec{n} (\nabla \cdot \vec{p}) = \vec{n} \left[\nabla \cdot \left(\frac{\vec{q}}{T} \right) \right] = \vec{n} \left[\frac{T \nabla \cdot [\vec{q}] - \nabla [T] \cdot \vec{q}}{T^2} \right] \\ (\nabla \vec{p}) \vec{n} = \left[\nabla \left(\frac{\vec{q}}{T} \right) \right] \vec{n} = \left[\frac{T (\nabla \vec{q}) - (\nabla T) \otimes \vec{q}}{T^2} \right] \vec{n} = \left[\frac{T (\nabla \vec{q}) - (\nabla T) \otimes \vec{q}}{T^2} \right] \vec{n} \\ [(\vec{p} \cdot \nabla) \vec{n}] \cdot \vec{n} = 0 \\ \text{if } \vec{p} \perp \vec{n} \Longrightarrow [\vec{p} (\nabla \cdot \vec{n})] \cdot \vec{n} = 0 \,. \end{gathered} \tag{D.24}$$

Two distinct cases are identified:

- $\vec{p}$ is perpendicular to $\vec{n}$;
- $\vec{p}$ is not perpendicular to $\vec{n}$.

D.1.3.1 $\vec{p}$ is perpendicular to $\vec{n}$

We known that:

$$\begin{gathered}[\vec{p}\,(\nabla\cdot\vec{n})]\cdot\vec{n}=0\\ \text{and}\\ \{[(\nabla T)\otimes\vec{q}]\,\vec{n}\}\cdot\vec{n}=\{[\vec{n}\cdot(\nabla T)]\,\vec{n}\}\cdot\vec{q}\;.\end{gathered}\tag{D.25}$$

Finally:

$$\begin{aligned}&\int_{\partial\mathcal{P}}\widetilde{\Phi}dl=\int_{\partial\mathcal{P}}\underbrace{\frac{\vec{q}}{T}}_{\vec{p}}\cdot\vec{t}_{\perp}dl=\int_{\mathcal{P}}[\nabla\times(\vec{n}\times\vec{p})]\cdot\vec{n}dS\\ &=\int_{\mathcal{P}}\underbrace{\left\{\frac{1}{T}(\nabla\cdot\vec{p})-\left\{\left[\frac{1}{T}(\nabla\vec{q})\right]\vec{n}\right\}\cdot\vec{n}\right\}}_{\frac{1}{T}div_{\mathcal{P}}[q]}dS-\int_{\mathcal{P}}\left\{\frac{(\nabla T)\cdot\vec{q}-\{[(\nabla T)\otimes\vec{q}]\,\vec{n}\}\cdot\vec{n}}{T^2}\right\}dS\\ &=\int_{\mathcal{P}}\frac{1}{T}div_{\mathcal{P}}[\vec{q}]dS-\int_{\mathcal{P}}\underbrace{\frac{\{(\nabla T)\cdot\vec{q}-\{[\vec{n}\cdot(\nabla T)]\,\vec{n}\}\cdot\vec{q}\}}{T^2}}_{\frac{1}{T^2}\nabla_{\mathcal{P}}[T]\cdot\vec{q}}dS\\ &=\int_{\mathcal{P}}\frac{1}{T}div_{\mathcal{P}}[\vec{q}]dS-\int_{\mathcal{P}}\frac{1}{T^2}\nabla_{\mathcal{P}}[T]\cdot\vec{q}dS=\int_{\mathcal{P}}div_{\mathcal{P}}[\frac{\vec{q}}{T}]dS\;.\end{aligned}\tag{D.26}$$

D.1.3.2 $\vec{p}$ is not perpendicular to $\vec{n}$

$$\begin{gathered}[\vec{p}\,(\nabla\cdot\vec{n})]\cdot\vec{n}\neq 0\\ \text{and}\\ \{[(\nabla T)\otimes\vec{q}]\,\vec{n}\}\cdot\vec{n}=\{[\vec{n}\cdot(\nabla T)]\,\vec{n}\}\cdot\vec{q}\,.\end{gathered}\tag{D.27}$$

Finally:

$$\begin{aligned}&\int_{\partial\mathcal{P}}\widetilde{\Phi}dl=\int_{\partial\mathcal{P}}\underbrace{\frac{\vec{q}}{T}}_{\vec{p}}\cdot\vec{t}_{\perp}dl=\int_{\mathcal{P}}[\nabla\times(\vec{n}\times\vec{p})]\cdot\vec{n}dS\\ &=\int_{\mathcal{P}}\underbrace{\left\{\frac{1}{T}(\nabla\cdot\vec{p})-\left\{\left[\frac{1}{T}(\nabla\vec{q})\right]\vec{n}\right\}\cdot\vec{n}\right\}}_{\frac{1}{T}div_{\mathcal{P}}[q]}dS-\int_{\mathcal{P}}\left\{\frac{(\nabla T)\cdot\vec{q}-\{[(\nabla T)\otimes\vec{q}]\,\vec{n}\}\cdot\vec{n}}{T^2}\right\}dS+\\ &\qquad-\int_{\mathcal{P}}[\vec{p}\,(\nabla\cdot\vec{n})]\cdot\vec{n}dS\text{ where }\vec{p}=\frac{\vec{q}}{T}\\ &=\int_{\mathcal{P}}\frac{1}{T}div_{\mathcal{P}}[\vec{q}]dS-\int_{\mathcal{P}}\underbrace{\frac{\{(\nabla T)\cdot\vec{q}-\{[\vec{n}\cdot(\nabla T)]\,\vec{n}\}\cdot\vec{q}\}}{T^2}}_{\frac{1}{T^2}\nabla_{\mathcal{P}}[T]\cdot\vec{q}}dS-\int_{\mathcal{P}}\left[\frac{\vec{q}}{T}(\nabla\cdot\vec{n})\right]\cdot\vec{n}dS\\ &=\int_{\mathcal{P}}\frac{1}{T}div_{\mathcal{P}}[\vec{q}]dS-\int_{\mathcal{P}}\frac{1}{T^2}\nabla_{\mathcal{P}}[T]\cdot\vec{q}dS-\int_{\mathcal{P}}\left[\frac{\vec{q}}{T}(\nabla\cdot\vec{n})\right]\cdot\vec{n}dS\\ &=\int_{\mathcal{P}}div_{\mathcal{P}}\left[\frac{\vec{q}}{T}\right]dS-\int_{\mathcal{P}}\left[\left(\frac{\vec{q}}{T}\cdot\vec{n}\right)(\nabla\cdot\vec{n})\right]dS\,.\end{aligned}\tag{D.28}$$

D.2 Einstein notation

D.2.1 $div_{\mathcal{P}}[\vec{h}]$

$$\int_{\partial\mathcal{P}} \Phi dl = \int_{\partial\mathcal{P}} \vec{h}\cdot\vec{t}_{\perp} dl = \int_{\mathcal{P}} \left[\nabla\times\left(\vec{n}\times\vec{h}\right)\right]\cdot\vec{n} dS\,, \tag{D.29}$$

By means of Einstein notation, it is possible to express the vectorial product through the operator Levi-Civita, otherwise known as the Ricci Curbastro operator ε_{ijk}.
Remembering that:

$$\varepsilon_{ijk} = \begin{cases} 0 & \text{if at least two indices are equal} \\ 1 & \text{for every even permutation of the indices i, j, k with respect to 1, 2, 3} \\ -1 & \text{for every odd permutation of the indices i, j, k with respect to 1, 2, 3} \end{cases}$$

or alternatively:

$$\varepsilon_{ijk} = \frac{(i-j)(j-k)(k-i)}{2} \tag{D.30}$$

$$\begin{aligned} \nabla\times\left(\vec{n}\times\vec{h}\right) &= \varepsilon_{pqr}\partial_q\left(\vec{n}\times\vec{h}\right) = \varepsilon_{pqr}\varepsilon_{rij}\left(n_i h_j\right)_{,q} \\ &= \left(\delta_{pi}\delta_{qj}-\delta_{pj}\delta_{qi}\right)\left(n_{i,q}h_j + n_i h_{j,q}\right) \\ &= n_{p,q}h_q + n_p h_{q,q} - n_{q,q}h_p - n_q h_{p,q} \\ &= \left(\vec{h}\cdot\nabla\right)\vec{n} + \vec{n}\left(\nabla\cdot\vec{h}\right) - \vec{h}\left(\nabla\cdot\vec{n}\right) - \left(\vec{n}\cdot\nabla\right)\vec{h}\,, \end{aligned} \tag{D.31}$$

therefore:

$$\begin{aligned} &\int_{\mathcal{P}} \left[\nabla\times\left(\vec{n}\times\vec{h}\right)\right]\cdot\vec{n} dS = \int_{\mathcal{P}} \left[n_{p,q}h_q + n_p h_{q,q} - n_{q,q}h_p - n_q h_{p,q}\right] n_p dS \\ &= \int_{\mathcal{P}} \left[h_{q,q} - n_q h_{p,q} n_p\right] dS = \int_{\mathcal{P}} \left\{\left(\nabla\cdot\vec{h}\right) - \left[\left(\nabla\vec{h}\right)\vec{n}\right]\cdot\vec{n}\right\} dS = \int_{\mathcal{P}} div_{\mathcal{P}}[\vec{h}] dS\,. \end{aligned} \tag{D.32}$$

D.2.2 $div_{\mathcal{P}}[\widehat{c}\vec{h}]$

$$\int_{\partial\mathcal{P}} \widehat{\Phi} dl = \int_{\partial\mathcal{P}} \underbrace{\widehat{c}\vec{h}}_{\vec{g}}\cdot\vec{t}_{\perp} dl = \int_{\mathcal{P}} \left[\nabla\times\left(\vec{n}\times\vec{g}\right)\right]\cdot\vec{n} dS\,, \tag{D.33}$$

where:

$$\begin{gathered} \nabla\times\left(\vec{n}\times\vec{g}\right) = \varepsilon_{plr}\varepsilon_{rij}\left(n_i g_j\right) = n_p g_{l,l} - n_l g_{p,l} + n_{p,l}g_l - n_{l,l}g_p \\ \text{but:} \\ g_l = \widehat{c}h_l \rightarrow g_{l,l} = \widehat{c}_{,l}h_l + \widehat{c}h_{l,l} \quad g_{p,l} = \widehat{c}_{,l}h_p + \widehat{c}h_{p,l}\,. \end{gathered} \tag{D.34}$$

Finally:

$$\int_{\mathcal{P}} [\nabla \times (\vec{n} \times \vec{g})] \cdot \vec{n} dS = \int_{\mathcal{P}} \left[n_p g_{l,l} - n_l g_{p,l} + n_{p,l} g_l - n_{l,l} g_p \right] n_p dS$$

$$n_{p,l} g_l n_p = n_{l,l} g_p n_p = 0$$

$$= \int_{\mathcal{P}} \left[n_p \left(\widehat{c}_{,l} h_l + \widehat{c} h_{l,l} \right) - n_l \left(\widehat{c}_{,l} h_p + \widehat{c} h_{p,l} \right) \right] n_p dS$$

$$= \int_{\mathcal{P}} [\underbrace{\widehat{c}_{,l} h_l}_{l \to p} + \widehat{c} h_{l,l}] - \left[n_l \widehat{c}_{,l} h_p n_p + n_l \widehat{c} h_{p,l} n_p \right] dS \tag{D.35}$$

$$= \int_{\mathcal{P}} \left[\widehat{c} \left(h_{l,l} - n_l h_{p,l} n_p \right) + \left(\widehat{c}_{,p} - n_l c_{,l} n_p \right) h_p \right] dS$$

$$= \int_{\mathcal{P}} \widehat{c} div_{\mathcal{P}}[\vec{h}] dS + \int_{\mathcal{P}} \nabla_{\mathcal{P}}[\widehat{c}] \cdot \vec{h} dS = \int_{\mathcal{P}} div_{\mathcal{P}}[\widehat{c}\vec{h}] dS \, .$$

D.2.3 $div_{\mathcal{P}}[\frac{\vec{q}}{T}]$

$$\int_{\partial \mathcal{P}} \widetilde{\Phi} dl = \int_{\partial \mathcal{P}} \underbrace{\frac{\vec{q}}{T}}_{\vec{p}} \cdot \vec{t}_{\perp} dl = \int_{\partial \mathcal{P}} \vec{p} \cdot \vec{t}_{\perp} dl$$

where, thanks to what we have seen in the previous section, we can state that: (D.36)

$$\int_{\partial \mathcal{P}} \vec{p} \cdot \vec{t}_{\perp} dl = \int_{\partial \mathcal{P}} (\vec{n} \times \vec{p}) \, d\vec{l} = \int_{\mathcal{P}} [\text{ rot } (\vec{n} \times \vec{p})] \cdot \vec{n} dS \, ,$$

where:

$$\nabla \times (\vec{n} \times \vec{p}) = \varepsilon_{rlm} \varepsilon_{mij} \left(n_i p_j \right) = n_{r,l} p_l - n_{l,l} p_r + n_r p_{l,l} - n_l p_{r,l}$$

but:

$$p_l = \frac{q_l}{T} \rightarrow p_{l,l} = \frac{T q_{l,l} - q_l T_{,l}}{T^2} \quad p_{r,l} = \frac{T q_{r,l} - T_{,l} q_r}{T^2} \tag{D.37}$$

Finally:

$$\begin{aligned}
&\int_{\mathcal{P}} [\nabla \times (\vec{n} \times \vec{p})] \cdot \vec{n} dS = \int_{\mathcal{P}} \left[n_r p_{l,l} - n_l p_{r,l} + n_{r,l} p_l - n_{l,l} p_r \right] n_r dS \\
&= \int_{\mathcal{P}} \left[n_r \left(\frac{T q_{l,l} - q_l T_{,l}}{T^2} \right) - n_l \left(\frac{T q_{r,l} - T_{,l} q_r}{T^2} \right) + n_{r,l} p_l - n_{l,l} p_r \right] n_r dS \\
&= \int_{\mathcal{P}} \left[\left(\frac{T q_{l,l} - q_l T_{,l}}{T^2} \right) - n_l \left(\frac{T q_{r,l} - T_{,l} q_r}{T^2} \right) n_r \right] dS \\
&= \int_{\mathcal{P}} \left[\frac{1}{T} \left(q_{l,l} - n_l q_{r,l} n_r \right) - \frac{1}{T^2} \left(\underbrace{q_l T_{,l}}_{l \to r} - n_l T_{,l} q_r n_r \right) \right] dS = \\
&\int_{\mathcal{P}} \left[\frac{1}{T} \underbrace{\left(q_{l,l} - n_l q_{r,l} n_r \right)}_{div_{\mathcal{P}}(\vec{q})} - \frac{1}{T^2} \underbrace{\left(T_{,r} - n_l T_{,l} n_r \right)}_{\nabla_{\mathcal{P}}(T)} q_r \right] dS \\
&= \int_{\mathcal{P}} \frac{1}{T} div_{\mathcal{P}}[\vec{q}] dS - \int_{\mathcal{P}} \frac{1}{T^2} \nabla_{\mathcal{P}}[T] \cdot \vec{q} dS = \int_{\mathcal{P}} div_{\mathcal{P}}[\frac{\vec{q}}{T}] dS \, .
\end{aligned} \tag{D.38}$$

D.2.4 $T\vec{h} \cdot \nabla_{\mathcal{P}}[\mu^\eta]$

$$\begin{aligned}
T\vec{h} \cdot \nabla_{\mathcal{P}}[\mu^\eta] &= T \left(\mu^\eta_{,p} - n_l \mu^\eta_{,l} n_p \right) h_p \\
\mu^\eta \vec{h} \cdot \nabla_{\mathcal{P}}[T] &= \mu^\eta \left(T_{,p} - n_l T_{,l} n_p \right) h_p \\
T\vec{h} \cdot \nabla_{\mathcal{P}}[\mu^\eta] + \mu^\eta \vec{h} \cdot \nabla_{\mathcal{P}}[T] &= T \left(\mu^\eta_{,p} - n_l \mu^\eta_{,l} n_p \right) h_p + \mu^\eta \left(T_{,p} - n_l T_{,l} n_p \right) h_p \\
\left[T \mu^\eta_{,p} + \mu^\eta T_{,p} - \left(n_l \mu^\eta_{,l} n_p + n_l T_{,l} n_p \right) \right] h_p &= \\
\left[\left(T \mu^\eta \right)_{,p} - n_l \left(\mu^\eta_{,l} + T_{,l} \right) n_p \right] h_p &= \vec{h} \cdot \nabla_{\mathcal{P}}[T \mu^\eta] \\
\Longrightarrow & \\
T\vec{h} \cdot \nabla_{\mathcal{P}}[\mu^\eta] + \mu^\eta \vec{h} \cdot \nabla_{\mathcal{P}}[T] &= \vec{h} \cdot \nabla_{\mathcal{P}}[T \mu^\eta] \, .
\end{aligned} \tag{D.39}$$

D.2.5 $\nabla_{\mathcal{P}}[f(y,z)]$

We want to prove that:

$$\nabla_{\mathcal{P}} f(y,z) = \frac{\partial f}{\partial y} \nabla_{\mathcal{P}}[y] + \frac{\partial f}{\partial z} \nabla_{\mathcal{P}}[z] \, , \tag{D.40}$$

where:

$$\begin{aligned}
\nabla_{\mathcal{P}}[f(y,z)] &= \{\nabla[f(y,z)]\} - \{\vec{n}\cdot\nabla[f(y,z)]\}\vec{n} \\
&= \left\{\frac{\partial f}{\partial y}\nabla[y] + \frac{\partial f}{\partial z}\nabla[z]\right\} - \left\{\vec{n}\cdot\left[\frac{\partial f}{\partial y}\nabla[y] + \frac{\partial f}{\partial z}\nabla[z]\right]\right\}\vec{n} \\
&= \frac{\partial f}{\partial y}\{\nabla[y] - [\vec{n}\cdot\nabla[y]]\,\vec{n}\} + \frac{\partial f}{\partial z}\{\nabla[z] - [\vec{n}\cdot\nabla[z]]\,\vec{n}\} \\
&= \frac{\partial f}{\partial y}\nabla_{\mathcal{P}}[y] + \frac{\partial f}{\partial z}\nabla_{\mathcal{P}}[z]\,.
\end{aligned} \tag{D.41}$$

Considering f as a function of vector quantities:

$$\begin{aligned}
\nabla_{\mathcal{P}}[f(\vec{y},\vec{z})] = f_{,p} - n_l f_{,l} n_p &= \frac{\partial f}{\partial y_k} y_{k,p} + \frac{\partial f}{\partial z_k} z_{k,p} - n_l\left[\frac{\partial f}{\partial y_k} y_{k,l} + \frac{\partial f}{\partial z_k} z_{k,l}\right] n_p \\
&= \frac{\partial f}{\partial y_k}\left[y_{k,p} - n_l y_{k,l} n_p\right] + \frac{\partial f}{\partial z_k}\left[z_{k,p} - n_l z_{k,l} n_p\right] \\
&= \frac{\partial f}{\partial \vec{y}}\nabla_{\mathcal{P}}[\vec{y}] + \frac{\partial f}{\partial \vec{z}}\nabla_{\mathcal{P}}[\vec{z}]\,.
\end{aligned} \tag{D.42}$$

Appendix E

Experimental insights

E.1 Fluorescence resonance energy transfer (FRET)

Fluorescence resonance energy transfer (FRET) is a further important experimental typology. Thanks to is possible to investigate the interplay between two protein on the cell membrane, basically exploiting the emission spectrum characteristic of two different fluorochrome use to labeled the molecules of interest. Specifically, the donor has to have fluorochrome with an emission spectrum that overlaps with the absorption spectrum of fluorochrome of the acceptor. Therefore, if these two proteins come in contact and bind (making a complex), taking to the two fluorochromes to a distance closer than 5 nm, by resonance one fluorochrome can transfer energy (from the absorbed light) to the other. Intriguingly, illuminating the complex at the characteristic wavelength of the donor, the fluorescence produced has the characteristic wavelength of the acceptor. Finally, measuring the change in donor fluorescence when it is colocalized with the acceptor, can lead to the FRET quantification [9] (chapter 9).
Currently, this work has been used to demonstrate the direct interaction between VEGFR2 and integrin.

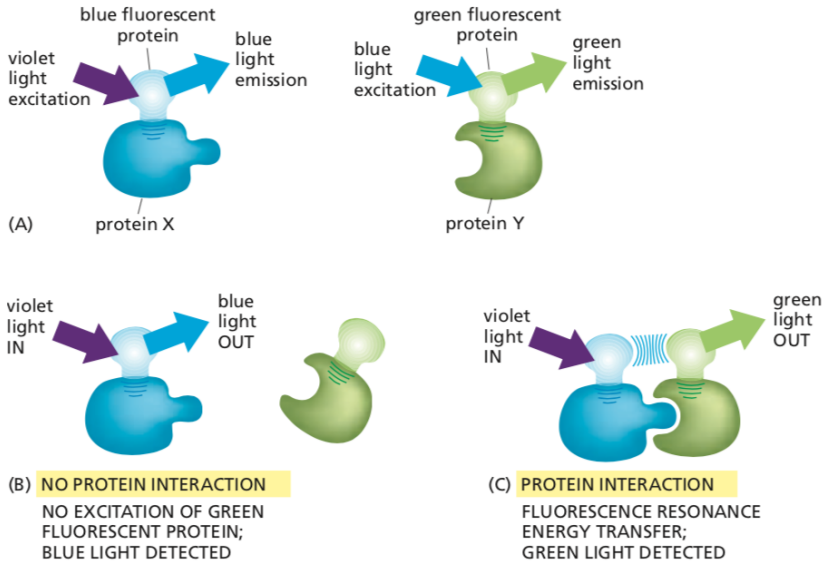

Figure E.1: A specific "X" protein is fuse with a definite blue fluorescent molecule. Similarly, a further "Y" protein is fuse with distinctive green fluorescent ones. Specifically, if violet light hits blue proteins, they emit blue light and coherently, if blue light hits green proteins, they emit green light. Therefore, if "X" and "Y" proteins are interacting, and violet light stimulates blue proteins, they emit blue light which in turn will excite green proteins owing to green light emissions. Accordingly, FRET analysis can study when and where two specific proteins are interplaying inside the cell. Adapted from [9]

E.2 Fluorescence recovery after photobleaching (FRAP)

FRAP is a diffuse methodology in much dynamic application in cellular biology. Cytoskeletal rearrangements, mitosis, cellular adhesion, etc. are just a few fields of application of this technique [159]. Such a procedure provides for the use of a high-intensity laser beam able to bleaching, in a specific and restricted area on the cell surface, the fluorescence of the labeled receptors. All this is necessary in order to observe over time, the total or partial reconstitution of the initial fluorescence, inasmuch as this datum is purely correlated to the lateral diffusion of the receptors (for time-span observation of minutes) and to the new generation (new synthesis) of receptors (for long time-span observation). Effectively, the bleaching procedure irreparably damages the fluorescence of the receptors hit by the laser beam, ensuring that the future measured fluorescence intensity is due to other molecules. In the current work, FRAP analysis is strictly correlated with the measurement of two kinetic parameters: the diffusion constant D and the mobile fraction (M_f) [31] (chapter 2).

The first one, when neither active transport nor flow insists on the receptor, expresses the rate of protein motion; indeed, this quantity is correlated with the mean squared displacement of a receptor that moving along a random path in a given observed time.

The second represents the number of fluorescent proteins that can diffuse inside the ROI during the observation time duration. Not only that, even the percentage of immobilized receptors (im-

mobile fraction) could be deduced on the basis of the present experiment. In fact, a failure to recover the initial fluorescence can be caused by the presence of immobile receptors, which not being able to diffuse remain to occupy the portion of space affected by the laser. Such a relevant phenomenon could be caused either by cytoskeleton interaction with these immobilized receptors or, alternatively, due to the presence of diffusion barriers that are responsible for lower mobility [31] (chapter 2).

The following mathematical expression denotes the fluorescence recovery curve after photobleaching:

$$\mathcal{I}_t = M_f \left[1 - \exp\left(-\tau t\right)\right] . \tag{E.1}$$

Where:

- $\mathcal{I}_t$ represents the intensity recovery after a specific t;
- t depicts the instant to whom we do the observation;
- $M_f = \dfrac{\mathcal{I}_\infty - \mathcal{I}_i}{\mathcal{I}_i - \mathcal{I}_0}$ is the mobile fraction of fluorescent proteins [159];
- $\mathcal{I}_i$ is the initial fluorescent;
- $\mathcal{I}_0$ is the fluorescence after photobleaching;
- $\mathcal{I}_\infty$ is the plateau value reach by the intensity after photobleaching;
- τ denotes the frequency correlated at the time necessary to recover half of the maximum fluorescence.

The diffusivity ($\mathbb{D}$ $\left[\mu m^2/s\right]$) value resulting from the following formula (Soumpasis equation [160]):

$$\mathbb{D} = 0.224 * \omega^2 / t_{1/2} , \tag{E.2}$$

wherein ω is the radius of the bleaching area and $t_{1/2}$ is the span time necessary to reach half of the final fluorescent intensity ($\mathcal{I}_{\frac{1}{2}} = \dfrac{\mathcal{I}_\infty + \mathcal{I}_0}{2}$ [159]).

The diffusivity ($\mathbb{D}$) arise from FRAP analysis can lead to misleading results. In fact, exist multiply factors that can impact the diffusivity of a receptor, perhaps making it grow dramatically; just think at the above-mentioned interaction between transmembrane protein and the cytoskeleton, or protein-protein interaction (e.g. interaction with co-receptors) or again the collision with other kinds of molecules [31] (chapter 2). Therefore, it could be that receptors do not assume the numerical value predict by the theory (e.g. Stokes-Einstein formula[1]).

[1] In a given volume, the diffusion constant of a free particle is given by the following Stoke-Einstein formula $\mathbb{D} = \dfrac{\kappa_B T}{6\pi\eta l}$. Where T denotes the temperature, constant inside a cell, η the solution viscosity, κ_B is the constant of Boltzmann, and finally, l represents the radius of the receptor molecule. It seems obvious that following the present formula only η and l are the variables able to influence the value of $\mathbb{D}$, but, from what has been said above, we understand that such a statement is dangerously false. [31] (chapter 2)

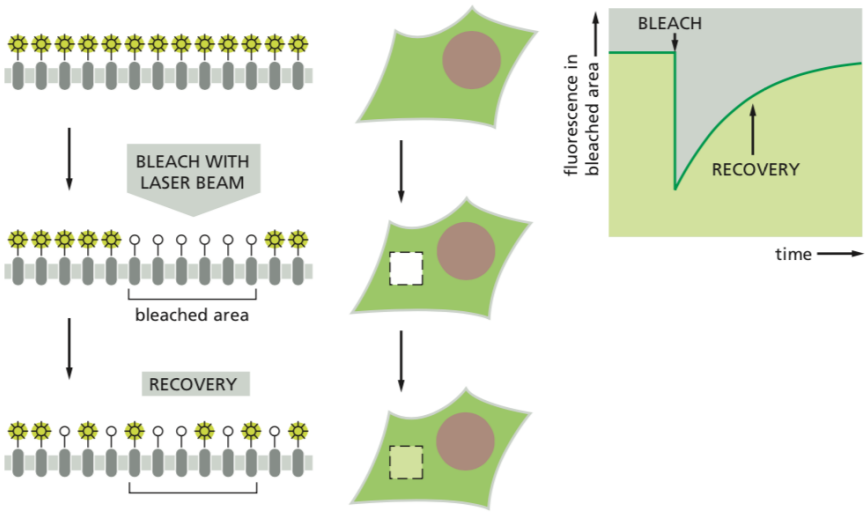

Figure E.2: Main operating mechanisms of FRAP analysis, with which it is possible to detect both the immobile fraction of the labeled protein and its diffusivity. Adapted from [9]

E.3 Single particle tracking (SPT)

The SPT procedure is based on microscopy techniques (e.g. Total Internal Reflection Fluorescence Microscopy - TIRFM-). In fact, by marking the receptor with fluorescent molecular groups it is possible, through acquires a very high number of photograms for the unit time and by means of computational elaboration, to reconstruct the trajectory of the labeled molecule that diffuses on the lipid bilayer. Comprehend how a single protein can move along the membrane and compute its velocity, as is possible through SPT, could make the difference in the interpretation of the experimental result. Indeed, understand the kind of motion of the receptors, linked with its velocity, might help to decipher if the receptor is anchored at the cytoskeleton or is undergoing some chemical interaction with co-receptors or ligands. However, a further important feature of this kind of experiment is the possibility to be able to study how membrane domains can impact the receptor dynamics [9] (chapters 9 and 10).

E.4 Surface Plasmon Resonance (SPR)

Association and dissociation rate constant as well as equilibrium constant and chemical affinities are the main kinetics parameters that have been possible to measure and deduces by means of SPR. SPR provides a real-time (label-free) investigation of the biomolecular interaction [31] (chapter 2), [161]. Practically, by means of SPR is possible to probe the interplay between a specific kind of molecule, that is immobilized on the SPR sensor surface, and an analyte in solution, which can, in this way, studying their affinity [162].

SPR is mainly made by a high refractive index material, cover by a thin metal film (usually gold, thanks to its inherent stability), and a chamber-flow. Hitting this material with a monochromatic p-polarized source of light, with an appropriate specific angulation, is possible to induce a physical phenomenon that causes a surface plasmon generation. Specifically, this happens because of the

energy that the light transfer to the free electrons of the gold layer. Particularly, we call evanescence wave, that part of the incident light, that for a specific angle of incidence (resonance angles), is capable of matching with the plasmons(i.e. free oscillating electrons) of the metal film producing an SPR. Interestingly, the mass concentration on the metal film, measured in resonance units (RU), affects the SPR signal [161].

Hence, if we let a soluble molecule called analyte fluxing in the flow-chamber shown in Fig. E.3a over the gold layer (immobilized protein-coated), we can provide a quantification of the kinetics parameters of the chemical reaction involved between the analyte and fixed proteins. In fact, the (probable) affinity between the immobilized molecules attached at the gold layer and the analyte, provides a chemical interaction that changes the mass concentration on the metal film E.3b, inducing, therefore, a variation in the refractive index of the golden layer itself [31] (chapter 2).

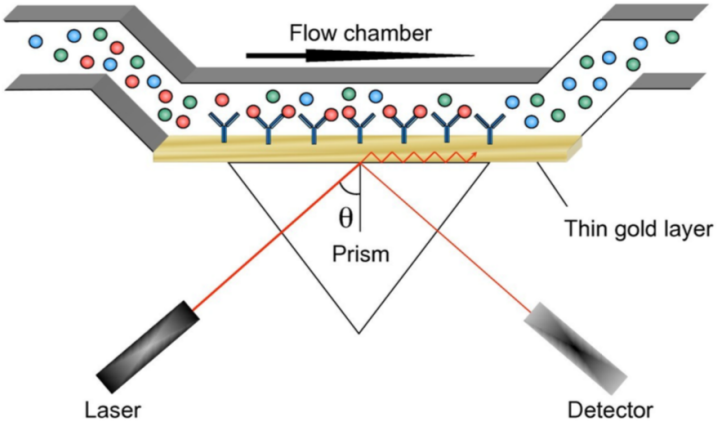

(a) A flow chamber in a customary SPR instrument is here shown. The gold layer is coated by biomolecules that have a specific affinity with the analyte, which is injected and let flow over the chip surface [31] (chapter 2).

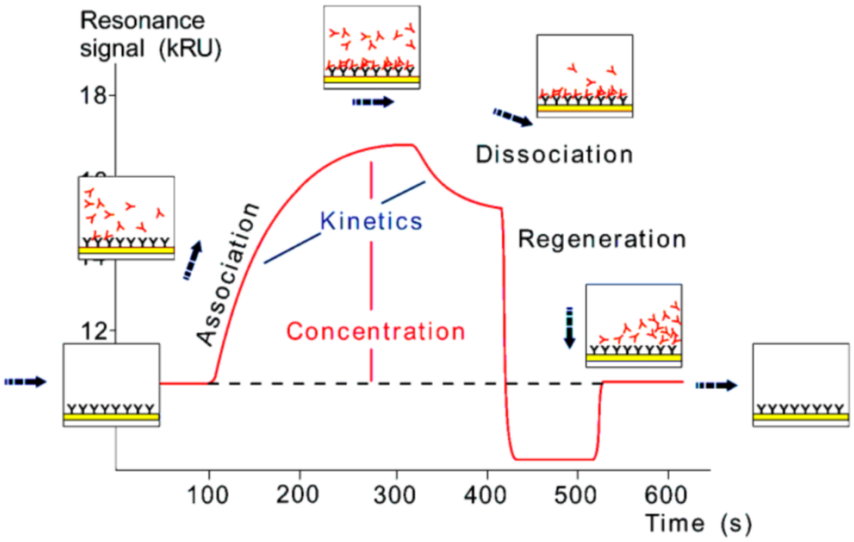

(b) The kinetics constant of the chemical interaction between the immobilized molecules and the analyte are deducible, owing to continuous monitoring provide by the sensor device [31] (chapter 2).

Figure E.3

Part III

A large deformations framework describes membrane dynamics

Mechanical modeling of a cell is a very challenging and fascinating task. New unexplored principles and laws are hidden behind the mechanical behavior of a living cell, highlighting how animated matter is different from inanimate one [3] (chapter 1). The cell actively evolves its internal structure based on the environmental conditions, and so also the progress of mechanical conditions in the surrounding environment. Cells undergo complex mechanical interplays, such as cell-cell, cell-substrate, and cell-fluid interactions. Further, any "cell-microenvironment" mechanical interplay induces the evolvement and the triggering of polymers that make up the cytoskeleton whose activities could is affected by the entropic effect. Actually, all the cell components, which are very small, undergo unavoidably thermal and entropic effects that require explanations given by statistical mechanics [3] (chapter 1).

Typically, the mechanical response within a cell (that is a three-dimensional body), is ruled at the same time by the coexist of elements with a mainly linear structure (e.g. filaments and bundles of actin and microtubules) and curvilinear two-dimensional shell-structures (e.g. cell membrane or lipid rafts), that need to be opportune coordinate to well capture the phenomenology show by the experiments [3] (chapter 1). This makes the mechanical description of a cell extremely challenging.

Following we present a new theoretical scheme embedded in the continuum thermodynamics framework (chapter 6) and the corresponding numerical formulations, with the consequently co-designing of in-silico and in-vitro simulations (chapters 7 and 8). Nevertheless, it has to be clear that all the constitutive parameters as well as the best stoichiometric arrangement of reactions (4.1), (4.2), and (4.6) will be inherited from the previous Part of the thesis (chapters 4 and 5).

Chapter 6

A framework for modeling cells spreading, motility, and the relocation of proteins on advecting lipid membranes

The response of cells during spreading and motility is dictated by several multi-physics events, which are triggered by extracellular cues and occur at different time-scales. For this sake, it is not completely appropriate to provide a cell with classical notions of the mechanics of materials, as for "rheology" or "mechanical response". Rather, a cell is an alive system with constituents that show a reproducible response, as for the *contractility* for single stress fibers or for the mechanical response of a biopolymer actin network, but that reorganize in response to external cues in a non-exactly-predictable and reproducible way. Aware of such complexity, in this note we aim at formulating a multi-physics framework for modeling cell spreading and motility, accounting for the relocation of proteins on advecting lipid membranes.

Receptors dynamic along cell membrane is a key factor in several biological phenomena, as for angiogenesis, tumor metastasis, endocytosis, and exocytosis. Angiogenesis is a multistep process in which endothelial cells are affected by several extracellular stimuli, including growth factors, extracellular matrix, and parenchymal and stromal cells. In this process, growth factor receptors, as well as adhesion receptors, convey the extracellular signaling in a coordinate intracellular pathway promoting cell proliferation, migration, and their reorganization in active vessels [163]. Integrins are a family of cell adhesion receptors that support and modulate several cellular functions required for tumor metastasis. They can directly contribute to the control and progress of metastatic dissemination. During tumor development, changes in this family of receptors impact the ability of tumor cells to interact with their environment and enable metastatic cells to convert to a migratory and invasive phenotype. Integrins regulate each step of the metastasis and affect tumor cell survival and interaction with changing environments in transit from the primary tumor to distant target organs [164]. Receptor-mediated endocytosis is a process by which cells absorb metabolites, hormones, proteins, and, in some cases, viruses by the inward budding of the plasma membrane (invagination). This process forms vesicles containing the absorbed substances and is strictly mediated by receptors on the surface of the cell [165].

Whereas uncountable papers have been published on the biology of cells spreading, motility and, the relocation of proteins on advecting lipid membranes, the mathematical modeling definitely

lags behind experiments and overall received much less attention. Although nowadays widespread literature in mechanobiology exists [166], the relocation of proteins and their interaction with the reorganizing cytoskeleton in the biological phenomena mentioned above is still an ongoing research topic, let alone the formulation of efficient algorithms and computational solvers for three-dimensional simulations [167].
In this part of the thesis, we attempt at defining a multi-physics scheme for the modeling of cells spreading, motility, and the relocation of proteins on advecting lipid membranes, framing the mathematical setting within the mechanics and thermodynamics of continua [142], stemming from seminal works [106, 113, 119] and accounting for recent literature, either connected to the endocytosis of virus in human and animal cells [132, 130, 133] or ligand-receptor mediated raft formation [136], chemotaxis [137], surface-associated caveolae mechanotransduction [135].

The general framework illustrated in this part of the thesis applies to growth and remodeling, too, falling within the category of the theory of finite growth according to the terminology defined in [2]. The chapter is designed as follows. After a nomenclature of the main symbols and the definition of operators in a Lagrangian setting, we focus in section 6.2 on the relocation and reaction of receptors on a lipid membrane that advects. The topic is purposely presented in a broad sense, in order to be applicable to several possible receptors-ligands interactions: specific applications - carried out in [138], [140] and in the companion works embedded in the current work of thesis - deals with the relocation of vascular endothelial growth factor receptors and integrins during endothelial cell adhesion and spreading. In spite of the generality, section 6.2 is self-contained and includes the description of Reynold's theorem on a surface that advects, of the equations that rule proteins transport on an advecting lipid membrane, and eventually of the receptors-ligand interactions, in form of chemical reactions, that take place concurrently with relocation. A rather similar approach has been taken in section 6.3, which concerns the relocation and reaction of actin to form biopolymers within the cytosol. The mechanical evolution of the cell is discussed afterward in section 6.4: besides stating the classical balance laws (of linear and angular momentum), the section is accompanied by an extensive discussion on boundary conditions, aimed at showing that Neumann type of conditions, due to electrostatic interactions, are most likely not responsible for cell spreading and motion in view of the modest amount of energy involved in those interactions compared to the bulk energy of a cell. We concluded therefore that spreading is a result of extensional and contractile forces exerted by pseudopodia and the cytoskeleton machinery [97]. Those forces have been investigated further in section 6.5, where the thermodynamics of receptors' motion on the membrane was studied at first up to the constitutive theory and the kinetics of the receptors-ligand interaction. The analysis of the thermo-chemo-mechanics of cells is the last section of this work: in it, we highlight the role of strain and stress decompositions in order to model cell adhesion, protrusion, contractility.

Nomenclature

Notation

Vectors $\vec{a}$ will be denoted by an over-right-arrow, second-order tensors $\boldsymbol{A}, \boldsymbol{a}$ by bold face. This notation does not apply to operators.

Operators

- the symbol $\mathrm{tr}[-]$ denotes the trace operator
- the symbol $\mathrm{div}[-]$ denotes the divergence operator in the current configuration, i.e. $\mathrm{div}\left[\vec{f}\right] = \partial f_i/\partial x_i$
- the symbol $\mathrm{div}_{\mathcal{P}}[-]$ denotes the divergence operator restricted at the surface $\mathcal{P}$ in the current configuration
- the symbol $\mathrm{Div}[-]$ denotes the referential divergence operator, i.e. $\mathrm{Div}\left[\vec{f}\right] = \partial f_i/\partial X_i$
- the symbol $\mathrm{Div}_{\mathcal{P}_R}[-]$ denotes the referential divergence operator restricted at the surface $\mathcal{P}_{\mathcal{R}}$
- the symbol $\nabla[-]$ denotes the gradient operator in the current configuration
- the symbol $\nabla_{\mathcal{P}}[-]$ denotes the gradient operator restricted at the surface $\mathcal{P}$ in the current configuration
- the symbol $\mathrm{Grad}[-]$ denotes the referential gradient operator
- the symbol $\mathrm{Grad}_{\mathcal{P}_R}[-]$ denotes the referential gradient operator restricted at the surface $\mathcal{P}_{\mathcal{R}}$
- the symbol $\mathrm{curl}[-]$ denotes the curl operator in the current configuration
- the symbol $\mathrm{Curl}[-]$ denotes the curl operator in the referential configuration
- the symbol $\Delta[-]$ denotes the Laplace operator in the current configuration
- the symbol $\Delta_{\mathcal{P}}[-]$ denotes the Laplace operator restricted at the surface $\mathcal{P}$ in the current configuration
- the symbol $\bigtriangleup[-]$ denotes the Laplace operator in the referential configuration
- the symbol $\bigtriangleup_{\mathcal{P}_{\mathcal{R}}}[-]$ denotes the Laplace operator restricted at the surface $\mathcal{P}_{\mathcal{R}}$ in the referential configuration
- the symbol $\cdot$ denotes the single contraction of two vectors
- the symbol : denotes the double contraction of two tensors
- the symbol $\otimes$ denotes the tensor product between two vectors
- the symbol $\times$ denotes the vector or cross product between two vectors
- the symbols $||\vec{a}||^2$, $||\boldsymbol{A}||^2$ denote the squared norm of vector $\vec{a}$ or tensor $\boldsymbol{A}$
- the symbol ^{T} denotes transposition of a tensor
- the symbol $^{-1}$ denotes the inverse of a tensor

Variables and fields

- the symbol t denotes time
- the symbol $\Omega(t) \in \mathbb{R}^3$ denotes a volume that advects, where referential counterparts inherit the subscript $_R$
- the symbol $\partial\Omega(t)$ denotes the surface of $\Omega(t)$, where referential counterparts inherit the subscript $_R$
- the symbol $\mathcal{P}(t) \subset \partial\Omega(t)$ denotes a part of $\partial\Omega(t)$, where referential counterparts inherit the subscript $_R$
- the symbol $\partial\mathcal{P}(t)$ denotes the boundary of $\mathcal{P}(t)$, where referential counterparts inherit the subscript $_R$
- the symbol $\vec{v}_{adv}(\vec{x},t)$ denotes the velocity of advection at place $\vec{x}$ and time t
- the symbol $\vec{n}(\vec{x},t)$ denotes the outward normal at place $\vec{x}$ and time t
- the symbol $\vec{t}_{\perp}(\vec{x},t)$ denotes the normal to the curve $\partial\mathcal{P}(t)$ at a generic place $\vec{x}$ and time t

- the symbol $\vec{t}_{||}(\vec{x},t)$ denotes the vector tangent to the curve $\partial\mathcal{P}(t)$ at a generic place $\vec{x}$ and time t
- the symbol $\boldsymbol{l}(\vec{x},t)$ denotes the velocity gradient at place $\vec{x}$ and time t
- the symbol $\boldsymbol{d}(\vec{x},t)$ denotes the stretching at place $\vec{x}$ and time t
- the symbol $\boldsymbol{F}(\vec{X},t)$ denotes the deformation gradient at point $\vec{X}$ and time t
- the symbol $\boldsymbol{C}(\vec{X},t)$ denotes the right Cauchy-Green tensor at point $\vec{X}$ and time t
- the symbol $\boldsymbol{P}(\vec{X},t)$ denotes the first Piola stress tensor at point $\vec{X}$ and time t
- the symbol $J(\vec{X},t)$ denotes the determinant $\det[\boldsymbol{F}]$ at point $\vec{X}$ and time t
- the symbol $j(\vec{X},t)$ denotes the areal jacobian at point $\vec{X}$ and time t
- the symbol $\vec{n}_R(\vec{X},t)$ denotes the outward normal at point $\vec{X}$ and time t
- the symbol $\vec{t}(\vec{x},t)$ denotes the contact and surface forces acting on $\partial\Omega(t)$, where referential counterparts inherit the subscript $_R$
- the symbol $\vec{b}(\vec{x},t)$ denotes the body forces acting on $\Omega(t)$, where referential counterparts inherit the subscript $_R$
- the symbol $\mathbb{1}$ denotes the identity matrix

- the symbol m_e denotes the molar mass of a generic species e
- the symbol c_e denotes the molarity of a generic species e
- the symbol ρ_e denotes the density of a generic species e
- the symbol $\bar{s}_e$ denotes the mass supply of a generic species e
- the symbol s_e denotes the molar supply of a generic species e
- the symbol $\vec{\hbar}_e$ denotes the density flux of a generic species e
- the symbol $\vec{h}_e$ denotes the molar flux of a generic species e
- the symbol μ_e^u denotes the change in specific energy provided by a unit supply of moles of a generic species e
- the symbol μ_e^η denotes the change in specific entropy provided by a unit supply of moles of a generic species e
- the symbol μ_e denotes the chemical potential of a generic species e
- the symbol $c_e^{\max}$ denotes the saturation limit of a generic species e
- the symbol ϑ_e denotes the non-dimensional ratio between the concentration of a generic species e and $c_e^{\max}$
- the symbol w denotes the reaction rate of a reaction
- the symbol A denotes the affinity of a reaction
- the symbols k_f and k_b denote the kinetic constants of the forward and backward reaction
- the symbols $\Delta G^0(T)$ denotes the standard Gibbs free-energy of formation
- the symbols K_{eq} denotes the equilibrium constant

Constants and parameters

- the symbol R denotes the universal gas constant
- the symbol $\mathfrak{u}$ denotes the receptor mobility
- the symbol $\mathfrak{D}$ denotes the receptor diffusivity
- the symbol α denotes the infinitely fast kinetics parameter
- the symbol G denotes the bulk modulus for a regularized NeoHookean formulation
- the symbol κ denotes the shear modulus for a regularized NeoHookean formulation

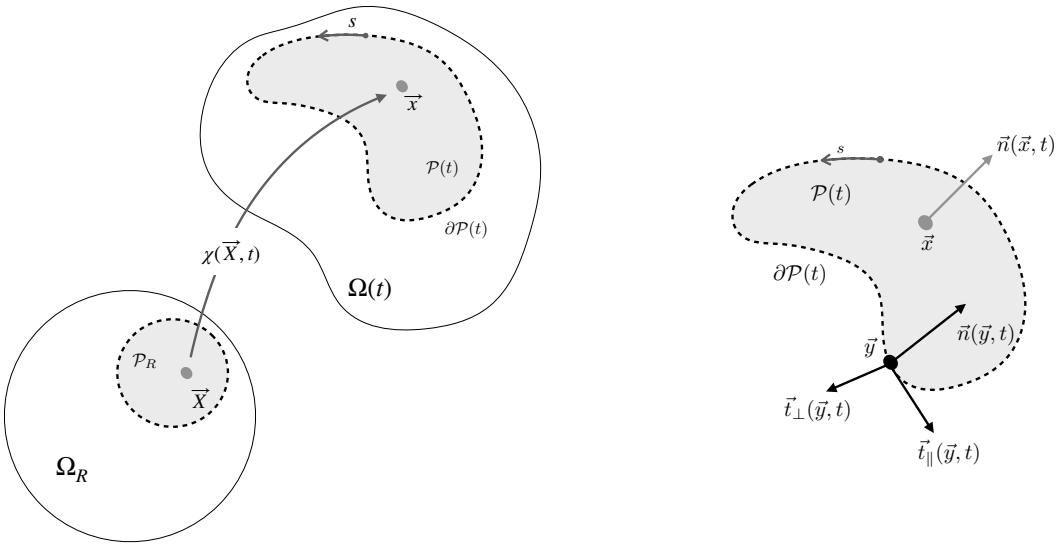

(a) (b)

Figure 6.1: Notation. (a) The reference body Ω_R and the deformed body $\Omega(t)$. Note that $\vec{x} \in \mathcal{P}(t)$ implies $\vec{X} \in \mathcal{P}_R$. (b) Frenet frame at point $\vec{y} \in \partial\mathcal{P}(t)$ and the normal vector $\vec{n}$ at point $\vec{x} \in \mathcal{P}(t)$.

6.1 Definitions

Denote with $\Omega(t)$ a volume that advects, and with $\partial\Omega(t)$ its surface. A spatial point $\vec{x} \in \Omega(t)$ is defined as the image of a (material) point $\vec{X}$ in a reference configuration Ω_R through a smooth function $\chi(\vec{X},t)$ termed *motion* [142]. Following [142] (page 61), we will name *deformation* the snapshot of a motion at a fixed time t:

$$\chi_t(\vec{X}) = \chi(\vec{X},t) \,.$$

The deformation is assumed to be a one-to-one map. In addition, denoting the deformation gradient with

$$\boldsymbol{F} = \mathrm{Grad}\,[\,\chi_t\,] \,,$$

the requirement $J = \det[\,\boldsymbol{F}\,] > 0$ holds. Define on the surface a part $\mathcal{P}(t) \subset \partial\Omega(t)$ as in Fig. 6.1a, and consider a scalar function $f(\vec{x},t)$ with $\vec{x} \in \mathcal{P}(t)$. Denote with

$$\vec{v}_{adv}(\vec{x},t) = \mathrm{d}\vec{x}/\mathrm{d}t$$

the velocity of advection at location $\vec{x}$ and time t; such a velocity has an arbitrary direction, i.e. it is not necessarily tangent to $\partial\Omega(t)$.

The *Frenet-Serret* reference frame at a generic point $\vec{y} \in \partial\mathcal{P}(t)$ is defined as in Fig. 6.1b, in terms of the two unit vectors $\vec{t}_\parallel(\vec{y},t)$ (tangent) and $\vec{t}_\perp(\vec{y},t)$ (normal). The vector $\vec{n}(\vec{y},t)$ (binormal) is here

taken of non-unit length, being the imagine in $\Omega(t)$ of a unit vector $\vec{n}_R$ in the reference configuration Ω_R, by means of the contravariant transformation

$$\vec{n} = \boldsymbol{F}^{-T}\,\vec{n}_R\,.$$

On the other hand, the following covariant transformations hold:

$$\vec{t}_{\parallel_R} = \boldsymbol{F}^{-1}\vec{t}_{\parallel}\,, \qquad \vec{t}_{\perp_R} = \boldsymbol{F}^{-1}\vec{t}_{\perp}\,,$$

with the obvious implication that $\vec{t}_{\parallel_R}$ and $\vec{t}_{\perp_R}$ are not unit vectors. The Frenet formulae holds, namely:

$$\kappa\,\vec{t}_{\perp} = -\frac{\partial \vec{t}_{\parallel}}{\partial s}\,, \qquad \tau\,\vec{t}_{\perp} = \frac{\partial}{\partial s}\left(\frac{\vec{n}}{|\vec{n}|}\right)\,, \qquad \kappa\,\vec{t}_{\parallel} - \tau\,\frac{\vec{n}}{|\vec{n}|} = \frac{\partial \vec{t}_{\perp}}{\partial s}\,,$$

where κ denotes the curvature and τ the torsion.

The *projected gradient operator* of a scalar field f on a surface $\mathcal{P}$ is defined as follows

$$\nabla_{\mathcal{P}}[f] = \nabla[f] - \frac{\vec{n}\cdot\nabla[f]}{|\vec{n}|^2}\,\vec{n}\,, \tag{6.1a}$$

in the current configuration, whereas in the reference configuration it reads

$$\mathrm{Grad}_{\mathcal{P}_R}[f] = \mathrm{Grad}[f] - \vec{n}_R\cdot\mathrm{Grad}[f]\,\vec{n}_R\,, \tag{6.1b}$$

The *projected divergence operator* of a vector field $\vec{v}$, which has an arbitrary direction, on a surface $\mathcal{P}$ is defined as follows

$$\mathrm{div}_{\mathcal{P}}[\vec{v}] = \mathrm{div}[\vec{v}] - \frac{\vec{n}\cdot\boldsymbol{l}\vec{n}}{|\vec{n}|^2}\,, \tag{6.2a}$$

$$\mathrm{Div}_{\mathcal{P}_R}[\vec{v}_R] = \mathrm{Div}[\vec{v}] - \vec{n}_R\cdot\mathrm{Grad}[\vec{v}_R]\vec{n}_R\,, \tag{6.2b}$$

in the current and reference configurations, respectively. Tensor $\boldsymbol{l}$ is the gradient of $\vec{v}$, $\boldsymbol{l} = \nabla[\vec{v}]$. Note that $\boldsymbol{l}$ in eq. (6.2a) can be replaced by its symmetric part $\boldsymbol{d} = \mathrm{sym}[\boldsymbol{l}]$, since for any skew-symmetric tensor $\boldsymbol{w}$ it holds $\vec{n}\cdot\boldsymbol{w}\vec{n} = 0$. Alternative forms for the projected divergence operators are

$$\mathrm{div}_{\mathcal{P}}[\vec{v}]\,\mathcal{P} = \mathrm{curl}\left[\frac{\vec{n}}{|\vec{n}|}\times\vec{v}\right]\cdot\frac{\vec{n}}{|\vec{n}|}\,, \qquad \mathrm{Div}_{\mathcal{P}_R}[\vec{v}] = \mathrm{Curl}\left[\frac{\vec{n}_R}{|\vec{n}_R|}\times\vec{v}_R\right]\cdot\frac{\vec{n}_R}{|\vec{n}_R|}\,. \tag{6.3a}$$

Provided sufficient smoothness, the divergence theorem holds also for advecting membranes, in the form:

$$\int_{\mathcal{P}(t)} \mathrm{div}_{\mathcal{P}}[\vec{g}]\,\mathcal{P}\,\mathrm{d}a = \int_{\partial\mathcal{P}(t)} \vec{g}\cdot\vec{t}_{\perp}\,\mathrm{d}\ell\,. \tag{6.4}$$

The proof of this theorem (see Appendix F.1), as well as for all other theorems not explicitly stated in this section, can be found in the Appendix F.

Moreover, we will make use of the following identity

$$\frac{\mathrm{d}\,J\sqrt{\vec{n}_R\cdot\boldsymbol{C}^{-1}\vec{n}_R}}{\mathrm{d}t} = J\,|\vec{n}|\,\left(\mathrm{div}[\vec{v}_{adv}] - \frac{\vec{n}\cdot\boldsymbol{d}\vec{n}}{|\vec{n}|^2}\right)\,, \tag{6.5a}$$

$$\nabla[f\,\vec{v}_{adv}] = \nabla[f]\otimes\vec{v}_{adv} + f\,\boldsymbol{l}\,, \tag{6.5b}$$

in deriving the Reynold's theorem on a surface that advects. The two identities which will be proved in Appendix F.2.

6.2 Relocation and reaction of receptors on a lipid membrane that advects

6.2.1 Reynold's theorem on a surface that advects

Reynold's theorem on $\mathcal{P}(t)$ reads as follows:

$$\frac{\mathrm{d}}{\mathrm{d}t}\int_{\mathcal{P}(t)} f\,\mathrm{d}a = \int_{\mathcal{P}(t)} \frac{\partial f}{\partial t} + \mathrm{div}_{\mathcal{P}}\left[f\,\vec{v}_{adv}\right]\,\mathrm{d}a\,, \tag{6.6}$$

where $\vec{v}_{adv}(\vec{x},t)$ is the velocity of advection at location $\vec{x}$ and time t.

Denote with $\vec{n}(\vec{x},t)$ the outward normal at point $\vec{x}$ and time t, and with $\boldsymbol{d}(\vec{x},t)$ the stretching (i.e. the symmetric part of the velocity gradient $\boldsymbol{l}(\vec{x},t)$) at point $\vec{x}$ and time t. Note that the point $\vec{x}$ is constrained to be in $\mathcal{P}(t)$ and similarly its reference counterpart, $\vec{X}$ is constrained to be in $\mathcal{P}_R$. Hence,

$$\frac{\mathrm{d}\,f(\vec{x},t)}{\mathrm{d}t} = \frac{\partial\, f(\vec{x},t)}{\partial t} + \nabla_{\mathcal{P}}\left[f(\vec{x},t)\right]\cdot\vec{v}_{adv}(\vec{x},t).$$

To prove eq. (6.6), denote with $\mathrm{d}a$ the infinitesimal area in $\mathcal{P}(t)$ and with $\mathrm{d}a_R$ its counterpart in the reference configuration $\mathcal{P}_R$. They are related by Nanson's formula

$$\mathrm{d}a = j\,\mathrm{d}a_R\,,$$

where [142, 168]:

$$j = J\,|\boldsymbol{F}^{-T}\vec{n}_R| = J\,\sqrt{\vec{n}_R\cdot\boldsymbol{C}^{-1}\vec{n}_R}\,. \tag{6.7}$$

Owing to eq. (6.5b), one writes

$$\begin{aligned}
\frac{\mathrm{d}}{\mathrm{d}t}\int_{\mathcal{P}(t)} f(\vec{x},t)\,\mathrm{d}a &= \frac{\mathrm{d}}{\mathrm{d}t}\int_{\mathcal{P}_R} f(\varphi(\vec{X},t),t)\,J\sqrt{\vec{n}_R\cdot\boldsymbol{C}^{-1}\vec{n}_R}\,\mathrm{d}a_R\\
&= \int_{\mathcal{P}_R}\frac{\mathrm{d}\,f(\varphi(\vec{X},t),t)}{\mathrm{d}t}\,J\sqrt{\vec{n}_R\cdot\boldsymbol{C}^{-1}\vec{n}_R}\,\mathrm{d}a_R + \int_{\mathcal{P}_R} f(\varphi(\vec{X},t),t)\frac{\mathrm{d}\,J\sqrt{\vec{n}_R\cdot\boldsymbol{C}^{-1}\vec{n}_R}}{\mathrm{d}t}\,\mathrm{d}a_R\\
&= \int_{\mathcal{P}(t)}\frac{\mathrm{d}\,f(\vec{x},t)}{\mathrm{d}t}\,\mathrm{d}a + \int_{\mathcal{P}_R} f(\varphi(\vec{X},t),t)\frac{\mathrm{d}\,J\sqrt{\vec{n}_R\cdot\boldsymbol{C}^{-1}\vec{n}_R}}{\mathrm{d}t}\,\mathrm{d}a_R\\
&= \int_{\mathcal{P}(t)}\frac{\partial\, f(\vec{x},t)}{\partial t} + \nabla_{\mathcal{P}}\left[f(\vec{x},t)\right]\cdot\vec{v}_{adv}(\vec{x},t)\,\mathrm{d}a + \int_{\mathcal{P}_R} f(\varphi(\vec{X},t),t)\,J\,|\vec{n}|\,\left(\mathrm{div}\left[\vec{v}_{adv}\right] - \frac{\vec{n}\cdot\boldsymbol{d}\vec{n}}{|\vec{n}|^2}\right)\mathrm{d}a_R\\
&= \int_{\mathcal{P}(t)}\frac{\partial\, f(\vec{x},t)}{\partial t} + \nabla_{\mathcal{P}}\left[f(\vec{x},t)\right]\cdot\vec{v}_{adv}(\vec{x},t) + f(\vec{x},t)\,\mathrm{div}\left[\vec{v}_{adv}(\vec{x},t)\right]\,\mathrm{d}a\,,
\end{aligned}$$

whence eq. (6.6) comes out.

By taking $f = 1$, eq. (6.6) depicts the area evolution of $\mathcal{P}(t)$ as

$$\frac{\mathrm{d}}{\mathrm{d}t}\int_{\mathcal{P}(t)}\mathrm{d}a = \int_{\mathcal{P}(t)}\mathrm{div}_{\mathcal{P}}\left[\vec{v}_{adv}\right]\,\mathrm{d}a\,.$$

It is intuitive that advection with velocity in the tangent plane has the capacity of modifying the surface area, however this property is not restricted to tangent advection. In other words, even

$\vec{v}_{adv}(\vec{x},t) \propto \vec{n}(\vec{x},t)$ can alter the surface, as for the homothetic expansion of a rubber balloon. Reynold's theorem (6.6) can be also restated as

$$\frac{\mathrm{d}}{\mathrm{d}t}\int_{\mathcal{P}(t)} f(\vec{x},t)\,\mathrm{d}a = \int_{\mathcal{P}(t)} \frac{\mathrm{d}\,f(\vec{x},t)}{\mathrm{d}t} + f(\vec{x},t)\,\mathrm{div}_{\mathcal{P}}\left[\vec{v}_{adv}\right]\,\mathrm{d}a\,. \tag{6.8}$$

and is a restriction on surfaces of the classical Reynold's transport relation on volumes (see [142], section 16 among others).

6.2.2 Mass transport on a surface that advects

6.2.2.1 Mass balance in the current configuration for a convecting species

Consider a generic species a at a point $\vec{x}$ on the surface $\partial\Omega(t)$. Species a convects with velocity $\vec{v}_a(\vec{x},t)$. The latter entails the dragging, or advection, velocity $\vec{v}_{adv}(\vec{x},t)$ and another velocity that is due to many possible physics, as for diffusion or migration. If *internalization of species from the membrane* is not allowed, the net velocity $\vec{v}_a - \vec{v}_{adv}$ lays in the tangent plane of the membrane and

$$(\vec{v}_a - \vec{v}_{adv})\cdot\vec{n} = 0\,. \tag{6.9}$$

Since species are modeled on a membrane, which is a two-dimensional manifold, the surface density ρ_a of species a measures the mass of the species per unit surface. The *density* flux vector of species a, denoted with $\vec{\hbar}_a$, is the product of the surface density times the net velocity of species a, i.e.

$$\vec{\hbar}_a = \rho_a\,(\vec{v}_a - \vec{v}_{adv})\,. \tag{6.10}$$

Define on the surface a part $\mathcal{P}(t) \subset \partial\Omega(t)$ as in Fig. 6.1. The flux of species a across the boundary $\partial\mathcal{P}(t)$ is

$$\int_{\partial\mathcal{P}(t)} \vec{\hbar}_a\cdot\vec{t}_{\perp}\,\mathrm{d}\ell$$

and the mass balance of species a in the advecting configuration $\mathcal{P}(t)$ reads

$$\frac{\mathrm{d}}{\mathrm{d}t}\int_{\mathcal{P}(t)} \rho_a(\vec{x},t)\,\mathrm{d}a + \int_{\partial\mathcal{P}(t)} \vec{\hbar}_a\cdot\vec{t}_{\perp}\,\mathrm{d}\ell = \int_{\mathcal{P}(t)} \bar{s}_a(\vec{x},t)\,\mathrm{d}a\,, \tag{6.11}$$

where $\bar{s}_a(\vec{x},t)$ is the surface mass supply[1] of species a. By means of the divergence theorem (6.4) and of Reynold's transport theorem in the form (6.8), balance law (6.11) becomes

$$\int_{\mathcal{P}(t)} \frac{\mathrm{d}\rho_a}{\mathrm{d}t} + \rho_a\,\mathrm{div}_{\mathcal{P}}\left[\vec{v}_{adv}\right] + \mathrm{div}_{\mathcal{P}}\left[\vec{\hbar}_a\right]\,\mathrm{d}a = \int_{\mathcal{P}(t)} \bar{s}_a(\vec{x},t)\,\mathrm{d}a\,.$$

Since it holds for all $\mathcal{P}(t)$, it eventually localizes as

$$\frac{\mathrm{d}\rho_a}{\mathrm{d}t} + \rho_a\,\mathrm{div}_{\mathcal{P}}\left[\vec{v}_{adv}\right] + \mathrm{div}_{\mathcal{P}}\left[\vec{\hbar}_a\right] = \bar{s}_a(\vec{x},t)\,. \tag{6.12}$$

This formulation of the mass conservation law has been considered also in [169]. The mass balance can be finally written in terms of surface molarity c_a (in moles or molecules per unit surface), by division by the molar or molecular mass (m_a) of species a. By denoting with $c_a = \rho_a/m_a$, $s_a = \bar{s}_a/m_a$, and $\vec{h}_a = \vec{\hbar}_a/m_a$ the local balance (6.12) becomes

$$\frac{\mathrm{d}c_a}{\mathrm{d}t} + c_a\,\mathrm{div}_{\mathcal{P}}\left[\vec{v}_{adv}\right] + \mathrm{div}_{\mathcal{P}}\left[\vec{h}_a\right] = s_a(\vec{x},t)\,. \tag{6.13}$$

[1] As an example, in biology cells may produce proteins that move to the lipid membranes from the cytosol.

6.2.2.2 Mass balance in the reference configuration for a convecting species

The mass balance (6.13) can be rephrased in the reference configuration at point $\vec{X}$ and time t. To this aim, define the reference molarity of species a as

$$c_{a_R}(\vec{X},t) = c_a(\vec{x}(\vec{X},t),t)\; j(\vec{X},t)\;, \tag{6.14}$$

the reference flux vector $\vec{h}_{a_R}(\vec{X},t)$ and the reference mass supply $s_{a_R}(\vec{X},t)$ as

$$\vec{h}_{a_R} = j\boldsymbol{F}^{-1}\,\vec{h}_a(\vec{x}(\vec{X},t),t)\;, \qquad s_{a_R} = j\,s_a(\vec{x}(\vec{X},t),t)\;, \tag{6.15}$$

respectively, where [142, 168]:

$$j = J\,|\boldsymbol{F}^{-T}\vec{n}_R| = J\,\sqrt{\vec{n}_R\cdot\boldsymbol{C}^{-1}\vec{n}_R}\;. \tag{6.16}$$

The referential form of the mass balance (6.13) can be derived from the mass balance in the form (6.11), and reads

$$\frac{\partial c_{a_R}}{\partial t} + \mathrm{Div}_{\mathcal{P}_R}\left[\vec{h}_{a_R}\right] = s_{a_R}\;. \tag{6.17}$$

To prove eq. (6.17), consider the mass balance in the form (6.11), yet written in terms of molarity:

$$\frac{\mathrm{d}}{\mathrm{d}t}\int_{\mathcal{P}(t)} c_a(\vec{x},t)\,\mathrm{d}a + \int_{\partial\mathcal{P}(t)} \vec{h}_a\cdot\vec{t}_\perp\,\mathrm{d}\ell = \int_{\mathcal{P}(t)} s_a(\vec{x},t)\,\mathrm{d}a\;, \tag{6.18}$$

and make use of Nanson's formula to write

$$\frac{\mathrm{d}}{\mathrm{d}t}\int_{\mathcal{P}(t)} c_a(\vec{x},t)\,\mathrm{d}a = \frac{\mathrm{d}}{\mathrm{d}t}\int_{\mathcal{P}} c_a(\vec{X},t)\,j(\vec{X},t)\,\mathrm{d}a_R = \int_{\mathcal{P}}\frac{\partial}{\partial t}\,c_{a_R}(\vec{X},t)\,\mathrm{d}a_R\;,$$

it will be proved in Appendix F.3 that it holds:

$$\vec{h}_a\cdot\vec{t}_\perp\,\mathrm{d}\ell = \vec{h}_{a_R}\cdot\vec{t}_{\perp_R}\,\mathrm{d}\ell_R\;, \tag{6.19}$$

whence the mass balance in the form (6.18) writes in the reference configuration as

$$\int_{\mathcal{P}}\frac{\partial c_{a_R}}{\partial t}\,\mathrm{d}a_R + \int_{\partial\mathcal{P}}\vec{h}_{a_R}\cdot\vec{t}_{\perp_R}\,\mathrm{d}\ell_R = \int_{\mathcal{P}} s_{a_R}\,\mathrm{d}a_R\;. \tag{6.20}$$

By means of the divergence theorem (6.4), the latter becomes

$$\int_{\mathcal{P}}\frac{\partial c_{a_R}}{\partial t} + \mathrm{Div}_{\mathcal{P}_R}\left[\vec{h}_{a_R}\right]\mathrm{d}a_R = \int_{\mathcal{P}} s_{a_R}\,\mathrm{d}a_R$$

and since it holds for all $\mathcal{P}$, it eventually localizes as eq. (6.17).

6.2.3 Relocation and reaction

A two-steps mechanism defines the process of combination and generation of a protein complex. The first stage wherein the formation of an encounter complex happens, namely where free proteins show few specific interactions and assume many orientations. Whereupon, a second phase in which the formation of the final complex takes place. It has to be clear that the electrostatic interactions predominantly govern the encounter complex; importantly, if the orientations of the reactants are perfectly matched, the final complex is formed, vice-versa if this does not occur, proteins come back to be free [170, 171].

The two steps mechanism which describes the formation of a protein complex reads:

$$\mathrm{R}+\mathrm{L}\underset{k_{-1}}{\overset{k_1}{\rightleftarrows}}\mathrm{C}^*\underset{k_{-2}}{\overset{k_2}{\rightleftarrows}}\mathrm{C}\,, \tag{6.21}$$

where R and L are the receptors (R) and ligands (L) free proteins, C^* represents the encounter complex and C is the final complex. In eq. (6.21), k_1 and k_{-1} are the rate of formation and dissolution of the encounter complex, C^*, whereas k_2 and k_{-2} are the forward and reverse rate constants for formation of the final complex, C, from C^*.

Assuming that the formation of the encounter complex occurs whenever R and L are separated by an encounter distance smaller than r, then $k_1 = 2Q[D(\mathrm{R})+D(\mathrm{L})]$, $k_{-1} = 2[D(\mathrm{R})+D(\mathrm{L})]r^{-2}$. Here $D(\mathrm{R})$ and $D(\mathrm{L})$ are the translational diffusion constants for protein motion in the membrane and the equilibrium constant for the encounter step, $K_d = Qr^2$, represents the area of a disk of radius r [107]. If the concentration of C^* is smaller than the concentration of free proteins or final complexes, it is a good approximation to set $\mathrm{d}C^*/\mathrm{d}t = 0$, leading to the binding-unbinding interaction

$$\mathrm{R}+\mathrm{L}\underset{k_b}{\overset{k_f}{\rightleftarrows}}\mathrm{C}\,, \tag{6.22}$$

most commonly used [107]. A similar approach has been taken in [138, 139] for the relocation of VEGFR-2 receptors and in [140] for integrins. Coefficients k_f and k_b are the kinetic constants of the forward and backward reactions, respectively. The rate of reaction (6.22), denoted with $w^{(6.22)}$and measured in $[\frac{mol}{m^2 s}]$, quantifies the net formation of (C) on the advecting membrane as the difference between the forward and backward reactions. Equation (6.17) shall be extended to account for the reaction (6.22) and tailored to species $a = R, L, C$.

Receptors (either free or bound into the complex) are distributed along the membrane together with other lipid species and proteins. They are assumed to freely move laterally, effects due to steric hindrance are not accounted for. The amount of proteins per unit area that can be placed at a membrane location $\vec{x}$ is thus limited by the actual size of the protein itself. This evidence ushers the definition of a saturation limit for the species, $c_a^{max}(\vec{x},t)$.

During their life, cells and their membranes undergo major *macroscopic* mechanical deformations. Studies on the red blood cell [172] suggest that the membrane deformation occur at constant area,

but this evidence does not appear to be supported by experiments in endothelial cells during spreading [97]. Individual protein and phospholipid can easily move laterally within the membrane, which results in a very low shear stiffness. The *fluid mosaic model* [20] captures this evidence, adding a questionable high resistance to areal expansion. Indeed the mechanisms that are in charge of areal expansion during cell spreading are complex and involve the micro-structural topology[2] of the membrane (as for flattening of invaginated membrane domains [173], i.e. the role of the caveole as membrane surface repository readily made available for fast geometrical evolution as during filopodia extension). The structure of the lipid membranes, however, induce to suppose that the saturation concentration $c_a^{max}(\vec{x},t)$, i.e. the maximum number of moles or molecules per unit area for any species a, remains unchanged in time in the current configuration. This choice in turn entails that the number of moles or molecules per unit area in the reference configuration is not constant and evolves in time following eq. (6.14), i.e.

$$c_{a_R}^{max}(\vec{X},t) = c_a^{max}(\vec{x}(\vec{X},t),t)\, j(\vec{X},t)\ . \tag{6.23}$$

Accordingly, the value of the non-dimensional ratio between the concentration of species a and its amount c_a^{max} at saturation,

$$\vartheta_a = c_a / c_a^{max} \tag{6.24}$$

in the current configuration remains unchanged in the reference configuration

$$\vartheta_{a_R}(\vec{X},t) = \vartheta_a(\vec{x},t)\ . \tag{6.25}$$

The kinetics of reaction (6.22) is modeled as for ideal systems via the law of mass action [144]

$$w^{(6.22)} = k_f \frac{\vartheta_L}{(1-\vartheta_L)} \frac{\vartheta_R}{(1-\vartheta_R)} - k_b \frac{\vartheta_C}{(1-\vartheta_C)}\ . \tag{6.26}$$

At chemical equilibrium, as $w^{(6.22)} = 0$, the concentrations obey the relation

$$\frac{k_f}{k_b} = \frac{\vartheta_C^{\rm eq}}{(1-\vartheta_C^{\rm eq})} \frac{(1-\vartheta_R^{\rm eq})}{\vartheta_R^{\rm eq}} \frac{(1-\vartheta_L^{\rm eq})}{\vartheta_L^{\rm eq}} = K_{\rm eq}^{(6.22)} \tag{6.27}$$

which defines the constant of equilibrium $K_{\rm eq}^{(6.22)}$ of reaction (6.22).

Far from the saturation limit, $(1-\vartheta_a) \sim 1$ for all a. Accordingly, the mass action law (6.26) simplifies as

$$w^{(6.22)} = \tilde{k}_f\, c_L\, c_R - \tilde{k}_b\, c_C \tag{6.28}$$

once the new constants

$$\tilde{k}_f = k_f (c_L^{max} c_R^{max})^{-1}\ , \qquad \tilde{k}_b = k_b (c_C^{max})^{-1}$$

are defined.

The diffusion of receptors and the viscous evolution of the cell during adhesion and migration appear to be much slower than the interaction kinetics, i.e. the time required to reach chemical

[2] Multiscale investigations, however, fall out of the scope of the present thesis.

equilibrium is orders of magnitude smaller than the time-scale of other processes. For this reason, thermodynamic equilibrium may be invoked in place of a transient evolution, thus inferring the constraint $w^{(6.22)} = 0$ to the concentrations of species at all times. Far from saturation, equating (6.28) to zero implies that

$$c_C = \frac{c_R\, c_L}{\alpha}\,, \tag{6.29}$$

having denoted with α the following constant:

$$\alpha = \frac{\tilde{k}_b}{\tilde{k}_f} = \frac{c_R^{max}\, c_L^{max}}{c_C^{max}}\, \frac{1}{K_{\text{eq}}^{(6.22)}}\,. \tag{6.30}$$

In view of identity (6.29), the two concentrations c_R and c_L describe the problem in full, and the concentration of the complex can be deduced a posteriori.

In vivo experiments show that the complex molecules usually have a much smaller mobility than receptors, perhaps induced by their size. For in vitro experiments [138, 139, 140], ligands are prevented to flow onto the substrate: given that complex molecules result from the interaction with immobile ligands, they are macroscopically steady as well. Since receptors move along the membrane, reaction (6.22) traps mobile receptors and vice-versa [141]. In this work, analogously to [114] and what has been done in the previous part of the thesis, ligands and complex are assumed to be motionless, i.e.

$$\vec{h}_L = \vec{h}_C = \vec{0}\,. \tag{6.31}$$

The reaction rate $w^{(6.22)}(\vec{x},t)$, being a mass supply, shall transform as $s_a(\vec{x},t)$ according to eq. (6.15). The invariance of ϑ_a with the configuration and the analysis of the mass action law (6.26) imply that the forward and backward "constants", which encompass the dimensionality of $w^{(6.22)}(\vec{x},t)$, are not actually constants in the reference configuration. They rather change with time and with point $\vec{X}$ according to

$$k_{f_R}(\vec{X},t) = j(\vec{X},t)\, k_f\,, \qquad k_{b_R}(\vec{X},t) = j(\vec{X},t)\, k_b \tag{6.32}$$

with $j(\vec{X},t)$ as in (6.16). The equilibrium constant in the reference configuration, being the ratio of k_{f_R} and k_{b_R} remains independent upon the configuration. Eventually, the mass action law (6.26) in the reference configuration writes

$$w_R^{(6.22)} = k_{f_R}\, \frac{\vartheta_L}{(1-\vartheta_L)}\, \frac{\vartheta_R}{(1-\vartheta_R)} - k_{b_R}\, \frac{\vartheta_C}{(1-\vartheta_C)}\,. \tag{6.33}$$

In view of all considerations made so far, the local form (6.17) of the mass balance specify as follows (omitting the dependency upon $\vec{X}$ and t):

$$\frac{\partial c_{R_R}}{\partial t} + \text{Div}_{\mathfrak{P}_R}\left[\vec{h}_{R_R}\right] + w_R^{(6.22)} = s_{R_R}\,, \tag{6.34a}$$

$$\frac{\partial c_{L_R}}{\partial t} + w_R^{(6.22)} = 0\,, \tag{6.34b}$$

$$\frac{\partial c_{C_R}}{\partial t} - w_R^{(6.22)} = 0\,. \tag{6.34c}$$

Equation (6.34a) is defined on the membrane surface $\partial\Omega_R$, where the receptors flow. The supply s_{R_R} accounts for internalization or generation of proteins: it is the amount of receptors that are generated within the cell and reach the membrane or that internalize. It can be related to the change in the membrane area through a parameter κ_{R_R} as

$$\begin{aligned} s_{R_R}(\vec{X},t) &= \kappa_{R_R}\frac{\partial j}{\partial t} \\ &= \kappa_{R_R}\left[\,|\boldsymbol{F}^{-T}\vec{n}_R|J\,\mathrm{tr}\,[\boldsymbol{l}] - \frac{J}{2}\frac{1}{|\boldsymbol{F}^{-T}\vec{n}_R|}\,\vec{n}_R\cdot\boldsymbol{C}^{-1}\frac{\partial \boldsymbol{C}}{\partial t}\boldsymbol{C}^{-1}\vec{n}_R\right]. \end{aligned} \tag{6.35}$$

At all points at which ligands and receptors do not interact, the reaction rate $w_R^{(6.22)}$ vanishes. Equation (6.34b) is rather defined in the location where ligands stand. In vitro, a given amount of ligands (which can be thought of as the initial condition of eq. (6.34b) are spread upon a microscope slide. Finally, eq. (6.34c) is defined in the contact zone between the cell and the slide where reaction (6.22) takes place.

It is convenient to rephrase eq. (6.34b) in terms of the "ligands made available for the reaction" in place of the "ligands spread on the slide". The former ligands are the ones "felt" at a point on the membrane as the distance from such a point and the substrate, where ligands are spread out, becomes sufficiently small.
Such a distance can be understood as a cutoff, within which the formation of an encounter complex, C^*, becomes possible as a consequence of diffusion, as made clear in [170, 171, 107, 174]. Despite the size of the cutoff distance remains inaccurately estimated, it was established to be on the order of tens nanometers [107, 106]. It arises form the interplay of attractive and repulsive forces between either two cells or a cell and a substrate. Indeed, negative electrical charge carried by cells generates repulsive electrostatic forces - *repulsive barrier* - which is further enriched by an additional resistance provided by the compression of the glycocalyx proteins. Rather, electrodynamic van der Waals forces are expected to be attractive [107]. Both van der Waals and compressive forces are characterized as non-specific long ranged forces, whereas cell adhesion is generally mediated by the specific short ranged receptor-ligand interactions, which can cause cell adhesion much more tightly than the non-specific electrical forces [107, 114]. Cells separated by a distance less than, or equal to, the cutoff distance should form a zone of adhesion with the substrate by means of local fluctuations in receptors density, so that small regions of increased density can penetrate through the resisting potential to react with the source of ligands on substrate [106].
This point of view, which corresponds to the picture of tight receptor-ligand bond as a set of weak non covalent physical interactions [175], is made explicit by a supply function s_{L_R}, that vanishes at long ranges and rapidly reaches the initial concentration of ligands available for the reaction at short distances

$$\frac{\partial c_{L_R}}{\partial t} + w_R^{(6.22)} = s_{L_R}\,. \tag{6.36}$$

The ligand supply $s_{L_R}(\vec{X},t)$ becomes available for the reaction during the spreading of the cell. It seems to be logically related to: i) a gap function between the substrate rich in ligands and the cell membrane *in the current configuration*; ii) a lag in time, namely a point-wise function of an internal variable that activates when the gap function is below some threshold and is related to the chemical kinetics of the binding-unbinding reaction (6.22). In this form, all three equations (6.34a), (6.34c), (6.36) can be written on the membrane $\vec{X}\in\partial\Omega_R$.

Assuming that the time scale of the chemical reaction is much faster than other processes, the concentrations of species may be governed by thermodynamic equilibrium at all times. The concentration of complex c_{C_R} relates then to the others by the equation $w^{(6.22)} = 0$, which leads to eq. (6.29) in the current configuration. Making use of mapping (6.14), eq. (6.29) relates the concentration of complex in the reference configuration c_{C_R} to the concentration of ligands and receptors in the same configuration c_{L_R}, c_{R_R} as follows

$$c_{C_R} = \frac{c_{R_R}\, c_{L_R}}{\alpha_R(\vec{X},t)}\,, \qquad \alpha_R(\vec{X},t) = \alpha\, j(\vec{X},t)\,, \tag{6.37a}$$

with constant α defined in eq. (6.30). Transformation (6.37a) is consistent with the assumption (6.23) made on how saturations transform.

In conclusion, exploiting identity (6.37a), the two concentrations c_{R_R} and c_{L_R} fully describe the problem in the assumption of infinitely fast kinetics, whereas the concentration of the complex can be deduced a posteriori. The two governing equations descend from eqs. (6.34) and read:

$$\frac{\partial c_{R_R}}{\partial t} + \frac{\partial c_{C_R}}{\partial t} + \mathrm{Div}_{\mathcal{P}_R}\left[\vec{h}_{R_R}\right] = s_{R_R}\,, \qquad \vec{X} \in \partial\Omega_R\,, \tag{6.37b}$$

$$\frac{\partial c_{L_R}}{\partial t} + \frac{\partial c_{C_R}}{\partial t} = s_{L_R}\,, \qquad \vec{X} \in \partial\Omega_R\,. \tag{6.37c}$$

Equations (6.37), with associated initial conditions

$$c_{R_R}(\vec{X},0) = c^0_{R_R}(\vec{X})\,, \qquad c_{L_R}(\vec{X},0) = 0\,, \qquad c_{C_R}(\vec{X},0) = 0$$

and Dirichlet-Neumann boundary conditions define the relocation of receptors that undergo binding-unbinding reactions on the reference configuration of a membrane that advects. These are balance equations and as such hold for any constitutive behavior for the mass flux. These equations are *coupled to the mechanical evolution of the cell* (i.e. adhesion, spreading, migration) through the function $s_{L_R}(\vec{X},t)$, which "transfers" ligands on the membrane according to the geometry of the cell.
Generation and/or internalization phenomena of receptors are taking into account by means of the mass supply $s_{R_R}(\mathbf{X},t)$. $s_{R_R}(\mathbf{X},t)$, it can be related to the change in the membrane area through a parameter κ_{R_R} as:

$$s_{R_R}(\mathbf{X},t) = \kappa_{R_R}\frac{\partial j}{\partial t}\,. \tag{6.38}$$

Now we study the expression $\dfrac{\partial j}{\partial t}$ where $j = |\mathbf{F}^{-T}\mathbf{n}_R|J$.

$$\frac{\partial j}{\partial t} = \frac{\partial |\mathbf{n}|}{\partial t}J + |\mathbf{n}|\frac{\partial J}{\partial t}\,. \tag{6.39}$$

From F.19:

$$\frac{d\left[J\sqrt{\mathbf{n}_R\cdot\mathbf{C}\mathbf{n}_R}\right]}{dt} = J|\mathbf{n}|\left[\mathrm{div}\,(\mathbf{v}_b) - \frac{\mathbf{n}\cdot(\mathbf{dn})}{|\mathbf{n}|^2}\right]\,. \tag{6.40}$$

We know that:

$$\begin{gathered}\mathbf{C}=\mathbf{F}^T\mathbf{F}\quad \mathbf{C}^{-1}=\mathbf{F}^{-1}\mathbf{F}^{-T}\\ \mathbf{l}=\dot{\mathbf{F}}\mathbf{F}^{-1}\quad \mathbf{l}^T=\mathbf{F}^{-T}\dot{\mathbf{F}}^T\\ \frac{\partial\mathbf{C}^{-1}}{\partial t}=-\mathbf{C}^{-1}\frac{\partial\mathbf{C}}{\partial t}\mathbf{C}^{-1}\\ \mathbf{n}\cdot(\mathbf{dn})=\mathbf{n}^T\mathbf{dn}=\left(\mathbf{F}^{-T}\mathbf{n}_R\right)^T\mathbf{d}\left(\mathbf{F}^{-T}\mathbf{n}_R\right)=\mathbf{n}_R^T\mathbf{F}^{-1}\mathbf{dF}^{-T}\mathbf{n}_R\end{gathered}\tag{6.41}$$

Now we want to proof that $\mathbf{F}^{-1}\mathbf{dF}^{-T}=\frac{1}{2}\mathbf{C}^{-1}\frac{\partial\mathbf{C}}{\partial t}\mathbf{C}^{-1}$.

$$\begin{gathered}\frac{1}{2}\mathbf{C}^{-1}\frac{\partial\mathbf{C}}{\partial t}\mathbf{C}^{-1}=\frac{1}{2}\mathbf{F}^{-1}\mathbf{F}^{-T}\left(\dot{\mathbf{F}}^T\mathbf{F}+\mathbf{F}^T\dot{\mathbf{F}}\right)\mathbf{F}^{-1}\mathbf{F}^{-T}=\\ =\frac{1}{2}\mathbf{F}^{-1}\mathbf{F}^{-T}\dot{\mathbf{F}}^T\underbrace{\mathbf{F}\mathbf{F}^{-1}}_{\mathbf{I}}\mathbf{F}^{-T}+\frac{1}{2}\mathbf{F}^{-1}\underbrace{\mathbf{F}^{-T}\mathbf{F}^T}_{\mathbf{I}}\dot{\mathbf{F}}\mathbf{F}^{-1}\mathbf{F}^{-T}=\\ =\frac{1}{2}\mathbf{F}^{-1}\underbrace{\mathbf{F}^{-T}\dot{\mathbf{F}}^T}_{\mathbf{l}^T}\mathbf{F}^{-T}+\frac{1}{2}\mathbf{F}^{-1}\underbrace{\dot{\mathbf{F}}\mathbf{F}^{-1}}_{\mathbf{l}}\mathbf{F}^{-T}=\mathbf{F}^{-1}\underbrace{\frac{1}{2}\left(\mathbf{l}^T+\mathbf{l}\right)}_{\mathbf{d}}\mathbf{F}^{-T}=\mathbf{F}^{-1}\mathbf{dF}^{-T}\end{gathered}\tag{6.42}$$

$$\begin{gathered}\frac{d\left[J\sqrt{\mathbf{n}_R\cdot\mathbf{C}\mathbf{n}_R}\right]}{dt}=J|\mathbf{n}|\ \mathrm{div}\ (\mathbf{v}_b)-J\frac{\mathbf{n}\cdot(\mathbf{dn})}{|\mathbf{n}|}=\\ =J|\mathbf{F}^{-T}\mathbf{n}_R|\ \mathrm{div}\ (\mathbf{v}_b)-\frac{J}{|\mathbf{F}^{-T}\mathbf{n}_R|}\mathbf{n}\cdot(\mathbf{dn})=\\ =J|\mathbf{F}^{-T}\mathbf{n}_R|\ \mathrm{div}\ (\mathbf{v}_b)-\frac{J}{|\mathbf{F}^{-T}\mathbf{n}_R|}\frac{1}{2}\mathbf{n}_R\cdot\mathbf{C}^{-1}\frac{\partial\mathbf{C}}{\partial t}\mathbf{C}^{-1}\mathbf{n}_R=\\ J|\mathbf{F}^{-T}\mathbf{n}_R|\underbrace{\mathrm{div}\ (\mathbf{v}_b)}_{Tr(\mathbf{l})}-\frac{J}{2|\mathbf{F}^{-T}\mathbf{n}_R|}\mathbf{n}_R\cdot\mathbf{C}^{-1}\frac{\partial\mathbf{C}}{\partial t}\mathbf{C}^{-1}\mathbf{n}_R\end{gathered}\tag{6.43}$$

$$\begin{aligned}s_{R_R}(\mathbf{X},t)&=\kappa_{R_R}\frac{\partial j}{\partial t}\\ &=\kappa_{R_R}\left[J|\mathbf{F}^{-T}\mathbf{n}_R|Tr(\mathbf{l})-\frac{J}{2|\mathbf{F}^{-T}\mathbf{n}_R|}\mathbf{n}_R\cdot\mathbf{C}^{-1}\frac{\partial\mathbf{C}}{\partial t}\mathbf{C}^{-1}\mathbf{n}_R\right]\end{aligned}\tag{6.44}$$

$$s_R=\kappa_R\frac{\partial j}{\partial t}=\kappa_R\left[J|\mathbf{F}^{-T}\mathbf{n}_R|Tr(\mathbf{l})-\frac{J}{2|\mathbf{F}^{-T}\mathbf{n}_R|}\mathbf{n}_R\cdot\mathbf{C}^{-1}\frac{\partial\mathbf{C}}{\partial t}\mathbf{C}^{-1}\mathbf{n}_R\right]\tag{6.45}$$

where we know: $s_{R_R}=s_R J|\mathbf{F}^{-T}\mathbf{n}_R|$.
Thanks to the (6.37a) two governing equations descend from (6.37) and read:

$$\begin{aligned}&\frac{\partial c_{R_R}}{\partial t}+\mathrm{Div}_{\mathcal{P}_R}\left[\mathbf{h}_{R_R}\right]+\frac{\partial c_{C_R}}{\partial t}=s_{R_R}\,,\\ &\frac{\partial c_{L_R}}{\partial t}+\frac{\partial c_{C_R}}{\partial t}=s_{L_R}\,.\end{aligned}\tag{6.46}$$

Now we wanto to evalueted the expression $\frac{\partial c_{C_R}}{\partial t}$. By means of (6.37a) and (6.44):

$$\frac{\partial c_{C_R}}{\partial t}=\frac{\frac{\partial}{\partial t}\left(c_{R_R}c_{L_R}\right)\alpha_R-\left(c_{R_R}c_{L_R}\right)\frac{\partial\alpha_R}{\partial t}}{\alpha_R^2}$$

where:

$$\frac{\partial \alpha_R}{\partial t} = \alpha \frac{\partial j}{\partial t} = \alpha \left[J|\mathbf{F}^{-T}\mathbf{n}_R| Tr(\mathbf{l}) - \frac{J}{2|\mathbf{F}^{-T}\mathbf{n}_R|}\mathbf{n}_R \cdot \mathbf{C}^{-1}\frac{\partial \mathbf{C}}{\partial t}\mathbf{C}^{-1}\mathbf{n}_R \right]$$

therefore:

$$\begin{aligned}
\frac{\partial c_{C_R}}{\partial t} &= \frac{\alpha_R c_{L_R}\frac{\partial c_{R_R}}{\partial t} + \alpha_R c_{R_R}\frac{\partial c_{L_R}}{\partial t} - \alpha c_{R_R} c_{L_R}\frac{\partial j}{\partial t}}{\alpha_R^2} = \\
&= \frac{c_{L_R}\frac{\partial c_{R_R}}{\partial t} + c_{R_R}\frac{\partial c_{L_R}}{\partial t}}{\alpha_R} - \frac{\alpha c_{R_R} c_{L_R}\frac{\partial j}{\partial t}}{\alpha_R^2} = \\
&= \frac{c_{L_R}\frac{\partial c_{R_R}}{\partial t} + c_{R_R}\frac{\partial c_{L_R}}{\partial t}}{\alpha_R} - \frac{\alpha c_{R_R} c_{L_R}\left[J|\mathbf{F}^{-T}\mathbf{n}_R| Tr(\mathbf{l}) - \frac{J}{2|\mathbf{F}^{-T}\mathbf{n}_R|}\mathbf{n}_R \cdot \mathbf{C}^{-1}\frac{\partial \mathbf{C}}{\partial t}\mathbf{C}^{-1}\mathbf{n}_R \right]}{\alpha_R^2} = \\
&= \frac{c_{L_R}\frac{\partial c_{R_R}}{\partial t} + c_{R_R}\frac{\partial c_{L_R}}{\partial t}}{\alpha_R} - \frac{\alpha c_{R_R} c_{L_R}\left[J|\mathbf{F}^{-T}\mathbf{n}_R| Tr(\mathbf{l}) - \frac{J^2}{2j}\mathbf{n}_R \cdot \mathbf{C}^{-1}\frac{\partial \mathbf{C}}{\partial t}\mathbf{C}^{-1}\mathbf{n}_R \right]}{\alpha_R^2}
\end{aligned}$$

We focus on the term $-\dfrac{\alpha c_{R_R} c_{L_R}\left[J|\mathbf{F}^{-T}\mathbf{n}_R| Tr(\mathbf{l}) - \frac{J^2}{2j}\mathbf{n}_R \cdot \mathbf{C}^{-1}\frac{\partial \mathbf{C}}{\partial t}\mathbf{C}^{-1}\mathbf{n}_R \right]}{\alpha_R^2}$:

first member

$$-\frac{\alpha c_{R_R} c_{L_R} J|\mathbf{F}^{-T}\mathbf{n}_R| Tr(\mathbf{l})}{\alpha_R^2} = -\frac{c_{R_R} c_{L_R} Tr(\mathbf{l})}{\alpha_R}$$

second member

$$\begin{aligned}
\frac{\alpha c_{R_R} c_{L_R}\frac{J^2}{2j}\mathbf{n}_R \cdot \mathbf{C}^{-1}\frac{\partial \mathbf{C}}{\partial t}\mathbf{C}^{-1}\mathbf{n}_R}{\alpha_R^2} &= \underbrace{\frac{\alpha}{2\alpha_R^2}\frac{J^2}{j}}_{1/2\alpha J|\mathbf{F}^{-T}\mathbf{n}_R|^3} c_{R_R} c_{L_R}\mathbf{n}_R \cdot \mathbf{C}^{-1}\frac{\partial \mathbf{C}}{\partial t}\mathbf{C}^{-1}\mathbf{n}_R = \\
&= \frac{c_{R_R} c_{L_R}}{2\alpha J|\mathbf{F}^{-T}\mathbf{n}_R|^3}\mathbf{n}_R \cdot \mathbf{C}^{-1}\frac{\partial \mathbf{C}}{\partial t}\mathbf{C}^{-1}\mathbf{n}_R
\end{aligned}$$

Finally:

$$\begin{aligned}
\frac{\partial c_{C_R}}{\partial t} &= \frac{1}{\alpha_R}\left[c_{L_R}\frac{\partial c_{R_R}}{\partial t} + c_{R_R}\frac{\partial c_{L_R}}{\partial t} \right] + c_{R_R} c_{L_R}\left[-\frac{Tr(\mathbf{l})}{\alpha_R} + \frac{\mathbf{n}_R \cdot \mathbf{C}^{-1}\frac{\partial \mathbf{C}}{\partial t}\mathbf{C}^{-1}\mathbf{n}_R}{2\alpha J|\mathbf{F}^{-T}\mathbf{n}_R|^3} \right] = \\
&= \frac{1}{\alpha_R}\left[c_{L_R}\frac{\partial c_{R_R}}{\partial t} + c_{R_R}\frac{\partial c_{L_R}}{\partial t} \right] + c_{R_R} c_{L_R}\left[-\frac{Tr(\mathbf{l})}{\alpha_R} + \frac{\mathbf{n}_R \cdot \mathbf{C}^{-1}\frac{\partial \mathbf{C}}{\partial t}\mathbf{C}^{-1}\mathbf{n}_R}{2\alpha_R|\mathbf{F}^{-T}\mathbf{n}_R|^2} \right] = \qquad (6.47) \\
&= \frac{1}{\alpha_R}\left[c_{L_R}\frac{\partial c_{R_R}}{\partial t} + c_{R_R}\frac{\partial c_{L_R}}{\partial t} \right] + \frac{c_{R_R} c_{L_R}}{\alpha_R}\left[-Tr(\mathbf{l}) + \frac{\mathbf{n}_R \cdot \mathbf{C}^{-1}\frac{\partial \mathbf{C}}{\partial t}\mathbf{C}^{-1}\mathbf{n}_R}{2|\mathbf{F}^{-T}\mathbf{n}_R|^2} \right]
\end{aligned}$$

in light of the above, the governing equations 6.46 become:

$$\begin{aligned}
&\frac{\partial c_{R_R}}{\partial t} + \mathrm{Div}_{\mathcal{P}_R}[\mathbf{h}_{R_R}] + \frac{1}{\alpha_R}\left[c_{L_R}\frac{\partial c_{R_R}}{\partial t} + c_{R_R}\frac{\partial c_{L_R}}{\partial t}\right] + \frac{c_{R_R}c_{L_R}}{\alpha_R}\left[-Tr(\mathbf{I}) + \frac{\mathbf{n}_R\cdot\mathbf{C}^{-1}\dfrac{\partial \mathbf{C}}{\partial t}\mathbf{C}^{-1}\mathbf{n}_R}{2|\mathbf{F}^{-T}\mathbf{n}_R|^2}\right] = s_{R_R}\,, \\
&\frac{\partial c_{L_R}}{\partial t} + \frac{1}{\alpha_R}\left[c_{L_R}\frac{\partial c_{R_R}}{\partial t} + c_{R_R}\frac{\partial c_{L_R}}{\partial t}\right] + \frac{c_{R_R}c_{L_R}}{\alpha_R}\left[-Tr(\mathbf{I}) + \frac{\mathbf{n}_R\cdot\mathbf{C}^{-1}\dfrac{\partial \mathbf{C}}{\partial t}\mathbf{C}^{-1}\mathbf{n}_R}{2|\mathbf{F}^{-T}\mathbf{n}_R|^2}\right] = s_{L_R}\,.
\end{aligned} \tag{6.48}$$

Such a model could be extend to a further formulation involving more than one chemical reactions, see next chapters and Appendix G.1.

6.3 Relocation and reaction of actin to form biopolymers

The extensive mathematical description made in section 6.2 will guide the modeling of the relocation and reaction of actin to form biopolymers in the cytosol, which will be summarized here in a shorter shape.

Biopolymers are composed of actin, a protein termed globular or G-actin in its monomeric form and F-actin when it forms filamentous polymers. In turn, actin filaments can bundle to form stress fibers, or cross-link to form polymer networks that allow the movement of the cell. Polymerization is usually triggered by extracellular signals. In the case of cell locomotion, for instance, the cell extends finger-like protrusions by which the cell "feels" the surrounding surface. As done in [129], the precise details of the signaling pathways are here ignored. Rather, the level of signaling is assumed given in the reference configuration by a function

$$\mathcal{C}(\vec{X},t) = \gamma_i \exp\left[-|\vec{x}(\vec{X},t) - \vec{y}_i|\right] \exp\left[-\frac{t-\tau_i}{\theta}\right] \tag{6.49}$$

that accounts for the location of discrete signaling points $\vec{y}_i$ in the surroundings emitting signals of intensity γ_i at time τ_i; θ is the decay constant of the signal. This approach in modeling the external stimulus is similar to the membrane activator in [176]. The transduction of the signal results in the polymerization of the actin filaments and their cross-linking or bundling. The formation of single actin filaments can be modeled as a bimolecular reaction similar to (6.21), as in [3]; in this section, the biopolymer turn-over will be described at a larger scale, involving the interplay between fundamental units and stress-fibers or pseudopodia, in the form

$$\mathrm{G} \underset{k_b}{\overset{k_f}{\rightleftarrows}} \mathrm{F} \tag{6.50}$$

with F denoting either one of the two biopolymers. The network or fiber formation rate of reaction (6.50), denoted with $w^{(6.50)}$, is influenced by mechanical stresses: stress fibers stability is favored by tension, for instance. For this reason, the stress tensor enters the chemical potential and the dissociation reaction of biopolymers. The kinetics of reaction (6.50) is modeled via the law of mass action, properly extended to account for signaling:

$$w^{(6.50)}(\vec{X},t) = \mathcal{C}(\vec{X},t)\, k_f \frac{\vartheta_G}{(1-\vartheta_G)} - \mathcal{D}(\vec{X},t)\, k_b \frac{\vartheta_F}{(1-\vartheta_F)}\,, \tag{6.51}$$

having already discussed the meaning of the ratio ϑ in eq. (6.24). Function $\mathcal{D}$ accounts for the role of the stress in the dynamic formation and dissociation of biopolymers, see for instance [129].

6.3.1 Mass transport in the cytosol

Consider a generic species a at a point $\vec{x}$ in the cytosol $\Omega(t)$. The mass balance of species a in the advecting configuration $\mathcal{Q}(t)$ localizes as

$$\frac{\mathrm{d}\rho_a}{\mathrm{d}t} + \rho_a \,\mathrm{div}\,[\vec{v}_{adv}] + \mathrm{div}\left[\vec{\hbar}_a\right] = \bar{s}_a(\vec{x},t)\,, \tag{6.52}$$

with $\vec{\hbar}_a$ and $\vec{v}_{adv}$ defined earlier in section 6.2.2.1, ρ_a is the density of species a. The mass balance can be restated in terms of molarity c_a (in moles or molecules per unit volume), by division by the molar or molecular mass (m_a) of species a. By denoting with $c_a = \rho_a/m_a$, $s_a = \bar{s}_a/m_a$, and $\vec{h}_a = \vec{\hbar}_a/m_a$ the local balance (6.52) becomes

$$\frac{\mathrm{d}c_a}{\mathrm{d}t} + c_a \,\mathrm{div}\,[\vec{v}_{adv}] + \mathrm{div}\left[\vec{h}_a\right] = s_a(\vec{x},t)\,. \tag{6.53}$$

The latter can be rephrased in the reference configuration at point $\vec{X}$ and time t. To this aim, define the reference molarity of species a as

$$c_{a_R}(\vec{X},t) = c_a(\vec{x}(\vec{X},t),t)\,J(\vec{X},t)\,, \tag{6.54}$$

the reference flux vector $\vec{h}_{a_R}(\vec{X},t)$ and the reference mass supply $s_{a_R}(\vec{X},t)$ as [142] (page 374)

$$\vec{h}_{a_R} = J\,\boldsymbol{F}^{-1}\,\vec{h}_a(\vec{x}(\vec{X},t),t)\,, \qquad s_{a_R} = J\,s_a(\vec{x}(\vec{X},t),t)\,, \tag{6.55}$$

respectively. The reaction rate $w^{(6.50)}(\vec{x},t)$, being a mass supply, shall transform according to eq. (6.55)b. The invariance of ϑ_a with the configuration and the analysis of the mass action law (6.51) imply that the forward and backward "constants", which encompass the dimensionality of $w^{(6.50)}(\vec{x},t)$, are not actually constants in the reference configuration. They rather change with time and with point $\vec{X}$ according to

$$k_{f_R}(\vec{X},t) = J(\vec{X},t)\,k_f\,, \qquad k_{b_R}(\vec{X},t) = J(\vec{X},t)\,k_b \tag{6.56}$$

The ratio k_{f_R}/k_{b_R} remains independent upon the configuration. The referential form of the mass balance equations eventually reads

$$\frac{\partial c_{G_R}}{\partial t} + \mathrm{Div}\left[\vec{h}_{G_R}\right] + w_R^{(6.50)} = s_{G_R}\,, \tag{6.57a}$$

$$\frac{\partial c_{F_R}}{\partial t} + \mathrm{Div}\left[\vec{h}_{F_R}\right] - w_R^{(6.50)} = s_{F_R}\,. \tag{6.57b}$$

As for the complex molecules, filaments usually have a much smaller mobility than monomers and might be assumed to be motionless, i.e.

$$\vec{h}_F = \vec{h}_{F_R} = \vec{0}\,. \tag{6.58}$$

The diffusion of monomers appears to be much slower than the interaction kinetics and the concentrations of species may be governed by thermodynamic equilibrium at all times [177]. The concentration of filaments c_{F_R} relates then to the monomers by the equation $w^{(6.50)} = 0$, mediated by the local amount of signaling and stress. Equations (6.57), with associated initial conditions

$$c_{G_R}(\vec{X},0) = c^0_{G_R}(\vec{X}) \,, \qquad c_{F_R}(\vec{X},0) = 0$$

and Dirichlet-Neumann boundary conditions define the relocation of monomers that undergo polymerization reactions in the reference configuration.

6.4 Mechanical evolution of the cell

Based upon the selection of the mechanisms that are supposed to govern the structural response of the cell, the balance laws of linear and angular momentum come out. Literature provides two basic approaches, whether the structural functions are demanded entirely to the cell membrane [98, 99, 101, 178, 179] or to the development of a cytoskeletal structure within the bulk of the cell [129, 119, 120, 118, 128, 121, 126, 123, 122, 180] (see also section 2.5). Studies on the red blood cell [172] suggest that the membrane deformation occur at constant area, but this evidence does not appear to be supported by experiments in endothelial cells during spreading. The influence of curvature on the elastic stiffness of the membrane appears to be related to the size of the cell [116] and seems to be negligible for endothelial cells of diameter $\sim 10\mu$m. These two evidences lead to consider the reorganization of the cytoskeleton through a network of actin filaments and microtubules the main responsible for the mechanical response of endothelial cells, coupled to a passive behavior dictated by the viscosity of the cytosol as in [129, 119, 180]. Accordingly, balance of linear and angular momentum will be formulated for the bulk of the cell rather than the membrane.

Forces in continuum mechanobiology are described spatially by *contact forces* between adjacent spatial regions (as for the forces exchanged by the substrate and the cell during adhesion), *surface forces* exerted on the boundary of the cell by the environment (as for the receptor-ligand attractive interaction [107, 108] and repulsive electrostatic interactions), *body forces* exerted on the interior points by the environment (as for the gravity or pseudopodia forces that preside migration). Contact and surface forces, acting on $\partial\Omega(t)$ will be denoted henceforth with $\vec{t}(\vec{x},t)$ whereas body forces will be denoted with $\vec{b}(\vec{x},t)$. Their referential counterparts will inherit the subscript $_R$. Throughout the rest of the current chapter (and subsequent ones), we will neglect inertia forces, although some authors [181] pinpointed the role of inertia forces during migration. Accordingly, the balance of linear and angular momentum, which are assumed to hold at each time for all spatial regions $\mathcal{Q}(t) \subseteq \Omega(t)$, read:

$$\int_{\partial\mathcal{Q}(t)} \vec{t}(\vec{x},t)\,\mathrm{d}a + \int_{\mathcal{Q}(t)} \vec{b}(\vec{x},t)\,\mathrm{d}v = \vec{0} \,, \tag{6.59a}$$

$$\int_{\partial\mathcal{Q}(t)} \vec{r}\times\vec{t}(\vec{x},t)\,\mathrm{d}a + \int_{\mathcal{Q}(t)} \vec{r}\times\vec{b}(\vec{x},t)\,\mathrm{d}v = \vec{0} \tag{6.59b}$$

with $\vec{r}$ denoting the position vector with respect to an arbitrary pole. Classical arguments of continuum mechanics lead to localize eqs. (6.59) in the reference configuration, in terms of the

(first) Piola stress tensor $\boldsymbol{P}$ and of the body forces measured per unit volume in the reference body

$$\vec{b}_R(\vec{X},t) = J(\vec{X},t)\,\vec{b}(\vec{x}(\vec{X},t),t)\,.$$

The referential local form of the balance of linear momentum reads

$$\mathrm{Div}\,[\boldsymbol{P}] + \vec{b}_R = \vec{0}\,, \qquad \vec{X} \in \Omega_R\,. \tag{6.60a}$$

The first Piola stress tensor $\boldsymbol{P}$ must satisfy the local angular momentum balance

$$\boldsymbol{P}\boldsymbol{F}^T = \boldsymbol{F}\boldsymbol{P}^T\,. \tag{6.60b}$$

6.4.1 Mechano-biological quantitative investigations on boundary conditions

Contact and surface forces are boundary conditions for problem (6.60a). They emanate from electrostatic long or short-range interactions, from receptor-ligand adhesion forces, as well as from contact tractions after adhesion. A vast literature [182, 183, 3] has been devoted to quantify the forces involved in these interaction mechanisms. It emerges that uncertainties remain in the establishment of realistic values for attraction forces, not surprisingly due to the complexity of the required experimental tasks.

Studies on the influence of non-specific *traction forces in cell adhesion* were performed at different time scales, from minutes - as for the spreading of a mouse embryonic fibroblasts on a matrix-coated surface [184] - to several hours - as for a bovine aortic endothelial cell on polyacrylamide gels [97] - for different cell sizes. Analyses refer mostly to the early stage of adhesion: as pointed out in [114], traction models are helpful under specific conditions and particularly in predicting isotropic early stage of cell adhesion, which is essentially independent of the cytoskeleton remodeling. Isotropic spreading is made possible by higher ligands densities; at lower densities of ligands, cells tend to spread anisotropically, by extending pseudopodia randomly along the cell membrane [97]. This has been made clear also in modeling micropipette-manipulated red blood cell attachment-detachment from a substrate [115], which was performed in ≈ 50 *ms* showings that after approximately a third of the adhesion-spreading time, the adhesion-traction forces level off and to further increase spreading area, receptor diffusion from a remote area of the cell to the spreading front is required. Roughly the same concept has been explored in [185], dealing with charged flexible particles that adhere to an oppositely charged rigid substrate due to electrostatic attraction forces. Surface forces drive the adhesion of small particles. The cell radius in the reference, unstressed configuration was considered in the micron/sub-micron range 1 μm in [185] or even smaller 12.5 *nm* in [116]. According to [113], adhesion and spreading also require transport of receptors from the apical to the basal part of the cell in order to generate attractive forces.

Initially, we do not account explicitly for integrins, as done in [123] among others, yet we will use the approaches in [123, 116] to discuss the magnitude of *traction forces in cell spreading*. According to [116], Neumann tractions emanate from short-range, noncovalent interactions between one receptor and one ligand due to polarization of a non-polar ligand molecule in the electrostatic field

of a charged receptor. The binding force on the membrane per unit area in the current configuration was given as

$$\vec{t}(\vec{x}) = -C(Kg_N+1)\left((Kg_N+1)^2+1\right) g_N^{-5} \exp(-2Kg_N)\,\rho_{rl}(\vec{x})\vec{e}_2 \tag{6.61}$$

where: g_N is the gap between receptors and ligands, $\rho_{rl}(\vec{x})$ is the minimum concentration of receptors and ligands at location $\vec{x}$, C is the number of weak noncovalent sub-bonds which form the interaction between one receptor and one ligand, K is the inverse of the Debye length. It is of course particularly complex to provide parameters with high accuracy: assuming that the values provided in [116] apply also to endothelial cells, one would set $C = 1.17 \times 10^{-7}\text{fN}\mu\text{m}^{-5}$, $K = 1$.

Parameter $\rho_{rl}(\vec{x})$ selected in [116] amounts at 10^5 receptors per μm^2, severely higher than the concentrations of species that have been measured in [138]. Such a parameter should be considered as a constant only if it refers to *all receptors on the membrane*, which is questionable. The protein transport affects the amount $\rho_{rl}(\vec{x})$ and couples mechanical deformation in the bulk and chemo-transport processes on the membrane. The resulting Neumann electrostatic attractive tractions are plotted with a continuous line in Fig. 6.2.

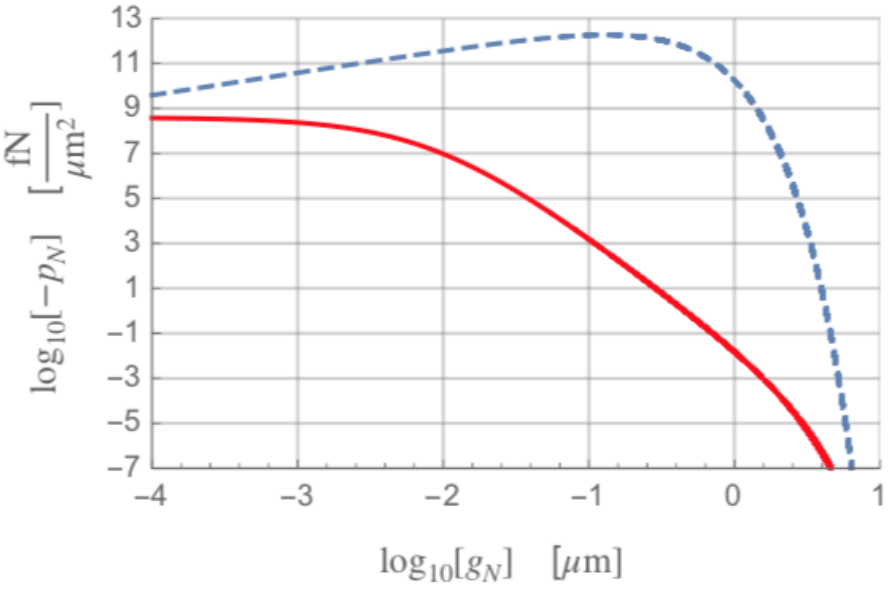

Figure 6.2: Comparison between binding forces on the membrane per unit area. Continuous line refers to eq. (6.61) adopted in [116], whereas the dashed line refers to eq. (6.62) used in [123].

These forces decrease when the distance between receptors and ligands grows, and are quite high at a strictly positive lower bound h_0 depicted as the gap between the cell and the substrate at contact. Authors in [116] suggest $h_0 = 9.0 \times 10^{-3}\mu\text{m}$. Repulsive forces are expected for distances below such a bound, as in Lennard-Jones potentials, yet this is not the case of equation (6.61). Attractive forces decay rapidly and at a distance of $0.5\mu\text{m}$ they amount to a few $\text{fN}/\mu\text{m}^2$. Their range being

so short, it is unlikely that those forces promote the cell spreading unless the characteristic size of the cell becomes very small (indeed, authors in [116] considered a cell with radius $12.5nm$, three orders of magnitude smaller than the measured radius of an endothelial cell in suspension - about $10\mu m$). Rather, electrostatic interactions grant attachment to the lower μslide once gravitational effects bring the cell in contact with the slide.
A further corroboration of this statement emerge from the analysis of attractive forces used in [123] to allow a cell to (partially) spread, namely

$$\vec{t}(\vec{x}) = -Q\frac{g_N}{\delta_p}\exp\left(-\frac{g_N}{\delta_p}\right)\vec{e}_2 \tag{6.62}$$

with Q, δ_p calibrated as $50\text{kPa} = 5\times 10^7 \text{fN}/\mu\text{m}^2$ and $0.13\mu\text{m}$, respectively. In order to foster cell spreading, these attraction forces result 4 orders of magnitude higher than (6.61) - see the dashed line in 6.2. there is apperently no justification in the literature for such a huge value of the ligand-receptor binding force acting on such a long-range extent. *Rather, these interactions are followed by the extension of pseudopodia from the cell body. As the cell begins to flatten against the substrate, it forms additional bonds, rearranges its cytoskeleton to form actin filaments and bundles, creating new focal adhesions.*

In conclusion, surface forces may drive the post-adhesion processes only for *small particle*s as the ones considered in [185] or [116]. The cell radius in the reference, unstressed configuration was in the micron/sub-micron range 1 μm in [185] or even smaller 12.5 nm in [116]. For ECs, interaction forces of electrostatic nature are followed by the extension of pseudopodia from the cell body. As the cell begins to flatten against the substrate, it forms additional bonds, rearranges its cytoskeleton to form actin filaments and bundles, creating new focal adhesions. Spreading thus is a result of extensional and contractile forces exerted by pseudopodia and the cytoskeleton machinery [97].

6.5 Thermodynamics

The quest of the right thermodynamic principles in mechanobiology is, on one hand, far from being understood and, from a wider perspective, it paves the way to boundless questions of philosophical and ethical nature, as for the establishment of a thermodynamics of life [186], which fall completely out of the scope of present paper. Major accomplishments have been recently achieved [14] in formulating fresh concepts that deviate from classical results of thermodynamics of non equilibrium. In this scientific area, which is nowadays flourishing, new fundamentals assertions are expected in the years to come. Being aware of these deficiencies, we admit that our formulation of non equilibrium thermodynamics [144, 141] may not be able to capture some principles of mechanobiology that rule the dynamic of receptors - as for the homeostatic constraint - and we are prone to deepen our formulation in future studies.

6.5.1 Thermodynamics of receptors motion on the membrane

6.5.1.1 Energy Balance

As in section 6.1, denote with $\Omega(t)$ the advecting cell, and with $\partial\Omega(t)$ its lipid membrane. Consider an arbitrary region $\mathcal{P}(t) \subset \partial\Omega(t)$. The first law of thermodynamics represents the balance of the

interplay among the internal energy of $\mathcal{P}(t)$, the heat transferred in $\mathcal{P}(t)$ and the power due to mass exchanged by receptor dynamics on $\mathcal{P}(t)$. The energy balance for the problem at hand reads:

$$\frac{\mathrm{d}\mathcal{U}}{\mathrm{d}t}(\mathcal{P}) = \mathcal{Q}_u(\mathcal{P}) + \mathcal{T}_u(\mathcal{P}) \,, \tag{6.63}$$

where $\mathcal{Q}_u$ is the power due to heat transfer and $\mathcal{T}_u$ is the power due to mass transfer. Denoting with $\partial\mathcal{P}(t)$ the bounding closed curve of $\mathcal{P}(t)$ (see Fig. 6.1), they read:

$$\begin{aligned} \mathcal{Q}_u &= \int_{\mathcal{P}} s_q \,\mathrm{d}a - \oint_{\partial\mathcal{P}} \vec{q}\cdot\vec{t}_\perp \,\mathrm{d}\ell \\ \mathcal{T}_u &= \int_{\mathcal{P}} \mu_L^u s_L + \mu_R^u s_R \,\mathrm{d}a - \oint_{\partial\mathcal{P}} \mu_R^u \vec{h}_R\cdot\vec{t}_\perp \,\mathrm{d}\ell \end{aligned} \tag{6.64a}$$

The time variation of net internal energy $\mathcal{U}$ thus corresponds to the power expenditure of two external agents: a heat contribution $\mathcal{Q}_u$ where s_q is the heat supplied by external agents and $\vec{q}$ is the heat flux vector; a mass contribution $\mathcal{T}_u$ in which the scalar ${}^u\mu_\beta$ denotes the change in specific energy provided by a unit supply of *moles* of species $\beta = L,R$. Mass supply s_L is the push-forward of the ligand supply $s_{L_R}(\vec{X},t)$ defined in eq. (6.36) and $\vec{h}_R$ is the flux of receptors along the membrane in the current configuration.

The net internal energy can be denoted in terms of specific internal energy u per unit surface, namely:

$$\mathcal{U}(\mathcal{P}) = \int_{\mathcal{P}} u \,\mathrm{d}a \,. \tag{6.65}$$

Applying the surface divergence theorem (6.4) and mass balances leads from (6.64) to

$$\mathcal{Q}_u = \int_{\mathcal{P}} s_q \,\mathrm{d}a - \int_{\mathcal{P}} \mathrm{div}_{\mathcal{P}}\left[\vec{q}\right] \mathrm{d}a \qquad \mathcal{T}_u = \int_{\mathcal{P}} \mu_L^u s_L + \mu_R^u s_R \,\mathrm{d}a - \int_{\mathcal{P}} \mathrm{div}_{\mathcal{P}}\left[\mu_R^u \vec{h}_R\right] \mathrm{d}a \,, \tag{6.66a}$$

whence the first law of thermodynamics arises[3]

$$\frac{\mathrm{d}}{\mathrm{d}t}\int_{\mathcal{P}} u \,\mathrm{d}a = \int_{\mathcal{P}} s_q - \mathrm{div}_{\mathcal{P}}\left[\vec{q}\right] - \mathrm{div}_{\mathcal{P}}\left[\mu_R^u \vec{h}_R\right] + \mu_L^u s_L + \mu_R^u s_R \,\mathrm{d}a \,.$$

It can be pulled back to the reference configuration in view of definitions of reference molarity of species $c_{a_R}(\vec{X},t)$ in eq. (6.14), of the reference flux vector $\vec{h}_{a_R}(\vec{X},t)$ and of the reference mass supply $s_{a_R}(\vec{X},t)$ in eq. (6.15), which readily extends to heat fluxes and supplies

$$\frac{\mathrm{d}}{\mathrm{d}t}\int_{\mathcal{P}_R} u_R \,\mathrm{d}A = \int_{\mathcal{P}_R} s_{q_R} - \mathrm{Div}_{\mathcal{P}_R}\left[\vec{q}_R\right] - \mathrm{Div}_{\mathcal{P}_R}\left[\mu_{R_R}^u \vec{h}_{R_R}\right] + \mu_{L_R}^u s_{L_R} + \mu_{R_R}^u s_{R_R} \,\mathrm{d}A \,. \tag{6.68}$$

Since it must hold for any region $\mathcal{P}_R$, the local form of the first principle can be derived exploiting the mass balance equations (6.34a), (6.34c), (6.36) in the reference configuration

$$\begin{aligned} \frac{\mathrm{d}u_R}{\mathrm{d}t} &= s_{q_R} - \mathrm{Div}_{\mathcal{P}_R}\left[\vec{q}_R\right] - \vec{h}_{R_R}\cdot\mathrm{Grad}_{\mathcal{P}_R}\left[\mu_{R_R}^u\right] \\ &\quad + \mu_{R_R}^u \frac{\partial c_{R_R}}{\partial t} + \mu_{L_R}^u \frac{\partial c_{L_R}}{\partial t} + \mu_{C_R}^u \frac{\partial c_{C_R}}{\partial t} + \left(\mu_{R_R}^u + \mu_{L_R}^u - \mu_{C_R}^u\right) w_R^{(6.22)} \,. \end{aligned} \tag{6.69}$$

[3] Since it must hold for any region $\mathcal{P}(t)$, the current configuration local form of the first principle can be derived exploiting Reynold's theorem (6.6) on $\mathcal{P}(t)$

$$\frac{\partial u}{\partial t} + \mathrm{div}_{\mathcal{P}}\left[u\,\vec{v}_{adv}\right] = s_q - \mathrm{div}_{\mathcal{P}}\left[\vec{q}\right] + \mu_R^u \frac{\partial c_R}{\partial t} + \mu_L^u \frac{\partial c_L}{\partial t} + \mu_C^u \frac{\partial c_C}{\partial t} - \vec{h}_R\cdot\nabla_{\mathcal{P}}\left[\mu_R^u\right] + \left(\mu_R^u + \mu_L^u - \mu_C^u\right) w^{(6.22)} \,. \tag{6.67}$$

6.5.1.2 Entropy balance equations

The second law of thermodynamics represents the balance of the interplay among the internal entropy of $\mathcal{P}$ and the entropy transferred in $\mathcal{P}$ due to mass exchange and heat transferred on $\mathcal{P}$. The entropy balance for the problem at hand reads:

$$\frac{\mathrm{d}S}{\mathrm{d}t}(\mathcal{P}) - \frac{\mathrm{d}S_{irr}}{\mathrm{d}t}(\mathcal{P}) = \mathcal{Q}_\eta(\mathcal{P}) + \mathcal{T}_\eta(\mathcal{P}) \,, \tag{6.70}$$

where S is the net internal entropy of $\mathcal{P}$, S_{irr} is the entropy produced inside $\mathcal{P}$, Q_η the entropy per unit time due to heat transfer, $\mathcal{T}_\eta$ the entropy per unit time due to mass transfer. The individual contributions read:

$$Q_\eta = \int_{\mathcal{P}} \frac{s_q}{T}\,\mathrm{d}A - \oint_{\partial\mathcal{P}} \frac{\vec{q}}{T}\cdot\vec{t}_\perp\,\mathrm{d}\ell \,, \tag{6.71a}$$

$$T_\eta = \int_{\mathcal{P}} \mu_L^\eta\, s_L + \mu_R^\eta\, s_R\,\mathrm{d}A - \oint_{\partial\mathcal{P}} \mu_R^\eta\,\vec{h}_R\cdot\vec{t}_\perp\,\mathrm{d}\ell \,. \tag{6.71b}$$

The scalar μ_β^η denotes the change in specific entropy provided by a unit supply of moles of species β. Equation (6.70) stems from the non-trivial assumption that mechanics does not contribute directly to the total entropy flow in the entropy balance equation [141]. The second law of thermodynamics states that:

$$\frac{\mathrm{d}S_{irr}}{\mathrm{d}t} \geq 0. \tag{6.72}$$

Analogously to the energy counterpart, we define the specific internal entropy η per unit volume and write the entropy imbalance in the reference configuration as

$$\frac{\mathrm{d}}{\mathrm{d}t}\int_{\mathcal{P}_R} \eta_R\,\mathrm{d}A + \int_{\mathcal{P}_R} -\frac{s_{q_R}}{T} + \mathrm{Div}_{\mathcal{P}_R}\left[\frac{\vec{q}_R}{T}\right] - \mu_{L_R}^\eta\, s_{L_R} - \mu_{R_R}^\eta\, s_{R_R} + \mathrm{Div}_{\mathcal{P}_R}\left[\mu_{R_R}^\eta\,\vec{h}_{R_R}\right]\,\mathrm{d}A \geq 0 \,.$$

After multiplication by $T \geq 0$, replacing $-s_{q_R} + \mathrm{Div}_{\mathcal{P}_R}[\vec{q}_R]$ by means of the energy balance (6.69), and some simple algebra, the local form of the entropy imbalance becomes

$$\begin{aligned} T\,\frac{\mathrm{d}\eta_R}{\mathrm{d}t} - \frac{\mathrm{d}u_R}{\mathrm{d}t} + \frac{\partial c_{R_R}}{\partial t}\left[\mu_{R_R}^u - T\,\mu_{R_R}^\eta\right] + \frac{\partial c_{L_R}}{\partial t}\left[\mu_{L_R}^u - T\,\mu_{L_R}^\eta\right] + \frac{\partial c_{C_R}}{\partial t}\left[\mu_{C_R}^u - T\,\mu_{C_R}^\eta\right] + \\ - \frac{1}{T}\,\vec{q}_R\cdot\mathrm{Grad}_{\mathcal{P}_R}[T] + T\,\vec{h}_{R_R}\cdot\mathrm{Grad}_{\mathcal{P}_R}\left[\mu_{R_R}^\eta\right] - \vec{h}_{R_R}\cdot\mathrm{Grad}_{\mathcal{P}_R}\left[\mu_{R_R}^u\right] \\ + \left(\mu_{R_R}^u - T\,\mu_{R_R}^\eta + \mu_{L_R}^u - T\,\mu_{L_R}^\eta - \mu_{C_R}^u + T\,\mu_{C_R}^\eta\right) w_R^{(6.22)} \geq 0 \,. \end{aligned} \tag{6.73}$$

Denote with $\beta = R, L, C$ and with the symbols $\mu_{\beta_R}, A_R^{(6.22)}$ the quantities

$$\mu_{\beta_R} = \mu_{\beta_R}^u - T\,\mu_{\beta_R}^\eta \tag{6.74}$$

$$A_R^{(6.22)} = -\mu_{R_R} - \mu_{L_R} + \mu_{C_R} \,. \tag{6.75}$$

By noting that:

$$T\,\vec{h}_{R_R}\cdot\mathrm{Grad}_{\mathcal{P}_R}\left[\mu_{R_R}^\eta\right] = \vec{h}_{R_R}\cdot\mathrm{Grad}_{\mathcal{P}_R}\left[T\,\mu_{R_R}^\eta\right] - \vec{h}_{R_R}\cdot\mathrm{Grad}_{\mathcal{P}_R}[T]\,\mu_{R_R}^\eta$$

one finally writes the entropy imbalance as:

$$T\,\frac{\mathrm{d}\eta_R}{\mathrm{d}t} - \frac{\mathrm{d}u_R}{\mathrm{d}t} + \frac{\partial c_{R_R}}{\partial t}\,\mu_{R_R} + \frac{\partial c_{L_R}}{\partial t}\,\mu_{L_R} + \frac{\partial c_{C_R}}{\partial t}\mu_{C_R} + \\ - \left(\frac{1}{T}\,\vec{q}_R + \mu^{\eta}_{R_R}\,\vec{h}_{R_R}\right)\cdot \mathrm{Grad}_{\mathcal{P}_R}[\,T\,] - \vec{h}_{R_R}\cdot\mathrm{Grad}_{\mathcal{P}_R}[\,\mu_{R_R}\,] \\ - A_R^{(6.22)}\,w_R^{(6.22)} \geq 0\,. \tag{6.76}$$

6.5.1.3 Helmholtz Free Energy and thermodynamic restrictions

The referential specific Helmholtz free energy per unit volume is defined as:

$$\psi_R = u_R - T\,\eta_R \tag{6.77}$$

and is taken as a function of temperature and concentrations, $\psi_R\,(T, c_{R_R}, c_{L_R}, c_{C_R})$. It thus hold:

$$T\,\frac{\mathrm{d}\eta_R}{\mathrm{d}t} - \frac{\mathrm{d}u_R}{\mathrm{d}t} = -\,\frac{\mathrm{d}\psi_R}{\mathrm{d}t} - \eta_R\,\frac{\partial T}{\partial t} = -\,\frac{\partial \psi_R}{\partial c_{L_R}}\frac{\partial c_{L_R}}{\partial t} - \frac{\partial \psi_R}{\partial c_{R_R}}\frac{\partial c_{R_R}}{\partial t} - \frac{\partial \psi_R}{\partial c_{C_R}}\frac{\partial c_{C_R}}{\partial t} - \left(\eta_R + \frac{\partial \psi_R}{\partial T}\right)\frac{\partial T}{\partial t}$$

which can be plugged in (6.76) to derive the entropy imbalance in the Clausius-Duhem form:

$$\left(-\frac{\partial \psi_R}{\partial c_{R_R}} + \mu_{R_R}\right)\frac{\partial c_{R_R}}{\partial t} + \left(-\frac{\partial \psi_R}{\partial c_{L_R}} + \mu_{L_R}\right)\frac{\partial c_{L_R}}{\partial t} + \left(-\frac{\partial \psi_R}{\partial c_{C_R}} + \mu_{C_R}\right)\frac{\partial c_{C_R}}{\partial t} - \left(\eta_R + \frac{\partial \psi_R}{\partial T}\right)\frac{\partial T}{\partial t} + \\ - \frac{1}{T}\underline{\vec{q}_R}\cdot\mathrm{Grad}_{\mathcal{P}_R}[\,T\,] - A_R^{(6.22)}w_R^{(6.22)} - \vec{h}_{R_R}\cdot\mathrm{Grad}_{\mathcal{P}_R}[\,\mu_{R_R}\,] \geq 0 \tag{6.78}$$

with $\underline{\vec{q}_R} = \vec{q}_R + T\,\mu^{\eta}_{R_R}\vec{h}_{R_R}$. This inequality must hold for any value of the time derivative of the temperature and of the referential concentrations c_{R_R}, c_{L_R}, and c_{C_R}. Since they appear linearly in the inequality, the factors multiplying them must be zero, as otherwise it would be possible to find a value for the time derivatives that violate the inequality. Therefore, the following restrictions apply

$$\mu_{R_R} = \frac{\partial \psi_R}{\partial c_{R_R}}, \qquad \mu_{L_R} = \frac{\partial \psi_R}{\partial c_{L_R}}, \qquad \mu_{C_R} = \frac{\partial \psi_R}{\partial c_{C_R}}, \qquad \eta_R = -\frac{\partial \psi_R}{\partial T}\,. \tag{6.79}$$

In view of formula (6.79), the amount μ_β declared in eq. (6.74) acquires the meaning of *chemical potential* and hence the term $A^{(6.22)}$ in eq. (6.75) turns out to be the *affinity of the reaction* (6.22). Further remarks on this thermodynamic approach can be found in [141] and in chapter 3.2.

Equation (6.79) yields to the so called Clausius-Plank inequality:

$$-\frac{1}{T}\underline{\vec{q}_R}\cdot\mathrm{Grad}_{\mathcal{P}_R}[\,T\,] - A_R^{(6.22)}w_R^{(6.22)} - \vec{h}_{R_R}\cdot\mathrm{Grad}_{\mathcal{P}_R}[\,\mu_{R_R}\,] \geq 0 \tag{6.80}$$

that splits under the assumptions of Curie's principle and thermal equilibrium in the following set of inequalities:

$$\frac{1}{T}\underline{\vec{q}_R}\cdot\mathrm{Grad}_{\mathcal{P}_R}[\,T\,] + \vec{h}_{R_R}\cdot\mathrm{Grad}_{\mathcal{P}_R}[\,\mu_{R_R}\,] \leq 0\,, \tag{6.81a}$$

$$A_R^{(6.22)}\,w_R^{(6.22)} \leq 0\,. \tag{6.81b}$$

6.5.1.4 Constitutive theory

We will assume henceforth that the lipid membrane is in thermal equilibrium, i.e. $\mathrm{Grad}_{\mathcal{P}_R}[T] = \vec{0}$, and that the Helmholtz free energy density is additively decomposed into three separate parts:

$$\psi_R(c_{R_R}, c_{L_R}, c_{C_R}) = \psi_R^R(c_{R_R}) + \psi_R^L(c_{L_R}) + \psi_R^C(c_{C_R}) \tag{6.82}$$

meaning that the contribution of species are uncoupled, neglecting molecular friction that would lead to a Maxwell-Stefan description of transport. The free energy density of mobile guest atoms interacting with a host medium is described by an ideal solution model, which stems from a statistical mechanics description of the entropy for isolated systems in terms of the density of states, i.e. the number of possible molecular configurations [150] in the case of two-state systems. Making recourse to Stirling's approximation, one finds that the formula for combinations provides the following free energy density for the continuum approximation of mixing [150] of the generic species $\beta = R, L, C$

$$\psi_R^\beta(c_{\beta_R}) = \mu_{\beta_R}^0 c_{\beta_R} + RTc_{\beta_R}^{max}\left[\vartheta_{\beta_R}\ln\vartheta_{\beta_R} + (1-\vartheta_{\beta_R})\ln(1-\vartheta_{\beta_R})\right] , \tag{6.83}$$

with ϑ_{β_R} defined in (6.25) as the ratio between the concentration and the saturation limit for each species in the reference configuration. The chemical potential descends from eq. (6.79)

$$\mu_{\beta_R} = \frac{\partial \psi_R^\beta}{\partial c_{\beta_R}} = \mu_{\beta_R}^0 + RT\left(\ln\vartheta_{\beta_R} - \ln\left(1-\vartheta_{\beta_R}\right)\right) . \tag{6.84}$$

A strategy to meet the thermodynamic restriction (6.81a) is to model the flux of receptors by Fickian-diffusion, that linearly correlates $\vec{h}_{R_R}$ to the gradient of its chemical potential μ_{R_R}:

$$\vec{h}_{R_R} = -\boldsymbol{M}_R(c_R)\,\mathrm{Grad}_{\mathcal{P}_R}[\mu_{R_R}] \tag{6.85}$$

by means of a positive definite mobility tensor $\boldsymbol{M}_R$. The following isotropic non linear specialization for the mobility tensor $\boldsymbol{M}_R$ is chosen [149]

$$\boldsymbol{M}_R(c_{R_R}) = \mathbb{\mu}_R\, c_{R_R}^{max}\,\vartheta_{R_R}\,(1-\vartheta_{R_R})\,\mathbb{1} , \tag{6.86}$$

where $c_{R_R}^{max}$ is the saturation limit for receptors, and $\mathbb{\mu}_R > 0$ is the *mobility* of receptors. Definition (6.86) represents the physical requirement that both the pure ($c_{R_R} = 0$) and the saturated ($c_{R_R} = c_{R_R}^{max}$) phases have vanishing mobilities. Neither the mobility $\mathbb{\mu}_R$ nor the saturation concentration $c_{R_R}^{max}$ are assumed to change in time. Whereby experimental data indicate an influence of temperature, stresses, or concentrations, such a limitation can be removed without altering the conceptual picture. Noting that

$$\mathrm{Grad}_{\mathcal{P}_R}[\mu_{R_R}] = \frac{RT}{c_{R_R}^{max}}\frac{1}{\vartheta_{R_R}(1-\vartheta_{R_R})}\,\mathrm{Grad}_{\mathcal{P}_R}[c_{R_R}] ,$$

Fick's Law (6.85) specializes as

$$\vec{h}_{R_R} = -\mathbb{D}_R\,\mathrm{Grad}_{\mathcal{P}_R}[c_{R_R}] , \tag{6.87}$$

where $\mathbb{D}_R = \mathbb{\mu}_R RT$ is the receptor *diffusivity*.

6.5.1.5 Chemical kinetics

The chemical kinetics of reaction (6.22) is modeled via the law of mass action (6.33). Experimental evidences [138] show that: (i) the equilibrium constant (6.27) is high, thus favoring the formation of ligand-receptor complex and the depletions of receptors and ligands; (ii) the diffusion of receptors on the cell membrane is much slower than interaction kinetics. Accordingly, it can be assumed that the reaction kinetics is infinitely fast, in the sense that the time required to reach chemical equilibrium is orders of magnitude smaller than the time-scale of other processes. For these reasons we assume that the concentrations of species are ruled by thermodynamic equilibrium at all times, and the concentration of complex c_{C_R} is related to the others by the equation (6.37a). This very same equation could be derived imposing

$$A^{(6.22)} = 0 \, .$$

Simple algebra allows deriving eq. (6.37a), provided that to the equilibrium constant $K_{\text{eq}}^{(6.22)}$ the alternative definition

$$K_{\text{eq}}^{(6.22)} = \exp\left(-\frac{\Delta G^0}{RT}\right) \tag{6.88}$$

is given, where $\Delta G^0 = \mu_C^0 - \mu_L^0 - \mu_R^0$ is the standard Gibbs free energy.

6.5.2 Thermo-chemo-mechanics of cells

Endothelial cells show two main paradigmatic mechanical attitudes: active and passive. Active response is related to the ability of the cell to change, as a result of external cues, its own cytoskeletal conformation, i.e. to reorganize the morphology of the biopolymer net that provides the structural resistance during adhesion (to the ECM or to other cells), migration (e.g. chemotaxis, mechanotaxis, and durotaxis) and division (e.g.. mitosis). Passive, instead, refers to the mechanical response that each component of the cell has inasmuch material bodies, in accordance with their own internal structure and as a result of external actions.

6.5.2.1 Energy balance

Define in the bulk an arbitrary region $Q(t) \subset \Omega(t)$. The energy balance for the problem at hand, using the notation introduced in [141], reads:

$$\frac{\mathrm{d}\,\mathcal{U}}{\mathrm{d}t}(Q) = \mathcal{W}_u(Q) + \mathcal{Q}_u(Q) + \mathcal{T}_u(Q) \, , \tag{6.89}$$

with $\mathcal{U}$ the net internal energy of Q, $\mathcal{W}_u$ the mechanical external power, $\mathcal{Q}_u$ the power due to heat transfer, $\mathcal{T}_u$ the power due to mass exchanged by actin dynamics on $Q(t)$. It is assumed that each of these processes is *energetically separable* in the balance. The individual contributions read:

$$\mathcal{W}_u(Q) = \int_Q \vec{b} \cdot \vec{v} \, \mathrm{d}\Omega + \int_{\partial Q} \vec{t} \cdot \vec{v} \, \mathrm{d}\Gamma \, , \tag{6.90a}$$

$$\mathcal{Q}_u(Q) = \int_Q s_q \, \mathrm{d}\Omega - \int_{\partial Q} \vec{q} \cdot \vec{n} \, \mathrm{d}\Gamma \, , \tag{6.90b}$$

$$\mathcal{T}_u(Q) = \int_Q {}^u\mu_G \, s_G + {}^u\mu_F \, s_F \, \mathrm{d}\Omega - \int_{\partial Q} {}^u\mu_G \, \vec{h}_G \cdot \vec{n} \, \mathrm{d}\Gamma \, . \tag{6.90c}$$

Assumption (6.58) has been accounted for in the mass transfer contribution $\mathcal{T}_u(Q)$.
The time variation of net internal energy $\mathcal{U}$ corresponds to the power expenditure of external agencies: a mechanical contribution $\mathcal{W}_u$ due to body forces $\vec{b}$ and surface tractions $\vec{t}$ that do work on velocities $\vec{v}$; a heat contribution $\mathcal{Q}_u$ where s_q is the heat supplied by external agencies and $\vec{q}$ is the heat flux vector; a mass contribution $\mathcal{T}_u$ in which the scalar ${}^u\mu_\beta$ denotes the change in specific energy provided by a unit supply of *moles* of $\beta = G, F$ actin. Mass supply s_β is the push-forward of the supply $s_{\beta_R}(\vec{X},t)$ defined in eq. (6.55) and $\vec{h}_G$ is the flux of G-actin in the current configuration.

Standard application of the divergence theorem and of balance equations leads from (6.90a) to

$$\mathcal{W}_u(Q) \;=\; \int_Q \boldsymbol{\sigma} : \boldsymbol{l}\, \mathrm{d}\Omega \,. \tag{6.91}$$

where $\boldsymbol{l}$ is the gradient of velocity tensor, i.e. $\boldsymbol{l} = \nabla[\vec{v}]$ and $\boldsymbol{\sigma}$ is the Cauchy stress tensor. Since it is well known that

$$\boldsymbol{\sigma} : \boldsymbol{l}\, \mathrm{d}\Omega = \boldsymbol{P} : \dot{\boldsymbol{F}}\, \mathrm{d}\Omega_R = \boldsymbol{S} : \dot{\boldsymbol{E}}\, \mathrm{d}\Omega_R \,,$$

the mechanical power expenditure can be written in terms of the first Piola-Kirchoff stress $\boldsymbol{P} = J\boldsymbol{\sigma}\boldsymbol{F}^{-T}$ or of the second Piola-Kirchoff stress $\boldsymbol{S} = \boldsymbol{F}^{-1}\boldsymbol{P}$ in the referential configuration. Analogously, by defining the referential heat flux $\vec{q}_R = J\boldsymbol{F}^{-1}\vec{q}$ and making use of Nanson's formula, it holds

$$\vec{q}\cdot\vec{n}\, \mathrm{d}\Gamma = \vec{q}_R \cdot \vec{n}_R\, \mathrm{d}\Gamma_R \,. \tag{6.92}$$

As usual in the thermodynamics of continua, see e.g. [142], one can make use of the specific internal energy u_R per unit volume in the reference configuration to write the referential local form of the first principle as

$$\begin{aligned} \frac{\mathrm{d}u_R}{\mathrm{d}t} &= \boldsymbol{S} : \dot{\boldsymbol{E}} \; + s_{q_R} - \mathrm{Div}\,[\vec{q}_R] - \vec{h}_{G_R} \cdot \mathrm{Grad}\left[\mu^u_{G_R}\right] \\ &\quad + \mu^u_{G_R} \frac{\partial c_{G_R}}{\partial t} + \mu^u_{F_R} \frac{\partial c_{F_R}}{\partial t} + \left(\mu^u_{G_R} - \mu^u_{F_R}\right) w_R^{(6.50)} \,. \end{aligned} \tag{6.93}$$

6.5.2.2 Entropy imbalance

The second law of thermodynamics represents the balance of the interplay among the internal entropy of Q and the entropy transferred in it due to mass exchange and heat transferred. We make the non-trivial assumption that mechanics does not contribute directly to the total entropy flow in the entropy balance equation, as profoundly elaborated in [144, 187]. The entropy balance for the problem at hand reads:

$$\frac{\mathrm{d}\mathcal{S}}{\mathrm{d}t}(Q) - \frac{\mathrm{d}\mathcal{S}_i}{\mathrm{d}t}(Q) = \mathcal{Q}_\eta(Q) + \mathcal{T}_\eta(Q) \,, \tag{6.94}$$

where $\mathcal{S}$ is the net internal entropy of Q, $\mathcal{S}_i$ is the entropy produced inside Q, $\mathcal{Q}_\eta$ the entropy per unit time due to heat transfer, $\mathcal{T}_\eta$ the entropy per unit time due to mass transfer. The individual contributions read:

$$\mathcal{Q}_\eta(Q) \;=\; \int_Q \frac{s_q}{T}\, \mathrm{d}\Omega - \int_{\partial Q} \frac{\vec{q}}{T}\cdot\vec{n}\, \mathrm{d}\Gamma \,, \tag{6.95}$$

$$\mathcal{T}_\eta(Q) \;=\; \int_Q {}^\eta\mu_G\, s_G + {}^\eta\mu_F\, s_F\, \mathrm{d}\Omega - \int_{\partial Q} {}^\eta\mu_G \vec{h}_G \cdot \vec{n}\, \mathrm{d}\Gamma \,. \tag{6.96}$$

The second law of thermodynamics states that

$$\frac{\mathrm{d}\,\mathcal{S}_i}{\mathrm{d}t}(Q) \geq 0\,.$$

As for the energy, one can make use of the specific internal entropy η_R per unit referential volume to localize and rephrase the entropy imbalance in terms of internal energy taking advantage of identity (6.93) and of the sign definiteness of temperature :

$$\begin{aligned} T\,\frac{\mathrm{d}}{\mathrm{d}t}\,\eta_R - \frac{\mathrm{d}u_R}{\mathrm{d}t} + \boldsymbol{S} : \dot{\boldsymbol{E}} \; + \frac{\partial c_{G_R}}{\partial t}\,\mu_{G_R} + \frac{\partial c_{F_R}}{\partial t}\,\mu_{F_R} + \\ - \left(\frac{1}{T}\,\vec{q}_R + \mu^{\eta}_{G_R}\vec{h}_{G_R}\right)\cdot \mathrm{Grad}\,[\,T\,] - \vec{h}_{G_R}\cdot\mathrm{Grad}\,[\,\mu_{G_R}\,] - A^{(6.50)}_R\,w^{(6.50)}_R \geq 0\,, \end{aligned} \tag{6.97}$$

having denoted with $\beta = G, F$ and with the symbols $\mu_{\beta_R}, A^{(6.50)}_R$ the quantities

$$\mu_{\beta_R} = \mu^{u}_{\beta_R} - T\,\mu^{\eta}_{\beta_R} \tag{6.98}$$

$$A^{(6.50)}_R = -\mu_{G_R} + \mu_{F_R}\,. \tag{6.99}$$

6.5.2.3 Helmholtz free energy and thermodynamic restrictions

The referential specific Helmholtz free energy per unit volume $\psi_R\,(T, c_{G_R}, c_{F_R}, \boldsymbol{C}, \boldsymbol{\xi})$, defined as in (6.77), is taken as a function of temperature, strains (either $\boldsymbol{C}$ or $\boldsymbol{E}$), concentrations c_{G_R}, c_{F_R}, and of some kinematic internal variables $\boldsymbol{\xi}$ that compare with the usual meaning in inelastic constitutive laws [142, 168, 187, 5, 188, 189]. It follows that

$$T\,\frac{\mathrm{d}\eta_R}{\mathrm{d}t} - \frac{\mathrm{d}u_R}{\mathrm{d}t} = -\frac{\mathrm{d}\psi_R}{\mathrm{d}t} - \eta_R\,\frac{\partial T}{\partial t}\,, \tag{6.100}$$

which can be inserted in (6.97) to derive the entropy imbalance in final form:

$$\begin{aligned} -\frac{\mathrm{d}\psi_R}{\mathrm{d}t} - \eta_R\,\frac{\partial T}{\partial t} + \boldsymbol{S} : \dot{\boldsymbol{E}} \; + \frac{\partial c_{G_R}}{\partial t}\,\mu_{G_R} + \frac{\partial c_{F_R}}{\partial t}\,\mu_{F_R} + \\ - \left(\frac{1}{T}\,\vec{q}_R + \mu^{\eta}_{G_R}\vec{h}_{G_R}\right)\cdot \mathrm{Grad}\,[\,T\,] - \vec{h}_{G_R}\cdot\mathrm{Grad}\,[\,\mu_{G_R}\,] - A^{(6.50)}_R\,w^{(6.50)}_R \geq 0\,. \end{aligned} \tag{6.101}$$

In view of the stated functional dependency of the free energy, its total derivative with respect to time reads:

$$\frac{\mathrm{d}}{\mathrm{d}t}\,\psi_R(T, c_{G_R}, c_{F_R}, \boldsymbol{C}, \boldsymbol{\xi}) = \frac{\partial \psi_R}{\partial T}\,\frac{\partial T}{\partial t} + \frac{\partial \psi_R}{\partial c_{G_R}}\,\frac{\partial c_{G_R}}{\partial t} + \frac{\partial \psi_R}{\partial c_{F_R}}\,\frac{\partial c_{F_R}}{\partial t} + \frac{\partial \psi_R}{\partial \boldsymbol{C}} : \dot{\boldsymbol{C}} + \frac{\partial \psi_R}{\partial \boldsymbol{\xi}} : \frac{\partial \boldsymbol{\xi}}{\partial t} \tag{6.102}$$

The Clausius-Duhem inequality yields:

$$\left(-\frac{\partial \psi_R}{\partial c_{G_R}} + \mu_{G_R}\right)\frac{\partial c_{G_R}}{\partial t} + \left(-\frac{\partial \psi_R}{\partial c_{F_R}} + \mu_{F_R}\right)\frac{\partial c_{F_R}}{\partial t} + \frac{\partial T}{\partial t}\left(-\eta_R - \frac{\partial \psi_R}{\partial T}\right) + \dot{\boldsymbol{C}} : \left(\frac{1}{2}\,\boldsymbol{S} - \frac{\partial \psi_R}{\partial \boldsymbol{C}}\right) +$$

$$-\frac{\partial \psi_R}{\partial \boldsymbol{\xi}} : \frac{\partial \boldsymbol{\xi}}{\partial t} - \left(\frac{1}{T} \vec{q}_R + \mu_{G_R}^{\eta} \vec{h}_{G_R} \right) \cdot \mathrm{Grad}\,[T] - \vec{h}_{G_R} \cdot \mathrm{Grad}\,[\mu_{G_R}] - A_R^{(6.50)} w_R^{(6.50)} \geq 0 \,. \tag{6.103}$$

This inequality must hold for any value of the time derivative of the temperature, the referential concentrations, the strain tensor. Since they appear linearly in the inequality, the factors multiplying them must be zero, as otherwise it would be possible to find a value for the time derivatives that violate the inequality. Therefore, the following prescriptions apply

$$\boldsymbol{S} = 2\,\frac{\partial \psi_R}{\partial \boldsymbol{C}}\,, \qquad \eta_R = -\frac{\partial \psi_R}{\partial T}\,, \qquad \mu_{G_R} = \frac{\partial \psi_R}{\partial c_{G_R}}\,, \qquad \mu_{F_R} = \frac{\partial \psi_R}{\partial c_{F_R}}\,. \tag{6.104a}$$

The internal force, conjugate to $\boldsymbol{\xi}$, will be denoted with the symbol $\boldsymbol{\chi}$, i.e.

$$\boldsymbol{\chi}_R = -\frac{\partial \psi_R}{\partial \boldsymbol{\xi}}\,. \tag{6.104b}$$

Equation (6.104a) yields to the Clausius-Plank inequality, which under the assumptions of Curie symmetry principle [144], can be written as

$$\boldsymbol{\chi}_R : \dot{\boldsymbol{\xi}} \geq 0\,, \tag{6.105a}$$

$$\left(\frac{1}{T} \vec{q}_R + \mu_{G_R}^{\eta} \vec{h}_{G_R} \right) \cdot \mathrm{Grad}\,[T] + \vec{h}_{G_R} \cdot \mathrm{Grad}\,[\mu_{G_R}] \leq 0\,, \tag{6.105b}$$

$$A_R^{(6.50)} w_R^{(6.50)} \leq 0\,. \tag{6.105c}$$

6.5.2.4 Decompositions.

The stress filed $\boldsymbol{S}$ will be additively decomposed in the sum of the active and passive contributions, analogously to generalized Maxwell models

$$\boldsymbol{S} = \boldsymbol{S}_{active} + \boldsymbol{S}_{passive}\,. \tag{6.106}$$

Active response is related to cytoskeletal reorganization in stress fibers and pseudopodia, whereas the passive response reflects the mechanical behavior that each component of the cell has inasmuch material bodies. Although the "additive decomposition" of the total stress is the most common way to model the activation process inside "active materials", its validity remains a subject strongly debated by the scientific community. For instance, a further way to describe the phenomenon of activation is present in literature; specifically, this is called the "active strain" approach, and involves a multiplicative decomposition of the strain gradient tensor in an elastic and active part, is also proposed $\boldsymbol{F} = \boldsymbol{F}^e \boldsymbol{F}^a$, similarly to the classical plasticity and growth and morphogenesis theories [190].

We base the theory for pseudopodia on a multiplicative decomposition of the deformation gradient

$$\boldsymbol{F} = \boldsymbol{F}^e \, \boldsymbol{F}^c\,. \tag{6.107}$$

Tensor $\boldsymbol{F}^c$, named *swelling distortion* is the local distortion of the material neighborhood of a point due to a volumetric swelling (de-swelling) owing to the phase change of actin, from monomeric to a

network of filaments. Its representation will be taken as $\boldsymbol{F}^c = \lambda^c \mathbb{1}$, assuming therefore that a dense network of actin filaments form in pseudopodia. This approach conforms well for lamellipodia, but it might result in inappropriate for slender and highly oriented microstructures seen in filopodia, which might be better captured by the protrusion-contraction uniaxial tensors presented in [181] or [191]. The following identities can be easily assessed:

$$\det[\boldsymbol{F}^c] = J^c = \lambda^{c3}\,, \qquad \dot{J}^c/J^c = 3\,\dot{\lambda}^c/\lambda^c\,, \qquad \boldsymbol{l}^c = \dot{\boldsymbol{F}}^c\,\boldsymbol{F}^{c-1} = \dot{J}^c/(3J^c)\mathbb{1}\,. \tag{6.108}$$

We assume that changes in J^c occur because of changes in filaments $J^c = J^c(c_{F_R})$ and define the partial molar volume of the pseudopodia as

$$\Omega_C(c_{F_R}) = \frac{\mathrm{d}J^c}{\mathrm{d}c_{F_R}} \tag{6.109}$$

and it holds

$$\dot{J}^c = \Omega_C(c_{F_R})\,\frac{\partial c_{F_R}}{\partial t}\,. \tag{6.110}$$

The decomposition (6.107) leads to a multiplicative decomposition for the left Cauchy-Green tensor, too:

$$\boldsymbol{C} = \boldsymbol{C}^e\,\boldsymbol{C}^c \tag{6.111}$$

with the swelling factor $\boldsymbol{C}^c = J^{c2/3}\,\mathbb{1}$ and the elastic factor $\boldsymbol{C}^e = J^{c-2/3}\,\boldsymbol{C}$. A classical [149] specification of $J^c(c_{F_R})$ is the affine map

$$J^c(c_{F_R}) = 1 + (c_{F_R} - c^0_{F_R})\,\Omega_C \tag{6.112}$$

with a constant partial molar volume $\Omega_C > 0$.

In the realm of viscoelasticity, if is also common to perform a multiplicative decomposition of the deformation gradient $\boldsymbol{F}^e$ into volumetric $\boldsymbol{F}^{e^v}$ and isochoric $\boldsymbol{F}^{e^i}$ factors

$$\boldsymbol{F}^e = \boldsymbol{F}^{e^v}\,\boldsymbol{F}^{e^i}\,. \tag{6.113}$$

The volumetric factor $\boldsymbol{F}^{e^v} = J^{e1/3}\,\mathbb{1}$ turns out to be completely identified by the determinant of $\boldsymbol{F}^e$, whereas the isochoric factor $\boldsymbol{F}^{e^i} = J^{e-1/3}\,\boldsymbol{F}^e$ obeys to the constraint $\det\left[\boldsymbol{F}^{e^i}\right] = 1$. The decomposition (6.113) leads to a multiplicative decomposition for the left Cauchy-Green tensor, too:

$$\boldsymbol{C}^e = \boldsymbol{C}^{e^v}\,\boldsymbol{C}^{e^i}\,, \tag{6.114}$$

with volumetric factor $\boldsymbol{C}^{e^v} = J^{e2/3}\,\mathbb{1}$ and the isochoric factor $\boldsymbol{C}^{e^i} = J^{e-2/3}\,\boldsymbol{C}^e$.

6.5.2.5 Constitutive theory

Two among the several ways to satisfy the thermodynamic restriction (6.105b) have been discussed in [141] (and in the previous part of the current thesis) in the framework of trapping. Here, we proceed as for the membrane imposing that the cytosol stands in thermal equilibrium, whereby $\mathrm{Grad}[T] = \vec{0}$. The flow of actin monomers is linearly related to the gradient of their chemical potential by Fick's assumption, consistently with the thermodynamic restriction (6.105b):

$$\vec{h}_{G_R} = -\boldsymbol{M}_{G_R}(c_{G_R})\,\mathrm{Grad}[\mu_{G_R}]\,. \tag{6.115a}$$

The following isotropic non linear specialization for the mobility tensor $\boldsymbol{M}_{G_R}$ is chosen [149]

$$\boldsymbol{M}_{G_R}(c_{G_R}) = \mathbb{\mu}_{G_R} c_{G_R}^{max}\, \vartheta_{G_R}\,(1-\vartheta_{G_R})\,\mathbb{1}\,, \tag{6.116}$$

where $c_{G_R}^{max}$ is the saturation limit for receptors, and $\mathbb{\mu}_{G_R} > 0$ is the *mobility* of actin monomers. Assuming that the trapped species F has vanishing mobility is an alternative view of modeling the absence of their flux.

The Helmholtz free energy density ψ_R is modeled by decomposing it into separate parts: a thermal contribution ψ_R^{th}, a diffusive contribution ψ_R^{diff}, an elastic contribution ψ_R^{el}, and an inelastic (also called *configurational*) counterpart ψ_R^{in}

$$\psi_R(T, c_{G_R}, c_{F_R}, \boldsymbol{C}, \boldsymbol{\xi}) = \psi_R^{th}(T) + \psi_R^{\text{diff}}(c_{G_R}, c_{F_R}) + \psi_R^{el}(c_{F_R}, \boldsymbol{C}) + \psi_R^{in}(c_{F_R}, \boldsymbol{E}, \boldsymbol{\xi})\,. \tag{6.117}$$

This splitting is here taken for granted without motivation. We will not indulge in the description of ψ_R^{th} (see [141] in case of interest) and we'll rather focus on the remaining parts.

Statistical mechanics depicts the entropy for isolated systems in terms of the density of states, the number of possible molecular configurations [150]. Making recourse to Stirling's approximation and since the entropy transforms with the volume by means of J, one finds that the following well-known expression of the entropy of mixing *in the reference configuration* arises, the universal gas constant R being the product of Boltzmann constant k_B and Avogadro's number:

$$\eta_{\beta_R}^{\text{diff}} = -RJ\, c_\beta^{max}\,\left(\vartheta_\beta\,\ln[\vartheta_\beta] + (1-\vartheta_\beta)\,\ln[1-\vartheta_\beta]\right)\,, \tag{6.118}$$

having denoted with $\beta = G, F$ and with ϑ_{β_R} the ratio

$$\vartheta_{\beta_R}(\vec{X}, t) = c_{\beta_R}/c_{\beta_R}^{max}\,. \tag{6.119}$$

We argued in eq. (6.23) that, in view of the structure of the lipid membranes, the maximum number of moles or molecules per unit area for any species remains unchanged in time in the current configuration. The same argument does not seem to apply for the bulk, hence we take henceforth that

$$c_{\beta_R}^{max}(\vec{X}, t) = c_\beta^{max}(\vec{x}(\vec{X}, t), t)\, J(\vec{X}, t) \tag{6.120}$$

is constant and write the free energy density for the continuum approximation of mixing [150] as

$$\begin{aligned}\psi_R^{\text{diff}}(c_{G_R}, c_{F_R}) = {} & \mu_{G_R}^0\, c_{G_R} + RT c_{G_R}^{max}\,[\vartheta_{G_R}\ln\vartheta_{G_R} + (1-\vartheta_{G_R})\ln(1-\vartheta_{G_R})] \\ & + \mu_{F_R}^0\, c_{F_R} + RT c_{F_R}^{max}\,[\vartheta_{F_R}\ln\vartheta_{F_R} + (1-\vartheta_{F_R})\ln(1-\vartheta_{F_R})]\,.\end{aligned} \tag{6.121}$$

Note that if the saturation is constant in the current configuration, an explicit coupling of the free energy of mixing with the deformation arises by means of J. A new stress would come out, in view of the thermodynamic prescription (6.104a).

Following [187], we will define visco-elastic materials based on the multiplicative decomposition (6.114). Specifically, the free energy for visco-elastic materials will be defined as follows

$$\psi_R^{el}(c_{F_R}, \boldsymbol{C}) + \psi_R^{in}(c_{F_R}, \boldsymbol{E}, \boldsymbol{\xi}) = \psi_R^{el,vol}(c_{F_R}, \boldsymbol{C}^{e^v}) + \psi_R^{el,iso}(c_{F_R}, \boldsymbol{C}^{e^i}) + \psi_R^{in}(c_{F_R}, \boldsymbol{E}^e - \boldsymbol{\xi})\,. \tag{6.122}$$

with ψ_R^{in} depending upon $\boldsymbol{E}^e$ by means of $\boldsymbol{C}^{e^i}$. The volumetric part of the elastic free energy is defined through J^e, highlighting the role of the swelling tensor and of the concentration of pseudopodia, since

$$\boldsymbol{C}^{e^v} = J^{e2/3}\,\mathbb{1} = J^{2/3}\,J^{c-2/3}\,\mathbb{1} = \left(\frac{J}{1+(c_{F_R}-c^0_{F_R})\,\Omega_C}\right)^{2/3}\mathbb{1} \tag{6.123}$$

in view of eq. (6.112). On the other end, it holds

$$\boldsymbol{C}^{e^i} = \boldsymbol{C}^e\,J^{e-2/3} = \boldsymbol{C}\,J^{c-2/3}\,J^{e-2/3} = \boldsymbol{C}\,J^{-2/3} \tag{6.124}$$

hence $\boldsymbol{C}^{e^i}$ depends merely upon the state of deformation and not upon the concentration of species. This outcome reverberates upon the energetic contributions $\psi_R^{el,iso}$ and ψ_R^{in}. The latter is such that

$$\frac{\partial\,\psi_R^{in}}{\partial\,\boldsymbol{E}} = -\frac{\partial\,\psi_R^{in}}{\partial\,\boldsymbol{\xi}}\,, \tag{6.125}$$

a property physically grounded in the rheological model of Maxwell, for which we refer to [187] or [192].

Provided that the above holds, the selection for ψ_R^{el} and ψ_R^{in} is arbitrary. Their selection shall be different in modeling the passive behavior or the active response of pseudopodia and stress fibers. The elastic, reversible behavior that occurs once the viscous effects vanish (ideally at $t \to \infty$) is captured by ψ_R^{el}. The inelastic free energy accounts for the non-equilibrium response due to viscosity - the so called *dissipation potential*. By thermodynamic restrictions (6.104) and identity (6.125)

$$\boldsymbol{\chi}_R = -\frac{\partial\,\psi_R^{in}}{\partial\,\boldsymbol{\xi}} = \frac{\partial\,\psi_R^{in}}{\partial\,\boldsymbol{E}} \tag{6.126a}$$

$$\boldsymbol{S} = 2\,\frac{\partial\,\psi_R^{el}}{\partial\,\boldsymbol{C}} + \boldsymbol{\chi}_R\,. \tag{6.126b}$$

According to eq. (6.126b), tensorial internal forces $\boldsymbol{\chi}_R$ can be interpreted as a *non-equilibrium stress tensor* of second Piola-Kirchoff kind, that accounts for the viscous response.

Inelastic internal entropy production (6.105a) was described by the internal flux variables $\boldsymbol{\xi}$ and by their energy-conjugate forces $\boldsymbol{\chi}_R$. A simple way to satisfy constraint (6.105a) is choosing a positive definite operator $\mathbb{L}$ such that

$$\boldsymbol{\chi}_R = \mathbb{L}\,\dot{\boldsymbol{\xi}}\,. \tag{6.127}$$

In case of isotropy, the fourth order operator $\mathbb{L}$ restricts to the scalar viscosity ν times the identity operator. Equations (6.126a), (6.127) provide evolution equations for $\boldsymbol{\chi}_R$ that allow the algorithmic integration of the constitutive law once a selection for the free energy densities ψ_R^{el} and ψ_R^{in} is made.

The chemical potential of G-actin monomers and of F-actin networks descends from thermodynamic prescriptions (6.104a), in the form

$$\mu_{G_R} = \frac{\partial\,\psi_R^{\text{diff}}(c_{G_R}, c_{F_R})}{\partial\,c_{G_R}} \tag{6.128a}$$

$$\mu_{F_R} = \frac{\partial \psi_R^{\text{diff}}(c_{G_R}, c_{F_R})}{\partial c_{F_R}} + \frac{\partial \psi_R^{el,vol}(c_{F_R}, \boldsymbol{C}^{e^v})}{\partial c_{F_R}} + \frac{\partial \psi_R^{el,iso}(c_{F_R}, \boldsymbol{C}^{e^i})}{\partial c_{F_R}} + \frac{\partial \psi_R^{in}(c_{F_R}, \boldsymbol{E}^e - \boldsymbol{\xi})}{\partial c_{F_R}} \,. \tag{6.128b}$$

While the chemical potential of actin monomers has merely an entropic nature, mechanical contributions enter the definition of the chemical potential of actin networks. Specifically, mechanics affects μ_{F_R} in the volumetric contribution $\psi_R^{el,vol}$ through the swelling tensor $\boldsymbol{C}^{e^v}$ (6.123), whereas the isochoric tensor $\boldsymbol{C}^{e^i}$ was proven to be independent upon the concentration of species in eq. (6.124). Nonetheless, the parameters of the viscoelastic loading-unloading law are expected to depend upon the extent of the polymerization reaction by means of the network concentration c_{F_R} in all terms of the mechanical free energy.

The mechanical effect on the chemical potential does not propagate into the mass flux because the mobility of actin network is assumed to be negligible. Mechanics however enters the affinity of polymerization reaction (6.50) in view of definition (6.99). The stress state is expected to favor polymerization nearby the lipid membrane and depolymerization towards the nucleus.

6.5.2.6 The multiscale scenario of cell viscoelasticity

Although the mechanical framework of the free energy depicted above is rather clear, a specialization of the constitutive equations has not been attempted here and in many cases (as for stress fibers and microtubules) it has not been attempted in the literature, to the best of our knowledge. The hindrance stands in the multiscale scenario of cell viscoelasticity: while the mechanical behavior and properties of intermediate filaments, actin filaments, and microtubules has been nowadays quite clarified, at least in terms of relative stiffness and strengths, bundles of the filaments, their response, polymerization, shape and time evolution are not yet captured by comprehensive models at the "macroscopic" scale through appropriate free energies. As a consequence, the ability of models to capture the mechanics of fundamental cellular processes (as chemotaxis, cell sprouting, junction and differentiation, endocitosys and exocitosys to cite a few) still requires abundant research before gaining predicting capabilities in simulations.

The cytoskeleton, an interconnected network of regulatory proteins and filamentous biological polymers, undergoes massive reorganization during cell deformation, especially after cell rolling and adhesion [3, 193] and in mediating, sensing and transduction of mechanical cues from the micro-environment [194]. Homogenized models for the mechanical response of a cell shall include in effective, macroscopic properties the polymerization/depolymerization of filaments, the process of cross-linking that determine the architecture of cytoskeletal filaments, and the passive mechanical properties of the cytosol. In view of the above, the thermodynamics of statistically-based continuum theories for polymers with transient networks [195, 196, 197, 125, 198] appear to be good candidates for the selection of free energies $\psi_R^{el}(c_{F_R}, \boldsymbol{C})$ and $\psi_R^{in}(c_{F_R}, \boldsymbol{E}, \boldsymbol{\xi})$. The need for statistical approaches to model the time-dependent response of polymers with reversible cross-links emerges since the overall response is influenced by the rate of assembly and disassembly of cross-linking factors that are controlled at the molecular level by actin nucleation, capping, severing factors, and by the activity of molecular motors such myosin-II, which, in combination with cross-linkers, appears to be responsible for the viscoelastic properties of the cytoskeleton [199]. At present, however, such a comprehensive model has not yet been proposed for the pseudopodia

driven cell motion. Classical models as hyperelastic Saint-Venant [181] or Newtonian viscous fluids [200] eventually surrounded by a hyperelastic, zero-thickness membrane [201] have been used for the pseudopodia, whereas a very large amount of literature concerns pseudopod dynamics (see for instance [202] and the large literature therein) or ameboid motion [203] with no account for their mechanical response. Different approaches to cell motility, as for active gel theory coupled to the classical theory of thin elastic shells, are also widely used [204] but are not discussed in this thesis. The framework described herein, including myosin dynamics, phase transformations between G-actin and F-actin, has been depicted in a set of publications by the group of H. Gomez [176, 205]. The flow of the F-actin network was treated as a Newtonian fluid and directed by its velocity. A one dimensional yet comprehensive model has been proposed in [206]. Not surprisingly, the nucleus and its meshwork of intermediate filaments formed mostly of proteins (nuclear lamina), contribute to the viscoelasticity of cells [207]. Depending upon the content of Lamins, the nucleus becomes more or less stiff, impacting cell migration: nuclear deformation facilitates cell migration through complex environments, whereas its stiffness may act as a mechanical barrier for a migratory cell [208]. Cells are capable to modify their viscoelasticity while migrating across confined spaces [209], a very intriguing mechanism yet complex to be captured macroscopically in view of its multiscale nature.

The multiscale scenario is invoked also for cell contractility. There are pieces of evidence [210] that the interaction among filaments, motors, and cross-linkers is mechanically stimulated. As reported in [194], *myosin binding to actin fibers occurs in a force-dependent manner, as well as the contractile response of actomyosin to extracellular stiffness*. According to [211], force feedback controls motor activity and increases density and mechanical efficiency of self-assembling branched actin networks, thus suggesting that those feedbacks could allow migratory cells adjusting their viscoelastic properties to favor migration. Mass transport and *cell contractility* have been accounted for in several publications with different degree of complexity [125, 180, 191]: to the best of our knowledge, however, the force transmission has always been modeled stemming from the similarity between the sarcomeric structure of stress fibers and the actin-myosin interactions in muscle cells. In [129] a multi-dimensional network of stress fibers was built on the notion of a representative volume element, in which stress fibers can form in any direction with equal probability. Average macroscopic stress is then recovered from the fiber tension, which in turn is generated by the cross-bridging cycles and described by a Hill-like relation [212] of viscoelastic nature. Anisotropic stress fibers distributions have been considered in [125], making use of Von Mises distribution functions at the "microscale" coupled to a directional averaging operator. The active contraction is described in terms of the change of fiber length and its rate of change, with a product formula of viscoelastic origin. Experimental evidences, however, seem to show that such a resemblance might be questionable in the dynamics and mechanics of endothelial cell spreading [97] and hence that the predictive capability of this family of models might be poor for this family of cells.

Finally, the *passive response of the cytosol*, provided mainly by the intermediate filaments attached to the nuclear and plasma membranes, has been modeled by several authors by means of classical models as linear elasticity [125], the finite strain generalization of Hooke's law [129] or a Neo-Hookean potential energy

$$\psi_R^{el}(\boldsymbol{C}^e) = \frac{G_0}{2}\left(I_1(\boldsymbol{C}^e) - 3\right), \qquad \psi_R^{in}(\boldsymbol{E}^e, \boldsymbol{\xi}) = \frac{G_0 - G_\infty}{G_0}\,\psi_R^{el}(\boldsymbol{E}^e - \boldsymbol{\xi}), \tag{6.129}$$

where G_0 is the initial shear modulus and G_∞ is the shear modulus at the end of the viscous processes. This classical choice of Helmholtz free energy is associated to efficient integration schemes, depicted in [192].

Within this chapter, we admit not being capable to include this rich and tangled scenario of multi-physics processes across multiple scales. We limit ourselves, being aware of several attempts to capture at least cell contractility [101, 178, 128, 121, 180, 14], to a simplistic formulation of viscoelasticity, which will be enriched in future investigations.

6.5.3 Regularized Neo-Hookean formulation

In the current section and in the subsequent chapter, in-silico models will be performed characterized by a mechanical behavior of the cell described by a regularized Neo-Hookean model ($\boldsymbol{S} = \boldsymbol{S}_{passive}$ - see (6.106) -). Therefore, we neglected the viscous behavior hereto discussed, and we focus only on the elastic one (6.129). According to the additive decomposition in an isochoric and volumetric part of the Helmholtz free energy (see (6.122) neglecting the inelastic contribute and expressing $\psi_R^{el,vol}$ as a function of J), we can write:

$$\psi_R^{el}(\boldsymbol{C}) = \psi_R^{el,vol}(J) + \psi_R^{el,iso}(\boldsymbol{C}^i)\,, \tag{6.130}$$

where:

$$\psi_R^{el,vol}(J) = \frac{\kappa}{2}\left[\ln(J)\right]^2\,, \tag{6.131a}$$

$$\psi_R^{el,iso}(\boldsymbol{C}^i) = \frac{G}{2}\left(\mathrm{tr}\left[\boldsymbol{C}^i\right] - 3\right)\,, \tag{6.131b}$$

with κ and G the bulk and shear modulus respectively, for a regularized NeoHookean formulation [192]. Therefore, narrowing the relation (6.126b) at the current case:

$$\boldsymbol{S} = 2\left(\frac{\partial \psi_R^{el,iso}}{\partial \boldsymbol{C}} + \frac{\partial \psi_R^{el,vol}}{\partial \boldsymbol{C}}\right)\,, \tag{6.132}$$

we attains:

$$\frac{\partial \psi_R^{el,iso}}{\partial \boldsymbol{C}} = \frac{G}{2}\frac{\partial}{\partial \boldsymbol{C}}\mathrm{tr}\left[J^{-\frac{2}{3}}\boldsymbol{C}\right] = \frac{G}{2}\underbrace{\frac{\partial J^{-\frac{2}{3}}}{\partial \boldsymbol{C}}}_{-\frac{1}{3}J^{-\frac{2}{3}}\boldsymbol{C}^{-1}}\mathrm{tr}\left[\boldsymbol{C}\right] + \frac{G}{2}J^{-\frac{2}{3}}\underbrace{\frac{\partial \mathrm{tr}\left[\boldsymbol{C}\right]}{\partial \boldsymbol{C}}}_{\mathbb{1}} \tag{6.133a}$$

$$= \frac{G}{2}\left[-\frac{1}{3}J^{-\frac{2}{3}}\boldsymbol{C}^{-1}\mathrm{tr}\left[\boldsymbol{C}\right] + J^{-\frac{2}{3}}\mathbb{1}\right] = -\frac{G}{2}\frac{1}{3}J^{-\frac{2}{3}}\left[-\frac{\mathrm{tr}\left[\boldsymbol{C}\right]}{3}\boldsymbol{C}^{-1} + \mathbb{1}\right]\,, \tag{6.133b}$$

$$\frac{\partial \psi_R^{el,vol}}{\partial \boldsymbol{C}} = \kappa\ln(J)\frac{1}{J}\underbrace{\frac{\partial J}{\partial \boldsymbol{C}}}_{\frac{J}{2}\boldsymbol{C}^{-1}} = \frac{\kappa}{2}\ln(J)\boldsymbol{C}^{-1}\,. \tag{6.133c}$$

Finally, exploiting the expressions between the first and second Piola-Kirchoff stress tensor ($\boldsymbol{P} = \boldsymbol{F}\boldsymbol{S}$), the balance of momentum (6.60a) becomes:

$$\mathrm{Div}\,[\boldsymbol{F}\boldsymbol{S}] + \vec{b}_R = \vec{0}\,, \qquad \vec{X} \in \Omega_R\,, \tag{6.134}$$

with $\boldsymbol{S}$ equal to:

$$\begin{aligned} \boldsymbol{S} &= 2\left(\frac{\partial \psi_R^{el,iso}}{\partial \boldsymbol{C}} + \frac{\partial \psi_R^{el,vol}}{\partial \boldsymbol{C}}\right) = 2\left[\frac{G}{2}\frac{1}{3}J^{-\frac{2}{3}}\left[-\frac{\mathrm{tr}\,[\boldsymbol{C}]}{3}\boldsymbol{C}^{-1} + \mathbb{1}\right] + \frac{\kappa}{2}\ln(J)\boldsymbol{C}^{-1}\right] \\ &= G\frac{J^{-\frac{2}{3}}}{3}\left[-\frac{\mathrm{tr}\,[\boldsymbol{C}]}{3}\boldsymbol{C}^{-1} + \mathbb{1}\right] + \kappa\ln(J)\boldsymbol{C}^{-1}\,. \end{aligned} \tag{6.135}$$

6.6 Concluding remarks

In this chapter, a multi-physics framework of protein relocation on the advecting lipid membrane during cell spreading and motion has been put forward. It sets the (continuum) thermodynamic background for simulations of receptor recruitment during migration. Throughout the next chapters of the current part of the thesis, we deal on simulations with the relocation of vascular endothelial growth factor receptors on advecting lipid membrane during endothelial cell adhesion and spreading. Those simulations may have a significant impact in biology and in the pharmacological treatment of cancer, either in view of their predictive nature in virtual experiments or by clearly identifying the sequence of processes that limit the relocation of targeted proteins during in vitro experiments.

The present framework still has significant limitations, yet by illustrating a complex and rigorous scenario it might be a cornerstone to account for several further processes. To cite a major phenomenon that has been insufficiently discussed here, the transport of the protein on the membrane is crucially coupled to the cytoskeleton reorganization, which is related to the motion of integrins on the membrane: the formation of focal adhesion sites is preliminary to stress fibers generation and contractility. Internalization of complexes is another phenomenon not included in this work. Further efforts, therefore, will be devoted to extending this framework to these and other challenging tasks.

We also aimed in this chapter (together with section 2.5) at recollecting recent publications from several schools on cell mechanics, encasing them in a unified framework, being aware that a comprehensive account of publications is significantly hard in view of the broadness of the literature in the field. We clarified that for some processes, as for contractility and protrusion, either a thermodynamically consistent formulation has not been devised yet or it stems from simplistic models that do not account for the microstructural evolution of the biopolymers. Even in this fascinating field, the last word is far from being spoken.

Chapter 7

Relocation of proteins on a lipid membrane that advects during endothelial cell adhesion and spreading

Cell adhesion to another cell or to ECM or on a substrate in static in-vitro experiments, is essential in the development and maintenance of tissues. This process is dominated by three stages [213]:

- an initial phase regarding the attachment to the substrate of the cell body;
- a second step govern by spreading and flattening of the cell;
- a third period characterized by the rearrangements of the actin cytoskeleton with consequent generation of FA.

To mimic the passive cell adhesion we adsorbed culture surface with a positively charged synthetic polymer of the amino acid L-lysine or D-lysine (Poly-Lysine). Poly-Lysine favors cell attachment, by uplifting the electrostatic interplay among cations of the culture surface and negatively-charged ions on the cell membrane. Since Poly-Lysine inhibits the re-organization of the stress fibers, by preventing the focal adhesion driven by integrins, it appears reasonable to uncouple the mechanical spreading of the cell and the modeling of chemical-transport processes along its membrane, as formulated in the previous chapter 6. Accordingly, mechanics in the bulk can be solved for as first and membranes processes at a later stage. This is not the general case, though. In accounting for the diffusion of integrins concurrently with cell spreading on a substrate that is filled with specific ligands rather than Poly-Lysine, uncoupling becomes less realistic. Models for cytoskeleton reorganization [118, 129, 123] must be taken into account in this alternative case, which entails focal adhesions and hence matching with the motion of integrins. Although, mass transport and cell contractility have been accounted for in several publications with different degree of complexity [125, 180, 191]: to the best of our knowledge, the force transmission has always been modeled stemming from the similarity between the sarcomeric structure of stress fibers and the actin-myosin interactions in muscle cells. Experimental pieces of evidence seem to show that such a resemblance might be questionable in the dynamics and mechanics of endothelial cell spreading [97] and hence that the predictive capability of this family of models might be poor for the target of the present thesis.
Therefore, in the first instance, a re-proposal of the decoupled model also for integrins (as it will

show in the next chapter 8) can represent an important intermediate-step capable of providing essential indications in order to build a fully two-way coupled model able to describe how integrins activities pair problem on the membrane with that in the bulk. Therefore, we attempt to including neither a rich and tangled scenario of multi-physics processes across multiple scales to ECs and their specific chemo-mechanical response [97], nor any description of the active behavior of this kind of cell.

Accordingly, we have consciously decided to solely take into account the passive response of the cell, recurring to a simplistic formulation of hyperelasticity (*Regularized Neo-Hookean formulation* - see section 6.5.3 -) both for nucleus and the cytoplasm (cytosol more organelles - see Fig. 7.1), where the contractile ability of the EC, usually ruled by the cytoskeleton machinery, is appropriately surrogated through suitably calibrated bulk forces inside the pseudopodia. Precisely, symmetric mechanical spreading of the EC is proposed, as a result of the ligands homogenous experimental conditions on the substrate (totally analogous to what has been observed in Part II of the thesis).

Precisely, in the current chapter, and in the next one, we aim to build a new in-silico formulation owing to the writing in a weak form of the governing equations explicated throughout the current Part of the thesis, leading the way towards new numerical approximations and solutions of the experimental outcomes proposed in chapter 4.
Such a mathematical framework is capable to describe and quantify the main phases of the mechanical spreading shown in chapter 5, and papers [138, 139] and so understand how, a "large deformations scheme", can impact the relocation and depletion of VEGFR2 and integrin on the cell membrane of an EC.

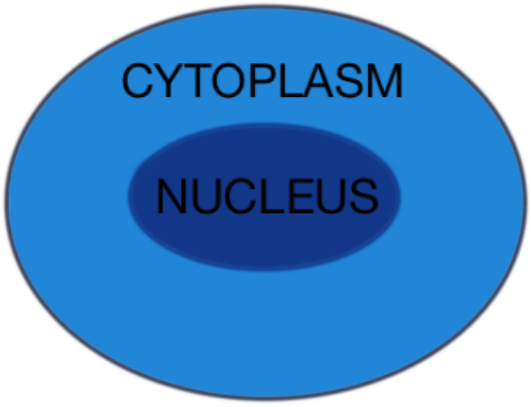

Figure 7.1: Illustration of an idealized EC composed of two distinct materials: nucleus and cytoplasm.

7.1 Experimental investigations and their numerical simulation

7.1.1 Biological evidence

The cell-cell interaction and adhesion are receptor-mediated processes: it is the affinity and avidity of receptors that modulate the adhesive forces during cell spreading and migration. As a paradigmatic study, consider the extravasation of EPCs, an important step in the neovascularization of a tumor mass. The luminal surface of blood vessels is coated with a carbohydrate-rich surface layer, consisting of adsorbed proteins and membrane-bound proteoglycans, collectively referred to as the *endothelial glycocalyx*. The thickness of the latter is on the order 400-500 nm in vivo, while in vitro cultured ECs express a glycocalyx thickness ranging from 29 to 118 nm [214]. The EPCs /ECs interaction is mediated by the endothelial glycocalyx receptors, without inducing the cytoskeletal reorganization.

Several reports assume that plasma membrane viscoelasticity, cytoplasmic viscosity, and cellular geometry are responsible for the mechanical deformation of cells, using erythrocytes as a cellular model of analysis. In this regard, it is important to pinpoint that erythrocytes can form neither stress fibers nor other actin networks, hence their remarkable mechanical properties must indeed originate solely from the architecture of their cell membrane. The influence of curvature on the elastic stiffness of the membrane appears to be related to the size of the cell [116].

In the first set of experiments, in order to focus on the adhesion phase of an EC, we plated ECs on the positively charged synthetic polymer of the amino acid L-lysine or D-lysine (Poly-Lysine). Poly-Lysine favors cell attachment, by uplifting the electrostatic interplay among cations of the culture surface and negatively-charged ions on the cell membrane. At the same time, poly-Lysine prevents the organization of focal adhesions and of stress fibers. Under these experimental conditions, cell spreading could be promoted only by electrostatic interactions, while the mechanical response of the cell relies on the membrane and on the passive response of the cytosol.

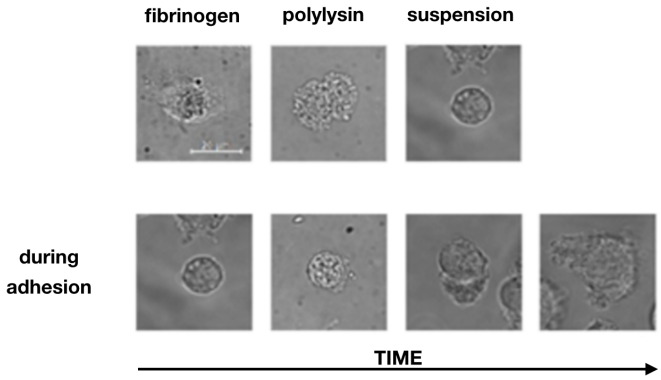

(a) Analysis over time of ECs seeded on Poly-Lysine ECM.

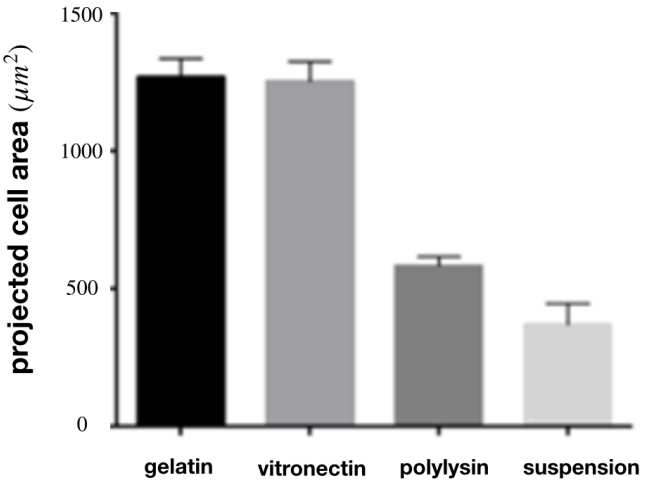

(b) Quantification of the projected cell area of EC on the substrate. Four different substrate conditions are explored, namely gelatine, vitronectin, Poly-Lysine, and in suspension.

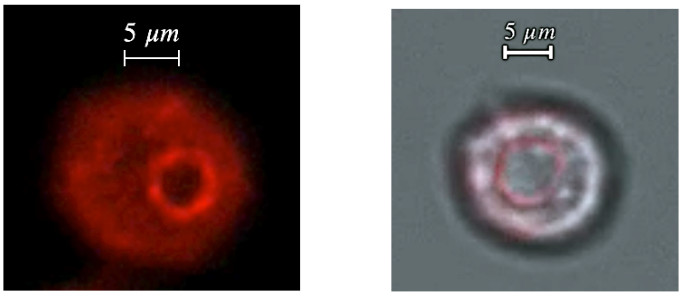

(c) Analysis over time of ECs on Poly-Lysine prove that the contact area, highlighted by a marked red *coffee-rings* is considerably lower than the projected cell area of the cells themself.

Figure 7.2

ECs were seeded on Poly-Lysine ECM and analyzed over time. As shown in experiments summarized by means of Fig. 7.2a, adherent ECs no longer fluctuate during the time-span of tests. Yet, they were unable to spread: two hours after seeding, the cell/ECM projected cell area (henceforth PA) was still about 520 μm^2 (see Fig. 7.2b). It has to be clear that, the values in Fig. 7.2b, represent the PA on the substrate; these data have not to be confused with that arise from the measurements of cell-substrate contact area (from here on CA), namely that corresponding to the effective portion of the cell membrane that is in touch with the substrate. Hence, PA represents the cell (3D-body) orthographic projection on a 2D-surface (substrate) that can be deduced even when the cell is not actually in contact with the substrate (e.g. suspension cell). Particularly, the CA correspondent to the experiments on Poly-Lysine, and so so the adhesion stage, is determined by Fig. 7.2c, wherein a pronounced red *coffee-rings* of actin is formed on the edge of the cell-substrate interface. Such a datum is approximately between 19 μm^2 and 38.5 μm^2 (data deduced through the values of diameters shown in Fig. 7.2c). This evidence unveils that electrostatic interactions do allow the attachment of cells, but not the spreading. On the contrary, when ECs adhere to fibronectin, microscope time-lapse shows that in 3-5 minutes membrane remodeling takes place after cells/ECM contact and several membrane protrusions sprout from the membrane increasing the contact area between the cell and the ECM, thus promoting the reorganization of the cellular cytoskeleton: two hours after seeding, the cell/ECM CA increased to 1200 μm^2 (see Fig. 7.2b).

Our experimental investigations confirm former studies on the influence of non-specific *traction forces in cell adhesion* were performed for different cell types at different time scales, from minutes - as for the spreading of mouse embryonic fibroblasts on a matrix-coated surface, [184] - to several hours - as for bovine aortic endothelial cells on polyacrylamide gels. Isotropic spreading is made possible by higher ligands densities; at lower densities of ligands, cells tend to spread anisotropically, by extending pseudopodia randomly along the cell membrane [97].

7.1.2 Experimental setup

ECs GM7373, from fetal bovine aortic, were transfected to co-express VEGFR2 and β_3-integrin. The first labeled with EYFP (Enhanced Yellow Fluorescent Protein, shown in green) the second one with an ECFP (Enhanced Cyan Fluorescent Protein, shown in red), as shown in Fig. 7.3 [52]. Transfected cells were cultured on glass coverslips that were flipped upside-down on gremlin- or fibrinogen-coated μslides. The geometrical evolution of the cell was recorded for 2 hours in time-lapse microscopy and Z stack sectioning to visualize the recruitment of VEGFR2 and β_3 integrin at the basal side of cells. During this timespan, cells slowly moved from the glass coverslip to adhere to the protein-coated substratum, as depicted in Fig. 7.4. Three mechanically relevant events can be identified after slide inversion: the detachment from the upper μslide, the floating and adhesion on the ligand rich μslide, and eventually the cell spreading onto the latter. Already past 6-8 minutes after the interaction with the substratum, VEGFR2 is found to the basal side of the membrane (i.e. that in close contact with immobilized gremlin). Subsequently, β_3 integrin undergoes a slow relocation that occurred 60- 120 minutes thereafter. Vice-versa, when cells were in contact with fibrinogen, higher levels of β_3 integrin were rapidly recruited, and a total absence of VEGFR2 polarization is observed [52].

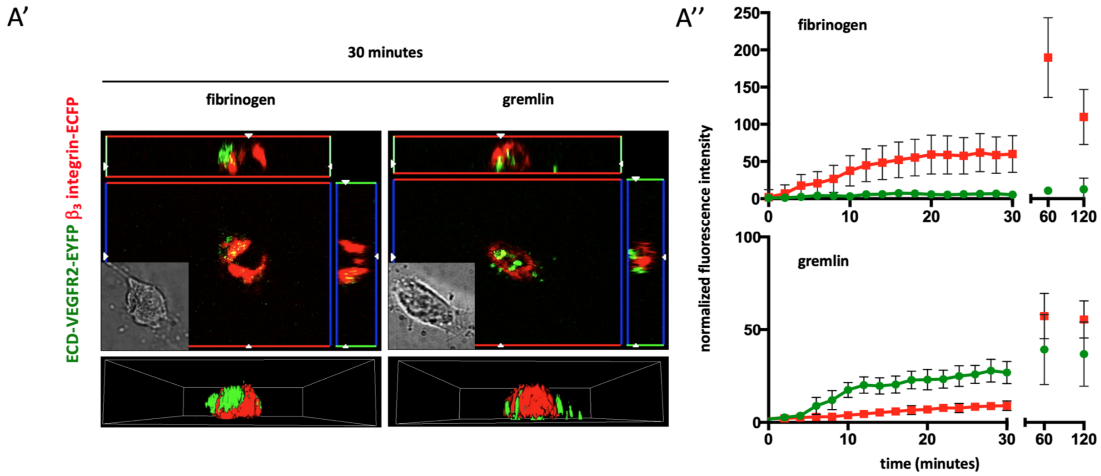

Figure 7.3: On coverslips were cultured GM7373 cells co-expressing ECD-VEGFR2-EYFP and β_3-ECFP. Experiments start when the coverslips were flipped on μslides coated by fibrinogen or gremlin, and then undergo 120 minutes of observation as discuss in chapter 4. Fluorescence intensity time evolution of VEGFR2 and integrin perceived at the basal side of ECs lying on a substrate enriched of gremlin and fibrinogen, as depicted in Fig. 4.1 and 4.2. Adapted from [52] and [31] (chapter 2).

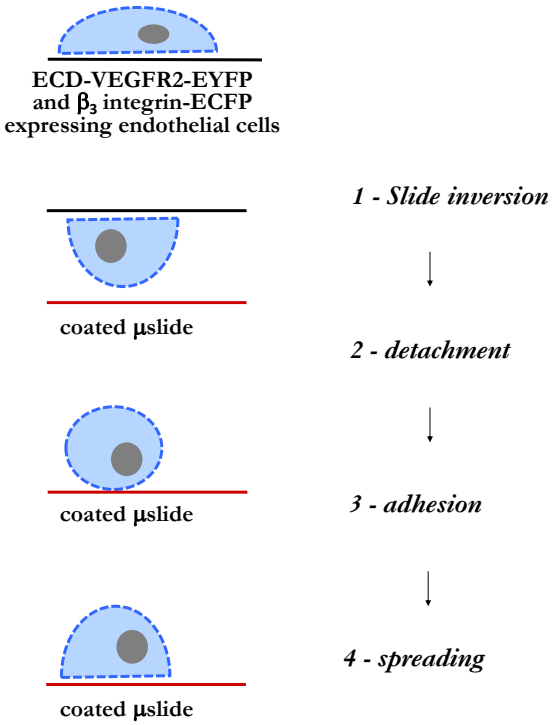

Figure 7.4: The four phases of the experimental process. Adapted from [52] and [31] (chapter 2).

7.1.3 Mechanical description of the 3d contact problem

Neglecting in this work the phase of mechanical detachment from the upper μslide, all other events depicted in Fig. 7.4 - the motion of an endothelial cell approaching the μslide during a finite deformation process, eventually coming into contact on a part of its boundary denoted by $\partial^C\Omega$ - have been accounted for. Because the glass-made μslides are flat, as depicted in Fig. 7.5 the normal

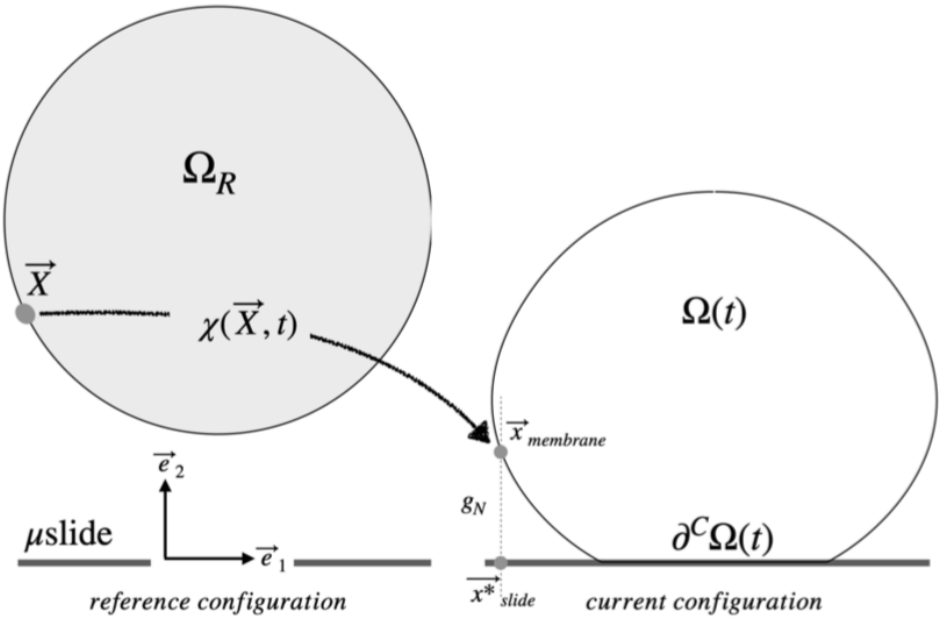

Figure 7.5: The notation for cell adhesion and spreading.

vector at a generic point $\vec{x}_{slide} \in \mu$slide is $\vec{n}_{slide} = \vec{e}_2$ and it remains unaltered in time. Accordingly, a single point $\vec{x}^*_{slide} \in \mu$slide is associated to a corresponding point $\vec{x}_{membrane} \in \partial\Omega(t)$ via the minimum distance method, by projecting $\vec{x}_{membrane}$ onto μslide (see [215] and Fig. 7.5). The inequality constraint

$$g_N = (\vec{x}_{membrane} - \vec{x}^*_{slide}) \cdot \vec{e}_2 \geqslant 0 \tag{7.1}$$

ensures that the cell and the substrate do not interpenetrate. The boundary value problem for the adhesion and spreading phases thus is formed by the balance of momentum equations (6.60), the interpenetration condition (7.1), and appropriate Neumann boundary conditions. Those arise in view of the mediation of transmembrane proteins and immobile ligands on the μslide.

The initial contact is mediated via integrin receptors on the cell surface. In this chapter, we do not account explicitly for integrins, as done in [123] among others, yet we will use the approaches in [123, 116] to discuss the magnitude of involved quantities, as shown in the previous chapter. Precisely, all the considerations that we have done regarding the works [123, 116] in 6.4.1, hold for the current chapter as well.

From these remarks (7.1.3 and 6.4.1) emerge that uncertainties remain in the establishment of realistic values for attraction forces, owing to the complexity of the related experimental tasks. On the other side, whereas their correct estimation is crucial in cell migration since cells shall detach focal

adhesions to allow motion, it is less relevant in the process of spreading. Accordingly, a simplistic approach that accounts for contact mechanics and disregards binding forces might still be effective to model the initial contact between a cell and a substrate, in view of the very short range of these interactions and the role that gravitational interactions must play at any rate. This approach shall be complemented by simulating the process of pseudopodia extension and cytoskeleton contractility that induce spreading [97].

Contact takes place when $g_N = 0$ and it is such a condition that defines the subpart $\partial^C\Omega(t) = \partial\Omega(t) \cap \mu$slide. It is indeed a simple case of contact mechanics, in the sense that the obstacle is given and it is fixed in time (i.e. we consider a rigid substrate, which approximates well the real glass-made μslide). In this regard, the global search for contact and the set-up of kinematical relations required by the contact constraint is straightforward, as depicted in Fig. 7.5. Tractions $\vec{t}_{slide}$ at all points $\vec{x}_{slide} \in \mu$slide have normal component $p_N = \vec{t}_{slide} \cdot \vec{e}_2$ and the Hertz-Signorini-Moreau linear complementarity conditions for frictionless contact read

$$g_N \geqslant 0\,, \qquad p_N \leqslant 0\,, \qquad p_N\, g_N = 0\ . \tag{7.2}$$

During the adhesion phase, the most appropriate description of tangential contact forces is rather unclear. We assume that the contact is frictionless in such a phase, allowing a sliding motion between the cell and the substrate justified by the chance that a new complex can be formed by a bound receptor jumping to a nearby free ligand [123]. Once the adhesion phase is completed, pseudopodia-driven protrusion machinery (F-actin polymerization, ARP 2/3 actin branching, filamin cross-linking, integrin-binding) takes place, driving the polymerization and reorganization of the cytoskeleton. Since at the stage reached by our research we are not able to account for a rigorous description of all these phenomena, we simulate these processes through the setup and growth in the time of bulk forces oriented axis-symmetrically, which surrogate the internal forces generated by the contractile machinery [97].

The boundary value problem for the adhesion and spreading phases thus is formed by the balance of momentum equations (6.60), the contact conditions (7.2), and the solvability conditions accompanied by appropriate Neumann boundary conditions.

Computationally, one writes the boundary value problem in a weak form in the reference configuration, selecting a strategy to numerically deal with the contact constraints. Among several possible algorithms, in the numerical simulations, we implemented two classical active set strategies, the Lagrange multiplier method [215] and the primal-dual active set strategy [216].

In the proposed approach, the mechanical spreading is independent upon the relocation of VEGFR2 on the lipid membrane. As such, the mechanical evolution is solved separately, using different time discretization too, from the problem of proteins relocation on the membrane. Note also that frictionless contact does not allow unique solvability unless the rigid body motion in the plane of the μslide is removed: to this aim, the average displacement in the μslide plane $\vec{e}_1 \times \vec{e}_3$ and rotations around the axis $\vec{e}_2$ are a priori imposed to vanish.

7.1.4 Transport description

The two balance equations (6.37), associated initial and boundary conditions, eventually the constitutive assumption (6.87) entirely govern the transport of receptors along the membrane. Together with the infinitely fast kinetics assumption (6.37a), the two-fields system of equations for c_{R_R}, c_{L_R} read at point $\vec{X} \in \partial\Omega_R$:

$$\frac{\partial c_{R_R}}{\partial t} - \frac{\partial c_{L_R}}{\partial t} - \mathrm{Div}_{\mathcal{P}_R}\left[\mathbb{D}_R \mathrm{Grad}_{\mathcal{P}_R}\left[c_{R_R}\right]\right] = s_{R_R} - s_{L_R} \,, \tag{7.3a}$$

$$\frac{\partial c_{L_R}}{\partial t} + \frac{\partial c_{C_R}}{\partial t} = s_{L_R} \,. \tag{7.3b}$$

An effective way of solving this system can be set up by noting that for the sum $c_{S_R} = c_{C_R} + c_{L_R}$ equation (7.3b) turns out to be an ordinary differential equation in time at point $\vec{X}$ rather than a PDE. Accordingly, one proceeds by direct integration in time

$$c_{S_R} = \int_0^t s_{L_R}(\vec{X},\tau)\,\mathrm{d}\tau = S_{L_R}(\vec{X},t) \,, \tag{7.4}$$

since initial concentration of ligands and complex is zero. Function $S_{L_R}(\vec{X},t)$ is, in view of the interpretation given to $s_{L_R}(\vec{X},\tau)$, the amount of ligands that the cell got in contact with onto the substrate at time t and location $\vec{X}$, pulled back to the reference configuration $\partial\Omega_R$. Such an interpretation clarifies that the evolution in time of $S_{L_R}(\vec{X},t)$ can be only be due to the gap function $g_N(\vec{X},t)$ and we may reasonably postulate a definition for S_{L_R} based on the physics that has been described right after equation (6.36):

$$S_{L_R}(\vec{X},t) = c_{L_R}^{max} \exp\left(-\frac{g_N(\vec{X},t)}{\ell_{chem}}\right) \,. \tag{7.5}$$

When $g_N(\vec{X},t)$, tuned by the *chemical length-scale* $\ell_{chem} > 0$, is sufficiently large then $S_{L_R}(\vec{X},t)$ is negligible and in fact no ligands are available on the membrane surface. On the other end, when $g_N(\vec{X},t)$ is zero and the membrane is in contact with the substrate, the available concentration is $c_{L_R}^{max}$, the maximum available concentration in the reference configuration.

Defining the difference $c_{D_R} = c_{R_R} - c_{L_R}$ and neglecting the role of internalization or generation of proteins, i.e. $s_{R_R} \sim 0$ (as infer in the chapter 5), the remaining governing equation becomes

$$\frac{\partial c_{D_R}}{\partial t} - \mathrm{Div}_{\mathcal{P}_R}\left[\mathbb{D}_R \mathrm{Grad}_{\mathcal{P}_R}\left[c_{R_R}\right]\right] = -s_{L_R} \,, \tag{7.6a}$$

to be solved under the constraint (6.37a), that writes

$$c_{R_R}^2(\vec{X},t) + \left[\alpha_R(\vec{X},t) - c_{D_R}(\vec{X},t)\right] c_{R_R}(\vec{X},t) - \alpha_R(\vec{X},t)\left[c_{S_R}(\vec{X},t) + c_{D_R}(\vec{X},t)\right] = 0 \,. \tag{7.6b}$$

The initial values PDE (7.6) will be solved for the unknown fields c_{D_R}, c_{R_R}, stemming from its weak form.

7.1.5 Weak formulation and finite elements discretization

Formally speaking, the weak formulation is obtained after multiplication of the strong form of the governing equation (7.6a) by a suitable set of time independent test functions (expressed here with a superposed caret), and performing an integration upon the domain, exploiting Green's formula with the aim of reducing the order of differentiation. Such a weak form, in terms of the unknown fields c_{D_R}, c_{R_R}, reads:

Find unknown fields $c_{D_R}(\vec{X},t)$, $c_{R_R}(\vec{X},t)$ - in the functional space $\mathcal{V}^{[0,t_f]}$ that accounts for initial conditions and the constraint (7.6b) *such that*

$$\int_{\mathcal{P}_R} \hat{c}(\vec{X}) \, \frac{\partial c_{D_R}(\vec{X},t)}{\partial t} \, - \mathrm{Grad}_{\mathcal{P}_R}\left[\hat{c}(\vec{X})\right] \cdot \mathbb{D}_R \, \mathrm{Grad}_{\mathcal{P}_R}\left[c_{R_R}(\vec{X},t)\right] + \hat{c}(\vec{X}) \, s_{L_R}(\vec{X},t) \; \mathrm{d}\mathcal{P}_R = 0 \quad (7.7)$$

for all functions $\hat{c}(\vec{X})$ that belong to a suitable functional space $\mathcal{V}$. The identification of the functional spaces $\mathcal{V}^{[0,t_f]}$, $\mathcal{V}$ falls beyond the scope of the present paper.

Note that there is no contribution defined on the boundary, because the cell membrane $\mathcal{P}_R$ The weak form (7.7) naturally leads to a semi-discrete problem, by approximating the space $\mathcal{V}$ by a finite dimensional space $\mathcal{V}_h$. To this aim, unknown fields $c_{D_R}(\vec{X},t)$, $c_{R_R}(\vec{X},t)$ will be approximated as a product of separated variables, by means of a basis $\{\varphi_i(\vec{X})\}$ of spatial shape functions and nodal unknowns that depend solely on time

$$c_{D_h}(\vec{X},t) = \varphi_j(\vec{X}) \, c_{D_R\,j}(t) \, , \qquad c_{R_h}(\vec{X},t) = \varphi_j(\vec{X}) \, c_{R_R\,j}(t) \, . \quad (7.8)$$

The Einstein summation convention is taken for repeated indexes. The semi-discrete approximate problem reads as follows: given $c_{0hR}(\vec{X})$ a suitable approximation of the initial datum $c_{0R}(\vec{X})$, for each $t \in [0,t_f]$ find $c_{D_R\,j}(t)$ and $c_{R_R\,j}(t)$ such that

$$\begin{aligned} &\int_{\mathcal{P}_R} \varphi_i(\vec{X}) \, \varphi_j(\vec{X}) \, \frac{\partial c_{D_R\,j}(t)}{\partial t} \, - \mathrm{Grad}_{\mathcal{P}_R}\left[\varphi_i(\vec{X})\right] \cdot \mathbb{D}_R \, \mathrm{Grad}_{\mathcal{P}_R}\left[\varphi_j(\vec{X})\right] \, c_{R_R\,j}(t) + \quad (7.9) \\ &\quad \varphi_i(\vec{X}) \, s_{L_R}(\vec{X},t) \; \mathrm{d}\mathcal{P}_R = 0 \, . \end{aligned}$$

Constraint (7.6b) shall be satisfied, either in L_2 sense or point-wise for $c_{D_R\,j}(t)$, $c_{R_R\,j}(t)$ at the discretization nodes. The weak form (7.7) is thus rephrased into the system of ordinary differential equations, whose solution is an approximation of the exact solution for each time t.

In order to obtain a full discretization of the weak form (7.7), we consider a uniform mesh for the time variable t and define $t_n = n\Delta t$ with $n = 0, 1, ...,$ and $\Delta t > 0$ being the time step. We integrate equation (7.9) in time in the generic interval t_{n-1}, t_n, to get

$$\begin{aligned} &\int_{\mathcal{P}_R} \varphi_i(\vec{X}) \, \varphi_j(\vec{X}) \, \mathrm{d}\mathcal{P}_R \, \left(c_{D_R\,j}(t_n) - c_{D_R\,j}(t_{n-1})\right) + \quad (7.10) \\ &\quad - \int_{\mathcal{P}_R} \mathrm{Grad}_{\mathcal{P}_R}\left[\varphi_i(\vec{X})\right] \cdot \mathbb{D}_R \, \mathrm{Grad}_{\mathcal{P}_R}\left[\varphi_j(\vec{X})\right] \, \mathrm{d}\mathcal{P}_R \int_{t_{n-1}}^{t_n} c_{R_R\,j}(t)\mathrm{d}t + \\ &\quad + \int_{\mathcal{P}_R} \varphi_i(\vec{X}) \, \left(S_{L_R}(\vec{X},t_n) - S_{L_R}(\vec{X},t_{n-1})\right) \, \mathrm{d}\mathcal{P}_R = 0 \end{aligned}$$

with $S_{L_R}(\vec{X},t)$ as in identity (7.5). Integral in time can be approximated with Newton-Cotes formulae, either second-order accurate as

$$\int_{t_{n-1}}^{t_n} c_{R_R j}(t)\mathrm{d}t \sim \frac{\Delta t}{2}\left[\, c_{R_R j}(t_n) + c_{R_R j}(t_{n-1}) \,\right]$$

or even with first-order accurate approximation formula

$$\int_{t_{n-1}}^{t_n} c_{R_R j}(t)\mathrm{d}t \sim \Delta t\; c_{R_R j}(t_{n-1})$$

which might be appealing because it provides to eq. (7.9) the nature of an explicit approximation scheme, that can be trivially solved for $c_{D_R j}(t_n)$. The constraint (7.6b) shall be solved afterwards for $c_{R_R j}(t_n)$.

Weak form (7.10) can be reshaped in dimensionless form, by means of a time-scale $\hat{t}$, a length-scale $\ell_{transport}$ and a reference value for concentration, which is taken to be $c_{L_R}^{max}$. Denoting with a star every dimensionless quantity, easy algebra leads from (7.10) to

$$\begin{aligned}
&\int_{\mathcal{P}_R} \varphi_i(\vec{X})\; \varphi_j(\vec{X})\; \mathrm{d}\mathcal{P}_R \left(c^*_{D_R j}(t_n) - c^*_{D_R j}(t_{n-1}) \right) + \qquad (7.11)\\
&\quad - \int_{\mathcal{P}_R} \frac{\mathbb{D}_R \hat{t}}{\ell^2_{transport}} \mathrm{Grad}^*_{\mathcal{P}_R}\left[\varphi_i(\vec{X}) \right] \cdot \mathrm{Grad}^*_{\mathcal{P}_R}\left[\varphi_j(\vec{X}) \right] \mathrm{d}\mathcal{P}_R \int_{t^*_{n-1}}^{t^*_n} c^*_{R_R j}(t^*)\,\mathrm{d}t^* + \\
&\quad + \int_{\mathcal{P}_R} \varphi_i(\vec{X}) \left(\exp(-\frac{g_N(\vec{X},t_n)}{\ell_{chem}}) - \exp(-\frac{g_N(\vec{X},t_{n-1})}{\ell_{chem}}) \right) \mathrm{d}\mathcal{P}_R = 0\,,
\end{aligned}$$

which shows clearly the roles of the chemical length scale, of the dimensionless diffusivity and hence the transport length scale, and of mechanics that rules the geometrical spreading. The time-scale interacts also with the mechanical time-scale associtaed with the viscous behavior, typically the relaxation time of the cell.
The finite element approximation of the chemo-transport model was implemented exploiting the high performance computing open source library deal.ii (https://www.dealii.org/).

7.1.6 Simulations

Since the machinery of cytoskeleton reorganization has not been included in the numerical simulations, the relocation of proteins on the cell does not affect the mechanical deformation. As a consequence, an algorithm has been successfully implemented, for which mechanical deformation within a given time step occurs, and transport coupled with receptors-ligands binding takes place on the updated membrane configuration. It can be easily transformed into a staggered approach in the case of two-way coupling.

7.1.6.1 Mechanical deformation

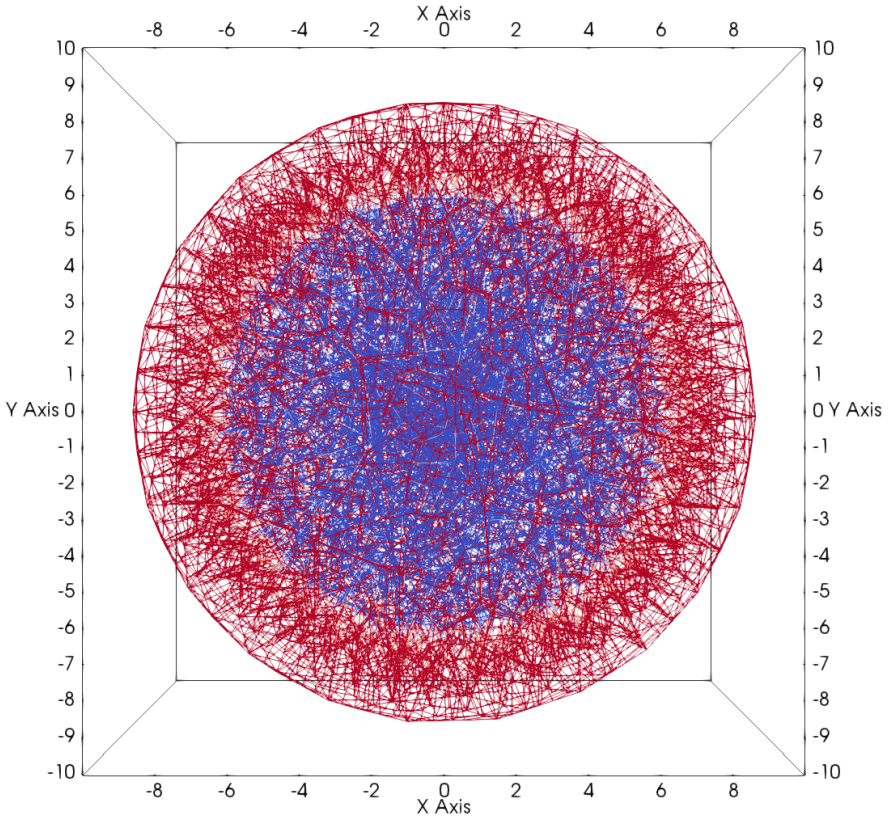

Figure 7.6: A 3D hexahedral tessellations with a total number of elements equal to 12578, is depicted. The color blue denotes the nucleus while the red one indicates the cytoplasm. Coherently, the external face of the boundary elements of the cytoplasm mesh, correspond to 1817 elements quadrilateral elements that discretizing the geometry of the cell surface.

Figure 7.4 identifies four main phases after slide inversion. We aim at capturing the response of the EC, the relocation of receptors and their binding with ligands during the processes of floating and adhesion on the ligand rich μslide, and eventually during the cell spreading onto the slide. EC has been idealized as two Neo-Hookean solid materials, represented the cytoplasm and the nucleus (see tesselation of the EC Fig. 7.6). Particularly, we set shear modulus $G = 72.99\ Pa$ and bulk modulus $\kappa = 25.641\ Pa$ (correlate to E $= 20\ Pa$ and $\nu = 0.37$) for the nucleus, whereas $G = 36.50\ Pa$ and $\kappa = 128.20\ Pa$ for the corresponding parameters of the cytoplasm (accord to E $= 10\ Pa$ and $\nu = 0.37$). Finally we ussume nucleus and cytoplasm densities equal to $\rho_{nuc} = 2\ g/m^3$ and $\rho_{cyt} = 1\ g/m^3$ respectively [217, 218].

A pictorial view of the geometrical evolution in the four phases is shown in Fig. 7.8 and 7.9.
The time required to complete the mechanical evolution of the cell, 600 s, was experimentally measured as reported in [138]. Mechanical deformation entails the adhesion, in which the cell attaches to the substrate and accommodates its cytoskeleton in response to binding forces of electro-static

nature, and the spreading, driven by pseudopodia, a temporary actin filament network that develops in the direction of motion. The floating and the adhesion are governed by gravitational forces and by electrostatic interactions at a very short range, estimated according to formula (6.61) by means of the gap function $g_N(\vec{X},t)$ used to define $S_{L_R}(\vec{X},t)$ in eq. (7.5). The time span of adhesion has been estimated at 300 seconds, according to the experimental pieces of evidence for complex formation in Fig. 7.10. The radius of the adhesion circular surface in our numerical simulations amounts to nearly 10.5 μm, while the spreading phase, which lasts a similar amount of time, reaches a final radius of about 20 μm. Protrusion forces description in the literature is still an ongoing research field. Some authors describe those forces to be located at the membrane: according to [177] protrusion forces act in the internal boundary of the membrane and are related to the integrin forces at the focal adhesion sites. The cell cortex was considered as an excitable system in [202]: that paper reproduced experimentally observed zig-zag behavior. Other authors and we follow this path of reasoning, model protrusion forces in the bulk of the cell. In [181], a decomposition of the deformation gradient was used to reproduce the cyclic phases of protrusion and contraction of the cell, which are tightly synchronized with the adhesion forces at the back and at the front of the cell. We follow here a similar approach: the cell senses the external sources at different spots of the membrane by tasting randomly several locations. Only one pseudopod in the direction of the most attractive one protrudes. This process is simulated by imposing bulk forces in the cytosol inversely proportional to the distance of the most attractive tasted location, tuned by means of a paraboloid filter function. This approach lacks the physical connection between the bulk forces and the actin polymerization, which will be accounted for in future research. Experiments show that the cell shape at the completion of the spreading maintains axis-symmetry, with an average radius of 20 μm (average measured on 50 EC) [138, 139]. These two data have been used to calibrate protrusion forces in the bulk, that amount at 6.2 times $|\vec{g}|$.

Finally, concerning the contact area at the end of the adhesion phase and at the end of the mechanical spreading they are approximately equal to 35.3 μm^2 e 1256.6 μm^2. Intriguingly, both the data are completely overlapping to the experimental results show in Fig. 7.2b, and 7.2c. Following, the diameters of the CAs at the end of the adhesion and spreading stage, have depicted (see Fig. 7.7b and 7.7c).

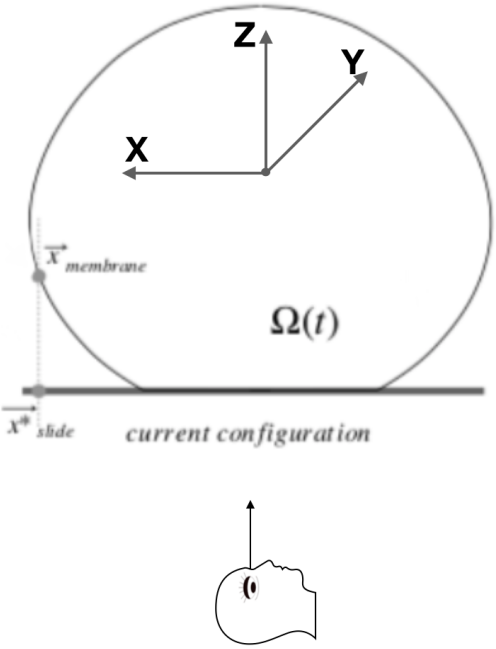

(a)

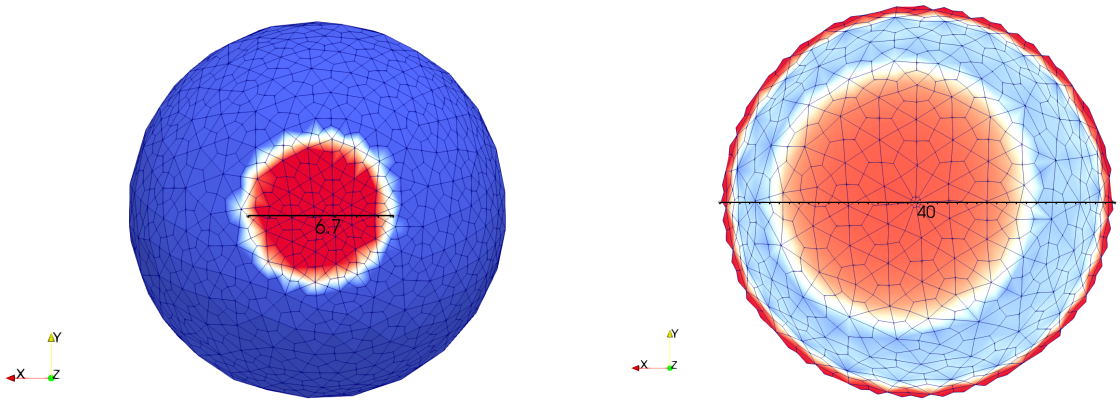

(b) $t = 300\,\mathrm{s}$ (c) $t = 600\,\mathrm{s}$

Figure 7.7: (a) Reference system in the current configuration and point of view of the observer from which to see the contact area between the cell membrane and the ligands coated substrate. (b) - (c) The diameter of the cell contact area is here depicted either at the end of the adhesion stage (6.7 μm) that at the last instant of the mechanical spreading phase (40 μm).

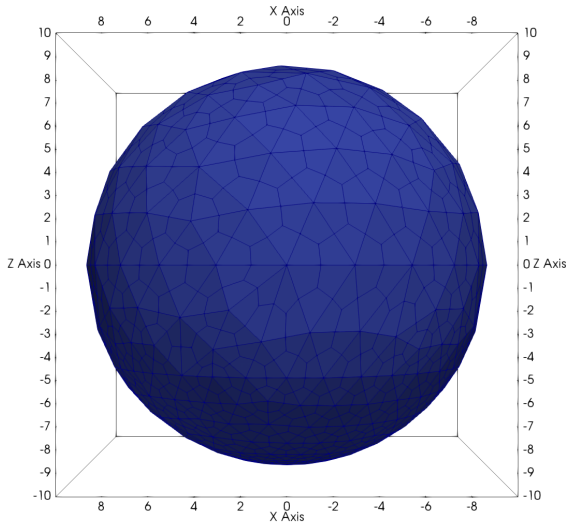

(a) $t = 0\,\mathrm{s}$

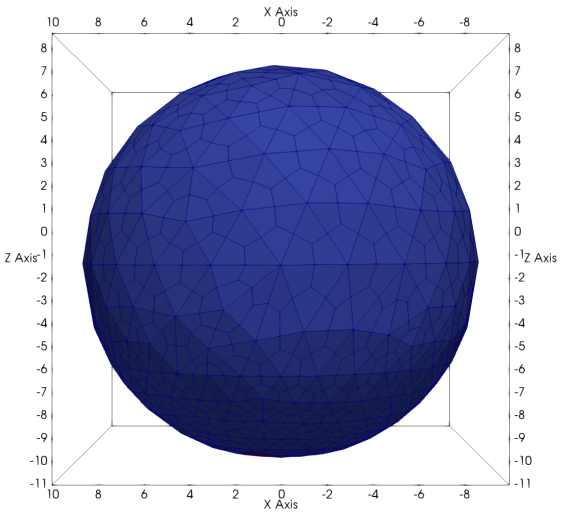

(b) $t = 120\,\mathrm{s}$

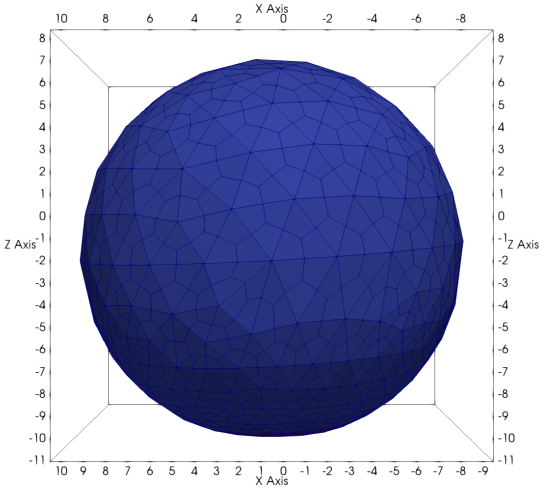

(c) $t = 240\,\mathrm{s}$

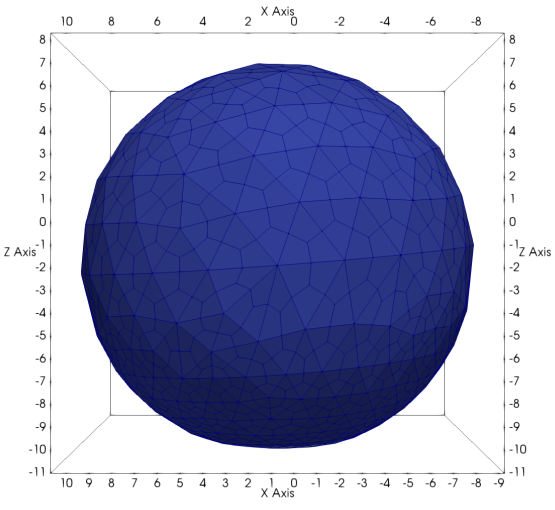

(d) $t = 300\,\mathrm{s}$

Figure 7.8: Cell-shape at the time instants $t = 0,\ 120,\ 240,\ 300\ s$.

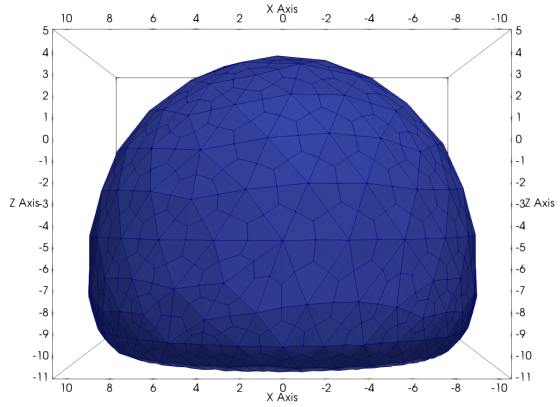

(a) $t = 360\,\mathrm{s}$

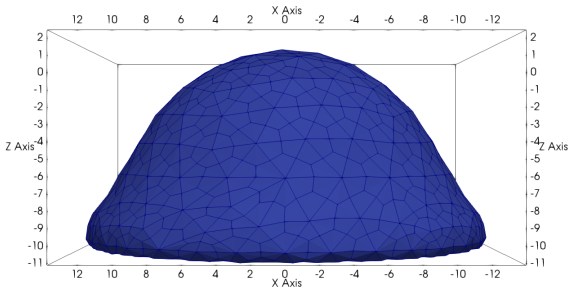

(b) $t = 480\,\mathrm{s}$

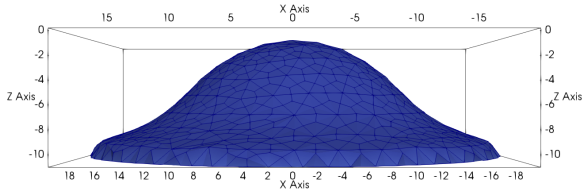

(c) $t = 600\,\mathrm{s}$

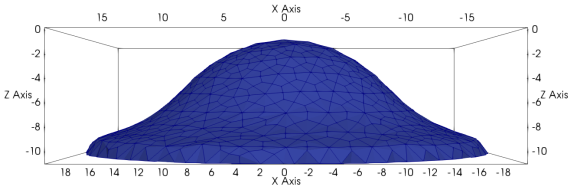

(d) $t = 7200\,\mathrm{s}$

Figure 7.9: Cell-shape at the time instants $t = 360,\ 480,\ 600,\ 7200,\ s$.

7.1.6.2 Cell membrane parameters and relocations of VEGFR2

As deeply discussed in chapters 4 and 5, the product C, in reaction:

$$\underbrace{\text{VEGFR2}}_{R} + \underbrace{\text{gremlin}}_{L} \underset{k_b}{\overset{k_f}{\leftrightarrows}} \text{C}\,, \tag{7.12}$$

is half of the whole complex that triggers the intracellular signal of the angiogenic stimulus. In equation (7.12), identification of symbols with reaction (6.22) has been carried out.

A short summary of the material parameters is here carried out.
In agreement with the governing equations shown in the former sections and chapter, parameters α from eq. (6.30) and the receptor diffusivity $\mathbb{D}_R$ (see eq. (6.87)) need to be experimentally measured, together with initial conditions $c^0_{R_R}(\vec{X})$. The chemical length scale $\ell_{chem} > 0$ for the amount of ligands $S_{L_R}(\vec{X},t)$ in eq. (7.5) shall be enforced, too.
As dealt with deeply in the previous part (Part II) of the thesis and described in [138], we estimated by means of Surface Plasmon Resonance, both the values of $c^{\max}_{L_R} = 16000\, molecules\mu\ m^{-2}$ (where again has been set $c^{max}_R = c^{max}_C$) and the standard Gibbs free energy $\Delta G_0 = -32949.0\ J/mol$, to be inserted in eq. (6.88) to derive the equilibrium constant of reaction (6.22), i.e. $K^{(7.12)}_{\text{eq}} = 354058.31692$. Receptor diffusivity, experimentally computed through Fluorescence Recovery After Photobleaching (FRAP), holds $\mathbb{D}_R = 0.198\ \mu m^2 s^{-1}$, [138]. According to available literature

[158], [48], the total number of molecules of VEGFR2 on the lipid bilayer of an EC is taken as 24000, providing an initial amount of receptors equal to 19.1 $molecules \cdot \mu m^{-2}$, supposed homogeneous on the surface of a spheric cell in suspension with radius $r = 10\ \mu m$. It is relevant to underline the difference with the models in surrogate mechanics; here, the cellular radius assumed for in-silico investigations has been set equal to 20 microns, that is, equal to the radius of the spreaded cell. Consequently, different radiuses mean different initial concentrations for VEGFR2 on the cell surface, because, in our formulations, the number of total receptor molecules (free plus bound) is maintained constant for all the time of the simulations (no internalization/externalization of receptors from/on the cell membrane). The gremlin that coats the substrate and is available for binding is not a priori experimentally deducible, since not every molecule is in the ideal condition to interplay with VEGFR2: contrariwise, it is very likely that many dimers have a not suitable orientation to chemically interact with the receptor monomers. These considerations prelude to the calibration of this datum by means of the current in-silico analysis.

7.1.6.3 Comparison between numerical and experimental outcomes

The numerical model here presented is the evolution of those shown in the preceding chapters (3.4 and 5) and of the papers [138] and [139]. In these works, a chemo-transport model was implemented, wherein the mathematical descriptions of the mechanical spreading of an EC on substrates enriched of ligands were suitably surrogated. For the purposes of the current chapter, the understanding of the three limiting processes that characterize the depletion of VEGFR2, inherited by the chapters and manuscripts above-mentioned, result pivotal.

The first phase corresponds to a moderated generation of complexes, as shown in Fig. 7.10. In this step, the VEGFR2 depletion is dominated by the chemical interaction between receptor and ligands during the adhesion between the cell membrane and substrate. The second phase, up to 600 s, is characterized by a very steep branch of the experimental curve. Comparison between experimental and numerical outcomes (see Fig. 7.10) shows how this step is strictly connected with the mechanical spreading of the cell: the cell-substrate contact dynamics drives the formations of complexes since the mechanical spreading makes new free receptors available for the binding with the ligands. Ultimately, the last branch of the experimental curve is dominated by a lower complex formation rate (from 600 s to 7200 s) and takes place after cell spreading thus being transport-dominated. Free VEGFR2, guided by concentration gradients, move from the apical part of the cell towards the basal one, where the reaction occurs and depletes receptors - see Fig. 7.11.

Numerical simulations allow quantification of parameters that can hardly be measured, as the number of ligands available to chemical interaction or the time span of adhesion/vs spreading or the forces exerted by pseudopodia driven motion. Evolution in time of the normalized total amount of complexes is depicted in Fig. 7.10, where values are made dimensionless by division with the corresponding data at the instant 1800 s after calibration of the concentration of ligands available in the substrate to 90 $molecules/\mu m^2$. In finding the correct fit of the experimental curve, the time spent for the adhesion and spreading phases are defined. By surrogated mechanics hypothesis we have inferred that these two-steps together require about 600 s (phase two). Now, improving the multi-fields formulation, it has been estimated that this step of the complex generation curve, is actually subdivided into two further periods: adhesion and spreading phase, and both last 300 s each.

In Table 7.1 are shown the numerical and experimental outcomes. Precisely, here it is tabled the evolution in time of the total amount of complexes (in-silico experiment) and the VEGR2 (in-vitro experiment) free and bound, in contact with the substrate.

Table 7.1: Co-designing between VEGFR2-fluorescence intensity (in-vitro experiments) and the number of complexes generating on the cell membrane (in-silico simulation) is provided. Specifically, both the total that dimensionless quantities are tabulated.

Time	FRAP	Error bars	Complex	Adimensional Complex	Adimensional FRAP	Adimensional error bars
0	1,8125	1,7470	0,0000	0,0000	-	-
120	2,6775	1,7774	2105,2746	0,1008	0,0995	0,0661
240	3,6175	2,0371	2941,2043	0,1408	0,1344	0,0757
360	8,8875	4,5427	8072,1388	0,3864	0,3303	0,1688
480	12,0225	5,1638	11954,5760	0,5722	0,4468	0,1919
600	17,4375	4,0251	14293,4851	0,6842	0,6481	0,1496
720	20,1325	4,3776	15205,1208	0,7278	0,7482	0,1627
840	19,6650	4,4217	16410,0491	0,7855	0,7308	0,1643
960	20,4075	4,5417	17406,2871	0,8332	0,7584	0,1688
1080	22,8600	4,7168	18100,4100	0,8664	0,8496	0,1753
1200	23,0375	5,5135	18747,8007	0,8974	0,8562	0,2049
1320	23,2725	4,8333	19328,7216	0,9252	0,8649	0,1796
1440	24,9150	5,5791	19843,2785	0,9499	0,9260	0,2073
1560	25,8650	4,7980	20262,9277	0,9700	0,9613	0,1783
1680	27,8800	6,0900	20598,0116	0,9860	1,0361	0,2263
1800	26,9075	5,9243	20890,5624	1,0000	1,0000	0,2202
3600	39,2718	18,8742	22723,3906	1,0877	1,4595	0,7014
7200	36,8140	17,3697	23079,7764	1,1048	1,3682	0,6455

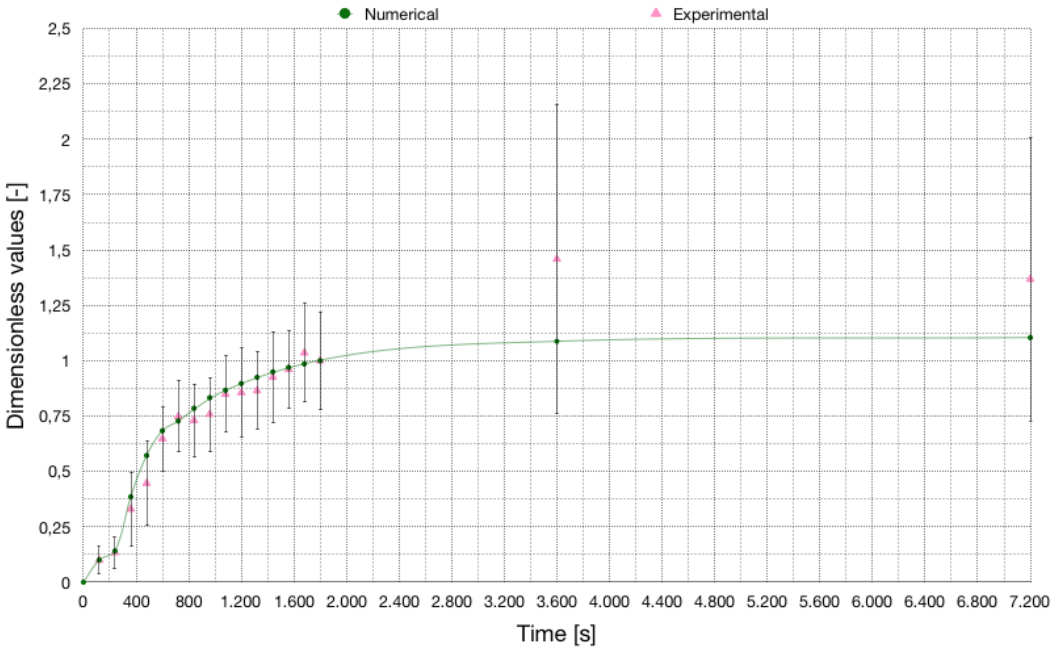

Figure 7.10: Numerical (dots with continuous line) and experimental (triangles with error bars) outcomes. Evolution in time of the normalized total amount of complexes.

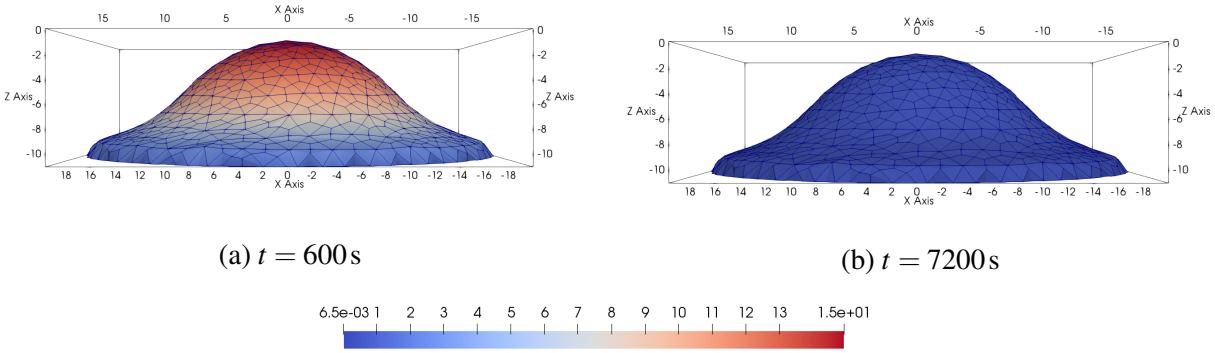

(a) $t = 600\,\mathrm{s}$

(b) $t = 7200\,\mathrm{s}$

(c) Legend

Figure 7.11: Diffusion of receptors after the spreading phase has been completed.

The evolution in time of the generated complexes is represented in Fig. 7.12, in which the basal portion of the cell (in contact with the μslide) is depicted (see 7.7a for better understand the point of view of the observer). Numerical simulations predict a homogeneous distribution of complexes in the contact region at the end of the adhesion phase Fig. 7.12(d). This behavior is due to the selected thermodynamic prescription for the transport of receptors, dictated by the gradient of concentration only. The pattern would have been different if the flux of receptors would have been influenced, for instance, by the membrane tension. Figure 7.13 depicts the evolution of complexes during the mechanical spreading phase. Due to the mechanics timescale is faster than that guided by receptors diffusion, the tendency of complexes to accumulate at the boundary of the cell-substrate contact area emerges quite clearly. Hence, the so-called “coffee rings" appear, as described in [138] and chapters 3.4 and 5 (see fig. 7.13(c)). At the end of the experimental time span (fig. 7.13(d)), a zone of a small concentration of complexes in the adhesion zone is clearly visible. Importantly, a slight asymmetry of the spatial distribution of the concentration of complexes on the cell membrane in contact with the substrate (see Fig. 7.12 and 7.13) is observable. This phenomenon arises as a consequence of the discretization of the cell geometry (see Fig. 7.6) coupled with the fact that the forces that guide the adhesion phase are totally related to gravity. Indeed, in a not discretized geometry framework, the vertical projection of the cell's center of mass (from here on CM) on the membrane, identify the initial contact-point (henceforth IC-P) between cell-surface and substrate during experiments like those previously introduced. Therefore, in this scenario, the resultant bulk forces that ruling the cell adhesion mechanism are perfectly aligned with the vertical line joining the CM and IC-P, favoring a fully symmetric spatial distribution either for the adhesion mechanism that for complexes concentration in the basal side of the cell. However, introducing the geometry discretization, the IC-P is not the first contact-point between cell membrane and substrate, rather will be another point on the cell membrane that will be closer to the IC-P the denser the tesselation. Hence, a small eccentricity among the resultant of the bulk forces and the IC-P has characterized the in-silico analysis, providing a tiny cell rolling mechanism during the adhesion phase. This is, in the end, what induces the asymmetries into the complexes' concentration spatial distribution. Moreover, the mechanical spreading and diffusion stages have inherited these asymmetries up to the result acquired by Fig. 7.12 and 7.13. Finally, from instant $t = 600\ s$ to $t = 7200\ s$ (see fig. 7.13 (c) - (d)), we observe how, on an unmodified cell geometry, free receptors are recruiteds in the basal side of the cell owing to gremlin, up to an almost homogeneous distribution of the bound VEGFR2.

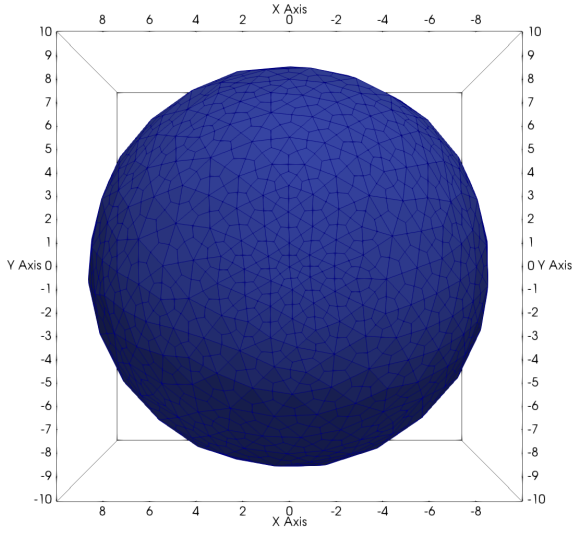

(a) $t = 0\,\mathrm{s}$

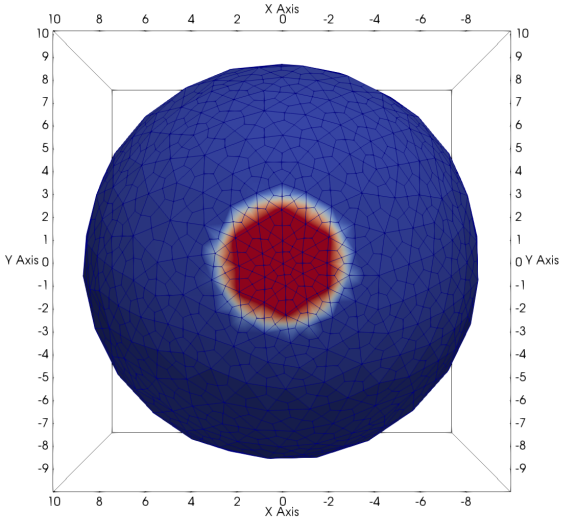

(b) $t = 120\,\mathrm{s}$

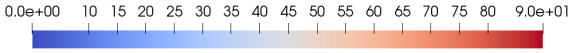

(c) Legend

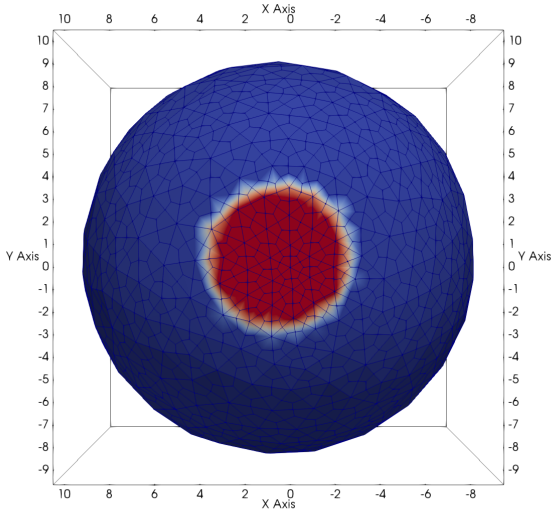

(d) $t = 240\,\mathrm{s}$

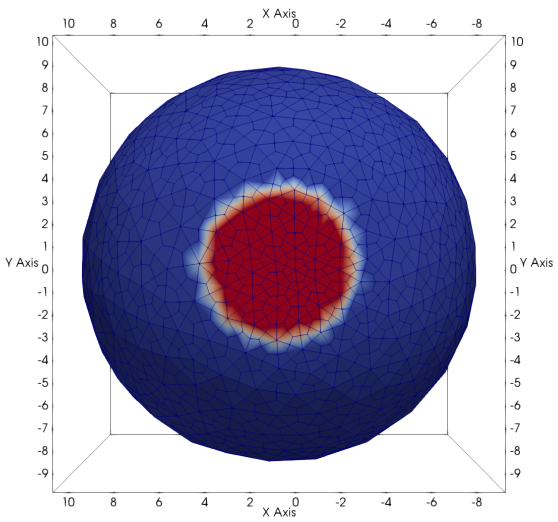

(e) $t = 300\,\mathrm{s}$

Figure 7.12: Basal distribution of complexes during the adhesion stage.

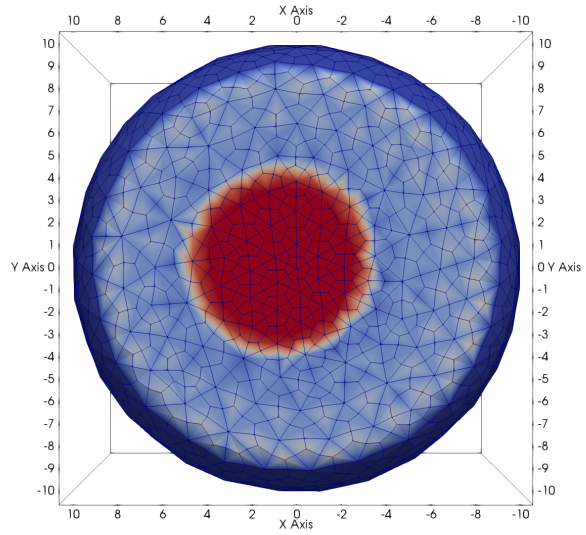

(a) $t = 360\,\mathrm{s}$

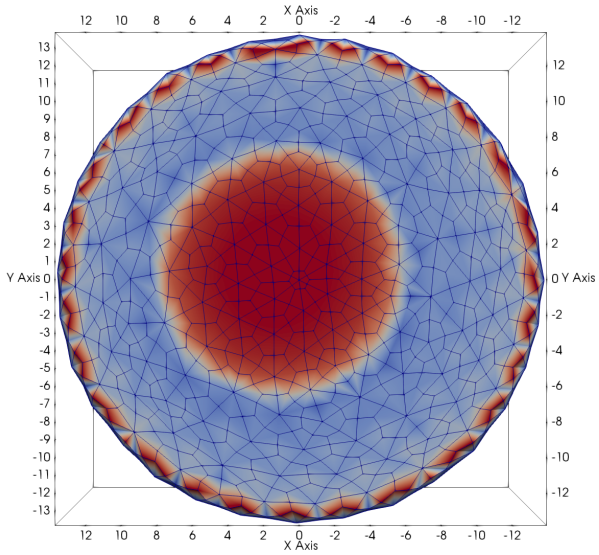

(b) $t = 480\,\mathrm{s}$

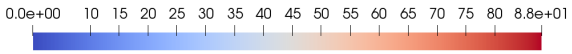

(c) Legend

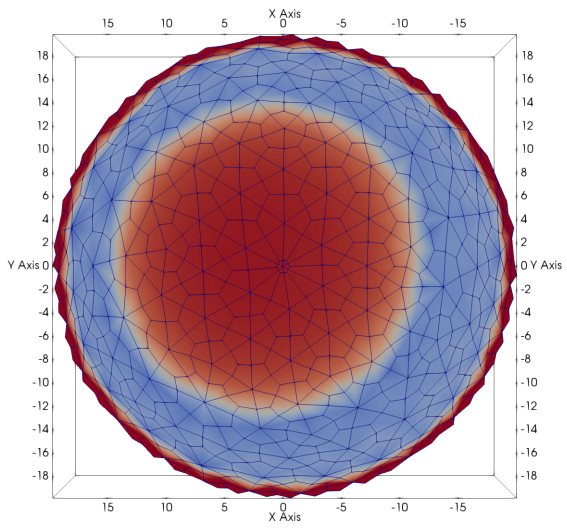

(d) $t = 600\,\mathrm{s}$

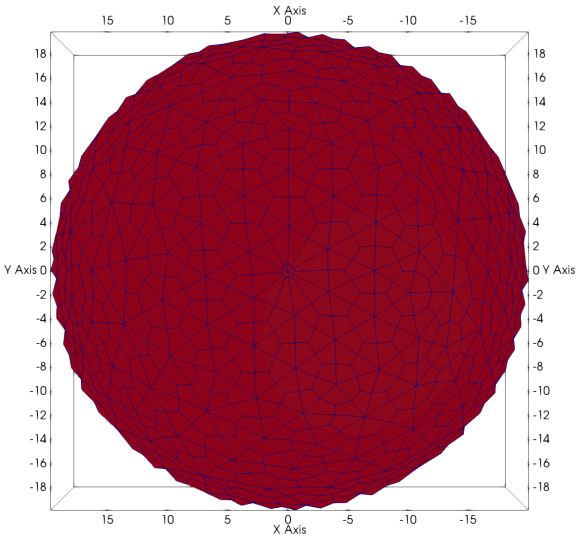

(e) $t = 7200\,\mathrm{s}$

Figure 7.13: Basal distribution of complexes during spreading stage (a)-(c) and at the end of the experimental time-span (d).

The time progression of all molecules targeted in this computational analysis is summarized in Fig. 7.14. Importantly, in the first 300 s of simulation, the total amount of ligands (free plus bound) in contact with the substrate (red-line) is perfectly overlapped on that of complexes (orange-line). This means that the chemo-diffusive phenomenon has timing compatible with those of cell-substrate contact mechanics. It clearly emerges, instead, that during spreading, from 300 s to 600 s, the amount of available ligands increases by a large extent and so the amount of ligands that go in contact with the substrate is so quickly and so high that the chemo-diffusive process leads to ligand depletion at a later time.

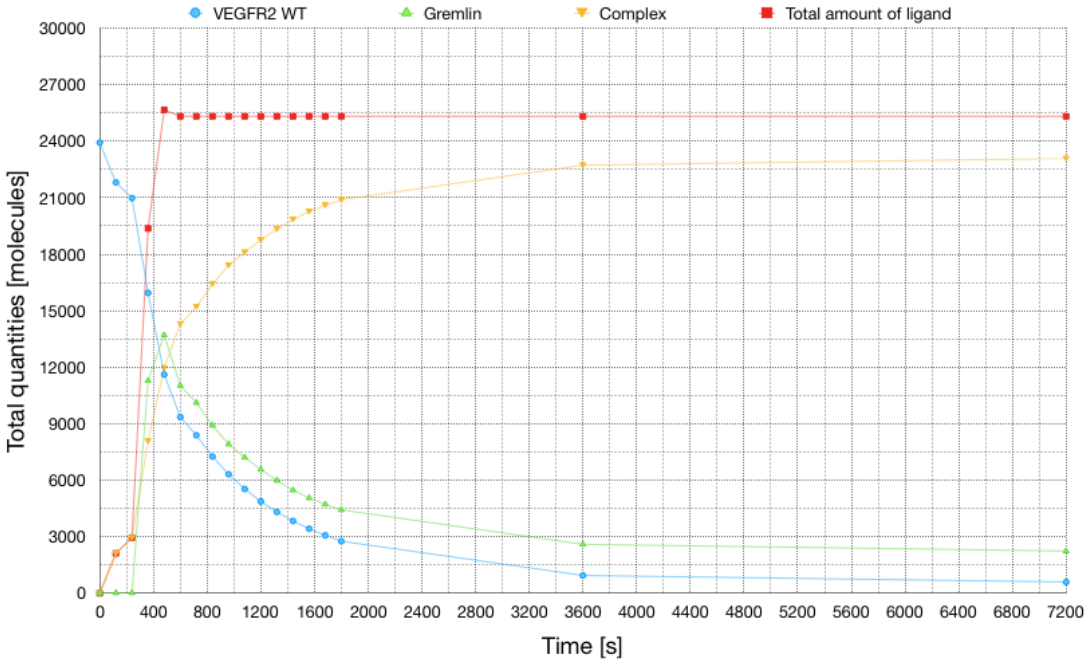

Figure 7.14: Time evolution of the total amount of molecules of receptors, complexes, free-ligands, and the complete amount of ligands (free plus bound) when $S_L = 90\ molecules/\mu m^2$.

It is important to highlights that distinct time-stepping has been implemented for each of the three stages characterizing the in-silico experiment, inasmuch as each of these phases is ruled in a different way by the physical phenomena so far described. Particularly, concerning the problem into the bulk, therefore confined to the first two stages, a constant time step has been fixed equal to:

- 0.5 s for adhesion phase;
- 0.1 s for the mechanical spreading stage.

Moreover, due to the fact that the time scale of the bulk and membrane processes are different as well, a sub-incrementation strategy for the numerical solution of the chemo-diffusive problem on the cell surface has been adopted for the above mentioned two phases. Hence, both for the adhesion and mechanical spreading stage, at every discrete instant wherein the problem into the bulk has

been solved, a further sub-incrementation of 90 substeps to solve the chemo-diffusive problem has been implemented. Finally, as regards the chemo-diffusion phase, no sub-incrementation has been necessary inasmuch as the cell geometry remained unchanged throughout this stage. Here, the constant time-stepping has been arranged to 0.05 s.

7.1.6.4 Low amount of gremlin

Analogously to what has been done in chapter 5, it is interesting to verify what happens if we try to guarantee, within the current formulation, that nearly 30% of free receptors remaining unbound in the apical side of the cell (anchored-receptors). In fact, by playing with the number of available gremlin in the substrate, specifically reducing them from 90 to about 60 $molecules/\mu m^2$, we can respect, by this artifact, the ratio between the total amount of free and bound receptors on the cell membrane.

Table 7.2: Co-designing between VEGFR2-fluorescence intensity (in-vitro experiments) and the number of complexes generating on the cell membrane (in-silico simulation) is provided for $S_L = 60\ molecules/\mu m^2$. Specifically, both the total that dimensionless quantities are tabulated.

Time	FRAP	Error bars	Complex	Adimensional Complex	Adimensional FRAP	Adimensional error bars
0	1.8125	1.7470	0.0000	0.0000	0.0674	0.0649
120	2.6775	1.7774	1422.8270	0.0864	0.0995	0.0661
240	3.6175	2.0371	1973.5409	0.1198	0.1344	0.0757
360	8.8875	4.5427	7432.5178	0.4514	0.3303	0.1688
480	12.0225	5.1638	11555.1774	0.7017	0.4468	0.1919
600	17.4375	4.0251	13275.4867	0.8062	0.6481	0.1496
720	20.1325	4.3776	14041.9600	0.8527	0.7482	0.1627 4
840	19.6650	4.4217	14953.0312	0.9081	0.7308	0.1643
960	20.4075	4.5417	15624.1197	0.9488	0.7584	0.1688
1080	22.8600	4.7168	16073.1926	0.9761	0.8496	0.1753
1200	23.0375	5.5135	16325.7133	0.9914	0.8562	0.2049
1320	23.2725	4.8333	16404.9998	0.9962	0.8649	0.1796
1440	24.9150	5.5791	16436.5035	0.9982	0.9260	0.2073
1560	25.8650	4.7980	16452.5141	0.9991	0.9613	0.1783
1680	27.8800	6.0900	16461.5263	0.9997	1.0361	0.2263
1800	26.9075	5.9243	16466.8527	1.0000	1.0000	0.2202
3600	39.2718	18.8742	16475.3274	1.0005	1.4595	0.7014
7200	36.8140	17.3697	16475.3348	1.0005	1.3682	0.6455

This approximation, which we know to be biologically wrong, could be accepted, preliminary, if we wanted to study only the dynamics of the receptor. However, by co-design the correspondent in-vitro and in-silico outcomes, we acknowledge the inaccuracy provided by this assumption (see Fig. 7.15), thus necessited to extend the current paradigm with a further one (see section 7.2).

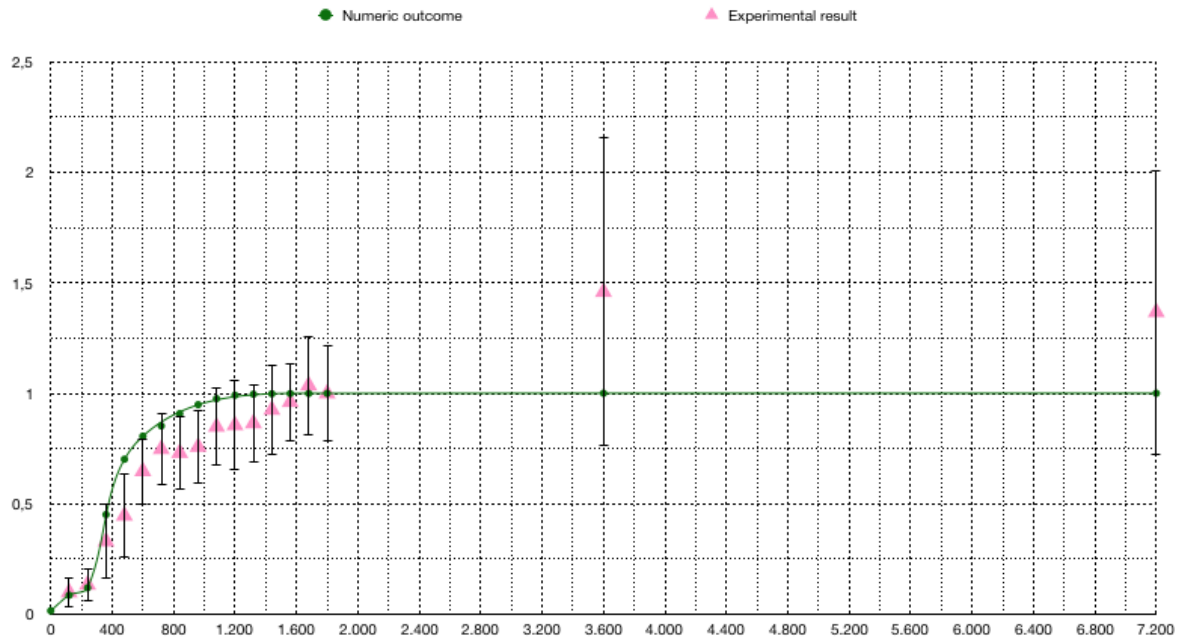

Figure 7.15: Numerical (continuous line) and experimental (dots with error bars). Evolution in time of the normalized total amount of complexes, when the available concentration of ligands in contact with the substrate is equal to 60 $molecules/\mu m^2$.

The following picture, Fig. 7.16, displays the evolution in time of the total amount of molecules on the cell membrane. Here, we can see how a considerable quantity of VEGFR2 keeps on free on the cell membrane. Such evidence, instead, does not happen in Fig. 7.14, where a total depletion of free receptors is manifested.

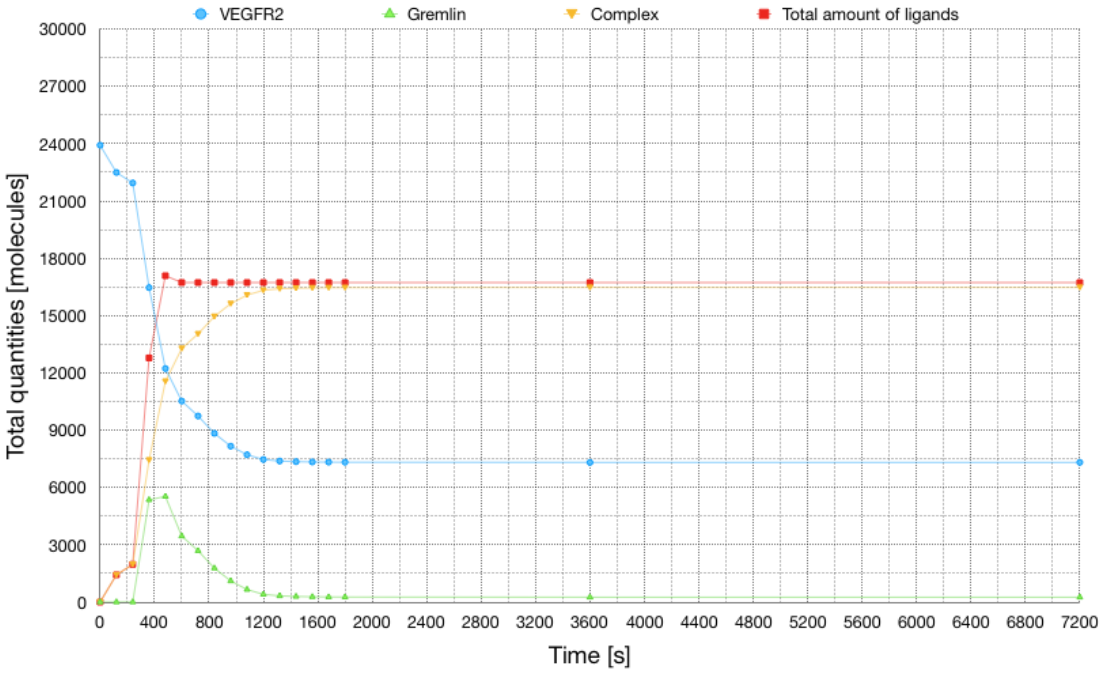

Figure 7.16: Time evolution of the total amount of molecules of receptors, complexes, free-ligands, and the complete amount of ligands (free plus bound) when $S_L = 60\ molecules/\mu m^2$.

7.1.6.5 Remarks and further development

Receptors-ligand interaction in the adhesion of a cell onto a substrate has been investigated in [113]. In this study, the adhesion requires transport of receptors from the apical to the basal part of the cell in order to generate attractive forces, since the mean receptor density on the membrane does not allow to overcome the elastic resistance against spreading. In recent publications [138, 139] three distinct phases of the relocation of receptors have been identified, each of which relates to a different physical mechanism. A fast interaction due to chemical bonding at adhesion precedes a mechanically dominated regime, in which free receptors are depleted to be engaged in complexes with ligands due to the spreading of the cell, driven by filopodia/lamellipodia migration processes. Finally, once a *macroscopic* steady-state mechanical configuration has been achieved, transport of receptors on the membrane continues and favor complex formation in localized spots. This three-phases evolution time-scale differs from the scenario depicted in [113].

A detailed study of cell adhesion to a substrate was proposed in [116]. Differently from the present formulation, the structural response of the cell was attributed in full to the membrane, modeled by means of an isotropic continuum model. The role of the spontaneous area dilation was clearly highlighted. Numerical simulations and conclusions, achieved on particularly small cells of radius 12.5nm, may not hold for endothelial cells. In particular, the range of action and the importance of binding force in the mechanical response largely differ from the conclusions stated here.

Figure 7.11(b) shows that at the end of the experimental time span, free receptor molecules almost vanish. This outcome contradicts the experimental evidence since the full depletion of VEGFR2 is prevented and the residual amount of free receptors in the apical side of the cell is in the order of 30% of the initial concentration. Precisely, the 77% of ECD-VEGFR2-EYFP on the lipid bilayer is found in a mobile form [138]. This datum could have been achieved numerically, by altering the initial value of available gremlin on the substrate to 60 $molecules/\mu m^2$ rather than 90 $molecules/\mu m^2$. In such a case, the correct final amount of free receptors is captured by the simulation, but the shape of the numerical curve largely differs from experimental data - see Fig. 7.15. We believe that this simulation is not reliable, since it does not grasp the physics of the experiment correctly (see section 7.1.6.4).

In fact, by imposing a low amount of initial gremlin, all available ligands are consumed and for this sake, a free receptors leftover arises. However, this is not the physical reason for which receptors do not deplete, rather it is due to a specific interplay of VEGFR2 with the cellular cortex. Such an interaction favors the internalization/externalization of receptors, which takes place during the normal angiogenic processes. Such an interplay slows down enormously the transport of the engaged receptors, nearly the 23% of them [138], to the point of making them basically immobile, at least compared to free receptors. All these considerations suggest that the right model for capturing the residue of receptors on the apical side would require a duplication of the species of receptors in a *free* set and an *immobile* part, capable to internalize/externalize. The depletion of free receptors will be complete, as in 7.11(b) and the residual will be due to the immobile VEGFR2 attached to the cellular cortex (see next chapter 7.2).

Note also that the internalization/externalization of receptors is known to take place at a longer timescale compared to the mechanical spreading. These events therefore shall interact with the diffusion of receptors after the geometrical evolution completes. We notice in Fig. 7.10 that the highest discrepancies between simulations and experiments arise exactly in such a phase. We infer that they might indeed be due to the above-mentioned physical processes that have not been accounted for.

Hence, we extend the current model to further numerical patterns involve the definition of the above-mentioned immobilized and mobile species of VEGFR2.

7.2 Immobilized receptor

Concerning the in-silico simulation of VEGFR2, either in "surrogatad mechanics" framework (chapters 3.4 and 5) that in the large deformations one (chapters 6 and 7), we dispose of models wherein all the VEGFR2 molecules are potentially free to move along the cell membrane. Indeed, with enough high-amount of ligands, the above-mentioned formulations always conduct towards a total depletion of free VEGFR2 on the cell membrane. However, this kind of phenomenon has no correspondence in the experimental reality (see FRAP analysis E.2), where we usually observe a considerable (according to the type of cell and kind of experiment) fraction of VEGFR2 molecules anchored ("immobilized-fraction" of VEGFR2) at the cytoskeleton [31] (chapter 2), [138, 139]. Consequently, in the experiment discussed in chapter 4, we can not observe a total depletion of

free VEGFR2 on the cell membrane, rather a total depletion of the mobile fraction of VEGFR2 participating in the experiment. Therefore, at the end of the experimental observation, we can attest that a not negligible amount of VEGFR2 remains fixed and free in the apical side of an EC spread on a ligands-coated substrate. Particularly, the in-vitro experiments presented in [31] (chapter 2), [138, 139], and chapters 4, 5, 7, and 8 of the current thesis, show a marked amount of fixed free receptors in the apical area of the cell membrane with consequent an uneven distribution of the VEGFR2 unbonded. These fixed receptors, henceforth called "immobilized free receptors", are characterized by having a very slowed motility, despite they are not linked to any types of ligands. Probably, this kind of specific behavior is the result of a complex dynamical interaction between this kind of VEGFR2 and the actin cellular cortex and other cell membrane components. Such interactions are under scrutiny by biologists.

Although we could play with the number of available ligands in order to respect the relation between free and bound VEGFR2 at the end of the simulation (as we have done in chapters 5, 7), this is an incomplete idealization of reality. Also, following such a path of reasoning, we could not surely start to set a mathematical model able to involve the possible cytoskeletal interaction that VEGFR2 is subjected in the current experiments.

Hence, the free receptors on the cell membrane are divisible in at least two subcategories: the first one called *immobilized* due to the interaction with the cell actin cortex, and the second one said *mobile* along the membrane. Therefore, a suitable duplication of the species of VEGFR2 is desirable in order to describe the coexistence of free mobile and immobile receptors. This inevitably leads to update the previous set of governing equations shown in section 6.2.3, accounting for the new experimental considerations.

Accordingly, we extend the previous relations, (6.22) and (6.34), through the following ones:

$$1)\quad V_{Im} + L_V \underset{k_b^1}{\overset{k_f^1}{\leftrightarrows}} C_1^{Im}\,, \tag{7.13a}$$

$$2)\quad V_M + L_V \underset{k_b^1}{\overset{k_f^1}{\leftrightarrows}} C_1^{M}\,. \tag{7.13b}$$

$$\frac{\partial c_{V_R^{Im}}}{\partial t} + w_R^{(7.13a)} = s_{V_R^{Im}}\,, \tag{7.14a}$$

$$\frac{\partial c_{V_R^{M}}}{\partial t} + \mathrm{Div}_{\mathcal{P}_R}\left[\vec{h}_{V_R^{M}}\right] + w_R^{(7.13b)} = s_{R_R^{M}}\,, \tag{7.14b}$$

$$\frac{\partial c_{L_{VR}}}{\partial t} + w_R^{(7.13a)} + w_R^{(7.13b)} = s_{L_{VR}}\,, \tag{7.14c}$$

$$\frac{\partial c_{C_{1R}}}{\partial t} = \frac{\partial c_{C_{1R}^{Im}}}{\partial t} + \frac{\partial c_{C_{1R}^{M}}}{\partial t}\,, \tag{7.14d}$$

$$\frac{\partial c_{C_{1R}^{Im}}}{\partial t} = w_R^{(7.13a)}\,, \tag{7.14e}$$

$$\frac{\partial c_{C_{1R}^{M}}}{\partial t} = w_R^{(7.13b)}\,. \tag{7.14f}$$

where the apex "Im" and "M" denote the immobilized and mobile species, respectively. Moreover, because the chemical interaction exerts by VEGFR2, fix, and mobile, with respect to the non-canonical ligand gremlin, is totally equivalent, all the specifications made in the previous chapters

on the receptor-ligand chemical interaction can be inherited. These comprised the infinitely fast kinetics hypothesis, which previously had conducted to the governing equation (6.37a), and now leads to the following relations:

$$c_{C_{1R}^{Im}} = \frac{c_{V_R^{Im}} c_{L_{VR}}}{\alpha_R} \qquad (7.15a) \qquad\qquad c_{C_{1R}^{M}} = \frac{c_{V_R^{M}} c_{L_{VR}}}{\alpha_R} \qquad (7.15b)$$

Therefore, together with eq .(7.15), the subsequent collection of equations complete the group of the current governing equations:

$$\frac{\partial c_{V_R^{Im}}}{\partial t} + \frac{\partial c_{C_{1R}^{Im}}}{\partial t} = s_{V_R^{Im}} \,, \qquad (7.16a)$$

$$\frac{\partial c_{V_R^{M}}}{\partial t} + \mathrm{Div}_{\mathcal{P}_R}\left[\vec{h}_{V_R^{M}}\right] + \frac{\partial c_{C_{1R}^{M}}}{\partial t} = s_{R_R^{M}} \,, \qquad (7.16b)$$

$$\frac{\partial c_{L_{VR}}}{\partial t} + \frac{\partial c_{C_{1R}^{Im}}}{\partial t} + \frac{\partial c_{C_{1R}^{M}}}{\partial t} = s_{L_{VR}} \,, \qquad (7.16c)$$

$$\frac{\partial c_{C_{1R}}}{\partial t} = \frac{\partial c_{C_{1R}^{Im}}}{\partial t} + \frac{\partial c_{C_{1R}^{M}}}{\partial t} \,, \qquad (7.16d)$$

where, now, the terms $s_{V_R^{Im}}$ and $s_{R_R^{M}}$, can potentially describe the internalization/externalization phenomena. However, also for these kind of problems we set $s_{V_R^{Im}} = s_{R_R^{M}} = 0$.

Table 7.3: Material papameters

Material parameters	values	Units
$\mathbb{D}_V$	0.198	$\mu m^2/s$
$\alpha_{(7.13a)} \equiv \alpha_R$	0.04519	$molecules/\mu m^2$
$\alpha_{(7.13b)} \equiv \alpha_R$	0.04519	$molecules/\mu m^2$

Table 7.4: Material papameters

Material parameters	values	Units
$c_{V_R}^{Im0}$	4.393	$molecules/\mu m^2$
$c_{I_R}^{M0}$	14,17	$molecules/\mu m^2$
$c_{L_{VR}}^{0}$	0	$molecules/\mu m^2$
$c_{C_{1R}}^{0}$	0	$molecules/\mu m^2$

In Tables 7.3 and 7.4 we can take a view of the material parameters ruling the current formulation. Interestingly, the initial concentration of immobilized receptors is computed accounting to

the FRAP analysis (see [138] and Appendix E.2), which show that 23% of VEGFR2 is anchored at the cytoskeleton. Therefore, at each point of the cell membrane, we denote that the 77% of VEGFR2 results to be mobile. Such values appear to be in contrast with those mentioned in chapters 5, 7 where we have assumed a percentage of the 30% of VEGFR2 present in the apical side of the cell at time $t = 7200\ s$. It is important to point out that these two percentage (23% and 30%) are correctly different from each other; in fact, the datum 30% does not describe a piece of local information, rather than the ratio among the total number of VEGFR2 free in the apical side of the EC compared to the global amount of this receptor on the cell membrane. These two percentages could match only in a perfect case of symmetry, that here we do not have. Knowing that it is trivial deduced $c_{V_R}^{Im0} = 0.23 * 19.1 = 4.393$, where 19.1 is the initial concentration corresponding to a total number of VEGFR2 equal to 24000 and a cell radius equal to 10 μm.

Table 7.5: Co-designing between VEGFR2-fluorescence intensity (in-vitro experiments) and the number of complexes generating on the cell membrane (in-silico simulation) is provided for a duplicate-species model. Specifically, both the total that dimensionless quantities are tabulated.

Time	FRAP	Error bars	Complex	Adimensional Complex	Adimensional FRAP	Adimensional error bars
0	1.8125	1.7470	0.0000	0.0000	-	-
120	2.6775	1.7774	1982.1244	0.1124	0.0995	0.0661
240	3.6175	2.0371	2929.2491	0.1661	0.1344	0.0757
360	8.8875	4.5427	7419.5159	0.4207	0.3303	0.1688
480	12.0225	5.1638	10526.2684	0.5968	0.4468	0.1919
600	17.4375	4.0251	12580.9120	0.7133	0.6481	0.1496
720	20.1325	4.3776	13290.4139	0.7536	0.7482	0.1627
840	19.6650	4.4217	14085.3412	0.7986	0.7308	0.1643
960	20.4075	4.5417	14860.5194	0.8426	0.7584	0.1688
1080	22.8600	4.7168	15515.1072	0.8797	0.8496	0.1753
1200	23.0375	5.5135	16078.1305	0.9116	0.8562	0.2049
1320	23.2725	4.8333	16511.9306	0.9362	0.8649	0.1796
1440	24.9150	5.5791	16852.1123	0.9555	0.9260	0.2073
1560	25.8650	4.7980	17143.5108	0.9720	0.9613	0.1783
1680	27.8800	6.0900	17404.8341	0.9869	1.0361	0.2263
1800	26.9075	5.9243	17636.7404	1.0000	1.0000	0.2202
3600	39.2718	18.8742	18955.5063	1.0748	1.4595	0.7014
7200	36.8140	17.3697	19221.7209	1.0899	1.3682	0.6455

Interestingly, the possible receptors that can interact with ligands are decreased with respect to the previous models. Hence, it is predictable a total depletion of the mobile species of VEGFR2 (as confirmed by Fig. 7.20b). Consequently, the trend of the numerical curve (see Fig. 7.17) maintains a similar shape to those shown in the preceding chapters, provide a suitable fitting well the experimental outcomes.

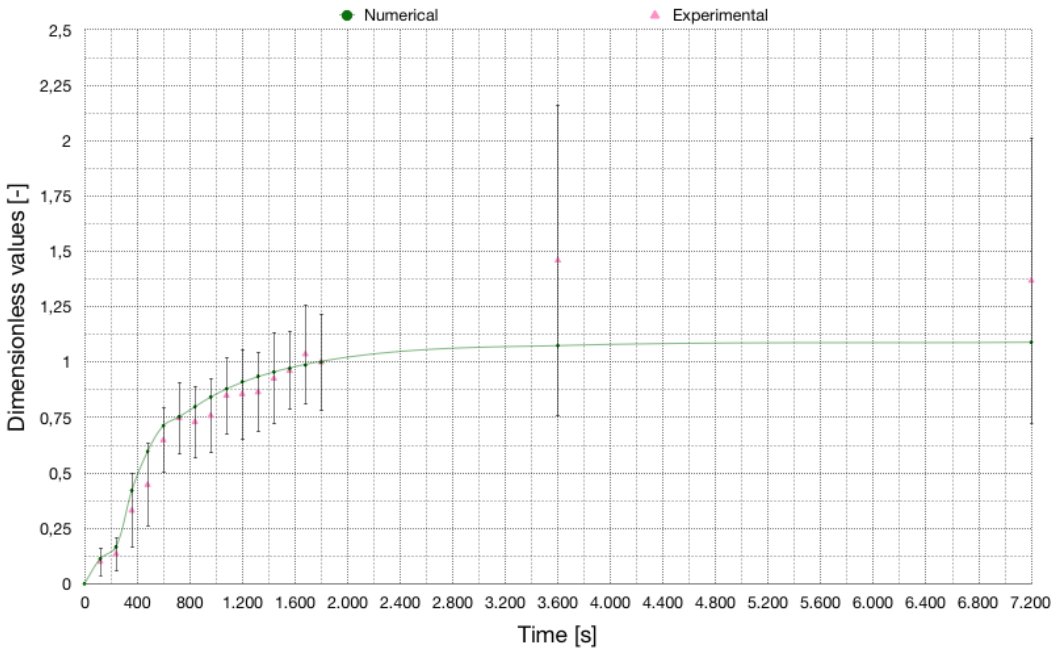

Figure 7.17: Numerical (continuous line) and experimental (dots with error bars) outcomes. Evolution in time of the normalized total amount of complexes (mobile plus immobilized).

Moreover, by means of Fig. 7.18, it can be observed that a non-negligible part of VEGFR2 remains on the apical part of the cell. Following, through Fig 7.20 we depicted the frames at the end of the mechanical spreading process and diffusion processes, for both immobilized mobile VEGFR2 respectively.

Finally, the evolution in the basal side of the cell of the complex is shown through Fig. 7.21 and 7.22 (see 7.7a for better understand the point of view of the observer), where a non-homogeneous concentration of complexes at the end of the analysis, suggests a possible high residual of availability of ligands present in the substrate (assumptions confirm by the graphic 7.23).

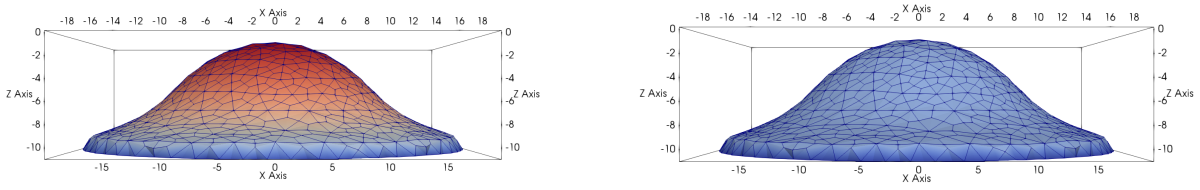

(a) $t = 600\,\mathrm{s}$ (b) $t = 7200\,\mathrm{s}$

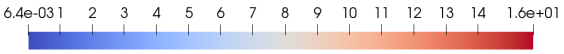

(c) Legend

Figure 7.18: Diffusion of receptors (immobilized plus mobile) after the spreading phase has not been completed.

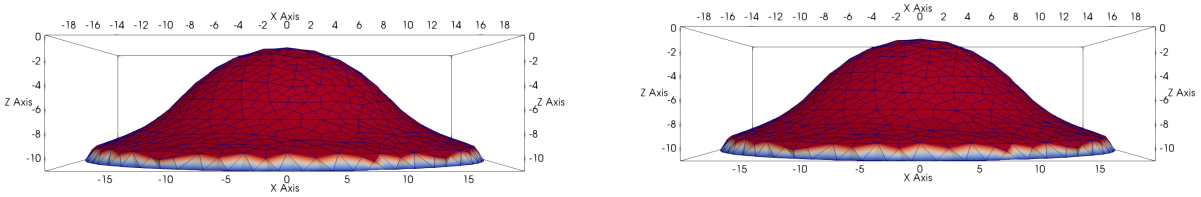

(a) $t = 600\,\mathrm{s}$ (b) $t = 7200\,\mathrm{s}$

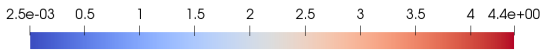

(c) Legend

Figure 7.19: No-diffusion of receptors after the spreading phase has been observed for immobilized species.

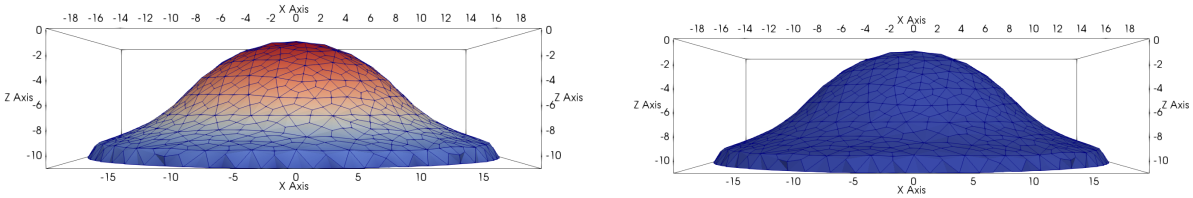

(a) $t = 600\,\mathrm{s}$ (b) $t = 7200\,\mathrm{s}$

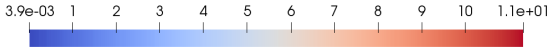

(c) Legend

Figure 7.20: Diffusion of mobile receptors after the spreading phase has been completed.

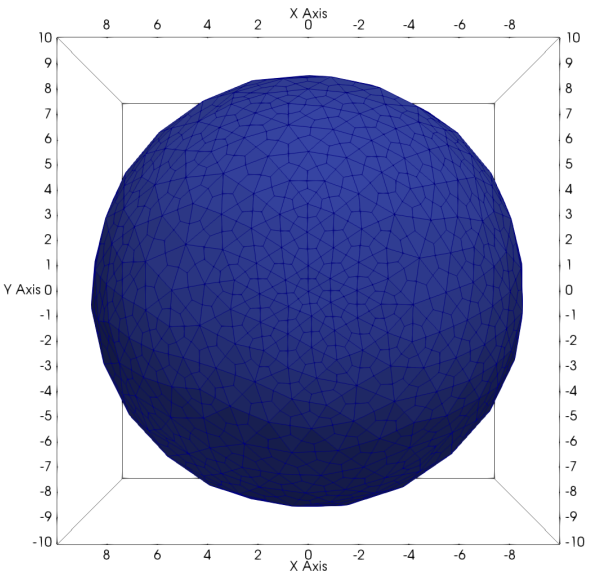

(a) $t = 0\,\mathrm{s}$

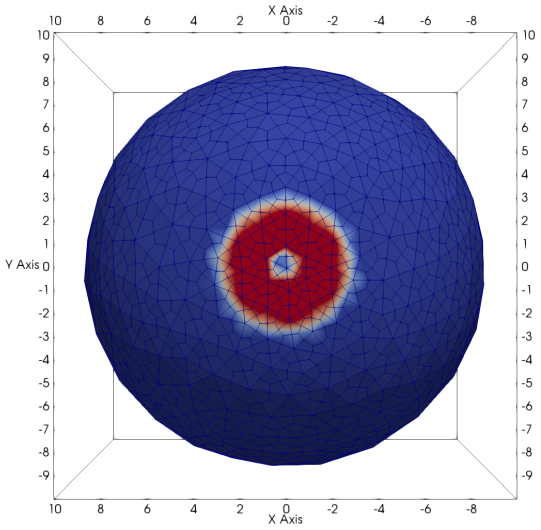

(b) $t = 120\,\mathrm{s}$

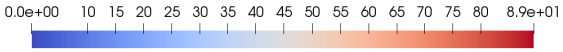

(c) Legend

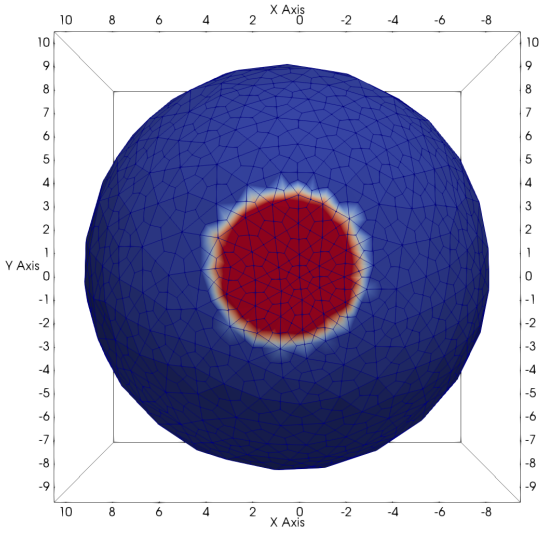

(d) $t = 240\,\mathrm{s}$

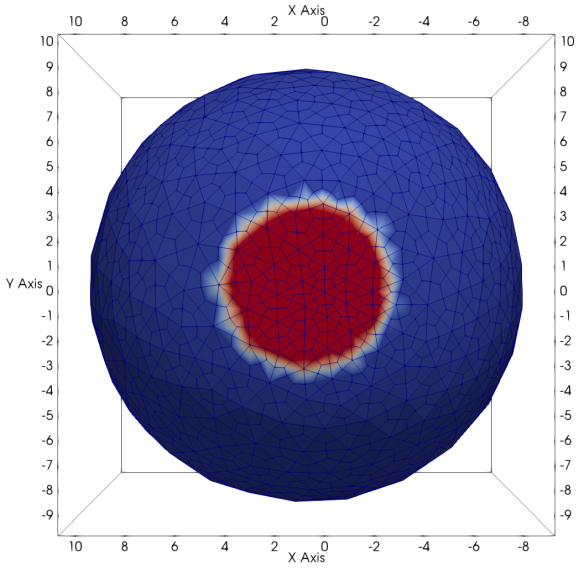

(e) $t = 300\,\mathrm{s}$

Figure 7.21: Basal distribution of the whole species of complexes (mobile and immobilized) during the adhesion stage.

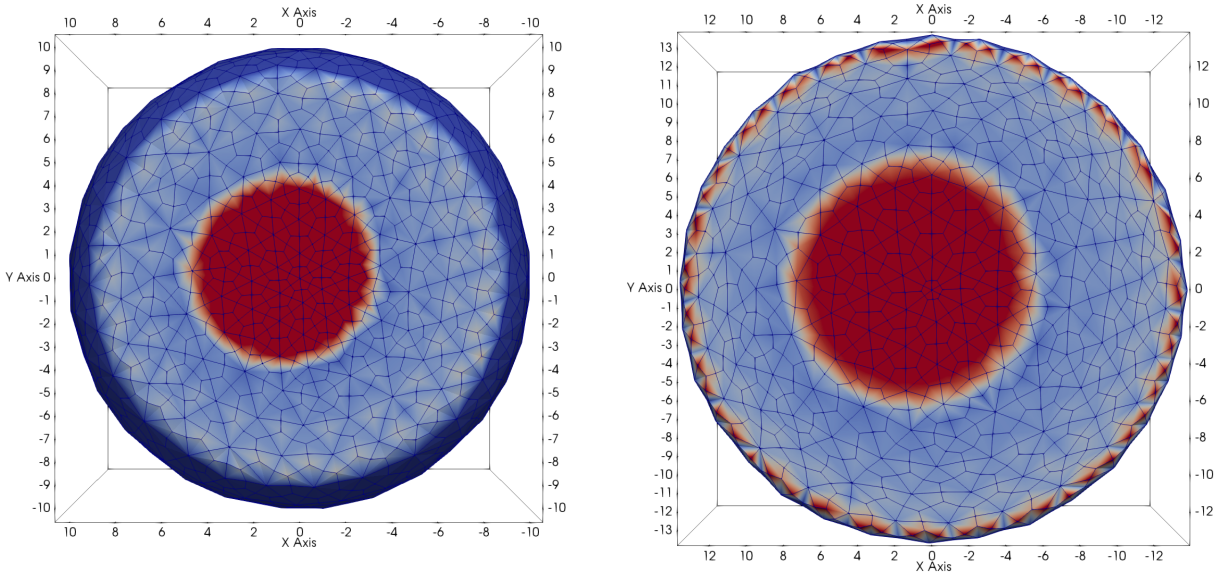

(a) $t = 360\,\mathrm{s}$ (b) $t = 480\,\mathrm{s}$

(c) Legend

(d) $t = 600\,\mathrm{s}$ (e) $t = 7200\,\mathrm{s}$

Figure 7.22: Basal distribution of the whole species of complexes (mobile and immobilized) during spreading stage (a)-(c) and at the end of the experimental time-span (d).

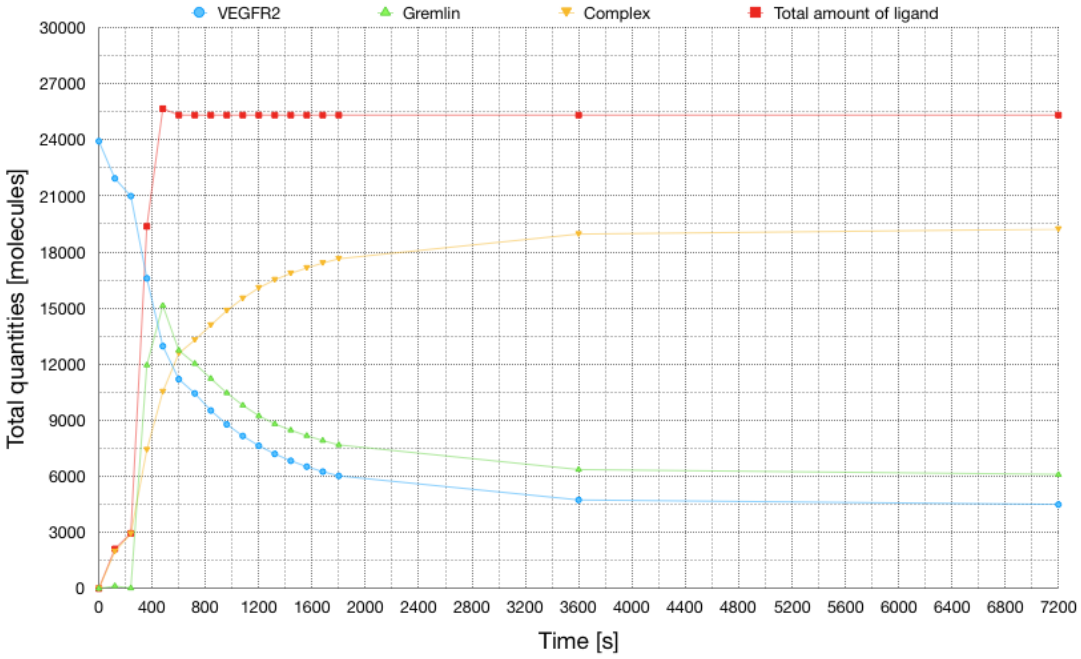

Figure 7.23: Time evolution of the total amount of molecules of receptors, complexes (mobile plus immobilized), free-ligands, and the complete amount of ligands (free plus bound) when $S_L = 90\ molecules/\mu m^2$.

7.3 Comparison between VEGFR2 and VEGFR2-R1032Q

Agree with what has been discussed in 2.3.1.3, in the current section we provide a study on the behavior of the specific mutation R1032Q of VEGFR2.

The biological aim of this part of the work is to discuss, verify and quantify what are the effects of the mutation R1032Q on the performance of the VEGFR2, either concerning the interaction with ligands, specifically, in these experiments, VEGF-A, that regarding its dynamic on the cellular membrane. In order to do this, we study the dynamics of this receptor, and of its corresponding unmutated (henceforth called VEGFR2 Wild Type or VEGFR2-WT), on CHO cells by means of two main experimental techniques: FRAP and the time-lapse microscopy that shows the VEGFR2 (R1032Q or WT) recruitment by immobilized VEGF-A.

Preliminarily, we have not tested if VEGFR2-R1032Q manifests the very same affinity and chemical kinetics with VEGF-A displayed by VEGFR2-WT, but we assume it. Such a supposition is congruent with the fact that the mutation R1032Q concerns the intracellular domains of the receptor not leading to any changes in the molecular conformation of its extracellular domains (domains D2 and D3). Particularly, we observe the substitution of arginine with glutamine in the VEGFR2-R1032Q catalytic site, leading to an improvement in kinase activity of the mutated receptor itself.

With the aids of FRAP analysis has been possible to evaluate how the R/Q substitution of residue 1032 can alter the mobility of the receptor. Hence, FRAP experiments on CHO cells that express hVEGFR2-WT-EYFP or hVEGFR2-R1032Q-EYFP have been set, with or without VEGF-A. Consequently, either the time necessary to recover the 50% of fluorescence in ROI that the corresponding mobile and immobile fractions have been measured for VEGFR2-WT and VEGFR2-R1032Q.

Table 7.6: FRAP-parameters corresponding to VEGFR2-WT and VEGFR2-R1032Q receptor.

Receptor	$0.224/t_{1/2}$	% of immobile fraction
VEGFR2-WT	0.021	35 %
VEGFR2-R1032Q	0.01045	64.5%

It is evident (see 7.6), how VEGFR2-WT has greater lateral motility than the R1032Q. Not only that, but significant results also arise from the time-lapse adhesion assay of CHO cells on a substrate coated by VEGF-A. Here, we observe that WT-receptor has greater motility also in terms of recruitment in the basal side of the cell.

7.3.1 In-silico analysis

It is very interesting to try to understand how the mutated receptor changes the behavior of the ECs in experiments such as those discussed in chapters 5 and 7, and section 7.2. In order to do that, we set a series of in-silico analysis that mimic the mechanical behavior of ECs tested and calibrated in section 7.1, but using, both for WT that R1032Q, the parameters (diffusivity and immobile fraction) deduced by the experiments on the CHO cells (see Tab.7.6).

Accordingly, a suitable measure of w^2 (i.e. the square of the radius of ROI - see Appendix E.2) is necessary for this purpose, that it has been inferred owing to the assumption that the diffusivity of the VEGFR2-WT in EC is equal to the diffusivity of the VEGFR2-WT in CHO cells ($\mathbb{D}_{V_{WT}}^{EC} = \mathbb{D}_{V_{WT}}^{CHO} = 0.198\ \mu m^2/s$). Therefore, thanks to the relation $\mathbb{D} = 0.224 * \omega^2/t_{1/2}$ (see eq. (E.2)), it is trivial obtain:

$$\frac{0.198 * t_{1/2}}{0.224} = \omega_{CHO}^2 = 9,43 \mu m^2 \,. \tag{7.17}$$

Hence, thanks to (7.17), we can deduce that the diffusivity of the VEGFR2-R1032Q is equal to $\mathbb{D}_{V_{R1032Q}} = 0.224 * \omega^2/t_{1/2} = 0,0985\ \mu m^2/s$.

7.3.1.1 Simulations on receptors with full depletion

In the current section, we compare the numerical curves that depict the complexes' recruitment both for VEGFR2-WT-VEGF-A that VEGFR2-E1032Q-VEGF-A.
Analyzing the data in Tab. 7.7, we can observe how, despite the WT receptor has a diffusivity greater than R1032Q, the total quantities of Complex-WT and R1032Q are almost similar. The current, in fact, is a model that leads to a full depletion of the receptors; indeed, no splitting of VEGFR2 in mobile and immobilized species has been here done. Therefore, the greater slowness of R1032Q is compensated by the fact that all the receptors can potentially move from the apical to the basal side of the cell, and so, at a long-term ($t = 7200\ s$), also the mutated receptor reaches the complete dwindling.

Table 7.7: Co-designing between the number of complexes generating on the cell membrane (in-silico simulation) correlated to receptors VEGFR2-WT and VEGFR2-R10312Q, respectively. Specifically, both the total that dimensionless quantities are tabulated.

Time	Complex-WT	Complex-R1032Q	Adimensional Complex-WT	Adimensional Complex-R1032Q
0	0,0000	0,0000	0,0000	0,0000
120	2105,2746	1740,4353	0,1008	0,0833
240	2941,2043	2753,3911	0,1408	0,1318
360	8072,1388	6620,3376	0,3864	0,3169
480	11954,5760	9518,4365	0,5722	0,4556
600	14293,4851	11479,0537	0,6842	0,5495
720	15205,1208	12292,0891	0,7278	0,5884
840	16410,0491	13010,4657	0,7855	0,6228
960	17406,2871	13750,2831	0,8332	0,6582
1080	18100,4100	14477,6438	0,8664	0,6930
1200	18747,8007	15160,8978	0,8974	0,7257
1320	19328,7216	15824,7614	0,9252	0,7575
1440	19843,2785	16361,3288	0,9499	0,7832
1560	20262,9277	16778,1826	0,9700	0,8031
1680	20598,0116	17149,2433	0,9860	0,8209
1800	20890,5624	17530,2588	1,0000	0,8391
3600	22723,3906	20996,5336	1,0877	1,0051
7200	23079,7764	22713,5303	1,1048	1,0873

Nevertheless, despite the two curves reach analogous final values, their trends explore very different quantities (see Fig. 7.24). Particularly, it is evident either from Fig. 7.24 that for Fig. 7.27, how the two curves are completed overlapped until the end of the adhesion phase ($t = 300\ s$). This means that the mechanical spreading of the cell, throughout this step, is not so quick and significant to highlights the different sizes of diffusivity of these receptors. For juxtaposed arguments, after the instant $t = 300\ s$ until the $t = 600\ s$ the curves move away from each other. Such a trend persists as long as there is a considerable amount of WT receptor that can migrate (see Tab. 7.7 instant $t = 1800\ s$), thereafter for each numerical outcome, the two curves tend to get closer. Finally, the basal distribution of the WT- and R1032Q-species of complexes upon completion of adhesion stage, spreading stage, and at the end of the experimental time-span are depicted in Fig. 7.25 and 7.26 (see 7.7a for better understand the point of view of the observer).

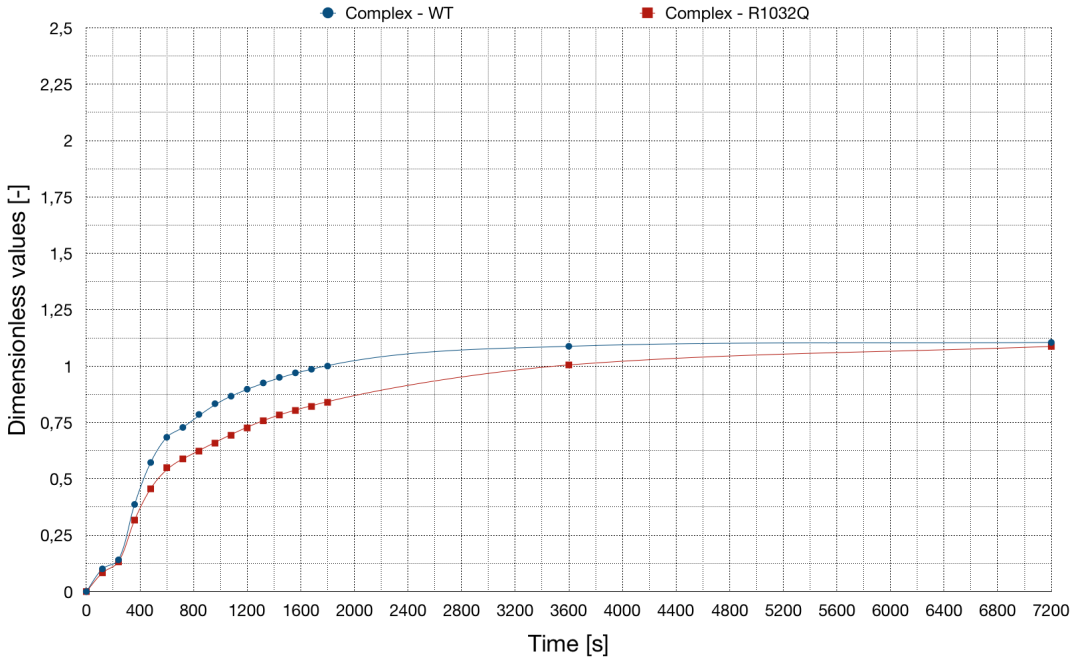

Figure 7.24: Evolution in time of the normalized total amount of complexes of VEGFR2-WT (continuous blue-line) and VEGFR2-R1032Q (continuous red-line).

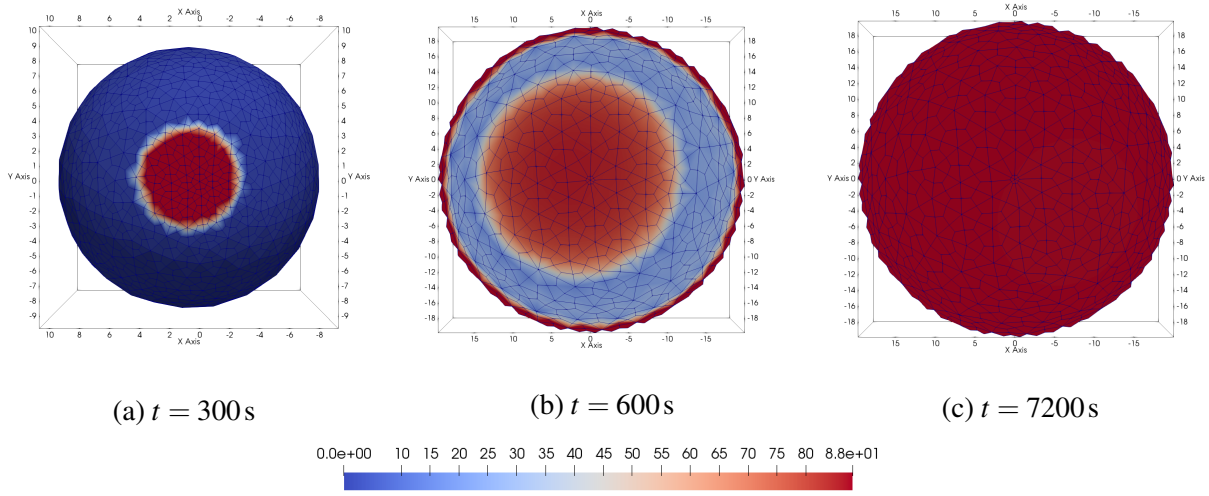

(a) $t = 300\,\mathrm{s}$ (b) $t = 600\,\mathrm{s}$ (c) $t = 7200\,\mathrm{s}$

(d) Legend

Figure 7.25: Basal distribution of the WT-species of complexes upon completion of adhesion stage (a), spreading stage (b), and at the end of the experimental time-span (d).

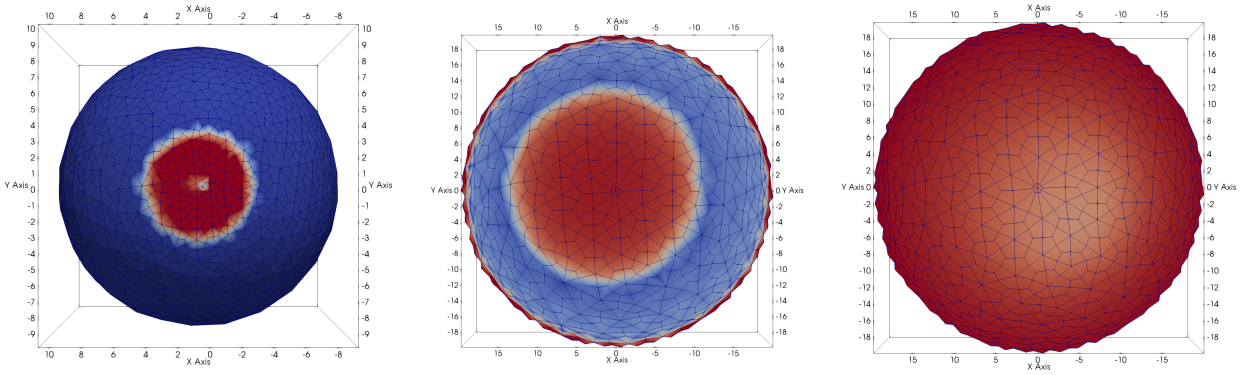

(a) $t = 300\,\mathrm{s}$ (b) $t = 600\,\mathrm{s}$ (c) $t = 7200\,\mathrm{s}$

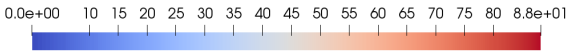

(d) Legend

Figure 7.26: Basal distribution of the WT-species of complexes upon completion of adhesion stage (a), spreading stage (b), and at the end of the experimental time-span (d).

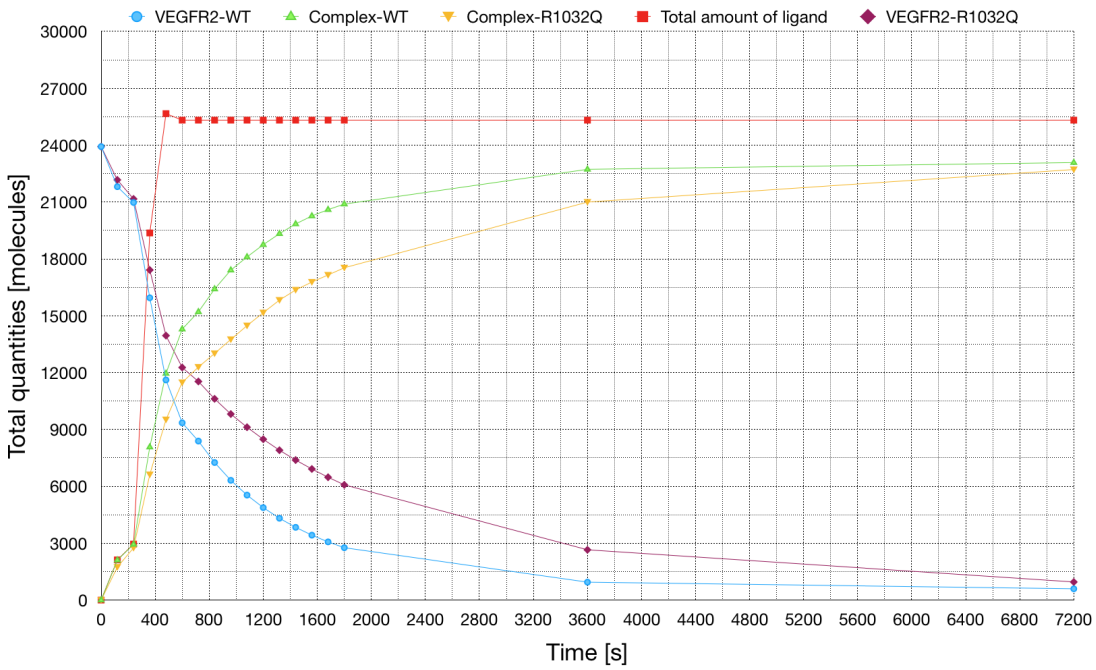

Figure 7.27: Time evolution of the total amount of molecules of receptors (WT and R1032Q), complexes (WT and R1032Q), free-ligands, and the complete amount of ligands (free plus bound) when $S_L = 90\ molecules/\mu m^2$.

7.3.1.2 Simulations with immobilized receptors

Different inferences arise from the analyses of Tab. 7.8, and Fig. 7.28, 7.31. Here, the model allows for accounting for two different species (mobile and immobilized) both for VEGFR2-WT and VEGFR2-R1032Q. Firstly, the total amount of complex generated in the basal side of the cell is considerably lower with respect to the antecedent section. Significantly, are the differences among the values presented in Tab. 7.7 and Tab. 7.8.

Table 7.8: Co-designing between the number of complexes (mobile plus immobilized) generating on the cell membrane (in-silico simulation) correlated to receptors VEGFR2-WT and VEGFR2-R10312Q, respectively. Specifically, both the total that dimensionless quantities are tabulated.

Time	Complex-WT	Complex-R1032Q	Adimensional Complex-WT	Adimensional Complex-R1032Q
0	0.0000	0.0000	0.0000	0.0000
120	1832.5553	1054.3656	0.1155	0.0665
240	2868.4190	1608.1412	0.1808	0.1014
360	7037.2058	5117.0622	0.4437	0.3226
480	9784.4864	6981.4241	0.6169	0.4402
600	11472.1348	7462.8892	0.7233	0.4705
720	12209.3933	7798.2001	0.7698	0.4917
840	12909.5766	8183.0337	0.8139	0.5159
960	13478.8934	8494.8370	0.8498	0.5356
1080	14022.9486	8790.6328	0.8841	0.5542
1200	14479.6310	9072.0667	0.9129	0.5720
1320	14870.3365	9329.0500	0.9375	0.5882
1440	15201.1000	9555.1283	0.9584	0.6024
1560	15469.2401	9749.7749	0.9753	0.6147
1680	15684.3609	9916.6583	0.9889	0.6252
1800	15861.1301	10060.9336	1.0000	0.6343
3600	16881.3626	11197.9580	1.0643	0.7060
7200	17083.9615	11648.5650	1.0771	0.7344

Moreover, such dissimilarities, all together, determine, ultimately, a total lack of superposition between the curves shown in Fig. 7.28, as well. Specifically, starting from the adhesion phase, we can note how the WT receptor manages to generate more complexes than R1032Q one. This happens, despite the very low rate of deformation that persists along with the first 300 s, inferring that the massive differences between the immobilized fractions of WT and mutated receptors play a pivotal role from the very beginning of the in-silico experiments. This is confirmed by Fig. 7.31, wherein the total amount of mutated complexes is not able to overlap the total number of available ligands.
Subsequently, the complexes formation curves manifest the same slopes until the instant $t = 400\ s$, namely, as far as the half of the mechanical spreading phase. The second part of this stage ($t =$

600 s), is closed by pronounced differences in the growths drawn up on the graph Fig 7.28. Here again, we can observe how the WT receptor must have access to a higher amount of mobile species and more diffusive, inasmuch as the *blue* curve, present a continuous growth as far as the instant $t = 3600\ s$. Afterward, we denote a slight reduction of the distance between the *red* curve and the *blue* one, which suggests that the mutated receptor, in proportion, has eroded less portion of the mobile species than the WT, owing to its low diffusivity. Finally, the basal distribution of the WT- and R1032Q-species of complexes upon completion of adhesion stage, spreading stage, and at the end of the experimental time-span are depicted in Fig. 7.29 and 7.30 (see 7.7a for better understand the point of view of the observer).

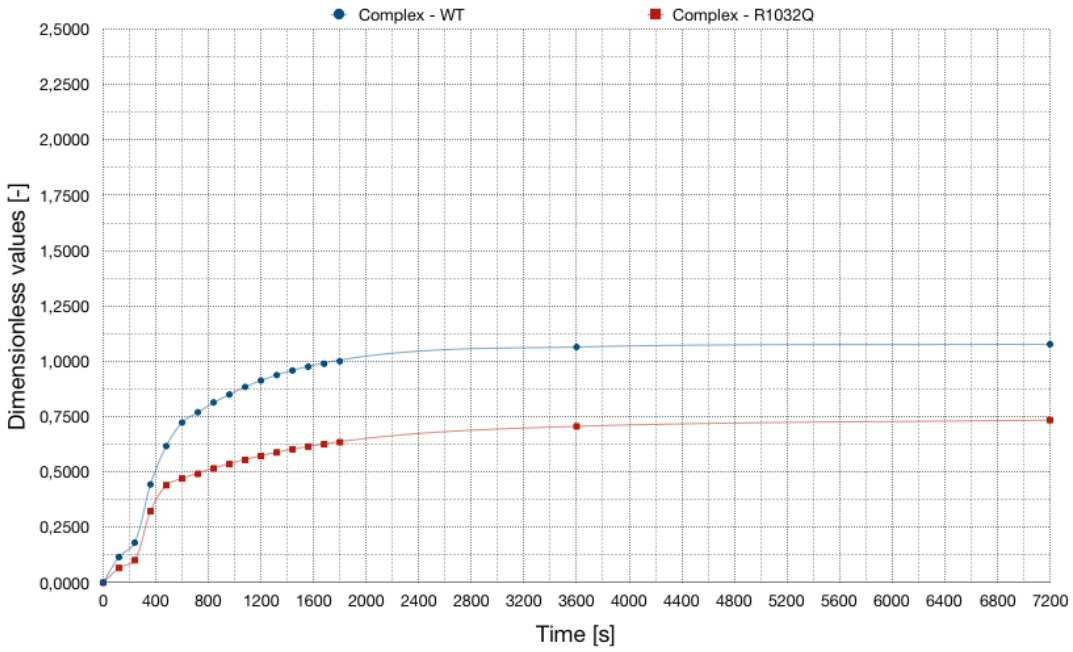

Figure 7.28: Evolution in time of the normalized total amount of complexes (mobile plus immobilized) of VEGFR2-WT (continuous blue-line) and VEGFR2-R1032Q (continuous red-line).

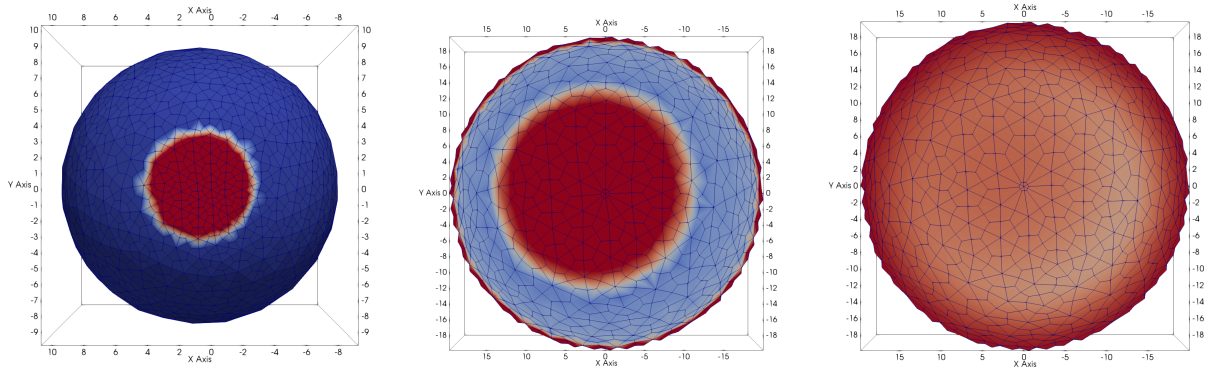

(a) $t = 300\,\mathrm{s}$ (b) $t = 600\,\mathrm{s}$ (c) $t = 7200\,\mathrm{s}$

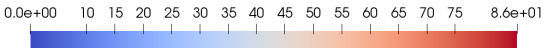

(d) Legend

Figure 7.29: Basal distribution of the whole WT-species of complexes (mobile and immobilized) upon completion of adhesion stage (a), spreading stage (b), and at the end of the experimental time-span (d).

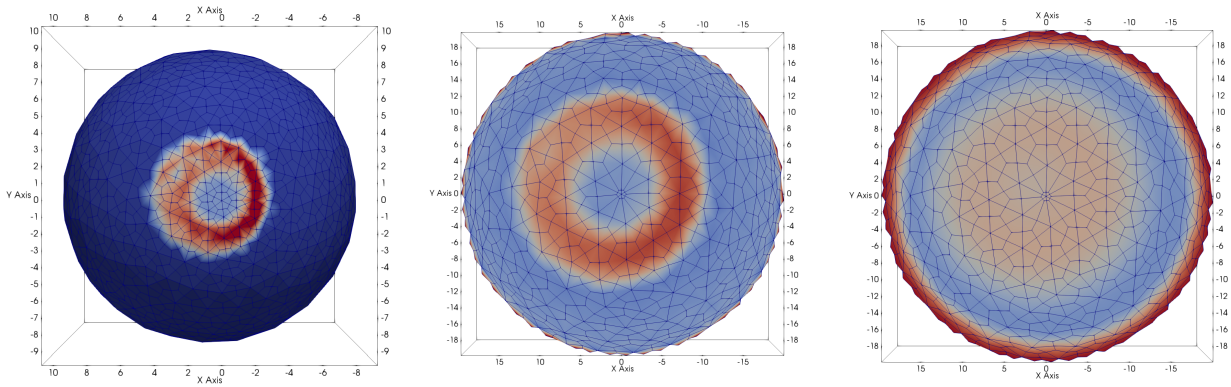

(a) $t = 300\,\mathrm{s}$ (b) $t = 600\,\mathrm{s}$ (c) $t = 7200\,\mathrm{s}$

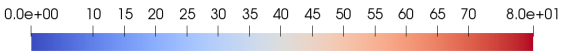

(d) Legend

Figure 7.30: Basal distribution of the whole R1032Q-species of complexes (mobile and immobilized) upon completion of adhesion stage (a), spreading stage (b), and at the end of the experimental time-span (d).

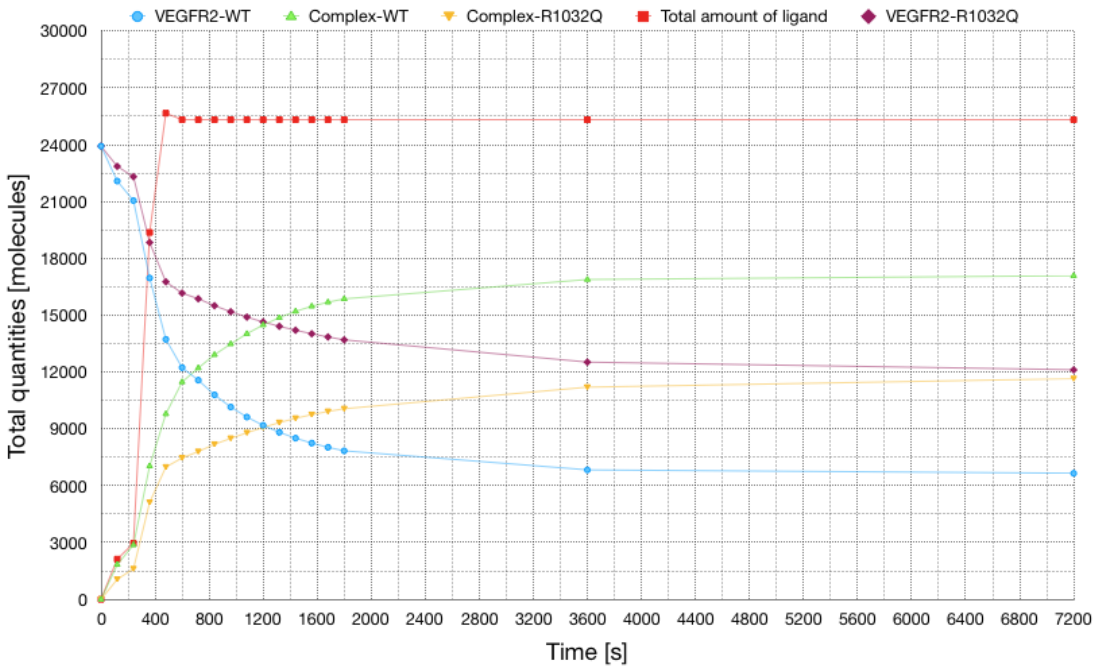

Figure 7.31: Time evolution of the total amount of molecules of receptors VEGFR2-WT and VEGFR2-R1032Q (mobile plus immobilized), complexes WT and R1032Q (mobile plus immobilized), free-ligands, and the complete amount of ligands (free plus bound) when $S_L = 90\, molecules/\mu m^2$.

Chapter 8

Large deformations framework to study integrin

Undoubtedly, integrin has a key role in the portrayal of angiogenic stimuli as well. Not just due to the fact that the mechanical deformation of EC is actively ruled by integrin itself (e.g. cellular adhesion and migration), but also because this receptor is pivotal in several processes characterizing VEGFR2 activities. In fact, with the aid of experimental evidence has been possible to observe how integrin acts as a co-receptor for VEGFR2, interplaying with the complex VEGFR2-gremlin, by prolonging and strengthening its intracellular signaling activity. Therefore, similarly to what we have shown the chapters 3.4 and 5, we provide some paradigmatic result describing the recruitment of integrin by fibrinogen during the mechanical spreading of an EC, and its interaction with VEGFR2.

Thereby, it seems clear how integrin corroborates angiogenesis by means of at least two distinctive chemical interactions, corresponding to as many configurational states of this protein, i.e. the bent-clasped (low affinity) and unbent-unclasped (high-affinity) conformation. Specifically, a low-affinity state is expressed when integrin work as a co-receptor inside the VEGFR2-gremlin-complex chemical interaction; whereas, the high-activity state is manifest by the integrin-linked to its own specific ligand. In light of all this, could be an important forward step in the mechanobiological characterization of the angiogenesis at the molecular level, extend and enrich the framework presented in sec. 6.2.3 with a model accounting for integrin and its chemical interplays with ligands and VEGFR2.

Basically, the aim of this section is to extend the work done under the "surrogated mechanics" hypothesis (see previous part of the thesis II), in the thermodynamics frame presented in the previous chapter (see chapter 6). Actually, these models could be interpreted as an intermedial step between the models presented in chapter 5 and a model in large deformation accounting of the active behavior of the cell. In fact, despite again we neglect the description of the active behavior of an EC, it is considered important to take an intermediate step throughout a simplified formulation, where the mechanical spreading of the cell is not coupled with the behavior of the adhesion molecules. Such an intermedial pattern could be essential to deal with a two-way coupling model among mechanical deformation of the nucleus and of the cytosol and receptor recruitment.

8.1 Integrin-fibrinogen interaction

Based on what we have presented in chapters 4 and 5 we approach to present formulation. It has to be clear that all the material parameters necessary to run the following in-silico analysis have been inherited by the above-mentioned works in the previous part of the thesis. Except for the evaluation of the concentration of the ligands available on the substrate, which will be inherited here from the estimates made in the previous chapter, and the assessment of $c^0_{I_R}$. In fact, similarly to what has happened in the former chapter 7 for the initial concentration of VEGFR2, the initial distribution of integrin on the cell membrane is assumed to equal to $c^0_{I_R} = 5.0134\, molecules/\mu m^2$ owing to an initial EC radius equivalent to 10 μm.

Following, we present the governing equations for a model of relocation and reaction of integrin on a lipid membrane that advects.

$$\underbrace{\text{Integrin}}_{I} + \underbrace{\text{Fibrinogen}}_{L_I} \underset{k_b}{\overset{k_f}{\leftrightarrows}} \text{C}_3 \,, \tag{8.1}$$

$$\frac{\partial c_{I_R}}{\partial t} + \text{Div}_{\mathcal{P}_R}\left[\vec{h}_{I_R}\right] + \frac{\partial c_{C_{3R}}}{\partial t} = 0 \,, \tag{8.2a}$$

$$\frac{\partial c_{L_{IR}}}{\partial t} + \frac{\partial c_{C_{3R}}}{\partial t} = s_{L_I} \,, \tag{8.2b}$$

$$[c_{C_{3R}}] = \frac{[c_{IR}]\,[c_{L_{IR}}]}{\alpha_{3R}} \,. \tag{8.2c}$$

Table 8.1: Co-designing between integrin-fluorescence intensity (in-vitro experiments) and the number of complexes generating on the cell membrane (in-silico simulation). Specifically, both the total that dimensionless quantities are tabulated.

Time	FRAP	Error bars	Complex	Adimensional Complex	Adimensional FRAP	Adimensional error bars
0	2.0200	10.3196	0.0000	0.0000	-	-
120	7.0275	11.8379	964.1132	0.1638	0.1172	0.1973
240	17.7100	14.9573	1614.5588	0.2743	0.2952	0.2494
360	20.8125	15.7440	2839.3696	0.4823	0.3470	0.2625
480	26.7050	18.4065	3894.0804	0.6615	0.4452	0.3069
600	37.5350	20.3823	4273.8683	0.7260	0.6257	0.3398
720	45.0000	22.2337	4541.5755	0.7714	0.7502	0.3707
840	48.5450	22.8354	4912.7127	0.8345	0.8093	0.3807
960	52.2100	24.0112	5251.4787	0.8920	0.8704	0.4003
1080	55.4000	24.6039	5478.0027	0.9305	0.9236	0.4102
1200	59.3875	26.0124	5626.4698	0.9557	0.9900	0.4336
1320	58.8700	25.5831	5720.0712	0.9716	0.9814	0.4265
1440	57.7225	24.5200	5781.8527	0.9821	0.9623	0.4088
1560	62.0475	25.5762	5826.8514	0.9898	1.0344	0.4264
1680	58.6325	24.3768	5860.9471	0.9956	0.9775	0.4064
1800	59.9850	24.7566	5887.1109	1.0000	1.0000	0.4127
3600	189.6127	53.7018	5997.5924	1.0188	3.1610	0.8953
7200	109.8590	36.9739	6065.9361	1.0304	1.8314	0.6164

Again, as shown in chapter 5, we can observe how the numerical outcomes result to be different with respect to the experimental ones after time $t = 1800\ s$. We infer that a so peculiar behavior is correlated to the mechanism of externalization of integrin on the cell membrane through vesicles invaginated under the lipid bilayer. Particularly, in these vesicles, integrins are preformed and so available to be active once exposed on the membrane.
Although in the current formulation we have neglected any kind of receptors internalization/externalization phenomena, it is in our ability to quantify how many integrin molecules are missing in order to align the numerical data with the experimental ones. In particular, it is trivial to compute (see Table 8.1) that at $t = 3600\ s$ the number of integrins foresaw by the in-vitro experiment is approximately 3.1 times of the in-silico one, and at $t = 7200\ s$ about 1.8 times.

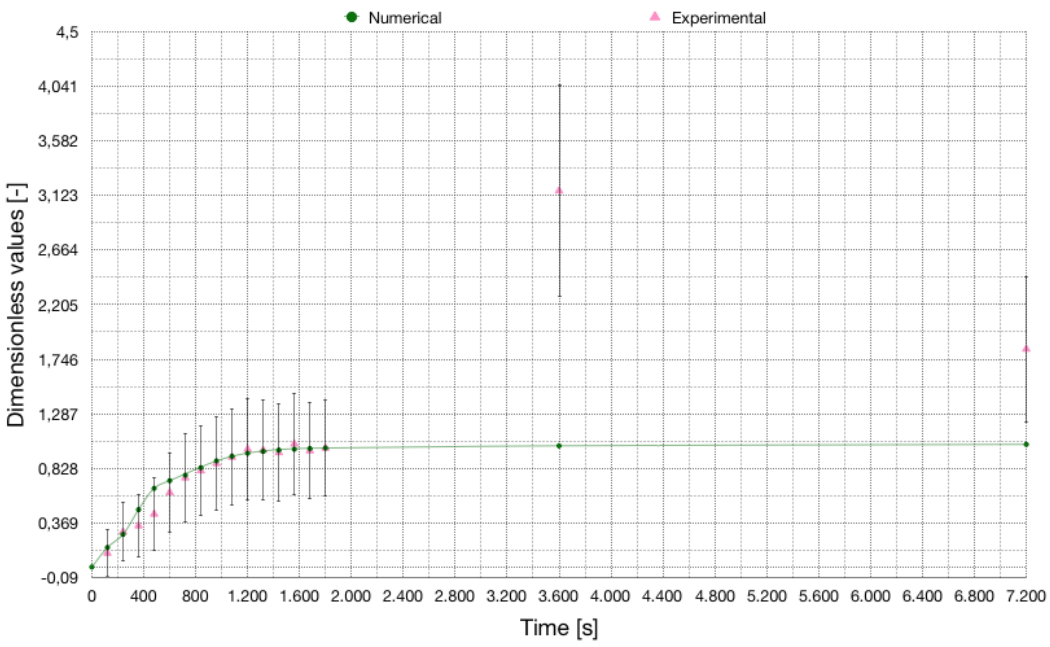

Figure 8.1: Numerical (continuous line) and experimental (dots with error bars) outcomes. Evolution in time of the normalized total amount of complexes.

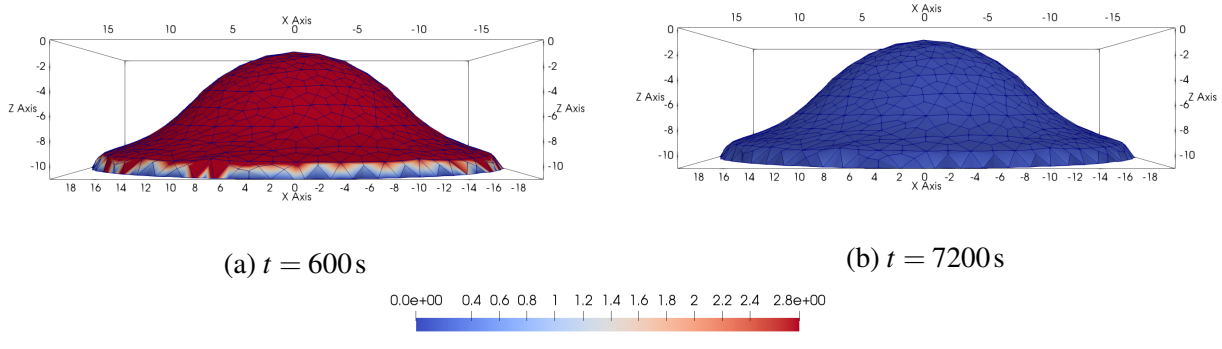

(a) $t = 600\,\mathrm{s}$

(b) $t = 7200\,\mathrm{s}$

(c) Legend

Figure 8.2: Diffusion of integrin after the spreading phase has been completed.

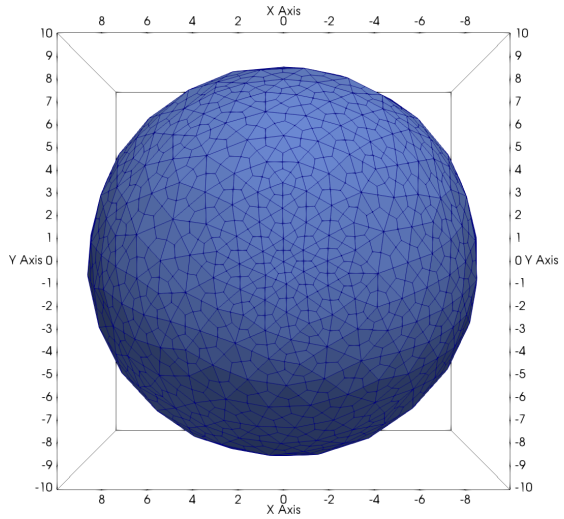

(a) $t = 0\,\mathrm{s}$

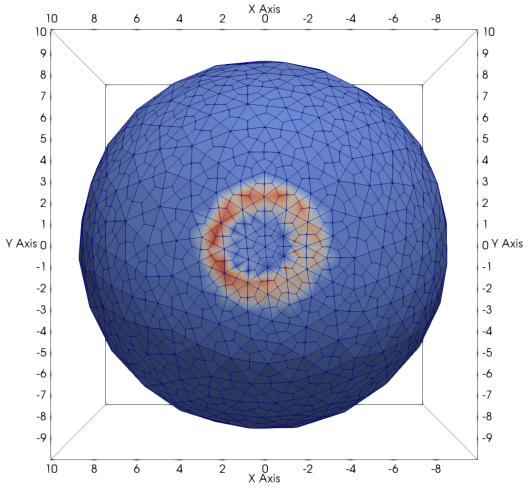

(b) $t = 120\,\mathrm{s}$

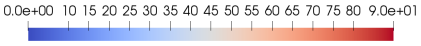

(c) Legend

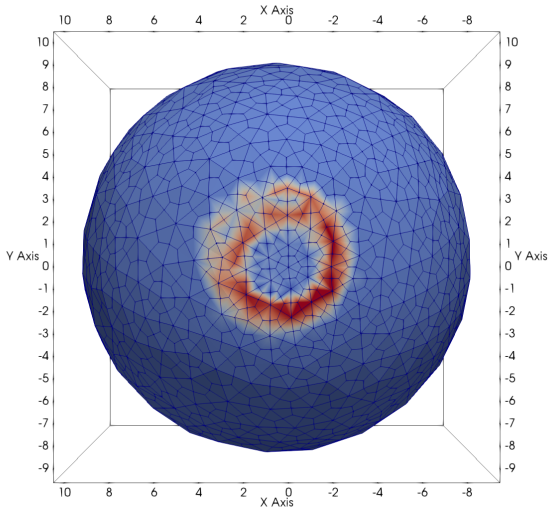

(d) $t = 240\,\mathrm{s}$

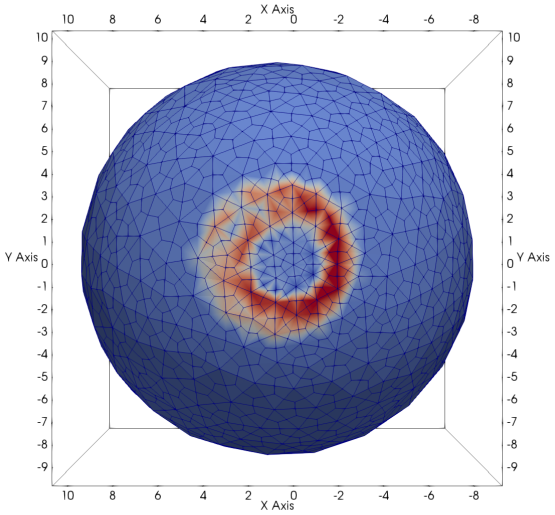

(e) $t = 300\,\mathrm{s}$

Figure 8.3: Basal distribution of complexes during the adhesion stage.

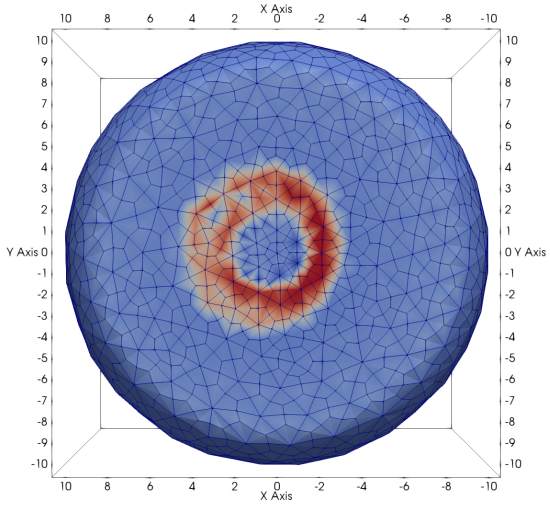

(a) $t = 360\,\mathrm{s}$

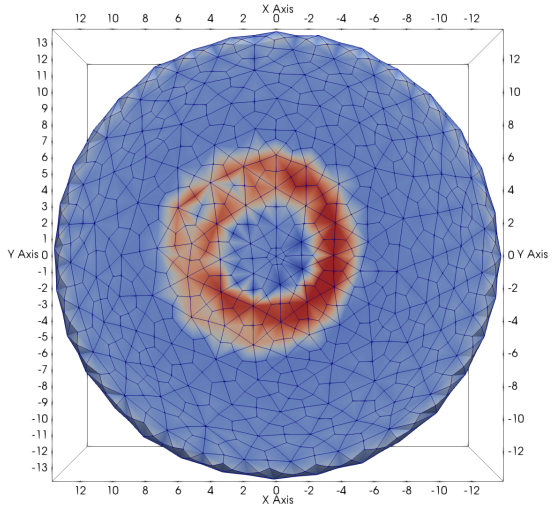

(b) $t = 480\,\mathrm{s}$

(c) Legend

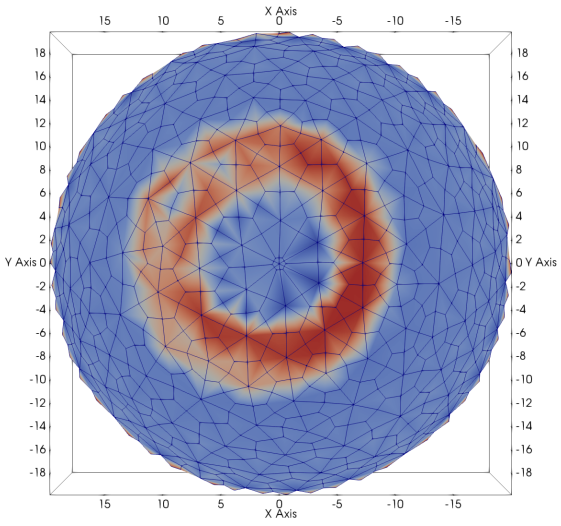

(d) $t = 600\,\mathrm{s}$

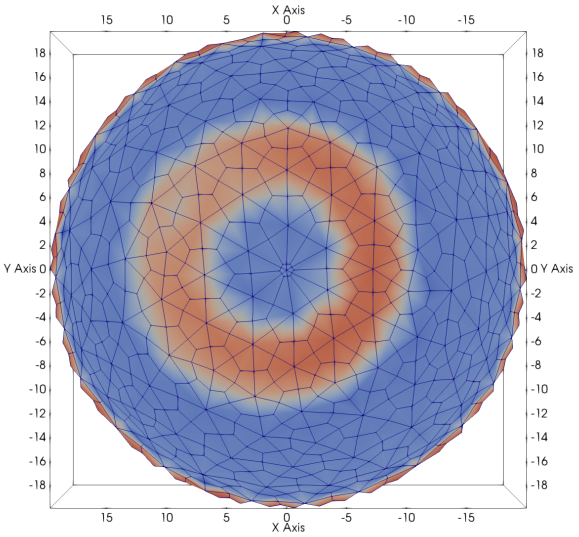

(e) $t = 7200\,\mathrm{s}$

Figure 8.4: Basal distribution of complexes during spreading stage (a)-(c) and at the end of the experimental time-span (d).

It is interesting to highlight how the low availability of integrin on the cell membrane with respect to the accessible fibrinogen (equal to gremlin - 90 molecules/μm^2- owing to the experimental consideration made in chapters 4 and 5) in touch with the basal side of the EC, provides the formation of two "coffee rings". The first one around the cell-substrate contact limit zone defined during the adhesion phase (see Fig. 8.3). The second one, likewise the previous one but at the end of the receptor diffusion stage (see Fig. 8.4), around the extreme contact zone between fibrinogen and lipid bilayer. Such a scenario was not capturable in the "surrogated mechanics" framework due to the fact that the mechanical spreading of the cell was defined by means of a uniform source of ligands in the fibrinogen mass balance equation. Hence, the first implication of this choice is a uniform mechanical spreading of the cell between $t = 0\ s$ and $t = 600\ s$. Instead, with the aid of the current formulation, we understand that this phase is at least characterized by two distinct behavior: adhesion (until $t = 300\ s$) and mechanical spreading (until $t = 600\ s$).

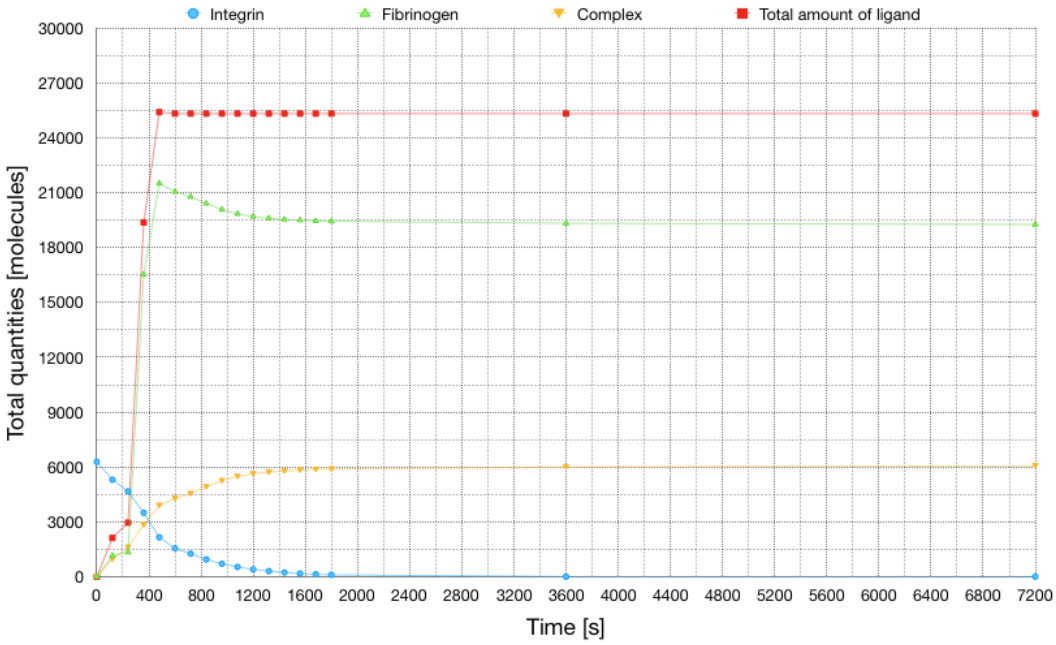

Figure 8.5: Time evolution of the total amount of molecules of integrin, complexes, free-ligands, and the complete amount of fibrinogen (free plus bound) when $S_{L_I} = 90\ molecules/\mu m^2$.

8.2 Integrin as a co-receptor for VEGFR2

As shown in section 5.2.5 is reasonable, from a biological point of view, to particularise our patterns at the cases in which integrin works like a co-receptor for VEGFR2. Therefore, the following, are the governing equations:

$$1)\quad V + L_V \underset{k_b^1}{\overset{k_f^1}{\leftrightarrows}} C_1\,, \tag{8.3a}$$

$$2)\quad C_1 + I \underset{k_b^2}{\overset{k_f^2}{\leftrightarrows}} \underbrace{C_1 I_l}_{C_2}\,, \tag{8.3b}$$

$$\frac{\partial c_{V_R}}{\partial t} + \mathrm{Div}_{\mathcal{P}_R}\left[\vec{h}_{V_R}\right] + \frac{\partial c_{C_{1R}}}{\partial t} + \frac{\partial c_{C_{2R}}}{\partial t} = 0\,, \tag{8.4a}$$

$$\frac{\partial c_{L_{VR}}}{\partial t} + \frac{\partial c_{C_{1R}}}{\partial t} + \frac{\partial c_{C_{2R}}}{\partial t} = s_{L_{VR}}\,, \tag{8.4b}$$

$$\frac{\partial c_{I_R}}{\partial t} + \mathrm{Div}_{\mathcal{P}_R}\left[\vec{h}_{I_R}\right] + \frac{\partial c_{C_{2R}}}{\partial t} = 0\,, \tag{8.4c}$$

$$c_{C_{1R}} = \frac{c_{V_R} c_{L_{VR}}}{\alpha_{1R}}\,, \tag{8.4d}$$

$$c_{C_{2R}} = \frac{c_{C_{1R}} c_{I_R}}{\alpha_{2R}}\,. \tag{8.4e}$$

The current simulation presents an amount of available gremlin equal to 80 $molecules/\mu m^2$, i.e. a small quantity compared to the 90 $molecules/\mu m^2$ so far used. Such a choice is due to our actual computational capacity. In fact, the intricate chemical interaction between integrin and VEGFR2 leads to a quick increment of the rate of depletion of the TKR-receptor with respect to what has been observed in the model with a single chemical reaction (see chapter 7). Consequently, a thickened of the tesselation shown by Fig. 7.6 is necessary to catch the correct results in presence of a ligands availability greater than 80 $molecules/\mu m^2$. Unfortunately, such a process, that has been already embedded in our codes through suitable re-mesh algorithms, implies a computational processing power improvement that nowadays we are not able to perform.

Likewise, integrin manifests an analogous rate erosion increase in a three couple chemical reactions pattern, as shown in section 5.2.6. For this reason, it is considered appropriate to provide, throughout section 8.3, the governing equations and some qualitative images depicted the outcomes, that define such a kind of formulation.

Table 8.2: Co-designing between integrin and VEGFR2 fluorescence intensity (in-vitro experiments) and the number of complexes generating on the cell membrane (in-silico simulation). Specifically, the total quantities are tabulated.

Time	FRAP VEGFR2	Error bars VEGFR2	FRAP integrin	Error bars integrin	C_2	C_1
0	1.8125	1.7470	2.0700	1.3727	0.0000	0.0000
120	2.6775	1.7774	2.1825	1.4993	942.0184	1897.2510
240	3.6175	2.0371	2.5650	1.3584	1555.5455	2632.4123
360	8.8875	4.5427	2.9550	1.4014	2785.3904	7938.8907
480	12.0225	5.1638	3.0775	1.5473	3733.3365	11835.3442
600	17.4375	4.0251	3.8900	1.7371	4614.0879	14477.7023
720	20.1325	4.3776	4.4750	1.6674	4777.5579	15026.1888
840	19.6650	4.4217	5.3775	1.5673	5111.3756	16163.8470
960	20.4075	4.5417	5.9175	1.9579	5352.7382	16992.9887
1080	22.8600	4.7168	6.6400	2.3900	5541.7365	17788.7539
1200	23.0375	5.5135	6.9850	1.9568	5679.8520	18464.4720
1320	23.2725	4.8333	7.8000	2.0404	5776.0682	18977.5215
1440	24.9150	5.5791	7.6800	2.4520	5850.7933	19438.8217
1560	25.8650	4.7980	8.4550	1.9578	5909.1244	19849.0170
1680	27.8800	6.0900	8.8375	2.0512	5955.1153	20201.5272
1800	26.9075	5.9243	9.0225	2.5968	5991.0090	20501.0436
3600	39.2718	18.8742	57.3603	12.2651	6142.8328	21829.7037
7200	36.8140	17.3697	55.5292	10.0477	6177.6460	21842.4365

Similarly to what is shown in section 5.2.5, the total amount of fluorescence of VEGFR2 is connected with the global number of C_1 (bound or not bound with C_2), inasmuch as experimentally it has been possible to visualize time-lapse the fluorescence connected to every single molecule both of VEGFR2 and integrin. Contextually, the fluorescence of integrin is correlated only with C_2.

Table 8.3: Co-designing between integrin and VEGFR2 fluorescence intensity (in-vitro experiments) and the number of complexes generating on the cell membrane (in-silico simulation). Specifically, the dimensionless quantities are tabulated.

Time	Adimensional C_2	Adimensional C_1	Adimensional VEGFR2	Adimensional error bars VEGFR2	Adimensional integrin	Adimensional error bars integrin
0	0.0000	0.0000	-	-	-	-
120	0.0459	0.0925	0.0995	0.0661	0.0811	0.0557
240	0.0759	0.1284	0.1344	0.0757	0.0953	0.0505
360	0.1359	0.3872	0.3303	0.1688	0.1098	0.0521
480	0.1821	0.5773	0.4468	0.1919	0.1144	0.0575
600	0.2251	0.7062	0.6481	0.1496	0.1446	0.0646
720	0.2330	0.7329	0.7482	0.1627	0.1663	0.0620
840	0.2493	0.7884	0.7308	0.1643	0.1999	0.0582
960	0.2611	0.8289	0.7584	0.1688	0.2199	0.0728
1080	0.2703	0.8677	0.8496	0.1753	0.2468	0.0888
1200	0.2771	0.9007	0.8562	0.2049	0.2596	0.0727
1320	0.2817	0.9257	0.8649	0.1796	0.2899	0.0758
1440	0.2854	0.9482	0.9260	0.2073	0.2854	0.0911
1560	0.2882	0.9682	0.9613	0.1783	0.3142	0.0728
1680	0.2905	0.9854	1.0361	0.2263	0.3284	0.0762
1800	0.2922	1.0000	1.0000	0.2202	0.3353	0.0965
3600	0.2996	1.0648	1.4595	0.7014	2.1318	0.4558
7200	0.3013	1.0654	1.3682	0.6455	2.0637	0.3734

Analyzing Fig. 8.6, we denote the very same trend observed in section 5.2.5, namely, integrin does not appropriately match the numerical results, manifesting a discrepancy among in-vitro and in-silico outcomes. Particularly, at time $t = 3600\ s$ and $t = 7200\ s$, the numerical complexes $C2$ in contact with the basal side of the cell are about 7.11 and 6.85 times less than the correspondent experimental data (see Tab. 8.2 and 8.3). Once again we find a similar qualitative trend to the results of the analyzes analogous to the surrogated mechanics framework. In fact, these results are considerably higher than the corresponding observed for the model integrin-fibrinogen in the previous section. Currently, we think that the reason for this peculiar tendency is correlated to the integrins clustering phenomenon inside FAs. Specifically, in the adhesion sites (FAs), integrins are recruited in their active configuration forming, together with other proteins, cluster molecules that are necessary to the mechanical signaling transduction among the cell and its own extracellular microenvironment. Such localization of integrin could affect the fluorescence perceived, and so underestimate the experimental results. This is a crucial point in the mechanical description of an EC, and a mathematical formulation able to take into account these behaviors (e.g. [121]) can point to specific biological experiments capable to interpret these phenomena.

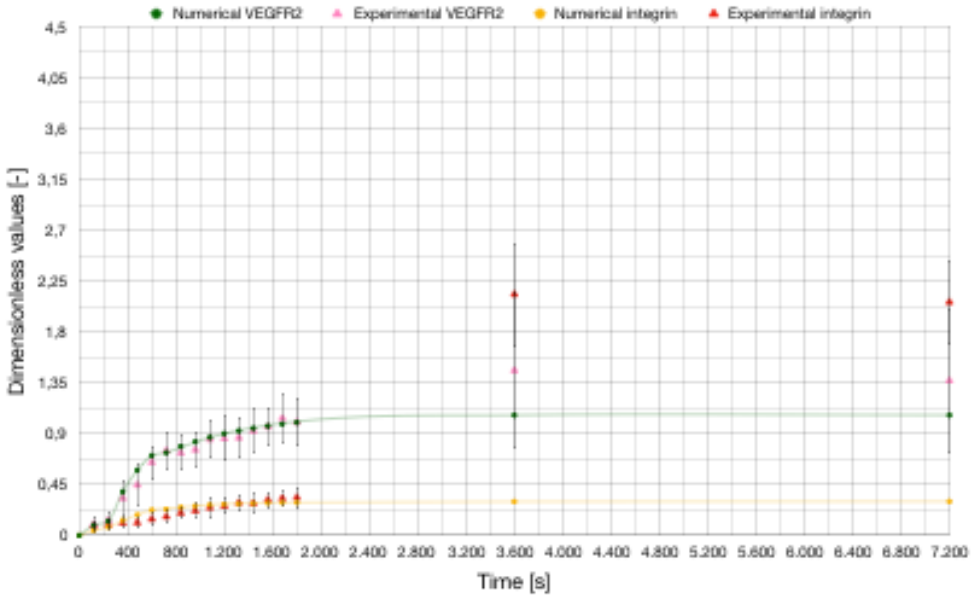

Figure 8.6: Numerical (continuous line) and experimental (dots with error bars) outcomes. Evolution in time of the normalized total amount of complexes.

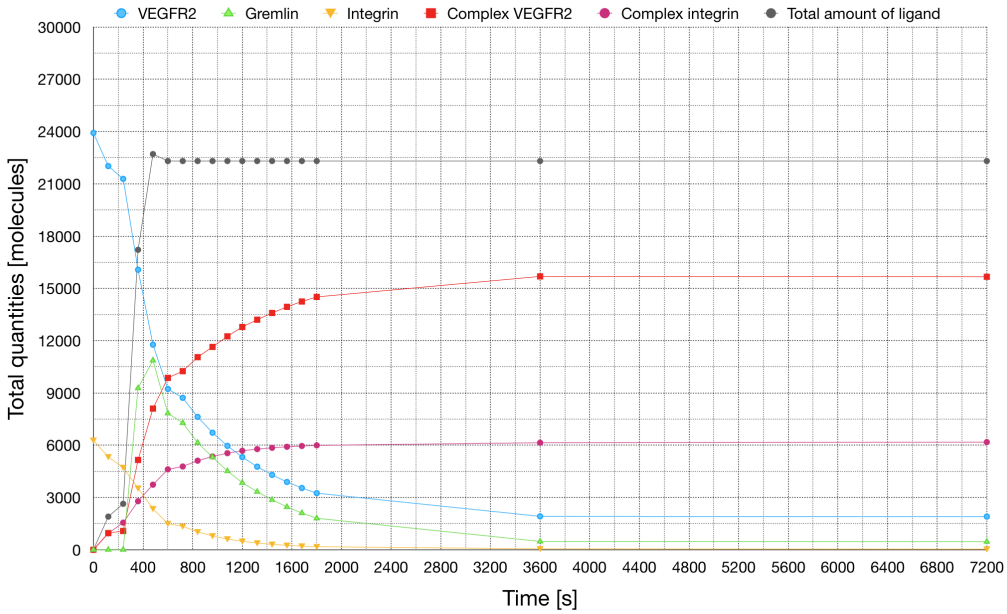

Figure 8.7: Time evolution of the total amount of molecules of receptors (VEGFR2 and integrin), complexes (C_1 and C_2), free-ligands, and the complete amount of gremlin (free plus bound) when $S_L = 80\ molecules/\mu m^2$.

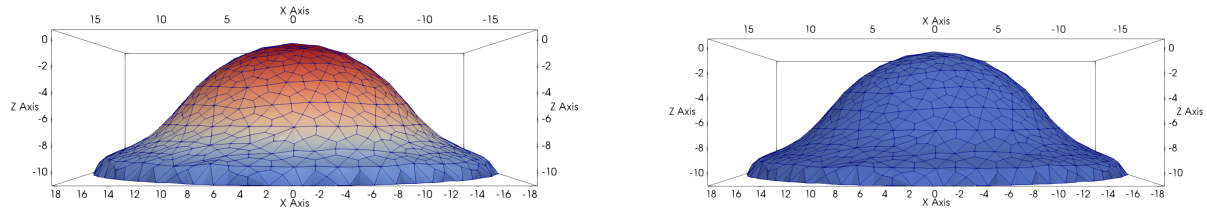

(a) $t = 600\,\mathrm{s}$ (b) $t = 7200\,\mathrm{s}$

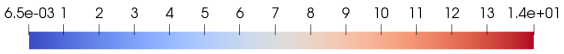

(c) Legend

Figure 8.8: Diffusion of VEGFR2 after the spreading phase has been completed.

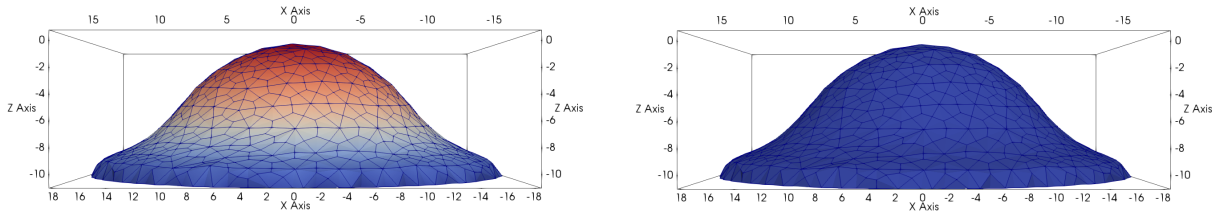

(a) $t = 600\,\mathrm{s}$ (b) $t = 7200\,\mathrm{s}$

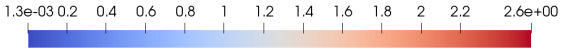

(c) Legend

Figure 8.9: Diffusion of integrin after the spreading phase has been completed.

Moreover, it is interesting to point out, by means the Fig. 8.10, 8.11, 8.12, and 8.13, how the evolution in time of C_1 and C_2 complexes are totally complemental.

If we take the images 8.11e and 8.13e as a comparative example, it is possible to see how, here, the areas with a higher concentration of complexes (darker red) and those with less (darker blue), are totally supplementary to each other, namely, the major concentration of C_1 happens where we have fewer molecules of C_2, and vice-versa.

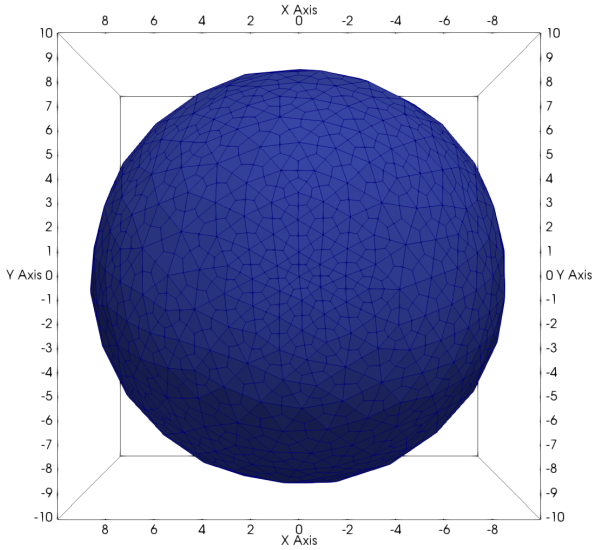

(a) $t = 0\,\mathrm{s}$

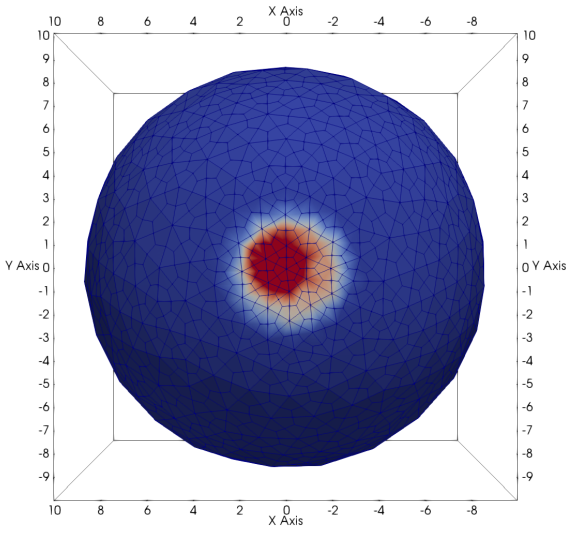

(b) $t = 120\,\mathrm{s}$

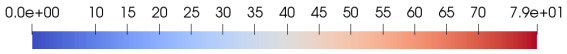

(c) Legend

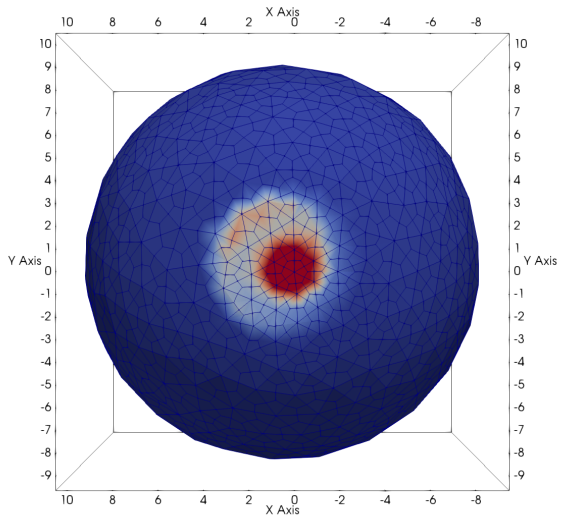

(d) $t = 240\,\mathrm{s}$

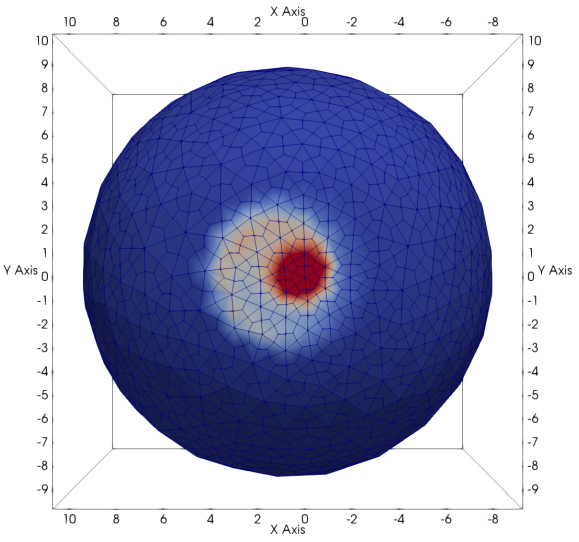

(e) $t = 300\,\mathrm{s}$

Figure 8.10: Basal distribution of complexes C_1 during the adhesion stage.

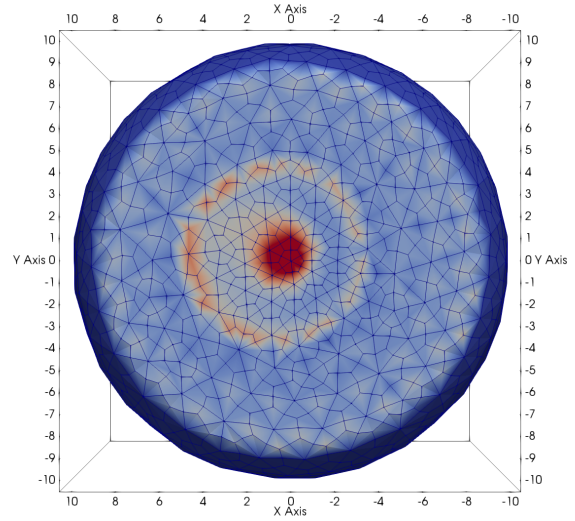

(a) $t = 360\,\mathrm{s}$

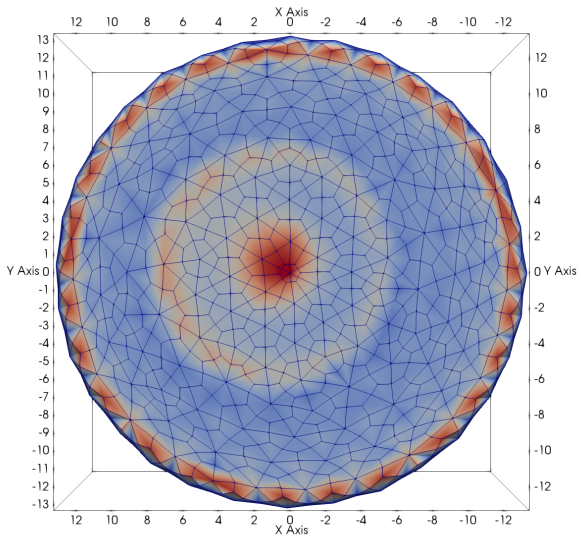

(b) $t = 480\,\mathrm{s}$

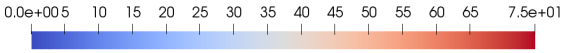

(c) Legend

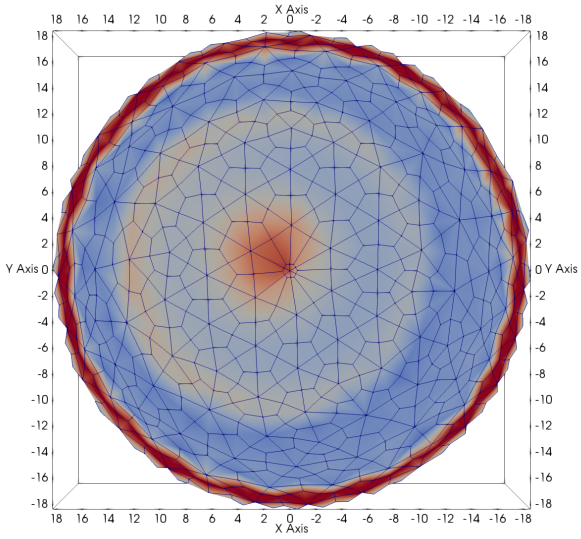

(d) $t = 600\,\mathrm{s}$

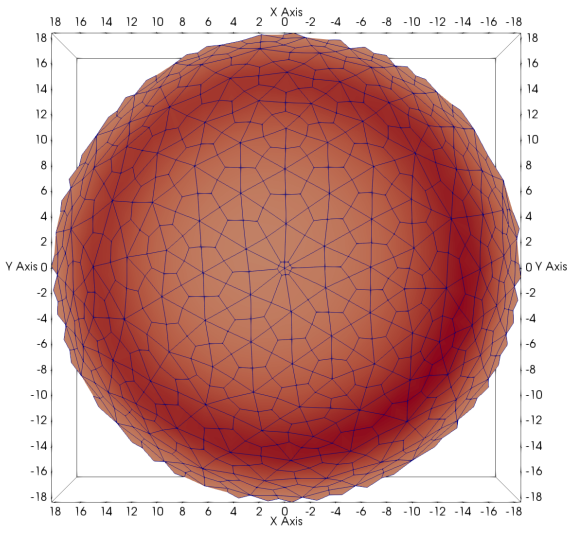

(e) $t = 7200\,\mathrm{s}$

Figure 8.11: Basal distribution of complexes C_1 during spreading stage (a)-(c) and at the end of the experimental time-span (d).

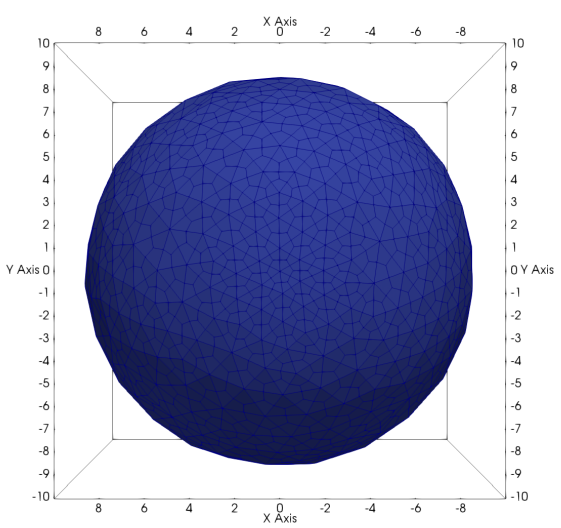

(a) $t = 0\,\mathrm{s}$

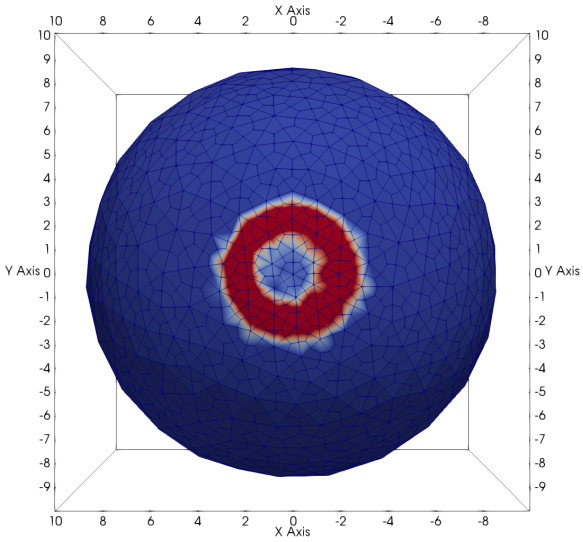

(b) $t = 120\,\mathrm{s}$

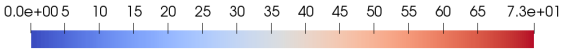

(c) Legend

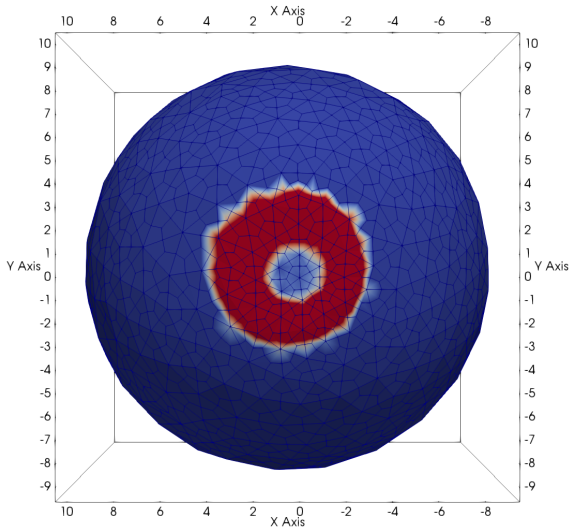

(d) $t = 240\,\mathrm{s}$

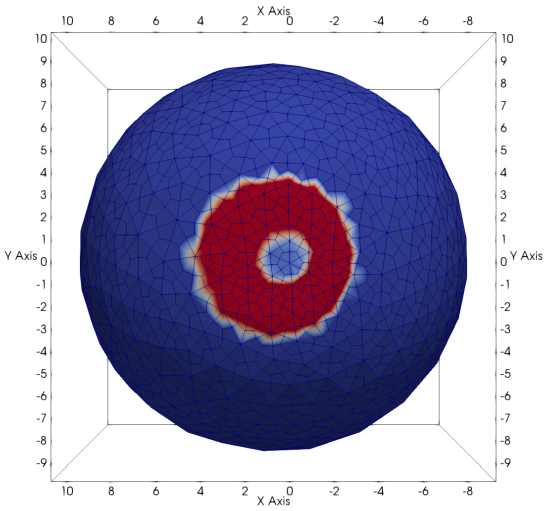

(e) $t = 300\,\mathrm{s}$

Figure 8.12: Basal distribution of complexes C_2 during the adhesion stage.

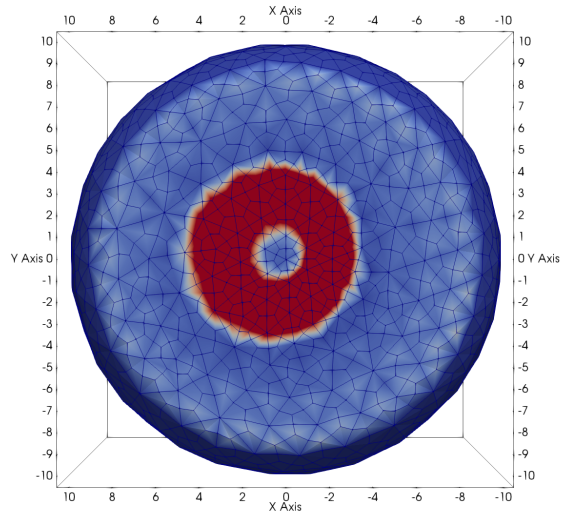

(a) $t = 360\,\mathrm{s}$

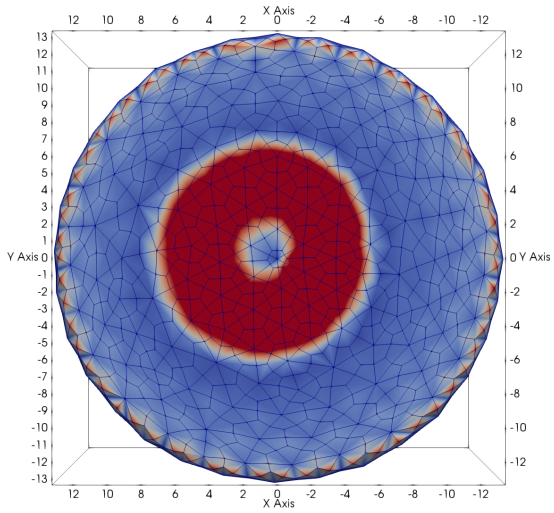

(b) $t = 480\,\mathrm{s}$

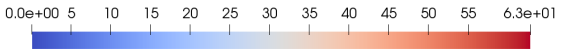

(c) Legend

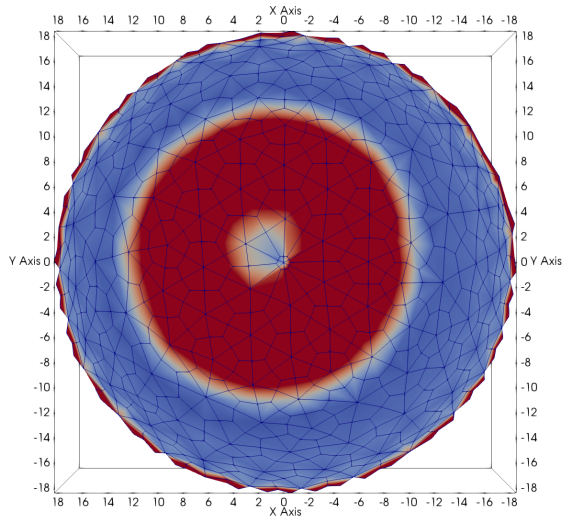

(d) $t = 600\,\mathrm{s}$

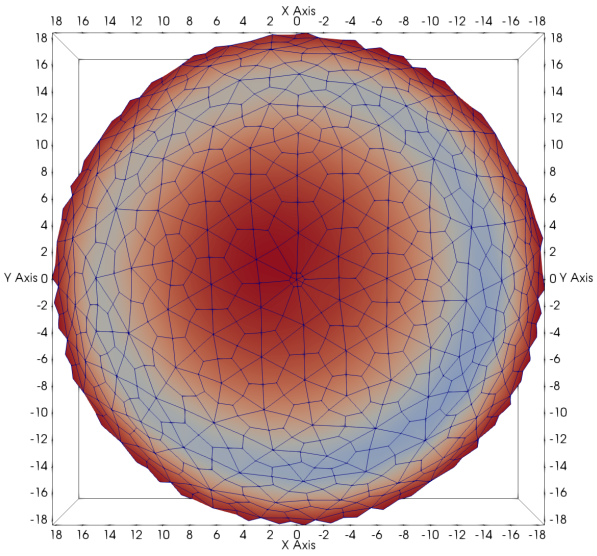

(e) $t = 7200\,\mathrm{s}$

Figure 8.13: Basal distribution of complexes C_2 during spreading stage (a)-(c) and at the end of the experimental time-span (d).

8.3 Formulation with three chemical reactions

The ability of VEGFR-2 to participate in a complex with integrin is well known, the close correlation between their activation and the multiphysical phenomena regulating EC dynamics remains still very restricted.
Here, we model either the VEGFR-2 membrane dynamics and that for integrin as well, by a multiphysics model, to identify how gremlin and fibrinogen stimulations induce the polarization of receptors in cell protrusions and in the basal aspect of ECs plated on a ligands-enriched ECM.

$$1)\quad V + L_V \underset{k_b^1}{\overset{k_f^1}{\leftrightarrows}} C_1\,, \tag{8.5a}$$

$$2)\quad C_1 + I \underset{k_b^2}{\overset{k_f^2}{\leftrightarrows}} \underbrace{C_1 I_l}_{C_2}\,, \tag{8.5b}$$

$$3)\quad I + L_I \underset{k_b^3}{\overset{k_f^3}{\leftrightarrows}} \underbrace{I_h L_I}_{C_3}\,. \tag{8.5c}$$

$$\frac{\partial c_{V_R}}{\partial t} + \mathrm{Div}_{\mathcal{P}_R}\left[\vec{h}_{V_R}\right] + w_R^{(8.5a)} = 0\,, \tag{8.6a}$$

$$\frac{\partial c_{L_{VR}}}{\partial t} + w_R^{(8.5a)} = s_{L_{VR}}\,, \tag{8.6b}$$

$$\frac{\partial c_{I_R}}{\partial t} + \mathrm{Div}_{\mathcal{P}_R}\left[\vec{h}_{I_R}\right] + w_R^{(8.5b)} + w_R^{(8.5c)} = 0\,, \tag{8.6c}$$

$$\frac{\partial c_{L_{IR}}}{\partial t} + w_R^{(8.5c)} = s_{L_{IR}}\,, \tag{8.6d}$$

$$\frac{\partial c_{C_{1R}}}{\partial t} + w_R^{(8.5b)} = w_R^{(8.5a)}\,, \tag{8.6e}$$

$$\frac{\partial c_{C_{2R}}}{\partial t} = w_R^{(8.5b)}\,, \tag{8.6f}$$

$$\frac{\partial c_{C_{3R}}}{\partial t} = w_R^{(8.5c)}\,. \tag{8.6g}$$

Experimental evidence shows that the time span required to reach chemical equilibrium is orders of magnitude less than the time scales necessary to reach mechanical and diffusive equilibrium. Accordingly, the infinitely fast kinetics hypothesis is assumed valid for each of the chemical interactions depicted by the expressions (8.5), leading to the subsequent relations:

$$c_{C_{1R}} = \frac{c_{V_R} c_{L_{VR}}}{\alpha_{1R}} \tag{8.7a}$$

$$c_{C_{2R}} = \frac{c_{C_{1R}} c_{I_R}}{\alpha_{2R}} \tag{8.7b}$$

$$c_{C_{3R}} = \frac{c_{I_R} c_{L_{IR}}}{\alpha_{3R}} \tag{8.7c}$$

Finally, substituting the expressions (8.6e), (8.6f), and (8.6g) in the remaining equations of (8.6), we build the set of Eqs. (8.8) that jointly with Eqs. (8.7) denote the governing equations for the current model.

$$\frac{\partial c_{V_R}}{\partial t} + \mathrm{Div}_{\mathcal{P}_R}\left[\vec{h}_{V_R}\right] + \frac{\partial c_{C_{1R}}}{\partial t} + \frac{\partial c_{C_{2R}}}{\partial t} = 0\,, \tag{8.8a}$$

$$\frac{\partial c_{L_{VR}}}{\partial t} + \frac{\partial c_{C_{1R}}}{\partial t} + \frac{\partial c_{C_{2R}}}{\partial t} = s_{L_{VR}}\,, \tag{8.8b}$$

$$\frac{\partial c_{I_R}}{\partial t} + \mathrm{Div}_{\mathcal{P}_R}\left[\vec{h}_{I_R}\right] + \frac{\partial c_{C_{2R}}}{\partial t} + \frac{\partial c_{C_{3R}}}{\partial t} = 0\,, \tag{8.8c}$$

$$\frac{\partial c_{L_{IR}}}{\partial t} + \frac{\partial c_{C_{3R}}}{\partial t} = s_{L_{IR}}\,. \tag{8.8d}$$

where the model parameters necessary to solve the eq. (8.8) and (8.7), are deducible from chapters 4 and 5. Nevertheless, the initial concentration of VEGFR2 (about 24000 $molecules$) and integrin (about 6300 $molecules$) are computed with respect to the surface of a spherical and in suspension cell with a radius equal to 10 μm.
Due to excessive computational burden, we can follow show qualitative results (see Fig. 8.14) on the current formulations. Therefore, we postpone any discussion on quantitative outcomes when we will dispose of greater computing power.
Although the spatial distribution of the complexes depicted in Fig. 8.14 does contemplate an amount of gremlin and fibrinogen available in the substrate considerably lower than the above deduce, 35 $molecules/\mu m^2$ and 35 $molecules/\mu m^2$, respectively, several interesting information is deducible. Interesting, are the complementary arrangements of C_1 and C_2 complexes (see Fig. 8.14a and 8.14b), where the zones with higher (red-colors) concentrations of the former correspond to lower (blue-colors) concentrations of the latter, and vice-versa. Moreover, due to the multiple participations of integrins in two chemical reactions and their low availability on the membrane, we observe that at the end of the adhesion phase (see Fig. 8.14c), the distribution of C_3 concentration is not homogeneous on the contact area between cell-substrate. Finally, all three spatial distributions manifest the generations of "coffee-rings" (see Fig. 8.14d, 8.14e, and 8.14f, and Fig. 8.14g, 8.14h, and 8.14i) on the edge of the cell-substrate contact surface.

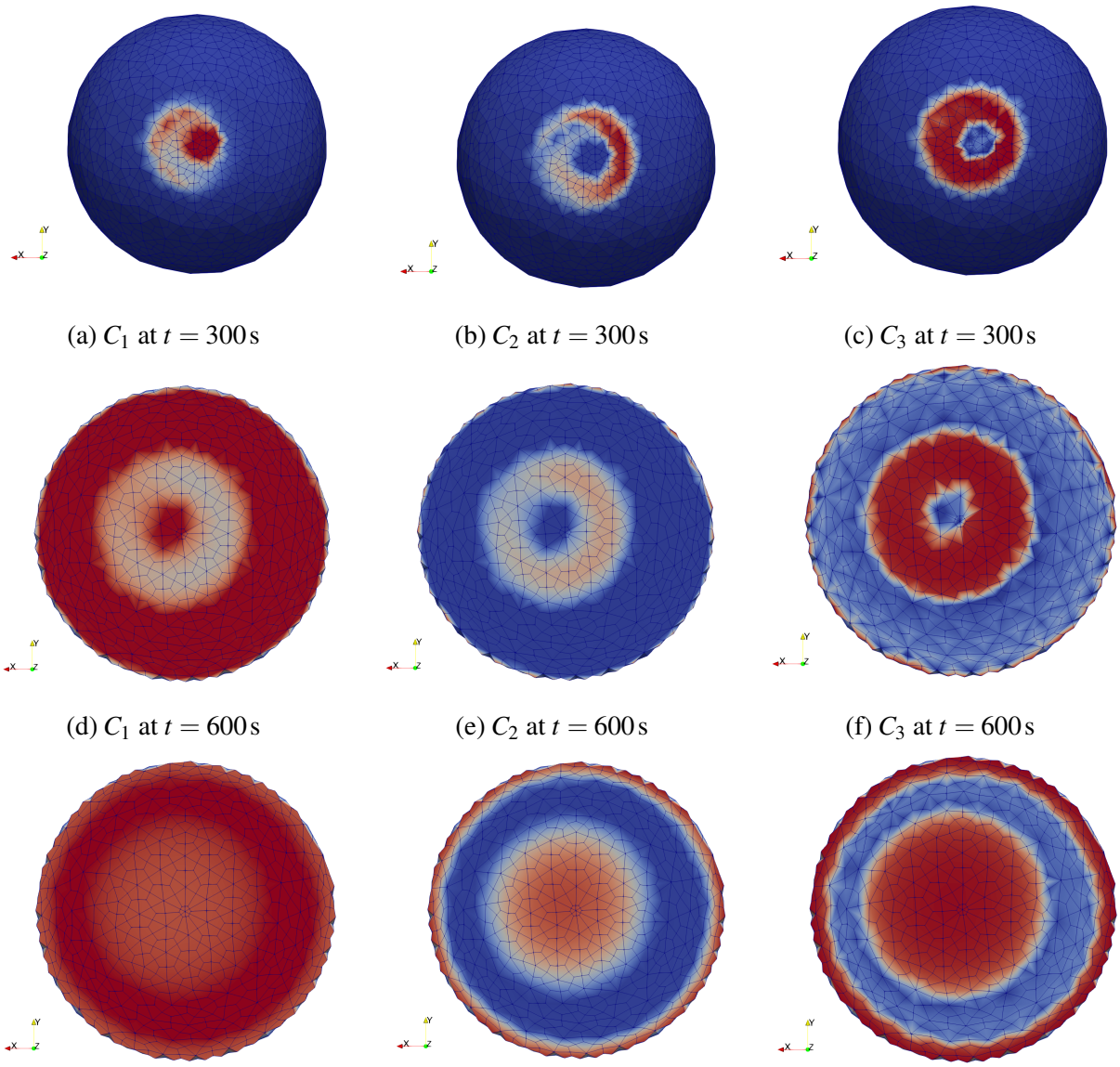

(a) C_1 at $t = 300\,\mathrm{s}$ (b) C_2 at $t = 300\,\mathrm{s}$ (c) C_3 at $t = 300\,\mathrm{s}$

(d) C_1 at $t = 600\,\mathrm{s}$ (e) C_2 at $t = 600\,\mathrm{s}$ (f) C_3 at $t = 600\,\mathrm{s}$

(g) C_1 at $t = 7200\,\mathrm{s}$ (h) C_2 at $t = 7200\,\mathrm{s}$ (i) C_3 at $t = 7200\,\mathrm{s}$

Figure 8.14: Basal distribution of complexes C_1, C_2, and C_3 upon completion of adhesion stage (a),(b), and (c), spreading stage (d), (e), and (f), and diffusion stage (g),(h), and (i), respectively.

Appendix F

Demonstrations

F.1 Divergence theorem on $\mathcal{P}(t)$

The following outcome extends the divergence theorem to advecting membranes.

$$\int_{\mathcal{P}(t)} \mathrm{div}_{\mathcal{P}}\,[\,\vec{g}\,]\;\mathrm{d}a = \int_{\partial\mathcal{P}(t)} \vec{g}\cdot\vec{t}_{\perp}\,\mathrm{d}\ell\,. \tag{F.1}$$

Proof: - Taking advantage of the Frenet formulae one has:

$$\int_{\partial\mathcal{P}(t)} \vec{g}\cdot\vec{t}_{\perp}\,\mathrm{d}\ell = \int_{\partial\mathcal{P}(t)} \vec{g}\cdot\frac{\vec{t}_{\parallel}\times\vec{n}}{|\vec{n}|}\,\mathrm{d}\ell = \int_{\partial\mathcal{P}(t)} \frac{\vec{n}\times\vec{g}}{|\vec{n}|}\cdot\vec{t}_{\parallel}\,\mathrm{d}\ell\,.$$

In view of Stokes' theorem, the latter holds

$$\int_{\partial\mathcal{P}(t)} \frac{\vec{n}\times\vec{g}}{|\vec{n}|}\cdot\vec{t}_{\parallel}\,\mathrm{d}\ell = \int_{\mathcal{P}(t)} \mathrm{curl}\left[\,\frac{\vec{n}}{|\vec{n}|}\times\vec{g}\,\right]\cdot\frac{\vec{n}}{|\vec{n}|}\,\mathrm{d}a$$

and the thesis is proved in view of definition (6.3a).

F.2 The time derivative of the areal jacobian

We aim at proving the following identities.
It holds:

$$\frac{\mathrm{d}\,J\sqrt{\vec{n}_R\cdot\boldsymbol{C}^{-1}\vec{n}_R}}{\mathrm{d}t} = J\,|\vec{n}|\,\left(\mathrm{div}\,[\,\vec{v}_{adv}\,] - \frac{\vec{n}\cdot\boldsymbol{d}\vec{n}}{|\vec{n}|^2}\right)\,. \tag{F.2}$$

Proof: - It is well known that

$$\frac{\mathrm{d}\,J}{\mathrm{d}t} = J\,\mathrm{div}\,[\,\vec{v}_{adv}\,]$$

and straightforward to prove that

$$\frac{\mathrm{d}\,\boldsymbol{C}^{-1}}{\mathrm{d}t} = -\,\boldsymbol{F}^{-1}\,(2\,\boldsymbol{d})\,\boldsymbol{F}^{-T}\,.$$

By noting that

$$|\vec{n}| = \sqrt{\vec{n}_R \cdot \boldsymbol{C}^{-1}\vec{n}_R}\,,$$

assertion (F.2) immediately descends.
Defining a base $\mathbf{u},\mathbf{v},\mathbf{w}$ for the domain of $\mathbf{S}$ (where $\mathbf{S}$ is a second-order tensor), we can prove:

$$\det(\mathbf{S}) = \frac{[(\mathbf{Su})\times(\mathbf{Sv})]\cdot(\mathbf{Sw})}{[\mathbf{u}\times\mathbf{v}]\cdot\mathbf{w}}\,. \tag{F.3}$$

We know that the mixed product between the component of bases is correlated to the volume of the parallelepiped denoted by the own vectors. Let $L\mathbf{E}_1, L\mathbf{E}_2, L\mathbf{E}_3$ be the local base of a material point of the reference configuration and $L\mathbf{FE}_1, L\mathbf{FE}_2, L\mathbf{FE}_3$ the correspondent in the current one. We know that:

$$\begin{aligned} dV &= (L\mathbf{E}_1 \times L\mathbf{E}_2)\cdot L\mathbf{E}_3 = L^3\left[(\mathbf{E}_1\times\mathbf{E}_2)\cdot\mathbf{E}_3\right]\,,\\ dv &= (L\mathbf{FE}_1 \times L\mathbf{FE}_2)\cdot L\mathbf{FE}_3 = L^3\left[(\mathbf{FE}_1\times\mathbf{FE}_2)\cdot\mathbf{FE}_3\right]\,, \end{aligned} \tag{F.4}$$

therefore:

$$\begin{aligned} \frac{dv}{dV} = \frac{L^3\left[(\mathbf{E}_1\times\mathbf{E}_2)\cdot\mathbf{E}_3\right]}{L^3\left[(\mathbf{FE}_1\times\mathbf{FE}_2)\cdot\mathbf{FE}_3\right]} = \frac{\left[(\mathbf{E}_1\times\mathbf{E}_2)\cdot\mathbf{E}_3\right]}{\left[(\mathbf{FE}_1\times\mathbf{FE}_2)\cdot\mathbf{FE}_3\right]} = J = \det(\mathbf{F})\,,\\ JdV = dv\,. \end{aligned} \tag{F.5}$$

By analogy:

$$(\mathbf{Su})\times(\mathbf{Sv}) = \det(\mathbf{S})\mathbf{S}^{-T}\mathbf{u}\times\mathbf{v}\,, \tag{F.6}$$

$$dA = L^2|\mathbf{E}_1\times\mathbf{E}_2| = L^2|\mathbf{E}_3| = L^2\,, \tag{F.7}$$

$$\begin{aligned} \mathbf{FE}_1\times\mathbf{FE}_2 = \det(\mathbf{F})\mathbf{F}^{-T}(\mathbf{E}_1\times\mathbf{E}_2) = J\mathbf{F}^{-T}\mathbf{E}_3\,,\\ da = |L\mathbf{FE}_1\times L\mathbf{FE}_2| = L^2|\mathbf{FE}_1\times\mathbf{FE}_2| = L^2J|\mathbf{n}| = L^2J|\mathbf{F}^{-T}\mathbf{n}_R|\,. \end{aligned} \tag{F.8}$$

hence:

$$\begin{aligned} \frac{da}{dA} = J|\mathbf{F}^{-T}\mathbf{n}_R|\,,\\ dAJ|\mathbf{F}^{-T}\mathbf{n}_R| = da\,. \end{aligned} \tag{F.9}$$

We want to prove the following identities:

$$\begin{aligned} \nabla[f\mathbf{v}_b] &= \mathbf{v}_b\otimes\nabla[f] + f\mathbf{l}\,,\\ \frac{d\left[J\sqrt{\mathbf{n}_R\cdot\mathbf{C}^{-1}\mathbf{n}_R}\right]}{dt} &= J|\mathbf{n}|\left(\text{ div }[\mathbf{v}_b] - \frac{\mathbf{n}\cdot\mathbf{dn}}{|\mathbf{n}|^2}\right)\,, \end{aligned} \tag{F.10}$$

where f is a scalar function and $\mathbf{C}$ is the right-Cauchy-Green tensor. It has to be clear:

$$\begin{aligned} |\mathbf{F}^{-T}\mathbf{n}_R| = \sqrt{\left(\mathbf{F}^{-T}\mathbf{n}_R\right)\cdot\left(\mathbf{F}^{-T}\mathbf{n}_R\right)} = \sqrt{\left(\mathbf{F}^{-T}\mathbf{n}_R\right)\cdot\left(\mathbf{n}_R^T\mathbf{F}^{-1}\right)} =\\ \sqrt{\mathbf{n}_R\cdot\left[\mathbf{F}^{-1}\left(\mathbf{F}^{-T}\mathbf{n}_R\right)\right]} = \sqrt{\mathbf{n}_R\cdot\left[\mathbf{F}^{-1}\mathbf{F}^{-T}\mathbf{n}_R\right]} = \sqrt{\mathbf{n}_R\cdot\left[\mathbf{C}^{-1}\mathbf{n}_R\right]} = \sqrt{\mathbf{n}_R\cdot\mathbf{C}^{-1}\mathbf{n}_R}\,. \end{aligned} \tag{F.11}$$

We know that:

$$\frac{d\left[J\sqrt{\mathbf{n}_R\cdot\mathbf{C}^{-1}\mathbf{n}_R}\right]}{dt} = \frac{dJ}{dt}\left[\sqrt{\mathbf{n}_R\cdot\mathbf{C}^{-1}\mathbf{n}_R}\right] + J\frac{d\left[\sqrt{\mathbf{n}_R\cdot\mathbf{C}^{-1}\mathbf{n}_R}\right]}{dt} \tag{F.12}$$

focusing on the first terms:

$$\begin{aligned}\frac{d}{dt}\left[\det(\mathbf{S})\right] &= \left\{\det(\mathbf{S})Tr\left[\left(\frac{d\mathbf{S}}{dt}\right)\mathbf{S}^{-1}\right]\right\}, \\ \frac{d}{dt}\left[\det(\mathbf{F})\right] &= \left\{\det(\mathbf{F})Tr\left[\left(\frac{d\mathbf{F}}{dt}\right)\mathbf{F}^{-1}\right]\right\},\end{aligned} \tag{F.13}$$

we can found the following relation:

$$\frac{d}{dt}\left[\det(\mathbf{F})\right] = JTr\left(\dot{\mathbf{F}}\mathbf{F}^{-1}\right) = JTr(\mathbf{l}) = J\ \text{div}\ (\mathbf{v}_b)\,. \tag{F.14}$$

Concerning the term $\dfrac{d\left[\sqrt{\mathbf{n}_R\cdot\mathbf{C}^{-1}\mathbf{n}_R}\right]}{dt}$, we can deduce that:

$$\begin{aligned}\frac{d}{dt}\sqrt{\mathbf{n}_R\cdot\mathbf{C}^{-1}\mathbf{n}_R} = \frac{d}{dt}|\mathbf{F}^{-T}\mathbf{n}_R| = \frac{d}{dt}|\mathbf{n}| = \\ \frac{1}{2}\frac{\left[\dfrac{d\mathbf{n}}{dt}\cdot\mathbf{n}+\mathbf{n}\cdot\dfrac{d\mathbf{n}}{dt}\right]}{|\mathbf{n}|} = \frac{\dfrac{d\mathbf{n}}{dt}\cdot\mathbf{n}}{|\mathbf{n}|}\,.\end{aligned} \tag{F.15}$$

Now, we are interested to understand the expression of $\dfrac{d\mathbf{n}}{dt}$, hence:

$$\begin{aligned}\frac{d\mathbf{n}}{dt} &= \frac{d\mathbf{F}^{-T}}{dt}\mathbf{n}_R + \mathbf{F}^{-T}\frac{d\mathbf{n}_R}{dt} \\ \text{where: } &\frac{d\mathbf{n}_R}{dt} = 0 \\ \frac{d\mathbf{n}}{dt} &= \frac{d\mathbf{F}^{-T}}{dt}\mathbf{n}_R\end{aligned} \tag{F.16}$$

knowing that $\dfrac{d\mathbf{A}^{-1}}{dt} = -\mathbf{A}^{-1}\dot{\mathbf{A}}\mathbf{A}^{-1}$ and substituting $\mathbf{A}$ with $\mathbf{F}$, we derived:

$$\begin{aligned}\frac{d\mathbf{n}}{dt} = \frac{d\mathbf{F}^{-T}}{dt}\mathbf{n}_R &= -\mathbf{F}^{-T}\dot{\mathbf{F}^{T}}\mathbf{F}^{-T}\mathbf{n}_R\,, \\ \text{where: } \mathbf{F}^{-T}\dot{\mathbf{F}^{T}} &= \mathbf{l}^{T}\,, \\ \frac{d\mathbf{n}}{dt} &= -\mathbf{l}^{T}\mathbf{F}^{-T}\mathbf{n}_R = -\mathbf{l}^{T}\mathbf{n}\,,\end{aligned} \tag{F.17}$$

therefore:

$$J\frac{d}{dt}\sqrt{\mathbf{n}_R\cdot\mathbf{C}^{-1}\mathbf{n}_R} = -J\frac{\dfrac{d\mathbf{n}}{dt}\cdot\mathbf{n}}{|\mathbf{n}|} = -J\frac{\left(\mathbf{l}^{T}\mathbf{n}\right)\cdot\mathbf{n}}{|\mathbf{n}|} = -J\frac{\mathbf{n}\cdot(\mathbf{dn})}{|\mathbf{n}|}\,. \tag{F.18}$$

In the end, it holds:

$$\begin{aligned}\frac{d\left[J\sqrt{\mathbf{n}_R\cdot\mathbf{C}^{-1}\mathbf{n}_R}\right]}{dt} = \frac{dJ}{dt}\left[\sqrt{\mathbf{n}_R\cdot\mathbf{C}^{-1}\mathbf{n}_R}\right] + J\frac{d\left[\sqrt{\mathbf{n}_R\cdot\mathbf{C}^{-1}\mathbf{n}_R}\right]}{dt} = \\ J\ \text{div}\ (\mathbf{v}_b)|\mathbf{n}| - J\frac{\mathbf{n}\cdot(\mathbf{dn})}{|\mathbf{n}|} = J|\mathbf{n}|\left[\ \text{div}\ (\mathbf{v}_b) - \frac{\mathbf{n}\cdot(\mathbf{dn})}{|\mathbf{n}|^2}\right]\,.\end{aligned} \tag{F.19}$$

F.3 Flux across the boundary

It holds:

$$\vec{h}_a \cdot \vec{t}_\perp \, \mathrm{d}\ell = \vec{h}_{a_R} \cdot \vec{t}_{\perp_R} \, \mathrm{d}\ell_R \, . \tag{F.20}$$

Proof: -
Recognizing that tangent vectors usually convect with the body, we can state that $\mathbf{t}_\parallel = \mathbf{F}\mathbf{t}_{\parallel R}$, so:

$$\begin{aligned} \mathbf{h}_a \cdot \mathbf{t}_\perp = \mathbf{h}_a \cdot \left(\mathbf{t}_\parallel \times \frac{\mathbf{n}}{|\mathbf{n}|} \right) = \mathbf{t}_\parallel \cdot \left(\frac{\mathbf{n}}{|\mathbf{n}|} \times \mathbf{h}_a \right) = \\ = \left(\frac{\mathbf{n}}{|\mathbf{n}|} \times \mathbf{h}_a \right) \cdot (\mathbf{F}\mathbf{t}_{\parallel R}) = \mathbf{F}^T \left(\frac{\mathbf{n}}{|\mathbf{n}|} \times \mathbf{h}_a \right) \cdot \mathbf{t}_{\parallel R} \end{aligned} \tag{F.21}$$

where $|\mathbf{t}_\perp| = 1$ and through the follow relations $(\mathbf{a} \times \mathbf{b}) \cdot \mathbf{c} = (\mathbf{b} \times \mathbf{c}) \cdot \mathbf{a} = (\mathbf{c} \times \mathbf{a}) \cdot \mathbf{b}$ and $(\mathbf{F}\mathbf{v}) \cdot \mathbf{u} = (\mathbf{F}^T \mathbf{u}) \cdot \mathbf{v}$. The subsequent rules are pivotal for the aim:

$$\begin{gathered} \mathbf{M}\mathbf{a} \times \mathbf{M}\mathbf{b} = \det(\mathbf{M}) \mathbf{M}^{-T} (\mathbf{a} \times \mathbf{b}) \\ \text{where: } \mathbf{F} = \mathbf{M}^{-1} \text{ and } \mathbf{M} = \mathbf{F}^{-1} \\ \det(\mathbf{M}) = \det(\mathbf{F}^{-1}) = \frac{1}{J} \end{gathered} \tag{F.22}$$

therefore:

$$\begin{aligned} \mathbf{F}^T \left(\frac{\mathbf{n}}{|\mathbf{n}|} \times \mathbf{h}_a \right) \cdot \mathbf{t}_{\parallel R} = J \left[\underbrace{\frac{1}{J}}_{\det(\mathbf{F}^{-1}) \equiv \det(\mathbf{M})} \underbrace{\mathbf{F}^T}_{\mathbf{M}^{-T}} \left(\underbrace{\frac{\mathbf{n}}{|\mathbf{n}|} \times \mathbf{h}_a}_{\mathbf{a} \times \mathbf{b}} \right) \right] \cdot \mathbf{t}_{\parallel R} = \\ = J \left[\left(\mathbf{F}^{-1} \frac{\mathbf{n}}{|\mathbf{n}|} \right) \times \left(\mathbf{F}^{-1} \mathbf{h}_a \right) \right] \cdot \mathbf{t}_{\parallel R} = J \mathbf{t}_{\parallel R} \cdot \left[\left(\mathbf{F}^{-1} \frac{\mathbf{n}}{|\mathbf{n}|} \right) \times \left(\mathbf{F}^{-1} \mathbf{h}_a \right) \right] = \\ = J \left(\mathbf{F}^{-1} \mathbf{h}_a \right) \cdot \left[\mathbf{t}_{\parallel R} \times \left(\mathbf{F}^{-1} \frac{\mathbf{n}}{|\mathbf{n}|} \right) \right] = \frac{J}{|\mathbf{n}|} \left[\mathbf{t}_{\parallel R} \times \left(\mathbf{F}^{-1} \mathbf{n} \right) \right] \cdot \left(\mathbf{F}^{-1} \mathbf{h}_a \right) = \\ = \frac{J}{|\mathbf{n}|} \left[\mathbf{t}_{\parallel R} \times \left(\underbrace{\mathbf{F}^{-1} \mathbf{F}^{-T}}_{\mathbf{C}^{-1}} \mathbf{n}_R \right) \right] \cdot \left(\mathbf{F}^{-1} \mathbf{h}_a \right) = \frac{J}{|\mathbf{n}|} \left[\mathbf{t}_{\parallel R} \times \left(\mathbf{C}^{-1} \mathbf{n}_R \right) \right] \cdot \left(\mathbf{F}^{-1} \mathbf{h}_a \right) \, . \end{aligned} \tag{F.23}$$

We have to note that the application of a second-order tensor like $\mathbf{C}^{-1}$ to a first-order tensor $\mathbf{n}_R$ it is a first-order tensor with a component along the local Frenet axes $\mathbf{n}_R$, $\mathbf{t}_\parallel$, $\mathbf{t}_\perp$. Hence:

$$\mathbf{C}^{-1} \mathbf{n}_R = z_n \mathbf{n}_R + z_\parallel \mathbf{t}_\parallel + z_\perp \mathbf{t}_\perp \tag{F.24}$$

$$\begin{aligned} \frac{J}{|\mathbf{n}|} \left[\mathbf{t}_{\parallel R} \times \left(\mathbf{C}^{-1} \mathbf{n}_R \right) \right] \cdot \left(\mathbf{F}^{-1} \mathbf{h}_a \right) = \frac{J}{|\mathbf{n}|} z_n \left[\mathbf{t}_{\parallel R} \times \mathbf{n}_R \right] \cdot \left(\mathbf{F}^{-1} \mathbf{h}_a \right) + \\ + \frac{J}{|\mathbf{n}|} z_\parallel \left[\underbrace{\mathbf{t}_{\parallel R} \times \mathbf{t}_{\parallel R}}_{0} \right] \cdot \left(\mathbf{F}^{-1} \mathbf{h}_a \right) + \frac{J}{|\mathbf{n}|} z_\perp \left[\mathbf{t}_{\parallel R} \times \mathbf{t}_{\perp R} \right] \cdot \left(\mathbf{F}^{-1} \mathbf{h}_a \right) \end{aligned} \tag{F.25}$$

We know that $\mathbf{n}_R$ is a unit vector unlike $\mathbf{t}_{\|R}$, therefore we take:

$$\begin{aligned}\mathbf{t}_{\perp R} &= \frac{\mathbf{t}_{\|R}\times\mathbf{n}_R}{|\mathbf{t}_{\|R}|}\text{ unit vector}\,,\\ \mathbf{n}_R &= \frac{\mathbf{t}_{\|R}\times\mathbf{t}_{\perp R}}{|\mathbf{t}_{\|R}|}\text{ unit vector}\,.\end{aligned} \tag{F.26}$$

$$\begin{aligned}&\frac{J}{|\mathbf{n}|}z_n\left[\mathbf{t}_{\|R}\times\mathbf{n}_R\right]\cdot\left(\mathbf{F}^{-1}\mathbf{h}_a\right)+\frac{J}{|\mathbf{n}|}z_\perp\left[\mathbf{t}_{\|R}\times\mathbf{t}_{\perp R}\right]\cdot\left(\mathbf{F}^{-1}\mathbf{h}_a\right)=\\ &=\frac{J}{|\mathbf{n}|}z_n|\mathbf{t}_{\|R}|\mathbf{t}_{\perp R}\cdot\left(\mathbf{F}^{-1}\mathbf{h}_a\right)-\frac{J}{|\mathbf{n}|}z_\perp|\mathbf{t}_{\|R}|\mathbf{n}_R\cdot\left(\mathbf{F}^{-1}\mathbf{h}_a\right)\,.\end{aligned} \tag{F.27}$$

We denote:

$$\mathbf{h}_{aR}=|\mathbf{n}|J\mathbf{F}^{-1}\mathbf{h}_a\Longrightarrow\mathbf{h}_a=\frac{1}{|\mathbf{n}|J}\mathbf{F}\mathbf{h}_{aR} \tag{F.28}$$

and then:

$$\begin{aligned}&\frac{J}{|\mathbf{n}|}z_n|\mathbf{t}_{\|R}|\mathbf{t}_{\perp R}\cdot\left(\mathbf{F}^{-1}\mathbf{h}_a\right)-\frac{J}{|\mathbf{n}|}z_\perp|\mathbf{t}_{\|R}|\mathbf{n}_R\cdot\left(\mathbf{F}^{-1}\mathbf{h}_a\right)=\\ &=z_n|\mathbf{t}_{\|R}|\mathbf{t}_{\perp R}\cdot\left(\frac{J}{|\mathbf{n}|}\frac{|\mathbf{n}|}{|\mathbf{n}|}\mathbf{F}^{-1}\mathbf{h}_a\right)-z_\perp|\mathbf{t}_{\|R}|\mathbf{n}_R\cdot\left(\frac{J}{|\mathbf{n}|}\frac{|\mathbf{n}|}{|\mathbf{n}|}\mathbf{F}^{-1}\mathbf{h}_a\right)=\\ &=z_n\frac{|\mathbf{t}_{\|R}|}{|\mathbf{n}|^2}\mathbf{t}_{\perp R}\cdot\left(\underbrace{J|\mathbf{n}|\mathbf{F}^{-1}\mathbf{h}_a}_{\mathbf{h}_{aR}}\right)-z_\perp\frac{|\mathbf{t}_{\|R}|}{|\mathbf{n}|^2}\mathbf{n}_R\cdot\left(\underbrace{J|\mathbf{n}|\mathbf{F}^{-1}\mathbf{h}_a}_{\mathbf{h}_{aR}}\right)=\\ &=z_n\frac{|\mathbf{t}_{\|R}|}{|\mathbf{n}|^2}\mathbf{t}_{\perp R}\cdot\mathbf{h}_{aR}-z_\perp\frac{|\mathbf{t}_{\|R}|}{|\mathbf{n}|^2}\mathbf{n}_R\cdot\mathbf{h}_{aR}\,.\end{aligned} \tag{F.29}$$

We arrive at the following relation $\mathbf{h}_a\cdot\mathbf{t}_\perp=z_n\frac{|\mathbf{t}_{\|R}|}{|\mathbf{n}|^2}\mathbf{t}_{\perp R}\cdot\mathbf{h}_{aR}-z_\perp\frac{|\mathbf{t}_{\|R}|}{|\mathbf{n}|^2}\mathbf{n}_R\cdot\mathbf{h}_{aR}$.

We know:

$$\begin{aligned}0=\mathbf{h}_a\cdot\mathbf{n}&=\frac{1}{J|\mathbf{n}|}\left(\mathbf{F}\mathbf{h}_{aR}\right)\cdot\left(\mathbf{F}^{-T}\mathbf{n}_R\right)=\\ &=\frac{1}{J|\mathbf{n}|}\left(\mathbf{F}^{-1}\mathbf{F}\mathbf{h}_{aR}\cdot\mathbf{n}_R\right)=\frac{1}{J|\mathbf{n}|}\mathbf{h}_{aR}\cdot\mathbf{n}_R\end{aligned} \tag{F.30}$$

$$\begin{aligned}z_n&=\mathbf{C}^{-1}\mathbf{n}_R\cdot\mathbf{n}_R=\left(\mathbf{F}^T\mathbf{F}\right)^{-1}\mathbf{n}_R\cdot\mathbf{n}_R=\\ &=\mathbf{F}^{-1}\mathbf{F}^{-T}\mathbf{n}_R\cdot\mathbf{n}_R=\mathbf{F}^{-T}\mathbf{n}_R\cdot\mathbf{F}^{-T}\mathbf{n}_R=|\mathbf{n}|^2\end{aligned} \tag{F.31}$$

and finally:

$$\mathbf{h}_a\cdot\mathbf{t}_\perp=z_n\frac{|\mathbf{t}_{\|R}|}{|\mathbf{n}|^2}\mathbf{t}_{\perp R}\cdot\mathbf{h}_{aR}-z_\perp\frac{|\mathbf{t}_{\|R}|}{|\mathbf{n}|^2}\underbrace{\mathbf{n}_R\cdot\mathbf{h}_{aR}}_{0}=|\mathbf{t}_{\|R}|\mathbf{t}_{\perp R}\cdot\mathbf{h}_{aR}$$

knowing that:

$$dl=\sqrt{d\mathbf{x}\cdot d\mathbf{x}}=|\mathbf{t}_\||d\lambda=d\lambda\quad dl_R=\sqrt{d\mathbf{X}\cdot d\mathbf{X}}=|\mathbf{t}_{\|R}|d\lambda \tag{F.32}$$

we can deduce:

$$\begin{aligned}\mathbf{h}_a\cdot\mathbf{t}_\perp(\mathbf{x})&=|\mathbf{t}_{\|R}|\mathbf{t}_{\perp R}(\mathbf{X})\cdot\mathbf{h}_{aR}\\ \mathbf{h}_a\cdot\mathbf{t}_\perp(\mathbf{x})d\lambda&=|\mathbf{t}_{\|R}|\mathbf{t}_{\perp R}(\mathbf{X})\cdot\mathbf{h}_{aR}d\lambda\\ \mathbf{h}_a\cdot\mathbf{t}_\perp(\mathbf{x})dl&=\mathbf{h}_{aR}\cdot\mathbf{t}_{\perp R}(\mathbf{X})dl_R\,.\end{aligned}$$

Appendix G

Possible improvements of the chemo-transpo-mechanical model

G.1 Formal extension in the large deformations framework of the expressions (3.82) provide in chapter 3.4

Following we provide a formal extension in the large deformation framework of the expressions (3.82) provide in chapter 3.4.

$$1)\quad V + L_V \underset{k_b^1}{\overset{k_f^1}{\leftrightarrows}} C_1\,, \tag{G.1a}$$

$$2)\quad C_1 + I \underset{k_b^2}{\overset{k_f^2}{\leftrightarrows}} \underbrace{C_1 I_l}_{C_2}\,, \tag{G.1b}$$

$$3)\quad I + L_I \underset{k_b^3}{\overset{k_f^3}{\leftrightarrows}} \underbrace{I_h L_I}_{C_3}\,. \tag{G.1c}$$

$$\frac{\partial c_{V_R}}{\partial t} + \mathrm{Div}_{\mathcal{P}_R}\left[\vec{h}_{V_R}\right] + \frac{\partial c_{C_{1R}}}{\partial t} + \frac{\partial c_{C_{2R}}}{\partial t} = 0\,, \tag{G.2a}$$

$$\frac{\partial c_{L_{VR}}}{\partial t} + \frac{\partial c_{C_{1R}}}{\partial t} + \frac{\partial c_{C_{2R}}}{\partial t} = s_{L_{VR}}\,, \tag{G.2b}$$

$$\frac{\partial c_{I_R}}{\partial t} + \mathrm{Div}_{\mathcal{P}_R}\left[\vec{h}_{I_R}\right] + \frac{\partial c_{C_{2R}}}{\partial t} + \frac{\partial c_{C_{3R}}}{\partial t} = 0\,, \tag{G.2c}$$

$$\frac{\partial c_{L_{IR}}}{\partial t} + \frac{\partial c_{C_{3R}}}{\partial t} = s_{L_{IR}}\,, \tag{G.2d}$$

$$\frac{\partial c_{C_{3R}}}{\partial t} = w_R^{(G.1c)}\,, \tag{G.2e}$$

$$\frac{\partial c_{C_{1R}}}{\partial t} + \frac{\partial c_{C_{2R}}}{\partial t} = w_R^{(G.1a)}\,, \tag{G.2f}$$

$$\frac{\partial c_{C_{2R}}}{\partial t} = w_R^{(G.1b)}\,. \tag{G.2g}$$

Extending the eq. (6.37a) to the current model:

$$c_{C_{1R}} = \frac{c_{R_R} c_{L_{RR}}}{\alpha_{1R}} \tag{G.3a}$$

$$c_{C_{2R}} = \frac{c_{C_{1R}} c_{I_R}}{\alpha_{2R}} = \frac{c_{R_R} c_{L_{RR}} c_{I_R}}{\alpha_{1R}\alpha_{2R}} \tag{G.3b}$$

$$c_{C_{3R}} = \frac{c_{I_R} c_{L_{IR}}}{\alpha_{3R}} \tag{G.3c}$$

where:

$$\frac{\partial c_{C_{1R}}}{\partial t} = \frac{1}{\alpha_R^{(1)}}\left[c_{L_{VR}}\frac{\partial c_{V_R}}{\partial t} + c_{V_R}\frac{\partial c_{L_{VR}}}{\partial t}\right] + \frac{c_{V_R}c_{L_{VR}}}{\alpha_R^{(2)}}\left[-Tr(\mathbf{l}) + \frac{\mathbf{n}_R\cdot\mathbf{C}^{-1}\dfrac{\partial \mathbf{C}}{\partial t}\mathbf{C}^{-1}\mathbf{n}_R}{2|\mathbf{F}^{-T}\mathbf{n}_R|^2}\right]$$

$$\frac{\partial c_{C_{2R}}}{\partial t} = \frac{1}{\alpha_R^{(2)}}\left[c_{C_{1R}}\frac{\partial c_{I_R}}{\partial t} + c_{I_R}\frac{\partial c_{C_{1R}}}{\partial t}\right] + \frac{c_{I_R}c_{C_{1R}}}{\alpha_R^{(2)}}\left[-Tr(\mathbf{l}) + \frac{\mathbf{n}_R\cdot\mathbf{C}^{-1}\dfrac{\partial \mathbf{C}}{\partial t}\mathbf{C}^{-1}\mathbf{n}_R}{2|\mathbf{F}^{-T}\mathbf{n}_R|^2}\right] =$$

$$= \frac{1}{\alpha_R^{(2)}}\left\{c_{C_{1R}}\frac{\partial c_{I_R}}{\partial t} + \frac{c_{I_R}}{\alpha_R^{(1)}}\left[c_{L_{VR}}\frac{\partial c_{V_R}}{\partial t} + c_{V_R}\frac{\partial c_{L_{VR}}}{\partial t}\right] + \frac{c_{I_R}c_{V_R}c_{L_{VR}}}{\alpha_R^{(2)}}\left[-Tr(\mathbf{l}) + \frac{\mathbf{n}_R\cdot\mathbf{C}^{-1}\dfrac{\partial \mathbf{C}}{\partial t}\mathbf{C}^{-1}\mathbf{n}_R}{2|\mathbf{F}^{-T}\mathbf{n}_R|^2}\right]\right\} +$$

$$+\frac{c_{I_R}c_{C_{1R}}}{\alpha_R^{(2)}}\left[-Tr(\mathbf{l}) + \frac{\mathbf{n}_R\cdot\mathbf{C}^{-1}\dfrac{\partial \mathbf{C}}{\partial t}\mathbf{C}^{-1}\mathbf{n}_R}{2|\mathbf{F}^{-T}\mathbf{n}_R|^2}\right],$$

where:

$$c_{C_{1R}} = \frac{c_{V_R}c_{L_{VR}}}{\alpha_R^{(1)}} =$$

$$= \frac{1}{\alpha_R^{(2)}}\left\{\frac{c_{V_R}c_{L_{VR}}}{\alpha_R^{(1)}}\frac{\partial c_{I_R}}{\partial t} + \frac{c_{I_R}}{\alpha_R^{(1)}}\left[c_{L_{VR}}\frac{\partial c_{V_R}}{\partial t} + c_{V_R}\frac{\partial c_{L_{VR}}}{\partial t}\right] + \frac{c_{I_R}c_{V_R}c_{L_{VR}}}{\alpha_R^{(1)}}\left[-Tr(\mathbf{l}) + \frac{\mathbf{n}_R\cdot\mathbf{C}^{-1}\dfrac{\partial \mathbf{C}}{\partial t}\mathbf{C}^{-1}\mathbf{n}_R}{2|\mathbf{F}^{-T}\mathbf{n}_R|^2}\right]\right\} +$$

$$+\frac{c_{I_R}c_{V_R}c_{L_{VR}}}{\alpha_R^{(1)}\alpha_R^{(2)}}\left[-Tr(\mathbf{l}) + \frac{\mathbf{n}_R\cdot\mathbf{C}^{-1}\dfrac{\partial \mathbf{C}}{\partial t}\mathbf{C}^{-1}\mathbf{n}_R}{2|\mathbf{F}^{-T}\mathbf{n}_R|^2}\right]$$

$$\frac{\partial c_{C_{3R}}}{\partial t} = \frac{1}{\alpha_R^{(3)}}\left[c_{L_{IR}}\frac{\partial c_{I_R}}{\partial t} + c_{I_R}\frac{\partial c_{L_{IR}}}{\partial t}\right] + \frac{c_{I_R}c_{L_{IR}}}{\alpha_R^{(3)}}\left[-Tr(\mathbf{l}) + \frac{\mathbf{n}_R\cdot\mathbf{C}^{-1}\dfrac{\partial \mathbf{C}}{\partial t}\mathbf{C}^{-1}\mathbf{n}_R}{2|\mathbf{F}^{-T}\mathbf{n}_R|^2}\right]. \tag{G.4}$$

Thanks to the realtions (G.2) and (G.4) we can deduce the following four governing equations:

First equation

$$\frac{\partial c_{I_R}}{\partial t}+\mathrm{Div}_{\mathcal{P}_R}[\mathbf{h}_{I_R}]+\frac{1}{\alpha_R^{(3)}}\left[c_{L_{IR}}\frac{\partial c_{I_R}}{\partial t}+c_{I_R}\frac{\partial c_{L_{IR}}}{\partial t}\right]+\frac{c_{I_R}c_{L_{IR}}}{\alpha_R^{(3)}}\left[-Tr(\mathbf{l})+\frac{\mathbf{n}_R\cdot\mathbf{C}^{-1}\frac{\partial\mathbf{C}}{\partial t}\mathbf{C}^{-1}\mathbf{n}_R}{2|\mathbf{F}^{-T}\mathbf{n}_R|^2}\right]+$$
$$+\frac{1}{\alpha_R^{(2)}}\left\{\frac{c_{V_R}c_{L_{VR}}}{\alpha_R^{(1)}}\frac{\partial c_{I_R}}{\partial t}+\frac{c_{I_R}}{\alpha_R^{(1)}}\left[c_{L_{VR}}\frac{\partial c_{V_R}}{\partial t}+c_{V_R}\frac{\partial c_{L_{VR}}}{\partial t}\right]+\frac{c_{I_R}c_{V_R}c_{L_{VR}}}{\alpha_R^{(1)}}[-Tr(\mathbf{l})+\right.$$
$$\left.+\frac{\mathbf{n}_R\cdot\mathbf{C}^{-1}\frac{\partial\mathbf{C}}{\partial t}\mathbf{C}^{-1}\mathbf{n}_R}{2|\mathbf{F}^{-T}\mathbf{n}_R|^2}\right]\right\}+\frac{c_{I_R}c_{V_R}c_{L_{VR}}}{\alpha_R^{(1)}\alpha_R^{(2)}}\left[-Tr(\mathbf{l})+\frac{\mathbf{n}_R\cdot\mathbf{C}^{-1}\frac{\partial\mathbf{C}}{\partial t}\mathbf{C}^{-1}\mathbf{n}_R}{2|\mathbf{F}^{-T}\mathbf{n}_R|^2}\right]=s_{I_R} \tag{G.5}$$

Second equation

$$\frac{\partial c_{L_{IR}}}{\partial t}+\frac{1}{\alpha_R^{(2)}}\left[c_{L_{IR}}\frac{\partial c_{I_R}}{\partial t}+c_{I_R}\frac{\partial c_{L_{IR}}}{\partial t}\right]+\frac{c_{I_R}c_{L_{IR}}}{\alpha_R^{(3)}}\left[-Tr(\mathbf{l})+\frac{\mathbf{n}_R\cdot\mathbf{C}^{-1}\frac{\partial\mathbf{C}}{\partial t}\mathbf{C}^{-1}\mathbf{n}_R}{2|\mathbf{F}^{-T}\mathbf{n}_R|^2}\right]=s_{L_{IR}} \tag{G.6}$$

Third equation

$$\frac{\partial c_{V_R}}{\partial t}+\mathrm{Div}_{\mathcal{P}_R}[\mathbf{h}_{V_R}]+\frac{1}{\alpha_R^{(1)}}\left[c_{L_{VR}}\frac{\partial c_{V_R}}{\partial t}+c_{V_R}\frac{\partial c_{L_{VR}}}{\partial t}\right]+\frac{c_{V_R}c_{L_{VR}}}{\alpha_R^{(1)}}\left[-Tr(\mathbf{l})+\frac{\mathbf{n}_R\cdot\mathbf{C}^{-1}\frac{\partial\mathbf{C}}{\partial t}\mathbf{C}^{-1}\mathbf{n}_R}{2|\mathbf{F}^{-T}\mathbf{n}_R|^2}\right]+$$
$$+\frac{1}{\alpha_R^{(2)}}\left\{\frac{c_{V_R}c_{L_{VR}}}{\alpha_R^{(1)}}\frac{\partial c_{I_R}}{\partial t}+\frac{c_{I_R}}{\alpha_R^{(1)}}\left[c_{L_{VR}}\frac{\partial c_{V_R}}{\partial t}+c_{V_R}\frac{\partial c_{L_{VR}}}{\partial t}\right]+\frac{c_{I_R}c_{V_R}c_{L_{VR}}}{\alpha_R^{(1)}}[-Tr(\mathbf{l})+\right.$$
$$\left.+\frac{\mathbf{n}_R\cdot\mathbf{C}^{-1}\frac{\partial\mathbf{C}}{\partial t}\mathbf{C}^{-1}\mathbf{n}_R}{2|\mathbf{F}^{-T}\mathbf{n}_R|^2}\right]\right\}+\frac{c_{I_R}c_{V_R}c_{L_{VR}}}{\alpha_R^{(1)}\alpha_R^{(2)}}\left[-Tr(\mathbf{l})+\frac{\mathbf{n}_R\cdot\mathbf{C}^{-1}\frac{\partial\mathbf{C}}{\partial t}\mathbf{C}^{-1}\mathbf{n}_R}{2|\mathbf{F}^{-T}\mathbf{n}_R|^2}\right]=s_{V_R} \tag{G.7}$$

Fourth equation

$$\frac{\partial c_{L_{VR}}}{\partial t}+\frac{1}{\alpha_R^{(1)}}\left[c_{L_{VR}}\frac{\partial c_{V_R}}{\partial t}+c_{V_R}\frac{\partial c_{L_{VR}}}{\partial t}\right]+\frac{c_{V_R}c_{L_{VR}}}{\alpha_R^{(1)}}\left[-Tr(\mathbf{l})+\frac{\mathbf{n}_R\cdot\mathbf{C}^{-1}\frac{\partial\mathbf{C}}{\partial t}\mathbf{C}^{-1}\mathbf{n}_R}{2|\mathbf{F}^{-T}\mathbf{n}_R|^2}\right]+$$
$$+\frac{1}{\alpha_R^{(2)}}\left\{\frac{c_{V_R}c_{L_{VR}}}{\alpha_R^{(1)}}\frac{\partial c_{I_R}}{\partial t}+\frac{c_{I_R}}{\alpha_R^{(1)}}\left[c_{L_{VR}}\frac{\partial c_{V_R}}{\partial t}+c_{V_R}\frac{\partial c_{L_{VR}}}{\partial t}\right]+\frac{c_{I_R}c_{V_R}c_{L_{VR}}}{\alpha_R^{(1)}}[-Tr(\mathbf{l})+\right. \tag{G.8}$$
$$\left.+\frac{\mathbf{n}_R\cdot\mathbf{C}^{-1}\frac{\partial\mathbf{C}}{\partial t}\mathbf{C}^{-1}\mathbf{n}_R}{2|\mathbf{F}^{-T}\mathbf{n}_R|^2}\right]\right\}+\frac{c_{I_R}c_{V_R}c_{L_{VR}}}{\alpha_R^{(1)}\alpha_R^{(2)}}\left[-Tr(\mathbf{l})+\frac{\mathbf{n}_R\cdot\mathbf{C}^{-1}\frac{\partial\mathbf{C}}{\partial t}\mathbf{C}^{-1}\mathbf{n}_R}{2|\mathbf{F}^{-T}\mathbf{n}_R|^2}\right]=s_{L_{VR}}$$

G.2 Interaction between mobile and immobilized VEGFR2 and integrin

It could be interesting to update and extend the model presented in section 8 with the current frame involving an appropriate duplication of the species for VEGFR2 (mobile and immobilized).

1) $V_{Im} + L_R \underset{k_b^2}{\overset{k_f^2}{\leftrightarrows}} C_1^{Im}$, (G.9a)

2) $V_M + L_R \underset{k_b^2}{\overset{k_f^2}{\leftrightarrows}} C_1^{M}$, (G.9b)

3) $C_1^{Im} + I \underset{k_b^3}{\overset{k_f^3}{\leftrightarrows}} C_2^{Im}$, (G.9c)

4) $C_1^{M} + I \underset{k_b^3}{\overset{k_f^3}{\leftrightarrows}} C_2^{M}$, (G.9d)

5) $I + L_I \underset{k_b^1}{\overset{k_f^1}{\leftrightarrows}} C_3$. (G.9e)

$$\frac{\partial c_{V_R^{Im}}}{\partial t} + w_R^{(G.9a)} = s_{V_R^{Im}} , \tag{G.10a}$$

$$\frac{\partial c_{V_R^{M}}}{\partial t} + \mathrm{Div}_{\mathcal{P}_R}\left[\vec{h}_{V_R^{M}}\right] + w_R^{(G.9b)} = 0 , \tag{G.10b}$$

$$\frac{\partial c_{L_{VR}}}{\partial t} + w_R^{(G.9a)} + w_R^{(G.9b)} = s_{L_{VR}} , \tag{G.10c}$$

$$\frac{\partial c_{I_R}}{\partial t} + \mathrm{Div}_{\mathcal{P}_R}\left[\vec{h}_{I_R}\right] + w_R^{(G.9c)} + w_R^{(G.9d)} + w_R^{(G.9e)} = 0 , \tag{G.10d}$$

$$\frac{\partial c_{L_{IR}}}{\partial t} + w_R^{(G.9e)} = s_{L_{IR}} , \tag{G.10e}$$

$$\frac{\partial c_{C_{1R}}}{\partial t} = \frac{\partial c_{C_{1R}^{Im}}}{\partial t} + \frac{\partial c_{C_{1R}^{M}}}{\partial t} , \tag{G.10f}$$

$$\frac{\partial c_{C_{2R}}}{\partial t} = \frac{\partial c_{C_{2R}^{Im}}}{\partial t} + \frac{\partial c_{C_{2R}^{M}}}{\partial t} , \tag{G.10g}$$

$$\frac{\partial c_{C_{1R}^{Im}}}{\partial t} + w_R^{(G.9c)} = w_R^{(G.9a)} , \tag{G.10h}$$

$$\frac{\partial c_{C_{1R}^{M}}}{\partial t} + w_R^{(G.9d)} = w_R^{(G.9b)} , \tag{G.10i}$$

$$\frac{\partial c_{C_{2R}^{Im}}}{\partial t} = w_R^{(G.9c)} , \tag{G.10j}$$

$$\frac{\partial c_{C_{2R}^{M}}}{\partial t} = w_R^{(G.9d)} , \tag{G.10k}$$

$$\frac{\partial c_{C_{3R}}}{\partial t} = w_R^{(G.9e)} . \tag{G.10l}$$

One more time, we recognize valid the infinitely fast kinetics hypothesis which, based on the chemical interactions (G.9), conduct to the following relations:

$$c_{C_{1R}^{Im}} = \frac{c_{V_R^{Im}} c_{L_{VR}}}{\alpha_{1R}} \tag{G.11a}$$

$$c_{C_{1R}^{M}} = \frac{c_{V_R^{M}} c_{L_{VR}}}{\alpha_{1R}} \tag{G.11b}$$

$$c_{C_{2R}^{Im}} = \frac{c_{C_{1R}^{Im}} c_{I_R}}{\alpha_{2R}} \tag{G.11c}$$

$$c_{C_{2R}^{M}} = \frac{c_{C_{1R}^{M}} c_{I_R}}{\alpha_{2R}} \tag{G.11d}$$

$$c_{C_{3R}} = \frac{c_{I_R} c_{L_{IR}}}{\alpha_{3R}} \tag{G.11e}$$

Finally, these complete the set of the current governing equations:

$$\frac{\partial c_{V_R^{Im}}}{\partial t} + \frac{\partial c_{C_{1R}^{Im}}}{\partial t} + \frac{\partial c_{C_{2R}^{Im}}}{\partial t} = s_{V_R^{Im}} , \tag{G.12a}$$

$$\frac{\partial c_{V_R^M}}{\partial t} + \mathrm{Div}_{\mathcal{P}_R}\left[\vec{h}_{V_R^M}\right] + \frac{\partial c_{C_{1R}^M}}{\partial t} + \frac{\partial c_{C_{2R}^M}}{\partial t} = 0\,, \tag{G.12b}$$

$$\frac{\partial c_{L_{VR}}}{\partial t} + \frac{\partial c_{C_{1R}^{Im}}}{\partial t} + \frac{\partial c_{C_{2R}^{Im}}}{\partial t} + \frac{\partial c_{C_{1R}^M}}{\partial t} + \frac{\partial c_{C_{2R}^M}}{\partial t} = s_{L_{VR}}\,, \tag{G.12c}$$

$$\frac{\partial c_{I_R}}{\partial t} + \mathrm{Div}_{\mathcal{P}_R}\left[\vec{h}_{I_R}\right] + \frac{\partial c_{C_{2R}^{Im}}}{\partial t} + \frac{\partial c_{C_{2R}^M}}{\partial t} + \frac{\partial c_{C_{3R}}}{\partial t} = 0\,, \tag{G.12d}$$

$$\frac{\partial c_{L_{IR}}}{\partial t} + \frac{\partial c_{C_{3R}}}{\partial t} = s_{L_{IR}}\,, \tag{G.12e}$$

$$\frac{\partial c_{C_{1R}}}{\partial t} = \frac{\partial c_{C_{1R}^{Im}}}{\partial t} + \frac{\partial c_{C_{1R}^M}}{\partial t}\,, \tag{G.12f}$$

$$\frac{\partial c_{C_{2R}}}{\partial t} = \frac{\partial c_{C_{2R}^{Im}}}{\partial t} + \frac{\partial c_{C_{2R}^M}}{\partial t}\,. \tag{G.12g}$$

where the Eqs. (G.12f) and (G.12g) confirm the above-formulated assumption that the doubling of species of VEGFR2 does not affect the chemical interaction either between VEGFR2 and gremlin or among VEGFR2-gremlin-complex with integrin.

G.3 Interaction between mobile and immobilized VEGFR2 with mobile and immobilized integrin

Intriguingly, integrin as well could be subdivided into a mobile and immobilized species. Indeed, actin filaments present in the inner part of an EC, are involved by integrin activation in several biological processes including angiogenesis. Hence, in order to extend what has been just presented in section G.2, we present a multiphysics model involving an appropriate duplication of the species both VEGFR2 and integrin.

$$1)\ V_{Im} + L_R \underset{k_b^1}{\overset{k_f^1}{\leftrightarrows}} C_1^{Im}\,, \tag{G.13a}$$

$$2)\ V_M + L_R \underset{k_b^1}{\overset{k_f^1}{\leftrightarrows}} C_1^{M}\,, \tag{G.13b}$$

$$3)\ C_1^{Im} + I_{Im} \underset{k_b^2}{\overset{k_f^2}{\leftrightarrows}} C_2^{Im(1Im)} \equiv C_{2A}^{Im}\,, \tag{G.13c}$$

$$4)\ C_1^{M} + I_{Im} \underset{k_b^2}{\overset{k_f^2}{\leftrightarrows}} C_2^{Im(1M)} \equiv C_{2B}^{Im}\,, \tag{G.13d}$$

$$5)\ C_1^{Im} + I_{M} \underset{k_b^2}{\overset{k_f^2}{\leftrightarrows}} C_2^{M(1Im)} \equiv C_{2A}^{M}\,, \tag{G.13e}$$

$$6)\ C_1^{M} + I_{M} \underset{k_b^2}{\overset{k_f^2}{\leftrightarrows}} C_2^{M(1M)} \equiv C_{2B}^{M}\,, \tag{G.13f}$$

$$7)\ I_{Im} + L_I \underset{k_b^3}{\overset{k_f^3}{\leftrightarrows}} C_3^{Im}\,, \tag{G.13g}$$

$$8)\ I_{M} + L_I \underset{k_b^3}{\overset{k_f^3}{\leftrightarrows}} C_3^{M}\,. \tag{G.13h}$$

$$\frac{\partial c_{V_R^{Im}}}{\partial t} + w_R^{(G.13a)} = s_{V_R^{Im}} \,, \tag{G.14a}$$

$$\frac{\partial c_{V_R^{M}}}{\partial t} + \mathrm{Div}_{\mathcal{P}_R}\left[\vec{h}_{V_R^{M}}\right] + w_R^{(G.13b)} = 0 \,, \tag{G.14b}$$

$$\frac{\partial c_{L_{VR}}}{\partial t} + w_R^{(G.13a)} + w_R^{(G.13b)} = s_{L_{VR}} \tag{G.14c}$$

$$\frac{\partial c_{I_R^{Im}}}{\partial t} + w_R^{(G.13c)} + w_R^{(G.13d)} + w_R^{(G.13g)} = s_{I_R^{Im}} \,, \tag{G.14d}$$

$$\frac{\partial c_{I_R^{M}}}{\partial t} + \mathrm{Div}_{\mathcal{P}_R}\left[\vec{h}_{I_R^{M}}\right] + w_R^{(G.13e)} + w_R^{(G.13f)} + w_R^{(G.13h)} = 0 \,, \tag{G.14e}$$

$$\frac{\partial c_{L_{IR}}}{\partial t} + w_R^{(G.13g)} + w_R^{(G.13h)} = s_{L_{IR}} \,, \tag{G.14f}$$

$$\frac{\partial c_{C_{1R}}}{\partial t} = \frac{\partial c_{C_{1R}^{Im}}}{\partial t} + \frac{\partial c_{C_{1R}^{M}}}{\partial t} \,, \tag{G.14g}$$

$$\frac{\partial c_{C_{2R}}}{\partial t} = \frac{\partial c_{C_{2AR}^{Im}}}{\partial t} + \frac{\partial c_{C_{2BR}^{Im}}}{\partial t} + \frac{\partial c_{C_{2AR}^{M}}}{\partial t} + \frac{\partial c_{C_{2BR}^{M}}}{\partial t} \,, \tag{G.14h}$$

$$\frac{\partial c_{C_{3R}}}{\partial t} = \frac{\partial c_{C_{3R}^{Im}}}{\partial t} + \frac{\partial c_{C_{3R}^{M}}}{\partial t} \,, \tag{G.14i}$$

$$\frac{\partial c_{C_{1R}^{Im}}}{\partial t} + w_R^{(G.13c)} + w_R^{(G.13e)} = w_R^{(G.13a)} \,, \tag{G.14j}$$

$$\frac{\partial c_{C_{1R}^{M}}}{\partial t} + w_R^{(G.13d)} + w_R^{(G.13f)} = w_R^{(G.13b)} \,, \tag{G.14k}$$

$$\frac{\partial c_{C_{2AR}^{Im}}}{\partial t} = w_R^{(G.13c)} \,, \tag{G.14l}$$

$$\frac{\partial c_{C_{2BR}^{Im}}}{\partial t} = w_R^{(G.13d)} \,, \tag{G.14m}$$

$$\frac{\partial c_{C_{2AR}^{M}}}{\partial t} = w_R^{(G.13e)} \,, \tag{G.14n}$$

$$\frac{\partial c_{C_{2BR}^{M}}}{\partial t} = w_R^{(G.13f)} \,, \tag{G.14o}$$

$$\frac{\partial c_{C_{3R}^{Im}}}{\partial t} = w_R^{(G.13g)} \,, \tag{G.14p}$$

$$\frac{\partial c_{C_{3R}^{M}}}{\partial t} = w_R^{(G.13h)} \,. \tag{G.14q}$$

Eqs. (G.15) are the relations that link the concentrations of reactants with those of products, arising from the infinitely fast kinetics hypothesis.

$$c_{C_{1R}^{Im}} = \frac{c_{V_R^{Im}} c_{L_{VR}}}{\alpha_{1R}} \tag{G.15a}$$

$$c_{C_{2AR}^{Im}} = \frac{c_{C_{1R}^{Im}} c_{I_R^{Im}}}{\alpha_{2R}} \tag{G.15b}$$

$$c_{C_{2BR}^{Im}} = \frac{c_{C_{1R}^{M}} c_{I_R^{Im}}}{\alpha_{2R}} \tag{G.15c}$$

$$c_{C_{3R}^{Im}} = \frac{c_{I_R^{Im}} c_{L_{IR}}}{\alpha_{3R}} \tag{G.15d}$$

$$c_{C_{1R}^{M}} = \frac{c_{V_R^{M}} c_{L_{VR}}}{\alpha_{1R}} \tag{G.15e}$$

$$c_{C_{2AR}^{M}} = \frac{c_{C_{1R}^{Im}} c_{I_R^{M}}}{\alpha_{2R}} \tag{G.15f}$$

$$c_{C_{2BR}^{M}} = \frac{c_{C_{1R}^{M}} c_{I_R^{M}}}{\alpha_{2R}} \tag{G.15g}$$

$$c_{C_{3R}^{M}} = \frac{c_{I_R^{M}} c_{L_{IR}}}{\alpha_{3R}} \tag{G.15h}$$

The remaining governing equations read as follows:

$$\frac{\partial c_{V_R^{Im}}}{\partial t} + \frac{\partial c_{C_{1R}^{Im}}}{\partial t} + \frac{\partial c_{C_{2AR}^{Im}}}{\partial t} + \frac{\partial c_{C_{2AR}^{M}}}{\partial t} = s_{R_R^{Im}} \,, \tag{G.16a}$$

$$\frac{\partial c_{V_R^{M}}}{\partial t} + \mathrm{Div}_{\mathcal{P}_R}\left[\vec{h}_{V_R^{M}}\right] + \frac{\partial c_{C_{1R}^{M}}}{\partial t} + \frac{\partial c_{C_{2BR}^{Im}}}{\partial t} + \frac{\partial c_{C_{2BR}^{M}}}{\partial t} = 0 \,, \tag{G.16b}$$

$$\frac{\partial c_{L_{VR}}}{\partial t} + \frac{\partial c_{C_{1R}^{Im}}}{\partial t} + \frac{\partial c_{C_{2AR}^{Im}}}{\partial t} + \frac{\partial c_{C_{2AR}^{M}}}{\partial t} + \frac{\partial c_{C_{1R}^{M}}}{\partial t} + \frac{\partial c_{C_{2BR}^{Im}}}{\partial t} + \frac{\partial c_{C_{2BR}^{M}}}{\partial t} = s_{L_{VR}} \,, \tag{G.16c}$$

$$\frac{\partial c_{I_R^{Im}}}{\partial t} + \frac{\partial c_{C_{2AR}^{Im}}}{\partial t} + \frac{\partial c_{C_{2BR}^{Im}}}{\partial t} + \frac{\partial c_{C_{3R}^{Im}}}{\partial t} = s_{I_R^{Im}} \,, \tag{G.16d}$$

$$\frac{\partial c_{I_R^{M}}}{\partial t} + \mathrm{Div}_{\mathcal{P}_R}\left[\vec{h}_{I_R^{M}}\right] + \frac{\partial c_{C_{2AR}^{M}}}{\partial t} + \frac{\partial c_{C_{2BR}^{M}}}{\partial t} + \frac{\partial c_{C_{3R}^{M}}}{\partial t} = 0 \,, \tag{G.16e}$$

$$\frac{\partial c_{L_{IR}}}{\partial t} + \frac{\partial c_{C_{3R}^{Im}}}{\partial t} + \frac{\partial c_{C_{3R}^{M}}}{\partial t} = s_{L_{IR}} \,, \tag{G.16f}$$

$$\frac{\partial c_{C_{1R}}}{\partial t} = \frac{\partial c_{C_{1R}^{Im}}}{\partial t} + \frac{\partial c_{C_{1R}^{M}}}{\partial t} \,, \tag{G.16g}$$

$$\frac{\partial c_{C_{2R}}}{\partial t} = \frac{\partial c_{C_{2AR}^{Im}}}{\partial t} + \frac{\partial c_{C_{2BR}^{Im}}}{\partial t} + \frac{\partial c_{C_{2AR}^{M}}}{\partial t} + \frac{\partial c_{C_{2BR}^{M}}}{\partial t} \,, \tag{G.16h}$$

$$\frac{\partial c_{C_{3R}}}{\partial t} = \frac{\partial c_{C_{3R}^{Im}}}{\partial t} + \frac{\partial c_{C_{3R}^{M}}}{\partial t} \,. \tag{G.16i}$$

Part IV

Fluctuations in living cells

Chapter 9

Fluctuations in living cells

In the current section, we present a summary of the work, that has been done during my experience abroad at the University of Cambridge under the supervision of Professor Vikram Deshpande financed by means of a scholarship provided by the Guido Berlucchi Foundation (Young Researchers Mobility Programme). Such collaboration has been prematurely interrupted due to coronavirus pandemic (after 2 months on the six planned) and below we will show the results.

The goals of the work were to try to understand the competition mechanism between haptotaxis and durotaxis, where the in-silico replication of the experimental results on fibroblast dictated by the paper [219], is the target. In order to do that, base on the statistical mechanics framework, suitable explained in the paper [14], we provide a simplified idealization of these cells by means of a 2D study on fibroblast constrained to maintain an elliptical shape.
The chapter is structured as follows: a first introduction (9.1) wherein the theoretical insights are presented (mainly deduce by the papers of [180, 128], and [14]), and finally, a second part (9.2) where the numerical results on the behavior of the cell, constrained to maintain an elliptic shape, are shown.

9.1 Theoretical insights

In order to satisfy either the several observations that attest to cells fluctuating response during in-vitro experiments and in order to bypass the uncertainty and ignorance on the determination of all intracellular processes that happen in every biological phenomenon (lack of information), it has been introduced in the paper [14], a statistical mechanics framework for living cells. Such a theory allow the accounting of a very relevant concept that hereto has remained unexplored throughout the thesis, namely the concept of cellular homeostasis.

Homeostasis expresses the will of living organisms to maintain a steady-state condition, adapting themself to the environment (time-depending) condition. This phenomenon is manifest at every scale of observation of living matter and actually, biologists associate the term homeostasis to describe the healthy-steady condition connected with the human body, organs, tissue, or cells. Exemplary, are those autoregulation mechanisms that maintain constant vital parameters like, temperature, osmotic pressure, ph, etc., all connected with the homeostatic machinery. It is evident

as homeostasis acts as an internal constraint in a living system, avoiding reaching state-condition incompatible with life.

In the current chapter, we focus on the homeostasis of the intracellular environment, which affects the behavior of a cell allowing it to avoid death. In fact, the living cell maintains a sort of steady-state equilibrium, henceforth called homeostatic equilibrium, that allows them to maintain their own vital activities. Specifically, in [14] it is assumed that cells are entropic and so that they manifest fluctuations in order to support the homeostasis; such an attitude is here modeled accounting for a specific internal constraint during entropy maximisation procedure for the definition of homeostatic equilibrium (see further section). Actually, the framework shown by the work [14] is an impressive change of perspective in the study and modeling of living cells. This conjecture would explain the reason why the replication of an identical in-vitro experiment does not provide the very same results but variability in the experimental observations. In fact, if it is true that cells are entropic, what biologists see in their experiments are nothing but the manifestations of the microstates accessible at the thermodynamic system called cell.

9.1.1 Analogies among the classic and homeostatic ensemble

Observing the interphase period of a cell cycle (usually valid for times observation from a few hours to few days), during an in-vitro experiment, is possible to attest that the values of physics-observables show fluctuations and variabilities. This uncertainty in the results is characteristic of living systems and mark their complexity. The assumption upon which is based on the current model is that such an uncertainty in the results is due to the entropic nature of homeostatic equilibrium [14].

In order to describe the macro-world through the behavior of particles constituent the micro one, we should study each individual molecule[1] that composes the macroscopic system. However, considering that inside a mole of a substance is present a huge amount of constituents (in the order of the number of Avogadro[2]), the attempt to describe every single particle evolution is practically an impossible path. Nevertheless, we can study the average properties of this huge set of particles, by means of statistical analysis [12].

Actually, we will provide a further method to utilize the statistical mechanic's architecture, which will be a real paradigmatic change in the study of cellular activities.
In fact, in the current chapter, we are interested in the statistical mechanics' description of the thermodynamic equilibrium state. Actually, a qualitative comparison among canonical and grand canonical ensembles describing the equilibrium state for closed and open systems will be provided with the homeostatic ensemble describing the (dynamic-) homeostatic equilibrium.

In classical or phenomenological thermodynamics, systems at the equilibrium state are fully described by a suitable characteristic function[3] [143] (pages 248). Such characteristic functions, also

[1] For instance, in a gaseous substance, the motion of the molecules and atoms is unceasing and continuously in evolution, obviously even at the so-call thermodynamic stable equilibrium state, i.e. the state where usually macroscopic observables do not change in time [12].

[2] $\mathcal{N}_A \simeq 6 \times 10^{23}$.

[3] All the properties of a system at equilibrium state, are deducible by means of derivations or algebraic manipula-

called thermodynamic potentials are generally the entropy or the internal energy rather than their Legendre transformation, which usually tend to assume a maximum or minimum value at a stable equilibrium state [145] (page 76). According to the typology of the equilibrium system itself (e.g. corresponding to an isolated or closed, rather than open system), and depending on the independent variables [143, 145, 12, 13] (pages 248-250, 75-83, 80 and 88-97 respectively), one of the possible above mentioned thermodynamic potential become the more suitable in order to describe the equilibrium state of the system.

In statistical thermodynamics, we observe an analogous situation; namely, to every statistical ensemble [12] (page 30) corresponds to a specific choice of the independent variables, and consequently, an opportune expression of a probability distribution of the microstates and partition function [12] (page 80). For each individual cases, we will arrange the suitable thermodynamic potential $\mathcal{M}$, that is connected to the partition function (Z), by the following relation [12] (page 80):

$$\mathcal{M} = -\kappa_B T \ln(Z) \tag{9.1}$$

where $\mathcal{M}$ could be the Helmholtz free-energy (systems that exchange energy with the environment in the form of heat) or Gibbs free-energy (systems that exchange energy by changing volume as well) [12].

For sake of clarifying we discuss briefly a very notorious example, i.e. the statistical mechanic description of a system (closed) that exchanges energy (heat) with a thermal bath (reservoir[4] with thermal or heat capacity ideally tending to infinity) with a temperature equal to T_R. The probability distribution of the microstates of the system is well captured by the canonical ensemble. By means of entropy maximisation (trough the Lagrange multipliers method) under the constraint that the total energy (reservoir plus system) remain constant, we can deduce the notorious Boltzmann distribution [14, 12].

According to the features of this problem, the suitable independent variables to describe the phenomenology are $(T,V,\mathbf{n})$, and not the usual variables $(E,V,\mathbf{n})$ exhibited by an isolated system, inasmuch as the internal energy can fluctuate whereas the temperature is fixed by the reservoir. In phenomenological thermodynamics, these are the natural independent variables of the thermodynamic potential called Helmholtz free-energy (Ψ - largely used in the models presented throughout the thesis). Accordingly, following the (9.1), we found:

$$\Psi(T,V,\mathbf{n}) = -\kappa_B T_R \ln\left(Z(T,V,\mathbf{n})\right) \tag{9.2}$$

where $\kappa_B T_R$ is indicative of the distribution parameter [14]. Such a relationship acts as a bridge between the macro and the micro world allowing the full description of the system described above [12] (page 71).
It is very interesting how we can obtain the expression (9.2) without any modeling neither the thermal interaction nor all the dynamic time evolution of each molecule that composes the system [14].

tions of the opportune characteristic function [143] (pages 248)

[4]Specificity of reservoir description are well describe in [143] (page 87) and [12] (page 61)

Similarly to the practical impossibility to describe every single evolution of each particle forming a gaseous system in a stable equilibrium state, we clash with the impractical attempt to describe the multiple intracellular processes that support the dynamic homeostatic equilibrium of a cell. Every biological process is characterized by several intracellular signaling, whose interconnections determine a definite behavior of the cell. The triggering of the angiogenic stimulus too is characterized by multiple intracellular signaling cascades, mainly starting from VEGFR2 interaction with its ligands, and not all of these are well-known. Moreover, arise several experimental evidence of statistical effects and non-thermal fluctuations in living cells [14].

Summing up, the authors of [14] build a statistical thermodynamics framework for living cells, assuming that living cells are entropic and describing their homeostatic state (valid for the interphase period of the cell cycle), accounting for the concept of homeostatic ensemble involving the cellular homeostasis as a suitable additional internal constraint for entropy maximisation. It has to be clear that this internal constraint avoids the cell to reach its thermodynamic equilibrium state corresponding to the state of death of it [14].

9.1.2 Homeostatic ensemble

We start defining the thermodynamic system and the conditions that characterize it. Focusing on standard in vitro experiments, such as what we explained in the previous chapters, we can observe a cell adhere to a substrate enriched with ligands, where both, cell and substrate are immersed in a nutrient broth. The latter provides to the cell the opportune nutrients to survive. Moreover, owing to this nutrient bath, the cell, and the substrate, are maintained at constant temperature and pressure. Likewise of a system in contact with a heat reservoir, we do not focus on all the set-up, rather we give priority to the description of an open system composed of the adherent cell and the substrate, where the nutrients bath work like a reservoir.

In such a framework, the experimental evidence supports some of the fundamental hypotheses envisaged.
Firstly, in order to change its morphology, a cell spends much more time with respect to that necessary for internal proteins reorganization. Therefore, it follows that during the proteins rearrangement within the cell, the morphology could be assumed fixed and so the environment pressure and the thermodynamic temperature are the unique constraints for the cell. Therefore, such a thermodynamic system, at the thermodynamic equilibrium, is governed by the Gibbs free energy thermodynamic potential [14].

Subsequently, it is known that during the homeostatic state the cell morphology fluctuates. It maintains an equilibrium distribution of morphological states that stems from entropy function maximisation undergone to a specific internal constraint. Specifically, this constraint is the mechanism that forces/allows the cell to remains at the homeostatic equilibrium. This restraint is made explicit stating that, during morphology fluctuations, the average amount, inside the cell, of the sum of chemical species is retained; explicitly, the cell keeps an average value of the Gibbs free-energy (G_0) upon all the morphological states. Intriguingly, such a constraint can be estimated when the cell can manifest one and only one morphological state, namely when it is in suspension. In this situation, $G_0 = G$, ensuring a known value at the constraint necessary for the above-mentioned

entropy maximisation. Also, it has to be clear the average Gibbs free-energy is characteristic of the type of cell but independent of the surrounding environment [14].

It is, therefore evident, how thermodynamic and homeostatic equilibrium are different. Practically, attains the homeostatic equilibrium, a net transfer of species is permitted among the system (substrate and adherent cell) and nutrient bath, if and only if the average amount of species inside the system remain constant, whereas a net energy transfer is avoided. Concerning the thermodynamical equilibrium, instead, neither a net transfer of energy nor species is allowed among system and bath, inasmuch as these quantities have to be fixed within isolated arrangement (system and nutrient bath together).
Homeostatic equilibrium is actually a dynamic equilibrium, that persists to avoid cell thermodynamic decadence. However, pinpointing the homeostatic equilibrium by means of a conventional way to entropy maximisation (similarly to classical equilibrium analysis) establishes a method to redefining the equilibrium state for living cells involving the notion of the homeostatic ensemble joint to that of homeostatic temperature ζ [14].

9.1.3 Model formulation

This statistical mechanics description of cells, similarly to the classical one, embeds the loss of information on the velocity and position of every particle (molecules) of the system (cell+ECM). In fact, macro variables are experimentally uncontrollable and only the pressure, temperature, and species concentration of the nutrient bath are manageable. Nevertheless, a further missing of details is manifested, namely the incertitude on the cell shape, that is an outcome obtained throughout homeostatic processes, concluding that, the cell form is not accurately ruled [14].

9.1.3.1 Molecular and morphological microstates

A twofold level of microstates is here introduced: molecular and morphological. These are justified by the deterministic correlation between the intracellular molecular arrangement and the cell shape.
In the first kind of microstate, the position and velocity of the total amount of species inside the system have a definite arrangement. Similar to the ensembles defined in classical statistical mechanics, the ensemble of molecular microstates is the collection of the sum of the molecular microstates in a specific molecular macrostate. This latter represents the probability distribution capable to provide the possibility to find a particular molecular microstate into this specific ensemble [14].
The second one, instead, is usually made by a huge number of molecular microstates, generally speaking, denoted the cell shape. Specifically, these molecular microstates are characteristic and so specific members of a given morphological microstate. Once more, we can define the ensemble of morphological microstates as the group of morphological microstates to a distinct morphological macrostate. Importantly, these morphological microstates are determined by the mapping/connection of material points on the ECM to those on the cell membrane. Whereas, all the points not in contact with the ECM are subjected to a given fixed pressure, namely that established by the nutrient bath [14].

9.1.3.2 Timescales consideration

From experimental evidence prove that subsists a considerable difference in the time evolution of molecular and morphological macrostate. Specifically the former evolves on the order of seconds whereas the latter of minutes, where the homeostatic equilibrium is maintained for hours. Typically, the diffusion rate of species inside the cell is what sets a limit at the time evolution of the molecular macrostate. Whereas, passing from a morphological microstate to another, entails cell shape mutation, a phenomenon that needs the rearrangement of the cytoskeletal machinery. Such a separation of the timescales allows for to elaborated the correct restraints on the system [14].

9.1.3.3 Entropy definition

In order to define the molecular and morphological ensembles via entropy maximisation, it is necessary to introduce:

- $P^{(i)}$, i.e. molecular microstate probability;
- $P^{(i,j)}$, i.e. the (joint) probability to find the molecular microstate (i) in the morphological microstate (j).

The joint probability $P^{(i,j)}$ is correlated to the probability of morphological microstate $P^{(j)}$, by the following relation:

$$P^{(i,j)} = P^{(i|j)}\ P^{(j)} \tag{9.3}$$

where $P^{(i|j)}$ is the probability to be in (i) knowing to be in (j). Hence, the total Gibbs entropy reads as:

$$I_T = -\sum_i P^{(i)} \ln P^{(i)} \tag{9.4}$$

It is a known fact that a specific molecular microstate can form part only of a single morphological microstate, therefore:

$$\begin{aligned}
I_T &= -\sum_i P^{(i)} \ln P^{(i)} = -\sum_j \sum_{i\in j} P^{(i,j)} \ln P^{(i,j)} && (9.5)\\
&= -\sum_j \sum_{i\in j} P^{(i|j)}\ P^{(j)} \ln\left(P^{(i|j)}\ P^{(j)}\right) && (9.6)\\
&= -\sum_j \sum_{i\in j} \left[P^{(i|j)}\ P^{(j)} \ln\left(P^{(i|j)}\right) + P^{(i|j)}\ P^{(j)} \ln\left(P^{(j)}\right)\right] && (9.7)\\
&= -\sum_j P^{(j)} \underbrace{\sum_{i\in j} P^{(i|j)} \ln\left(P^{(i|j)}\right)}_{-I_M^{(j)}} - \underbrace{\sum_j P^{(j)} \ln\left(P^{(j)}\right)}_{-I_\Gamma} \underbrace{\sum_{i\in j} P^{(i|j)}}_{1} && (9.8)\\
&= \sum_j P^{(j)} I_M^{(j)} + I_\Gamma && (9.9)
\end{aligned}$$

wherein $I_M^{(j)}$ and I_Γ are the entropy of the molecular microstates find in (j) and the entropy of the morphological microstates, respectively.

9.1.3.4 The setting of equilibrium in the range of seconds

On the basis of these considerations, over a period of time of few seconds, we can require that $dP^{(j)} = 0$, and so optimize I_T by imposing only $dP^{(i|j)} \neq 0$. Moreover, two conditions act on the system, namely the temperature and pressure that are fixed by the nutrient bath. It is evident how the total enthalpy of the system plus the bath (isolated set-up) has to be constant, similarly to the isobaric-isothermal ensemble. Significantly, in order to respect all the metabolic processes occurring inside the cell, the number of molecular species cannot be fixed [14].
Hence, knowing that $\sum_{i\in j} P^{(i|j)} = 1$ and $\sum_{i\in j} P^{(i|j)} h^{(i)} = H^{(j)}$ (constraints of the optimization problem), it is possible to impose the entropy maximisation [14]:

$$
\begin{aligned}
d\left[\sum_j P^{(j)} I_M^{(j)} + I_\Gamma - \lambda\left(\sum_{i\in j} P^{(i|j)} h^{(i)} - H^{(j)}\right) - (\lambda_0 - 1)\left(\sum_{i\in j} P^{(i|j)} - 1\right)\right] = 0 \\
\sum_j \underbrace{dP^{(j)}}_{0} I_M^{(j)} + \sum_j P^{(j)} dI_M^{(j)} + \underbrace{dI_\Gamma}_{0} - \lambda\left(\sum_{i\in j} dP^{(i|j)} h^{(i)}\right) - (\lambda_0 - 1)\left(\sum_{i\in j} dP^{(i|j)}\right) = 0 \\
\underbrace{\sum_j P^{(j)} dI_M^{(j)}}_{dI_M^{(j)} \sum_j P^{(j)} = dI_M^{(j)}} - \lambda\left(\sum_{i\in j} dP^{(i|j)} h^{(i)}\right) - (\lambda_0 - 1)\left(\sum_{i\in j} dP^{(i|j)}\right) = 0
\end{aligned}
$$

where $h^{(i)}$ is the enthalpy of the molecular microstates, and the above-mentioned restraints are enforced by means of the Lagrange multipliers λ and λ_0. Also, we have exploited the fact that $dI_M^{(j)}$ does not depend on (j) [14].
Finally, for every $(i) \in (j)$ with $P^{(i|j)}$ arbitrary and independent, we have [14]:

$$
\begin{aligned}
dI_M^{(j)} - \lambda\left(\sum_{i\in j} dP^{(i|j)} h^{(i)}\right) - (\lambda_0 - 1)\left(\sum_{i\in j} dP^{(i|j)}\right) = 0 \\
-\left[\sum_{i\in j} dP^{(i|j)} \ln\left(P^{(i|j)}\right) + \sum_{i\in j} \frac{P^{(i|j)}}{P^{(i|j)}} dP^{(i|j)}\right] - \lambda\left(\sum_{i\in j} dP^{(i|j)} h^{(i)}\right) - (\lambda_0 - 1)\left(\sum_{i\in j} dP^{(i|j)}\right) = 0 \\
-\sum_{i\in j}\left[+1 + \lambda h^{(i)} + (\lambda_0 - 1)\right] dP^{(i|j)} = 0
\end{aligned}
$$

$$
\ln\left(P_{eq}^{(i|j)}\right) + \lambda h^{(i)} + \lambda_0 = 0 \tag{9.10}
$$

$$
P_{eq}^{(i|j)} = \frac{\exp\left(-\lambda h^{(i)}\right)}{\exp\left(\lambda_0\right)} \tag{9.11a}
$$

$$
Z_M^{(j)} = \sum_{i\in j} \exp\left(-\lambda h^{(i)}\right) = \exp\left(\lambda_0\right) \tag{9.11b}
$$

$$
P_{eq}^{(i|j)} = \frac{\exp\left(-\lambda h^{(i)}\right)}{Z_M^{(j)}} \tag{9.11c}
$$

$$-\frac{1}{\lambda}\left[\ln\left(Z_M^{(j)}\right)+\ln\left(P_{eq}^{(i|j)}\right)\right]=h^{(i)} \tag{9.11d}$$

where the molecular partition function is denoted with $Z_M^{(j)}$. Knowing that $Z_M^{(j)}=\sum_{i\in j}\exp\left(-\lambda h^{(i)}\right)$, we can prove:

$$\begin{aligned}\frac{dZ_M^{(j)}}{d\lambda}&=\sum_{i\in j}-h^{(i)}\exp\left(-\lambda h^{(i)}\right)\\ \frac{d\ln\left(Z_M^{(j)}\right)}{d\lambda}&=\frac{1}{Z_M^{(j)}}\frac{dZ_M^{(j)}}{d\lambda}=-\frac{1}{Z_M^{(j)}}\sum_{i\in j}h^{(i)}\exp\left(-\lambda h^{(i)}\right).\end{aligned} \tag{9.12}$$

Therefore:

$$H^{(j)}=\sum_{i\in j}P_{eq}^{(i|j)}h^{(i)}=\sum_{i\in j}\exp\left(\frac{-\lambda h^{(i)}}{Z_M^{(j)}}\right)h^{(i)}=-\frac{d\ln\left(Z_M^{(j)}\right)}{d\lambda}. \tag{9.13}$$

By introducing the maximised molecular entropy $S_M^{(j)}\equiv\max_{P^{(i|j)}}\left[I_M^{(j)}\right]$, it is possible to found:

$$\begin{aligned}H^{(j)}&=\sum_{i\in j}P_{eq}^{(i|j)}h^{(i)}=-\frac{\sum_{i\in j}P_{eq}^{(i|j)}\left[\ln\left(Z_M^{(j)}\right)+\ln\left(P_{eq}^{(i|j)}\right)\right]}{\lambda}\\ &=-\frac{1}{\lambda}\underbrace{\sum_{i\in j}P_{eq}^{(i|j)}\left[\ln\left(P_{eq}^{(i|j)}\right)\right]}_{S_M^{(j)}}-\frac{1}{\lambda}\sum_{i\in j}P_{eq}^{(i|j)}\left[\ln\left(Z_M^{(j)}\right)\right]\\ S_M^{(j)}&=\lambda H^{(j)}+\ln\left(Z_M^{(j)}\right).\end{aligned} \tag{9.14}$$

Owing to the eq. (9.14) we deduce that $\frac{\partial S_M^{(j)}}{\partial H^{(j)}}=\lambda$, but, at the same time, by means of the definition $\frac{\partial H^{(j)}}{\partial S_M^{(j)}}=\kappa_B T$, we can determine $\lambda=\frac{1}{\kappa_B T}$. Similarly to expression (9.1), we found:

$$H^{(j)}-\kappa_B T S_M^{(j)}=-\kappa_B T\ln\left(Z_M^{(j)}\right) \tag{9.15}$$

We are going to introduce now the Gibbs free energy for the current problem:

$$\begin{aligned}\mathcal{G}^{(j)}&\equiv\sum_{i\in j}P^{(i|j)}h^{(i)}-\kappa_B T I_M^{(j)}\\ \mathcal{G}^{(j)}&\equiv\sum_{i\in j}P^{(i|j)}h^{(i)}+\kappa_B T\sum_{i\in j}P^{(i|j)}\ln\left(P^{(i|j)}\right)\end{aligned} \tag{9.16}$$

where $G^{(j)}\equiv\min_{P^{(i|j)}}\left[\mathcal{G}^{(j)}\right]$ when $P^{(i|j)}=P_{eq}^{(i|j)}$. Hence, the (9.15), become:

$$\begin{aligned}G^{(j)}&=-\kappa_B T\ln\left(Z_M^{(j)}\right),\\ G^{(j)}&=H^{(j)}-\kappa_B T S_M^{(j)}.\end{aligned} \tag{9.17}$$

Let $U^{(j)} = \kappa_B T S_M^{(j)} - pV + \sum_\alpha \chi_\alpha^{(j)} N_\alpha^{(j)}$ be the expression (Euler relation - see also (C.2) -) of the internal energy of the morphological microstates (j), where [14]:

- p is the pressure and V the volume;
- $\chi_\alpha^{(j)}$ is the chemical potential refering to the species α;
- $N_\alpha^{(j)}$ is the mean quantity of α species in (j), with $\sum_{i\in j} P^{(i|j)} n_\alpha^{(i)} = N_\alpha^{(j)}$;
- $n_\alpha^{(i)}$ is the average amount of species α in the molecular microstate.

It is known (see the corresponding Appendix C) that $H^{(j)} = U^{(j)} + pV = \kappa_B T S_M^{(j)} + \sum_\alpha \chi_\alpha^{(j)} N_\alpha^{(j)}$, therefore the Gibbs free energy assumes the following expression [14]:

$$G^{(j)} = \sum_\alpha \chi_\alpha^{(j)} N_\alpha^{(j)} \,. \tag{9.18}$$

9.1.3.5 The setting of the equilibrium in the range of hours

In the case where $P^{(j)}$ evolves up to find the "equilibrium state", and so for a timespan of many minutes (hours), the entropy function reads as follow [14]:

$$\begin{aligned} I_T^{'} &= \sum_j P^{(j)} I_M^{(j)} + I_\Gamma = -\sum_j P^{(j)} \underbrace{\sum_{i\in j} P_{eq}^{(i|j)} \ln\left(P_{eq}^{(i|j)}\right)}_{S_M^{(j)}} \underbrace{-\sum_j P^{(j)} \ln\left(P^{(j)}\right)}_{-I_\Gamma} \\ &= -\frac{1}{\kappa_B T} \sum_j P^{(j)} \left(G^{(j)} - H^{(j)}\right) - \sum_j P^{(j)} \ln\left(P^{(j)}\right) \end{aligned} \tag{9.19}$$

wherein the expression of the molecular entropy is equal to that attain at its equilibrium expression. Maximising $I_T^{'}$ will make it possible to deduce the equilibrium distribution $P_{eq}^{(j)}$. Intriguingly, in the case that the unique constraint place in the optimization processes is $\sum_j P^{(j)} = 1$, we achieve the expression [14]:

$$P_{eq\ (dead)}^{(j)} = \frac{\exp\left[\left(G^{(j)} - H^{(j)}\right)/\kappa_B T\right]}{\sum_j \exp\left[\left(G^{(j)} - H^{(j)}\right)/\kappa_B T\right]} \tag{9.20}$$

that correspond to the gran isothermal and isobaric canonical distribution, that lead to the thermodynamic potential (gran potential):

$$\begin{aligned} \Xi &\equiv \kappa_B T \ln Z_\Xi \,, \\ Z_\Xi &= \sum_j \exp\left[\left(G^{(j)} - H^{(j)}\right)/\kappa_B T\right] \,. \end{aligned} \tag{9.21}$$

Such a kind of equilibrium leads to having the same concentration of mobile species both in the system that in the bath, an event that we know being avoided by a living cell, except at its death. Living cells, therefore, have different behavior [14].
Cells attain the homeostatic (steady-)state equilibrium. In the current framework, this tendency of

the system is mathematically codified imposing a further restraint, namely that the average Gibbs free-energy remains steady all along with homeostatic equilibrium [14]:

$$\sum_j P^{(j)} G^{(j)} = \overline{G}\,. \tag{9.22}$$

Moreover, in order to ensure that the temperature stays fix, not only for the order of seconds but also for hours, we need to impose another constraint, i.e $\sum_j P^{(j)} H^{(j)} = \overline{H}$. Again, it is possible to administer these limitations, through the Lagrange multipliers during (9.19) maximisation. Hence [14]:

$$\begin{aligned} &-d\left[\frac{1}{\kappa_B T}\sum_j P_{eq}^{(j)}\left(G^{(j)}-H^{(j)}\right)+\sum_j P_{eq}^{(j)}\ln\left(P_{eq}^{(j)}\right)\right. \\ &\left.+\zeta_1\left(\sum_j P_{eq}^{(j)}G^{(j)}-\overline{G}\right)+\lambda_2\left(\sum_j P_{eq}^{(j)}H^{(j)}-\overline{H}\right)+(\lambda_1-1)\left(\sum_j P_{eq}^{(j)}-1\right)\right]=0\,. \end{aligned} \tag{9.23}$$

Similarly to the previous case, we have to notice that $P_{eq}^{(j)}$ is arbitrary, therefore:

$$\begin{aligned} &-\left[\frac{1}{\kappa_B T}\sum_j dP_{eq}^{(j)}\left(G^{(j)}-H^{(j)}\right)+\sum_j dP_{eq}^{(j)}\ln\left(P_{eq}^{(j)}\right)-\sum_j dP_{eq}^{(j)}\right. \\ &\left.+\zeta_1\left(\sum_j dP_{eq}^{(j)}G^{(j)}\right)+\lambda_2\left(\sum_j dP_{eq}^{(j)}H^{(j)}\right)+(\lambda_1-1)\left(\sum_j dP_{eq}^{(j)}\right)\right]=0 \end{aligned} \tag{9.24}$$

$$\begin{aligned} &-\left[\frac{1}{\kappa_B T}\sum_j dP_{eq}^{(j)}\left(G^{(j)}-H^{(j)}\right)+\sum_j dP_{eq}^{(j)}\ln\left(P_{eq}^{(j)}\right)\right. \\ &\left.+\zeta_1\left(\sum_j dP_{eq}^{(j)}G^{(j)}\right)+\lambda_2\left(\sum_j dP_{eq}^{(j)}H^{(j)}\right)+\lambda_1\left(\sum_j dP_{eq}^{(j)}\right)\right]=0\,. \end{aligned} \tag{9.25}$$

Consequently:

$$-\frac{\left(G^{(j)}-H^{(j)}\right)}{\kappa_B T}-\ln\left(P_{eq}^{(j)}\right)-\zeta_1 G^{(j)}-\lambda_2 H^{(j)}-\lambda_1=0 \tag{9.26}$$

$$\begin{aligned} P_{eq}^{(j)} &= \exp\left[-\frac{\left(G^{(j)}-H^{(j)}\right)}{\kappa_B T}-\zeta_1-G^{(j)}-\lambda_2 H^{(j)}-\lambda_1\right] \\ &= \exp\left[-\underbrace{\left(\zeta_1+\frac{1}{\kappa_B T}\right)}_{\zeta}G^{(j)}-\left(\lambda_2-\frac{1}{\kappa_B T}\right)H^{(j)}\right]\exp\left[-\lambda_1\right] \\ &= \frac{1}{\exp\left[\lambda_1\right]}\exp\left[-\zeta G^{(j)}-\left(\lambda_2-\frac{1}{\kappa_B T}\right)H^{(j)}\right] \\ &= \frac{1}{Z}\exp\left[-\zeta G^{(j)}-\left(\lambda_2-\frac{1}{\kappa_B T}\right)H^{(j)}\right], \end{aligned} \tag{9.27}$$

where Z is the partition function for the morphological microstates, and owing to the fact that $\sum_j P^{(j)} = 1$, we derive [14]:

$$Z \equiv \sum_j \exp\left[-\zeta G^{(j)} - \left(\lambda_2 - \frac{1}{\kappa_B T}\right) H^{(j)}\right] = \exp\left[\lambda_1\right] . \tag{9.28}$$

In statistical mechanics, in a given thermodynamic (homeostatic) equilibrium state, knowing the partition function means determines all the thermodynamic variables. As a result, the average enthalpy and Gibbs free-energy stems for [14]:

$$\begin{aligned} \overline{G} &= -\frac{\partial \ln Z}{\partial \zeta} , \\ \overline{H} &= -\frac{\partial \ln Z}{\partial \overline{\lambda}} = -\frac{\partial \ln Z}{\partial \lambda_2} , \text{with: } \overline{\lambda} = \lambda_2 - \frac{1}{\kappa_B T} . \end{aligned} \tag{9.29}$$

Moreover:

$$\begin{aligned} P_{eq}^{(j)} &= \frac{1}{Z} \exp\left[-\zeta G^{(j)} - \left(\lambda_2 - \frac{1}{\kappa_B T}\right) H^{(j)}\right] \\ P_{eq}^{(j)} Z &= \exp\left[-\zeta G^{(j)} - \left(\lambda_2 - \frac{1}{\kappa_B T}\right) H^{(j)}\right] \\ \sum_j P^{(j)} \left[\ln P_{eq}^{(j)} + \ln Z\right] &= \sum_j P^{(j)} \left[-\left(\zeta_1 + \frac{1}{\kappa_B T}\right) G^{(j)} - \left(\lambda_2 - \frac{1}{\kappa_B T}\right) H^{(j)}\right] \\ -S_\Gamma + \ln Z &= -\left(\zeta_1 + \frac{1}{\kappa_B T}\right) \overline{G} - \left(\lambda_2 - \frac{1}{\kappa_B T}\right) \overline{H} \\ S_\Gamma &= \ln Z + \zeta \overline{G} + \overline{\lambda} \overline{H} \\ \frac{1}{\kappa_B T}\left(\overline{G} - \overline{H}\right) - I_\Gamma &= -\ln Z - \zeta_1 \overline{G} - \lambda_2 \overline{H} \\ S_T &= \ln Z + \zeta_1 \overline{G} + \lambda_2 \overline{H} \end{aligned} \tag{9.30}$$

where $S_T \equiv \max_{P^{(j)}} \left[I_T^{'}\right]$ is the maximised entropy.
Significantly, it has to be clear that the temperature constraint is valid either in short that in long timescale, therefore observing that Gibbs free-energy does not depend on enthalpy [14].:

$$\begin{aligned} \frac{\partial S_T}{\partial \overline{G}} &= \zeta_1 = \zeta - \frac{1}{\kappa_B T} , \\ \frac{\partial S_\Gamma}{\partial \overline{G}} &= \zeta , \\ \frac{\partial S_T}{\partial \overline{H}} &= \lambda_2 = \frac{1}{\kappa_B T} , \end{aligned} \tag{9.31}$$

where S_Γ is the morphological entropy and $\overline{\lambda} = 0$.
Finally, the eq. (9.27) become:

$$\begin{aligned} P_{eq}^{(j)} &= \frac{1}{Z} \exp\left[-\zeta G^{(j)}\right] , \\ Z &= \sum_j \exp\left[-\zeta G^{(j)}\right] . \end{aligned} \tag{9.32}$$

A pivotal characteristic of the present formulation is given by the loss of information resulting from the impossibility of knowing the large number of variables associated with homeostatic processes (some of which are not precisely known) and the volatility of ions motion (Brownian). Similar to what happens in a standard statistical mechanics set-up, the lack of knowledge corresponds to a production of entropy, in this specific case of morphological entropy. If this does not happen, namely if we could precisely know all the variables of homeostatic processes, the production of morphological entropy would be equal to zero and the increase in molecular entropy would guide the trajectory pursued by the thermodynamic set-up (under the constraints of T and p constant). Hence, given the uncertainty on the biological mechanisms of homeostasis, it is preferred to represent the uncertainty, in a coarse-grained model, by introducing morphological entropy. Analogously to what we can observe in in-vitro models (statistics of biological observables), through a statistical mechanics model for living cells, it is possible to determine the possible states permissible to the system [14].

For instance, a fundamental role in the transformation of cell morphology is played by the polymerization of actin (as explained in chapter 6 and section 2.1.2). The impossibility of fully describing and predicting every single process of similar phenomena makes the model summarized here interesting. Importantly, it is precisely the application of $\sum_j P^{(j)} G^{(j)} = \overline{G}$ (restraints) the core of the homeostatic statistical mechanics scheme, a framework able to capture either the natural trend of living cells to avoid achieving the dead-matter thermodynamic equilibrium that the high volatility of the biological statics observable. It is critical to understand that in the current formulation, an extended version of the a priori assumption is added to the standard one. Consequently, it is stated that, in the morphological macrostate, the system is balanced with the greatest part of morphological microstates, presuming that the massive quantity of homeostatic operations offers the capability to the system to have access to morphological microstates. This is similar to the customary a priori assumption. In fact, in classical statistical mechanics, the system can access every molecular microstate owing to Hamiltonian mechanics [14].

In statistical mechanics, it is shared the method to take a view of the statistical ensemble as the collection of (virtual) copies of the system, each of which corresponding to every microstate. Particularly, we can see the homeostatic ensemble as the group of copies of the system as many as the number of morphological microstates. The distribution $P_{eq}^{(j)}$ determines how the above-mentioned copies, each one with the corresponding $G^{(i)}$, are spread in the homeostatic ensemble. Through the (9.31) we can see how the parameter ζ is connected with the morphological entropy I_Γ. Hence, a relevant result of this formulation consists of the following formal equivalence: *"the distribution parameter ζ, similar to $1/T$ (inverse of thermodynamic temperature) that connect average enthalpy and molecular entropy, defines the rate of variation of S_Γ with $\overline{G}$, and besides, ζ defines the increment of incertitude in the morphological microstates in a similar fashion to $1/T$ for the molecular ones"*. This is the reason why $1/\zeta$ is called *homeostatic temperature*. In fact, this parameter estimates the fluctuation in a long observation time (differently for T). Finally, it has to be clear that ζ is a property of the system and not of the whole set-up. This is the main reason that avoids defining a micro-homeostatic ensemble [14].

Again, as previously anticipated, we can establish a strict connection between the partition function and the thermodynamic potential (homeostatic potential) for the problem, comparatively with

what happens in the canonical (Helmholtz free-energy) or isobaric-isothermal (Gibbs free-energy) ensemble. Starting to (9.32), it is possible to deduce:

$$\mathcal{M} = -\frac{1}{\zeta}\ln Z\,. \tag{9.33}$$

Moreover, $1/\zeta$ is an indicator for the cell state (biochemical state) providing high values (P_{eq} tends to be uniform) for the high variability of the observations, and low for lower variations of the distribution (peaked P_{eq}). Furthermore, these parameters depend on ECM or, for in-vitro experiments, cell-substrate (or scaffolds). Clearly, $1/\zeta = 0$ when there are no uncertainties in the morphological microstate and the cell adopts a singular (unique) morphological microstate with traction-free surfaces (cell in suspension) [14].

9.1.3.6 Homeostatic constraint calculation

In a living cell, through a homeostatic statistical mechanics scheme, homeostasis is framed as an internal constraint able to maintain the average amount of the molecular species in the cell itself. Intriguingly, such restraint does not depend primarily on the microenvironment surrounding the cell, but on the kind of cell, we are studying [14].

In the current section, we want to explain that is the $G^{(j)}$, namely the Gibbs free-energy in the morphological microstates, the mathematical function through which the homeostatic constraint is conveyed [14].

In this scenario, it plays a relevant rule a cell in suspension (free-standing). Experimental pieces of evidence show negligible cell form fluctuations for cells in suspension. Consistently, through the statistical model introduced here, a single equilibrium morphological microstate is predicted for the free-standing cell. This is coherent with the resolution of a boundary problem which needs research of the minimum of the Gibbs free energy for a system with a single equilibrium state. In fact, differently from a cell laid on an ECM, a suspension cell has spatially uniform boundary conditions (e.g. atmospheric pressure). Therefore, it can not manifest several morphological microstates, as those corresponding to various equilibrated tractions among cells and ECM due to their contact dynamic. Nevertheless, although it may seem natural to assign a spherical shape to cells in this specific free-standing condition, this is wrong. Indeed, it must be clear that the shape of a suspended cell varies according to the type of cell that we are analyzing [14].

It is known that the expression of the Gibbs free-energy of morphological microstates follows the eq. (9.15), hence, for a cell in suspension, it reads:

$$G_S = \sum_{cell(\alpha)} \chi_\alpha^S N_\alpha^S\,. \tag{9.34}$$

Moreover, we need to account for the free-energy provide by the ECM, that in this set-up remain isolated by the cell, therefore:

$$G_{ECM}^S = \sum_{ECM(\beta)} \chi_\beta^S N_\beta^S\,. \tag{9.35}$$

When the cell goes in contact with the ECM, the morphological microstate manifests the following Gibbs free-energy:

$$G^{(j)} = \sum_{system(\delta)} \chi_\delta^{(j)} N_\delta^{(j)} = G_S + G_{ECM}^S + \Delta G^{(j)} \tag{9.36}$$

where an additional term has been to be taken into account, namely the interaction energy between ECM and cell ($\Delta G^{(j)}$). In fact, the chemical and physical interplay between cell and ECM cause either energetic changes in the surface energy of ECM that the appearance of the tractions exerts by the cell on the matrix. Moreover, for a simple system (see [143] (page 263)), with temperature and pressure fixed by the surroundings, it is possible to take advantage of the Gibbs-Duhem relation (see also (C.3)) and deduced [14]:

$$\begin{aligned} \Delta G^{(j)} &= \sum_{system(\delta)} \Delta\chi_\delta^{(j)} N_\delta^{(j)} + \chi_\delta^{(j)} \Delta N_\delta^{(j)} \\ \sum_{system(\delta)} \Delta\chi_\delta^{(j)} N_\delta^{(j)} &= 0 \quad \text{owing to Gibbs-Duhem relation} \\ \Delta G^{(j)} &= \sum_{cell(\alpha)} \chi_\alpha^S \Delta N_\alpha^{(j)} + \sum_{ECM(\beta)} \chi_\beta^S \Delta N_\beta^{(j)} \end{aligned} \tag{9.37}$$

where ΔN implies a variation of molecule species after cell-ECM interactions. Hence, the average Gibbs free-energy reads as follow:

$$\begin{aligned} \overline{G} &\equiv \sum_j P^{(j)} G^{(j)} = \sum_j P^{(j)} G_S + \sum_j P^{(j)} G_{ECM}^S + \sum_j P^{(j)} \Delta G^{(j)} \\ &= \sum_{cell(\alpha)} \chi_\alpha^S N_\alpha^S + \sum_{ECM(\beta)} \chi_\beta^S N_\beta^S + \sum_j P^{(j)} \left[\sum_{cell(\alpha)} \chi_\alpha^S \Delta N_\alpha^{(j)} + \sum_{ECM(\beta)} \chi_\beta^S \Delta N_\beta^{(j)} \right] \\ &= \sum_{cell(\alpha)} \chi_\alpha^S \sum_j P^{(j)} \underbrace{\left(N_\alpha^S + \Delta N_\alpha^{(j)} \right)}_{N_\alpha^{(j)}} + \sum_{ECM(\beta)} \chi_\beta^S \sum_j P^{(j)} \underbrace{\left(N_\beta^S + \Delta N_\beta^{(j)} \right)}_{N_\beta^{(j)}} \\ &= \sum_{cell(\alpha)} \chi_\alpha^S \underbrace{\sum_j P^{(j)} N_\alpha^{(j)}}_{\overline{N}_\alpha} + \sum_{ECM(\beta)} \chi_\beta^S \underbrace{\sum_j P^{(j)} N_\beta^{(j)}}_{\overline{N}_\beta} , \end{aligned} \tag{9.38}$$

where $\overline{N}$ expresses the average value of the molecular species in the morphological microstates. Several considerations are opportune at this point:

- we introduce the hypothesis that ECM is elastic, which implies $\Delta N_\beta^{(j)} = 0$
- the microenvironment surrounding the cell has no implications on the value of $\overline{N}_\alpha$, hence $\overline{N}_\alpha = N_\alpha^S$.

Therefore, the (9.38) assumes the form:

$$\overline{G} \equiv \sum_j P^{(j)} G^{(j)} = G_S + G_{ECM}^S \, . \tag{9.39}$$

Finally, accepting a model for cell describe in [180, 14] for $G^{(j)}$ ($\overline{G} \equiv \sum_j P^{(j)} G^{(j)} = G_S$ with $G^S_{ECM} = 0$), it is possible to derive through the ensemble average the form of G_S:

$$\sum_j P^{(j)} G^{(j)} \equiv \frac{1}{Z} \sum_j G^{(j)} \exp\left(\zeta G^{(j)}\right) = G_S \tag{9.40}$$

when the constant pressure, exercised by the bath, is the unique external load. Interesting, for a long period of observation we know $\overline{G}$ but do not the parameter distribution ζ. Viceversa, for a short time span, the thermodynamic temperature is known ex-ante while is the $\overline{H}$ that needs to be calculated [14].

9.1.4 Elliptic-cell's behavior

We consider now 2D-Elliptic cells placed on a substrate that mimics the behavior of the ECM. In this specific configuration (elliptic geometry), the cell is fully described by λ_1 and λ_2 or the two dimensionless semi-axes of the ellipse 9.1.

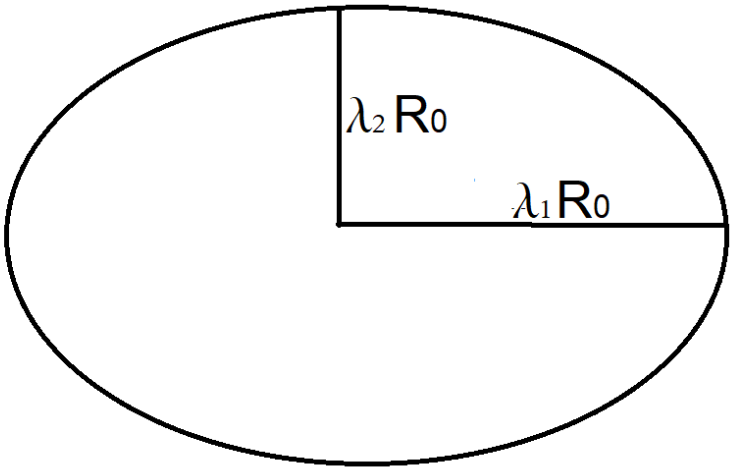

Figure 9.1: An elliptic cell spread on ECM with homogeneous chemo-mechanical features. R_0 is the radius of the cell in the reference configuration.

This work allows us to understand if an elliptic configuration can guarantee qualitatively correct information on cell behavior. In particular, we are going to explore the cell's responses to a non-ligand-coated substrate (elastic substrate, by testing various stiffnesses), although in the following theoretical treatment a ligands-coated substrate will be also accounted for (see Appendix H). It easily to deduce that for a uniform substrate the orientation of the ellipse does not matter. We can hypothesize that the cell is without a nucleus and that its Gibbs free energy can be described by means of the energetic model defined in [14] and [128].

9.1.4.1 Equations in supporting the calculations

In this section, we try to explain the fundamental equations of our formulation. This implies the deduction of the equations that allow us to calculate $\hat{G}_{tot} = \hat{G}_{cyto} + \hat{G}_{elast} + \hat{G}_{sub}$ for non-ligand-coated substrate and $\hat{G}_{tot} = \hat{G}_{cyto} + \hat{G}_{elast} + \hat{G}_{sub} + \hat{G}_{adh}$ for a ligand-coated substrate. Where:

- $\hat{G}_{cyto}$ is the energy per unit volume of the cytoplasm;
- $\hat{G}_{elast}$ is the energy per unit volume of the passive elasticity;
- $\hat{G}_{sub}$ is the energy per unit volume of the substrate;
- $\hat{G}_{adh}$ is the energy per unit volume due to adhesion.

It has to be clear that $\hat{G}_{tot} = \dfrac{G_{tot}}{V_0}$ where V_0 is the volume of the cell in the reference configuration and henceforth we call $G_0 = -24.0801 KPa$ the value of the Gibbs-free energy of a cell in suspension without nucleus.

$\hat{G}_{cyto}$'s computation for an elliptic cell

Let $\hat{G}_{cyto} = \rho_0 \kappa_B T \ln(\hat{N}_u)$ be the expression of the energy per unit volume of the cytoplasm, where $\hat{N}_u$, the unique unknown, is derived by iteration on the following expressions:

$$\begin{aligned} &\hat{N}_u + \frac{1}{V_0} \int_V \int_{-\frac{\pi}{2}}^{\frac{\pi}{2}} \hat{\eta} \hat{n}^{ss} d\phi dV = 1 \\ &\hat{\eta}\left(x_i, \phi\right) = \frac{\hat{N}_u \hat{\eta}_{max} \exp\left[\dfrac{\hat{n}^{ss}\left(\mu_u - \mu_b\right)}{\kappa_B T}\right]}{\pi \hat{n}^{ss} \hat{\eta}_{\max} + \hat{N}_u \exp\left[\dfrac{\hat{n}^{ss}\left(\mu_u - \mu_b\right)}{\kappa_B T}\right]} \end{aligned} \tag{9.41}$$

where:

- ρ_0 is the density of the stress-fibers packages per unit volume;
- $\hat{N}_u$ is the normalized number of unbound stress fibers determined by iteration on the previous equation;
- $\kappa_B T$ is the thermodynamic temperature.

Note that for an elliptic cell $\hat{n}_i^{ss} = \dfrac{\lambda_i}{\lambda_{ss}}$ where $\lambda_{ss} = \dfrac{1}{1+1.2}$.

$\hat{G}_{elast}$'s computation for an elliptic cell

The passive elasticity in the $2D$ setting is given by a $2D$ specialization of the Ogden-type hyperelastic strain energy density function:

$$\begin{aligned} \hat{G}_{elast} = \frac{1}{V_0} \int_{V_{cell}} \frac{2\mu}{m^2} \left[\left(\frac{\lambda_I}{\lambda_{II}}\right)^{\frac{m}{2}} + \left(\frac{\lambda_{II}}{\lambda_I}\right)^{\frac{m}{2}} - 2 \right] + \frac{\kappa}{2} \left(\lambda_I \lambda_{II} - 1\right)^2 \\ + \overline{\kappa} \mathcal{H}\left(J_c - \lambda_I \lambda_{II}\right) \ln\left(\lambda_I \lambda_{II} + 1 - J_c\right) \end{aligned} \tag{9.42}$$

where:

- λ_1 and λ_2 are the principal stretches;
- μ and κ are the shear modulus and in-plane bulk modulus respectively;
- m is a material constant governing the nonlinearity of the deviatoric elastic response;
- $\overline{\kappa} \mathcal{H}\left(J_c - \lambda_I \lambda_{II}\right) \ln\left(\lambda_I \lambda_{II} + 1 - J_c\right)$ is added to the passive energetic contribute modulated by $\overline{\kappa} = 1\ GPa$ when the areal stretch $\lambda_I \lambda_{II}$ drops below $J_c = 0.6$, with $\mathcal{H}(\cdot)$ denoting the Heaviside step function;
- λ_{III} is the further principal stretch and due to the assumption of incompressible behavior of the cell has the following expression $\lambda_{III} = \dfrac{1}{\lambda_I \lambda_{II}}$.

The passive Cauchy stress, given in terms of the principal (passive) Cauchy stresses, reads as follows:

$$\sigma^p_{ij} p^{(k)}_j = \sigma^p_k p^{(k)}_i \equiv \lambda_k \frac{\partial \Phi_{elast}}{\partial \lambda_k} \tag{9.43}$$

where $p^{(k)}_i$ $(k = I,II)$ are the unit vectors in the principal direction.

$\hat{G}_{sub}$'s computation for an elliptic cell

The energetic contribute exercised by the cell tractions on the substrate is here shown. Specifically, in the current formulation, these are connected with stresses provided by the active mechanical behavior of the cell (stress-fibers) and the passive one (Ogden model). The free-energy of the substrate writes as follows:

$$\hat{G}_{sub} = \frac{1}{V_0} \int_A \frac{1}{2} \frac{(T_1^2 + T_2^2)}{k_{sub}} dA \tag{9.44}$$

where:

- T_1 and T_2 are the value of the tractions along the directions x_1 and x_2;
- A is the area of the substrate in contact with the part of the cell membrane that produces tractions;
- k_{sub} is the stiffness of the elastic substrate.

In Appendix H, the theoretical formulations that explicated the energetic contribute related to the adhesion phenomena have been provided..

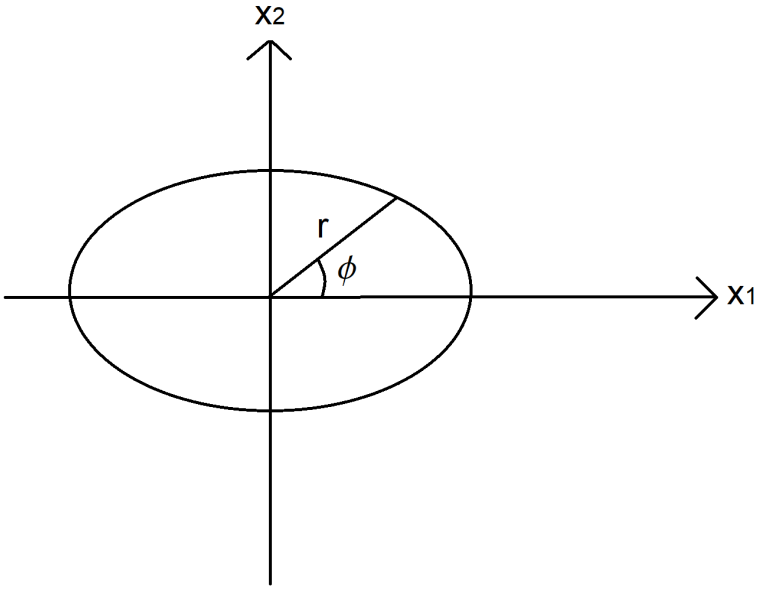

Figure 9.2: Elliptic cell spread on ECM with homogeneous chemo-mechanical features.

Tractions' computation for an elliptic cell The expression of the deformation gradient at principal directions reads as follow:

$$F = \begin{pmatrix} \lambda_1 & 0 \\ 0 & \lambda_2 \end{pmatrix} \tag{9.45}$$

Let $n_1 = \dfrac{\lambda_2 \cos(\phi)}{\sqrt{\lambda_2 \cos(\phi)^2 + \lambda_1 \sin(\phi)^2}}$ and $n_2 = \dfrac{\lambda_1 \sin(\phi)}{\sqrt{\lambda_2 \cos(\phi)^2 + \lambda_1 \sin(\phi)^2}}$ be the components of the normal versor to the ellipse.
Let σ_1 and σ_2 the Cauchy principal stress. The force per unit length along the cell periphery is:

$$f_1 = (\sigma_1 n_1)t \quad f_2 = (\sigma_2 n_2)t \tag{9.46}$$

in which t is the current thickness of the $2D$ cell.
We now "smear" these forces over the whole cell by assuming tractions vary linearly from the center of the ellipse. We consider direction along a define $R = R0\sqrt{\lambda_1 \cos(\phi)^2 + \lambda_2 \sin(\phi)^2}$ where $R0$ is the radius of the cell in the reference configuration. Let T_i with $i = 1,2$ be the tractions (variables along r as $T_i = \mathtt{k}r$) exert by the cell, such that:

$$\begin{aligned} &\int_0^R T_i r d\phi dr = \int_0^R f_i dr d\phi \\ &\frac{\mathtt{k}R^3}{3} = (\sigma_i n_i)tR \Longrightarrow \mathtt{k} = \frac{3(\sigma_i n_i)t}{R^2} \\ &T_i = \frac{3(\sigma_i n_i)t}{R^2} r \,. \end{aligned} \tag{9.47}$$

According to this, we dispose of a traction distribution over the whole cell, that satisfies the global equilibrium of forces, and can be used to calculate the work exerted on the Winkler foundation.

9.2 Numerical results

In order to deduce with enough accuracy the correct step of the discretization of λ_1 and λ_2, an analysis able to determine the probability distribution of the spread area and aspect ratio will be implemented in this specific geometric configuration. Accordingly, we have varied λ_1 and λ_2 in the following range:

$$\begin{aligned} \lambda_1 &= (d\lambda : d\lambda : 15) * R0 \\ \lambda_2 &= (d\lambda : d\lambda : 15) * R0 \end{aligned} \tag{9.48}$$

where $d\lambda = 0.01$ is the aforementioned discretization step, and $R0 = 30\mu m$ is the radius of the cell in suspension.

For each pair (λ_1, λ_2) we can evaluate the Gibbs free-energy of the configuration, $G(\lambda_1, \lambda_2)$ and probability distribution $P(\lambda_1, \lambda_2)$ (as well as ζ and Z). Importantly, it has to be highlighted that we use the definition of conditional probability to find $P(\lambda_1)$ and $P(\lambda_2)$:

$$P(\lambda_1) = \int_{\lambda_2} P(\lambda_1, \lambda_2) d\lambda_2 \,, \quad P(\lambda_2) = \int_{\lambda_1} P(\lambda_1, \lambda_2) d\lambda_1 \,. \tag{9.49}$$

Now, to determine $P(A)$ (where A stands for the area) and $P(ASR)$ (where ASR stands for the aspect ratio), we know that different pairs of (λ_1, λ_2) give the same area. However, the probability of obtaining a pair $(\lambda_1^i, \lambda_2^i)$ is independent of any other pair $(\lambda_1^j, \lambda_2^j)$. Hence:

$$\begin{aligned} P(A) &= \sum_{\lambda_1,\lambda_2} P(\lambda_1,\lambda_2) \text{ with } \lambda_1 \cdot \lambda_2 = A \,, \\ P(ASR) &= \sum_{\lambda_1,\lambda_2} P(\lambda_1,\lambda_2) \text{ with } \max\left\{\frac{\lambda_1}{\lambda_2}, \frac{\lambda_2}{\lambda_1}\right\} = ASR \,. \end{aligned} \tag{9.50}$$

Since λ_1 and λ_2 are independent variables, $P(\lambda_1,\lambda_2) = P(\lambda_1)P(\lambda_2)$, it is attained:

$$\begin{aligned} P(A) &= \sum_{\lambda_1,\lambda_2} P(\lambda_1)P(\lambda_2) \text{ with } \lambda_1 \cdot \lambda_2 = A \,, \\ P(ASR) &= \sum_{\lambda_1,\lambda_2} P(\lambda_1)P(\lambda_2) \text{ with } \max\left\{\frac{\lambda_1}{\lambda_2}, \frac{\lambda_2}{\lambda_1}\right\} = ASR \,, \\ P(T) &= \sum_{\lambda_1,\lambda_2} P(\lambda_1)P(\lambda_2) \text{ with } T_i = \frac{3(\sigma_i n_i)t}{R^2} r \,. \end{aligned} \tag{9.51}$$

The above-mentioned distributions are shown below:

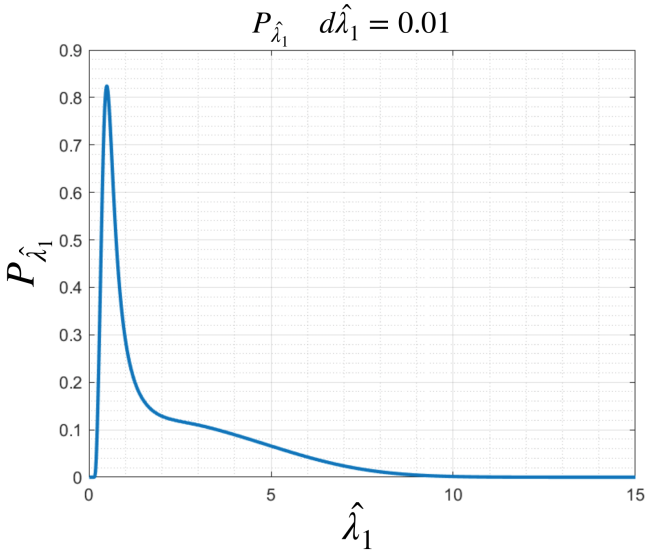

(a)

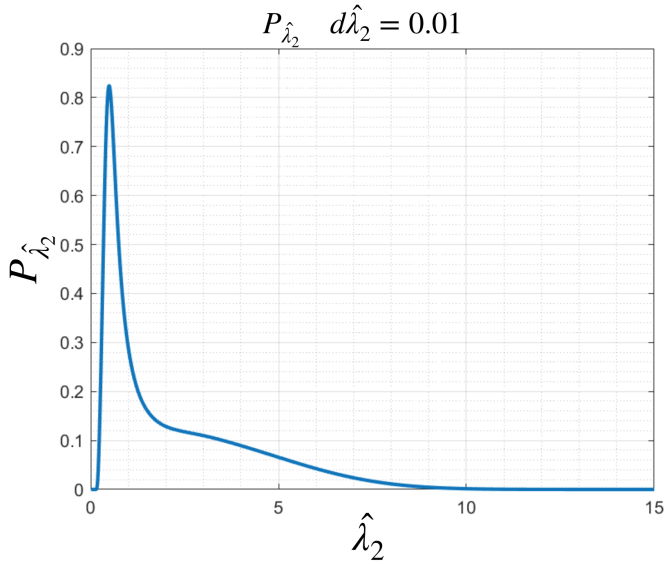

(b)

Figure 9.3: Figures show the distribution $P(\hat{\lambda}_1)$ and $P(\hat{\lambda}_2)$, expressed in terms of the dimensionless values. Average values are $\overline{\lambda}_1 = 2.2199$ and $\overline{\lambda}_1 = 2.2199$.

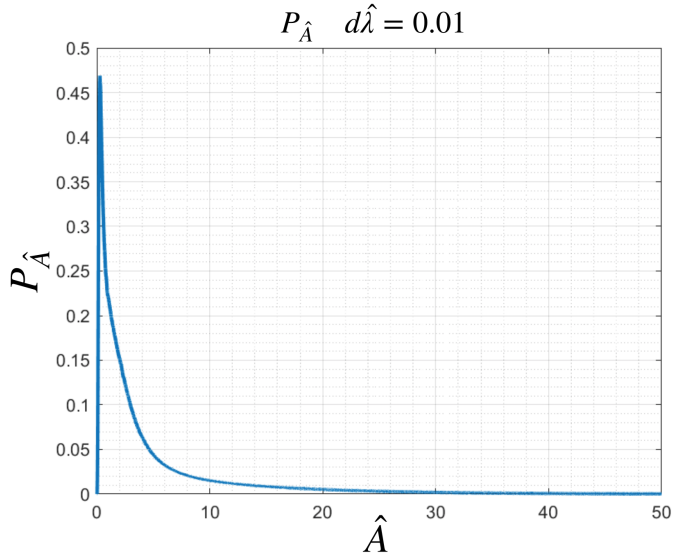

(a)

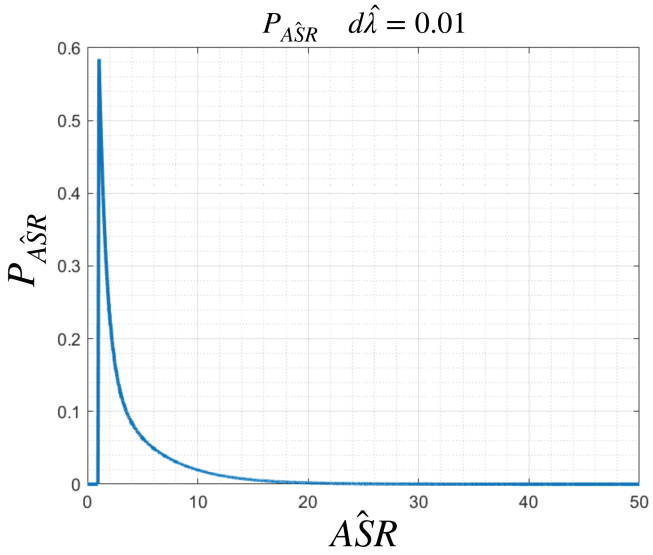

(b)

Figure 9.4: Figures show the distribution $P(\hat{A})$ and $P(A\hat{S}R)$, expressed in terms of the dimensionless values. Average values are $\overline{A} = 2.4154$ and $\overline{ASR} = 2.5320$.

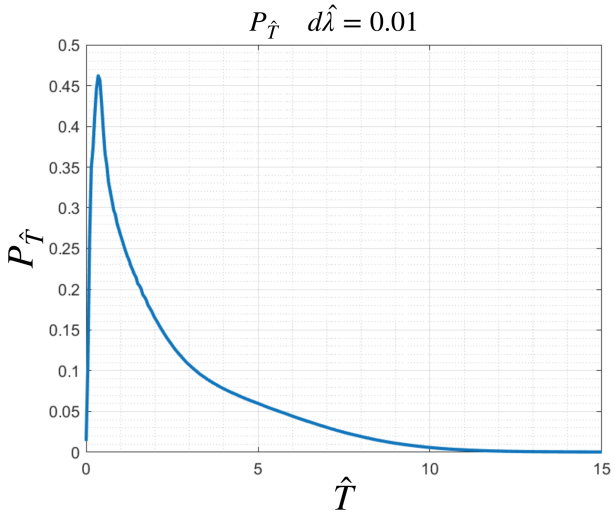

Figure 9.5: Figures show the distribution $P(\hat{T})$ average, expressed in terms of the dimensionless values. Average values are $\overline{T} = 2.1314$.

An appropriate analysis of the sensitivity of ζ and Z over $d\lambda_1$ and $d\lambda_2$ (with the stiffness of the substrate is infinite) (Tab. 9.2) allows us to reduce the discretization step considerably, decreasing the computational burden.

$d\lambda$	0.001	0.0025	0.005	0.01	0.025
ζ	0.0114	0.0114	0.0114	0.0114	0.0114
Z	16.891	16.8910	16.8911	16.8912	16.8956
P	3.1001	3.1001	3.1002	3.1002	3.1004

$d\lambda$	0.05	0.1	0.25	0.5	1
ζ	0.0114	0.0114	0.0116	0.0091	0.0313
Z	16.9084	16.9412	16.9401	18.2966	12.5524
P	3.1012	3.1031	3.1089	3.1257	3.2824

Each value in the table corresponds to an "x" in the respective graphs: Effectively, it is evident how

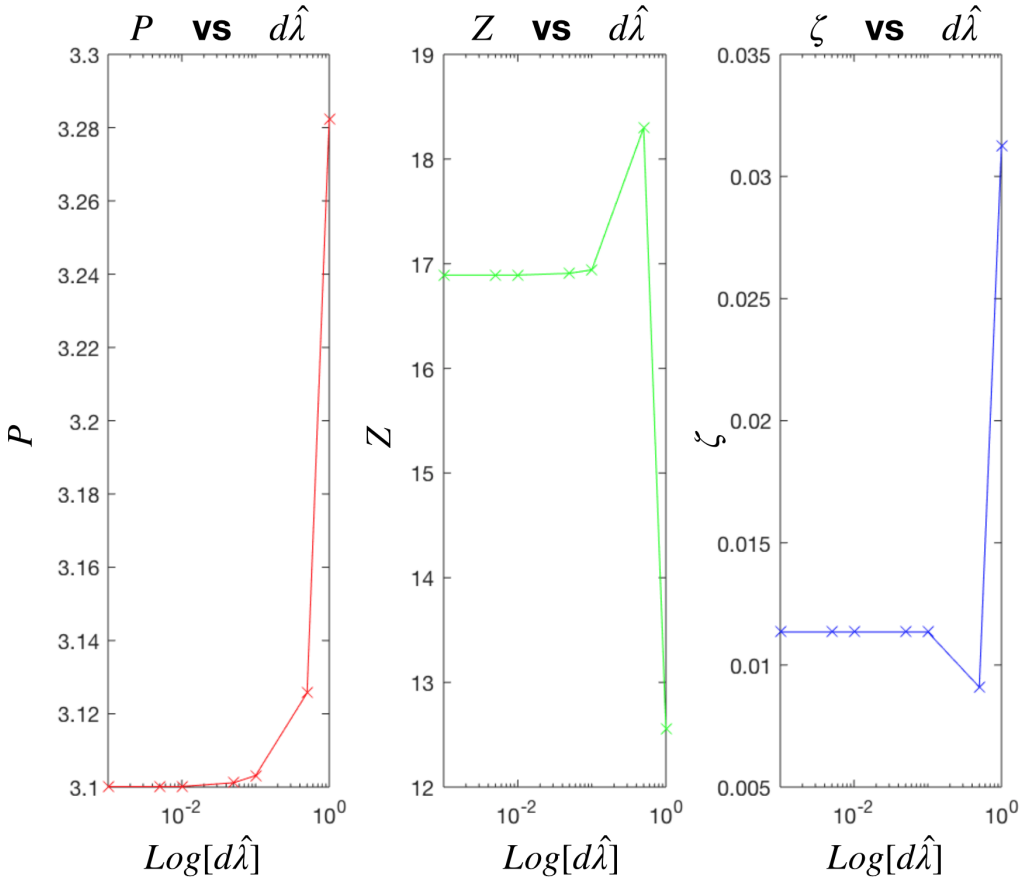

Figure 9.6

the sensitivity of Z, ζ, and P, correlated to $d\lambda \leq 0.01$ is imperceptible.

9.2.1 Elastic Winkler substrate

We are going to analyze the energetical response, of an elliptical cell, as the substrate stiffness varies ($\hat{K}_{sub} = \frac{K_{sub} t_0}{E_c}$[5]) with the discretization step for λ_1 and λ_2 established with sufficient reasonableness in the previous section. Consistently, we find more accessible configurations for the homostatic ensemble and therefore a greater uncertainty in the shape of the cell, measured through the morphological temperature $1/\zeta$, for rigid substrates than a soft one.

$\hat{K}_{sub}$	0.001	0.01	0.1	1	5	10	50
ζ	1	0.0352	0.0137	0.0116	0.0114	0.0114	0.0114
Z	413175832.7772	5.2189	11.2896	15.6608	16.5385	16.7003	16.8480
P	43.9195	2.4989	2.7531	3.0304	3.0791	3.0888	3.0976

$\hat{K}_{sub}$	100	250	500	1000	1e4	1e10
ζ	0.0114	0.0114	0.0114	0.0114	0.0114	0.0114
Z	16.8683	16.8807	16.8850	16.8871	16.8890	16.8912
P	3.0988	3.0995	3.0998	3.0999	3.1000	3.1002

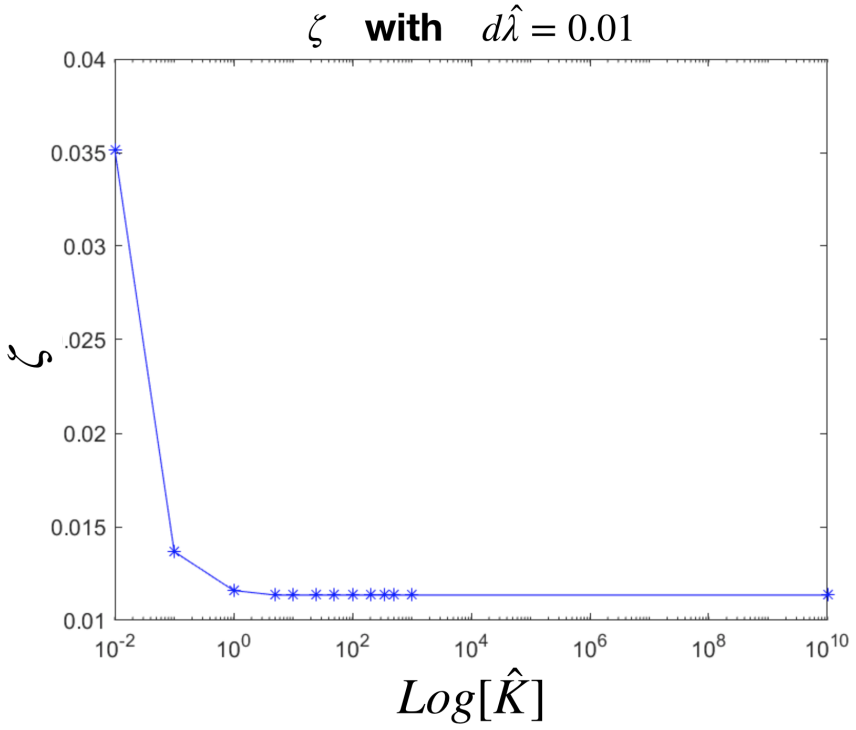

Figure 9.7

In particular, through Fig. 9.7, 9.8a, and 9.8b, we can infer how ζ are practically unchanged for the value of $\hat{K} \geq 5$. Similarly, for Z and P as well, although in a less evident way, we observe a stabilization of the corresponding values for $\hat{K} = 5$.

[5] Let $t_0 = 1.5\ \mu m$ and $E_c = 5\ KPa$ be the thickness and stiffness of the cell, respectively

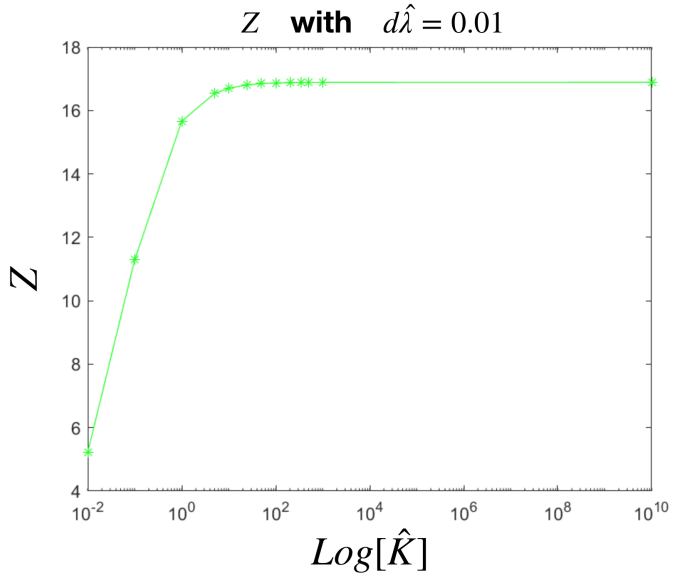
Z with $d\hat{\lambda} = 0.01$
Z
$Log[\hat{K}]$

(a)

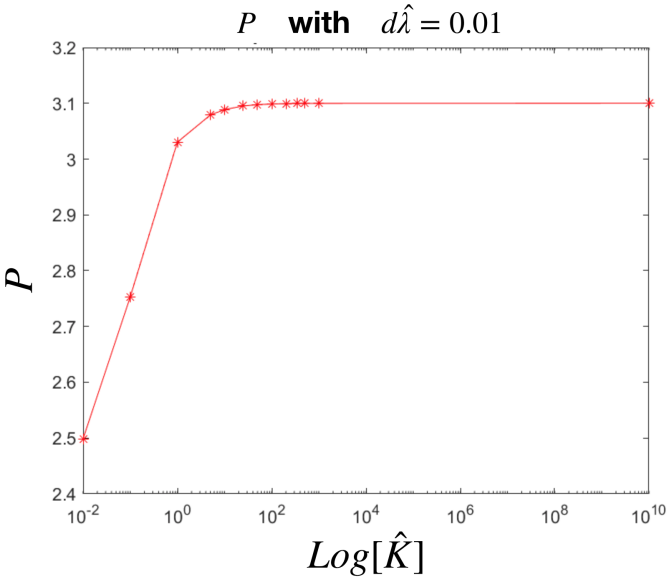
P with $d\hat{\lambda} = 0.01$
P
$Log[\hat{K}]$

(b)

Figure 9.8

An energetic analysis that highlights and quantifies the contribution of $\hat{G}_{sub}$ to $\hat{G}_{tot}$ may be interesting. In order to do that, a comparison among the minimum values assumed by $\hat{G}_{sub\ min}$ varying the substrate stiffness has been done.
Hence, the pair (λ_2, λ_1), due to the symmetry of the problem, minimize $\hat{G}_{tot}$. Calculating $\hat{G}_{tot} = -84.3721$, $\lambda_{1_{min}} = 0.49$, and $\lambda_{2_{min}} = 4.22$ it is possible to obtain:

$\hat{K}_{sub}$	0.001	0.01	0.1	1	5	10	25
$\hat{G}_{sub\,\min}$	654.6681	65.4668	6.5467	0.6547	0.1309	0.0655	0.0262

$\hat{K}_{sub\,\min}$	50	100	200	350	500	1000	1e4	1e10
$\hat{G}_{sub\,\min}$	0.0131	0.0065	0.0033	0.0019	0.0013	6.5467e-4	6.5467e-5	6.5467e-11

$\hat{K}_{sub}$	0.001	0.01	0.1	1	5	10	25
$err_{sub\,\min}$	775.9637	77.5964	7.7596	0.7760	0.1552	0.0776	0.0310

$\hat{K}_{sub\,\min}$	50	100	200	350	500	1000	1e4	1e10
$err_{sub\,\min}$	0.0155	0.0078	0.0039	0.0022	0.0016	7.7596e-4	7.7596e-5	0

where: $err = \left(\hat{G}_{tot\,\min}(k_i) - \hat{G}_{tot\,\min}(k_{1e10})\right) / \hat{G}_{tot\,\min}(k_{1e10})$

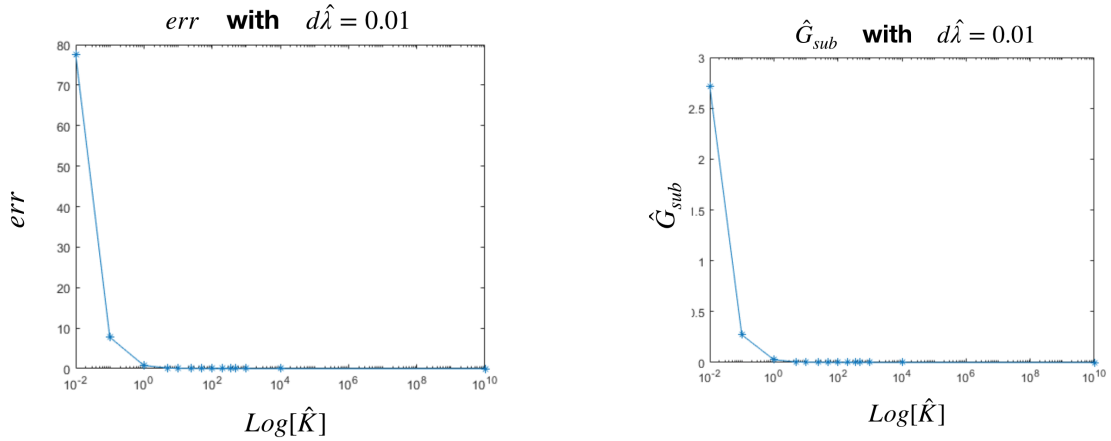

(a) (b)

Figure 9.9

It is, therefore, evident that $\hat{G}_{sub\ min}$ result to be relevant for soft substrate where lower stiffness allows higher deformations.

9.2.2 Cell free from any geometrical constraints

It may be of interest to set a comparison between the 2D-elliptic cell and cell with no-geometric restrictions. In order to support these calculations, the substrate stiffness has been fixed equal to $\hat{K}_{sub} = 1$.

The values of the single contributions of the Gibbs free energy, for a cell-free from geometric constraints, have been resumed in the following tabs corresponding to the values of ζ equal to 0.267 and 0.272.

ζ	0.267	0.272
$\hat{G}_{tot}^{mean}$	-23.50	-23.72
$\hat{G}_{cyto}^{mean}$	-72.56	-71.46
$\hat{G}_{elas}^{mean}$	23.67	22.70
$\hat{G}_{sub}^{mean}$	25.39	25.05
$\hat{A}_{mean}$	1.76	1.74
$A\hat{S}R_{mean}$	3.24	3.20
$\hat{T}_{mean}$	3.75	3.75

ζ	0.267	0.272
$\hat{G}_{tot}^{variance}$	12.19	11.93
$\hat{G}_{cyto}^{variance}$	22.41	20.62
$\hat{G}_{elas}^{variance}$	13.84	12.39
$\hat{G}_{sub}^{variance}$	9.08	8.94
$\hat{A}_{variance}$	0.24	0.23
$A\hat{S}R_{variance}$	1.48	1.40
$\hat{T}_{variance}$	0.75	0.75

where, for $\zeta = 0.272$, we observe better compliance between $\hat{G}_{tot}^{mean}$ and G_0. Hence, comparing numerical outcomes corresponding to elliptic geometry and cell without geometrical constraints, we attain the following results:

Quanties	Ellipse Ensamble	Ellips min value	Cell Ensamble ($\zeta = 0.272$)
$\hat{G}_{tot}$	-23.94	-83.71	-23.72
$\hat{G}_{cyto}$	-112.74	-132.94	-71.46
$\hat{G}_{elas}$	83.15	48.57	22.70
$\hat{G}_{sub}$	5.65	0.65	25.05
$\hat{A}$	2.39	2.06	1.74
$A\hat{S}R$	3.35	8.57	3.20
$\hat{T}$	1.24	0.21	3.75

Therefore, it can be inferred how the elliptical configuration is not enough accurate, and so not very reliable, in describing the behavior of a cell on a rigid substrate. Particularly, $\hat{G}_{sub}$ correspondence to the elliptic cell is five-time lower than infer by means of a general approach, highlighting an underestimate of this energetic contribution. Similarly, the average traction exerted by the elliptic cell on the substrate is significantly lower (three-times), as well.

Appendix H

$\hat{G}_{adh}$'s computation for an elliptic cell

$\hat{G}_{adh}$'s computation for an elliptic cell

In the case of a ligand-coated elastic Winkler substrate, we need to extend what we have just seen. So far, we implicitly assumed an unlimited supply of adhesion proteins as well as extracellular proteins to form adhesion complexes and thereby neglected the contribution of adhesion to $\hat{G}_{tot}$. Here, we need to extend the previous approach for the case of a finite quantity of both FA proteins and extracellular collagen and thus explicitly include an adhesion contribution to $\hat{G} = \hat{G}_{cyto} + \hat{G}_{elast} + \hat{G}_{sub} + \hat{G}_{adh}$.

$$\hat{G}_{adh} = A_0 C_0 \chi_C / V_0 \tag{H.1}$$

where:

- C_0 is the homogeneous surface density of integrin for a cell in suspension;
- A_0 and V_0 are the reference area and volume of the cell respectively;
- χ_c is the chemical potential of the integrins at equilibrium.

The integrins are mobile over the surface membrane and, at equilibrium, their chemical potentials are spatially uniform. Here, χ_c is unknown but easily computable by means of the iteration on the following equations:

$$\begin{aligned} \chi_C &= \kappa_B T \ln\left(\frac{\overline{C}_{eq}(x_i)}{1-\overline{C}_{eq}(x_i)}\right) - \frac{F(x_i)^2}{k_s} \\ A_0 C_0 &= C_r \int_A \overline{C}_{eq}(x_i) dA \end{aligned} \tag{H.2}$$

where:

- Cr is the number of integrin sites per unit area on the cell membrane;
- $\overline{C}_{eq}(x_i) = \dfrac{C_I^{eq}(x_i)}{C_r}$ in which C_I^{eq} is the concentration of integrin at the equilibrium;
- $F(x_i)$ is the force that each integrin molecule transmits and it is related with the traction by the expression $F(x_i) = \sqrt{T_1^2(x_i) + T_2^2(x_i)}/N_H$;

- N_H is the ligand density per unit area on the surface of the elastic Winkler substrate;
- k_s is the stiffness of the FA complex undertook to a force $F(x_i)$ and a stretch Δ;

The number of ligands per unit area, N_H, can be expressed as surface collagen density ρ_{col} through the following expression:

$$\rho_{col} = N_H M_{col}/N_A \tag{H.3}$$

where M_{col} is the molar mass of collagen, and N_A is Avogadro's constant. We assume a uniform surface collagen distribution with its own stiffness adding to that of the substrate. In particular, we know that $(N_A/M_{col}) * \rho_{col} = N_H$ where $N_A/M_{col} = 500/30$. There is a further question that we have to answer: how can we change $\hat{G}_{sub}$ in light of the presence of ligands? Under the elastic Winkler substrate hypothesis, we can argue that the substrate stiffness (elastic plus ligands) are ideally equivalent to two springs in series. For this reason, we can derive the following expression:

$$\frac{1}{V_0}\int_A \frac{1}{2}\frac{(T_1^2+T_2^2)}{k_{sub}}dA \tag{H.4}$$

where $k_{sub} = \dfrac{k_{el}k_{lig}}{k_{el}+k_{lig}}$.

Chapter 10

Conclusions and future developments

The present Ph.D. thesis, embedded in the newly emerging scientific discipline called mechanobiology, is the result of the multidisciplinary partnership between the group of biologists (experimentalists) headed by Professor Stefania Mitola (Department of Molecular and Translational Medicine of the University of Brescia) and the group of engineers (modelers) led by Professor Alberto Salvadori (Department of Mechanical and Industrial Engineering of the University of Brescia).

The importance of a multidisciplinary approach The in-vitro and/or in-vivo experimental observations reveal a highly complex and interconnected reality. The physical-mathematical modeling and the subsequent computational analysis discloses some of the hidden key mechanisms of living matter. Hence, interdisciplinarity has been the keyword of our work, where we have combined contributes from experimentalists and modelers, aiming at mutual contamination of scientific knowledge and methodologies, in order to set a mechanobiology group, which gave birth to an *Interdepartmental Center for International Research in Mechanobiology*, capable to describe and quantify the mechanical contribution to cellular activities.
The communion of intent between biologists and engineers grants the interpretative and predictive capabilities to models. The current theoretical knowledge combined with the growing capacity for calculating and processing experimental data togheter with the greater availability of high-precision tools available to biologists, demands the construction of an exact science that combines physics, biology, and engineering.

Motivations We have discussed why it could be relevant to provide a mechanobiological description of the complex phenomena correlated to new blood vessel formation (i.e. *angiogenesis*). Particularly, we have specified how angiogenesis is a target of several therapeutic strategies. It emerged that triggering or defusing the angiogenic stimulus could be, at the same time, vital to defeating many diseases. Typically, pathological conditions connected to ischemias (e.g. coronary, cardiac, limb, artery ischemias) provide a substantial reduction of vascular perfusion, revealing the need for a pro-angiogenic technique able, by means of a new network of blood vessels, to afford oxygen and nutrients in order to replenish tissues health. Viceversa, pathologies such as some types of cancer, use the angiogenic machinery (tumor angiogenesis) to the purpose to grow and develop until the metastasization occurs. Nevertheless, there are still limitations from the clinical point of view that do not allow the perfect interruption or triggering of angiogenesis, and all these

therapeutical treatments are not in line with the expectations, yet.
In order to circunvent this problem, studies have been put in place to understand how, at the early stage of angiogenesis, the recruitment of endothelial cells (ECs) is dominated by the growth factors conveyancec (e.g. VEGF and BMP). For this reason, we proposed to study the dynamic of activation and polarization of the ECs modulated by the VEGF receptor. Accordingly, we have analyzed angiogenesis from the perspective of a single endothelial cell setting in-vitro experiment, where we can observe and study the relocation of free VEGFR-2 and co-receptors like integrin, induced by ligands such as gremlin and fibrinogen, respectively. Moreover, it has been highlighted how mutations in specific domains of VEGFR2 can determine variations in the response of this transmembrane protein to ligands stimulations, which in this thesis has been provided by VEGF-A.
Therefore, the construction of in-silico simulations could have a significant impact in biology and in the pharmacological treatment of pathological angiogenic events, either in view of their predictive nature in virtual experiments or by clearly identifying the sequence of processes that limit the relocation of targeted proteins during in vitro experiments.

In-vitro experiments In chapter 4 the experimental data on time-lapse analysis adhesion assays [138, 51, 52] have been shown. These experiments examined how VEGFR2 and integrin have been relocated and recruited by two distinct ligands, i.e. gremlin and fibrinogen. Experiments on a substrate enriched on gremlin proved that VEGFR2 and integrin have been recruited from this ligand, although the latter receptor only after a long-time of observation. According to this experiment, it has been possible to denote how, at the end of the experiments (7200 s), about 30% of the total amount of VEGFR2 remained in the apical side of the cell, hence ECs avoid the total depletion of VEGFR2 on the cell membrane. Concerning the time-lapse analysis of adhesion assays on a substrate enriched with fibrinogen, integrin recruitment, and its relocation on the cell membrane have been shown, but at the same time, no significant rearrangement of VEGFR2 has been observed.
Such data have been enriched by further important biological results (e.g. by means of SPR, FRAP, and FRET experiments, see chapter 4), that allowed the estimations of a large number of constitutive parameters necessary for in-silico replications of the time-lapse experiments. However, not all have been experimentally determined, leaving the burden of calibration to an appropriate co-design between numerical and experimental results.

10.1 Multi-physical models and results

Three different kinds of multi-physical models have been proposed throughout the dissertation, to each of which, has been dedicated a Part of the thesis, i.e. Part II, Part III, and Part IV, respectively. Each of them expresses the mathematical coding of the mechanical behavior of a single-cell and its interaction with a substrate, trying to replicate explicit in-vitro experiments. Specifically, what sets them apart is the thermodynamic modeling that has been adopted and the duration of the in-vitro experiments to be described. Therefore, Parts II and III have arisen from the same thermodynamic approach, studying in-vitro experiments lasting two hours. In Part IV instead, a paradigmatic change of cell behavior (idealization proposed in the paper [14]), assuming that cells are entropic and a statistical mechanics scheme being necessary to describe the fluctuations observed during

biological experimental manifestations in notionally equivalent tests, on a timescale from hours to few days (i.e. the interphase period of the cell cycle).

Chemo-transport-mechanical models

Thermodynamically consistent "multiphysics" models have been here tailored to the above-mentioned experiments in order to describe the diffusion of free receptors on the cell membrane (transport) during the mechanical spreading of an EC (mechanics), encoding their ability to chemically interact with immobile ligands (chemistry) that cover the substrate in contact with the cell itself. The ultimate goal has been to reproduce/replicate the experimental evidence arise by in-vitro tests shown in chapter 4 through suitable in-silico trials. It has to be clear that in this formulation ligands have been assumed fix in the substrate while the receptors are free to move along the cell membrane. Therefore the generation of complexes is ruled by a trapping mechanism such as shown in paper [139] that governed the chemical reaction between free and immobilized molecules.
Moreover, such a model accounts for the diffusion of VEGFR2 and integrin on the cell membrane of EC, and the complex cell-substrate contact-dynamic. However, the latter is framed in two different ways, that ultimately distinguish the multi-physics formulation from Part II to Part III.

Chemo-transport model - Part II -

Part II, precisely in chapter 3, dealt with a chemo-transport model wherein the cell-substrate contact dynamics has been codified by means of a source of ligands in mass balance equations, allowing to not embed a mechanical contribution within the Helmholtz free-energy definition. This assumption, which we call *Surrogated Mechanics*, has led to a simplified description of the membrane events, whereas the cell geometry has been fixed as spheric and rigid. Such a formulation has been successfully published in [140], which is the extension of the works [138, 139].

Results In order to come to the complete calibration of the constitutive parameters necessary to describe a fully-coupled model that involved the three chemical reactions (3.1), (3.2), and (3.3), a gradual approach has been adopted in chapter 5, i.e. the progressive construction of four in-silico experiments. Through the first model, it has been possible to correlate characteristic physics phenomena with two/three defining phases the form of the time evolution of the total complexes curve, namely:

- an initial steep branch of the curve, firstly guided by receptor-ligand chemical interaction (i.e. the starting contact between the cell and the substrate) and then by a chemo-mechanical evolution of the cell-contact dynamic processes (after prime contact until 600 s);
- a final mechanism that has been driven primarily by the diffusive properties of free molecules of VEGFR2 (from 600 s to 7200 s).

The last result has confirmed that the internalization/externalization of VEGFR2 on the cell membrane is self-balanced in this experiments, therefore, the assumption that has precluded the existence of source terms, in the mass balance equations for VEGFR2, turned out to be correct.
Concerning integrin has been highlighted that neglecting receptors' internalization/externalization phenomena is not correct. This prediction is consistent with the experimental observations that

underline how high quantities of integrins are preformed and ready to be poured into the cellular membrane, through vesicles present in the cytoplasm. Nevertheless, thanks to the availability of a mathematical model that describes the experimental reality, we have been able to quantify that the integrins necessary to fully overlap the in-vitro curve with the numerical one have to be about double those provided by the current numerical curve. We further quantified stoichiometry between the molecules of integrin and VEGFR2-gremlin-Complex and estimated parameters that are hardly measurable. In the end, a well-matching between numerical and experimental results was obtained up to the instant 1800 s with evident discrepancies for greater times. Specifically, it has been possible to quantify, for $t > 1800$ s, that the amount of integrin in in-silico trials has been 4-5 times lower than in in-vitro ones. The biological motivations of this achievement have been equivalently correlated, as for the case o integrin-fibrinogen interaction, to the high availability of integrin inside vesicles under the cell membrane ready to be poured out on the cell surface. However, such a discrepancy in the number of integrin externalized between the model presented in pattern with one reaction and two reactions has been somewhat surprising. Effectively, a required higher amount of membrane-exposed receptors for the high-affinity integrin model was to be expected. Nevertheless, such unexpected prediction could be related to possible clustering phenomena of integrin at the sites of adhesion with fibrinogen for reaction (3.3), which can lead to an underestimation of the fluorescence of the receptor itself during in-vitro observations.

Finally, concerning the model showing all three of the above chemical-reaction, we have set exclusively an in-silico experiment, inasmuch as no biological models have been built for a similar problem. Therefore, prediction on the trend of the curves of the evolution of the total amount of complexes C_1, C_2, C_3 has been done when gremlin and fibrinogen coexist on the substrate. In this frame, we have provided the ratio in which each complex could be found respectively to the others. Intriguingly, it has been observed that the quantity of complex C_3, at instant $t = 1800$ s (i.e. the last moment in which there is perfect overlap between numerical and experimental data in previous patterns), is about five-time C_2, expressing how integrin is found more at adhesion sites rather than as a co-receptor of VEGFR2 in this simulations.

Chemo-transport model for proteins relocation on advecting membranes - Part III -

A multi-physics framework of protein relocation on the advecting lipid membrane during cell spreading and motion has been put forward in chapter 6 (and accepted for publication on [220]). Two preliminary assumptions have been done at the head of this formulation, namely:

- the structural contribute by the cell membrane is negligible with respect to that provided by the cytoskeleton in the bulk of the cell;
- it has been considered a one-way coupled model.

The former one is supported by experimental evidence that has shown that the structural response of the EC stems from complex biological mechanisms that arise in its volume. The second hypothesis instead, has not any biological roots, but, in the first approximation has allowed to establish that the mechanical spreading of the cell is independent on the receptor diffusion on the cell membrane. This is a simplification of the real fully-coupled mechanical behavior of an EC. Furthermore, the latter has been here characterized by a study on the relocation and reaction of

actin to form biopolymers that lead to consider the reorganization of the cytoskeleton through a network of actin filaments, coupled to a passive behavior dictated by the viscosity of the cytosol.

Afterward, through chapters 7, and 8 we have dealt with numerical simulations with the relocation of VEGFR2 (wild type or mutated R1032Q) on advecting lipid membrane during endothelial cell adhesion and spreading (chapter 7) and integrin receptor (chapter 8). Here, the mechanical behavior of an EC has been idealized, in first approximation, by *Regularized Neo-Hookean* formulation, ignoring the active mechanical cell attitude of the EC.

Results On the basis of the findings from the surrogate mechanics models it has been defined the construction of in-silico models under a large-deformations scheme.
Three distinct phases of the relocation of VEGFR2 have been identified, each of which relates to a different physical mechanism (see chapter 7). Nevertheless, this three-phases evolution time-scale extends the scenario shown under *surrogated mechanics* assumption. In fact, having included the mechanical description of an EC, we have been capable, either to describe with greater accuracy the form of the generation curve of the total number of complexes on the cell membrane of an EC as well as to quantified the forces ruling those steps dominated by mechanical behavior of the cell itself.
Precisely, a fast interaction due to chemical bonding at adhesion, mechanically dominated by gravitational force, characterized the first 300 s of the curve of total complexes generation. This step precedes a mechanically dominated regime (300 s-600 s), in which free receptors are depleted to be engaged in complexes with ligands due to the spreading of the cell, driven by filopodia/lamellipodia migration processes. Specifically, this process is actually correlated to the contractility of EC, a phenomenon connected with the active behavior of cells, a description that has been neglected in the current simulations. Therefore, the mechanical spreading of the cell has here been captured by the introduction of suitable bulk forces qualified to mimic the filopodia/lamellipodia migration processes. These bulk forces have been estimated equal to 6.2 times the magnitude of the gravitation one, a value required to induce a spread radius of cell equivalent to 20 μm (averaged value observed on measurements of 50 ECs). Moreover, once a macroscopic steady-state mechanical configuration has been achieved, transport of receptors on the membrane continues and favors complex formation in localized spots (600 s-7200 s). Finally, it is important to underline that the measurements cell-substrate contact areas provided by the in silico model, both at the end of the adhesion phase (300 s) and at the end of the diffusion phase (7200 s), are totally superimposable to the corresponding in-vitro values, namely approximately 35.3 μm^2 and 1256.6 μm^2, respectively. Again, such a formulation has allowed quantifying the available gremlin on the substrate in contact with the cell surface re-evaluating it to 90 $molecules/\mu m^2$.
Interestingly, although the numerical curve well-match the experimental one, this outcome contradicts the biological evidence arisen from the in-vitro experiments, inasmuch conducing to the full depletion of VEGFR2 on the cell surface.
These considerations have suggested that the right model for capturing the residue of receptors on the apical side would require a duplication of the species of VEGFR2 in a free set and an immobile part. wherein the free species "M" reach a complete depletion at the end of the analysis. Accordingly, in section 7.2 has been provided the results arisen from this evaluates formulation.

Moreover, in section 7.3, it has been applied both the above-mentioned formulations, namely with

or without duplication of species, on the study of the effect of the mutation R1032Q on the recruitment of VEGFR2 by the canonical ligand VEGFA. Notably, these in-silico simulations have been supported by further experimental results on VEGFR2 wild type (WT) and VEGFR2-R1032 on CHO cells. The aim of these studied has been that to provide a characterization of VEGFR2-R1032 behavior when exposed by an EC. Therefore, it has been inherited the timing of the three above-mentioned phases describing the mechanism of the complex formations for an EC but using material parameters measured by the novel experiments on CHO cells. Such results, compared with those on VEGFR2-WT, have highlighted a less amount of complexes generation related to the mutated receptor throughout the 7200 s of simulation, and so respective slower recruitment by the VEGFA on this kind of receptor.

Finally, through chapter 8 we have analyzed the in-silico replications of the in-vitro experiments specified by the chemical reactions that involve integrin.
Actually, describing integrin, i.e. the main receptor devoted to the mechanical interaction between EC-microenvironment, through a model with no active characterization of EC contractility, may a strong restriction; however, the current elaborations have been intended as an intermediate step. Future ones will involve the active mechanical description of EC and a two-way coupled formulation.

Homeostatic model for cells and its results - Part IV -

Arisen from a collaboration with Professor Vikram Deshpande (Department of Mechanics of the University of Cambridge) and financed by Guido Berlucchi Foundation (Young Researchers Mobility Programme), this Part of the thesis has aimed to study the competition between haptotaxis and durotaxis based on the experimental results on fibroblast dictated by the paper [219], and described by means of a theoretical scheme, embedded in a statistical mechanics framework and explained in paper [14]. Particularly, a simplified idealization of the experimental reality has been defined by means of a 2D study on fibroblast restrained to maintain an elliptical shape. This work, corresponding to the experience abroad of the author of the thesis was suddenly stopped after two months on the six expected due to the coronavirus pandemic.

Results The current Part of the thesis has been framed on the phenomenon of homeostasis for the intracellular environment by means of the formulations of a statistical ensemble for cells, elaborated in the work [14].
Such a characterization has been necessary to elaborate the numerical description, proposed in section 9.2 of the behavior of a cell that has been forced to maintain an elliptic shape.
Co-designing among numerical analysis on elliptic cells and cells free to assume any geometrical configuration, have demonstrated predictive inability, by the model with simplified (elliptical) geometry, to fully describe the correct interaction between cell and substrate. Particularly, an evident underestimation of the Gibbs free-energy contribution connected to the substrate activities as well as to that associated with the tractions values generated by the cell has arisen. Specifically, the former result to be five-times and the latter three-times lower than inferred on a cell without geometrical restraint.

10.2 Future developments

The encouraging results obtained through the multiphysics models presented in the thesis are pushing us to improve them by implementing newly detailed formulations. Either from the theoretical point of view that numerical, the above-described results can suggest us the way to take.

Thermodynamics considerations

The quest for the right thermodynamic principles in mechanobiology is far from being understood and, from a wider perspective, it paves the way to boundless questions of philosophical and ethical nature, as for the establishment of thermodynamics of life [221], which fall completely out of the scope of the present thesis. Major accomplishments have been achieved by [14] in formulating fresh concepts that deviate from classical results of thermodynamics of non-equilibrium. In this scientific area, which is nowadays flourishing, new fundamentals assertions are expected in the years to come. Being aware that classical formulations of non-equilibrium thermodynamics [144, 146] may not be able to capture some principles of mechanobiology that rule the dynamic of receptors - as for the homeostatic constraint [222], we are prone to deepen our formulation in future studies.

Particularly, the pattern framed in a pure continuum thermodynamic scheme can represent with enough accuracy the experimental evidence on the time span defined by the in-invitro trials in chapter 4, therefore two hours. Viceversa, the one arisen from the work [14], is able to describe living cells' behavior over a time scale that, from few hours, can rach a few days, including the tendency of these systems to maintain the so-called homeostatic equilibrium.
Coding the homeostatic constraint, from a thermodynamic point of view, is a crucial step for all models describing living matter. [14] did it by means a paradigmatic change of the study of living cells, from deterministic to statistic; actually, this is much more than a simple coarse-grained model, indeed it is assumed that cells are entropic and so that they manifest fluctuations in order to support the homeostasis.
However, on restricted time observation phenomena, classical results of thermodynamics of non-equilibrium could be useful yet, as confirmed by the patterns in Parts II and III of the thesis. Although we are persuaded by the thermodynamical arguments proposed by statistical mechanics theoretical frameworks in order to coarse-grain out the homeostatic process variables as shown in [14], we are equally convinced that a deterministic representation of the cell's attitudes, for a short time of the biological observations (two-hours time span), could be acceptable. According to this, in order to extend the formulation proposed in Parts II and III, we will improve this continuum thermodynamic framework providing the following features.

Two-way coupled models

Combining either the description of the chemo-diffusive problem of integrin receptor on the cell membrane (including modeling of the clustering procedure manifested by this receptor in adhesion sites [121] and the internalization/externalization phenomena) that the active description of the mechanical behavior of EC extending the model presented in chapter 6 it will be possible up-grade

the one-way coupled model hereto discussed in a two-way coupled formulations. Therefore, in this new scheme, the receptors' (integrin) activities on the lipid bilayer will cooperate to organize the mechanical response of an EC, promoting adhesions sites formations and guiding the arrangement of stress-fibers. Accordingly, a thermodynamically motivated model describing the stress-fibers (SFs) remodeling, and so the actin-myosin II interaction during the SFs reorganization, is recommended. Accordingly, if the contractile machinery of SFs within ECs is similar to that manifests inside muscle sarcomeres (as shown within fibroblasts) the model formulation proposed by [180] will be taken into account, otherwise, alternative and innovative models will be necessary.
Moreover, a coarse-grained model based on principles of statistical mechanics is necessary to connect the microscopic properties of the actin network with the macroscopic ones determinable at the continuum scale. Hence, a further extension of this pattern could arise by means of a statistical continuum theory for the study of the actin transient network both in globular (G-actin) and filamentous (F-actin) form able to motivated the innovative characterization of the mechanical description of cell motility guided by actin polymerization. This will be a direct extending the formulation derived in chapter 6.

Statistical continuum theory for the study of the actin transient network Actin polymerization is an intracellular activity connected to cell motion. This phenomenon provides the forces necessary for cell-shape evolution by means of a branched and dendritic array formation of F-actin. Specifically, actin polymerization guides lamellipodium generation, namely a cell protrusion playing a pivotal role in the initial phase of the cell migration [223]. Hence, with the aid of the theoretical framework elaborated by F.J. Vernerey and co-workers [195], we aim to describe the F-actin cytoskeleton devoted to generating cell protrusions. Hence, the grounded concept here is the idealization of actin monomers (G-actin) like monodisperse (or polydisperse if we also accounting for other polymers networks such as microtubules) polymers inside the cytoplasm that contextually, by means of their polymerization, become generators of F-actin chains that support the actin network in the cell protrusions.
The chains configuration can be statistically described by the distribution function.

With the purpose of describing the process of polymerization and/or depolymerization of G-actin into F-actin, and vice-versa, we will take into account the polymerization-depolymerization process.
Practically, referring to the deformation gradient decomposition (6.107) ($\boldsymbol{F} = \boldsymbol{F}^e \, \boldsymbol{F}^c$) provided in chapter 6, we will assume that the viscoelastic behavior of the EC is connected with the tensor $\boldsymbol{F}^e$ and fully described by a dynamical characterization of the evolution of the F-actin-network. In such a framework, the viscoelastic machinery will be outlined by the mechanism of the attachment and detachment of filaments of actin while the polymerization-depolymerization phenomena will rule the density of the total chain available to make the actin lattice. This contribution, combined with that provided by the swelling distortion tensor, will describe the dense network of actin filaments within pseudopodia.

Acknowledgments

The group of Mechanobiology, of which the author of the thesis is a member, is gratefully indebted to the company *Ferriera Valsabbia* for the support of its research through a devoted fellowship. Moreover, the author of the thesis acknowledges the support of *Guido Berlucchi Foundation Young Researchers Mobility Programme* concern the abroad experience at the University of Cambridge.

Ringraziamenti

Sono numerose le persone a cui devo rivolgere i miei ringraziamenti per questi lunghi ed intensi tre anni di dottorato di ricerca.

Ringrazio il Professor Alberto Salvadori e la Professoressa Stefania Mitola, ai quali mi lega un sentimento di profondo rispetto e sentita gratitudine, per essersi dimostrati mentori ancor prima che relatori. Ringrazio anche il Professor Gian Paolo Beretta per la disponibilità dimostratami.

Grazie a tutti i colleghi e amici dell'm4lab (*https://m4lab.unibs.it*) e del gruppo di ricerca della Professoressa Stefania Mitola con i quali ho condiviso gioie e fatiche del triennio di dottorato e ho potuto imparare tantissime cose. Un sentito ringraziamento va ad Alberto Ippolito per essersi dimostrato una persona splendida ed un vero amico durante il periodo che ho trascorso a Cambridge.

Vorrei inoltre manifestare l'eterna gratitudine che provo nei confronti della mia famiglia e della famiglia di Greta attraverso le parole di Albert Einstein: "*Cento volte al giorno ricordo a me stesso che la mia vita interiore e esteriore sono basate sulle fatiche di altri uomini, vivi e morti, e che io devo fare il massimo sforzo per dare nella stessa misura in cui ho ricevuto.*"

Infine, voglio dire grazie a Greta, mia moglie, per il suo continuo sostegno, per il suo amore incondizionato e per aver condiviso insieme a me ogni istante di questi tre anni, consapevole che il raggiungimento di questo obiettivo decreterà l'inizio di una nuova avventura insieme perché "*Nessuno è felice, come chi sa di esser amato (Alda Merini).*"

Bibliography

[1] Giovanni Chieffi, Silvana Dolfini, Massimo Malcovati, Riccardo Pierantoni, and Maria Luisa Tenchini. *Biologia e genetica*. EdiSES, 2005.

[2] D. Ambrosi, M. Ben Amar, C. J. Cyron, A. DeSimone, A. Goriely, J. D. Humphrey, and E. Kuhl. Growth and remodelling of living tissues: perspectives, challenges and opportunities. *J R SOC INTERFACE*, 16:20190233, 2019.

[3] C.R. Jacobs, H. Huang, and R.Y. Kwon. *Introduction to Cell Mechanics and Mechanobiology*. Garland Science, Taylor and Francis Group, 2013.

[4] A. Bejan. Discipline in thermodynamics. *Energies*, 13(2487):8, 2020.

[5] E.B. Tadmor, R.E. Miller, and R.S. Elliott. *Continuum Mechanics and Thermodynamics: From Fundamental Concepts to Governing Equations*. Cambridge University Press, 2011.

[6] H.B. Callen. *Thermodynamics and an Introduction to Thermostatics.* New York: John Wiley and Sons, second edition, 1985.

[7] A Bejan. Constructal-theory network of conducting paths for cooling a heat generating volume. *Int. J. Heat Mass Transfer*, 40(4):799–816, 1996.

[8] G. P. Beretta. The fourth law of thermodynamics: steepest entropy ascent. *Phil. Trans. R. Soc. A*, 378(37820190168):799–816, 2020.

[9] Bruce Alberts, A. Johnson, J. Lewis, D. Morgan, M. Raff, K. Roberts, and P. Walter. *Molecular Biology of THE CELL.* New York : Garland Science, 6th ed. edition, 2015.

[10] R.P. Feynman. *The great conservation principles (https://youtu.be/a6n0HSJ5jEE)*. In the Messenger Lectures series titled 'The Character of Physical Law' given at Cornell University by Richard Feynman and recorded by BBC. London: BBC., 1964.

[11] D. A. Fletcher and R. D. Mullins. Cell mechanics and the cytoskeleton. *Nature*, 463(7280):485–492, 2010.

[12] Domenico Gazzillo. *Termodinamica statistica*. libreriauniversitaria.it, 2013.

[13] E. Fermi. *TERMODINAMICA*. Bollati Boringhieri, 1972.

[14] S.S. Shishvan, A. Vigliotti, and V.S. Deshpande. The homeostatic ensemble for cells. *BIOMECH MODEL MECHAN*, 17:1631–1662, 2018.

[15] J. Schöneberg, F. De Lorenzi, B. Theek, A. Blaeser, D. Rommel, A. J. C. Kuehne, F. Kieβling, and H. Fischer. Engineering biofunctional in vitro vessel models using a multilayer bioprinting technique. *Scientific Reports*, 8(10430), 2018.

[16] Klotzsch. E. and G. J. Schütz. A critical survey of methods to detect plasma membrane rafts. *Philos Trans R Soc Lond B Biol Sci*, 368(1611)(20120033), 2012.

[17] B. Gumí-Audenis, L. Costa, F. Carlá, F. Comin, F. Sanz, and M. I. Giannotti. Structure and nanomechanics of model membranes by atomic force microscopy and spectroscopy: Insights into the role of cholesterol and sphingolipids. *Membranes (Basel)*, 6(4)(58), 2016.

[18] S. Bhattacharya and S. Haldar. Interactions between cholesterol and lipids in bilayer membranes. role of lipid headgroup and hydrocarbon chain-backbone linkage. *Biochim Biophys Acta*, 1467(1):39–53, 2000.

[19] A. Marmagne, M. Ferro, T. Meinnel, C. Bruley, L. Kuhn, J. Garin, H. Barbier-Brygoo, and G. Ephritikhine. A high content in lipid-modified peripheral proteins and integral receptor kinases features in the arabidopsis plasma membrane proteome. *Mol Cell Proteomics*, 6(11):1980–96, 2007.

[20] S.J. Singer and G.L. Nicolson. The fluid mosaic model of the structure of cell membranes. *SCIENCE*, 175(4023):720–731, 1972.

[21] J. Yu, D. A. Fischman, and T. L. Steck. Selective solubilization of proteins and phospholipids from red blood cell membranes by nonionic detergents. *J Supramol Struct*, 1(3):233–48, 1973.

[22] R. Lindner and H.Y. Naim. Domains in biological membranes. *Experimental Cell Research*, 315(17):2871–2878, 2009.

[23] K. Simons and E. Ikonen. Functional rafts in cell membranes. *Nature*, 387(6633):569–72, 1997.

[24] G. J. Doherty and H. T. McMahon. Mechanisms of endocytosis. *Annu Rev Biochem*, 78:857–902, 2009.

[25] I. Levental, D. Lingwood, M. Grzybek, Ü. Coskun, and K. Simons. Palmitoylation regulates raft affinity for the majority of integral raft proteins. *PNAS*, 107(51):22050–22054, 2010.

[26] G.R. Chichili and W. Rodgers. Cytoskeleton–membrane interactions in membrane raft structure. *Cellular and Molecular Life Sciences volume*, 66:2319–2328, 2009.

[27] B. Sinha, D. Köster, R. Ruez, P. Gonnord, M. Bastiani, D. Abankwa, Stan R.V., G. Butler-Browne, B. Vedie, B. Johannes, N. Morone, R.G. Parton, G. Raposo, P. Sens, C. Lamaze, and P. Nassoy. Cells respond to mechanical stress by rapid disassembly of caveolae. *Cell*, 144(3):402–413, 2011.

[28] A. Echarri and M.A. Del Pozo. Caveolae - mechanosensitive membrane invaginations linked to actin filaments. *J Cell Sci.*, 128(15):2747–2758, 2015.

[29] P. Nassoy and C. Lamaze. Stressing caveolae new role in cell mechanics. *Trends Cell Biol*, 22(7):381–9, 2012.

[30] P. Thomsen, K. Roepstorff, M. Stahlhut, and B. van Deurs. Caveolae are highly immobile plasma membrane microdomains, which are not involved in constitutive endocytic trafficking. *Molecular Biology of the Cell*, 13(1):238–250, 2015.

[31] V. Damioli. *A mechano-biological model of the coupling between cellular contractility and VEGFR2/VEGF interactions*. PhD thesis, University of Brescia, 2018.

[32] F. Tovar-Lopez, P. Thurgood, C. Gilliam, N. Nguyen, E. Pirogova, K. Khoshmanesh, and S. Baratchi. A microfluidic system for studying the effects of disturbed flow on endothelial cells. *Front Bioeng Biotechnol*, 7(81), 2019.

[33] S. J. Plowman and J. F. Hancock. Ras signaling from plasma membrane and endomembrane microdomains. *Biochim Biophys Acta*, 1746(3):274–83, 2005.

[34] P. Sharma, R. Varma, R. C. Ira Sarasij, K. Gousset, G. Krishnamoorthy, M. Rao, and S. Mayor. Nanoscale organization of multiple gpi-anchored proteins in living cell membranes. *Cell*, 116(4):577–89, 2004.

[35] D. Goswami, K. Gowrishankar, S. Bilgrami, S. Ghosh, R. Raghupathy, R. Chadda, R. Vishwakarma, M. Rao, and S. Mayor. Nanoclusters of gpi-anchored proteins are formed by cortical actin-driven activity. *Cell*, 135(6):1085–97, 2008.

[36] T. S. van Zanten, A. Cambi, M. Koopman, B. Joosten, C. G. Figdor, and M. F. Garcia-Parajo. Hotspots of gpi-anchored proteins and integrin nanoclusters function as nucleation sites for cell adhesion. *Proc Natl Acad Sci U S A*, 106(44):18557–62, 2009.

[37] S. Saha, I-H Lee, A. Polley, J. T. Groves, M. Rao, and S. Mayor. Diffusion of gpi-anchored proteins is influenced by the activity of dynamic cortical actin. *Mol Biol Cell*, 26(22):4033–45, 2015.

[38] T. Tian, A. Harding, K. Inder, S. Plowman, R.G. Parton, and J.F. Hancock. Plasma membrane nanoswitches generate high-fidelity ras signal transduction. *Nature Cell Biology*, 9:905–914, 2007.

[39] A.D. Douglass and R.D. Vale. Single-molecule microscopy reveals plasma membrane microdomains created by protein-protein networks that exclude or trap signaling molecules in t cells. *Cell*, 121(6):937–950, 2005.

[40] M.-J. Yu, T. Pisitkun, G. Wang, J.F. Aranda, P.A. Gonzales, D. Tchapyjnikov, R.-F. Shen, M.A. Alonso, and M.A. Knepper. Large-scale quantitative lc-ms/ms analysis of detergent-resistant membrane proteins from rat renal collecting duct. *Am J Physiol Cell Physiol*, 295(3):C661–678, 2008.

[41] M. Yanagida, H. Nakayama, F. Yoshizaki, T. Fujimura, K. Takamori, H. Ogawa, and K. Iwabuchi. Proteomic analysis of plasma membrane lipid rafts of hl-60 cells. *Proteomics*, 7(14):2398–2409, 2007.

[42] D.L. MacLellan, H. Steen, R.M. Adam, M. Garlick, D. Zurakowski, S.P. Gygi, M.R. Freeman, and K.R. Solomon. A quantitative proteomic analysis of growth factor-induced compositional changes in lipid rafts of human smooth muscle cells. *Proteomics*, 5(18):4733–4743, 2005.

[43] G.R. Chichili and W. Rodgers. Clustering of membrane raft proteins by the actin cytoskeleton. *J Biol Chem*, 282(50):36682–36691, 2007.

[44] C. F. Natale, J. Lafaurie-Janvore, M. Ventre, A. Babataheri, and A. I. Barakat. Focal adhesion clustering drives endothelial cell morphology on patterned surfaces. *J R Soc Interface*, 16(158)(20190263), 2019.

[45] R. Lugano, M. Ramachandran, and A. Dimberg. Tumor angiogenesis: causes, consequences, challenges and opportunities. *Cellular and Molecular Life Sciences*, 77:113–127, 2020.

[46] M. S. Patil, S. C. Cartland, and M. M. Kavurma. Trail signals, extracellular matrix and vessel remodelling. *Vasc Biol.*, 2(1):R73–R84, 2020.

[47] E. Gazzerro, R.C. Pereira, V. Jorgetti, S. Olson, A.N. Economides, and E. Canalis. Skeletal overexpression of gremlin impairs bone formation and causes osteopenia. *Endocrinology*, 146(2):655–665, 2005.

[48] H. Stabile, S. Mitola, E. Moroni, M. Belleri, S. Nicoli, D. Coltrini, F. Peri, A. Pessi, L. Orsatti, F. Talamo, V. Castronovo, David Waltregny, Franco Cotelli, D. Ribatti, and M. Presta. Bone morphogenic protein antagonist drm/gremlin is a novel proangiogenic factor. *BLOOD*, 109(5):1834–1840, 3 2007.

[49] G. Neufeld, T. Cohen, S. Gengrinovitch, and Z. Poltorak. Vascular endothelial growth factor (VEGF) and its receptors. *FASEB J.*, 13(1):9–22, 1999.

[50] S. Mitola, C. Ravelli, E. Moroni, V. Salvi, D. Leali, K. Ballmer-Hofer, L. Zammataro, and M. Presta. Gremlin is a novel agonist of the major proangiogenic receptor VEGFR2. *BLOOD*, 116(18):3677–3680, November 2010.

[51] C Ravelli, S Mitola, M Corsini, and M Presta. Involvement of $\alpha_v\beta_3$ integrin in gremlin-induced angiogenesis. *ANGIOGENESIS*, 16(1):235–43, 2013.

[52] C. Ravelli, E. Grillo, M. Corsini, D. Coltrini, M. Presta, and S. Mitola. β_3 integrin promotes long-lasting activation and polarization of vascular endothelial growth factor receptor 2 by immobilized ligand. *ARTERIOSCL THROM VAS*, 35(10):2161–2171, 2015.

[53] Elisabetta Grillo, Cosetta Ravelli, Michela Corsini, Kurt Ballmer-hofer, Pasqua Oreste, Giorgio Zoppetti, Chiara Tobia, Roberto Ronca, Marco Presta, and Stefania Mitola. Monomeric gremlin is a novel vascular endothelial growth factor receptor-2 antagonist. *Oncotarget*, 7(23):35353 – 35368, 2016.

[54] S. Kumar and V. M. Weaver. Mechanics, malignancy, and metastasis: The force journey of a tumor cell. *Cancer Metastasis Rev.*, 28(1-2):1745–1770, 2009.

[55] C. Bonnans, J. Chou, and Z. Werb. Remodelling the extracellular matrix in development and disease. *Nat Rev Mol Cell Biol.*, 15(12):786–801, 2014.

[56] J.K. Mouw, G. Ou, and V.M. Weaver. Extracellular matrix assembly: a multiscale deconstruction. *Nat Rev Mol Cell Biol.*, 15(12):771–785, 2014.

[57] F. T. Bosman and I. Stamenkovic. Functional structure and composition of the extracellular matrix. *Journal of Pathology*, 200(4):423–428, 2003.

[58] A. Ullrich and J. Schlessinger. Signal transduction by receptors with tyrosine kinase activity. *Cell*, 61(2):203–12, 1990.

[59] M.K. Paul and A.K. Mukhopadhyay. Tyrosine kinase - role and significance in cancer. *Int J Med Sci.*, 1(12):101–115, 2004.

[60] T. Pawson, G. D. Gish, and P. Nash. Sh2 domains, interaction modules and cellular wiring. *Trends Cell Biol*, 11(12):504–11, 2001.

[61] M. A. Lemmon. Ligand-induced erbb receptor dimerization. *Exp Cell Res*, 315(4):638–48, 2009.

[62] M. A. Lemmon and J. Schlessinger. Cell signaling by receptor tyrosine kinases. *Cell*, 141(7):1117–34, 2010.

[63] J.B. Casaletto and A. McClatchey. Spatial regulation of receptor tyrosine kinases in development and cancer. *Nat Rev Cancer*, 12(6):387–400, 2012.

[64] A. I. S*é*galiny, M. Tellez-Gabriel, M.-F. Heymann, and D. Heymann. Receptor tyrosine kinases: Characterisation, mechanism of action and therapeutic interests for bone cancers. *J Bone Oncol*, 4(1):1–12, 2015.

[65] I. Nilsson, F. Bahram, X. Li, L. Gualandi, S. Koch, M. Jarvius, O. S*ö*derberg, A. Anisimov, I. Kholov*á*, B. Pytowski, M. Baldwin, S. Yl*ä*-Herttuala, K. Alitalo, J. Kreuger, and L. Claesson-Welsh. Vegf receptor 2/-3 heterodimers detected in situ by proximity ligation on angiogenic sprouts. *EMBO J*, 29:1377–1388, 2010.

[66] C. Ruch, G. Skiniotis, M.O. Steinmetz, T. Walz, and K. Ballmer-Hofer. Structure of a vegf–vegf receptor complex determined by electron microscopy. *Nature Structural & Molecular Biology volume*, 14:249–250, 2007.

[67] Y. Yang, P. Xie, Y. Opatowsky, and J. Schlessinger. Direct contacts between extracellular membrane-proximal domains are required for vegf receptor activation and cell signaling. *PNAS*, 107(5):1906–1911, 2010.

[68] S. Koch, S. Tugues, X. Li, L. Gualandi, and L. Claesson-Welsh. Signal transduction by vascular endothelial growth factor receptors. *Biochem J*, 437(2):169–183, 2011.

[69] R Soldi, S Mitola, M Strasly, P Defilippi, G Tarone, and F Bussolino. Role of alphavbeta3 integrin in the activation of vascular endothelial growth factor receptor-2. *EMBO J*, 18(4):882–892, 1999.

[70] S. Garrido-Urbani, P.F. Bradfield, B.P.-L. Lee, and B.A. Imhof. Vascular and epithelial junctions: a barrier for leucocyte migration. *Biochem Soc Trans*, 36(2):203–211, 2008.

[71] J.A. NAGY, E. VASILE, D. FENG, C. SUNDBERG, L.F. BROWN, E.J. MANSEAU, A.M. DVORAK, and H.F. DVORAK. Vegf-a induces angiogenesis, arteriogenesis, lymphangiogenesis, and vascular malformations. *Cold Spring Harb Symp Quant Biol*, 67:227–238, 2002.

[72] P.M. Bauer, J. Yu, Y. Chen, R. Hickey, P.N. Bernatchez, R. Looft-Wilson, Y. Huang, F. Giordano, R.V. Stan, and W.C. Sessa. Endothelial-specific expression of caveolin-1 impairs microvascular permeability and angiogenesis. *PNAS*, 102(1):204–209, 2005.

[73] R. Bhattacharya, N. Kang-Decker, D.A. Hughes, P. Mukherjee, V. Shah, M.A. McNiven, and D. Mukhopadhyay. Regulatory role of dynamin-2 in vegfr-2/kdr-mediated endothelial signaling. *FASEB J*, 19(12):1692–1694, 2005.

[74] J.G. Donaldson. Arf6 and its role in cytoskeletal modulation. *Methods Mol Biol*, 189:191–198, 2002.

[75] L. Labrecque, I. Royal, D.S. Surprenant, C. Patterson, D. Gingras, R. B*é*liveau, and C.-H. Heldin. Regulation of vascular endothelial growth factor receptor-2 activity by caveolin-1 and plasma membrane cholesterol. *Mol Biol Cell*, 14(1):334–347, 2003.

[76] M.G. Lampugnani, F. Orsenigo, M.C. Gagliani, C. Tacchetti, and E. Dejana. Vascular endothelial cadherin controls vegfr-2 internalization and signaling from intracellular compartments. *J Cell Biol*, 174(4):593–604, 2006.

[77] P. Carmeliet, Y.S. Ng, D. Nuyens, G. Theilmeier, K. Brusselmans, I. Cornelissen, E. Ehler, V.V. Kakkar, I. Stalmans, V. Mattot, J.C. Perriard, M. Dewerchin, W. Flameng, A. Nagy, F. Lupu, L. Moons, D. Collen, P.A. D'Amore, and D.T. Shima. Impaired myocardial angiogenesis and ischemic cardiomyopathy in mice lacking the vascular endothelial growth factor isoforms vegf164 and vegf188. *NAT MED*, 5(5):495–502, 1999.

[78] S. Esser, M.G. Lampugnani, M. Corada, E. Dejana, and W. Risau. Vascular endothelial growth factor induces ve-cadherin tyrosine phosphorylation in endothelial cells. *J CELL SCI*, 111(Pt 13):1853–1865., 1998.

[79] C.J. Peach, L.E. Kilpatrick, R. Friedman-Ohana, K. Zimmerman, M.B. Robers, K.V. Wood, J. Woolard, and S.J. Hill. Real-time ligand binding of fluorescent VEGF-A isoforms that discriminate between VEGFR2 and NRP1 in living cells. *CELL CHEM BIOL*, 25(10):1208–1218, 2018.

[80] C. Ravelli, S. Mitola, M. Corsini, and M. Presta. Involvement of $\alpha_v\beta_3$ integrin in gremlin-induced angiogenesis. *ANGIOGENESIS*, 16(1):235–243, 2013.

[81] K.R. Molhoek, G. Erdag, Jk Rasamny, C. Murphy, D. Deacon, J.W. Patterson, C.L. Slingluff, and D.L. Brautigan. Vegfr-2 expression in human melanoma: Revised assessment. *Int J Cancer.*, 129(12):2807–2815, 2011.

[82] R. A. Toledo, E. Garralda, M. Mitsi, T. Pons, J. Monsech, E. Vega, Á. Otero, M. I. Albarran, N. Baños, Y. Durán, V. Bonilla, F. Sarno, M. Camacho-Artacho, T. Sanchez-Perez, S. Perea, R. Álvarez, A. De Martino, D. Lietha, C. Blanco-Aparicio, A. Cubillo, O. Domínguez, J. L. Martínez-Torrecuadrada, and M. Hidalgo. Exome sequencing of plasma dna portrays the mutation landscape of colorectal cancer and discovers mutated vegfr2 receptors as modulators of antiangiogenic therapies. *Clin. Canc. Res.*, 24(15):3550–3559, 2018.

[83] A. Loaiza-Bonilla, C. E. Jensen, S. Shroff, E. Furth, P. A. Bonilla-Reyes, A. F. Deik, and J. Morrissette. Kdr mutation as a novel predictive biomarker of exceptional response to regorafenib in metastatic colorectal cancer. *Cureus*, 8(2), 2016.

[84] T. C. Knepper, M. L. Freeman, G. T. Gibney, H. L. McLeod, and J. S. Russell. Clinical response to pazopanib in a patient with kdr-mutated metastatic basal cell carcinoma. *Jama Dermatology*, 153(6):607–609, 2017.

[85] D. R. Kumar and R. Bose. Analysis of somatic mutations across the kinome reveals loss-of-function mutations in multiple cancer types. *Sci. Rep.*, 7 (1)(6418), 2017.

[86] D.R. Senger and G.E. Davis. Angiogenesis. *Cold Spring Harb Perspect Biol*, 3(8)(a005090), 2011.

[87] Brian P Eliceiri. Integrin and growth factor receptor crosstalk. *CIRC RES*, 89(12):1104–1110, 2001.

[88] R. O. Hynes. Integrins: Bidirectional, allosteric signaling machines. *CELL*, 110(6):673–687, 2002.

[89] D Valdembri and G Serini. Regulation of adhesion site dynamics by integrin traffic. *CURR OPIN CELL BIOL*, 24(5):582–91, 2012.

[90] David A. Calderwood. Integrin activation. *J CELL SCI*, 117(5):657–666, 2004.

[91] M. Klagsbrunl and M. A. Moses. Molecular angiogenesis. *Chem Biol.*, 6(8):R217–24, 1999.

[92] IF. Tannock. The relation between cell proliferation and the vascular system in a transplanted mouse mammary tumour. *Br J Cancer*, 22(2):258–73, 1968.

[93] J. Folkman. Tumor angiogenesis: therapeutic implications. *N Engl J Med*, 285(21):1182–6, 1971.

[94] A. Herrera, M. Herrera, N. Guerra-Perez, C. Galindo-Pumariño, M. J. Larriba, V. García-Barberán, B. Gil, S. Giménez-Moyano, R. Ferreiro-Monteagudo, P. Veguillas, Candia. A., R. Peña, J. Pinto, M.L. García-Bermejo, A. Muñoz, A.G. de Herreros, F. Bonilla, and C. Carrato, A. & Peña. Endothelial cell activation on 3d-matrices derived from pdgf-bb-stimulated fibroblasts is mediated by snail1. *Oncogenesis*, 7(76), 2018.

[95] D. H. Ausprunk and H. J. Berman. Spreading of vascular endothelial cells in culture: Spatial reorganization of cytoplasmic fibers and organelles. *Tissue and Cell*, 10(4):707–724, 1978.

[96] L. Lamalice, F. Le Boeuf, and J. Huot. Endothelial cell migration during angiogenesis. *Circ Res.*, 100(6):782–94, 2007.

[97] Cynthia A. Reinhart-King, Micah Dembo, and Daniel A. Hammer. The dynamics and mechanics of endothelial cell spreading. *BIOPHYS J*, 89(1):676–689, jul 2005.

[98] J. F. Joanny, K. Kruse, J. Prost, and S. Ramaswamy. The actin cortex as an active wetting layer. *EUR PHYS J E*, 36(5), 2013.

[99] K. Kruse, J. F. Joanny, F. Jülicher, J. Prost, and K. Sekimoto. Generic theory of active polar gels: A paradigm for cytoskeletal dynamics. *EUR PHYS J E*, 16(1):5–16, 2005.

[100] M. C. Marchetti, J. F. Joanny, S. Ramaswamy, T. B. Liverpool, J. Prost, Madan Rao, and R. Aditi Simha. Hydrodynamics of soft active matter. *Reviews of Modern Physics*, 85(3):1143–1189, 2013.

[101] J. Prost, F. Jülicher, and J. F. Joanny. Active gel physics. *Nature Physics*, 11(2):111–117, 2015.

[102] W. Helfrich. Elastic properties of lipid bilayers: theory and possible experiments. *Z. Naturforsch.*, 28:693–703, 1973.

[103] A. Agrawal and D. J. Steigmann. Boundary-value problems in the theory of lipid membranes. *CONTINUUM MECH THERM*, 21(1):57–82, 2009.

[104] D. Steigmann and A. Agrawal. Electromechanics of polarized lipid bilayers. *Mathematics and Mechanics of Complex Systems*, 4(1):31–54, 2016.

[105] A. Agrawal and D. J. Steigmann. A model for surface diffusion of trans-membrane proteins on lipid bilayers. *Z ANGEW MATH MECH*, 62(3):549, 2011.

[106] L.B. Freund and Y. Lin. The role of binder mobility in spontaneous adhesive contact and implication for cell adhesion. *J MECH PHYS SOLIDS*, 52:2455–2472, 2004.

[107] G.I. Bell. Models for the specific adhesion of cells to cells. *SCIENCE*, 200(4342):618–627, 1978.

[108] G.I. Bell, M Dembo, and P. Bongrand. Cell adhesion. competition between nonspecific repulsion and specific bonding. *BIOPHYS J*, 45(6):1051–1064, 1984.

[109] B. Goldstein, C. Wofsy, and G. Bell. Interactions of low density lipoprotein receptors with coated pits on human fibroblasts: Estimate of the forward rate constant and comparison with the diffusion limit. *Proc Natl Acad Sci USA*, 78(9):5695–5698, 1981.

[110] M. Dembo and B. Goldstein. Theory of equilibrium bindign of symmetric bivalent haptens to cell surface antibody: Application to histamine release from basophils. *J IMMUNOL*, 121(1):345–353, 1978.

[111] R.C. Lee, T.R. Gowrishankar, R.M. Basch, K.K. Patel, and D.E. Golan. Cell shape-dependent rectification of surface receptor transport in a sinusoidal electric field. *BIOPHYS J*, 64:44–57, 1993.

[112] A. Boulbitch, Z. Guttenberg, and E. Sackmann. Kinetics of membrane adhesion mediated by ligand-receptor interaction studied with a biomimetic system. *BIOPHYS J*, 81(5):2743–2751, 2001.

[113] V. Shenoy and L. Freund. Growth and shape stability of a biological membrane adhesion complex in the diffusion-mediated regime. *PNAS*, 102(9):3213–3218, 2005.

[114] P. Liu, Y. Zhang, Q. Cheng, and C. Lu. Simulation of the spreading of a vesicle on a substrate surface mediated by receptor-ligand binding. *J MECH PHYS SOLIDS*, 55(6):1166–1181, 2007.

[115] Q. Cheng, P. Liu, H. Gao, and Y. Zhang. A computational modeling for micropipette-manipulated cell detachment from a substrate mediated by receptor-ligand binding. *J MECH PHYS SOLIDS*, 57:205–220, 2009.

[116] A.F. Golestaneh and B. Nadler. Modeling of cell adhesion and deformation mediated by receptor-ligand interactions. *BIOMECH MODEL MECHANOBIOL*, 15:371–387, 2016.

[117] R. Deshpande, Y.T Cheng, M.W. Verbrugge, and A. Timmons. Diffusion induced stresses and strain energy in a phase-transforming spherical electrode particle. *J ELECTROCHEM SOC*, 158(6):A718–A724, 2011.

[118] V Deshpande, M Mrksich, R M McMeeking, and A G Evans. A bio-mechanical model for coupling cell contractility with focal adhesion formation. *J MECH PHYS SOLIDS*, 56:1484–1510, 2008.

[119] Vikram S. Deshpande, Robert M. McMeeking, and Evans. A bio-chemo-mechanical model for cell contractility. *PNAS*, 103(45):17064–17065, 2006.

[120] Vikram S. Deshpande, Robert M. McMeeking, and Anthony G. Evans. A model for the contractility of the cytoskeleton including the effects of stress-fibre formation and dissociation. *Proceedings of the Royal Society A: Mathematical, Physical and Engineering Sciences*, 463(2079):787–815, 2007.

[121] R.M. McMeeking and V.S. Deshpande. A bio-chemo-mechanical model for cell contractility, adhesion, signaling, and stress-fiber remodeling. In G.A. Holzapfel and R.W. Ogden, editors, *Biomechanics: Trends in Modeling and Simulation.*, volume 20 of *Studies in Mechanobiology, Tissue Engineering and Biomaterials*, pages 53–81. Springer, 2017.

[122] W. Ronan, V.S. Deshpande, R.M. McMeeking, and J.P. McGarry. Numerical investigation of the active role of the actin cytoskeleton in the compression resistance of cells. *J MECH BEHAV BIOMED*, 14:143–157, 2012.

[123] W. Ronan, V.S. Deshpande, R.M. McMeeking, and J.P. McGarry. Cellular contractility and substrate elasticity: a numerical investigation of the actin cytoskeleton and cell adhesion. *BIOMECH MODEL MECHANOBIOL*, 13(417-435), 2014.

[124] C. Obbink-Huizer, C.W.J. Oomens, S. Loerakker, J. Foolen, C.V.C. Bouten, and Baaijens F.P.T. Computational model predicts cell orientation in response to a range of mechanical stimuli. *Biomech Model Mechanobiol*, 13(1):227–236, 2014.

[125] F.J. Vernerey and M. Farsad. A constrained mixture approach to mechano-sensing and force generation in contractile cells. *J MECH BEHAV BIOMED*, 4(8):1683–1699, 2011.

[126] A. Pathak, R.M. McMeeking, A.G. Evans, and V.S. Deshpande. An analysis of the cooperative mechano-sensitive feedback between intracellular signaling, focal adhesion development, and stress fiber contractility. *J APPL MECH*, 78, 2011.

[127] A. Vigliotti, R.M. McMeeking, and V.S. Deshpande. Simulation of the cytoskeletal response of cells on grooved or patterned substrates. *J R SOC INTERFACE*, 12(20141320), 2015.

[128] E. McEvoy, V.S. Deshpande, and P. McGarry. Free energy analysis of cell spreading. *J MECH BEHAV BIOMED*, 74:283–295, 2017.

[129] V. Deshpande, R.M. McMeeking, and A.G. Evans. A model for the contractility of the cytoskeleton including the effects of stress-fiber formation and dissociation. *P R SOC A*, 463:787–815, 2007.

[130] H. Gao, W. Shi, and L. Freund. Mechanics of receptor-mediated endocytosis. *PNAS*, 102(27):9469–9474, 2005.

[131] P. Decuzzi and M. Ferrari. The receptor-mediated endocytosis of nonspherical particles. *BIOPHYS J*, 94(10):3790–3797, 2008.

[132] H. Gao. Probing mechanical principles of cell–nanomaterial interactions. *J MECH PHYS SOLIDS*, 62:312–339, 2014.

[133] T. Wiegold, S. Klinge, R.P. Gilbert, and G.A. Holzapfel. Computational modeling of adhesive contact between a virus and a cell during receptor driven endocytosis. *PROC APPL MATH MECH*, 19(e201900161), 2019.

[134] H. Shin, J.H. Haga, T. Kosawada, K. Kimura, Y.S. Li, S. Chien, and G.W. Schmid-Schönbein. Fine control of endothelial vegfr-2 activation: caveolae as fluid shear stress shelters for membrane receptors. *BIOMECH MODEL MECHAN*, 18:5–16, 2019.

[135] A. Liberman, M. Mussel, G. Kario, D. Sprinzak, and U. Nevo. Modelling cell surface dynamics and cell–cell interactions using cell studio: a three-dimensional visualization tool based on gaming technology. *J R SOC INTERFACE*, 16(20190264), 2019.

[136] A.R. Carotenuto, L. Lunghi, V. Piccolo, M. Babaei, K. Dayal, N. Pugno, M. Zingales, L. Deseri, and M. Fraldi. Mechanobiology predicts raft formations triggered by ligand-receptor activity across the cell membrane. *J MECH PHYS SOLIDS*, 141, 2020.

[137] F. Bubba, T. Lorenzi, and F.R. Macfarlane. From a discrete model of chemotaxis with volume-filling to a generalized patlak–keller–segel model. *PROC R SOC A*, 476(20190871), 2020.

[138] V. Damioli, A. Salvadori, G.P. Beretta, C. Ravelli, and S. Mitola. Multi-physics interactions drive VEGFR2 relocation on endothelial cells. *SCI REP-UK*, 7(1):16700, 2017.

[139] A. Salvadori, V. Damioli, C. Ravelli, and S. Mitola. Modeling and simulation of VEGF receptors recruitment in angiogenesis. *MATH PROBL ENG*, page 4705472, 2018.

[140] M Serpelloni, M Arricca, V Damioli, C Ravelli, E Grillo, S Mitola, and A Salvadori. A model of integrin and vegf receptors recruitment on endothelial cells. In BE Abali and I Giorgio, editors, *Developments and Novel Approaches in Biomechanics and Metamaterials*, pages 163–198. Springer International Publishing, Cham, 2020.

[141] A. Salvadori, R.M. McMeeking, D. Grazioli, and M. Magri. A coupled model of transport-reaction-mechanics with trapping. Part I - small strain analysis. *J MECH PHYS SOLIDS*, 114:1–30, 2018.

[142] M.E. Gurtin, E. Fried, and L. Anand. *The Mechanics and Thermodynamics of Continua*. Cambridge University Press, 2010.

[143] Elias P Gyftopoulos and Gian Paolo Beretta. *THERMODYNAMICS: Foundation and Applications*. Mineola, N.Y. : Dover Publications, INC., 2005.

[144] S.R. De Groot and P. Mazur. *Non-Equilibrium Thermodynamics*. Dover, 1984.

[145] Ilya Prigogine and Dilip Kondepudi. *Termodinamica: dalle macchine termiche alle strutture dissipative*. Bollati Boringhieri, 2002.

[146] I. Prigogine. Time, structure and fluctuations. *Nobel Lecture*, (37820190168):799–816, 8 December1977.

[147] I. Prigogine. Time, structure and fluctuations. *Phys. Rev*, 37(37820190168):405–426, 15 February 1931.

[148] F. Benfanati and G. P. Beretta. The fourth law of thermodynamics: steepest entropy ascent. *J. Non-Equilib. Thermodyn.*, 43(2):101–110, 2018.

[149] L. Anand. A Cahn-Hilliard-type theory for species diffusion coupled with large elastic-plastic deformations. *J MECH PHYS SOLIDS*, 60(12):1983–2002, 2012.

[150] S. Shell. *Thermodynamics and statistical mechanics: an integrated approach*. Cambridge University Press, 2015.

[151] R. DeHoff. *Thermodynamic in material science*. CRC Press - Taylor and Francis, 2006.

[152] A. Quarteroni and A. Valli. *Numerical approximation of partial differential equations*. Springer Verlag, Berlin, 1997.

[153] O. Rossier, V. Octeau, J.-B. Sibarita, C. Leduc, B. Tessier, D. Nair, V. Gatterdam, O. Destaing, C. Albigès-Rizo, R. Tampé, L. Cognet, D. Choquet, B. Lounis, and G. Giannone. Integrins β_1 and β_3 exhibit distinct dynamic nanoscale organizations inside focal adhesions. *Nature Cell Biology*, 14:1057–1067, 2012.

[154] R.R. Hantgan, M.C. Stahle, and S.T. Lord. Dynamic Regulation of Fibrinogen: Integrin $allb\beta_3$ Binding. *Biochemistry*, 49, 43:9217–9225, 2010.

[155] E. Makogonenko, G. Tsurupa, K. Ingham, and L. Medved. Interaction of Fibrin(ogen) with Fibronectin: Further Characterization and Localization of the Fibronectin-Binding Site. *Biochemistry*, 41:7907–7913, 2002.

[156] S. Benedetto, R. Pulito, C. Geninatti, G. Tarone, S. Aime, L. Silengo, and J. Hamn. Quantification of the expression level of integrin receptor $\alpha_v\beta_3$ in cell lines and mr imaging with antibody-coated iron oxide particles. *Magnetic Resonance in Medicine*, 56(4):711–716, 2006.

[157] R. Soldi, S. Mitola, M. Strasly, P. Defilippi, G. Tarone, and F. Bussolino. Role of $\alpha_v\beta_3$ integrin in the activation of vascular endothelial growth factor receptor-2. *The EMBO journal*, 18(4):882–892, February 1999.

[158] D. Maiolo, S. Mitola, D. Leali, G. Oliviero, C. Ravelli, A. Bugatti, L.E. Depero, M. Presta, and P. Bergese. Role of Nanomechanics in Canonical and Noncanonical Pro-angiogenic Ligand/VEGF Receptor-2 Activation. *J AM CHEM SOC*, page 120823144733008, August 2012.

[159] J. Lippincott-Schwartz, E.L. Snapp, and R.D. Phair. The development and enhancement of frap as a key tool for investigating protein dynamics. *Biophysical Journal*, 115(7):1146–1155, 2018.

[160] M. Kang, C.A. Day, A.K. Kenworthy, and E. DiBenedetto. Simplified equation to extract diffusion coefficients from confocal frap data. *Traffic*, 13(12):1589–1600, 2012.

[161] R.V. Stahelin. Surface plasmon resonance: a useful technique for cell biologists to characterize biomolecular interactions. *Mol Biol Cell.*, 24(7):883–886, 2013.

[162] J. Homola. Present and future of surface plasmon resonance biosensors. *Analytical and Bioanalytical Chemistry volume*, 137:528–539, 2003.

[163] K Bentley and S. Chakravartula. The temporal basis of angiogenesis. *Phil. Trans. R. Soc. B*, 372: 20150522, 2017.

[164] Brunhilde Felding-Habermann. Integrin adhesion receptors in tumor metastasis. *CLIN EXP METASTAS*, 20(3):203–213, 2003.

[165] W. Stillwell. *An Introduction to Biological Membranes: Composition, Structure and Function*, chapter 17 - Moving Components Through the Cell: Membrane Trafficking, pages 369–379. Elsevier B.V., 2016.

[166] G. Huang, F. Xu, G. Genin, and T. Lu. Mechanical microenvironments of living cells: a critical frontier in mechanobiology. *ACTA MECH SINICA*, 35 (2):265–269, 2019.

[167] A. You, L. Zhou, W. Li, C. Huang, and Y. Du. Mechanical microenvironment as a key cellular regulator in the liver. *ACTA MECH SINICA*, 35 (2):289–298, 2019.

[168] S. Paolucci. *Continuum Mechanics and Thermodynamics of Matter*. Cambridge University Press, 2016.

[169] M. Mikucki and Y.C. Zhou. Curvature-driven molecular flow on membrane surface. *SIAM J APPL MATH*, 77(5):1587–1605, 2017.

[170] M. Ubbink. The courtship of proteins: Understanding the encounter complex. *FEBS Letters*, 583:1060–1066, 2009.

[171] T. Selzer and G. Schreiber. New insights into the mechanism of protein-protein association. *PROTEINS*, 45:190–198, 2001.

[172] E. Evans. New membrane concept applied to the analysis of fluid shear and micro-pipette deformed red blood cells. *BIOPHYS J*, 13(9):941–954, 1973.

[173] P Sens and MS Turner. Budded membrane microdomains as tension regulators. *PHYS REV E*, 73:031918, Mar 2006.

[174] P. Bongrand. Ligand-receptor interactions. *REP PROG PHYS*, 62:921–968, 1999.

[175] Bruce Alberts. *Molecular biology of the cell*. New York : Garland Science, 4th ed. edition, 2002.

[176] A Moure and H. Gomez. Three-dimensional simulation of obstacle-mediated chemotaxis. *BIOMECH MODEL MECHANOBIOL*, 17(5):1243–1268, 2018.

[177] F.J. Vernerey and M. Farsad. A mathematical model of the coupled mechanisms of cell adhesion, contraction and spreading. *J MATH BIOL*, 68:989–1022, 2014.

[178] Ernest Latorre, Sohan Kale, Laura Casares, Manuel Gómez-González, Marina Uroz, Léo Valon, Roshna V. Nair, Elena Garreta, Nuria Montserrat, Aránzazu del Campo, Benoit Ladoux, Marino Arroyo, and Xavier Trepat. Active superelasticity in three-dimensional epithelia of controlled shape. *NATURE*, 563(7730):203–208, 2018.

[179] M. Rahimi and M. Arroyo. Shape dynamics, lipid hydrodynamics, and the complex viscoelasticity of bilayer membranes. *PHYS REV E*, 86:011932, Jul 2012.

[180] A. Vigliotti, W. Ronan, F.P.T. Baaijens, and V.S. Deshpande. A thermodynamically motivated model for stress-fiber reorganization. *BIOMECH MODEL MECHAN*, 15:761–789, 2016.

[181] R Allena. Cell migration with multiple pseudopodia: Temporal and spatial sensing models. *B MATH BIOL*, 75(2):288–316, 2013.

[182] J.N. Israelachvili. *Intermolecular and Surface Forces*. Academic Press, 2011.

[183] R. Milo and R. Phillips. *Cell Biology By The Numbers*. Garland Science, Taylor and Francis Group, 2016.

[184] B.J. Dubin-Thaler, G. Giannone, H-G. Döbereiner, and Sheetz M.P. Nanometer analysis of cell spreading on matrix-coated surfaces reveals two distinct cell states and steps. *BIOPHYS J*, 86:1794–1806, 2004.

[185] T. Sohail, T. Tang, and B. Nadler. Adhesive contact of a fluid-filled membrane driven by electrostatic forces. *INT J SOLIDS STRUCT*, 50:2678–2690, 2013.

[186] E. Schrödinger. *What is Life – the Physical Aspect of the Living Cell.* . Cambridge University Press, 1944.

[187] G. Holzapfel. *Nonlinear Solid Mechanics: A Continuum Approach for Engineering*. John Wiley & Sons, Ltd., 2001.

[188] J.C. Simo. A framework for finite strain elastoplasticity based on maximum plastic dissipation and the multiplicative decomposition: Part I. Continuum formulation. *COMPUT METHOD APPL M*, 66(2):199 – 219, 1988.

[189] J.C. Simo. A framework for finite strain elastoplasticity based on maximum plastic dissipation and the multiplicative decomposition. Part II: Computational aspects. *COMPUT METHOD APPL M*, 68(1):1 – 31, 1988.

[190] G. Giantesio, A. Musesti, and D. Riccobelli. A comparison between active strain and active stress in transversely isotropic hyperelastic materials. *J Elast*, 137:63–82, 2019.

[191] S. Hervas-Raluy, J. M. Garcia-Aznar, and M. J. Gomez-Benito. Modelling actin polymerization: the effect on confined cell migration. *BIOMECH MODEL MECHANOBIOL*, 18(4):1177–1187, 2019.

[192] J.C. Simo and T.J.R. Hughes. *Computational inelasticity*. Springer-Verlag, New York, 1998.

[193] Qi Wen and Paul A. Janmey. Polymer physics of the cytoskeleton. *CURR OPIN SOLID ST M*, 15(5):177 – 182, 2011.

[194] Elias H. Barriga and Roberto Mayor. Adjustable viscoelasticity allows for efficient collective cell migration. *SEMIN CELL DEV BIOL*, 93:55 – 68, 2019.

[195] R Brighenti and F.J. Vernerey. A simple statistical approach to model the time-dependent response of polymers with reversible cross-links. *COMPOS PART B-ENG*, 115:257 – 265, 2017.

[196] F.J. Vernerey, R. Long, and R. Brighenti. A statistically-based continuum theory for polymers with transient networks. *J MECH PHYS SOLIDS*, 107:1 – 20, 2017.

[197] F.J. Vernerey. Transient response of nonlinear polymer networks: A kinetic theory. *J MECH PHYS SOLIDS*, 115:230 – 247, 2018.

[198] O. Lieleg, K.M. Schmoller, M.M.A.E. Claessens, and A.R. Bausch. Cytoskeletal polymer networks: Viscoelastic properties are determined by the microscopic interaction potential of cross-links. *BIOPHYS J*, 96(11):4725 – 4732, 2009.

[199] Michael Murrell, Patrick W. Oakes, Martin Lenz, and Margaret L. Gardel. Forcing cells into shape: the mechanics of actomyosin contractility. *NAT REV MOL CELL BIO*, 16(8):486–498, 2015.

[200] EJ. Campbell and P. Bagchi. A computational model of amoeboid cell swimming. *PHYSICS OF FLUIDS*, 29(10):101902, 2017.

[201] EJ. Campbell and P Bagchi. A computational study of amoeboid motility in 3d: the role of extracellular matrix geometry, cell deformability, and cell–matrix adhesion. *BIOMECH MODEL MECHANOBIOL*, 2020.

[202] RM Cooper, NS Wingreen, and EC Cox. An excitable cortex and memory model successfully predicts new pseudopod dynamics. *PLoS ONE*, 7(3):e33528, 2012.

[203] Zahra Eidi. Discrete modeling of amoeboid locomotion and chemotaxis in dictyostelium discoideum by tracking pseudopodium growth direction. *SCI REP-UK*, 7(1):12675, Oct 2017.

[204] C Bächer and S Gekle. Computational modeling of active deformable membranes embedded in three-dimensional flows. *PHYS REV E*, 99:062418, Jun 2019.

[205] A Moure and H Gomez. Phase-field modeling of individual and collective cell migration. *ARCH COMPUT METHOD E*, 2019.

[206] C Giverso and L Preziosi. Mechanical perspective on chemotaxis. *PHYS REV E*, 98:062402, 2018.

[207] Sangkyun Cho, Jerome Irianto, and Dennis E. Discher. Mechanosensing by the nucleus: From pathways to scaling relationships. *J CELL BIOL*, 216(2):305–315, 01 2017.

[208] Katarina Wolf, Mariska te Lindert, Marina Krause, Stephanie Alexander, Joost te Riet, Amanda L. Willis, Robert M. Hoffman, Carl G. Figdor, Stephen J. Weiss, and Peter Friedl. Physical limits of cell migration: Control by ECM space and nuclear deformation and tuning by proteolysis and traction force. *J CELL BIOL*, 201(7):1069–1084, 06 2013.

[209] Hawa-Racine Thiam, Pablo Vargas, Nicolas Carpi, Carolina Lage Crespo, Matthew Raab, Emmanuel Terriac, Megan C. King, Jordan Jacobelli, Arthur S. Alberts, Theresia Stradal, Ana-Maria Lennon-Dumenil, and Matthieu Piel. Perinuclear arp2/3-driven actin polymerization enables nuclear deformation to facilitate cell migration through complex environments. *NAT COMMUN*, 7(1):10997, 2016.

[210] Jonathan Fouchard, Démosthène Mitrossilis, and Atef Asnacios. Acto-myosin based response to stiffness and rigidity sensing. *CELL ADHES MIGR*, 5(1):16–19, 2011.

[211] Alba Diz-Muñoz, Daniel A. Fletcher, and Orion D. Weiner. Use the force: membrane tension as an organizer of cell shape and motility. *TRENDS CELL BIOL*, 23(2):47 – 53, 2013.

[212] A.V. Hill. The heat of shortening and the dynamic constants of muscle. *PROC R SOC B*, 126(136-195), 1938.

[213] A. A. Khalili and M. R. Ahmad. A review of cell adhesion studies for biomedical and biological applications. *Int J Mol Sci.*, 16(8):18149–18184, 2015.

[214] D. Chappell, M. Jacob, O. Paul, M. Rehm, U. Welsch, M. Stoeckelhuber, P. Conzen, and B. F. Becker. The glycocalyx of the human umbilical vein endothelial cell. *Circulation Research*, 104(11):1313–1317, 2009.

[215] P. Wriggers. *Computational Contact Mechanics*. Springer, 2006.

[216] S. Hüeber and B.I. Wohlmuth. A primal–dual active set strategy for non-linear multibody contact problems. *COMPUT METHOD APPL M*, 194(27):3147 – 3166, 2005.

[217] J.G. McGarry and P. J. Prendergast. A three-dimensional finite element model of an adherent eukaryotic cell. *Eur Cell Mater*, 7(27-33), 2004.

[218] S. Heyden and M. Ortiz. Investigation of the influence of viscoelasticity on oncotripsy. *Computer Methods in Applied Mechanics and Engineering*, 314:314–322, 2017.

[219] G. Jain, A. J. Ford, and P. Rajagopalan. Opposing rigidity-protein gradients reverse fibroblast durotaxis. *ACS Biomater Sci Eng*, 1(8):621–631, 2015.

[220] M Serpelloni, M Arricca, C Bonanno, and A Salvadori. A framework for modeling cells spreading, motility and the relocation of proteins on advecting lipid membranes. Accepted for publication on ACTA MECH SINICA, 2021.

[221] Erwin Schrödinger. *Che cos'è la vita? La cellula vivente dal punto di vista fisico*. Adelphi, 1995.

[222] A. B. C. Buskermolen, H. Suresh, S. S. Shishvan, A. Vigliotti, A. DeSimone, N. A. Kurniawan, C. V. C. Bouten, and V. S. Deshpande. Entropic forces drive cellular contact guidance. *Biophysical Journal*, 116(10):1994–2008, 2019.

[223] Jonathan Stricker, Tobias Falzone and Margaret Gardel. Mechanics of the F-actin Cytoskeleton. *J Biomech.*, 43(1):1–12, 2010.